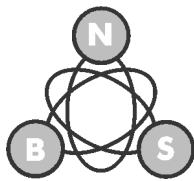


XLIX INTERNATIONAL SCIENTIFIC CONFERENCE ON INFORMATION, COMMUNICATION AND
ENERGY SYSTEMS AND TECHNOLOGIES



iCEEST 2014

Proceedings of Papers

Volume 2

Serbia, Niš, June 25 - 27, 2014

ICEST 2014 - XLIX INTERNATIONAL SCIENTIFIC CONFERENCE ON INFORMATION, COMMUNICATION AND ENERGY SYSTEMS AND TECHNOLOGIES, Serbia, Niš, June 25 - 27, 2014

Proceedings of Papers - Volume 2 of 2 volumes

Editor: Prof. Dr. Bratislav D. Milovanović

Technical Editor: Dr. Zoran Ž. Stanković

Technical Co-Editor: Aleksandra Đorić

Technical Support: Vladica Đorđević, Miloš Kostić, Ana Aleksić

Published by: Faculty of Electronic Engineering, University of Niš, Serbia

Printed by: NAIS PRINT Design, Niš, Serbia

Number of copies printed: 50

Printing of this edition has been financially supported by
Serbian Ministry of Education, Science and Technological Development

ISBN: 978-86-6125-109-2

CIP - Каталогизacija u publikaciji
Narodna biblioteka Srbije, Beograd

621.39(082)
537.8(082)
681.5(082)
004(082)
621.3(082)
37.02(082)

INTERNATIONAL Scientific Conference on Information, Communication and Energy Systems and Technologies (49th ; 2014 ; Niš)

Proceedings of Papers. Vol. 2 / XLIX International Scientific Conference on Information, Communication and Energy Systems and Technologies - ICEST 2014, Serbia, Niš, June 25-27, 2014 ; [organisers University of Niš, Faculty of Electronic Engineering ... [et al.] ; editor Bratislav D. Milovanović]. - Niš : Faculty of Electronic Engineering, 2014 (Niš : Nais Print Design). - X, str. 247-492 : ilustr. ; 30 cm

Tekst štampan dvostubačno. - Tiraž 50. - Bibliografija uz svaki rad. - Registar.

ISBN 978-86-6125-109-2

1. Faculty of Electronic Engineering (Niš)
a) Телекомуникације - Зборници b)
Микроталасна техника - Зборници c) Системи
аутоматског управљања - Зборници d)
Рачунарство - Зборници e) Електротехника -
Зборници f) Образовна технологија -
Зборници

COBISS.SR-ID 210191116

TABLE OF CONTENTS

VOLUME 1

ORAL SESSIONS

TELECOMMUNICATIONS SYSTEMS AND TECHNOLOGY

TST.1	Capacity Bounds of Lozenge Tiling Constraints	3
	B. Vasić, A. Krishnan <i>University of Arizona, USA</i>	
TST.2	New Iterative Method for Optimization of Quasilogarithmic Quantizer for Laplacian Source	7
	Z. Perić, A. Jovanović, M. Tančić <i>University of Niš, Serbia</i>	
TST.3	Analysis of some Wavelength Assignment Techniques in WDM Optical Networks	11
	S. Miladić, G. Marković* <i>University of East Sarajevo, Bosnia and Herzegovina</i> <i>*University of Belgrade, Serbia</i>	
TST.4	Performance Analysis of RF/FSO System with Interference at the Relay	15
	A. Cvetković, M. Petković, J. Anastasov <i>University of Niš, Serbia</i>	
TST.5	Performance Analysis of SIM-FSO System over Gamma-Gamma Atmospheric Channel	19
	M. Petković, N. Zdravković, Č. Stefanović, G. Đorđević <i>University of Niš, Serbia</i>	
TST.6	Comparative Cost-Capacity Analysis of the Advanced Wirelesses Heterogeneous Broadband Networks	23
	V. Nikolikj, T. Janevski* <i>Vip operator, Macedonia</i> <i>*University "Ss. Cyril and Methodius", Macedonia</i>	
TST.7	Improving Performance of Multimedia Web Transfer over WAN Connections.....	27
	H. Valchanov, M. Angelov <i>Technical University of Varna, Bulgaria</i>	
TST.8	An Approach of QoS by Admission Control of VoIP over WLANs	31
	V. Aleksieva <i>Technical University of Varna, Bulgaria</i>	

INFORMATICS AND COMPUTER SCIENCE

ICS.1	An Exact Interactive Method for Solving Multiple Objective Integer Problems	37
	V. Guliashki, L. Kirilov <i>Institute of Information and Communication Technologies, Bulgaria</i>	
ICS.2	Resource Allocation for Maximum Performance and Minimum Cost for 3-tier SaaS Application in Azure	41
	S. Ristov, M. Gusev, B. Koteska, G. Velkoski* <i>University "Ss. Cyril and Methodius", Macedonia</i> <i>*Innovation LLC, Macedonia</i>	
ICS.3	Avatar Concepts in Self Healthcare Systems	45
	M. Gusev, S. Ristov, A. Guseva* <i>University "Ss. Cyril and Methodius", Macedonia</i> <i>*Innovation LLC, Macedonia</i>	

ICS.4	Lexico-Semantic Collaborative Learning Framework.....	49
	M. Jovanović, D. Todosijević <i>University of Niš, Serbia</i>	
ICS.5	Definition of Transposition Base Opening System With the Algorithm of Machine Learning	53
	V. Vučković <i>University of Niš, Serbia</i>	
ICS.6	Models of Inductive Reasoning	57
	M. Ilić, V. Stanković* <i>College of Agriculture and Food Technology, Prokuplje, Serbia</i> <i>*University of Niš, Serbia</i>	
ICS.7	Prediction of the Stock Market Trend using LS-SVM based on Technical Indicators	61
	I. Marković, J. Stanković, M. Stojanović*, M. Božić <i>University of Niš, Serbia</i> <i>*College of Applied Technical Sciences, Serbia</i>	

COMPUTER SYSTEMS AND INTERNET TECHNOLOGIES I

CIT I.1	Evaluation of Application Level Mechanism for Reliable Smart Objects Communications	67
	I. Atanasov, M. Ivanov, E. Pencheva <i>Technical University of Sofia, Bulgaria</i>	
CIT I.2	An Approach to Design Web Services for Remote Entity Management	71
	I. Atanasov, N. Krastanov, E. Pencheva <i>Technical University of Sofia, Bulgaria</i>	
CIT I.3	Web Services Deployment in Microsoft Azure Cloud Computing Platform	75
	E. Srbinovska, P. Mitrevski <i>University "St.Kliment Ohridski", Macedonia</i>	
CIT I.4	Multipurpose Cloud-based Distance Learning Laboratory: A Case Study.....	79
	A. Donevski, S. Ristov, M. Gusev <i>University "Ss. Cyril and Methodius", Macedonia</i>	
CIT I.5	Parallelization of Machine Learning Methods Using CUDA.....	83
	G. Velkoski, M. Simjanoska*, S. Ristov*, M. Gusev* <i>Innovation LLC, Macedonia</i> <i>*University "Ss. Cyril and Methodius", Macedonia</i>	
CIT I.6	Data Mining Methodology for Web Users' Demographic Data Prediction.....	87
	V. Gega, I. Jolevski* <i>University for Information Science and Technology, Macedonia</i> <i>*University "Ss. Cyril and Methodius", Macedonia</i>	
CIT I.7	Improved Deflection Routing Method for Bufferless Networks-on-Chip.....	91
	I. Stojanović, M. Jovanović, S. Đošić, G. Đorđević <i>University of Niš, Serbia</i>	

COMPUTER SYSTEMS AND INTERNET TECHNOLOGIES II

CIT II.1	Realization of Universal HW/SW Module for Integration of Medical Laboratory Devices into Medical Information System.....	97
	A. Milenković, D. Janković, M. Stojković, A. Veljanovski, P. Rajković <i>University of Niš, Serbia</i>	
CIT II.2	Processing of Big Spatio-Temporal Data using MapReduce.....	101
	D. Stojanović, N. Stojanović <i>University of Niš, Serbia</i>	
CIT II.3	Incremental Development of e-Learning Systems for Mobile Platforms	105
	M. Frtunić, L. Stoimenov, D. Rančić <i>University of Niš, Serbia</i>	

CIT II.4	An Approach for Producing Long Term Statistics based on Weather Radar Data.....	109
	V. Mihajlović, M. Kovačević, D. Rančić <i>University of Niš, Serbia</i>	
CIT II.5	Comparison of Different Wireless Sensor Network Node Technologies.....	113
	M. Srbinovska, C. Gavrovski, V. Dimcev, Z. Kokolanski <i>University "Ss. Cyril and Methodius", Macedonia</i>	
CIT II.6	Immediate Assessment based Semantic e-Learning Evaluation Approach.....	117
	D. Todosijević, M. Jovanović <i>University of Niš, Serbia</i>	
CIT II.7	One Solution for Building Reconfigurable Multi-Projection Systems using the Adobe AIR Platform	121
	M. Radmanović, D. Tatić, D. Gajić <i>University of Niš, Serbia</i>	

RADIO COMMUNICATIONS, MICROWAVE TECHNIQUE AND ANTENNAS

RMA.1	ANN based Inverse Electro-Mechanical Modeling of RF MEMS Capacitive Switches	127
	T. Ćirić, Z. Marinković, T. Kim*, L. Vietzorreck*, O. Pronić-Rančić, M. Milijić, V. Marković <i>University of Niš, Serbia</i> <i>*TU München, Germany</i>	
RMA.2	Broadband Microstrip Doherty Amplifier Design and Linearization	131
	A. Đorić, A. Atanasković*, N. Maleš-Ilić*, B. Milovanović*, K. Blau** <i>Innovation Centre of Advanced Technology, Serbia</i> <i>*University of Niš, Serbia</i> <i>**Ilmenau University of Technology, Germany</i>	
RMA.3	A New Procedure for Extraction of Noise Wave Parameters of Microwave FETs	135
	V. Đorđević, Z. Marinković*, V. Marković*, O. Pronić-Rančić* <i>Innovation Centre of Advanced Technology, Serbia</i> <i>*University of Niš, Serbia</i>	
RMA.4	TLM Method with Z-transforms - Efficient Tool for Dispersive Anisotropic Structures Modelling.....	139
	M. Kostić, N. Dončov, Z. Stanković <i>University of Niš, Serbia</i>	
RMA.5	Band Gap Evaluation for Single, Dual and Triple Band Electromagnetic Band Gap Structures with Applied Geometrical Modifications	143
	I. Iliev, M. Nedelchev, E. Markov <i>University of Sofia, Bulgaria</i>	
RMA.6	Calculation of an Input Impedance of a Coax-fed Microstrip Circular Antenna using the TLM.....	147
	J. Joković, T. Dimitrijević, N. Dončov, B. Milovanović <i>University of Niš, Serbia</i>	
RMA.7	Dielectric Substrate Thickness Impact on Frequency Properties of Monopole Sierpinski Gasket Antenna	151
	P. Petkov, B. Bonev, T. Dimova <i>Technical University of Sofia, Bulgaria</i>	
RMA.8	Design Considerations for Splash Plate Reflector Antenna	153
	P. Petkov <i>Technical University of Sofia, Bulgaria</i>	

SIGNAL PROCESSING

SP.1	Power Disturbances Simulation and Analysis in Wavelet Domain	157
	M. Kostov, B. Gegov, M. Atanasovski*, M. Petkovski*, C. Mitrovski <i>University "St.Kliment Ohridski", Macedonia</i> <i>*Faculty of Technical Sciences, Bitola, Macedonia</i>	
SP.2	Comparison of Novel Designed Class of CIC FIR Filter Functions with Classical CIC Filters	161
	B. Stošić, V. Pavlović, D. Milić <i>University of Niš, Serbia</i>	
SP.3	ECG Signal Acquisition and Filtering	165
	M. Veljković, I. Janjić, D. Milić, D. Milović <i>University of Niš, Serbia</i>	
SP.4	Image Deblurring Methods and Image Quality Evaluation	169
	V. Guliashki, D. Dimov <i>Institute of Information and Communication Technologies, Bulgaria</i>	
SP.5	Combining Features by Query-time Weights Determination for Image Retrieval.....	177
	N. Neshov <i>Technical University of Sofia, Bulgaria</i>	
SP.6	Method for Colorization of the Original Photographs of Nikola Tesla.....	181
	V. Vučković, S. Spasić <i>University of Niš, Serbia</i>	
SP.7	The Effect of the Contrast Enhancement Processes on the Structural Entropy of Colonoscopic Images	185
	G. Csizmadia, S. Nagy <i>Szechenyi Istvan University, Hungary</i>	

WIRELESS COMMUNICATIONS

WC.1	Receiver Induced Intermodulation Interference in GSM-900	191
	P. Petkov, K. Angelov, I. Iliev, B. Bonev, V. Poulkov <i>Technical University of Sofia, Bulgaria</i>	
WC.2	Parametrical Analysis of DVB-T channels	195
	L. Jordanova, G. Karpov, D. Dobrev <i>Technical University of Sofia, Bulgaria</i>	
WC.3	Algorithms for APSK Constellation Optimization	199
	L. Jordanova, L. Laskov, D. Dobrev <i>Technical University of Sofia, Bulgaria</i>	
WC.4	Outage Performance of Dual-Hop AF Relaying System in Weibull-gamma Fading Environment.....	203
	J. Anastasov, A. Cvetković, D. Milović, D. Milić <i>University of Niš, Serbia</i>	
WC.5	Dynamic Characteristics of Selection Combining Receiver with Different Decision Algorithms	207
	D. Drača, A. Panajotović, N. Sekulović* <i>University of Niš, Serbia</i> <i>*College of Applied Technical Sciences, Serbia</i>	
WC.6	Comparative Performance Studies of Laboratory WEP IEEE 802.11g PTP Links	211
	J. Carvalho, C. Pacheco, H. Veiga, A. Reis <i>University of Beira Interior, Portugal</i>	
WC.7	Analysis of the SC Macrodiversity Reception in the Presence of Gamma Shadowed Nakagami-m Fading	215
	N. Simić, M. Milovanović, D. Milović <i>University of Niš, Serbia</i>	

ELECTRONIC COMPONENTS, SYSTEMS AND TECHNOLOGIES

EL.1	Start-Stop Ring Oscillators for GALS Designs.....	221
	G. Jovanović, M. Stojčev <i>University of Niš, Serbia</i>	
EL.2	FPGA Implementation of Digital PLL-based Frequency Synthesizer with Programmable Frequency Dividers	225
	M. Kovacheva, E. Stoumenov, I. Pandiev <i>Technical University of Sofia, Bulgaria</i>	
EL.3	Design and Realization of a Flexible Mains Switching Power Supply	229
	Z. Živanović, V. Smiljaković <i>IMTEL Komunikacije AD, Serbia</i>	
EL.4	Design and Realization of a Low Noise Power Converter.....	233
	Z. Živanović, V. Smiljaković <i>IMTEL Komunikacije AD, Serbia</i>	
EL.5	Verilog - A Noise Macromodel of Current Feedback Operational Amplifier with Improved Speed and Accuracy	237
	G. Valkov <i>Technical University of Sofia, Bulgaria</i>	
EL.6	Subtraction Procedure for ECG Drift Removing: High Level Synthesis with Compaan.....	241
	T. Shoshkov <i>Technical University of Sofia, Bulgaria</i>	

VOLUME 2

POSTER SESSIONS

COMPUTER SCIENCE AND INTERNET

CSI.1	Using IT Management Processes for Achieving Better Efficiency in the IT Service	247
	Y. Mitev, L. Kirilov <i>Institute of Information and Communication Technologies, Bulgaria</i>	
CSI.2	Technology Transfer Office “ICT for Energy Efficiency”: A Factor for Open Innovations	251
	R. Andreev, J. Doshev, I. Stoyanov <i>Institute of Information and Communication Technologies, Bulgaria</i>	
CSI.3	Usability Model for Evaluating the usability of Web-based GIS Applications.....	255
	N. Đorđević, D. Rančić, R. Simić, <i>University of Niš, Serbia</i>	
CSI.4	Development of Software Program for Direct Insertion into MySQL Database from Communication Interface	259
	G. Goranov, R. Hristova* <i>Technical University of Gabrovo, Bulgaria</i> <i>University of Sofia “St. Kliment Ohridski”, Bulgaria</i>	
CSI.5	Telemetry System for WRC Sport Cars. Mobile Part.	263
	H. Nenov, G. Hristova, P. Georgiev <i>Technical University of Varna, Bulgaria</i>	

CONTROL SYSTEMS

CS.1	Comparison Analysis of the Heading Accuracy of GPS, e-Compass and Gyroscope	267
	R. Miletičev, R. Kenov, I. Simeonov, E. Iontchev*	
	<i>Technical University of Sofia, Bulgaria</i>	
	<i>*Higher School of Transport "T. Kableshkov", Bulgaria</i>	
CS.2	Dynamic Compensation of the Gyro bias by e-Compass	271
	R. Miletičev, R. Kenov, I. Simeonov, E. Iontchev*	
	<i>Technical University of Sofia, Bulgaria</i>	
	<i>*Higher School of Transport "T. Kableshkov", Bulgaria</i>	
CS.3	Study on Control System of Permanent Magnet Linear Synchronous Motor	274
	B. Markov, V. Panov*	
	<i>University of Food Technologies, Bulgaria</i>	
	<i>Technical University of Sofia, Bulgaria</i>	
CS.4	Modular Development of Linear Induction Motor Control in Simulink Enviroment	278
	B. Markov	
	<i>University of Food Technologies, Bulgaria</i>	
CS.5	Evaluation of the Influence of the Human Factor on the Reliability of the Information and Control Systems in the Electric Power Industry	282
	Z. Hubenova, V. Gergov*	
	<i>Space Research and Technology Instit., Bulgaria</i>	
	<i>*Univ. of Transport "Todor Kableshkov", Bulgaria</i>	
CS.6	Generalized Forces of the Robotic System with Fractional Order Thermoviscoelastic Element	286
	M. Cajić, M. Lazarević*	
	<i>Mathematical Institute of the Serbian Academy of Sciences and Arts, Serbia</i>	
	<i>*University of Belgrade, Serbia</i>	
CS.7	Models of Objects of Control in the System for Monitoring and Dispatching on Metropolitan-Sofia	288
	E. Dimitrova	
	<i>Univ. of Transport "Todor Kableshkov", Bulgaria</i>	
CS.8	Design a Simple Hardware in the Loop Test-bed Platform for Educational Purposes	292
	M. Petkovski, A. Jurukovski*	
	<i>Faculty of Technical Sciences Bitola, Macedonia</i>	
	<i>*Mining and Energy Combine, Macedonia</i>	

ENGINEERING EDUCATION

EE.1	A Case Study Approach in Microcontroller Education	299
	V. Rankovska	
	<i>Technical University of Gabrovo, Bulgaria</i>	
EE.2	E-learning Module for Computer-aided Design in Moodle Platform	303
	G. Marinova, N. Stoyanov	
	<i>Technical University of Sofia, Bulgaria</i>	
EE.3	Various Approaches to Teach and Learn the Computer Architecture and Organization Cours	307
	G. Armenski, S. Ristov, M. Gusev, M. Kostoska	
	<i>University "Ss. Cyril and Methodius", Macedonia</i>	
EE.4	A Simple Hydraulic System as a Laboratory Equipment for Demonstrating On-Off Control	311
	M. Ristović, S. Labura, M. Naumović*	
	<i>University of East Sarajevo, Bosnia and Herzegovina</i>	
	<i>*University of Niš, Serbia</i>	

EE.5	Laboratory Equipment for Hydrogen Energy Education	315
	S. Letskovska, K. Seymenliyski, P. Rahnev*	
	<i>Burgas free University, Bulgaria</i>	
	<i>*As. Zlatarov University, Bulgaria</i>	

RADIO COMMUNICATIONS, TELECOMMUNICATIONS TECHNOLOGY AND ELECTROMAGNETICS

RTE.1	Complexity of the McEliece Cryptosystem based on GDBF Decoder for QC-LDPC Codes	321
	O. Al Rasheed, D. Drajić, P. Ivaniš, G. Đorđević*	
	<i>College of Applied Technical Sciences, Serbia</i>	
	<i>*University of Niš, Serbia</i>	
RTE.2	Probability of Collision in a Cooperative Relay Diversity Scheme in Nakagami Fading Channel	325
	N. Milošević, B. Dimitrijević, Z. Nikolić	
	<i>University of Niš, Serbia</i>	
RTE.3	Level Crossing Rate of Nakagami-m Signal Envelope Subjected to Gamma Shadowing	329
	D. Đošić, Č. Stefanović, D. Milić, D. Radenković, P. Spalević	
	<i>University of Niš, Serbia</i>	
RTE.4	Performance Analysis of MAMD Algorithms with QoS Parameters in Heterogeneous Network	333
	R. Dobrev	
	<i>Technical University of Sofia, Bulgaria</i>	
RTE.5	Simulation Estimation of Network and Quality Characteristics in Video Transmission over LTE Network	337
	G. Mihaylov, T. Iliev	
	<i>University of Ruse "Angel Kanchev", Bulgaria</i>	
RTE.6	Indoor Propagation Path Loss Modeling for Wireless Sensor Networks	341
	S. Savov, Z. Ganev	
	<i>Technical University of Varna, Bulgaria</i>	
RTE.7	ANN Model for DOA Estimation of Correlated Signals using Circular Antenna Array	343
	M. Stoilković, Z. Stanković*, B. Milovanović*, N. Dončov*	
	<i>Innovation Centre of Advanced Technology, Serbia</i>	
	<i>*University of Niš, Serbia</i>	
RTE.8	Localization of Mobile Users Stochastic Radiation Nature by using Neural Networks	347
	Z. Stanković, N. Dončov, I. Milovanović*, B. Milovanović, M. Stoilković**	
	<i>University of Niš, Serbia</i>	
	<i>*Singidunum University, Serbia</i>	
	<i>**Innovation Centre of Advanced Technology, Serbia</i>	
RTE.9	Design of a Printed Antenna Array in Rectangular Corner Reflector with Cosecant Square-Shaped Beam Pattern	351
	M. Milijić, A. Nešić*, B. Milovanović	
	<i>University of Niš, Serbia</i>	
	<i>*IMTEL Komunikacije AD, Serbia</i>	
RTE.10	Electromagnetic Modeling in Combination with Wave Digital Approach for Efficient Analysis of Microstrip Bandpass Filters with a Dual-Passband Response	355
	B. Stošić, N. Dončov	
	<i>University of Niš, Serbia</i>	
RTE.11	Three-Wire Star-Shaped Grounding Electrode in the Vicinity of the Semi-Cylindrically Shaped Ground Inhomogeneity	360
	N. Cvetković, D. Vučković, M. Stojanović, A. Ristić	
	<i>University of Niš, Serbia</i>	

DIGITAL SIGNAL PROCESSING

DSP.1	Research and Analysis of Methods for Localization of Audio Sources.....	367
	V. Hristov, S. Pleshkova-Bekjarska <i>Technical University of Sofia, Bulgaria</i>	
DSP.2	MIPFD Algorithm for Image Fire Detection	373
	B. Prlinčević, Z. Milivojević*, D. Brodić** <i>Polytechnic School for Vocational Studies, Serbia</i> <i>*College of Applied Technical Sciences, Serbia</i> <i>**University of Belgrade, Serbia</i>	
DSP.3	Image Edge Detection as Part of the Feature Extraction for Neural Network Realized with LabVIEW Application.....	377
	L. Docheva <i>Technical University of Sofia, Bulgaria</i>	
DSP.4	Digital Image Filtering with LabVIEW	381
	L. Docheva <i>Technical University of Sofia, Bulgaria</i>	
DSP.5	Robustness of SVD Watermarks in Video Sequences Encoded with H.264/AVC.....	385
	Z. Milivojević, Z. Veličković <i>College of Applied Technical Sciences, Serbia</i>	

ENERGY SYSTEMS AND EFFICIENCY

ESE.1	The Influence of the Power Systems from the Neighboring Countries, on the Fault Currents in the Macedonian Power System.....	391
	Lj. Trpezanovski, M. Atanasovski, M. Milosevski <i>Faculty of Technical Sciences Bitola, Macedonia</i>	
ESE.2	Station for Emulation of Load and Electrical Motors Testing.....	395
	M. Rosić, M. Božić, M. Bjekić <i>University of Kragujevac, Serbia</i>	
ESE.3	Modelling Self-excitation Overvoltage in an Induction Motor With Individual Compensation of Reactive Power	399
	M. Radić, Z. Stajić <i>University of Niš, Serbia</i>	
ESE.4	Multicriteria Analysis of the Smart Grid Project Efficiency.....	403
	A. Janjić, L. Velimirović*, S. Savić, M. Stanković <i>University of Niš, Serbia</i> <i>*Mathematical Institute of the Serbian Academy of Sciences and Arts, Serbia</i>	

MEASUREMENT SCIENCE AND TECHNOLOGY

MST.1	Acquisition System for Generation of the Test Signals with Standard Harmonic Disturbances.....	409
	M. Simić, D. Živanović, D. Denić, G. Miljković <i>University of Niš, Serbia</i>	
MST.2	Using Multifunction DAQ and LabVIEW for the Development of a Single-Channel EEG for Multiple Sclerosis Detection.....	413
	V. Mihaylov, K. Dimitrov, Y. Velchev, T. Mitsev <i>Technical University of Sofia, Bulgaria</i>	
MST.3	Model Development for Digital Stochastic Measurement of Noised EOG Signals.....	417
	J. Đorđević-Kozarov, P. Sovilj*, D. Mitić, V. Vujičić*, D. Radenković <i>University of Niš, Serbia</i> <i>*University of Novi Sad, Serbia</i>	

MST.4	Based on CPLD Programable Counter for Experimental Digital Electrical Energy Meter Part 2	421
	N. Draganov, T. Angelova <i>Technical University of Gabrovo, Bulgaria</i>	
MST.5	Artificial Neural Network-based Classification of Volatile Organic Compounds for Indoor Air Quality Control.....	425
	G. Georgiev, Z. Nenova, S. Ivanov <i>Technical University of Gabrovo, Bulgaria</i>	
MST.6	Experimental Digital Three-Phase Check Electrical Energy Meter Part 1.....	429
	N. Draganov <i>Technical University of Gabrovo, Bulgaria</i>	
MST.7	Research of Transmission Loss Properties of Thin Layered Sound Reduction Systems for Building Partition Elements.....	433
	T. Nedkov, S. Pleshkova-Bekjarska <i>Technical University of Sofia, Bulgaria</i>	
MST.8	The Acoustic Analysis of a Single Room	437
	V. Stojanović, Z. Milivojević, S. Dimitrijević <i>College of Applied Technical Sciences, Serbia</i>	

ELECTRONIC MATERIALS, COMPONENTS, SYSTEMS AND TECHNOLOGIES

ELT.1	Synthesis of Zeolite NaA with Facets by the Sol-gel Technology.....	443
	D. Georgiev, I. Petrov, T. Michalev, I. Pejchev <i>As. Zlatarov University, Bulgaria</i>	
ELT.2	The Removal of Cu(II) Ions from Aqueous Solutions on Synthetis Zeolite NaA.....	446
	T. Michalev, I. Petrov, I. Pejchev <i>As. Zlatarov University, Bulgaria</i>	
ELT.3	Electrical Properties of Piezo Polymer Nanocomposites and its Application.....	450
	L. Borisova, D. Kiryakova, A. Atanassov <i>As. Zlatarov University, Bulgaria</i>	
ELT.4	Impact of the Isolation Gap Position on the Voltage Gain Characteristics of Disc-Shaped Piezoelectric Transformers	454
	N. Nedev, Z. Nenova, T. Nenov <i>Technical University of Gabrovo, Bulgaria</i>	
ELT.5	High Frequency Inductive Power Transfer Device for Ultrasonic Applications.....	458
	N. Madzharov <i>Technical University of Gabrovo, Bulgaria</i>	
ELT.6	Efficiency Investigations of DC-DC Converter Supplying Power Amplifiers	463
	T. Brusev, B. Nikolova, G. Kunov, S. Vuchev <i>Technical University of Sofia, Bulgaria</i>	
ELT.7	Two-parametrical Control of Series Resonant DC-DC Converters that Operate with Common Load	467
	A. Vuchev, N. Bankov <i>University of Food Technologies, Bulgaria</i>	
ELT.8	Control Characteristics of High-Voltage Resonant DC/DC Converter	471
	N. Bankov, Y. Madankov, A. Vuchev <i>University of Food Technologies, Bulgaria</i>	
ELT.9	Three-Phase Soft-Switched Quasi Resonant DC Link Inverter for Motor Drive Application	475
	D. Spirov, N. Komitov <i>University of Food Technologies, Bulgaria</i>	

ELT.10	Matlab-Simulink Model of Three Phase BUCK Rectifier with Sinusoidal PWM	479
	G. Kunov, S. Vuchev <i>Technical University of Sofia, Bulgaria</i>	
ELT.11	Microprocessor-based Apparatus for Electrical Stimulation of Ruminant Meat	483
	I. Maslinkov, K. Kolev <i>University of Food Technologies, Bulgaria</i>	
ELT.12	A Microprocessor System for Food Quality Evaluation by Hyperspectral Images Processing	487
	K. Kolev <i>University of Food Technologies, Bulgaria</i>	
ELT.13	Preparation of Germanium Photo Detectors and Photovoltaic	491
	S. Letskovska, K. Seymenliyski <i>Burgas free University, Bulgaria</i>	

Session CSI:

**COMPUTER SCIENCE AND
INTERNET**

Using IT Management Processes for Achieving Better Efficiency in the IT Service

Yasen Mitev¹ and Leoneed Kirilov²

Abstract – This article aims to give the ITIL framework objectives, structure and functionalities. It is going to explain the rapidly growing IT business needs which had caused the development of this library of good practices. The outcomes which this framework gives to the companies using it is also discussed.

Keywords – IT management, ITIL, integration, service transition.

I. INTRODUCTION

During the last ten years ITIL (Information Technology Infrastructure Library) became most often used framework for managing IT processes. It contains full class with best practices which aim to support the delivery of an optimized IT service.

It provides full asset of guidelines how a certain situation about handling the IT service to be handled. This instructions are called best practices and they are based on the experience on many firms and enterprises. These practices ensure that the task is completed in the most efficient and cost effective way, that makes its resolution a part of the global strategy of the firm.

ITIL has been developed at the end of the '80s by the UK Government's Central Computer and Telecommunications Agency. Then ITIL didn't contain practices but just an asset of recommendations. Afterwards separate public and private sector organizations have started creating independent best practices sets, based on this recommendations. Until this moment there are 3 revisions created over the ITIL library: the second one was published on 2006 and the third one on June 2011.

The main subject of the all ITIL methodology is the IT service. All the practices are pointed to manage and support the IT service. The definition of service pointed in the The Official Introduction to the ITIL Service Lifecycle [1] is:

“A ‘service’ is a means of delivering value to customers by facilitating outcomes customers want to achieve without the ownership of specific costs and risks.”

II. KEY PRINCIPLES OF ITIL

The primary business goal of ITIL is to support the

¹Yasen Mitev is PhD student from the Institute of Information and Communication Technologies in BAS, Sofia Bulgaria, E-mail: yasen.mitev@gmail.com.

²Leoneed Kirilov is assoc. professor from the Institute of Information and Communication Technologies in BAS, Sofia Bulgaria, E-mail: lkirilov@iinf.bas.bg

company for achieving its primary business goals, by providing it with cost effective and highly productive IT environment. Following the context of this, its core principles can be summarized as follows:

- Adding value to the service
- Deliver high customer satisfaction
- Improve the usage of skills and experiences
- Improve the productivity
- Reduce the costs

ITIL is designed as a framework, which means that it provides only high level overview how the processes should follow and does not requires strict following for all of them [2]. This general rule is also being supported by the design of ITIL – it is structured in a way that allows the companies to use only the processes that they find for useful and applicable. All the processes are designed in a way that allows them to be used independently or together with the adjacent ones.

III. ITIL COEXISTENCE WITH OTHER MANAGEMENT FRAMEWORKS

In the most of the real life scenarios, the companies use different frameworks and standardizations that interfere in between. This mixture is needed for achieving the full asset of functions, necessary for the particular IT infrastructure. There are not limitations for ITIL to interfere with other frameworks as it offers only best practices with no obligatory character. These best practices also give guidelines how to effectively act with roles like a project manager in order to have effective cooperation. It is most often necessary the synergy between ITIL, a project management framework and an ISO or another standardization. There is a research [3] that studies the coexistence of four widely used frameworks and standardization:

- ITIL framework for managing the IT service
- CobiT – IT Governance framework that mainly focuses on the goal how the IT department and service should be controlled.
- CMMI – this is a framework focused on the software development. It aims to optimize the whole process of software product creation, increase its quality and optimize its cost.
- ISO9001 – standardization that assures general quality management levels.

The coexistence is described in Figure 1 [4]:

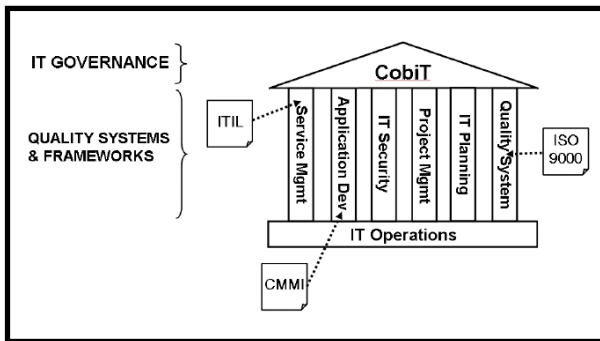


Fig. 1. Relationship of four frameworks to IT functions

IV. OTHER IT SERVICE MANAGEMENT FRAMEWORKS

Except ITIL, there are different solutions like frameworks, standardizations and methodologies that are available in the area of IT Service management (ITSM) [14]. They provide support for the management and the quality of the IT service. The most noticeable of them are: CMMI [5], Six Sigma [6], eTom [7]. It has to be mentioned that the listed solutions serve for the different areas of the ITSM and they cannot replace each-other for any purpose. There are also cases for co-existence between the different frameworks. Below we are going to review these solutions and highlight the main differences with ITIL.

CMMI is group of models that allows the processes in one organization to be benchmarked and therefore improved. Its main focus is over the processes for software development, support and management [5]. It has a five-stage measurement scale that represents the maturity level of the processes in a particular company. It is also being used as acknowledgement system that represents the company's quality of processes in front of customers and competitors. Despite of ITIL it does not provide exact guidelines how a particular task should be completed most effectively, but it is focused more on finding the process gaps and area of improvements.

Six Sigma is a methodology for minimizing the defects in the provided product or a service. It is achieving that goal by improvement the existent processes and continuous measurement of their effectiveness. There are following steps which are being universally followed: define, measure, analyze, design, and verify [6]. These processes are being very often followed together with ITIL processes like the supply management, quality management and etc. Six Sigma cannot be used independently like IT management process as it is intended only for eliminating the defects where a product is being produced to the customer.

ETOM (Enhanced Telecom Operations Map) is a business process framework that provides business processes aiming to achieve higher quality and efficiency as well as a common ground for collaboration between different teams and companies. The processes that ETOM provides are analogous to the ITIL processes but with the

specifics that they are more optimized for the Telecom industry [7]. Anyway, there are cases proving that ETOM is applicable in industries, different than the telecom one. It should be mentioned that the coexistence between ITIL and ETOM is possible after mapping the functions and roles between the both frameworks.

V. GOALS OF ITIL

The main goal of ITIL is to provide the IT managers as well as the whole organization with end-to-end processes which can allow them to have managed IT processes. These processes have to be able to continuously improve the organization's service. They also have to support meeting its strategic goals. This goal can be separated to the following sub-goals:

- User (account) satisfaction – this is the main goal which has to be reached when delivering the service. For achieving it, complicated mixture of sub goals have to meet. Satisfaction is most often periodically measured in organization level (quarter, half year, yearly). Of course the feedback by the affected users is also needed for this scoring.
- Optimized resource use – the Capacity Management ITIL process aims to involve needed resources in the most cost-efficient manner [8].
- Workflow optimization – Continual service improvement ITIL process is responsible for unstoppable workflow improvement
- Enhanced information security – regarding the ISO standard 17799:2000 [9] “Information security is achieved by implementing a suitable set of control, which can be policies practices, procedures, organizational structures and software functions. These controls need to be established to ensure that the specific security objectives of the organization are met.” That means that ITIL is not directly used to implement security but it may lead to enhanced security trough controlled processes. It is mainly achieved by the Availability management.
- Clear end-to-end monitoring – ITIL separates the monitoring activities in two parts:
 - o Proactive monitoring. By ITIL v.3 specification it is [10] “Monitoring that looks for patterns of Events to predict possible future Failures”.
 - o Reactive monitoring or just monitoring which by specification means “Repeated observation of a Configuration Item, IT Service or Process to detect Events and to ensure that the current status is known.”
- Clear roles defining – according to any ITIL's process there are set of roles. They are being assigned to one or

more employees. In particular cases some of these roles can be merged or replaced by the higher one as this cases are defined in the process.

VI. STAGES OF ITIL IMPLEMENTATION

THERE ARE TWO MAIN APPROACHES POSSIBLE APPROACHES WHEN IMPLEMENTING ITIL.

The first one is rarely used. It is applied mainly for startup companies which intend to use ITIL implementation from its beginning. As there is no any previous experience, they are no IT management processes followed. In that case there is no current process design schema that should be taken in account. Some cost and time are being safe, but there is additional focus on the company's strategy. In such type of startup companies, it is more difficult to forecast the future extension that relevantly makes the ITIL implementation roadmap. Also this roadmap is not as much optimized as expected. Very often different resources like manpower, meetings, hardware are not being utilized effectively during the expansion process. That leads to often changes of the project like suppressions, redesign, etc.

The second approach is used for the most companies. It is suitable for all the organizations that already have at least a couple of years experience and respectively some internal IT management processes in place. After taking the decision for enhancing these processes to achieve the company's goals, the phase for development of the deployment plan is in place. It can be separated into the four main stages:

- 1) Assess current ITSM processes
- 2) Create roadmap for ITIL implementation
- 3) Manage the transition and evaluate its progress
- 4) Continual service improvement

VII. ITIL STRUCTURE

Here we discuss mainly the newest version v3. of ITIL.

Between 2007 and 2011 (two editions), the third major version of ITIL was launched. This edition is providing more consistent decisions, following the fast growing IT technology progress as well as the modern business needs and outsource support model.

Version 3 of ITIL was covered into 5 main sets. There is also one additional which is often missed, because it is only a introduction book with a wide overview. The other five are:

- ITIL Service Strategy
- ITIL Service Design [11]
- ITIL Service Transition
- ITIL Service Operation
- ITIL Continual Service Improvement

These books are more directly oriented to the service provided.

On Figure 1 ITIL v3 Service Lifecycle is represented the structure of the ITIL v3 Framework. This shows that the Infrastructure Library is separated into 2 main components:

- The ITIL core
- The ITIL complimentary guidance.

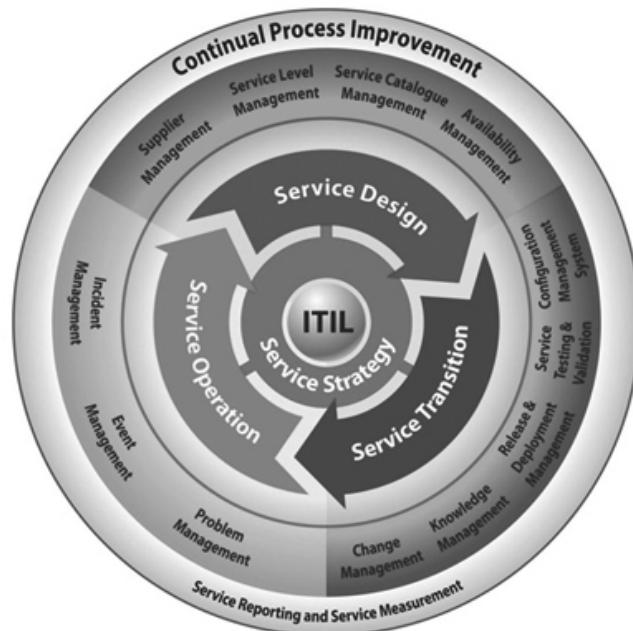


Fig. 1. ITIL v3 Service Lifecycle

VIII. IN WHICH ORGANIZATIONS ITIL IS APPLICABLE?

There is no official definition, or frame which says in what type of business the ITIL framework can be implemented successfully. Basically the framework is not dependent by the organization's type of business. It is wide applicable, as the processes are universal and not directly interfering with the main product of the business.

There can be entered a rule, that bigger companies adopt easier ITIL than the small ones. The reason is mainly lack of resources and unsure results expected. As said in "delivering effective support. Adopting ITIL to fit your IT Business Model" [1] after conduct qualitative research with focus group of 30 companies: "Many companies felt that they had insufficient resources to implement such rigorous IT support standards as ITIL. Negative attitudes centred on standards being too much hassle, too costly or just not important enough to spend time on."

IX. BENEFITS OF IMPLEMENTING ITIL

Based on a Forester Research Inc. questionnaire about "What were/are your main drives for investing in service management?" more than 2/3 of the companies had answered that they expect higher quality of the IT service and higher user satisfaction. Also almost half of them are aiming to

separate the IT departments into business service units. More than 40% expect to make cost savings with ITIL implementation. Here needs to be mentioned that the cost reducing is long term goal, as there are initial investments, which need to be made: for rearranging the human resources roles, to buy/create new software products, consulting services costs and etc.

X. ITIL v.3 MAIN SUBJECTS

One of the main principles in the third version of ITIL is that it is focused over the full cycle of the service, until the version 2 gives the main attention over specific activities around the service delivery and service support. This third version allows the ITIL to be more independent from the perspective of the industry type. It is also much easier to implement it due to the facilitated content.

There are also significant changes to the terminology in the new version.

ITIL v3 processes are separated into 5 core subjects: Service Strategy, Service Design, Service Transition, Service Operation, and Continual Service Improvement. As shown in Figure 3, these subjects can be separated into two main streams depending on the process orientation.

- Governance Processes - IT governance is defined as the leadership and organizational structures, processes and relational mechanisms that ensure that an organization's IT sustains and extends its strategy and objectives. [12]. As seen in Figure 3, the Governance processes include the Service Strategy and Continual Service Improvement processes.
- Operational processes – these are the Service Design, Service Transition, Service Operation processes. They are responsible for the actual delivery of the agreed service.

There are 26 processes in common, described in ITIL v3. The most important of them are showed horizontally in Figure 3. As you can see most of them are placed in multiple subjects. The corresponding part of the process is described at any subject separately.

XI. CONCLUSION

Based on the performed research over the structure of ITIL as well as its application and coexistence, we can conclude

that the mentioned framework provides effective toolset that allows effective management for the IT operations. Following its version history we can conclude that it is being adapted according to the demanding growth of the IT. We can point as challenge for the companies that want to adopt it the lack of clear instructions how to assess their environments and find the proper solution design for them.

REFERENCES

- [1] OGC - Office of Government Commerce, The Official Introduction to the ITIL Service Lifecycle, The Stationery Office, 2007, ISBN 9780113310616
- [2] A. White, Delivering Effective IT Support . Adopting ITIL to fit your IT Business Model, Numara Whitepaper, 2007
- [3] Setzer, T. Internet-Based Inf. Syst., Tech. Univ. Munchen, Garching Bhattacharya, K. ; Ludwig, H.; Network Operations and Management Symposium, 2008. NOMS 2008. IEEE; ISBN: 978-1-4244-2065-0
- [4] Cater-Steel, Aileen and Tan, Wui-Gee and Toleman, Mark; Challenge of adopting multiple process improvement frameworks; European Conference on Information Systems, Goteborg, Sweden, 2006
- [5] A. S. C. Marçal, B. C. C. de Freitas, F. S. Furtado Soares, M. E. S. Furtado, T. M. Maciel, A. D. Belchior, Blending Scrum practices and CMMI project management process areas, Innovations in Systems and Software Engineering, Volume 4, Issue 1, pp 17-29, 2008, ISSN 1614-5054
- [6] P. Nonthaleerak, L. Hendry, (2008) "Exploring the six sigma phenomenon using multiple case study evidence", International Journal of Operations & Production Management, Vol. 28 Iss: 3, pp.279 – 303
- [7] Chang, B-Y.,J. W. Hong, and B.-D. Chung, "Analysis of network operations management processes", KNOM Review, (2008)
- [8] Implementing Financial Management for IT - Office of Government Commerce, Service Delivery, The Stationery Office, 2001, ISBN: 0113300174
- [9] BS ISO/IEC 17799:2000 (BS 7799-1:2000). Information Technology - Code of Practice for Information Security Management. ISBN: 9780580402500
- [10] Office of Government Commerce (2001). Service Delivery. IT Infrastructure Library. The Stationery Office. ISBN 0-11-330017-4.
- [11] L. Hunnebeck, ITIL Service Design, The Stationery Office, 2011, ISBN 978-0113313051
- [12] De Haes, S. and Van Grembergen, W., "IT Governance and its Mechanisms", Information Systems Control Journal, 1), 2004.

Technology Transfer Office “ICT for Energy Efficiency”: A Factor for Open Innovations

Rumen Andreev, Jordan Doshev and Ilko Stoyanov¹

Abstract – Open innovation is a concept that focuses on the importance of external knowledge and collaboration between research organization and firms in enhancing firms’ innovation performance. In SME it is a complementary innovation activity to firms’ absorptive capacity. Its realization requires innovation agents like technology transfer offices fasten to research organizations. The paper presents the functions of such an office that works in the field of ICT and energy efficiency and is known as technology transfer offices “Information and Communication Technologies (ICT) for Energy Efficiency”.

Keywords – Open Innovation, Technology Transfer, ICT, Energy Efficiency

I. INTRODUCTION

Open innovation is defined as an act of systematically encouraging and exploring a wide range of internal and external sources for innovation opportunities, consciously integrating that exploration with organization’s capabilities and resources, and broadly exploiting those opportunities through multiple channels [1]. It is considered as a new conceptual framework in innovation literature that includes two different types of innovation activities [2], [3]. The first of them is known as *inbound open innovation* – technology exploration or acquisition. It concerns innovation activities, which base on external sources of knowledge and enhance internal technological capabilities of Small and Medium Enterprises (SME). The group of these activities covers technology scouting, external networking and participation, outsourcing research and development, customer involvement and inward licensing of Intellectual Property. The innovation activities of the second type are associated with the commercialization phase of an innovation process. They are named *outbound open innovations* that are carried out by external organizations, which are more suitable for commercialization of an innovative product. Outbound open innovation refers to such practices as venturing and outward licensing of intellectual property [4], [5].

The realization of an innovation process depends on the innovation system, in which it is carried out. The construction of a National Innovation System relates to the national innovation strategy. Bulgaria has such strategy that determines the National Innovation System, which simplified model is presented on Fig.1 [6]. The main components of this

system are Companies, Research and Education Organizations, Market demands and an innovation infrastructure that has to provide an environment, which ensures suitable conditions for starting, development and successful completion of an innovation process. Since the relationships between these components are complex, it is very difficult an organization that represents one of these components to support all relations in this complex system. But the successful work of the system is possible, if all its relations are available. That is why, it is appeared the component *Intermediary* that is responsible for the existence of all relationships, which sustains the system as a whole. The entities that represent this component are Technology Transfer Office (TTO), Innovation Centres, Agencies for Regional Development and others. They exist independently as agents, but they could be a result of their separation of representatives of other system’s components mainly Companies or Research and Education Organizations, or building up as an entirely new agent.

The purpose of this paper is to present a type of intermediary agents known as Technology Transfer Office. It is an element of innovation strategy of a research institute that is a member of Bulgarian Academy of Science – Institute of Information and Communication Technologies. The section two presents the function and role of the TTO “Information and Communication Technologies for Energy Efficiency”. Since the activities of a TTO concerns innovation activities that are regards as inbound open innovation, we could argument why it is more suitable to construct such an innovation agent in the framework of a research organization. The section three describes the main components of an innovation agent like Technology Transfer Office.

II. FUNCTION AND ROLES OF THE TTO “ICT FOR EE”

The function of the Technology Transfer Office is to support the establishment of a pro-innovation infrastructure in Bulgarian Academy of Sciences, to provide successful interaction between researchers and the industry and implementation of the national innovation strategy in the sectors of Energy Efficiency (EE) and Information and Communication Technologies (ICT). It has to be a factor for the development and enhancement of the ‘science to business’ relation, promotion of new knowledge and technologies transfer towards Bulgarian enterprises in support of their competitiveness and sustainable development.

¹Rumen Andreev, Jordan Doshev, Ilko Stoyanov are with The Institute of Information and Communication Technologies, Bulgarian Academy of Sciences, Acad. G. Bonchev str. Bl. 2, Sofia 1113, Bulgaria, E-mail: rumen@isdip.bas.bg

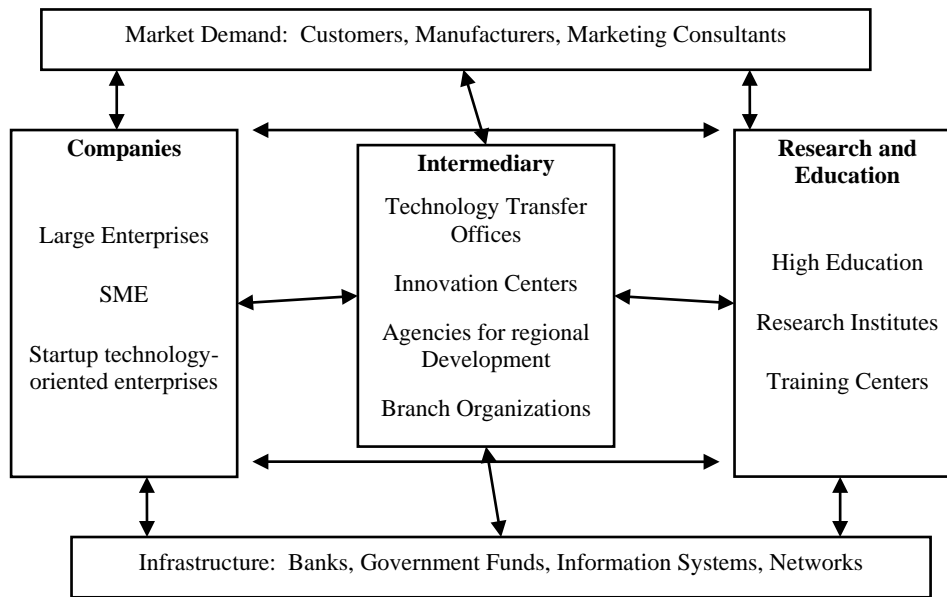


Fig.1. National Innovation System

To perform its function the TTO has to play roles, which realize the following specific goals and activities:

- Provision of information access to representatives of various professional groups to the TTO, and building a network of offices as a part of the European and national networks for technology transfer;
- Encouragement of research and development activities aimed at the development of innovative products, providing ICT-based energy efficiency, and introduction of novel technologies in enterprises with the purpose of achieving energy efficiency;
- Protection of intellectual property over the innovative products of RTD organizations, intended for Bulgarian private enterprises, municipal and state organizations;
- Being a coordinator and an intermediary in the field of energy efficiency innovations through ICT – this activity targets research organizations or individual researchers and inventors;
- Providing consulting and expert services in the field of technology transfer, intellectual property and financial management of innovation projects by engaging representatives of trade associations, non-governmental and intermediary organizations.

The main objectives and activities of the TTO “ICT for Energy Efficiency” (TTO “ICTEE”) require the performance of tasks that can be divided in the following four groups of services:

1. Information Services:

- Development of a database of energy efficiency related micro-, small and medium-sized enterprises;
- Constant networking with other Technology Transfer Offices from the National Innovation System of Bulgaria;
- Advancement of novel technological and scientific achievements in the field of energy efficiency and implementation of ICT;

- Support in promoting companies and their products;
- Establishment of contacts with research and development organizations and enterprises (foreign ones included); assistance with the establishment of collaborations between local and foreign companies;
- Organization of workshops, seminars, exhibitions, etc.

2. Consultancy Services:

- Evaluation and assistance in the protection of intellectual property and patent rights, legal support;
- Development, consultancy and coordination of new project proposals concerning the usage of ICT in the area of energy efficiency;
- Documentation development, certification and registration of new products;
- Market analysis of the market of ICT based energy efficiency innovation products.

3. Financial Services:

- Facilitation of easier access to external funding and support;
- Access to finance schemes;
- Promotion of energy efficiency related developments towards investment funds.

4. Technological Services:

- Transfer of technologies, innovations and know-how, scientific solutions to particular problems, related to the usage of ICT for energy efficiency;
- Technology valuation and technology audits;
- Pilot testing of energy efficiency technologies;
- Experts and consultants services, related to technology transfer.

III. A MODEL OF A TTO AGENT

The main characteristics of an agent are the followings [8, 9]:

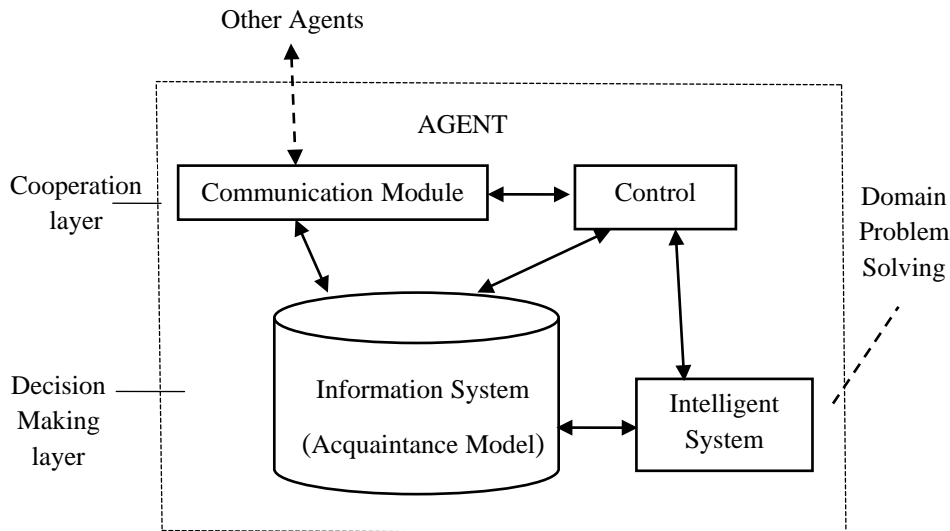


Fig. 2 Model of a TTO agent

- It is an entity with well-defined boundaries and interfaces, i.e. clearly identifiable;
- It solves problems and could be considered as an expert (problem solver);
- It is autonomous, i.e. self-controlled, self-organized;
- It performs a specific role (specific tasks);
- It exists (embedded) in particular environment, which is shared out among several agents;

The innovation environment that has to ensure the occurrence of an innovation process can adopt an agent-oriented view, since it has decentralized nature. The realization of an innovation depends on actors-mediators that work autonomously. Moreover, these agents need to interact, in order to either to achieve their individual objectives or to manage the dependencies that ensure from being situated in a common environment. In a specific innovation environment the main actors (technology transfer offices, innovation centres and others) participate in mini-societies devoted to specific objectives. The creation, operation and dissolutions of such societies are achieved by agents acting autonomously.

The description of the TTO “ICTEE” presents a conceptual model of a TTO agent that can serve for construction of its representation. It has to consist of components that are intended to realize the conceptual models in whole or partially. Figure 2 presents such a model. According to it an agent consists of two layers – *Decision Making Layer* and *Cooperation Layer*. The Decision Making Layer has two components: an intelligent system and information system. The intelligent system performs domain problem solving tasks. Some of them concern decision making. Their execution bases on information availability. The latter is provided by an information system that stores all necessary data and knowledge get by the agent. The Cooperation Layer is presented by a Communication Module and agent’s control.

The control module directs the intelligent system in such a way that the individual agent provides the necessary services,

which it is responsible to provide in accordance with its objective and role. As a part of the cooperation layer it controls the individual agent in such a way that it demonstrates co-ordinate behaviour towards the other agents and contributes to the integration of its intelligent system in the multi-agent environment. In other words, the cooperation layer manages interaction with the other agents and relates the local activity of the intelligent system to the global problem solving. This achieved through a control mechanism, which uses a set of data structures modelling the agent’s acquaintances (acquaintance models). Information (knowledge) contained in the Information system is used for planning co-ordinate activity and other social interaction. The interaction with the other agents is done by the communication module, which performs intelligent filtering and message routing.

IV. CONCLUSION

The activities that have to carry out a Technology Transfer Office concern not only inbound open innovation activities, but outbound open innovation activities, as well. The listed services that a TTO is necessary to provide are responsible for realization of technology scouting, external networking and participation, outsourcing research and development, customer involvement, inward and outward licensing of Intellectual Property.

ACKNOWLEDGEMENT

This document is created with financial support of the Project “Construction of Technology Transfer Office “Information and Communication Technologies for Energy Efficiency”, contract No: BG 161PO003-1.2.02-0001-C0001 with the Operational Programme “Development of the

Competitiveness of the Bulgarian Economy” 2007-2013, financed by the European Union via the European Regional Development Fund. The entire responsibility for the contents of the document rests with the Institute of Information and Communication Technologies, BAS, and under no circumstances can it be assumed that this document reflects the official position of the European Union and the Contracting Authority.

REFERENCES

- [1] J. D. Wit, B. Dankbaar, G. Vissers, “Open innovation: the new way of knowledge transfer?” *Journal of Business Chemistry*, vol. 4, no. 1, pp. 11-19, 2007.
- [2] H. Chesbrough, *Open innovation: The new imperative for creating and profiting from technology*, Boston, Harvard Business School Press, 2003.
- [3] V. Van de Vrande, W. Vanhaverbeke, O. Gassmann, "Broadening the scope of open innovation: past research, current state and future directions", *International Journal of Technology Management*, vol 52, no. 3/4, pp 221-235, 2010.
- [4] V. Van de Vrande, J.P.J. de Jong, W. Vanhaverbeke, M. de Rochemont, "Open innovation in SMEs: Trends, motives and management challenges", *Technovation*, vol 29, no. 6-7, pp 423-437, 2009
- [5] H., Chesbrough, A.K. Crowther, "Beyond high-tech: early adopters of open innovation in other industries", *R&D Management*, vol. 36, no. 3, pp 229-236, 2006.
- [6] Innovation Strategy of Bulgaria, www.min.government.bg
- [7] К. Костадинов, “Академичната наука като източник на иновации“, *Иновациите. Европейски, национални и регионални политики*, ред. на М. Петров, стр. 161-190, 2008, “ПИК”, ISBN 978-954-9456-12-7, София
- [8] N. R. Jennings, “An agent-based approach for building complex software systems”, *Communications of the ACM*, vol. 44, no. 4, pp. 35-41, 2001.
- [9] M. P. Singh, “Conceptual modeling for multiagent systems: applying interaction-oriented programming”, in LNCS, vol. 1565, P. P. Chen et al, Eds. Berlin Heidelberg: Springer-Verlag, pp.195-210, 1999,.

Usability Model for evaluating the usability of Web-based GIS applications

Nebojša D. Djordjević¹, Dejan D. Rančić² and Rajko Simić³

Abstract – This research aims to gain insight into evaluation methodology and to contribute to a higher standard of Web-based GIS applications (WGIS) evaluation in practice. This study proposed a suitable usability model for evaluating the usability of Web-based GIS applications. We explored existing usability standards and published usability models to determining an appropriate model for evaluating the usability of WGIS. The aim of review is that it may help to software developers and users to select the usable system on the basis of various attributes defined in the paper.

Keywords – Web-based GIS, usability, quality of use.

I. INTRODUCTION

Today, many various kinds of GIS applications are in everyday use. GIS is defined as a set of tools used to collect, store, retrieve, transform and display spatial data from the real world as defined previously [1-3].

Web-based geographic information systems (WGIS) are focused on end-users who have only a very limited knowledge of GIS, if any. This is why Web-based GIS applications should be designed very carefully and with a strong focus on their usability. Today, Web browser is used as a general multi-purpose client application. It provides “well-known” user environment because people are used to use Internet so they know how to work with a web browser. Furthermore, contemporary Web applications can provide adaptive user interface using many various technologies [4]. Because of many positives, including low costs per user, Web-based GIS applications (in general Internet applications) have become the most wide-spread GIS solutions [5]. Next advantage of Web-based GIS applications is their standardization and ability to use web services technology to cascade (mash-up) services into one application [6]. Concerning architecture, Web-based GIS applications are usually based on the n-tier client/server architecture.

A web-based GIS application means a browser supporting an application in order to make its information accessible. WGIS applications have client side and server side architecture over network. Client side is capable to edit and

improve performance, user access the GIS functions (information) through any internet browser on computer where people interact with GIS interface [7], [8]. Server side is using web remote in application server and address matching, where server is performing storage and process the data from central database to user query [8-10]. Database side is responsible, and consists of many different databases for different functionalities like store and access the server in order to return the data to the client server. Web browser is used for generating server requests and displays the data results [8].

One of the current goals of the Web engineering research is defining methods for ensuring usability. Usability is one relevant factor of the quality of Web applications. Recently, it has been receiving great attention, being recognized as a fundamental property for the success of Web applications. Defining methods for ensuring usability is therefore one of the current goals of the Web engineering research.

The notion of usability is a key theme in the human-computer interaction (HCI) literature. Determining the degree of usability is a process in which systems are evaluated in order to determine product-success using methods available to the evaluator.

One important success factor is, therefore, the need to warranty the levels of quality of the WGIS as software products [11]. High-quality software products are essential to provide value, and avoid potential negative consequences, for the stakeholders. Assessing the quality in use will allow WGIS application owners to estimate how usable a WGIS application might be and the user’s satisfaction.

These studies are certainly important as that would further deepen our understanding on factors that contributes towards the usability of WGIS applications.

In order to evaluate the quality of developed systems, a set of quality characteristics and criteria are required as a basis to describe the system quality. This set of characteristics and the relationship between them is called the Quality Model [12].

II. LITERATURE REVIEW OF USABILITY MODELS

Attempts to objectively evaluate usability of information systems are old. Many usability models have been proposed to allow software usability evaluation. The main purpose of the software product usability model is to specify and assess the level of usability of a product through internal measures of inherent properties of the software, and through external measures of the behavior of the system of which the software is part [12].

This section presents several usability models as the foundation for proposing an appropriate model for web site usability. Usability models are conceptual view and not only

¹Nebojša D. Djordjevic is with the Faculty of Electronic Engineering, Aleksandra Medvedeva 14, 18000 Nis, Serbia, E-mail: djnebojsa@open.telekom.rs.

²Dejan D. Rancic is with the Faculty of Electronic Engineering, Aleksandra Medvedeva 14, 18000 Nis, Serbia, E-mail: dejan.rancic@elfak.ni.ac.rs.

³Rajko Simic is with the Faculty of Electronic Engineering, Aleksandra Medvedeva 14, 18000 Nis, Serbia.

states the characteristics but also indicates how those characteristics fit together. The selected models are the standard and acceptable model includes Eason Model (1984), Shackel Model (1991), Nielsen Model (1993), ISO 9241-11 (1998), ISO 9126 (2001), QUIM model (2006), ISO 25010 (2010) and 2Q2U (2010).

Eason's Model [13] characterized usability into three sections based on their independency on the platform in which the task is being performed i.e. Task Characteristics, User Characteristics, System Characteristics and User Reaction which is variable dependent. Later, Shackel [14] gave the importance of usability engineering and the relativity of its concept. He gave the four important characteristics of usability namely effectiveness, learnability, flexibility, attitude. Nielsen Model [15] studied and recognized usability as an important attribute to influence the acceptance of a product. He divided acceptability into practical and social acceptance and further on gave five sub attributes of usability namely learnability, efficiency, memorability, errors, and satisfaction. The international organization of standardization gave a model consisting of three basic sub attributes namely effectiveness, efficiency, and satisfaction [16] (ISO 9214-11, 1998). Moving ahead, ISO 9126 [12] laid down the following sub attributes of usability namely understandability, learnability, operability, attractiveness, usability compliance.

Some researchers has combine ISO 9126 and ISO 9241 attributes and develop new model that has effectiveness, efficiency, satisfaction, learnability and security as attributes [17]. Usability standards provided by ISO can be broadly classified into two categories first, product-oriented standards (ISO 9126, 2001; ISO 14598, 2001) and second, process-oriented standards (ISO 9241, 1992/2001; ISO 13407, 1999).

QUIM (Quality in Use Integrated Measurement) [18] is a consolidated model for usability measurement and metrics. It combines various standard and model such as ISO 9241 and ISO 9126 and unified into a single consolidated, hierarchical model. It outlines methods for establishing quality requirements as well as identifying, implementing, analyzing, and validating both process and product quality metrics. This model appropriate for novice users that have little knowledge of usability and can be applied by usability experts and non-experts QUIM model consists of 10 factors and subdivided into 26 criteria or measurable criteria, and finally into specific metrics consists 127 specific metrics. The 10 factors consists Efficiency, Effectiveness, Satisfaction, Learnability, Productivity, Safety, Trustfulness Accessibility, Usefulness and Universality.

ISO has recently developed a new more comprehensive definition of quality in use, which has usability, flexibility and safety as subcharacteristics that can be quantified from the perspectives of different stakeholders, including users, managers and maintainers. It describes a practical method for identifying contextual aspects of usability in software systems, and for helping ensure that usability evaluations reflect the context of use and give data with acceptable validity.

ISO/IEC 25010 is the new standard of software product quality that is awaiting publication, and is a part of the new series of SQuaRE (Software product Quality Requirements

and Evaluation) standards [19]. ISO/IEC 25010 is an evolution of the ISO/IEC 9126 and defines a more complete and detailed quality in use model. According to both standards, the quality of a system can be assessed as the extent to which the system satisfies the stated and implied needs of its various stakeholders.

The modelling framework, 2Q2U [20], is designed to flexibly evaluate the external quality for a GIS application for usability and user experience by flexibly combining and relating the concepts of actual usability and actual UX.

Actual Usability, degree to which specified users can achieve specified goals with effectiveness in use, efficiency in use, learnability in use, and accessibility in use in a specified context of use. Actual usability is measured and evaluated in a real operational environment where real users perform actual specified tasks. To this aim, they modelled four characteristics, namely, efficiency in use, effectiveness in use, learnability in use and accessibility in use as shown in Fig. 1. Actual User Experience (UX), degree to which specified users can achieve actual usability, safety, and satisfaction in use in a specified context of use. Actual UX is evaluated not only by measures and indicators of user performance – as in actual usability-, but also by means of satisfaction instruments.

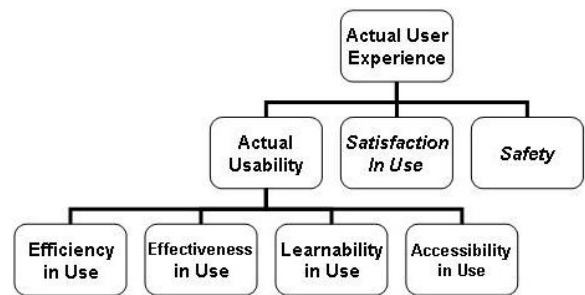


Fig 1. Model composition representing actual usability and actual UX.

2Q2U aligns with the intention of the ISO 25010 standard which encourages tailoring for relative importance of characteristics depending on the situation: "It is not practically possible to measure all ...relative importance of quality characteristics will depend on the product and application domain. So the model should be tailored before use..."

In fact, each author can propose his own usability model to cover all important issues and to take aim of an evaluation into account [21].

III. ANALYSIS OF USABILITY MODELS

During the decades, different literature described various models and attributes of usability. We based our methodology to explore published usability models. This paper, discussed how the usability models and their attributes are evolved.

In this section, a comparison between the availability of the characteristics (called factors or attributes in some usability models) within the eight usability models will be presented. Table 1 presents this comparison, at the end this table you will

find the number of the corresponding characteristics for each usability model.

There are many attributes in each model but there has similarity between the models. From Table 1, 6 attributes are selected based on frequency in each model and other study made by researchers to see the similarity. The attribute that have been selected are effectiveness, efficiency, satisfaction, safety, learnability and flexibility.

TABLE I
A COMPARISON BETWEEN THE USABILITY MODEL

Factors or attributes	Eason	Shackel	Nielsen	ISO 9241-11	ISO 9126	QUIM	ISO 25010	2Q2U
Effectiveness		√		√		√	√	√
Efficiency	√		√	√		√	√	√
Satisfaction			√	√		√	√	√
Safety						√	√	√
Learnability	√	√	√		√	√		√
Flexibility		√				√*	√	√
6	2	3	3	3	1	6	5	6

*Accessibility

From the 6 characteristics, there are only two characteristics (i.e. „efficiency“ and „learnability“) which are belonging to six usability models. Two characteristic belong to five usability models, that is, the „effectiveness“ and „satisfaction“ characteristics. And, one characteristic (i.e. „safety“) is defined in three usability models and („flexibility“) is defined in four usability models.

IV. DISCUSSION

There are a number of usability models in software engineering literature, each one of these usability models consists of a number of usability characteristics. These usability characteristics could be used to reflect the usability of the software product from the view of that characteristic. Selecting which one of the usability models to use is a real challenge. In this paper, we have discussed and compared the following usability models: Eason Model, Shackel Model, Nielsen Model, ISO 9241-11, ISO 9126, QUIM model, ISO 25010 and 2Q2U.

Based on the discussion of the eight usability models and on the comparison between them, the following comments could be written:

1. The ISO 25010 usability model is the most useful one since it has been built based on an international consensus and agreement from all the country members of the ISO organization.
2. However, based on table 1, it can be concluded that among the usability model, 2Q2U model is more complete than other models and suitable to be used in the WGIS usability because it consolidated model based on previous works and model.

For customizing these characteristics especially for web applications, a wide range of usability guidelines and

checklists were studied. It is important to emphasize the fact that the analyzed quality characteristics are those concerning the quality in use and those that are of interest to the end users of WGIS applications.

Since all of these characteristics affect the use of WGIS applications by final users, they were adapted to the WGIS application context. However, other sub-characteristics were not included because they could be considered as not being sufficiently relevant for WGIS application usage.

The 25010 standard categorizes learnability as an internal/external quality subcharacteristic under the operability characteristic. We propose to include learnability in use as a characteristic of usability in use to account for the learning process and the importance of context of use. The satisfaction attribute selectable because to determine whether the web application is usable or not. In addition, more satisfying experiences sometimes lead to better learning performance in the future. Safety is a quality in use characteristic defined by ISO 25010.

Quality in use is the degree to which a product or system can be used by specific users to meet their needs to achieve specific goals in specific contexts of use. A quality in use model composed of four characteristics (Usability in use, Satisfaction in use, Safety in use and Flexibility in use) that relate to the outcome of interaction when a software product is used in a particular context of use. Some of characteristics are further subdivided into sub-characteristics. Each characteristic can be assigned to different activities of stakeholders, for example, the interaction of an operator or the maintenance of a developer.

The characteristics and sub-characteristics of the model are specified below.

1. **Usability** in use: The extent to which a WGIS application can be used by specific users to achieve specified goals with effectiveness, efficiency and satisfaction in a specified context of use.

1.1. Effectiveness in use [12, 16, 19]: The degree to which the WGIS application can be used by the users to achieve their specific goals with accuracy and completeness in a specified context of use.

1.2. Efficiency in use [12, 16, 19]: The degree of resources consumed by WGIS application users in relation to the effectiveness reached in a specific context of use.

1.3. Learnability in use [20], degree to which specified users can learn efficiently and effectively while achieving specified goals in a specified context of use.

2. **Satisfaction** in use [12, 16, 19]: the WGIS application users' degree of satisfaction with regard to achieving their pragmatic and hedonic goals in a given context of use.

3. **Safety** in use [15, 16, 19]: The degree, to which the WGIS application does not, under specified conditions, lead to a state in which the personal security of its users is endangered and economic damage is caused.

3.1. Personal Security Risk [19, 22]: the degree of expected impact of harm to the personal security of the portal's users or clients in the intended contexts of use.

3.2. Economic damage risk [19, 22]: the degree of expected impact of causing economic damage to the web

portal users owing to insecure operations in the intended contexts of use.

4. **Flexibility** in use: the degree to which the quality in use requirements for WGIS application can be achieved in different contexts of use and for as many users as possible.

4.1. Accessibility [19], [23]: the degree of effectiveness, efficiency, safety and satisfaction, when people with the widest range of capabilities use the web portal.

4.2. Personalization [24]: the degree to which the users can modify certain aspects of the portal to suit their specific preferences and needs.

The quality in use model adapted for WGIS application is shown in Fig.2.

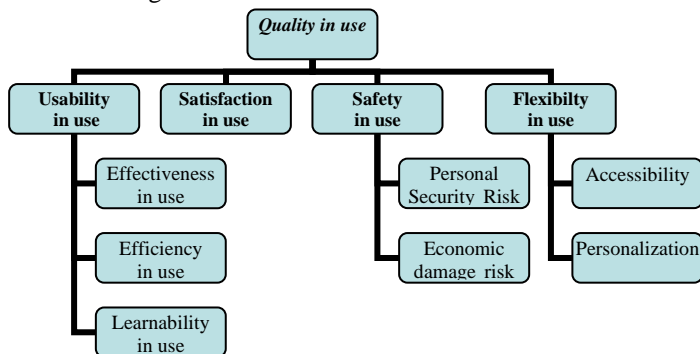


Fig. 2. Quality in use model for WGIS application

V. CONCLUSION

Researchers have not developed yet any model that precisely describes usability definition and all its attributes that takes into account the varying aspects of usability.

This paper provides a detailed analytical comparison of the various attributes, to achieve a more thorough view of the usability strengths and weaknesses. So they can get help in decision making and avoid costly mistakes when choosing WGIS applications. Since different users have different priorities during the usage of system, we consider final usability attributes to decide whether the particular WGIS application being developed is acceptable overall or not by them. Therefore this paper recommends a combination of these attributes into consideration of usability decision making for WGIS.

There are two immediate contributions of this work: comparison and analysis of existing usability model and identification of usability characteristics for WGIS.

REFERENCES

- [1] P. A. Burrough, "Principles of Geographical Information Systems for Land Resources Assessment", ISBN-10: 0198545924, Oxford University Press, New York, USA, 1986.
- [2] P. A. Burrough, and R. A. McDonnell, "Principles of Geographical Information Systems", 1998.
- [3] GIS Cloud. (2010, December, 21). [Online] available: <http://www.giscloud.com/>
- [4] H. M. El-Bakry, A. M. Riad, M. Abu-Elsoud, S. Mohamed, A. E. Hassan, M. S. Kandel, N. Mastorakis "Adaptive User Interface for Web Applications," in RECENT ADVANCES in BUSINESS ADMINISTRATION: Proceedings of the 4th WSEAS International Conference on BUSINESS ADMINISTRATION (ICBA '10), University of Cambridge, UK, February 20-22, 2010, pp. 190-211.
- [5] P. A. Longley, M. F. Goodchild, D. J. Maguire, and D. W. Rhind, Geographic information systems and science. 2nd ed. New York: John Wiley & Sons, 2005, chap. 7 and 11.
- [6] T. Brunclik, "Aggregating Remote Map Services with Local Cascading WMS Server," in Proc. of the 6th WSEAS Int. Conf. on Artificial Intelligence, Knowledge Engineering and Data Bases, Corfu Island, Greece, February 16-19, 2007, pp. 250-254.
- [7] G. Luciano, and V. Elisabetta, "Web Usability Today: Theories, Approach and methods", Towards Cyber Psychology: Mind, Cognitions and Society in the Internet Age, Amsterdam, IOS Press, 2003.
- [8] M. Man, and et al, "An architecture for Web-based GIS System for Artified Reefs", Universiti Malaya 50603 Kuala Lumpur, 2009.
- [9] H. Lan, and C.D. Martin, "A Web-based GIS Tool for Managing Urban Geological Hazard Data", Canada, 2009.
- [10] H. Lan, and et al, "A Web-based GIS for managing and assessing landslide of Likert scale and visual analog scale as response options in children questionnaires", Copernicus Publications on behalf of the European Geosciences Union, 2009.
- [11] Liu, C.-T., T.C. Du, and H.-H. Tsai, "A study of the service quality of general portals", Information & Management, 46(1): pp. 52-56, 2009.
- [12] ISO/IEC 9126-1, "Software engineering – Product quality - Part 1: Quality model", ISO, 2001.
- [13] Eason (1984): Towards the experimental study of usability, Behaviour and Information Technology, Vol. 3(2), pp. 133-143.
- [14] Shackel, B. (1991): Usability – Context, framework, definition, design and evaluation. In Human Factors for Informatics Usability, ed. Brian Shackel and Simon J. Richardson, 21–37. New York, Cambridge University Press.
- [15] Nielsen, J. (1993): Usability Engineering, Academic Press.
- [16] ISO 9241-11, "Ergonomic requirements for office work with visual display terminals (VDTs) – Part 11: Guidance on usability," Geneva, Switzerland: Author., 1998.
- [17] A. Abran, A. Khelifi, W. Suryn, and A. Seffah, "Usability Meanings and Interpretations in ISO Standards," Software Quality Journal, vol. 11, November 2003, pp. 325-338.
- [18] Seffah, A., Donyae, M., Kline, R.B. and Padda, H.K. (2006): Usability measurement and metrics: A consolidated model, Software Quality Control, Vol. 14, No. 2, pp. 159–178.
- [19] ISO/IEC CD 25010.3, "Systems and software engineering – Software product Quality Requirements and Evaluation (SQuARE) – Software product quality and system quality in use models", ISO (2010).
- [20] Lew P., Olsina L., Li Zhang, (2010) Quality, Quality in Use, Actual Usability and User Experience as Key Drivers for Web Application Evaluation, Lecture Notes in Computer Science, Volume 6189, Web Engineering, Pages 218-232.
- [21] N. E. Fenton, and S. L. Pfleeger, *Software metrics: A Rigorous and Practical Approach*. 2nd ed. Boston: PWS Publishing Company, 1997, chap. 9.
- [22] S. Gounaris, D. S., "Assessing service quality on the web: Evidence from business to consumer portals", The Journal of Services Marketing, pp. 17:529, 2003.
- [23] T. Kuo, L. I., C. Huang et al., "Measuring user's perceived portal service quality: An empirical study Total Quality Management and Business Excellence", pp. 16:309, 2005.
- [24] N. Manouselis and D.G. Sampson, "Multiple Dimensions of User Satisfaction as Quality Criteria for Web Portals", in ICWI, IADIS, pp. 535-542, 2004.

Development of Software Program for Direct Insertion into MySQL Database from Communication Interface

Goran Goranov¹ and Radoslava Hristova²

Abstract–Personal computers changed the style of work in solving measurement problems forever. Devices with a measuring function increasingly give way to the computer system which enables the gathering, processing and analysis of the measured results. Widespread approach is the combination of comprehensive measurement hardware with personal computers, and thus creating a measurement system dependent on the software. In this paper we propose software which periodically recorded information from LPT parallel port into MYSQL relational database.

Keywords–Analog to Digital System, MYSQL data base, PHP, Universal Serial Bus, Local Print Terminal

I. INTRODUCTION

The basic idea of the current work is to present the possibility for WEB-based monitoring of certain parameters of input interfaces in production environment.

In a measuring computer the most used input interfaces are Local Print Terminal (LPT), Universal serial bus (USB) and communication serial port (COM) ports [1,6,7]. In any case, an external measurement system has to be used in order to collect the information built on the basis of a high-speed multichannel analog-to-digital converters [2]. For this purpose a measuring module has been developed. The structure of the module is shown in Figure 1.

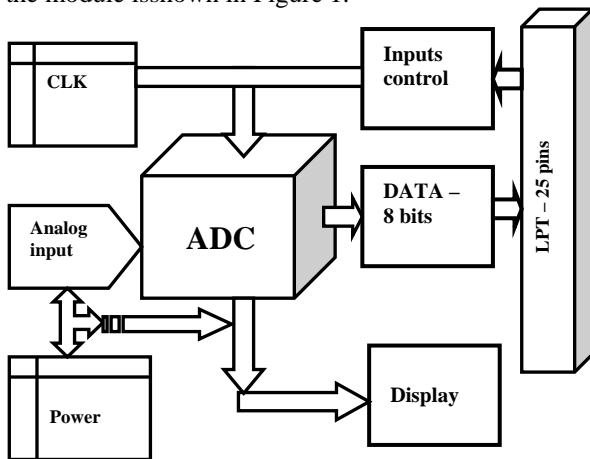


Fig.1. Digital to Analog Converter System

The analog digital converter (ADC) module management is done entirely from the personal computer (PC), by selecting the analog input or alternate analog inputs in order to account more channels. For ADC is used an IC ADC0808N – fig.1(a). In order to compare the measured and recorded value from the personal computer and this one coming from the input of the LPT port, a single mode of the ADC is provided. The signal is visualized on the 8 - light emission diodes (LED)

In order to access the recorded data from the PC, we have to configure the measuring computer as WEB server. The essential part here is that the data are stored into the relational database and can be visualised through the WEB.

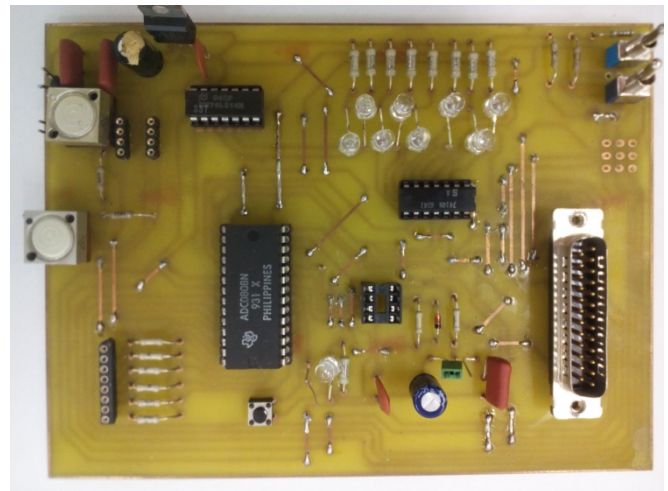


Fig.1.(a) Analog to Digital Converter Board

II. THE WEB SERVER AND THE SOFTWARE

The paper format must be A4 (210×297 mm²). The margins are given in Table 1. For the Web server configuration Apache HTTP server, MySQL – relational database system and PHPMyAdmin – a web-based user interface for access to MySQL are used. All components are installed as a part of the XAMP package [3]. For setting up the application a new database has to be created. In our case the name of the database is LPT. Also a table with corresponding columns has to be created. They are described in Table 1 and shown in Figure 2.

```

mysql> create database lpt;
mysql> use lpt;
mysql> create table data(
  id int auto_increment primary key,
  port varchar(100),
  data varchar(100),
  time date time,
  data10 varchar(100));
mysql> select * from data;
    
```

¹Goran Danailov Goranov, Dept. Electronics Technical University of Gabrovo, Bulgaria Faculty of Electrotechnics and Electronics, g_goranov@tugab.bg

²Radoslava Danailova Hristova, Dept. Computer Informatics University of Sofia “St. Kliment Ohridski”, Faculty of Mathematics and Informatics, Sofia, Bulgaria radoslava@fmi.uni-sofia.bg

TABLE I
LPT - DATABASE AND TABLE DATA

id	port	data	time	data10
1	0378	00FF	2013-05-25 22:06:36	255
2	0378	00FF	2013-05-25 22:06:41	255

#	Name	Type	Collation	Attributes	Null	Default
1	id	int(11)			No	None
2	port	varchar(100)	latin1_swedish_ci		No	None
3	data	varchar(100)	latin1_swedish_ci		No	None
4	time	datetime			No	None
5	data10	varchar(100)	latin1_swedish_ci		No	None

Fig.2. Diagram of table- DATA

The created database has to be monitored and optimised according to the time for reading and inserting into it. This is due to the fact that the developed software will insert entries into the database in a very short time (1min. -60min.). On the other hand this data has to be read and displayed by the WEB-based application.

SOFTWARE DEVELOPMENT

The software is developed using language C/C++. For the development an integrated development environment - Microsoft Visual Studio is used [4]. The developed program has the following algorithm:

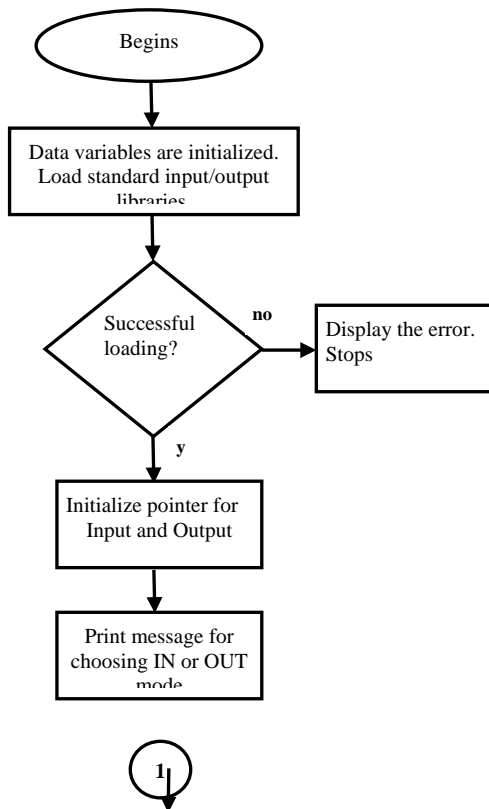


Fig.3. Program algorithm (Part 1)

First the data variables are initialised and the standard library for input/output operation is loaded. This library is used for reading and writing into the input interfaces [5]. If the library is loaded successfully the program continues, otherwise the program displays the error message and exits.

After that the pointers to the input and output functions for reading and writing are allocated. To the user is shown message for choosing the mode - IN or OUT (Fig. 3).

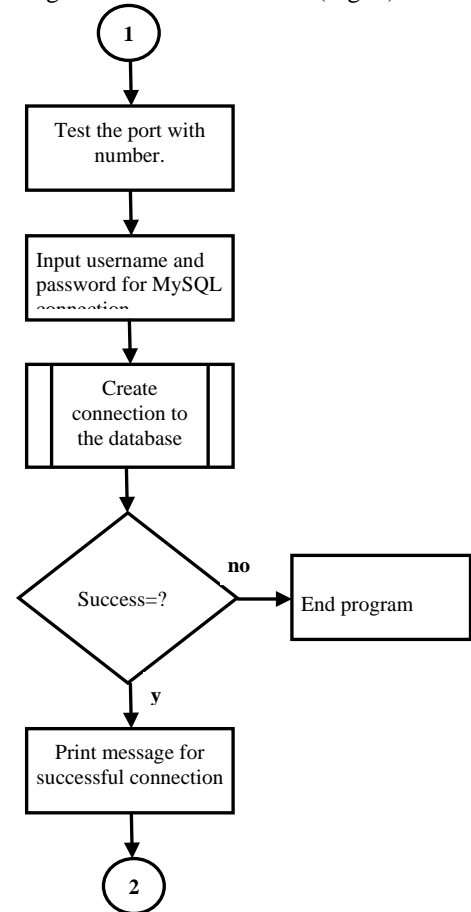


Fig.4. Program algorithm (Part 2)

After the user chooses the type of operation the corresponding branch is executed. Currently the program implemented only the IN mode.

After the user chooses IN mode, he enters the time interval for inserts and the user name and password for database connection. If the connection is not successful the program is ended. Otherwise the user is printed message for successful connection. (Fig. 4)

In eternal loop program reads data from the port on every N seconds, where N is previously defined and insert the data into the database. (Fig. 5)

III. THE RESULTS

The software is compiled and built into executable file, which can be loaded into DOS console. The software works on 32 bit operating systems. As it was shown above first we have to choose IN or OUT mode for the terminals of the LPT

port (Fig. 6). This is done by writing into the registry with address 37Ah, bit C5 in log. 1 (Fig. 7)

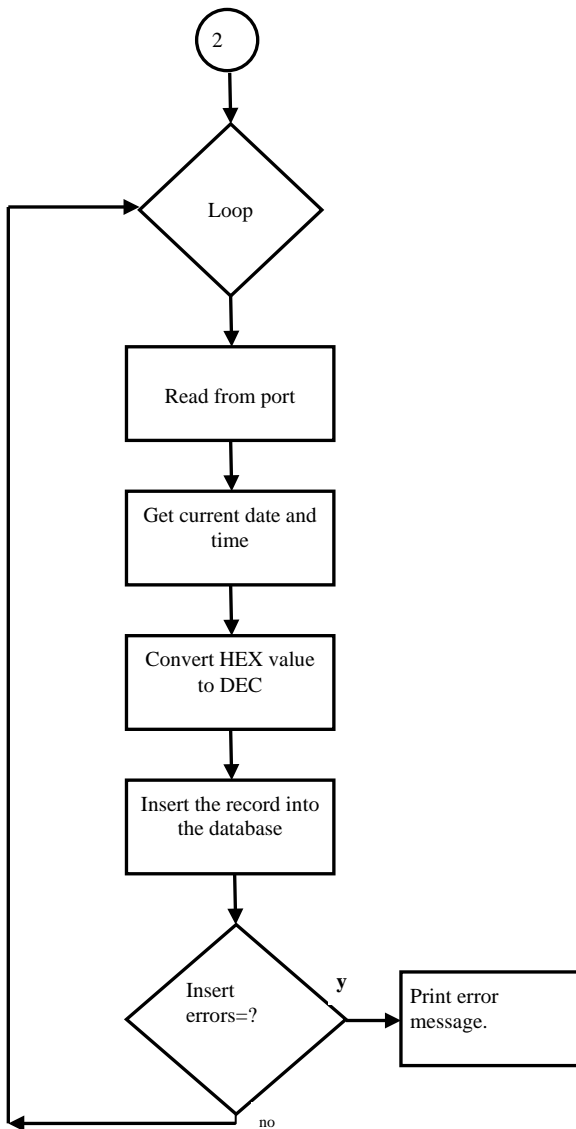


Fig.5. Program algorithm (Part 3)

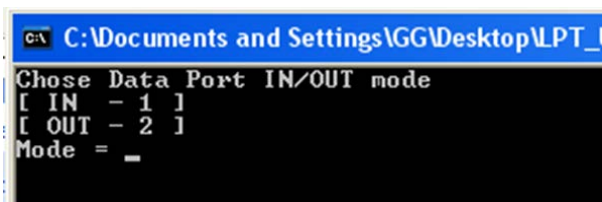


Fig. 6. ChoosetoLPTisinput or output

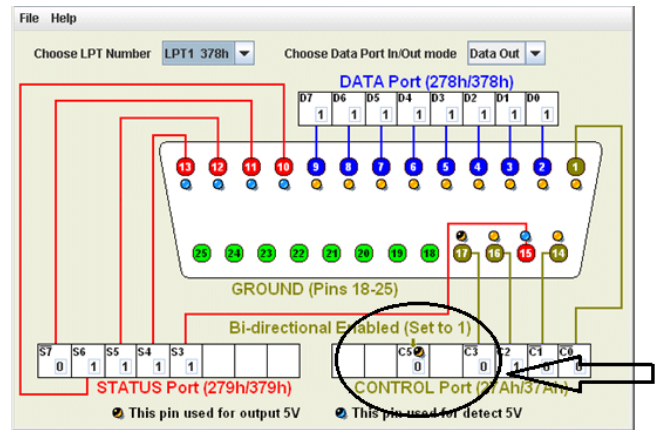


Fig.7. The control bit for select a pin is input

After initialization of the LPT port we input the time in seconds for data insertions (Fig. 8). Frequency of recording is limited due to considerations of database load. In this case, the possibilities are from 1 second to 60.

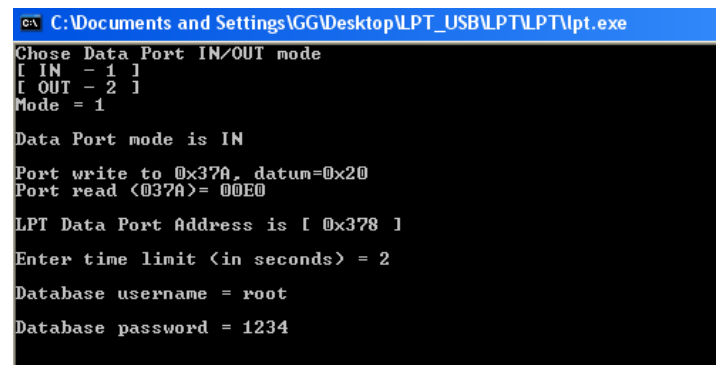


Fig.8. Insert data base user name and password

We input the username and the password for database connection and the time. In Fig. 8 the time is limited to 2 seconds. The connection between the program and the database is done through ODBC drivers for MySQL. They are additionally installed and configured (Fig.9).

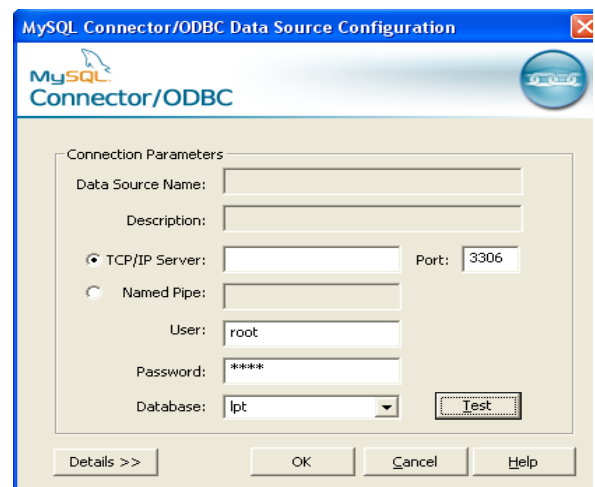


Fig.9. Driver for connection whit data base

As a result the measured data is stored into the database. For every record the date and time are stored (Fig.10)

```

C:\Documents and Settings\GG\Desktop\LPT_USB\LPT\LPT
Database username = root
Database password = 1234
>>>> Successfully connected to MySQL <<<<
>>>> Press !X! to exit <<<<
Inserting data into MySQL...
>> insert into data(port,data,time) values
<'0378','00FF','2013-06-18 19:31:50'>
Sleeping 2 seconds ...
Inserting data into MySQL...
>> insert into data(port,data,time) values
<'0378','00FF','2013-06-18 19:31:52'>

```

Fig.10. Writing in data base – intervals is 2 second

The console has to be active, i.e. minimized for the time the information will be gathered. The stored data into the database (Fig.11) can be additionally processed and displayed into the WEB-based application.

id	port	data	time	data10
1	0378	00FF	2013-05-25 22:06:36	255
2	0378	00FF	2013-05-25 22:06:41	255
3	0378	00FF	2013-05-25 22:06:46	255
4	0378	00FF	2013-05-25 22:06:51	255
5	0378	00FF	2013-05-25 22:06:56	255
6	0378	00FF	2013-05-25 22:07:01	255
7	0378	00FF	2013-05-25 22:07:06	255
8	0378	00FF	2013-05-25 22:07:11	255
9	0378	00FF	2013-05-25 22:07:16	255
10	0378	00FF	2013-05-25 22:07:21	255
11	0378	00FF	2013-05-25 22:07:27	255
12	0378	00FF	2013-05-25 22:07:32	255

Fig.11.Stored data into the database

However, for the purpose dynamic PHP web application has to be developed. The application will allow remote monitoring of the port processes (through the web) and also sorting the information, parameters classifications and drawing graphics for the collected data. This however is a matter of a further development.

IV. CONCLUSION

The presented work purpose an example solution for reading data from the LPT port and writing it to the MySQL database. The benefit of this solution is that it allows remote monitoring of port processes through the website. Developed is a ADC module connected to LPT port on the PC. Developed and software under windows to record the information in the database. Computer is configured as a WEB server, has a developed simple website to check the parameters.

REFERENCES

- [1] *USB deserves more support*, "Business", *Boston Globe Online* (Simson), 1995-12-31, retrieved 2011-12-12.
- [2] Meshurment Computing, USB-2500 Series DAC board, 2014.
- [3] XAMP, <http://www.apachefriends.org/index.html>.
- [4] Microsoft Visual Studio, <http://www.visualstudio.com/en-us> 2014.
- [5] D. Beattie Jr., Test interface to inport32.dll, <http://www.logix4u.net/inpout32.htm>, 2006.
- [6] C. Janssen, "What is a Universal Serial Bus (USB)". Techopedia. Retrieved 2014-02-12.
- [7] Dataproducts D-Sub 50 Parallel". *Hardware Book*. Retrieved 2008-01-25.
- [8] L. Welling, Laura Thomson, "PHP and MySQL web development" fourth edition, 2009.

Telemetry System for WRC Sport Cars. Mobile Part.

Hristo Nenov¹, Galina Hristova², Plamen Georgiev³

Abstract – Nowadays, the success of the rally pilots depends on the quality of the notes of the co-driver. This is too subjective factor even for people with great experience. This paper shows an approach that supports the preparation of a strategy for the competition by reducing subjective factors and providing concrete solutions.

Keywords – Mobile technologies, Software, GPS, Models.

I. INTRODUCTION

The using of technologies, as a tool, for problem solving is part of daily life. A similar approach is used in WRC Rally Championship. There, high cost equipment and facilities provide many details about the behaviour of racing cars. Necessity to optimize their driving can be done very efficiently by low priced technology. The system which is described in this paper is using a mobile phone like data-harvest module and server machine for data analysis.

II. “FORCESPEEDO” SYSTEM BASED ON ANDROID MOBILE TECHNOLOGIES

A. Mobile Technologies

Mobile technology is the technology used for cellular communication. Mobile code division multiple access (CDMA) technology has evolved rapidly over the past few years [4].

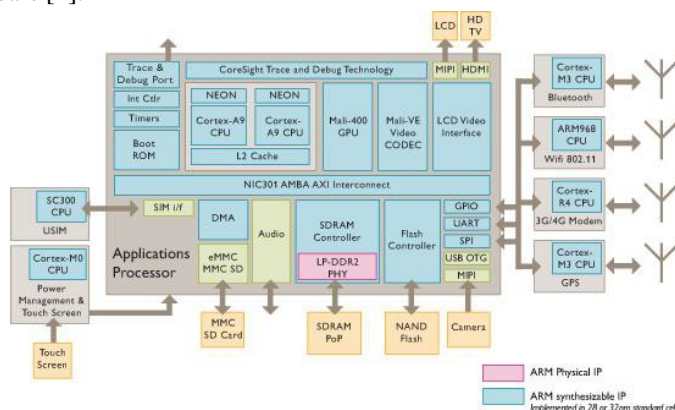


Fig.1 Mobile architecture from ARM [3]

¹Hristo Nenov is with the Faculty of Automation and Computing at Technical University of Varna, 1 “Studentska” str. 9000, Bulgaria, E-mail: h.nenov@tu-varna.bg.

²Galina Hristova, ³Plamen Georgiev are with the Faculty of Automation and Computing at Technical University of Varna, 1 “Studentska” str. 9000, Bulgaria

Since the start of this millennium, a standard mobile device has gone from being no more than a simple two-way pager to being a device for data collection based on different sensors and tool for various calculation procedures. their use is mainly based on direct manipulation, using touch inputs that loosely correspond to real-world actions, like swiping, tapping, pinching and reverse pinching to manipulate on-screen objects. Internal hardware such as accelerometers, gyroscopes and proximity sensors are used by some applications to respond to additional user actions, for example adjusting the screen from portrait to landscape depending on how the device is oriented. But, not only this. Combination of integration of such peripheral devices and the possibility of mobility gives programmers a great potential for creativity. From ordinary communication device it can be easily transform to intelligence tool for solving of interesting problems.

B. Android Operating System

Many types of mobile operating systems (OS) are available for smartphones, including: Android, BlackBerry OS, webOS, iOS, Symbian, Windows Mobile Professional (touch screen), Windows Mobile Standard (non-touch screen), and Bada. Android mobile operating system (OS) which is developed by Google, is the first completely open source mobile OS [1,2,4] and second (if not already the first) by popularity. These two characteristics were the reason Android to be chosen like platform for the telemetry system.

C. “ForceSpeedo” System

The performance of one rally car depends on sense of the driver and the quality of co-driver notes. Unfortunately, however good they are still remains a subjective factor.

The aim of the system is to improve the results of the rally pilot. This is based on several main processes:

- Data collecting in real time;
- Analyzing of the aggregated data into the server;
- Building the model of optimal performance.

Creation of etalon model based on objective factors and quantitative assessment, give possibility to evaluate the style and performance of the driver and to fix mistakes or to improve some details.

The system has two main modules – Android OS device which is in the car for data collection and remote server for final analysis of data and preparing the models of driving. The topic of the current paper is mobile part of the system.

The data which is necessary for the post analysis consist of a lot of coefficients and formulas. They are separated in two categories:

- statistic data from experiments;
- data collected from the car in real time.

The information from the car has connection with accelerating (throttle management), decelerating (brake management), the current speed of the car, lateral forces during cornering (G) and forces under braking / acceleration (G). The “G” forces are complex factor about speed characteristics and steering.

To collect the needed data the application use the information from peripheral devices (sensor) in mobile phone:

- GPS sensor;
- accelerometer ;

D. System Implementation

The interface of the mobile application includes speedometer for the current speed of the car, status of communication with the GPS sensor and information about “G” forces.



Fig. 2. “Speedometer” interface

The “map” display section shows a graphical presentation of the recorded data (data from GPS sensor) which describe the movement of the car.



Fig. 3. “Map” interface

Logs” display present recorded data as text. This is actually the information that will be sending to the server.

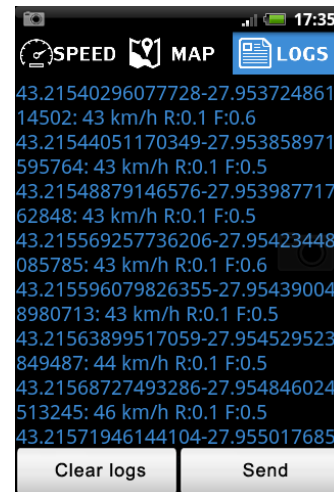


Fig.4. “Logs” interface

The role of different displays in mobile application is just to show that it works correctly. The main process is collecting of data.

When the user consider that that the process of data storing is finished , has possibility to send in to the server by Internet. Internet connection is only required when sending data to the server after the reading. At the time of reporting data is written to a local file and only needs a GPS connection. All reported data from the specified traverse route is sent to the server with the same key - date and time of transmission by which encapsulated and displayed together in the interface of the server side.

III. CONCLUSION

System for enhancing performance of rally driver in the race is Implemented and presented in this paper. The system is fully operational. After the tests, additional adjustments in the software and how to use the mobile device were made. Data received by it reached the required accuracy and are suitable for behavioral analysis and development of strategies for the different Stages in the race

ACKNOWLEDGEMENT

This paper is developed in the frames of project NP 12/2014 “Research on mobile technologies and their use in the management of remote and mobile objects”.

REFERENCES

- [1] M. Wolfson, *Android Developer Tools Essentials*, by Copyright © 2013
- [2] W. Ableson, *Android in Action*, Third Edition ©2012 by Manning Publications Co
- [3] <http://arm.com/>
- [4] http://www.openhandsetalliance.com/android_overview.html.

Session CS:

CONTROL SYSTEMS

Comparison Analysis of the Heading Accuracy of GPS, E-compass and Gyroscope

Rosen Miletiev¹, Radostin Kenov², Ivaylo Simeonov³, Emil Iontchev⁴

Abstract – A comparison analysis for heading determination is described that includes the effects of pitch and roll as well as the magnetic properties of the vehicle. Using 3D MEMS magnetic sensor and a linear accelerometer, a low-cost compass system can be realized which accuracy is compared with the GPS and gyroscope data. The proposed system has an integrated Kalman filter for the pitch and roll calculation to build a tilt compensated compass. The heading accuracy is better than the GPS COG data due to the high update rate – up to 75 Hz.

Keywords – heading angle, GPS, e-compass, gyroscope.

I. INTRODUCTION

Navigation is a key ability of mobile systems. The task of navigation can be divided into localization and path planning. Aim of localization is to estimate position and orientation of a mobile system with respect to its environment. The absolute position and heading angle determination of moving objects is necessary for their long term reliable operation. Commonly used heading sensors include difference odometers, gyros and electronic magnetic compasses as well as GNSS receivers [1-4]. The GPS has become the primary source of providing navigation information for most of the present vehicular navigation applications. However, the main disadvantages of GPS receivers towards the course estimation are recognized as a low update rate (usually 1 Hz) and the impossibility to provide continuous navigation solutions in the periods of no signal reception. On the contrary, an INS is a self-contained positioning device that continuously measures three orthogonal linear accelerations and three angular rates to calculate the required position. However, the error of accelerometers will be double integrated and cause position error that accumulate with time.

The current paper discusses the comparison analysis of the heading accuracy of the GPS receiver, MEMS gyroscope and tilt compensated e-compass. The designed heading determination system utilizes three of the above mentioned

sensors, i.e. an electronic compass, a GNSS receiver and a gyro which may work independently. The main subsystem is an electronic compass module. This part of the system allows heading calculation, based on the Earth magnetic field measurements after a calibration procedure implementation. The data of the GNSS receiver, gyroscope and electronic compass module are used to compare the accuracy and the stability towards heading determination. Primary the e-compass heading estimation may be based on the data of the three axis linear accelerometer where the accelerometer readings provide pitch and roll angle information which is used to correct the magnetometer data, but this tilt-compensated e-compass will not operate under freefall or high-g accelerations. This requires a Kalman filter implementation to calculate the proper pitch and roll values according to the gyroscope and accelerometer data.

II. BACKGROUND

The comparison analysis of the heading calculation is accomplished on the basis of the 9DoF inertial system shown at Fig. 1. It consists of 3 axes gyroscope, 3 axes accelerometer and 3 axes magnetometer as a part of 9DoF IMU system and Kalman filter which is integrated into the navigation processor. The roll and pitch angles are established according to the gyroscope and accelerometer data by the Kalman filter and the calculated angles are used in the e-compass to calculate heading on the basis of the tilt compensated compass equations.

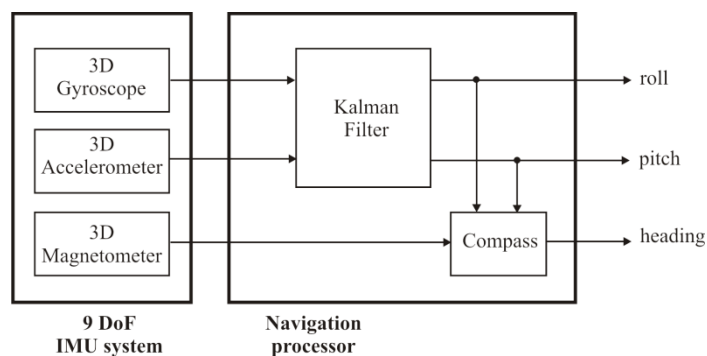


Fig. 1. Block diagram of the heading estimation system

A compass is shown at Fig. 2 with roll (θ) and pitch (ϕ) tilt angles referenced to the right and forward level directions. The X, Y, and Z magnetic readings may be transformed to the horizontal plane (X_h, Y_h) by applying the rotation equations shown in Eq. (1) [5].

$$\begin{aligned} X_h &= X \cdot \cos(\phi) + Y \cdot \sin(\theta) \cdot \sin(\phi) - Z \cdot \cos(\theta) \cdot \sin(\phi) \\ Y_h &= Y \cdot \cos(\theta) + Z \cdot \sin(\theta). \end{aligned} \quad (1)$$

¹Rosen Miletiev is with the Faculty of Telecommunications at Technical University of Sofia, 8 Kl. Ohridski Blvd, Sofia 1000, Bulgaria. E-mail: miletiev@tu-sofia.bg.

²Radostin Kenov is with the Faculty of Telecommunications at Technical University of Sofia, 8 Kl. Ohridski Blvd, Sofia 1000, Bulgaria. E-mail: rkenov@hotmail.com.

³Ivaylo Simeonov is with the Faculty of Computer Systems and Control at Technical University of Sofia, 8 Kl. Ohridski Blvd, Sofia 1000, Bulgaria. E-mail: ivosim@abv.bg.

⁴Emil Iontchev is with the Higher School of Transport "T. Kableskov" 158 Geo Milev Street, Sofia 1574, Bulgaria, E-mail: e_iontchev@yahoo.com.

Heading is defined as the angle in the local horizontal plane measured clockwise from a true North (earth's polar axis) direction. Pitch is defined as the angle between the aircraft's longitudinal axis and the local horizontal plane (positive for nose up). Roll is defined as the angle about the longitudinal axis between the local horizontal plane and the actual flight orientation (positive for right wing down) [6].

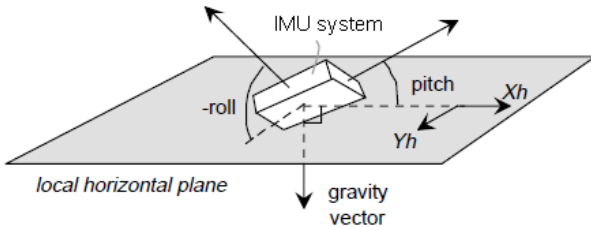


Fig. 2. Definition of the system angles

Heading is defined as the angle in the local horizontal plane measured clockwise from a true North (earth's polar axis) direction. Pitch is defined as the angle between the aircraft's longitudinal axis and the local horizontal plane (positive for nose up). Roll is defined as the angle about the longitudinal axis between the local horizontal plane and the actual flight orientation (positive for right wing down) [6].

Once the magnetic components are found in the horizontal plane, Eq. (1) can be used to determine heading. To account for the arcTan limits, the heading calculations must account for the sign of the Xh and Yh readings as shown below:

$$\begin{aligned} \text{Heading for } (X_h < 0) &= 180 - \arctan(Y_h/X_h) \\ \text{for } (X_h > 0, Y_h < 0) &= -\arctan(Y_h/X_h) \\ \text{for } (X_h > 0, Y_h > 0) &= 360 - \arctan(Y_h/X_h) \\ \text{for } (X_h = 0, Y_h < 0) &= 90 \\ \text{for } (X_h = 0, Y_h > 0) &= 270. \end{aligned} \quad (2)$$

III. COMPASS CALIBRATION

An application of electronic compasses in land vehicles poses serious problems with their installation and calibration. Magnetic disturbances from metal parts of the vehicle and its load, as well as from nearby objects passed by the vehicle may seriously affect the accuracy of measurements. The advantage of compass consists in its bounded errors, not increasing with the time of operation or the distance travelled by the vehicle.

When a two-axis (X,Y) magnetic sensor is rotated in the horizontal plane, the output plot of Xh vs. Yh will form a circle centered at the (0,0) origin. The effect of a magnetic disturbance on the heading is defined as circle distortions. Magnetic distortions may be recognized as hard iron and soft iron effects. The Hard iron distortions arise from permanent magnets on the compass platform. These distortions will remain constant and in a fixed location relative to the compass for all heading orientations therefore these effects add a constant magnitude field component along each axes of the sensor output. Hard and soft iron distortions depend from location to location within the same platform. The compass

has to be mounted permanently to its platform to get a valid calibration. A particular calibration is only valid for that location of the compass.

The calibration procedure is accomplished according to the algorithm, described at [7] which is based on the Merayo technique with a non iterative algorithm for scalar magnetometers calibration [8]. This calibration procedure tries to find the best 3D ellipsoid that fits the data set and returns the parameters of this ellipsoid. The algorithm returns the parameters of this ellipsoid (shape U and center c). The Ellipsoid equation is : $(v-c)^*(U^*U)(v-c) = 1$ with v a rough triaxes magnetometer measurement. The calibrated measurement is given by $w = U^*(v-c)$ [7].

The calibration data are extracted from the total amount of magnetic data for the specific calibration route which is a part of the test track (Fig. 3). The calibration route is chosen on the basis of its semi-circle shape and this route is passed four times to ensure the needed amount of calibration data.

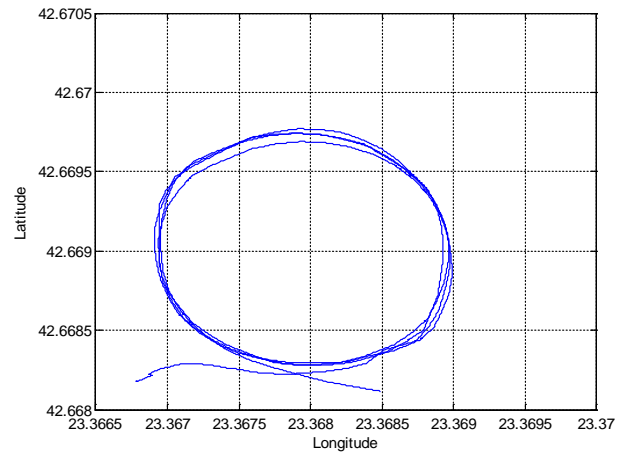


Fig. 3. The calibration route shape

As the calibration procedure is finished the calibrated magnetic data are shown at Fig. 4. The ellipsoid parameters are listed at Table I.

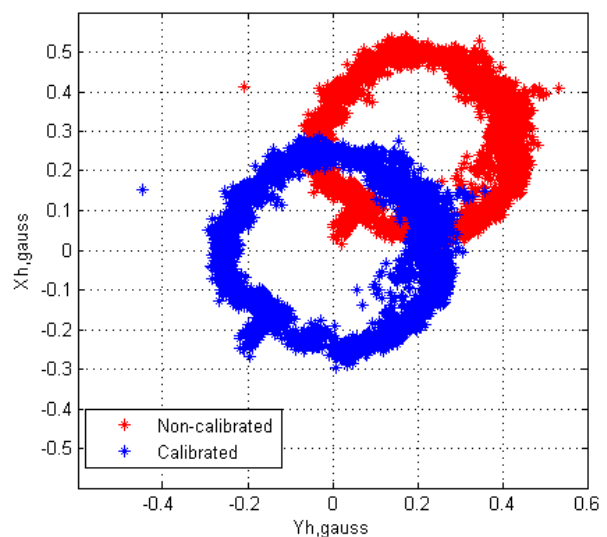


Fig. 4. Xh/Yh diagram before and after calibration

TABLE I
3D ELLIPSOID PARAMETERS

Parameter	Description	Value
a	sub axis (radius) of the X axis of the non-tilt ellipse	0.2362
b	sub axis (radius) of the Y axis of the non-tilt ellipse	0.2295
phi	orientation in radians of the ellipse (tilt)	0.7616
X0	center at the X axis of the non-tilt ellipse	0.0543
Y0	center at the Y axis of the non-tilt ellipse	0.3312
X0_in	center at the X axis of the tilted ellipse	0.2679
Y0_in	center at the Y axis of the tilted ellipse	0.2022
long axis	size of the long axis of the ellipse	0.4723
short axis	size of the short axis of the ellipse	0.4589

IV. HEADING ACCURASY ANALYSIS

The comparison analysis of the heading accuracy is accomplished by the test drive according to the track shown at Fig. 5. This test route also includes the calibration route shown at Figure 3 on the top of the tested one. This route combines a long straight line route and nearly circular calibration route. The heading calculations are made by the GPS receiver, three axes MEMS gyroscope and e-compass, calibrated according to the procedure described at the previous section.

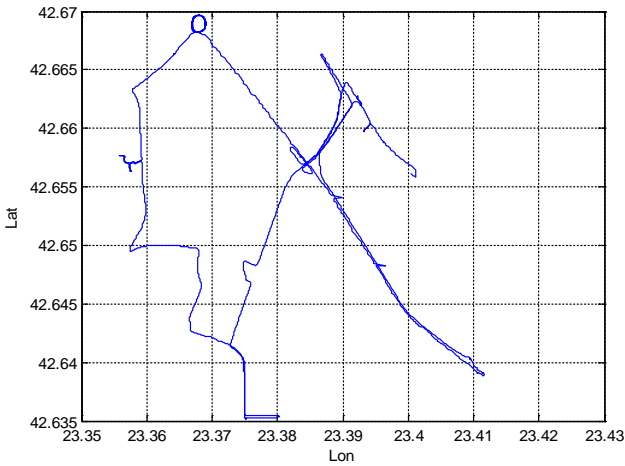


Fig. 5. The test drive track

The comparison of the short-term heading accuracy calculated by the e-compass versus GPS and gyroscope heading data is shown at Figs. 6 and 7 respectively. This comparison analysis is fulfilled on the calibration route as the e-compass is preliminary calibrated and also tilt compensated according to the roll and pitch values on the Kalman filter output. The gyroscope data are obtained after the gyroscope bias compensation according to the last gyroscope bias value

of the stationary object. The gyroscope course is calculated by the numerical integration of the compensated gyroscope data. It is clearly visible that the heading accuracy is very high of the tested navigation subsystems.

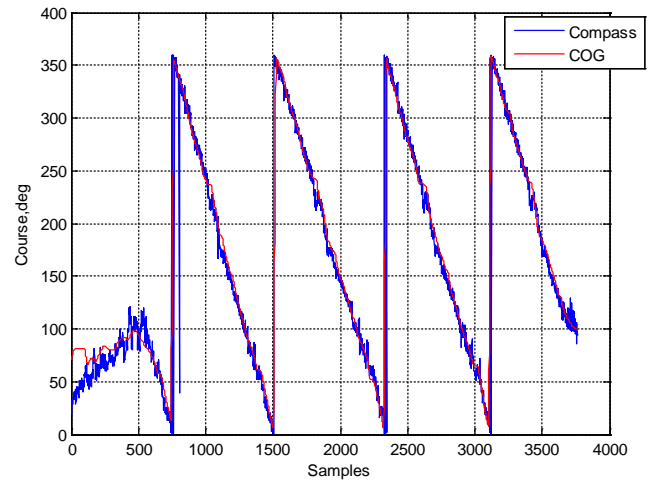


Fig. 6. Short-term heading accuracy (e-compass vs GPS receiver)

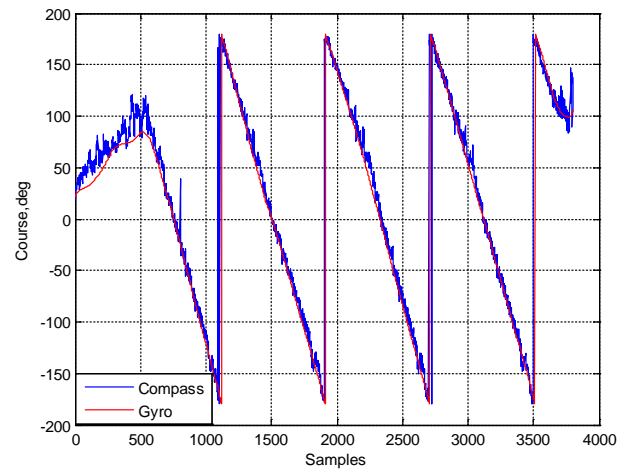


Fig. 7. Short-term heading accuracy (e-compass vs Gyro)

The comparison of the long-term heading accuracy shows slightly different picture. The heading accuracy of the e-compass remains unchanged while the object is non-stationary. Due to the high update rate of the magnetometer (up to 75Hz) the heading accuracy is higher than the GPS receiver which COG (course over ground) value is fixed at the last calculated value (Fig. 8). The long-term test also includes the short-term test shown between sample numbers $2,55 \div 2,6 \cdot 10^5$. Therefore the compass heading has long-term stability, but is noisy and requires an additional signal processing (high-pass filtering, smoothing, etc.).

In the same time the heading accuracy of the gyroscope subsystem is totally violated due to the time-varying gyroscope bias value (Fig. 9). Therefore the gyro has short-term stability but the accuracy is significantly decreased at a time which requires an adaptive gyro bias compensation.

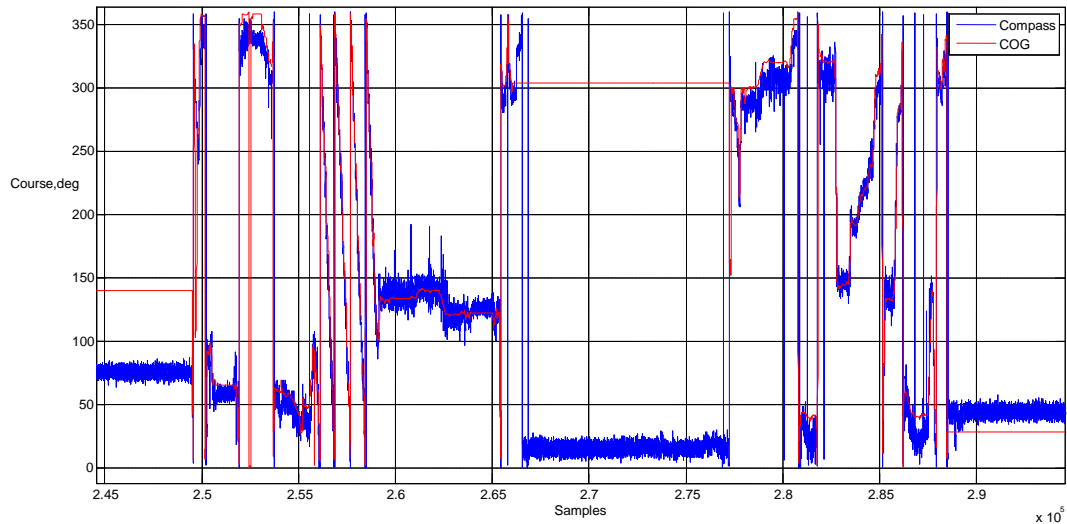


Fig. 8. Long-term heading accuracy of e-compass versus GPS data

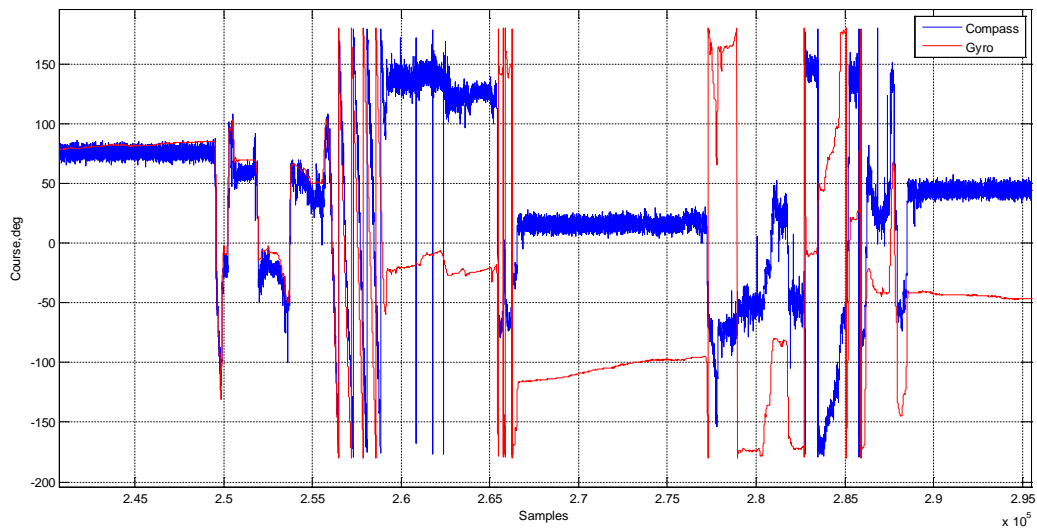


Fig. 9. Long-term heading accuracy of e-compass versus gyro data

V. CONCLUSION

The comparison analysis of the heading accuracy is accomplished using three independent subsystems – GPS receiver, tilt compensated e-compass and low cost gyro. The comparison analysis shows that the e-compass included as a subsystem in the inertial navigation systems may correctly calculate the object course for a long period of time while the gyroscope is distinguished only with a short-term accuracy and the long-term heading accuracy may be achieved only with the adaptive compensation of the bias offset. This compensation is out of the scope of this paper and will be discussed in our future work.

REFERENCES

- [1] M.J. Caruso, Applications of Magnetic Sensors for Low Cost Compass Systems, PLANS, London 2000, p. 177.
- [2] Q. Ladetto, V. Gabaglio, B. Merminod, *Combining Gyroscopes, Magnetic Compass and GPS for Pedestrian Navigation*, KIS, Banff, Canada 2001, p. 205.
- [3] J. Stephen, G. Lachapelle, *J. Navigation* 54, 297 (2001).
- [4] Electronic Tilt Compensation, Application Note AN-00MM-004, Memsic 2008.
- [5] T. Ozyagcilar - Implementing a Tilt-Compensated eCompass using Accelerometer and Magnetometer Sensors, Freescale Semiconductor, Document Number: AN4248, Rev.3, 01/2012.
- [6] M.J. Caruso, Applications of Magnetic Sensors for Low Cost Compass Systems, Honeywell, SSEC.
- [7] A. Barraud, Magnetometers calibration, 03/2009.
- [8] J. Merayo et al. "Scalar calibration of vector magnetometers", *Meas. Sci. Technol.* 11 (2000) 120-132.

Dynamic Compensation of the Gyro Bias by E-compass

Rosen Miletiev¹, Radostin Kenov², Ivaylo Simeonov³, Emil Iontchev⁴

Abstract – The paper discusses the dynamic compensation of the gyroscope bias offset based on the e-compass data. The static compensation is not very effective process because the bias offset depends from the temperature, supply voltage, chip statistics, etc. and bias instability (BI) refers to the additive error in a gyroscope's output with stochastic characteristics. The compensation is very important if the magnetic field data are lost or there are magnetic disturbances caused by soft-iron or hard-iron effects. The experiments are accomplished to proof the gyroscope bias offset compensation ability of the system.

Keywords – gyro bias, e-compass, compensation.

I. INTRODUCTION

The integration of the inertial data defines the most important problem of this navigation system – an unlimited error accumulation [1]. Typical factors, which have influence on the inertial sensor accuracy may be described as follows – null offset (bias), temperature hysteresis, gyroscope sensitivity to the linear accelerations, sampling noise, non – orthogonal sensor axes, etc. [2,3]. The additive error leads to the unlimited error accumulation due to the data integration. The bias offset is the main source of integration errors in IMU systems when velocity and distance are calculated on the bases of the accelerometer and gyroscope data. In the most of cases these errors may be grow rapidly if the bias offset is not be compensated.

In our previous paper [4] we proposed the dynamic compensation method based on the e-compass data which requires a smooth filter to eliminate data spikes generated by the differentiation step. The current paper this disadvantages is overcome by using the training and working gyroscope modes. The detection of the modes is based on the analysis of the total linear object acceleration.

II. BIAS COMPENSATION ALGORITHM

The bias compensation algorithm is based on the information of the linear accelerometer and e-compass. The

¹Rosen Miletiev is with the Faculty of Telecommunications at Technical University of Sofia, 8 Kl. Ohridski Blvd, Sofia 1000, Bulgaria. E-mail: miletiev@tu-sofia.bg.

²Radostin Kenov is with the Faculty of Telecommunications at Technical University of Sofia, 8 Kl. Ohridski Blvd, Sofia 1000, Bulgaria. E-mail: rkenov@hotmail.com.

³Ivaylo Simeonov is with the Faculty of Computer Systems and Control at Technical University of Sofia, 8 Kl. Ohridski Blvd, Sofia 1000, Bulgaria, E-mail: ivosim@abv.bg.

⁴Emil Iontchev is with the Higher School of Transport “T. Kableskov” 158 Geo Milev Street, Sofia 1574, Bulgaria, E-mail: e_iontchev@yahoo.com.

system calculates the pitch, roll and yaw angles (Fig. 1) by means of the Kalman filter and e-compass. The corrected Z gyro data are calculated by subtraction of the raw Z gyro data with the last known mean value while the switch was closed.

If the object is stationary for a certain period of time (n_{lim} samples) the switch is closed (Fig. 1) and the raw gyro data are integrated for time duration τ_u . The obtained calculated heading angle is compared with the e-compass heading angle and the result rotation angle is divided to the integration time to calculate the average gyro bias value which is subtracted from the raw data. If the object is non-stationary the last obtained average gyro value is not updated until the object become stationary again. The state of the object is detected according to the total linear acceleration $A = \sqrt{A_x^2 + A_y^2 + A_z^2}$

(Fig. 2). If this acceleration exceeds the given threshold value A_{lim} then the object is defined as non-stationary and the switch is opened. In this case the correction is made by the last known bias value.

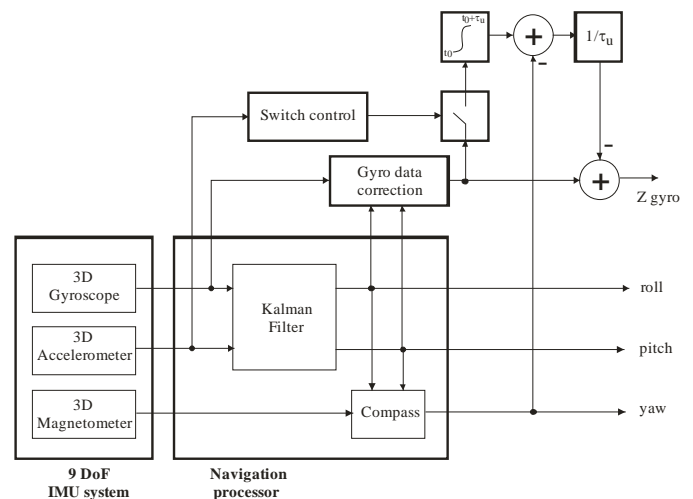


Fig. 1. Bias compensation algorithm

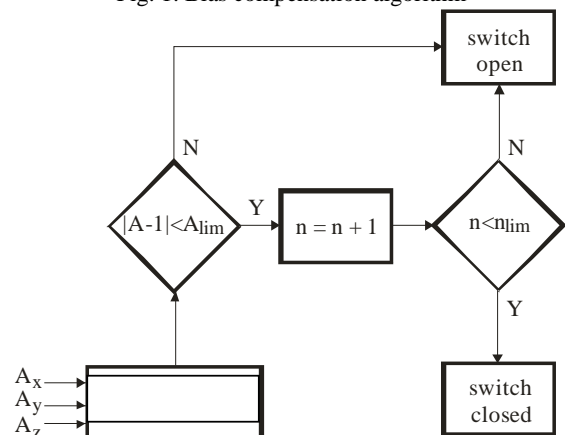


Fig. 2. Switch control algorithm

The bias calculation algorithm is accomplished after the gyro correction block. The data are corrected on the basis of the object tilt angles according to the equations (Fig. 3).

$$\begin{bmatrix} \dot{\phi}(t) \\ \dot{\theta}(t) \\ \dot{\psi}(t) \end{bmatrix} = \begin{bmatrix} 1 & \sin \phi(t) \tan \theta(t) & \cos \phi(t) \tan \theta(t) \\ 0 & \cos \phi(t) & -\sin \phi(t) \\ 0 & \frac{\sin \phi(t)}{\cos \theta(t)} & \frac{\cos \phi(t)}{\cos \theta(t)} \end{bmatrix} \begin{bmatrix} \omega_{\phi}(t) \\ \omega_{\theta}(t) \\ \omega_{\psi}(t) \end{bmatrix}$$

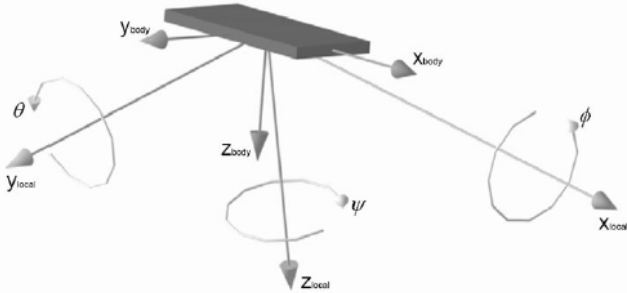


Fig. 3. Gyro data tilt compensation [5]

The proposed algorithm is tested using the hardware platform described in our previous paper [4].

III. EXPERIMENTAL DATA ANALYSIS

The comparison analysis of the bias compensation is accomplished by the test drive. The inertial data are measured using a sampling frequency equal to 20Hz and the total measurement time is set to 18000s which corresponds to $3,6 \cdot 10^5$ data samples. The threshold values A_{lim} and n_{lim} are set to 0.1 and 1200 respectively.

The data analysis results of the switch control algorithm is shown at Fig. 4 and the Z angular acceleration graphics before and after bias compensation is shown at Fig. 5. The result of the comparison analysis between the proposed algorithm and the static compensation are written at Table I and are illustrated at Fig. 6.

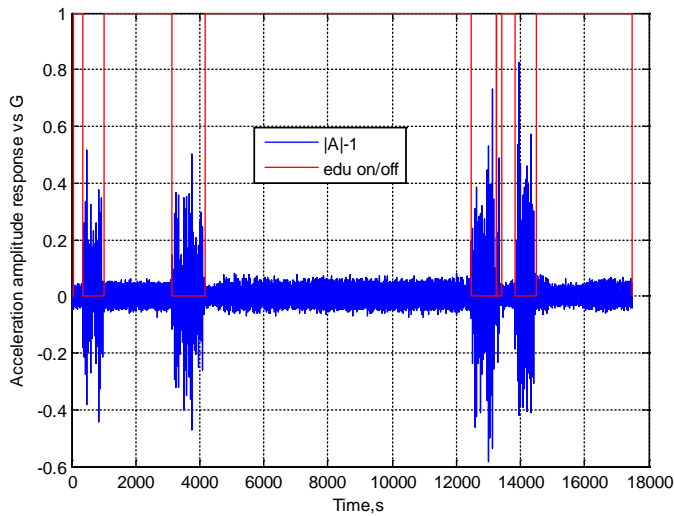


Fig. 4. Illustration of the switch control algorithm

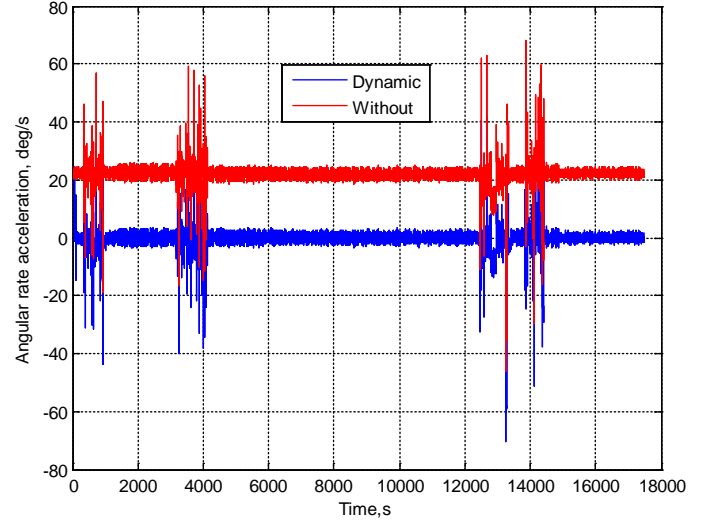


Fig. 5. Angular acceleration graphics before and after dynamic bias compensation

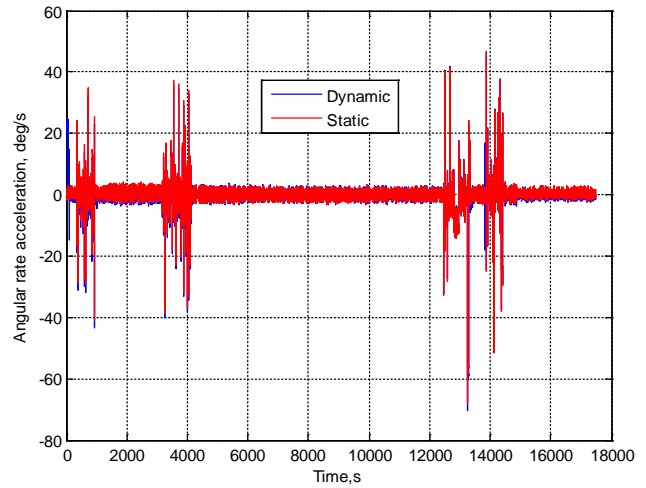


Fig. 6. Angular acceleration graphics with static and dynamic compensation

TABLE I
EXPERIMENTAL RESULT SUMMARY

Sample interval*	Gyro bias, deg/s		
	Without ompensation	With static compensation	With dynamic compensation
$1 \dots 6 \cdot 10^3$	22,705	$8,60 \cdot 10^{-1}$	$4,50 \cdot 10^{-3}$
$2 \cdot 10^4 \dots 6 \cdot 10^4$	22,477	$6,19 \cdot 10^{-1}$	$-1,79 \cdot 10^{-2}$
$9 \cdot 10^4 \dots 2,4 \cdot 10^5$	21,856	$-7,48 \cdot 10^{-14}$	$1,55 \cdot 10^{-6}$
$3 \cdot 10^5 \dots 3,5 \cdot 10^5$	22,229	$3,72 \cdot 10^{-1}$	$2,62 \cdot 10^{-5}$

*time intervals may be calculated by a sample interval divided by 20 (sampling frequency).

The static compensation is accomplished on the basis of the bias calculation between sample numbers $9 \cdot 10^4 \dots 2,4 \cdot 10^5$. In this sample interval the bias is fully compensated by the static compensation but in the other interval the bias values vary from 10^{-1} to 10^0 deg/s. In the same time the bias values are below 10^{-2} deg/s in all tested intervals.

IV. CONCLUSION

The current paper describes a gyro bias compensation algorithm which is based on the calculation of the mean value when the object is stationary according to the e-compass heading angle data. The object state is detected according to the total linear acceleration and the acceleration threshold. If the object is non-stationary the raw gyro data are processed by tilt compensation algorithm initially and bias compensation algorithm after that. If the object remains stationary for a certain period of time a new bias value is calculated.

The comparison analysis results show that the dynamic compensation algorithm reduces the bias values from 10^1 to 10^4 times compared to the static compensation.

REFERENCES

- [1] M.S. Grewal, L.R. Weil, A.P. Andrews, "Global Positioning Systems, Inertial navigation, and Integration", John Wiley & Sons, Inc., 2001.
- [2] B.W. Parkins, J.J. Spilker, Eds., *Global Positioning System: Theory and Applications*, Washington, DC: Amer. Inst. Aeronautics Astronautics, 1996, vol. II.
- [3] K.J. Walchko, "Low Cost Inertial Navigation: Learning To Integrate Noise And Find Your Way", A Master Of Science Thesis, University Of Florida, 2002.
- [4] R. Miletiev, R. Kenov, I. Simeonov, E. Iontchev, "Dynamic compensation of the gyroscope bias offset", XLVIII International Scientific Conference on Information, Communication and Energy Systems and Technologies ICEST 2013, 26 - 29 June 2013, Volume 1, pp.117-120.
- [5] E. Hadri, A. Benallegue, "Attitude estimation with gyros-bias compensation using low-cost sensors", Joint 48th IEEE Conference on Decision and Control and 28th Chinese Control Conference, Shanghai, P.R. China, December 16-18, 2009, pp.8077 – 8082.

Study on Control System of Permanent Magnet Linear Synchronous Motor

Bojidar Gueorguev Markov¹ and Vesko Krumov Panov²

Abstract – The study is forced on behaviour of control system of a linear synchronous motor at different loads and different speeds. Modelling and simulation is performed in Simulink environment. The proposed control model can be used as a dynamic study basis for linear synchronous motors with permanent magnets.

Keywords – Linear synchronous motor, Dynamic model, System control, Load, Speed.

I. INTRODUCTION

Approximately 50% of the produced energy is used for electric drives of different industrial systems [2]. Exceptional variety in the range of power and control could be recognized among the systems of automatic electric drive.

The automatic control systems for electric drive feature wide range of speed control; excellent control accuracy of the coordinates, speed and security; economy; good communication devices; easy service and maintenance; ecology etc.

In modern productions a number of auxiliary devices are built such as various sensors for speed feedback and position (precisious tacho generators, impulse sensors, code sensors, resolvers, etc.), electromechanical brakes, fan with forced cooling, driving screws, gearboxes etc [3].

These elements can increase additionally the fluctuations in the mechanisms, complicate the design and lead to greater complexity in managing with lower reliability.

Last decade was dedicated to different applications of linear motors. Driving systems for transport and material handling using linear motors now are part of the so-called gearless design.

Difficulties for large-scale production of linear drives are still high costing and difficult in preparing linear motors with an arbitrary profile and length. In addition, the magnets in the linear synchronous motors are made of expensive and rare metal. It is expected that prices of magnets will decline in response to the fast-paced production and development of technologies producing magnets [4]. The price of the linear motor depends on the length of the motor, and it is a 1.5 to 3 times higher than that of traditional rotary motor [7]. Despite these shortcomings, the interest in the deployment of linear drives in the industry is constantly growing. Growth of

interest in the usage of linear drives during the period between 1992-2005 can be seen on Fig. 1 [6]. For this period 272 presentations were published at the conference; 51 reports in magazines, which concerned the linear drives; three magazines have each published 2 reports of the conference with control plus linear motor in the title.

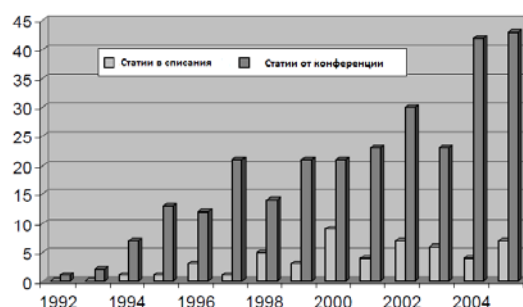


Fig. 1. Number of publications in which appears the name of the linear motor appears and their control according to IEEE Xplore

The main aim of the study is to create a simulation mathematical model in Simulink environment of the system control of linear synchronous motor with permanent magnets.

II. METHODS AND MEANS OF RESEARCH

The method which is applied to consider the dynamics of linear synchronous motor systems is based on principles of vector control. The means of the research is simulation modeling using Simulink system and SimPowerSystem.

III. MATHEMATICAL DESCRIPTION OF THE DYNAMIC MODEL OF THE LINEAR SYNCHRONOUS MOTOR WITH PERMANENT MAGNETS

The angular velocity of the linear synchronous motor with permanent magnets is connected to the linear synchronous speed of the motor by following equation [4], [5]:

$$\omega_e = \frac{\pi v}{\tau}, \quad (1)$$

where v - is a linear speed of movement; τ - poles pitch.

The equation of the electromagnetic balance can be written in the following form:

$$\vec{u} = R\vec{i} + \frac{d\vec{\lambda}}{dt} - \vec{\omega} \times \vec{\lambda}, \quad (2)$$

where $\vec{\omega} \times \vec{\lambda}$ - is the rate of change of voltage in a rotating magnetic field.

¹Bojidar Gueorguev Markov is with the Technical Faculty at University of Food Technology of Plovdiv, 26 Maritca Blvd, Plovdiv 4002, Bulgaria, e-mail: bojmarkov@abv.bg.

²Vesko Krumov Panov is with the Faculty of Mechanical Engineering at Technical University of Sofia, 8 Kl. Ohridski Blvd, Sofia 1000, Bulgaria.

Presenting scalar components of vector (2) on the axes d and q we can obtain voltage equations of linear synchronous motor with permanent magnets as follows:

$$\begin{cases} u_d = R \cdot i_d + L_d \frac{di_d}{dt} - \omega_e \cdot L_q \cdot i_q \\ u_q = R \cdot i_q + L_q \frac{di_q}{dt} + \omega_e L_d \cdot i_d + \lambda_f \cdot \omega_e \end{cases}, \quad (3)$$

where

u_d, u_q - are d, q axis stator voltage;

i_d, i_q - d, q axis stator current;

L_d, L_q - d, q-axis armature self-inductance;

R - stator winding resistance;

ω_e - angular velocity;

λ_f - flux linkage of permanent magnet.

The instantaneous electromagnetic power can be expressed by:

$$p_{em} = \frac{3}{2} \cdot \omega_e \cdot [\lambda_f + (L_d - L_q) i_d] i_q, \quad (4)$$

where p_{em} - is instantaneous electromagnetic power.

Linear force on the horizontal axis is determined by the formula:

$$F_x = \frac{p_{em}}{v} = \frac{3}{2} \cdot p \cdot \frac{\pi}{\tau} (\lambda_d \cdot i_q - \lambda_q \cdot i_d), \quad (5)$$

where p - is a pole pairs.

Linear force of the system in the present article is carried by the laws of vector control of electric motors. If the motor inductance is small as in the present study, the control of the flux will not give the desired result. A suitable method for control is, if the engine is controlled by the axis q, i.e. constancy of the vector in the inductor current. In this case it is assumed that the current in the axis d equals zero, i.e. $i_d = 0$.

Adopting this type of control, the equation of the electromagnetic force (5) is transformed into the following form:

$$F_x = \frac{p_{em}}{v} = \frac{3}{2} \cdot p \cdot \frac{\pi}{\tau} \cdot \lambda_d \cdot i_q. \quad (6)$$

The angle θ is determined by the formula:

$$\theta = \frac{d\omega}{dt} = \frac{\pi}{\tau} \cdot \frac{dv}{dt}. \quad (7)$$

A. Design of the System in Simulink Environment

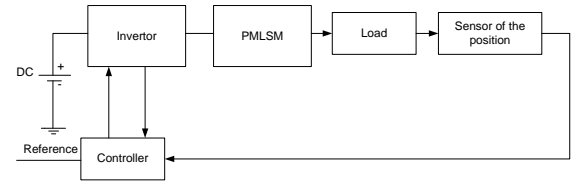


Fig. 2. Schematic control of linear synchronous motor with permanent magnets

The elements of the above shown scheme have the following realization in Simulink environment:

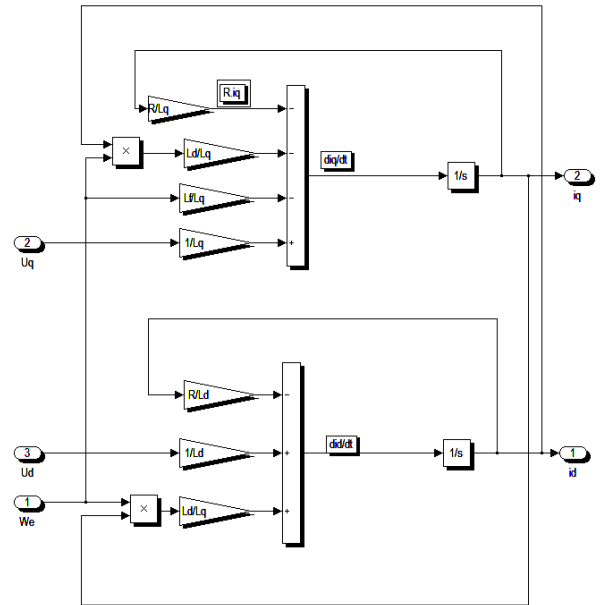


Fig. 3. Realization of voltage equations in Simulink environment

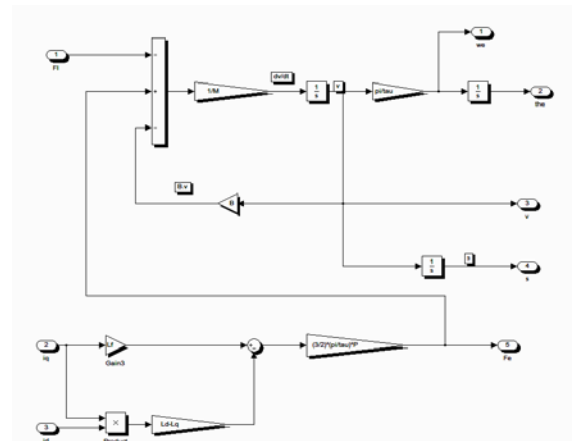


Fig. 4. Realization of the electromechanical part of a linear synchronous motor with permanent magnets in the Simulink environment

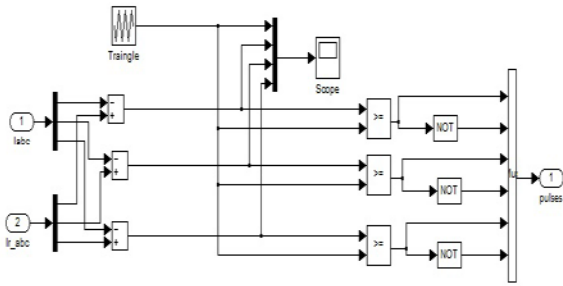


Fig. 5. Realization of the controller in the Simulink environment

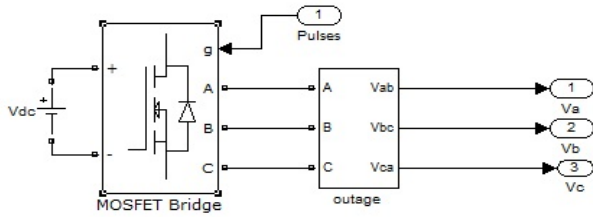


Fig. 6. Realization of the inverter in Simulink environment

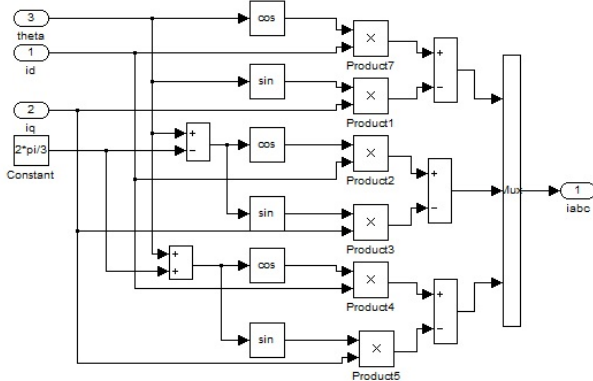


Fig. 7. Realization of modules for conversion of two-phase rotating frame into three-phase rotating frame

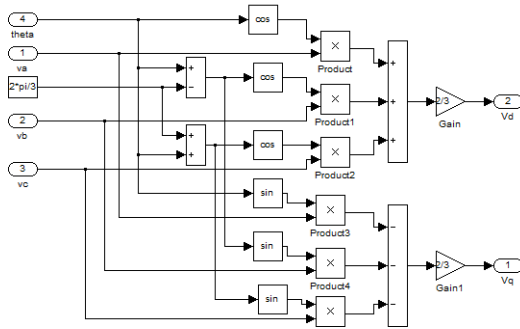


Fig. 8. Realization of the module for converting the three-phase coordinate system into a two-phase coordinate system

$B = 0,2 \text{ N.s/m}$; $M = 10 \text{ kg}$. Frequency of the inverter is 6000Hz .

The study is constructed by two essential cases, namely:

1. Constant speed and variable load,
2. Variable speed and variable load.

The results obtained in the simulation are presented in Figs. 9 and 10.

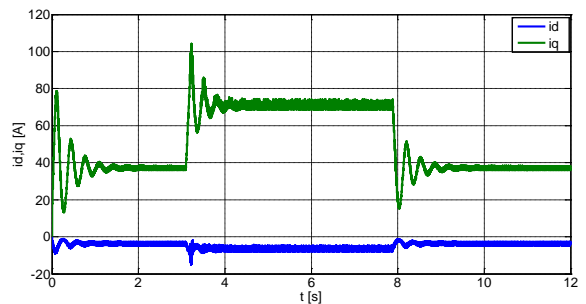
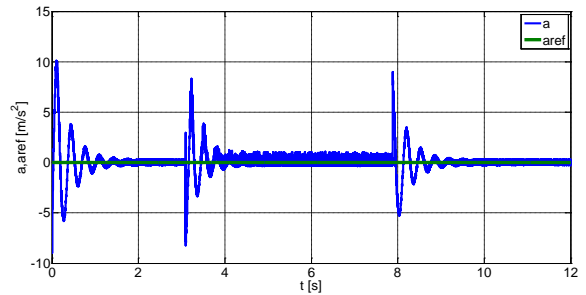
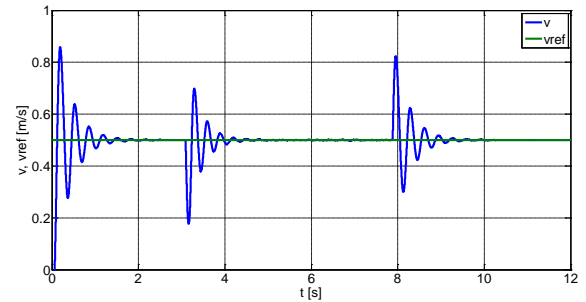
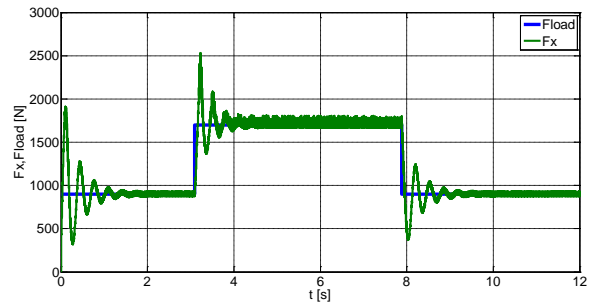


Fig. 9. Testing at a constant speed and variable load

IV. RESULTS AND DISCUSSION

Tested was performed by permanent magnets linear synchronous motor with the following data: $R = 3,2 \Omega$; $L_d = L_q = 8 \text{ mH}$; $\lambda_f = 83 \text{ Wb}$; $\tau = 33 \text{ mm}$; $p = 2$;

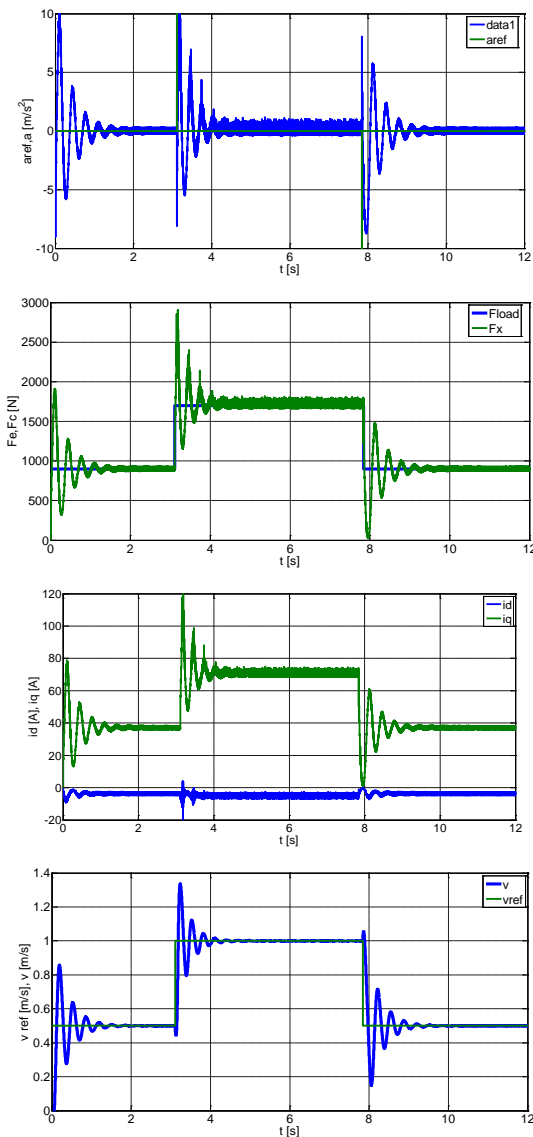


Fig. 10. Testing at variable speed and variable load

From simulations it can be seen that irrespectively of the reference speed and load, the engine is working job, and speed, and a force in the second half. The axis d current remains close to zero regardless of the load.

V. CONCLUSION

1. A simulation model of a control system of a linear synchronous motor with permanent magnets is developed.
2. The proposed control model can be used as a study basis for the dynamics of the linear synchronous motors with permanent magnets

REFERENCES

- [1] C.M. Ong, *Dynamic Simulation of Electric Machinery Matlab/Simuling*, Prentice-Hall, 1998.
- [2] B.K. Bose, "Power Electronics and AC Drives", Springer-Verlag, 1995.
- [3] K.L. Shi, T.F. Chan, Y.K. Wong, "Modeling of three-phase Induction Motor using Simulink", IEEE International Electrical Machines and Drives Conference IEMDC 2007, Wisconsin.
- [4] J.F. Gieras, Z.J. Piech, B.Z. Tomczuk, "Linear Synchronous motors: Transportation and Automation Systems", USA. CRC press LLC. 327 p. ISBN 0-8493-1859-9, 2000.
- [5] S.A. Nasar, I. Boldea, *Linear Electric Motors: Theory, Design, and Practical Applications*, Prentice-Hall, New Jersey, 1987.
- [6] IEEE Xplore release 2.1. Retrieved April 4, 2006, from <http://ieeexplore.ieee.org/>.
- [7] Permanent Magnets. - Financial Results & Limited Review for Dec 31, 2012 Mon, 14 Jan 2013 11:01:00.
- [8] Field Orientated Control of 3-Phase AC-Motors, Applikationsschrift BPRA073, Texas Instruments Europe, 1998.

Modular Development of Linear Induction Motor Control in Simulink Environment

Bojidar Gueorguev Markov

Abstract –In this paper, a modular Simulink implementation of a linear induction machine model is described in a step-by-step approach. With the modular system, each block solves one of the model equations; therefore, unlike black box models, all of the machine parameters are accessible for control and verification purposes. After the implementation, examples are given with the model used in different drive applications, such as open-loop constant V/Hz control.

Keywords – Linear induction motor, dynamic system, modular development, Simulink model.

I. INTRODUCTION

The modern adjustable frequency AC electric drive, in particular a linear induction drives, controlled by converter and programmable microcontroller. The advantage of linear drives is their works without gearbox and other transmission for transformation a rotation torque to linear force. The control of linear drives has small size and weight of the converter, ultimate protection, the ability to diagnose the state of the drive, the drive control of analog and digital signals, easy programming of work, ability to synchronize the joint work of the drives involved in the process and a number of other advantages are that opportunity for the mass deployment of frequency- adjustable asynchronous electric in practice. If not the straight requirements by the electrical drive in terms of range and accuracy of speed control it using simple schemes for scalar frequency regulation without speed feedback. These circuits operate on the principle U/f control with various ratios between of voltage and frequency. Creation of adequate models of frequency asynchronous electric drives, allow you to predict the behavior of the electric frequency. One possibility for modeling and management is driven by in Simulink environment. Simulink models of linear induction motors in are shown in [1-3], but these models are shown as "black boxes" without showing interconnections. Some of them [1-3] recommend using S-functions, which are software source codes for Simulink blocks. This technique does not fully utilize the power and ease of Simulink because S-function programming knowledge is required to access the model variables. S-functions run faster than discrete Simulink blocks, but Simulink models can be made to run faster using "accelerator" functions or producing stand-alone Simulink models. Both of these require additional expense and can be avoided if the simulation speed is not that critical. Another approach for traditionally induction motors is using the

Bojidar Gueorguev Markov is with the Technical Faculty at University of Food Technologies of Plovdiv, 26 Maritza Blvd, Plovdiv 4002, Bulgaria, e-mail: bojmarkov@abv.bg.

Simulink Power System [4] that can be purchased with Simulink. This blockset also makes use of S-functions and is not as easy to work with as the rest of the Simulink blocks. Reference [5] refers to an implementation approach similar to the one in this paper but fails to give any details. On the other side in this module doesn't have linear motor. In this paper, a modular, easy to understand Simulink linear induction motor model is described. With the modular system, each block solves one of the model equations therefore, unlike black box models, all of the machine parameters are accessible for control and verification purposes. Simulink induction machine model discussed in this paper has been featured in a recent graduate level text book [5], and it also has been used in [4-5], and [4-5] in their research.

II. LINEAR INDUCTION MOTOR MODEL

The linear induction machine d-q or dynamic equivalent circuit is shown in Fig. 1.

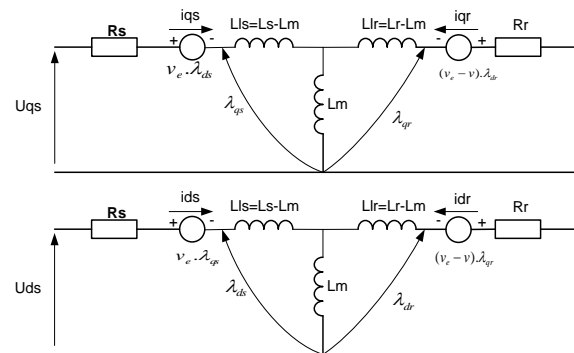


Fig.1. Dynamic model of linear induction motor

According to his model, the modeling equations in flux linkage form are as follows:

Equations should be centred and labelled. The example of equations is Eq. (1),

$$\frac{dF_{qs}}{dt} = v_b \cdot \left[U_{qs} - \frac{v_e}{v_b} \cdot F_{ds} + \frac{R_s}{x_{ls}} \cdot (F_{mq} + F_{qs}) \right] \quad (1)$$

$$\frac{dF_{ds}}{dt} = v_b \cdot \left[U_{ds} + \frac{v_e}{v_b} \cdot F_{qs} + \frac{R_s}{x_{ls}} \cdot (F_{md} + F_{ds}) \right] \quad (2)$$

$$\frac{dF_{qr}}{dt} = v_b \cdot \left[-\frac{(v_e - v)}{v_b} \cdot F_{dr} + \frac{R_r}{x_{lr}} \cdot (F_{mq} - F_{qr}) \right] \quad (3)$$

$$\frac{dF_{dr}}{dt} = v_b \cdot \left[\frac{(v_e - v)}{v_b} \cdot F_{qr} + \frac{R_r}{x_{lr}} \cdot (F_{md} - F_{dr}) \right] \quad (4)$$

$$F_{mq} = x_{ml}^* \left[\frac{F_{qs}}{x_{ls}} + \frac{F_{qr}}{x_{lr}} \right] \quad (5)$$

$$F_{md} = x_{ml}^* \left[\frac{F_{ds}}{x_{ls}} + \frac{F_{dr}}{x_{lr}} \right] \quad (6)$$

$$i_{qs} = \frac{1}{x_{ls}} \cdot (F_{qs} - F_{mq}) \quad (7)$$

$$i_{ds} = \frac{1}{x_{ls}} \cdot (F_{ds} - F_{md}) \quad (8)$$

$$i_{qr} = \frac{1}{x_{lr}} \cdot (F_{qr} - F_{mq}) \quad (9)$$

$$i_{dr} = \frac{1}{x_{lr}} \cdot (F_{dr} - F_{md}) \quad (10)$$

$$F_e = \frac{3}{2} \cdot \left(\frac{p}{2} \right) \cdot \left(\frac{\pi}{\tau} \right) \cdot \frac{1}{v_b} \cdot (F_{ds} \cdot i_{qs} - F_{qs} \cdot i_{ds}) \quad (11)$$

$$F_e - F_c = M \cdot \left(\frac{2}{p} \right) \frac{dv}{dt} \quad (12)$$

where,

d, q - axes of d, q coordinate reference frame;

s - primary variable;

r - secondary variable;

F_{ij} - the flux linkage ($i=q$ or d and $j=s$ or r);

U_{qs}, U_{ds} - q and d -axis primary voltages;

F_{mq}, F_{md} - q and d axis magnetizing flux linkages;

R_r, R_s - active secondary and primary resistances;

$x_{ls} = 2 \cdot f \cdot \tau \cdot L_{ls}$ - primary leakage reactance;

$x_{lr} = 2 \cdot f \cdot \tau \cdot L_{lr}$ - secondary leakage reactance;

$$x_{ml}^* = 1 / \left(\frac{1}{x_m} + \frac{1}{x_{ls}} + \frac{1}{x_{lr}} \right);$$

i_{qs}, i_{ds} - q and d -axis primary currents; i_{qr}, i_{dr} - q and d -axis secondary currents;

M - mass of the linear induction motor;

p - number of poles;

τ - pole pitch;

F_e - linear force;

F_c - load force;

$v_e = 2 \cdot \tau \cdot f$ - primary linear speed;

v_b - motor linear electrical base speed;

v - secondary linear speed.

The model of the linear induction motor can be represented by five differential equations shown above. To solve these equations, they must be presented in the form of state

equation, i.e.: $\dot{x} = A \cdot x + b$, where

$x = [F_{qs} \ F_{ds} \ F_{qr} \ F_{dr} \ v]^T$ is a state vector. Note that

$F_{ij} = \lambda_{ij} \cdot \omega_b$ where F_{ij} is the flux linkage ($i=q$ or d and $j=s$ or r) and λ_{ij} is the flux.

In this case, state-space form can be achieved by inserting (5) and (6) in (1-4) and collecting the similar terms together so that each state derivative is a function of only other state variables and model inputs. Then, the modeling Eqs. (1-4) and (12) of a squirrel cage induction motor in state-space become:

$$\frac{dF_{qs}}{dt} = v_b \left[U_{qs} - \frac{v_e}{v} \cdot F_{ds} + \frac{R_s}{x_{ls}} \cdot \left(\frac{x_{ml}^*}{x_{lr}} \cdot F_{qr} + \left(\frac{x_{ml}^*}{x_{ls}} - 1 \right) \cdot F_{qs} \right) \right] \quad (13)$$

$$\frac{dF_{ds}}{dt} = v_b \left[U_{ds} - \frac{v_e}{v} \cdot F_{qs} + \frac{R_s}{x_{ls}} \cdot \left(\frac{x_{ml}^*}{x_{lr}} \cdot F_{dr} + \left(\frac{x_{ml}^*}{x_{ls}} - 1 \right) \cdot F_{ds} \right) \right] \quad (14)$$

$$\frac{dF_{qr}}{dt} = v_b \left[-\frac{(v_e - v)}{v_b} \cdot F_{ds} + \frac{R_r}{x_{lr}} \cdot \left(\frac{x_{ml}^*}{x_{lr}} \cdot F_{qs} + \left(\frac{x_{ml}^*}{x_{lr}} - 1 \right) \cdot F_{qr} \right) \right] \quad (15)$$

$$\frac{dF_{dr}}{dt} = v_b \left[\frac{(v_e - v)}{v_b} \cdot F_{qr} + \frac{R_r}{x_{lr}} \cdot \left(\frac{x_{ml}^*}{x_{ls}} \cdot F_{qr} + \left(\frac{x_{ml}^*}{x_{lr}} - 1 \right) \cdot F_{dr} \right) \right] \quad (16)$$

$$\frac{dv}{dt} = \left(\frac{p}{2 \cdot M} \right) \cdot (F_e - F_c) \quad (17)$$

III. SIMULINK IMPLEMENTATION OF MODEL OF INDUCTION MOTOR

The inputs of a linear induction machine are the three-phase voltages, their fundamental frequency, and the load torque. The outputs, on the other hand, are the three-phase currents, and the secondary linear speed. The d - q model requires that all the three-phase variables have to be transformed to the two-phase synchronously rotating frame. Consequently, the linear induction machine model will have blocks transforming the three-phase voltages to the d - q frame and the d - q currents back to three-phase. The linear induction machine model implemented in this paper is shown in Fig. 2. It consists of five major blocks: the o - n conversion, abc - syn conversion, syn - abc conversion, unit vector calculation, and the induction machine d - q model blocks.

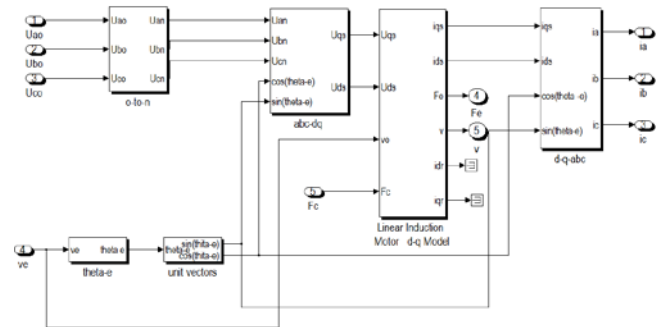


Fig. 2. The completed induction machine Simulink model

A. o-n block

This block is used for an isolated neutral system, otherwise it can be bypassed. The transformation done by this block can be represented as follows:

$$\begin{bmatrix} U_{an} \\ U_{bn} \\ U_{cn} \end{bmatrix} = \frac{1}{3} \begin{bmatrix} 2 & -1 & -1 \\ -1 & 2 & -1 \\ -1 & -1 & 2 \end{bmatrix} \begin{bmatrix} U_{a0} \\ U_{b0} \\ U_{c0} \end{bmatrix} \quad (18)$$

This is implemented in Simulink by passing the input voltages through a Simulink “Matrix Gain” block, which contains the above transformation matrix.

B. Unit vector calculation block

Unit vectors $\cos \theta_e$ and $\sin \theta_e$ are used in vector rotation blocks, “abc-syn conversion block” and “syn-abc conversion block”. The angle θ_e is calculated directly by integrating the frequency of the input three-phase voltages:

$$\theta_e = \int \omega_e dt, \quad (19)$$

where $\omega_e = (\pi / \tau) \cdot v$

The unit vectors are obtained simply by taking the sine and cosine of θ_e . This block is also where the initial rotor position can be inserted, if needed, by adding an initial condition to the Simulink “Integrator” block. Note that the result of the integration in (19) is reset to zero each time it reaches 2π radians so that the angle always varies between 0 and 2π .

C. abc-syn conversion block

To convert three-phase voltages to voltages in the two-phase synchronously rotating frame, they are first converted to two-phase stationary frame using (20) and then from the stationary frame to the synchronously rotating frame using (21).

$$\begin{bmatrix} U_{qs}^s \\ U_{ds}^s \end{bmatrix} = \begin{bmatrix} 1 & 0 & 0 \\ 0 & -\frac{1}{\sqrt{3}} & \frac{1}{\sqrt{3}} \end{bmatrix} \begin{bmatrix} U_{an} \\ U_{bn} \\ U_{cn} \end{bmatrix} \quad (20)$$

$$\begin{bmatrix} U_{qs} \\ U_{ds} \end{bmatrix} = \begin{bmatrix} \cos \theta_e & -\sin \theta_e \\ \sin \theta_e & \cos \theta_e \end{bmatrix} \begin{bmatrix} U_{qs}^s \\ U_{ds}^s \end{bmatrix} \quad (21)$$

where the superscript “s” refers to stationary frame. Eq. (20) is implemented similar to (18) because it is a simple matrix

transformation. Eq. (21), however, contains the unit vectors; therefore, a simple matrix transformation cannot be used. Instead, U_{ds} and U_{qs} are calculated using basic Simulink “Sum” and “Product” blocks.

D. syn-abc conversion block

This block does the opposite of the abc-syn conversion block for the current variables using (22) and (23) following the same implementation techniques as a point C:

$$\begin{bmatrix} i_{qs}^s \\ i_{ds}^s \end{bmatrix} = \begin{bmatrix} \cos \theta_e & \sin \theta_e \\ -\sin \theta_e & \cos \theta_e \end{bmatrix} \begin{bmatrix} i_{qs} \\ i_{ds} \end{bmatrix} \quad (22)$$

$$\begin{bmatrix} i_a \\ i_b \\ i_c \end{bmatrix} = \begin{bmatrix} 1 & 0 \\ -\frac{1}{2} & -\frac{\sqrt{3}}{2} \\ -\frac{1}{2} & \frac{\sqrt{3}}{2} \end{bmatrix} \begin{bmatrix} i_{qs}^s \\ i_{ds}^s \end{bmatrix} \quad (23)$$

E. Linear induction machine d-q model block

Fig. 3 shows the inside of this block where each equation from the induction machine model is implemented in a different block. First consider the flux linkage state equations because flux linkages are required to calculate all the other variables. These equations could be implemented using Simulink “State-space” block, but to have access to each point of the model, implementation using discrete blocks is preferred. Fig. 4 shows what is inside of the block solving (1). All the other blocks in Column 1 are similar to this block.

Once the flux linkages are calculated, the rest of the equations can be implemented without any difficulty. The blocks solving the rest of the equations are also organized in columns. The blocks in Column 2 solve (5) and (6). Eqs. (7-10) use the flux linkages to solve for the stator and rotor d and q currents. The fourth and the last column includes the electrical force calculation from (11) and the secondary element linear speed calculation using the last state Eq. (12); the implementation of which is shown in Fig. 5. The rotor speed information is required for the calculation of the secondary element flux linkages in Column 1; therefore, it is fed back to two blocks in this column. The resulting model is modular and easy to follow. Any variable can be easily traced using the Simulink ‘Scope’ blocks. The blocks in the first two columns calculate the flux linkages, which can be used in vector control systems in a flux loop. The blocks in Column 3 calculate all the current variables, which can be used in the current loops of any current control system and to calculate the three-phase currents. The two blocks of Column 4, on the other hand, calculate the torque and the speed of the linear induction machine, which again can be used in force control or speed control loops. These two variables can also be used to calculate the output power of the machine.

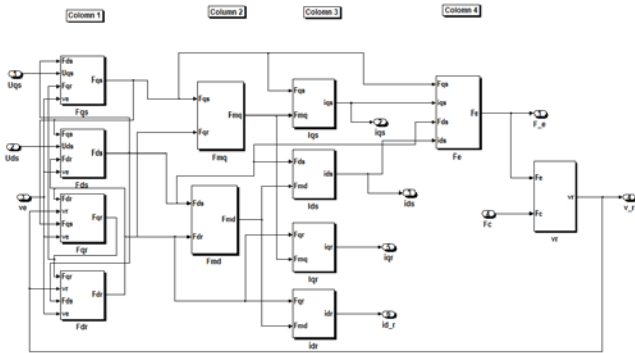


Fig. 3. Linear induction motor dynamic model in Simulink

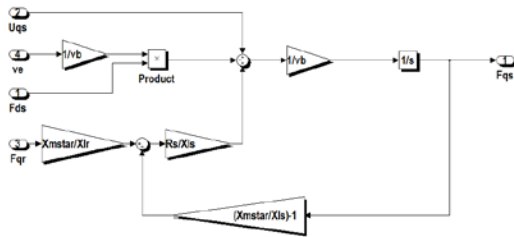


Fig. 4. Implementation one of module in column (1)

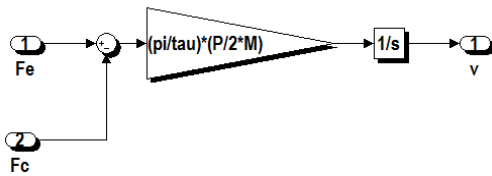


Fig. 5. Implementation of (12) in Simulink

IV. SIMULATION RESULTS

Fig. 6 shows the implementation of open-loop constant V/Hz control of a linear induction machine. This figure has two new blocks: command voltage generator and 3-phase PWM inverter blocks. The first one generates the three-phase voltage commands, and it is nothing more than a “syn-abc” block explained earlier. The latter first compares the reference voltage, v_{ref} to the command voltages to generate PWM signals for each phase, then uses these signals to drive three Simulink “Switch” blocks switching between $+V_d/2$ and $-V_d/2$ (V_d is dc link voltage). The open-loop constant V/Hz operation is simulated for 1.2s ramping up and down the speed command and applying step load torques. The results are plotted in Fig. 7 where the response of the drive to changes in the speed command and load disturbances can be observed.

V. CONCLUSION

In this paper, implementation of a modular Simulink model for linear induction machine simulation has been introduced. Unlike most other linear induction machine model implementations, with this model, the user has access to all the internal variables for getting an insight into the machine

operation. Any machine control algorithm can be simulated in the Simulink environment with this model without actually using estimators. If need be, when the estimators are developed, they can be verified using the signals in the machine model.

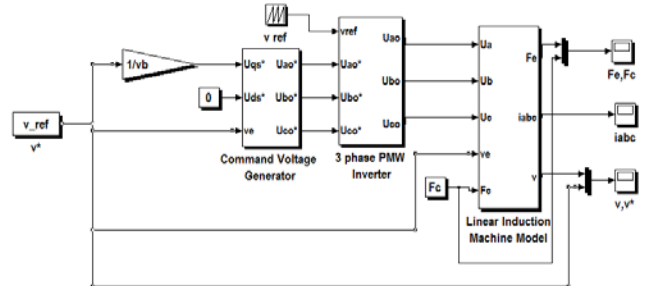


Fig. 6. Open loop constant V/Hz control Simulink model

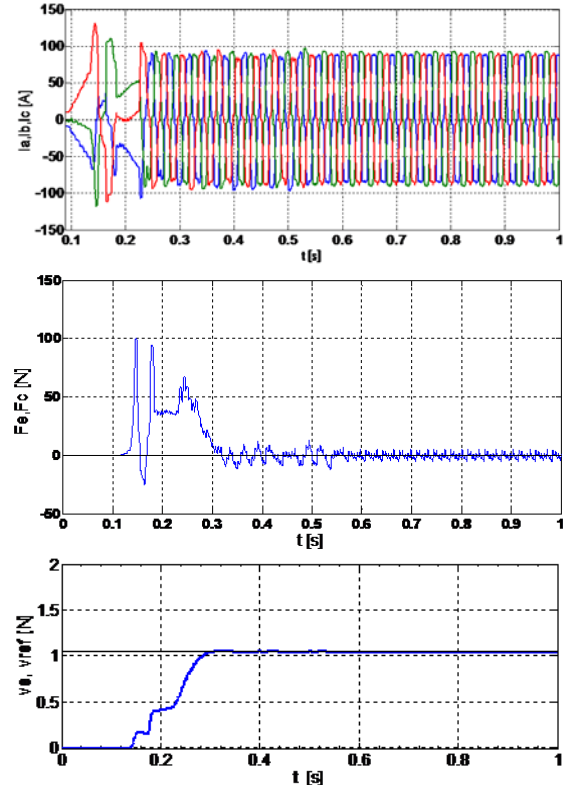


Fig. 7. Simulation results open loop constant V/Hz control

REFERENCES

- [1] H. Hamzeshbahmani, “Modeling and simulating of single side short stator linear induction motor with the end effect”, Journal of Electrical Engineering, Vol. 62, No 5, 2011, 302-308.
- [2] W. Xu, “Equivalent Circuits for Single-Sided Linear Induction Motors”, IEEE Transactions on Industry Applications 46 No. 6 (Nov/Dec 2010), 2410–2423.
- [3] F. Korkmaz, I. Topaloglu, R. Gurbuz, “Simulink Model of Vector Controlled Linear Induction Motor with end effect for electromagnetic Launcher System”, Elektronika ir Electrotechnika, ISSN 1392-1215, Vol. 20, No 1, 2014.
- [4] SimPowerSystem™, User’s Guide R2011b Hydro-Québec and the MathWorks, Inc.
- [5] N. Mohan, “Advanced Electric Drives. Analysis, Control and Modeling using Simulink®”, MNPERE, 2001.

Evaluation of the Influence of the Human Factor on the Reliability of the Information and Control Systems in the Electric Power Industry

Zoya Hubenova¹, Vladimir Gergov²

Abstract – In the article, there are presented the methods for evaluation of the reliability of the information and control systems of the dispatch station in the electric power industry, having into consideration the reliability of the human factor. There are examined several actual up-to-date methods of approach for the optimization of the influence of the human factor on the safety in such complex systems. There are analyzed the factors acting to the reliability of the human-operator and are suggested generalized criteria for their evaluation.

Keywords – Reliability, Information and Control Systems, Human Factor, Electric Power Industry.

I. INTRODUCTION

The up-to-date techniques and technologies (from the automobile to the Nuclear Power Plant) are characterized with a high degree of automatization, availability of information systems for receiving and processing of operational information for the working parameters of all main elements and units and the running of the processes as a whole.

The energy systems with their various equipment, huge number of sub-systems and complex connections between them are a natural object for application of a hierarchical approach in the development of their organization and management, including a wide spectrum of activities for organization, planning, control, constructing, assembly, operation, maintenance and development of information systems and technologies. In the up-to-date organization of the production of electrical energy and its supply and distribution by access and transportation systems, organized by different large companies, very complicated energy complexes arisen, gathering closely associated one to another systems. Their control is impossible without a quick and du decisions according high requirements for reliable and safety functioning, because possible failures in the energy system can have serious economic and social results. This requires a development and improvement of new methods in the organization and the control of huge energy systems.

The electro energetic system in Bulgaria is a complex corporate structure, including The National Electric Company

and 52 sub-divisions in the country, electricity distributing companies, the Thermo-electrical Power Station “Maritza-East”, The Nuclear Power Plant –Kozlodui. Each of its components is a complicated complex of different technical means, groups of people, gathered together within different departments and also include a combination of organizational and structural decisions (rules, service, etc.), organizational structure and technology of functioning [1].

A new tendency in the development of the power industry and the technical base worldwide is the replacement of the old equipment with new one. In the Electrical power stations and the substations, there are most often used systems for automation control, replacing the classic systems for distance control. The new quality high technology products ensure the safety and reliable operation of all technological processes.

The results from the investigations for the last 25 years show that nearly all accidents in the Nuclear power plants are because of human error but not because of technical defects and operation [2]. In many works for the investigation of the human factor (HF) there are mainly learnt the possible and potential reasons for human errors during the time preceding the accidents [3]. The HF is polysemantic and complex phenomenon dependent of different factors of the internal conditions and of the factors of external influences that lead in nowadays to different and not so actual evaluation of the reliability of the operator in the system “man-machine-environment”. During the projecting of the control system there are taken into consideration the main characteristics of the human-operator (HO), such as the time for reaction of the man and the time for the execution of the situation and taking decision and the time for the necessary command to be passed. In this way, in a time of continuous complicating of the technological processes, of power growth, controlled by man, the psycho-emotional stress and the fast tiredness of the operator increased. Actual become the tasks associated with the development of optimal operating conditions for each separate case and also the training of the staff. It is seen from the above that the man is the most responsible by one side and the most unreliable part by the other in such complex man-machine systems (MMS).

II. METHODS AND TECHNIQUES FOR THE EVALUATION OF THE HUMAN RELIABILITY

The various processes in the MMS carry the potential possibilities for mistakes of the staff, mainly in cases when the time that the operator has to take a decision is limited. Also the probability this problem to increase into a negative plan, is often very small. The most of the actions of the staff are

¹Zoya Hubenova is with the Space Research and Technology Institute – BAS, Acad G. Bonchev Str., Bl. 1, 1113 Sofia, Bulgaria, E-mail: zhubenova@space.bas.bg.

²Vladimir Gergov is with the University of Transport Todor Kableshkov, 158 Geo Milev str., 1574 Sofia, Bulgaria, E-mail: gergov@vtu.bg.

limited to the possibility to prevent the initial failure, preventing its growth into an emergency situation. To reach really objective evaluation, it is required analysis of the arisen because of human errors events. This is a hard and complicated process because of the existing limited concepts and lack of systematic description of the phenomenon.

The level of influence of the HF to the reliability of the system can be evaluated according the probability of appearance of mistakes during the process of functioning. The mistakes of the operator are usually connected with untrue interpretation of the incoming and analyzed by him data. It is considered that for the complex technical devices and complex computer tasks, the possibility for errors can reach 15% and for more ordinary one –the possibility for errors is from 1% to 5% [4, 5].

There is a big experience in the usage of methods for analysis of the risk in the human action and mainly in the nuclear power energy. The methods for preliminary estimation of the human errors are the most used for evaluation of the human reliability. The most famous and used in the practice theories are:

- THERT –Technique for Human Error Rate Prediction – Specifying the importance of the human errors in the technics;
- HCR – Human Cognitive Reliability – The reliability of the man related to his abilities. (according to Rasmussen);
- SLIM- Success Likelihood Index Method – Method of the indexes for possible success;
- DNE – Direct Numerical Estimation – Direct numerical evaluation-opinions (expert evaluation);
- MAPPS - Maintenance Personnel Performance Simulation – Method for modeling of the actions (errors) during the service of the technics.

The procedure for a system analysis of the human errors could have several steps according to the fact which of the mentioned methods are applied [6], [7].

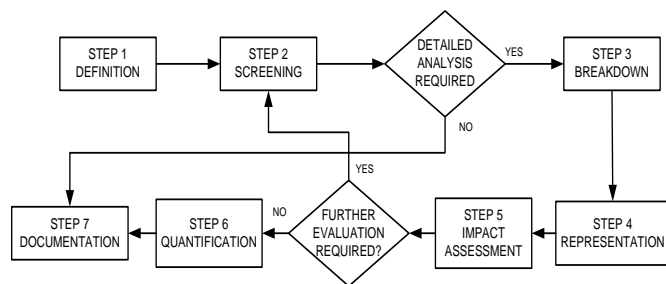


Fig. 1. System analysis of the errors

This procedure is known as SHARP –System Human Action Reliability Procedure and includes 6 steps and two stages: the first stage is executed by the system analytics, and the second –by specialist of the human factor:

Step 1: Defining of the human actions including activities for the accidents localization, repairs, etc. or all the actions that include errors of the staff that lead to failure in the operation of the whole system.

Step 2: Screening – selection of important events, errors that have a key importance for possibility of emergency situations.

Step 3: Separation- all the actions of the operator, requiring more careful analysis are separated which means that the action is divided into smaller elements/operations with the following characteristics:

- The ability to understand what should be done – separation by operations;
- Inability to define the system;
- Inability to execute the necessary actions;
- Expectation and system analysis of the safety;
- Necessity (possibility) to be worked-out an additional emergency plan, if there are found other errors of the operators;

Step 4: Representation –a full list with all errors and their analysis with similar actions;

Step 5: Specifying the interaction of the simple actions/operations and the influence to the next stages;

Step 6: Quantification- specifying the quality values of the probabilities for errors;

Step 7: Documentation.

The model of the human actions is known as Model of human action – SPAR-H and is connected with the processing of the information by man and by the computerized procedures. The SPAR-H model include elements from the planning and also the probability of the operators to be able successfully to fulfill the actions that are identified with procedures which correspond to: usage of operational procedures; the "Ergonomics and Human-Machine Interface (HMI)" – forming and qualitative receiving of information from displays and controllers; "Complexity" of the tasks;

Analysis of the human reliability (Human reliability analysis – HRA). A detailed description of the most often used techniques, associated with the first and the second generation of the HRA is the Method for prediction of the frequency of the human error (Technique for human error rate prediction – THERP) and the Method for evaluation of the human error and its decreasing (Human error assessment and reduction technique – HEART). The examination gives an adequate view for the advantages and the disadvantages of each technique in order to evaluate the reliability of the human operations. The method gives a computer modeling and practically recognizes all factors and experimental data for analysis of the human errors. (there is a standard for their applying - NUREC/CR-1278).

For HRA– Human Cognitive Reliability (Reliability of the human according his abilities) uses the taxonomy of Rasmussen [8]. The correlation between the human reliability and the time is given by:

$$NRP = \exp \left\{ \frac{t/T_{1/2} - C_{y_i}}{C_{n_i}} \right\}^{B_i}, \quad (1)$$

where, NRP is the probability for error (Non-Response Probability), t - available time, T_{av} - average time, C_{y_i} - retainment coefficient, connected with the mental process (specified according the Rasmussen factors), C_{n_i} - measuring factor, in a table there are defined the different factors such as

practical skills of the operator, tiredness, stress, interface quality, etc., B_i - the available time for the mentioned factors to be reported.

As an example it can be used one of the base values of the human error, recognizing the correct understanding of the information from the control panel [6].

TABLE I
ERRORS IN THE DEVICE READINGS

	Presenting of the information	Probability for error (HEP)	Indefiniteness (EF)
1.	Analogue device	0,003	3
2.	Digital device (less than 4 digits)	0,001	3
3.	Self-writing device	0,0006	3
4.	Printing device with many parameters	0,5	5
5.	Diagram device	0,01	3
6.	Digital device with indicating lamps for digits showing	0,001	3
7.	Incertitude, that the device is safe when no indication for check.	0,1	5
8.	More than three symbols	0,01	3
9.	Simple arithmetical calculations	0,01	3
10	Finding by the mean of arithmetic calculations/ accounts of readings out of range	0,05	5

III. SPECIFYING OF THE INFLUENCE OF THE HUMAN FACTOR ON THE RELIABILITY OF THE CONTROL SYSTEMS

Each component of the MMS executes functions and set programs having specific quick-operation, accuracy and reliability. The evaluation of the reliability of the system "man-machine" can be done in different methods: analytic, experimental, imitation. On the project stage, there are mostly used the computing methods that are based on the statistic data for the reliability and the time necessary to the operator to execute the rated functions, the reliability of the technical devices, the influence of different environment factors, the coordination between the operator and the technics, etc. The reliability of the technical devices of the system gives the probability for faulty-free operation during the time necessary for a message to be sent $P_T = 0,989$ and the readiness coefficient is $K_r = 0,958$.

When evaluating the reliability of the operator work, there are examined three possible regimes: 1) Normal conditions (without stress); 2) During lack of time; 3) During information overload.

It is found that the reliability of the operator depends on the algorithm and the variety of the executed operations which is described by the equation [9]:

$$P_{ho} = \exp \left(\sum_{j=1}^r \lambda_j T_j K_j \right) = \exp \left(\sum_{j=1}^r (1 - P_j) K_j \right), \quad (2)$$

where, P_j is the probability for execution of all operations of j-type without errors; λ_j - intensity of the errors of j-type; K_j - number of the executed operations of the j -type; r - number of the different types of operations ($j = 1, r$)

The readiness coefficient of the operator that is used for evaluation of the capacity of the system is defined by:

$$K_{ho} = 1 - T_0 / T, \quad (3)$$

where, T_0 is technical stop, the time when the operator is absent from the desk, when man does not process information; T - the full working time of the human operator.

If according the requirements for safety work of the operator it is necessary 10 min rest after 50 min work, then according to this indication the readiness coefficient of the operator will be: $K_{ho} = 0,833$. This testifies not only for "limited place" in the system but has influence to the organization of the working conditions and also to the system reliability [10]. According the calculations, the reliability of the operator is different when executing different types of operations: $P_{ho1} = 0,975$, $P_{ho2} = 0,960$, $P_{ho3} = 0,945$.

The errors of the operator are classified in three groups: misleading, disadvantages and negligence. They correspond to the cognitive stage in the different time intervals [7]:

Cognitive stage	Type of mistake
Training	Misleading
Knowing the Instructions	Insufficient knowledge
Execution	Negligence, mistakes

In this way, in order to specify the reliability of the system "man-machine", it is necessary to know the characteristics of the faulty-free operation and of the time needed for execution of the different actions being part of the activities algorithm of the HO. The tendency for decreasing of the operator mistakes is to be according the level of his training and practice [11].

The data shows that during the execution of the different operations, the operator has a high reliability – from 0.95 to 0.999. It has to be taken into consideration that the evaluation is done during an experiment, when the operator has past special training, the working conditions are specified (comfortable), etc. In the real life everything is more complicated and so less reliable.

IV. CONCLUSION

The using of a complex method for analysis of the reliability of the human factor, gives the possibility to achieve more complex and true picture in contrast to the filled out

probabilistic evaluation of the operator errors with determined indexes for his psycho-physiological state in real working conditions in the MMS. To increase the reliability of the operator in the field of the electric energy projects, during the operation of the MMS, it is necessary to cover the following most important principles:

- optimal separation of the control functions between the man and the machine;
- to choose automation devices adequate to the importance of the executed functions, connected with the safety;
- to create an optimal proportion between the activity of the operator and the systems supporting his activity;
- to create and use up-to-date interfaces “man-machine”.

The results from the complex approach for the analysis of the reliability of the operator activity can be used to specify the most rational variants of staffs when preparing the practical recommendations for the improvement of the means and ways to ensure effective functioning of the man in normal and accidental conditions on different energy projects.

REFERENCES

- [1] Sixth national report of Republic of Bulgaria for the convention for nuclear safety, Sofia 2013.
- [2] G. Simpson, T. Horberry, J. Joy, *Understanding Human Error in Mine Safety*, MPG Books Group, UK, 2009.
- [3] J.A. Forester, E. Susan, A.M. Kolaczowski, D.C. Bley, “An Overview of the Evolution of Human Reliability Analysis In the Context of Probabilistic Risk Assessment”, Risk & Reliability Analysis Department, 2009.
- [4] P. Pekka, “Human reliability analysis methods for probabilistic safety assessment”, VTT Automation, ESPOO, 2000.
- [5] K. Andersson, P. Pekka, “Integrated Sequence Analysis”, Technical Research Centre of Finland (VTT), 1998.
- [6] Human Reliability Assessment Training Course. USA, INEL, 1995.
- [7] D. Gertman, H. Blackman, J. Marble, J. Byers, C. Smith , “The SPAR-H Human Reliability Analysis Method”, Idaho National Laboratory, 2005.
- [8] J. Rasmussen, A.M. Pejtersen, L.P. Goodstein, *Cognitive Systems Engineering* New York: John Wily & Sons, Inc 1994.
- [9] R.L. Boring, D.I. Gertman, “Human Reliability Analysis for Computerized Procedures, Part Two: Applicability of Current Methods, Human Factors and Ergonomics Society”, 2006.
- [10] P. Getzov, Z. Hubenova, “Reliability Study of Operators within a Complex ergatic System”, *Journal Scientific and Applied Research*, vol. 4, 2013.
- [11] I. Dimitrov, S. Tanev, P. Getsov, P. Trendafilov, H. Hristov, L. Aleksiev, S. Doshev, “Scientific Research Complex for the Study of Human Operator in Extreme Conditions”, RAST 2011, 5-th International Conference – Resent Advances in Space Technologies, p.825, Istanbul, Turkey.
- [12] A. Pasquini, G. Pistolesi, A. Rizzo, “Reliability Analysis of Systems Based on Software and Human Resources”, *IEEE TRANSACTIONS ON RELIABILITY*, VOL. 50, NO. 4, 1.
- [13] M. Ahmed, L. Sharif, M. Kabir, M.A. Maimani, “Human Errors in Information Security”, *International Journal of Advanced Trends in Computer Science and Engineering*, Volume 1, No.3, 2012.
- [14] S. Andrew, J.A. Jacko, *The Human-Computer Interaction Handbook*, CRC Press, 30.10.2007.

Generalized Forces of the Robotic System with Fractional Order Thermoviscoelastic Element

Milan S. Cajić¹ and Mihailo P. Lazarević²

Abstract – In this paper, we analyze generalized forces of a discrete fractional order Kelvin-Voigt thermoviscoelastic element connected into a multibody robotic system. An efficient numerical approximation scheme is used to approximate fractional order derivative. The effects of fractional order derivative and temperature change on generalized forces are examined through the numerical example of simple three rigid body robotic system.

Keywords – Fractional calculus, thermoviscoelasticity, multibody dynamics.

I. INTRODUCTION

Thermal effects are present in the exploitation of robots under various conditions. Influence of such effects on rigid robotic parts as well as on the flexible one should not be neglected in the modelling and design procedure. In addition, these effects are having influence on the motion of the system and can change positioning trajectory of robot manipulators. However, available rigid body system modelling procedures are limiting our study to consideration of only discrete deformable elements in the system accounting the thermal effects. In the sense of Lagrange motion equations of the second kind, we consider a discrete rigid multibody system coupled with a fractional order thermoviscoelastic element. We derived generalized forces of the element based on the principle of virtual work (see [1] and [2]). In the literature, one can find many papers applying the fractional order viscoelasticity for the problems in structural mechanics or other applications in mechanics or control where use of fractional order derivatives or integrals is justified. By performing experiments, it has been concluded that fractional order viscoelastic models represent viscoelastic material behavior much better than classical viscoelastic models and in some cases, much less parameters are needed to fit experimental curves. In [3], one can find several fractional order models for different applications. Numerical approximation methods for fractional order derivatives one can find in [4] and [5].

In this paper, we introduce fractional order thermoviscoelastic element into a robotic system composed of multiple rigid bodies using generalized forces of the element. Element is connected to two different bodies in the system (see Fig. 1). For a numerical simulation, we use simple robotic

system composed of three rigid bodies.

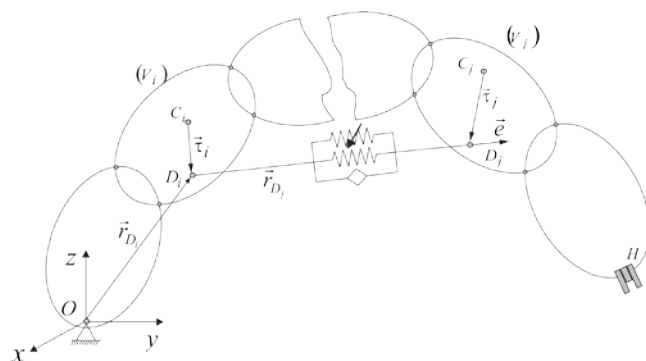


Fig. 1. Multibody robotic system with thermoviscoelastic element

II. FORMULATION OF THE PROBLEM

First, we give Lagrange motion equations of arbitrary multibody system in the covariant form as

$$\sum_{\alpha} a_{\alpha\gamma} \ddot{q}^{\alpha} + \sum_{\alpha=1}^n \sum_{\beta=1}^n \Gamma_{\alpha\beta,\gamma} \dot{q}^{\alpha} \dot{q}^{\beta} = Q_{\gamma}, \quad \alpha, \beta, \gamma = 1, \dots, n. \quad (1)$$

where with q^{α} and q^{β} we denote generalized coordinates, $\Gamma_{\alpha\beta,\gamma}$ are Christoffel symbols of the first kind, $a_{\alpha\gamma}$ are elements of the basic metric tensor and with Q_{γ} we denote generalized forces. In the above equation, we can introduce generalized forces such as gravitational forces, generalized control forces, semi dry friction forces etc. In our case, we will introduce generalized forces of the fractional order thermoviscoelastic element, which can be deformed only in the direction of the unit vector lying on the line which connects two different points on two different bodies in the system (see Fig. 1). Further, we propose a force-displacement relation of the element in the form

$$F_{KV} = (E_c + E_{KV})x + E_d {}^{RL}D_t^{\lambda}(x) - a_{KV} E_{KV} T, \quad (2)$$

where x is dilatation of the element, F_{KV} is force of the element, E_c and E_{KV} are stiffness's of the element, E_d is relaxation time, a_{KV} is thermo-dilatation constant and T is temperature of the element. The operator ${}^{RL}D_t^{\lambda}$ is fractional order derivative operator denoting the left Riemann-Liouville definition and which is given in the form

$${}^{RL}D_t^{\lambda}(x) = \frac{1}{\Gamma(n-\alpha)} \frac{d^n}{dt^n} \int_0^t (t-\tau)^{n-\alpha-1} x d\tau. \quad (3)$$

In Eq. (3) $x(q^i(t), q^{i+1}(t), \dots, q^k(t))$ is displacement of the element. It is equal to the difference of the instant length l of

¹Milan S. Cajić is with the Mathematical Institute of the Serbian Academy of Sciences and Arts, Kneza Mihaila 36, 11001 Belgrade, Serbia, E-mail: mcajic@mi.sanu.ac.rs.

²Mihailo P. Lazarević is with the Faculty of Mechanical Engineering University of Belgrade, Kraljice Marije 16, 11000 Belgrade, Serbia.

the element and constant initial length l_0 and it is a composite function depending of the generalized coordinates which are time dependent functions. Using the principle of virtual work we can derive generalized forces of the element where we obtain

$$Q_{\beta}^w = - \left[(E_{KV} + E_c) \cdot x \frac{\bar{l}}{l} \frac{\partial(\bar{l})}{\partial q^\alpha} + E_d \cdot \frac{\bar{l}}{l} \frac{\partial(\bar{l})}{\partial q^\alpha} \cdot D^\alpha(x) - \alpha_{KV} E_{KV} T \frac{\bar{l}}{l} \frac{\partial(\bar{l})}{\partial q^\alpha} \right] \quad (4)$$

III. NUMERICAL RESULTS

In our numerical simulation, we use robotic system composed of three rigid bodies and thermoviscoelastic element connected to the first and the third body in the system. We assumed the following generalized coordinates $q^1=0$, $q^2=0.1\sin(8t)$ and $q^3=0.1t$. Since displacement of the element is a composite function of generalized coordinates we cannot use classical chain rule for fractional derivative of a displacement. Thus, we use numerical approximation scheme proposed in [4] and [5] but for the case of a composite function. For the numerical calculations we used the following values of parameters: $E_c = 30[\text{N/m}]$, $E_e = 20[\text{N/m}]$, $E_d = 50[\text{s}^\alpha]$, $\alpha_{KV} = 0.0007[\text{m/C}^\alpha]$ and $l_0 = 0.7[\text{m}]$.

Values of second generalized force of the thermoviscoelastic element at room temperature and for different values of fractional order parameter are shown in Fig. 2. It can be noticed that decrease of the fractional order parameter softens the curve amplitude i.e. difference between values of generalized forces in time is less for lower fractional order derivatives than for the higher one. In Fig. 3, one can see the difference between values of the second generalized force for changes of temperature T in the range 0-60 [C°]. It is obvious that in general, an increase of the temperature decreases the value of generalized force. This effect depends on the temperature of the element and value of the thermo-dilatation constant α_{KV} , which is different for each material.

IV. CONCLUSION

Here, we analyzed generalized forces of the robotic system with thermoviscoelastic element. We showed that generalized forces depend of the element temperature but this influence is conditioned with the value of thermo-dilatation constant, which depends of the material properties. In addition, we showed that different viscoelastic properties of the element change the values of generalized forces significantly. By choosing the appropriate parameters of the model and fractional order parameter, which are normally obtained from experimental results, we can simulate real viscoelastic behavior much better than with classical integer order derivative models. The model proposed in this work can be

used for future investigation to develop a proper position control algorithm of a three body robotic system.

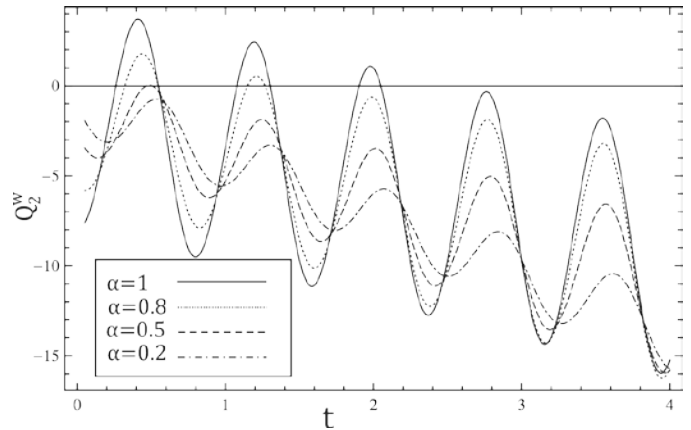


Fig. 2. Q_2^w for different α and $T = 25 [\text{C}^\circ]$

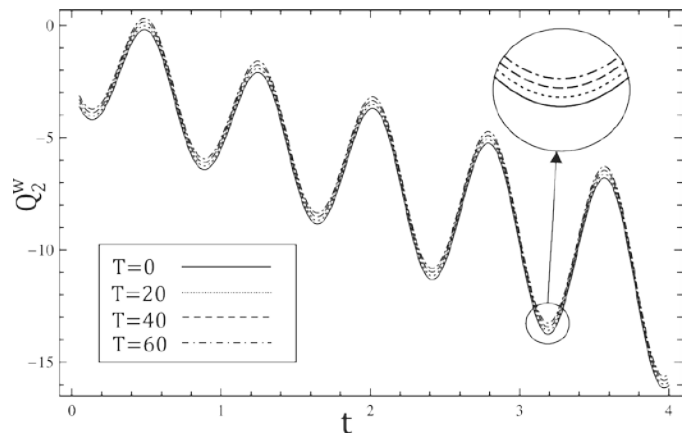


Fig. 3. Q_2^w for different T and $\alpha = 0.5$

ACKNOWLEDGEMENT

This research was sponsored by the research grants of the Serbian Ministry of Education, Science and Technological Development under the numbers OI 174001 and TR 35006.

REFERENCES

- [1] A.A. Shabana, *Computational Dynamics*, New York, John Wiley & Sons Ltd, 2010.
- [2] O.A. Goroško, K.S. Hedrih, "The construction of the Lagrange mechanics of the discrete hereditary systems", *Facta Universitatis - Series: Mechanics, Automatic Control and Robotics*, vol. 6, no. 1, pp. 1-22, 2007.
- [3] M.P. Lazarevic, Lj. Bucanovic, *Contribution to modeling and dynamical analysis of fractional order systems with basis of fractional calculus*, Belgrade, Faculty of Mechanical Engineering University of Belgrade, 2012 (in Serbian).
- [4] T.M. Atanacković, B. Stanković, "On a Numerical Scheme for Solving Differential Equations of Fractional Order", *Mech. Res. Commun.*, vol. 35, no. 7, pp. 429-438, 2008.
- [5] S. Pooseh, R. Almeida, D.F. Torres, "Numerical approximations of fractional derivatives with applications", *Asian J. Control.*, vol. 15, no. 3, pp. 698-712, 2013.

Models of Objects of Control in the System for Monitoring and Dispatching on Metropolitan-Sofia

Emiliya Dimitrova¹

Abstract – The purpose of this paper is establishment of models of SCADA – system DISIM that is incorporated into the Central Dispatching Post of Sofia Metropolitan. Its functions are related to a remote visualization and management of devices in Trains operation (DISIM-V) and Power transmission system (DISIM-E). These models are used as a basis for realization of a simulator of both SCADA systems.

Keywords – Dispatching systems, metropolitan, modelling.

I. INTRODUCTION

Dispatching system DISIM is implemented in Metropolitan Sofia. It is a complex structure of technical, software and organizational resources related to certain rules, providing control and operating on the train traffic process and power supply of the electrical equipment. Its purpose is to monitor and directly automatically control the processes and foremost to ensure the safety of passengers. In general, the control is performed automatically, while operating is done either automatically or through operator commands submitted by the dispatchers of the Central Dispatching Post (CDP). Therefore this is a contemporary Supervisory Control and Data Acquisition system (SCADA). It consists of several independent systems, the most important of which are DISIM-V for dispatching and control on the train traffic and DISIM-E for monitoring and control on the traction substations and electrical equipment [1], [6], [7]. The purpose of each SCADA-system is centralized data acquisition of remote geographical sites, information processing and visualization and generation of managerial impacts. The correct and reliable functioning of SCADA system is crucial for the functioning of the whole system [1], [2]. The point of the management is that these complicated technical systems implement an objective function when the external conditions are changed within fixed limits: their behavior is set up depending on the assessment of the external situation under a definite criterion in compliance with the fixed purpose. Therefore, the management is a process of forming the most effective behavior of the system aiming at implementation of appointed functions. The means for realization of management are the control units (where decision making is accomplished) and the actuators (which convert the information about the adopted decisions into actions directed towards achievement of management purposes). The following processes could be added to the more important and basic technological ones,

subject to management in the metropolitan:

- Operation of underground trains;
- Uninterruptible power supply of the rolling stock and many other consumers of electric power (for their own needs);
- Different engineering sanitary and technical structures (escalators, pumps, fans, heating and lighting);
- ensuring possibility for local management of trains in the region of each station;
- giving information to passengers for the remaining time until the arrival of the following train and etc.

The great complexity of these processes is determined by the fact that each one is distributed in all stations on the territory of the underground and the management has to cover all these parts. In this sense the metropolitan represents a typical non-concentrated object. It is known that many special requirements for automatic control of such objects independently of the manufacturing industry are presented [3]. The complexity of the processes in metropolitan is growing because of the management needs to ensure safe transport, according to strict European standards.

The aim of this paper is establishment of structural models and mathematical description of processes in object levels of SCADA-systems DISIM-V and DISIM-E. The suggested models could be used as a basis for elaboration of a simulator of both SCADA-systems.

II. STRUCTURAL MODEL OF A SYSTEM FOR MONITORING AND CONTROL ON METROPOLITAN-SOFIA

Each SCADA-system consists of three formal levels [1], [6], [7]: Upper (Dispatching) level, Communication level, Lower (Object) level. The overall structural model of the object level of the system DISIM-V for monitoring and dispatching on train traffic is shown in Fig. 1. Trains operation in the metropolitan is marked as an object of control which includes: all the trains situated along the route at a fixed moment, the elements of the railway track, the signaling devices. The right interaction between the trains and the elements of the railway track has to ensure running of the technical process under the given algorithm, in this case – the actual timetable of trains operation for a fixed period. Normally, different disturbing impacts (damages of the rolling stock or the railway track, incorrect actions of the operational staff and etc.) could influence the process passing. In most cases the disturbing actions represent a reason for discoordination of the system exit. Each discoordination, i.e. divergence from the timetable, has to be considered a warning for generation of a suitable management decision.

¹Emiliya Dimitrova is with Faculty of Communications and Electrical Equipment at the Todor Kableshkov University of Transport-Sofia, 158 Geo Milev Str., Sofia1574, Bulgaria, E-mail: edimitrova@bitex.bg.

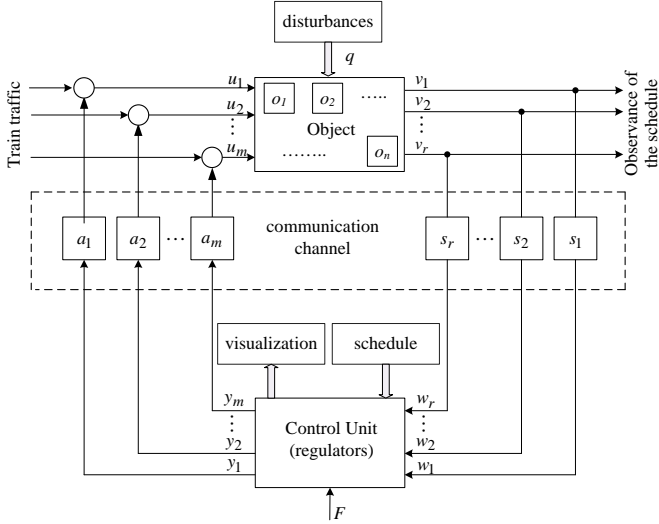


Fig. 1. Structural model of the object level of a system for dispatching and control on train traffic

All the trains operating along the section represent the system entrance. The system exit is the real implementation of the traffic timetable and the data reflecting the status of the different railway track elements. The information about the moment location of the trains is received from sensors s_i ($i=1\dots p$, where p is the number of the track circuits, mounted along the section). The rest part of sensors s_j ($j=p+1, \dots, r$) are situated in the signaling devices, points and other elements of the railway track. Actuators $a_1\dots a_m$ are used for the realization of switching of traffic lights, points, etc.

The overall structural model of the object level of the system DISIM-E for monitoring and control on traction substations and electrical equipment is shown in Fig. 2. In this case, the object of control includes all main physical objects liable to control and management by the system: complex switchgear 10kV (disconnecter and three-positional switchgear); traction transformer 10kV/825V; traction rectifiers; switchgear 825V; disconnecter 825V; transformer 10kV/0,4kV; disconnecter 0,4kV; charger devices and accumulator batteries. Most of the sensors and actuators are embedded in multifunction protection relays mounted at switchgears, transformers and other devices.

Data for normal state of these objects are embedded in the control unit memory. In contrast to DISIM-V system a fixed number of programmes, corresponding to the system reaction in case of arising of certain events, needs to be included in the managing device. These programmes establish an algorithm of switching over the object after assessment of the particular situation.

Visualization of the object status is envisaged in both models. It ensures monitoring by the dispatchers in the CDP and by the traffic manager on duty in the respective underground station.

In both models the object of control consists of n subsystems ($o_1\dots o_n$). It has m inputs of entering input effects $[u_1(t), \dots, u_m(t)] \in U$ and r outputs, which are obtained respectively the output signals of the system $[v_1(t), \dots, v_r(t)] \in V$.

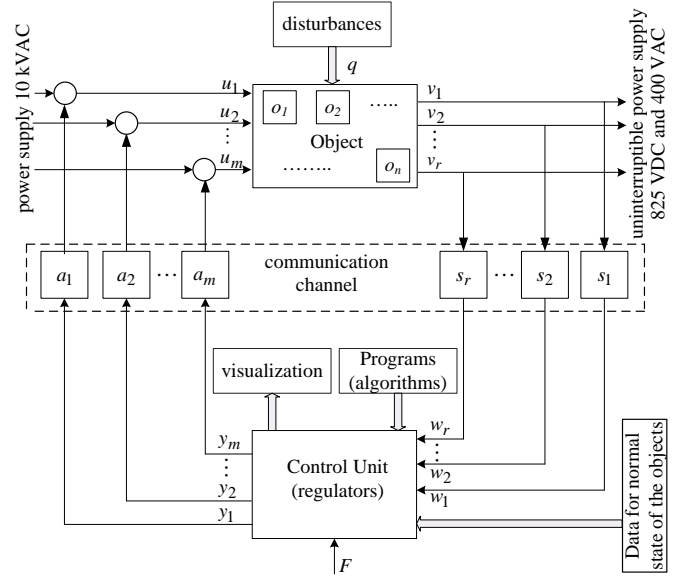


Fig. 2. Structural model of the object level of a system for monitoring and control on traction substations and electrical equipment

These signals are fed to the control unit by r number of sensors ($s_1\dots s_r$) [3].

The control unit has a corresponding number of r inputs ($w_1\dots w_r$) and m outputs ($y_1\dots y_m$). The control system affects on the object by m actuators ($a_1\dots a_m$).

The technical state X of the object of control is defined on the base of information received from the sensors and after computing operations. It can be interpreted as a technical grade of state G , which corresponds to a response of the control system.

Each state x_i of i -th subsystem, $i \in [1, n]$, expresses its current state. Thus $[x_1(t), \dots, x_n(t)] \in X$ expresses the current state of the object of control.

The transition of a subsystem from one state $x_i(t_1)$ to another $x_i(t_2)$ at $t_2 > t_1$ determines its dynamics. It may be a result from the action of external control signals or due to internal disturbances.

If at initial time t_0 the subsystem is in a state $x_i(t_0) \in X_0$ and there are no disturbances, then the change of its state is described by the equation:

$$x_i(t) = F[t, t_0, x_i(t_0)], \quad (1)$$

where F is objective function.

If the change in the state of the system is due to the action of an external signal, changes in the state is described by the equation

$$\dot{x}_i(t) = F[t, t_0, x_i(t_0), u(t)], \quad (2)$$

wherein the output signal is formed on:

$$v(t) = F[t, x_i(t), u(t)], \quad (3)$$

The dynamic model G_p of the object of control of the structures shown in Figs. 1 and 2 may be expressed in the form:

$$\begin{aligned} \dot{x}(t) &= A_p \cdot x(t) + B_p \cdot u(t) \\ v(t) &= C_p \cdot x(t) \end{aligned}, \quad (4)$$

where $x(t)$, $u(t)$, $v(t)$ and matrices with constant coefficients A_p , B_p и C_p are the relevant dimension.

Control unit is a specialized computing system and operates in discrete time with sampling period T . Programmable logic controllers (PLC) are widely used as control units in contemporary systems for monitoring and control on complex technical objects [1], [2], [7]. They offer high level of performance in the execution of the control program set in microprocessor. They are also equipped with a large number of digital and analog inputs and outputs, which can be increased by including additional expansion modules. PLC can be connected to a network and work as master or slave devices, and offer the ability to transmit data at high speed.

The technical state $Z(\kappa)$ of the control unit at the sample time κT can be expressed as a function of the technical state $Z(\kappa-1)$ in the preview sample time and information received on its inputs. Thus the dynamic model G_c of the control unit in the sample time kT can be expressed by the following equation

$$\begin{aligned} z(k) &= D \cdot z(k-1) + E \cdot w(k) \\ y(k) &= G \cdot z(k) + H \cdot w(k) \end{aligned}, \quad (5)$$

where $z(k) = z(kT)$, $w(k) = w(kT)$, $y(k) = y(kT)$ and matrices D , E , G and H are the relevant dimension. Each of these matrices consists of not only constant coefficients, but of regulators, associated to the appropriate input signal as well. Programmed PID (Proportional-Integral-Derivative) regulator allows the process control to accurately maintain setpoint by adjusting the control outputs. PID can be used to obtaining a fast response of a disturbance appearance. In steady state operation, it regulates the value of the output so as to drive the error e_i to zero. A measure of the error is given by the difference between the setpoint (the desired operating point of the appropriate sub-object of control) and the process variable (the actual operating point calculated on the base on the received information).

The principle of PID control is based upon the following equation that expresses the output, y_i , as a function of a proportional term, an integral term, and a differential term:

$$y_i(t) = K_i \cdot e_i + K_{iI} \cdot \int_0^t e_i \cdot dt + y_{i0} + K_{iD} \cdot \frac{\partial e_i}{\partial t}, \quad (6)$$

where:

$y_i(t)$ is the i^{th} output as a function of time ($i = 1 \dots m$);

K_i is the loop gain of the appropriate regulator;

e_i is the loop error (the difference between setpoint and process variable);

y_{i0} is the initial value of the i^{th} output.

In order to implement this control function in a digital description, the continuous function must be quantized into

periodic samples of the error value with subsequent calculation of the output. The corresponding equation, which is the basis for the solution of the digital algorithm, is:

$$\begin{aligned} y_i(k) &= K_i \cdot e_i(k) + K_{iI} \cdot \sum_{j=1}^k e_i(j) + y_{i0} + \\ &+ K_{iD} \cdot [e_i(k) - e_i(k-1)] \end{aligned}, \quad (7)$$

where: $y_i(k)$ is the calculated value of the i^{th} output at sample time k ; $e_i(k)$ is the value of the loop error of the appropriate regulator at sample time k ; $e_i(k-1)$ is the previous value of the loop error (at sample time $k-1$); $e_i(j)$ is the value of the loop error at sample time j ; K_{iI} is the proportional constant of the integral term of the i^{th} output signal:

$$K_{iI} = K_i \cdot \frac{T}{T_{iI}}, \quad (8)$$

T is the sample time (this is the cycle time at which the processor recalculates the output values); T_{iI} is the integration period of the i^{th} output (also called the integral time or reset); K_{iD} is the proportional constant of the differential term of the i^{th} output signal:

$$K_{iD} = K_i \cdot \frac{T_{iD}}{T}, \quad (9)$$

T_{iD} is the differentiation period of the i^{th} output (also called the derivative time or rate). The differential term is proportional to the change in the error.

As a result of the repetitive nature of the digital algorithm solution, a simplification in the Eq. (7), which must be solved at any sample time, can be made. The simplified equation is:

$$\begin{aligned} y_i(k) &= (K_i + K_{iI} + K_{iD}) \cdot e_i(k) + \\ &+ Y_i(k-1) - K_{iD} \cdot e_i(k-1) \end{aligned}, \quad (10)$$

where $Y_i(k-1)$ is the value of the integral term at sample time $k-1$ (also called the integral sum or the bias):

$$Y_i(k-1) = K_{iI} \cdot \sum_{j=1}^{k-1} e_j + y_{i0}. \quad (11)$$

The bias is the running sum of all previous values of the integral term. Several constants are also part of the integral term, the gain (K_i), the sample time (T), and the integral time or reset (T_{iI}), which is a time used to control the influence of the integral term in the output calculation.

In many control systems, it might be necessary to employ only one or two methods of loop control. Setting the value of the constant parameters makes the selection of the type of loop control desired. If the derivative action is not required and PI regulator may be used, then a value of 0.0 should be specified for the derivative time T_{iD} . If the integral action is also not required, then a value of infinity "INF" should be specified for the integral time T_{iI} . Even with no integral action, the value of the integral term might not be zero, due to the initial value of the integral sum y_{i0} . Then the proportioning

control continuously adjusts the output dependent on the relative values of the process variable and the setpoint. Many control designs incorporate offset as a digital programmable value that allows redefining the output requirement at the setpoint. A proportioning control without offset will settle out somewhere within the proportioning band but likely not on the setpoint. The offset may be used in conjunction with Integral time (reset) that allows for quicker settling at setpoint. Reset redefines the output requirements at the setpoint until the process variable and the setpoint are equal. PID functions allow for the precise control of difficult processes (for example control on the voltage, current, temperature, positioning of the actuators, etc.). Rate (Derivative time) is activated at a slope change of the error. Its effect applies the “brakes” in an attempt to prevent overshoot (or undershoot) on process upsets or startup. The process variable can be controlled without oscillations around the setpoint.

Most of the objects of control in SCADA-system DISIM are slowly acting – their reactions have low repeatable frequency. In this case there is no need to use more complicated regulators than P regulators.

The communication level for both systems is constructed in compliance with the principle of the Optical Open Transport Network (OTN). This is a digital communication network built up by nodes which are interconnected by a double optical fiber ring [6], [7], [8]. Because of the double ring structure, OTN guarantees an unparalleled degree of reliability. Should one fiber ring or node fails because of any reason (fire, rupture etc.), then the other ring and nodes take over immediately, thus keeping the whole network operational round the clock. The system will always find a way around any problem without affecting its users. The OTN nodes also offer redundancy of the main components such as power supplies, common logic cards and optical modules.

OTN allocates a dedicated amount of bandwidth to each application. Each application has its own 'lane' or layer in the fiber tunnel, with guaranteed bandwidth. This allows the all applications run smoothly on the OTN, without interfering with each other.

An OTN network is often applicable for extended transport environments such as tunnels, railways, subways, etc. All existing applications are linked by fully transparent manner. This network is “Open” because it transfers all available communication applications, provides Accident Prevention and limiting applications, includes Interface cards for voice, data, digital video and Ethernet [4], [8].

Dispatcher level realizes the logic functions in accordance with the requirements of the technology for the train traffic, passenger’s safety and monitoring and control on the electrical equipment. This process includes also functions of displaying the information and human-system dialogue (displaying track development, signals status, location and movement of trains at any time, status of all electrical equipment in the substation, etc.), as well as working-out and starting-up commands.

This level consist of functional modules representing these functions and appropriate one or more windows by which Dispatcher communicates with the system. Functions of this level are fully described in [1], [5], [9], [10].

III. CONCLUSION

The structural and functional models developed in this paper are the basis of elaboration of an imitation model of the system for monitoring and management of processes in the underground. Such model has been synthesized and a simulator of Dispatching SCADA systems DISIM-V and DISIM-E has been structured at Todor Kableshkov University of Transport. The imitation models of object levels of both systems have been installed on a server using special software. The dispatcher level has been installed on five computers that use the server for the communications with the objects. Opportunities for simulation of different real working regimes for both systems have been created. The trainers would be capable of coming in depth in the essence of the contemporary SCADA technologies adopted to be the main and increasingly perspective method for automatic management of complicated dynamic processes in crucial and critical fields in terms of safety and reliability.

A comprehensive survey of the contemporary, modern and effective SCADA-system DISIM is not possible due to the special working regime and admission in the CDP, local station posts (the work places of the traffic managers on duty) and substations. Thus, the availability of such a system model is extremely useful for personnel training and increasing the qualification of operational specialists in the metropolitan, electricity distribution companies and the railway infrastructure.

Many examinations on this simulator have been carried out and its proper work has been verified [5], [9], [10]. Thus an experimental verification of the developed models is done.

REFERENCES

- [1] E. Goranov, E. Dimitrova, *Remote Control Systems and Management in Transport*, University of transport, Sofia, 2010.
- [2] D. Bailey, E. Wright, *Practical SCADA for Industry*, Newness, ISBN: 978-0-7506-5805-8, 2003.
- [3] L. Baranov, *Models of automatic control systems*, МИИТ, Moscow, ISBN 978-5-7876-0022-3, 2008.
- [4] G. Clarke, D. Reynders, E. Wright, *Practical Modern SCADA Protocols*, Newness, ISBN: 978-0-7506-5799-0, 2004.
- [5] E. Dimitrova, “Laboratory SCADA – System for Control on Railway Traffic”. XLVIII International Scientific Conference ICESST 2013, Proceeding of papers, Vol. 2, pp.479-482.
- [6] Technical documentation of SCADA-system DISIM-V, 2012.
- [7] Technical documentation of SCADA-system DISIM-E, 2012.
- [8] OTN Systems – Dedicated Networks for Critical Environments, available on: <http://www.otn.be/>.
- [9] Е. Димитрова, “Симулатор на SCADA система за дистанционно управление на електросъоръжения”, Годишник на ТУ-София, том 63 кн.5/6, pp.313-320, ISSN 1311-0829, 2013.
- [10] Е. Димитрова, В. Димитров, “SCADA-система за управление на влакото движение – лабораторен симулатор”, Научни трудове на Русенския университет, том 52, серия 3.2, 91-95, ISSN 1311-3321, 2013.

Design a Simple Hardware in the Loop Test-bed Platform for Educational Purposes

Mile Petkovski¹ and Aleksandar Jurukovski²

Abstract – In this paper a simple hardware in the loop testing platform for educational purposes is considered. Dynamic model of speed servo is developed and implemented to the test-bed platform. Such system is purposed for testing physical controller. Different scenarios are defined at the test-bed platform side. Used equipment is general purposes and can be utilized for controller implementation as well as virtual plant model. Simulations are performed under different conditions and results are presented graphically using virtual instruments on the designed front panels.

Keywords – Speed servo, Dynamic model, Hardware In the Loop.

I. INTRODUCTION

Systems are created to solve problems. One can think of the systems approach as an organized way of dealing with a problem. System development life cycle means combination of various activities. In other words we can say that various activities put together are referred as system development life cycle, Fig.1.

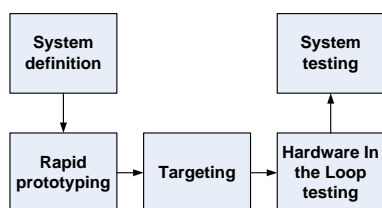


Fig. 1. System development life cycle

As the complexity of the hardware being controlled increases, the complexity of the embedded system that is designed to control the hardware is increased. In the System analysis and design terminology, the system development life cycle means model development and design and hardware and software implementation. Simulation is a technique that is used increasingly in the development and test of complex real-time embedded systems. Depending of facts that objects in the simulation process may be real and/or virtual, there is a few different types of approach, model in the loop (MIL), software in the loop (SIL) and hardware in the loop (HIL). Model in the loop is a real time simulation technique purposed for dynamical model testing. The Objectives of this type of

simulation are intended to functional validation and calibration of sub-system, models, evaluation interactions between subsystems, refinement of plant models. The main objectives of software in the loop simulation are functional validation of controller software architecture and verification of software implementation against model. The HIL simulation includes a mathematical model of the process and a hardware device you want to test.

System level testing is one of the major expenses in developing a complex product that incorporates embedded computing. The need to minimize time to market while simultaneously producing a thoroughly tested product presents tremendous challenges. Increasing levels of complexity in system hardware and software are making this problem more severe with each new generation of products. Additionally, any significant changes made to an existing product's hardware or software must be thoroughly regression-tested to confirm that the changes do not produce unintended effects [1].

Hardware in the Loop (HIL) simulation is becoming more prevalent tool for design, testing, adjustment and perfected stage of the electronic system development [2]. The practice of engineers abounds with examples of how the software controller, the part of the system software and hardware failures can lead to system failures, destruction of equipment and in some cases loss of life. These facts stand as a reminder that the testing technology must constantly improve and apply new technology to improve testing, increase test coverage and reduce the cost of testing.

In real HIL simulation system is replaced by a virtual model that operates in real time. Hardware in the loop simulations are increasingly used to evaluate the performance of the controllers. Software simulation results to develop a control system prepared in advance. In this case generally reduces the calculation time. The complexity of the equipment being tested is included in testing by adding a mathematical model that is about dynamic system. This mathematical model is stated as a simulation facility that is us the equipment that simulates. The HIL testing reduces the costs and risks, increasing reliability and quality, lower prices and has introduced changes more efficient development. The purpose of HIL simulation is to provide an effective platform for the development and testing of embedded real-time systems. As advanced HIL test method allows the prototype of the new equipment to be examined under a wide range of realistic conditions are safe and economically feasible.

In this paper we consider design phases of a simple test-bed platform for hardware in the loop simulation. Section two describes the theoretical background and development phases of dynamic model of components which speed servo consist off. The next section shows the implementation phases of dynamic model to the target HIL platform as a virtual model.

¹Mile Petkovski is with the Faculty of Technical sciences, Bitola, R. Macedonia, mile.petkovski@tfb.uklo.edu.mk.

²Aleksandar Jurukovski is with the Mining and Energy Combine, Bitola, R. Macedonia, aleksandarjurukovski@gmail.com.

Experimental results and conclusions are presented in the last two sections.

II. DYNAMIC MODEL OF SPEED SERVO

2.1. Modeling of DC permanent magnet motor

One of the most used actuators in control systems is a direct current (DC) motor. The general output variable of this actuator can be angular speed or angular displacement motion, but, coupled with wheels or drums and cables, can provide translation motion. In most applications the speed or position of the shaft of these motors must be accurately controlled. In order to design such velocity and position control systems it is necessary to obtain, analytically or experimentally, a mathematical model for the motor or system to be controlled.

Dynamic analysis and simplest process remains very complex if we want to give him a complete description [3]. Therefore, first and foremost when making mathematical model is to choose those assumptions that will simplify the description of the process. Usually, for this purpose a system that analyzed is divided into simple articles, subsystems suitable for analysis, and the total description is obtained by making the descriptions of all subsystems. The dynamic model of permanent magnet DC motor is shown in the following figure,

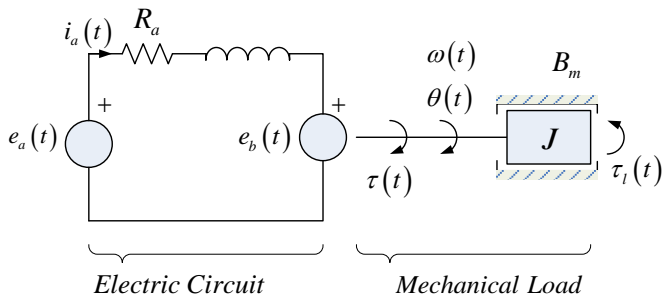


Fig. 2. Equivalent circuits for modeling of DC motor

Where the circuit element represents the motor model parameters are described in Table I.

TABLE I
MOTOR MODEL PARAMETER DESCRIPTION

$e_a(t)$	Applied armature voltage
$i_a(t)$	Armature current
$e_b(t)$	Back electromotive force
R_a	Armature resistance
L_a	Armature inductance
$\theta_m(t)$	Angular position
$\omega_m(t)$	Angular velocity
J	Rotor Inertia
B	Viscous friction

$\tau_m(t)$	Motor torque
$\tau_l(t)$	Load torque

Permanent magnet motor model presented above can be described by the two differential equations, one for electrical part and one for mechanical part. The differential equation for the armature electrical circuit is:

$$R_a i_a(t) + L_a \frac{di_a(t)}{dt} = e_a(t) - e_b(t) \quad (1)$$

The equation of motion, i.e. mechanical equation:

$$J_m \frac{d^2\theta_m(t)}{dt^2} + B_m \frac{d\theta_m(t)}{dt} = \tau_m(t) - \tau_l(t) \quad (2)$$

Interconnection between electrical and mechanical equations is realized by torque equation (3),

$$\tau_m(t) = K_\tau i_a(t) \quad (3)$$

and back electromotive force equation (4).

$$e_b = K_b \omega_m(t) \quad (4)$$

Replacing the motor torque (3) and back electromotive force (4) in electrical (1) and mechanical (2) equations, and applying Laplace transform, gives the following dynamic equation in the Laplace domain:

$$\begin{aligned} (sL_a + R_a)I_a(s) &= E_a(s) - K_b\Omega_m(s) \\ (sJ_m + B_m)\Omega_m(s) &= K_\tau I_a(s) - T_l(s) \end{aligned} \quad (5)$$

System of equations (5) can be used for generating the block diagram for dynamic system description presented at the Fig. 3.

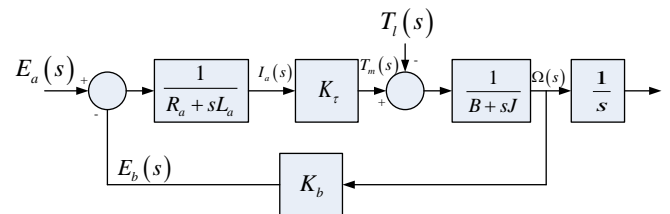


Fig. 3. Block diagram of the DC motor system

2.2. Modelling of tachogenerator

In certain speed of rotation of the rotor of tachogenerator, the rms value of the induced voltage can be explained by a linear equation:

$$E_{TG} = c_{TG}n \quad (6)$$

The expression (6) shows that the rms value of the output voltage of tachogenerator in idle mode is a linear function of speed of rotation n . It follows that tachogenerator can be modeled with a simple block - multiplication by a constant.

2.3. Modelling of a speed servo

Combining the models development above and utilizing control circuitry we can obtain the complete model of DC servo shown on Fig. 4.

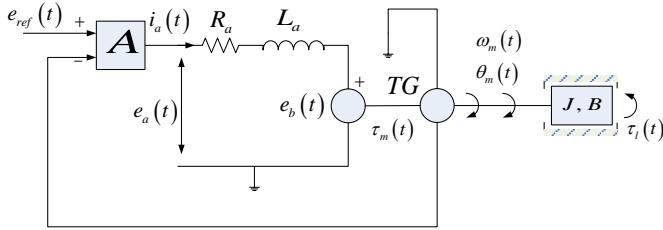


Fig. 4. Dynamic model of DC servo

Block 'A' stands for amplification, i.e. controller and 'TG' represents block of tachogenerator. The rest of the consisting components in block diagram of DC servo are described earlier.

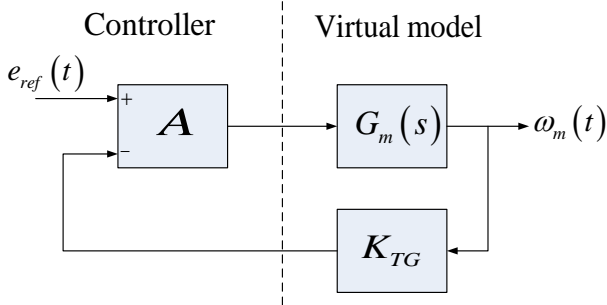


Fig. 5. Transfer function block diagram of DC servo

Block diagram of DC servo dynamic system model is presented on Fig. 5. During the following consideration the left side will be realized as a real controller and the right side which represent a controlled plant, in this case combination of DC motor and tachogenerator, will be implemented in a real hardware as a virtual model.

III. HIL TEST-BED DESIGN

The core platform of the presented hardware-in-the-loop approach is the Virtual Test Bed (VTB). The VTB is a dedicated environment for simulation and virtual prototyping of complex systems. The VTB allows for handling natural power flow, signal and data coupling between inter-connected devices and offers a combination of both topological and mathematical expressions in model formulation for a

comprehensive and efficient modelling process. The VTB also supports multiple layers modelling, wherein each layer can describe a different model complexity or a different behaviour. In addition to the powerful capabilities for modelling, the VTB is endowed with mechanisms for both wrapping and co-simulating with models developed in LabVIEW environment [4].

3.1. Controller design

The subject of this subsection is the development of the digital controller for power electronic circuit for governing speed servomechanism consisting of actuator - electric DC motor and angular velocity sensor. Motion control task can be realized by pulse-width modulation utilizing a bridge circuit configuration for powering the electric motor. Based on information obtained by the angular velocity sensor controller will change the width of the pulses in order to maintain a constant pre-specified speed of rotation. The prepared prototype controller implemented in Ni6008 acquisition card [5] will be connected to test hardware, the same type card, and scenarios in different operating conditions would be given interactively through a personal computer, Fig. 6.

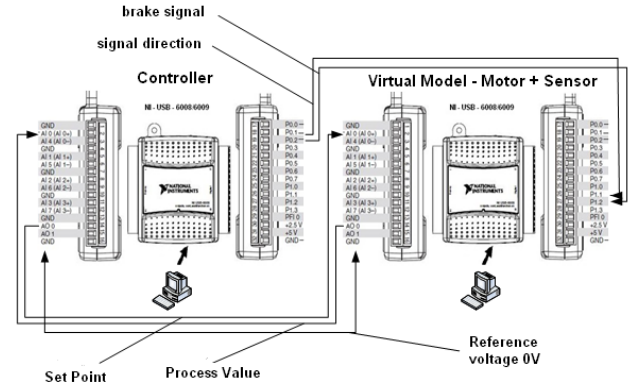


Fig. 6. Connection of used hardware

Block diagram of proposed controller incorporating PWM (Pulse Width Modulation) generator and feedback control with PID (Proportional Integral Derivative) circuit is presented on the Fig. 7.

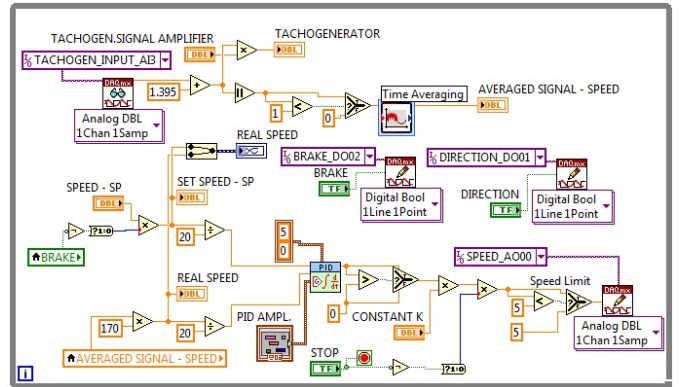


Fig. 7. Controller block diagram

Pulse width modulated signal can be obtained by a comparison of instantaneous value of saw-tooth signal and referent voltage. Varying the referent voltage results with the different duty cycle of PWM signal.

3.2. Virtual model implementation

In the case of testing with the principle of Hardware in the loop, the real object of control is replaced by a virtual model implemented in the hardware [5]. Block diagram of the virtual model developed in the previous section, implemented in this phase is given in Fig.8.

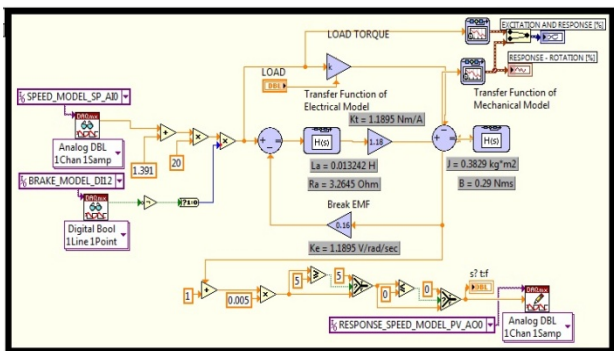


Fig. 8. Block Diagram of virtual plant model

Output signals of controller are input signals in virtual model and vice versa. Analogue signals are normalized according to acquisition card limits.

IV. EXPERIMENTAL RESULTS

Real time controller and virtual plant implemented in different hardware are undergone of testing. Different scenarios are generated and applied to the virtual model and results of experiment are presented on the next figures.

Experiments start with no load condition. Step response of the system with the absence of load torque is presented on the Fig. 9. It is obvious the behavior of second order system response with a vanishing oscillations. After some time since starting the resulting speed is equal to required speed.

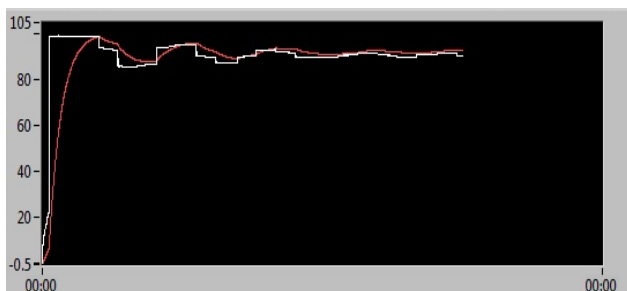


Fig. 9. No load torque step response

The results of another two starting scenarios are presented on the Fig. 10 and Fig. 11. The first scenario is application the

load torque during motor starting, and removing it after reaching set point, i.e. nominal motor speed.

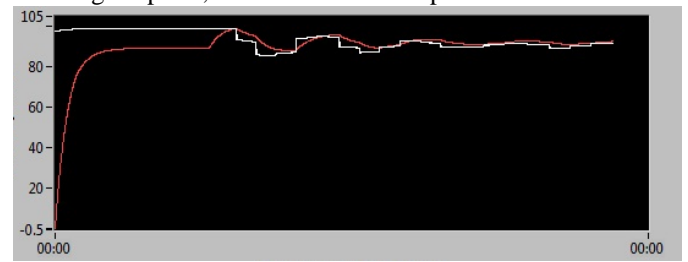


Fig. 10. Applied load torque during motor starting

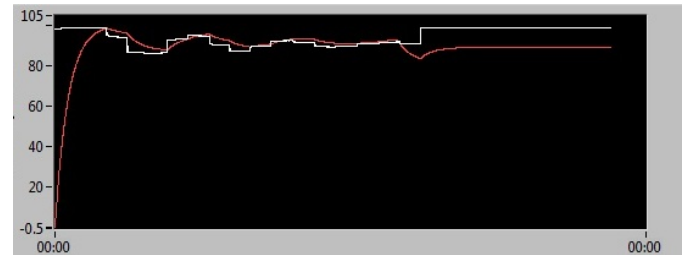


Fig. 11. Applied load torque after motor starting

At the moment of starting, controller responds with the increased excitation voltage as a reaction of applied external load torque to reach the given set point. When external load torque disappear the controller excitation voltage goes down followed by some decreasing oscillations due to the system order. The next figure shows scenario where the external load torque is applied after motor starting. At the moment of increased load torque the motor speed slow down, but after controller reaction with increased excitation voltage the motor speed reach its nominal value, set point.

V. CONCLUSION

HIL simulation is a technology where powerful modern electronic systems and their ancillary components are replaced with digital simulation in real time based on the physical model. This simulation is used to test the components as digital controller, which instead of being connected to real equipment under control is associated with HIL simulator and digital controller being tested feels like a real control system.

REFERENCES

- [1] P.M. Menghall, A.J. Laxmi, "Real Time Control of Electrical Machine and Drive: A Review", *International Journal of Advances in Engineering & Technology*, Sept. 2011, ISSN: 2231-1963.
- [2] B. Lu, A. Monti, R.A. Dougal, "Real-Time Hardware-In-the-Loop Testing During Design of Power Electronics Controls", *IECON 03*, The 29th Annual Conference, Roanoke, VA, USA, Nov. 2-6, 2003.
- [3] L. Lennart, *Modeling Of Dynamic Systems*, Prentice-Hall, Inc.1994.
- [4] LabView™, *Control Design and Simulation Module*, National Instruments Co. 2009.
- [5] NI USB-6008/6009 User Guide and Specifications, © 2004–2012 National Instruments Corporation.

Session EE:

ENGINEERING EDUCATION

A Case-Study Approach in Microcontroller Education

Valentina Rankovska¹

Abstract – In this paper an application of the case study approach in the microcontroller education is given. It is applied in the Bachelor's degree of Electronics in the Technical University of Gabrovo and it is implemented using various labkits. This approach is attractive for the students; it helps them to understand better the taught material and increases their motivation to study.

Keywords – Microcontrollers, Education, a Case-Study Approach, Development Boards.

I. INTRODUCTION

The progress of the microprocessor devices and systems is extremely dynamic since the occurrence of the microprocessors in the early 70's of the XX century to the modern microcontrollers and embedded systems.

The latter are applied in a wide range of areas - home and office appliances, automobiles, media and communication equipment, industrial applications, "smart home" and others. In many areas they solve monitoring and control problems, which have been solved formerly using for instance mechanical and electrical switching systems. This explains the wide variety of microcontrollers with a wide range of functionality and also the need for studying them. Moreover - the necessity of their inclusion in the curricula of disciplines such as biological engineering, agricultural engineering, forest resources, etc. [3], [10].

There are generally two main approaches to implement embedded microprocessor systems depending on the components used:

- Based on the traditional microcontrollers (single-chip microcomputers);
- Embedded systems integrated in programmable logic – Field-Programmable Gate Arrays (FPGA), Systems-On a Programmable Chip (SOPC), etc.

Regardless of the wide possibilities, which the innovative programmable logic integrated circuits give, the traditional microcontrollers will not soon be substituted by them generally because of the following reasons:

- The high level of complexity of the programmable logic devices, the development boards and software and their comparatively high price;
- In order to achieve optimal features and parameters of the designed systems, it is recommended to use Hardware Description Languages (HDLs). To study and apply them however additionally makes the design process more complex and expensive.

¹Valentina Rankovska is with the Faculty of Electrical Engineering and Electronics at Technical University of Gabrovo, 4 H. Dimitar str., Gabrovo 5300, Bulgaria, E-mail: rankovska@tugab.bg.

That is true especially when designing embedded systems of low and middle level of complexity, when it is necessary to achieve low cost price, when a low number of the devices will be produced, etc.

In the same time the microprocessor circuits education is plagued with problems, a result of various reasons:

- The abstract architecture of the microcontrollers and their programmability;
- The more and more complex architecture of the modern microcontrollers;
- The increasing volume of the supplied documentation;
- The adjustments and thinking of the present and future learners (students), who want to achieve quick and visible results at decreased analytical thinking;
- Additionally, to everything listed above – the presented results are for the education in Electronics. In many cases abroad microcontrollers are studied in Computer architectures-like courses, in which hardware and software of the digital and microprocessor systems are studied more detailed and for more time.

Microcontrollers have a much more complex architecture with various functions in comparison to integrated circuits that implement basic logic functions, or present simple logical nodes and blocks and can more easily be studied and researched. Furthermore, to study a block operation, for example a serial interface, is impossible without a control program for it. Or the students are required to obtain knowledge and skills both in the field of hardware and programming.

Along with all of this it is very difficult to appreciate immediately the end use of the microcontroller studied, and this further reduces the motivation of learners. One simple, but real application microprocessor unit presents not so complex electrical scheme, but is controlled by a program consisting for example of 100-200 lines (if it is in Assembler).

In the present work the application of the case-study approach in the Microprocessor Circuits course for the students in the bachelor's degree in Electronics at the Technical University of Gabrovo is presented.

II. MODERN TRENDS IN THE MICROCONTROLLER EDUCATION

In order to increase the effectiveness of the microcontroller education innovative means and approaches are continuously found and applied in terms of reducing workload of subjects, increasing prices of the development boards and kits and the above-mentioned problems in education:

- *Using complex and expensive development boards, applied in several courses* [4].

In Oregon State University a TekBots™ (a robotic base), is developed and implemented. It serves as a platform for learning in electrical and computer engineering (The students

purchase their own TekBot). Several years after a mechatronic variant for Mechanical Engineering is made and applied.

- *Possibilities to test the designed projects remotely*, via web, using development boards in the laboratory [2], [6], etc.

A good example is the possibility provided in the Siberian State University of Telecommunications and Information Sciences for remote experimentations [2]. The students (and not only as the access is free) can program the microcontroller ADuC842 on a development board, which includes peripherals, like 7-segment display, LEDs, real-time clock, digital thermometer, etc. The results could be monitored via webcam in real time. The necessary information and some examples are provided on the site.

- *Home Experimentation* [1], [2], [4]:

In the Institute of Computer Engineering at Vienna University of Technology the students studying Embedded systems, are supplied with labkits which they can borrow for a deposit of 70 euros [2]. They also could buy them if they wish. The labkits include a CD ROM with the necessary open source software and the Linux operating system. This helps them to begin working immediately without the necessity to install some software.

In the Electrical & Computer Engineering Department at Mississippi State University the students should purchase the parts kits (\$65) used for the hardware labs [1].

- *A gradual implementation of a complete embedded system*, including a control unit (microcontroller), sensors and actuators – for instance a simple robot, performing elementary functions [3], [10], [11].

This variant is applicable at the gradual growing of the knowledge and the skills in studying the selected microcontroller [11]. It is possible also to use it in making the course projects and applying a team-based design approach. Then several students could accomplish different operations implemented by the robot.

III. THE CASE-STUDY APPROACH IN THE MICROCONTROLLER EDUCATION

Designing a course relates generally two aspects: structure and content, taking into account the input connections, and the methodological tools used:

- **Concerning the structure and content of the course**

Microprocessor systems course is taught in the bachelor degree of Electronics (VI semester). Some of the input connections in the curriculum are related to high-level language programming (C language), pulse and digital circuits, sensors. That is the students have already learned a high-level programming language and the design and operation principles of basic digital circuits and blocks used in microcontrollers and embedded systems. The only other subject concerning these widespread control devices and systems is Embedded microcomputer systems studied in the eighth semester, but it is optional. This means that the students should be acquainted with a general purpose microcontroller and its application within only one discipline throughout the whole course. The workload of

Microprocessor systems course is 45 hours of lectures and 30 hours laboratory work. There are no seminars (as in the old curriculum), which could be used to design programs, used in the laboratory classes.

That is why the number of hours for some topics has been reduced drastically in the curriculum. They are related to the number formats, number systems conversions; phases of existence and design stages of microprocessor devices and systems, and some others. All this is in order to preserve the practical nature of the course - to have enough time for the students to learn the hardware, the programming of the microcontroller and to examine some simple case studies microprocessor devices.

The emphasis is on learning the hardware of the selected microcontroller and at the end of the course on practical aspects such as human-machine (microcontroller) interface and modern interfaces used in embedded microcomputer systems.

- **Concerning the used methodological tools**

The Microprocessor systems education for over 10 years is based on the widespread Microchip's 8-bit general purpose microcontrollers PIC12/16/18 which have a number of advantages [1].

Regarding to the programming languages studied at the universities and colleges various strategies are applied: using an assembler and a high-level language or only a high-level language (mostly C). In the presented course an assembly language and a C language are studied. Approximately two thirds of the workshops an assembler is studied and implemented and about one third of the hours - C. The students are already familiar with C from a former discipline. Presented in [1] study shows that this approach is correct.

The first four hours of the labs are devoted to the features and usage of the free integrated design environment MPLAB IDE (Microchip) and the software design stages. Immediately after that the students are involved into the realization of simple designs with simple assembler programs. The aim is to demonstrate them elementary microcontroller applications such as using buttons and LED indication. A variety of hardware tools is used: from simple models developed in the laboratory (Fig. 1 and Fig. 2), to more complex development systems containing a microcontroller and various peripherals and hardware debugging tools like In-Circuit Debuggers (ICD).

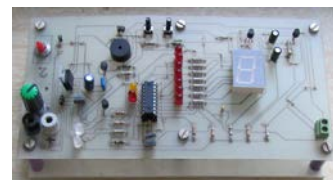


Fig. 1. Labkit 1 (with PIC16F84)

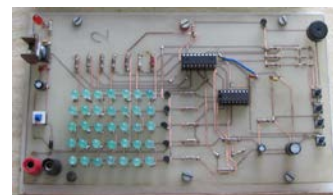


Fig. 2. Labkit 2 (with PIC16F84)

Some examples used in the Microprocessor systems lab: a development system with Microchip's ICD, and a development board BIGPIC5, produced by Mirkroelektronika [9] (Fig. 3).

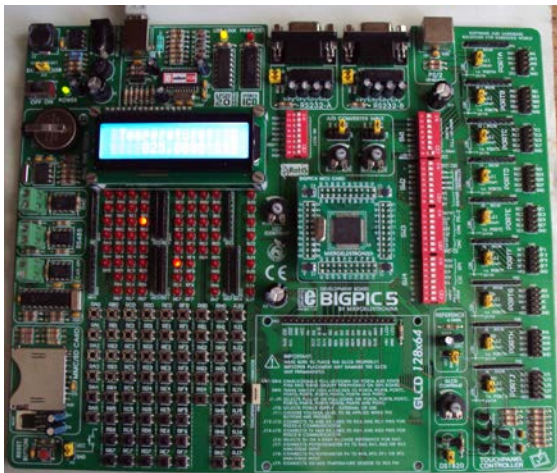


Fig. 3. BigPIC5 development board with PIC18F8520

Initially, in introducing the assembly language, it is appropriate to use ready models. The purpose is to allow the students to test their own elementary programs.

Thereafter the case study approach is applied, beginning with simple circuits to more complex projects, although the students are still not completely familiar with the hardware and the features of the microcontroller. This is done mainly in order not to lose the motivation of the students, because the consistent study of the individual microcontroller blocks operation (an old approach) seems an end in itself, abstract and not interesting for them.

Initially the students begin with using model boards (breadboards), on which they assemble simple circuits. The next task is to design and test simple programs which control the circuits (Fig. 4). The goal is to not accept the hardware as something given for granted, and to acquire skills to design, assemble and test an electrical schematic diagram.

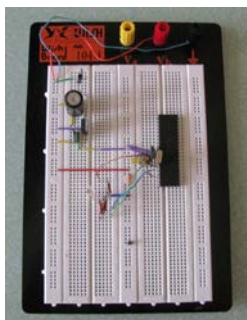


Fig. 4. The first breadboard project (with PIC16F874)

Traffic Lights Control System

It is appropriate to use the traffic lights as a case study in education [8], [12], [13]. It is an object well known to the students, and on the other hand relatively easy to control.

Fig. 5 shows a model of traffic lights used in the Microprocessor systems course. It also includes functions like

displaying the time left before changing the state of the traffic lights and detecting a stopped car in a street with low traffic. The detection is made by an infrared LED and a photodiode (shown in the left in Fig. 5 a).

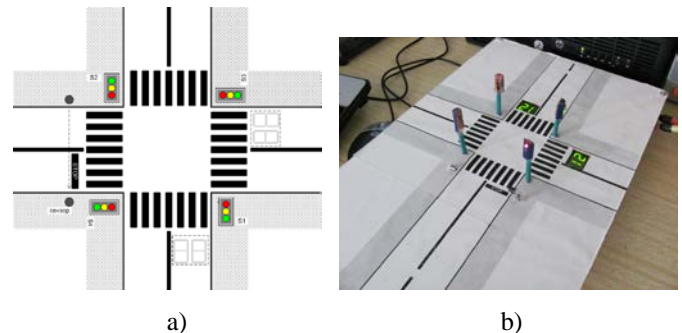


Fig. 5. Traffic Lights control with PIC16F627A

The control of the model can be configured for different variants: as an intersection of streets with equal priority where the time for the green and the red light is one and the same; when the traffic in one of the streets is with a higher priority (with more time for the green signal from that of the red); using the function for detecting a stopped vehicles.

There are possibilities to implement various algorithms: making time delays of different durations, generating control signals, controlling a 7-segment display, receiving and handling information from a sensor, etc. More complex variants are also possible such as changing the time durations according to the different parts of the day (for instance taking into account peak traffic intervals) and only a flashing warning signal at night, weekends, etc.

A DC Motor Control

Stepper and DC motors for low power applications are applied in a wide range of areas. Fig. 6 shows a DC motor controlling model based on PIC12F683. There are two goals: to control the object via a microcontroller and to present the features of the low-end microcontrollers of Microchip which have a low number of pins. There is also a potentiometer that can be used to change the rotation speed of the motor and a general purpose button, which can be used for example to change the mode of operation (e.g., the speed of the motor). These features also allow a variety of simple control algorithms implemented in C or Assembler.

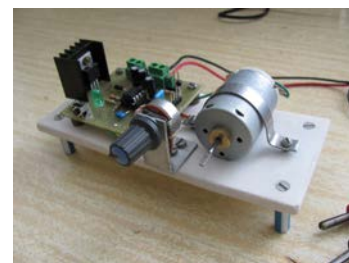


Fig. 6. A DC motor control with PIC12F683

An Electronic Badge

An effective real device, causing an interest among the students, is the Electronic badge (Fig. 7), realized with the PIC16F876A.

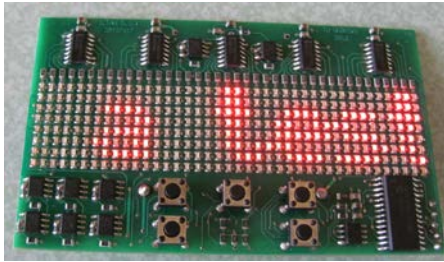


Fig. 7. An electronic badge with PIC16F876A and ICSP

The indication is implemented as a LED matrix 8x40. There is an opportunity for ICSP programming, allowing the students to easily reprogram the microcontroller to display different symbols.

The badge has five buttons that can be used for different operation modes and sub-modes. For example, initially it is shown to the students a ready, more complex operation algorithm, comprising two main modes: displaying information stored in the EEPROM with a lower or a higher speed, and changing the information in the EEPROM memory by using a kind of a stored character set. Then they can reprogram the microcontroller for different variants of simpler algorithms controlling the LED matrix.

Future work

It is necessary to enlarge the opportunities for the students to work alone and to increase the time for the practice. Since it is impossible to increase the time of the discipline, it is possible to give them the opportunity to work at home. It is difficult to supply them with labkits for home work in our conditions (either to borrow, or to buy them) because they are expensive. But it is possible to allow them to use the development boards and test their projects remotely, via a web server. That is our further goal, together with enlarging the variety of the boards used.

IV. CONCLUSION

In this paper an application of the case study approach in the microcontroller education is given. It is applied in the Bachelor's degree of Electronics in the Technical University of Gabrovo. It is implemented using various labkits, which number and variety should be increased. This approach is attractive for the students; it helps them to understand better the taught material and increases their motivation to study.

Of course it is not the only thing which should be done. The students are also supplied with course materials, which are an object of a continuous improvement [14].

The next step is to give them the opportunity to use remotely a "web-lab" at home.

ACKNOWLEDGEMENT

The present work is supported by the Science Research Fund at the Ministry of Education, Youth and Science under contract № E1403/2014.

REFERENCES

- [1] R.B. Reese, B.A. Jones, "Improving the Effectiveness of Microcontroller Education", IEEE SoutheastCon 2010 Conference Proceedings, pp. 172-175, Charlotte-Concord,NC, USA, 2010.
- [2] W. Elmenreich, Ch. Trodhandl, B. Weiss, "Embedded Systems Home Experimentation", 2nd IASTED International Conference on Education and Technology (ICET'06) Conference Proceedings, pp.11-15, Calgary, Alberta, Canada, 2006.
- [3] T.K. Hamrita, R.W. McClendon, "A New Approach for Teaching Microcontroller Courses, International Journal of Engineering Education, vol. 13, no. 4, pp.269-274, 1997. <http://www.ijee.ie/articles/Vol13-4/ijee984.pdf> (accessed in March, 2014)
- [4] A. Smit, D. Heer, R. Traylor, T. Fiez, "A Custom Microcontroller System Used as a Platform for Learning in ECE", ASEE Annual Conference Proceedings, ASEE 2004 Annual Conference and Exposition: Engineering Education Research's New Heights, pp. 2733-2740, 2004.
- [5] N. Manjikian, S. Simmons, "Evolution and Enhancements of a Microprocessor Systems Course", IEEE Trans., Education, vol. 42, no. 4, pp. 2395-2503, 1999.
- [6] Лаборатория с удаленным доступом для исследования работы микропроцессоров. Сибирский Государственный Университет Телекоммуникаций и Информатики. <http://www.labfor.ru/online/aduc> (accessed in March, 2014)
- [7] V. Proulx, J. Raab, R. Rasala, "Traffic Light: a Pedagogical Exploration Through a Design Space", Journal of Computing Sciences in Colleges, vol. 15, Issue 5, pp. 25-31, 2000.
- [8] <http://www.mikroe.com/>
- [9] T. Hamrita, W. Potter, B. Bishop. Robotics, Microcontroller, and Embedded Systems Education Initiatives at the University of Georgia. An Interdisciplinary Approach, International Journal of Engineering Education, vol. 21, no. 4, pp.730-738, 2005.
- [10] Т. Уилмшерст, Разработка встроенных систем с помощью микроконтроллеров PIC. Принципы и практические примеры, СПб, Корона-Век, 2008.
- [11] M.R.A. Purnomo, D.A. Wahab, A. Hassan, R.A. Rahmat, "Development of a Low Cost Smart Traffic Controller System", European Journal of Scientific Research, vol. 32 no.4, pp.490-499, 2009.
- [12] D. Rotake, S. Karmore, "Intelligent Traffic Signal Control System Using Embedded System", Innovative Systems Design and Engineering, vol 3, no 5, pp. 11-20, 2012.
- [13] <http://umis.tugab.bg/moodle/>

E-learning Module for Computer-Aided Design in Moodle Platform

Galia Marinova¹ and Nikolay Stoyanov²

Abstract – The paper describes an E-learning Module for Computer-Aided Design developed in Moodle platform implemented in Bachelor degree course in Telecommunications faculty in Technical University-Sofia. The E-learning Module is assisted by a specially developed online circuit calculator SMARTCircuitCalc which permits to generate parameters for individual projects to be simulated by students with ORCAD/PSPICE. Some observations on students' activities with the E-learning Module are commented.

Keywords – E-learning, Moodle, Computer-Aided-Design, Online circuit calculator, ORCAD/PSPICE.

I. INTRODUCTION

The open source platform Moodle is widely implemented in e-learning environments in universities all over the world. University courses for Computer-Aided Design and PSpice simulations can also be found in Moodle [2-5]. The paper describes an E-learning Module for Computer-Aided Design as a part of the project PROGRES-FTK in the Telecommunications faculty in Technical University – Sofia developed in Moodle Platform. The E-learning Module is created as an additional source of information, exercises, tests and projects for the course “Computer-aided design” for third year Bachelor degree students. The title of the Module is: **Computer-Aided Design of Communication Circuits with ORCAD/PSPICE and Other Tools**.

Since the main subject of the course “Computer-aided design” is focused on ORCAD/PSPICE applications, the E-learning module tends to add information for other CAD tools and to demonstrate wider application of ORCAD/PSPICE for communication circuits simulations in addition to those considered in regular laboratory exercises. An innovation in the E-module is its connection with a new developed online circuit calculator SMARTCircuitCalc which permits the generation of individual projects and tasks for students. Preliminary experiments with online assisted CAD course are presented in [1].

First the structure, the tests and the tasks in the E-learning Module are considered, then the new online circuit calculator SMARTCircuitCalc is described and then some observations on students' activity with the E-module is considered.

¹Galia Marinova is with the Faculty of Telecommunications at Technical University of Sofia, 8 Kl. Ohridski Blvd, Sofia 1000, Bulgaria, E-mail: gim@tu-sofia.bg.

²Nikolay Stoyanov is a student in the Faculty of Telecommunications at Technical University of Sofia, 8 Kl. Ohridski Blvd, Sofia 1000, Bulgaria.

II. STRUCTURE, TESTS AND TASKS IN THE E-LEARNING MODULE FOR COMPUTER-AIDED DESIGN

A. Structure of the E-learning Module for Computer-Aided Design

The E-learning module “**Computer-Aided Design of Communication Circuits with ORCAD/PSPICE and Other Tools**” is developed in Moodle 2.5+ platform and is organized in 5 topics:

Topic 1. Levels of Computer-Aided Design – analog, logical, digital, architectural, microprocessor. Daniel Gajsky Y model and J.P.Calvez classification are in the origin of this topic.

Topic 2. Computer-Aided Design tools – FilterCAD, AADE, PAC Designer, MMICAD, PSOC, WARP 6.2 and ISE WEBPACK. The main possibilities and applications of these tools are presented in this topic.

Topic 3. Simulator ORCAD/PSPICE. The architecture of the simulator ORCAD/PSPICE is presented and the features of ORCAD/Capture and ORCAD/PSPICE are considered in details.

Topic 4. Guidelines for analysis of different types of circuits with the simulator ORCAD/PSPICE – 20 types of circuits are considered: Audio amplifiers, Equalizers, PID controllers, Control system, Controller MAX854C, Circuit regulating the sound in a guitar, Signal oscillators – sinusoidal, pulse, “delay”, triangle, Programmable gain amplifiers, Filters with quartz crystals, Voltage regulator circuits, Circuits with timer 555.

Topic 5. Design of different parts of communication system – RF, digital and analog, with specialized and appropriate CAD tools. This topic includes recommendations and additional tools for PCB design of a communication system and mobile devices; Computer-aided design of communication system using MATLAB, ORCAD/PSPICE and a set of specialized online tools and platforms; Computer-aided design of power supplies, antennas, loudspeakers and microphones in communication systems.

All 5 topics are organized as follows:

- Learning objects, realized as presentations with included audio files for a set of subjects in the topic and additional knowledge units associated to the subjects.
- Learning test and
- Exam test.

In Topic 4 are included Tasks, Virtual simulators and a link with especially developed Online circuit calculator

SMARTCircuitCalc, which allows the personalization of students' projects and tasks.

There are 74 Learning Objects as presentations with audio files, 185 Knowledge units in a Virtual library, developed as a part of the project in the Telecommunications faculty, 5 Learning tests with 50 questions and 5 Exam test with 12 questions each.

Three MS-EXCEL based Virtual simulators and 13 tasks are added in Topic 4 which together with the online circuit calculator permit to define a large number of individual project for students home and/or class exercises. The E-learning Module **“Computer-Aided Design of Communication Circuits with ORCAD/PSPICE and Other Tools: is published on: <http://mdl.tu-sofia.bg/moodle/course/info.php?id=7&lang=en>.**

B. Tests in the E-learning Module

Two types of tests are included in each Topic in the E-Module – Learning tests and Exam tests.

The Learning tests are placed on the last pages of Lessons, realized through the Lesson activity in Moodle. The Learning objects of each topic are converted in SWF format and placed on the Lesson pages. All Lesson pages are accessible in parallel through push buttons. When a student makes an error in the Learning test, a feedback is foreseen to lead him back to the Learning object, which he has to revise in order to correct his error. These feedbacks are developed as a part of the personalization system in the e-learning system in the Telecommunications faculty. For all topics, a result of more than 70% to the Learning test is a precondition for access to Exam tests.

The Exam tests are realized through the Test activity in Moodle with the help of the Question Bank of the platform. The questions in the Exam tests are selected randomly from the Question Bank in Moodle, where an hierarchy of categories is created for each Topic. Four subcategories per Topic are developed with more than 10 questions each. When a concrete Exam test is generated for a student, 3 random questions are selected from each one of the 4 subcategories in the category for the Topic and an Exam test with 12 questions is proposed to the student.

Learning tests and Exam tests are limited in time and they allow no more than three attempts.

C. Tasks in the E-learning Module

The tasks in the E-learning Module are included in Topic 4.

Three MS-EXCEL based Virtual simulators are included in the E-learning Module, as follows:

- Virtual simulator for Audio amplifier design,
- Virtual simulator for Advanced audio amplifier design,
- Virtual simulator for Equalizer design.

Each Virtual simulator in MS-EXCEL is supported by a set of Knowledge units to help the student to design the circuits. The student has to extract himself the formulas and to make the circuit calculation in the MS-EXCEL file. The three circuits to be calculated are included in the Virtual simulators.

Figures 1a and 1b present the circuits of the Audio amplifier and the Advanced audio amplifier to be designed in the MS-EXCEL Virtual simulators. These three Virtual simulators are modifications of the online calculators in [7].

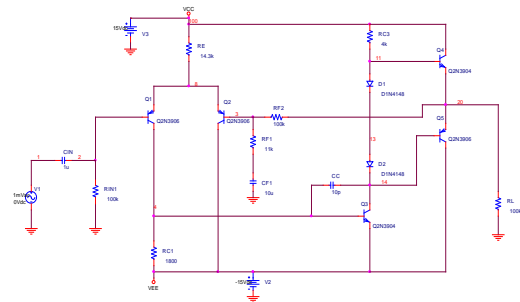


Fig. 1a. Audio amplifier circuit in MS-EXCEL Virtual simulator

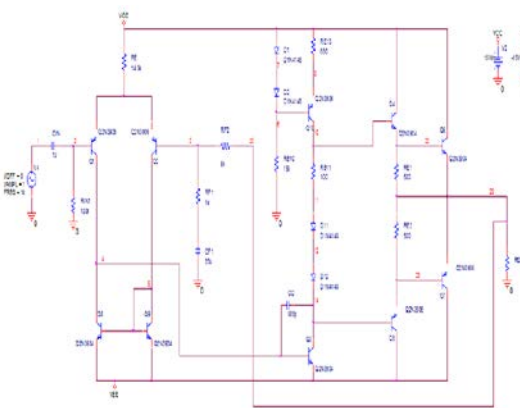


Fig. 1b. Advanced audio amplifier circuit in MS-EXCEL Virtual simulator

Thirteen tasks for analysis of different circuits with ORCAD/PSPICE are included in Topic 4. The MS-EXCEL Virtual simulators permit not only to test student on the corresponding circuits but when combined with the tasks for the audio amplifier, the advanced audio amplifier and the equalizer, to make comparison between calculated and PSPICE simulated results and if necessary to adjust the circuits' parameters. Besides the MS-EXCEL Virtual simulators, an additional tool is developed for personalization of the students' tasks and projects – the Online circuit calculator SMARTCircuitCalc which is described in next point.

III. ONLINE CIRCUIT CALCULATOR SMARTCIRCUITCALC

The Online circuit calculator called SMARTCircuitCalc is developed and associated to the E-module in order to generate personalized tasks and projects for students. SMARTCircuitCalc calculates elements values of circuits and models, as follows:

- Quartz crystal model parameters calculation,
- Calculation of a circuit with timer 555,
- Colpitts oscillator parameter calculation,
- Hartley oscillator parameter calculation.

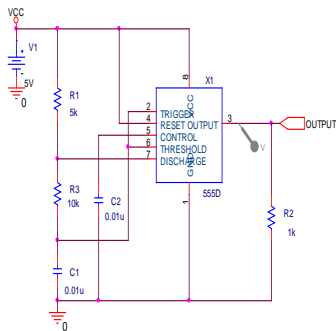


Fig. 2a. Circuit with timer 555 in SmartCircuitCalc

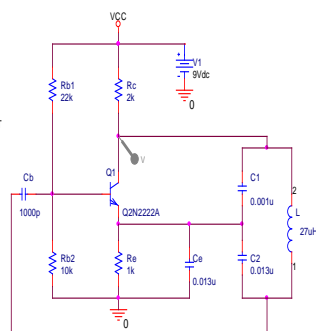


Fig. 2b. Colpitts oscillator circuit in SmartCircuitCalc

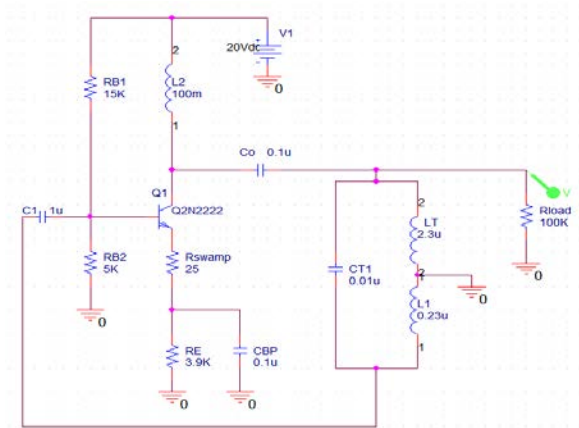


Fig. 2c. Hartley oscillator circuit in SmartCircuitCalc

The circuit with timer 555 and the circuits of the oscillators of Colpitts and Hartley included in SmartCircuitCalc are illustrated on Figs 2a, 2b and 2c.

The online calculation of quartz crystal model parameters is a modification of [9] and its function is to calculate the resonance frequency f_{res} , given the values of C_1 , C_2 and L , or given f_{res} , C_1 and C_2 to calculate the value of L .

The online calculator of a circuit with Timer 555 is a modification of [10] and its function is given R_1 , R_3 and C_1 from Fig.2a to calculate the frequency of the generated pulses f , the period T , the pulse width t_1 and the duty cycle – g .

The online calculator of the Colpitts oscillator is a modification of [11] and its function is given C_1 , C_2 , L from Fig.2b to calculate the frequency f of the generated sinusoidal signal.

The online calculator of a circuit of the Hartley oscillator is a modification of [12] and its function is given C , L from Fig.3c to calculates f and given C , L to calculate f .

These 4 online calculators permit to generate different specifications for the circuits with quartz crystals – filters and generators and for the timer 555, Colpitts and Hartley oscillators. Thus individual parameters are generated for the corresponding tasks for each student. The student is supposed to simulate his task with the individual specification and or circuit elements' values obtained from SMARTCircuitCalc. Individual students' projects are created by sets of Tasks.

A. Task on Harley oscillator circuit generated with SMARTCircuitCalc

Figs. 3a and 3b present the simulation of the Harley generator from Fig 2c, calculated for a 1MHz frequency. The circuit is then simulated in ORCAD/PSpice as shown on Fig.3b. The student should then determine the value of the period of the generated sinusoidal signal, which in the case of Fig3b is $1\mu s$ and correspond exactly to the 1MHz frequency determined in SMARTCircuitCalc.

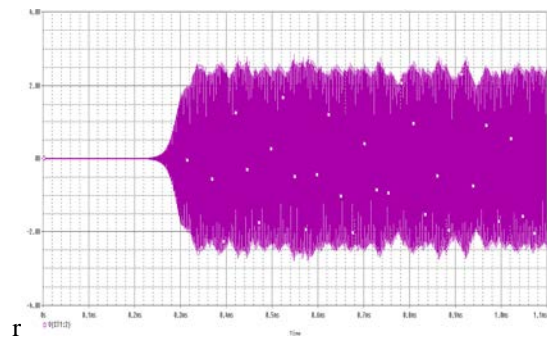


Fig. 3a. Output voltage of Hartley oscillator circuit simulated in ORCAD/PSpice

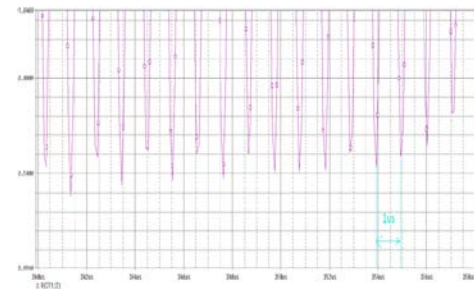


Fig. 3b. Period of the signal generated from Fig. 3a.

B. Task on Filter with quartz crystals circuit generated with SMARTCircuitCalc

Additional tools as AADE Filter Designer [8] are used together with SMARTCircuitCalc and ORCAD/PSpice for quartz crystal filter synthesis, calculation and simulation. On Fig.4a a filter with 2 quartz crystals is entered in AADE Filter Designer. Then the quartz crystal model parameters are calculated in SMARTCircuitCalc for a given resonance frequency 3.6MHz, as shown on Fig.4b. At that stage of personalization the student can simulate the filter from Fig.4a with AADE tool and/or with ORCAD/PSpice and then determine the circuit parameters and performance, as shown on Fig.4c.

The Online circuit calculator SMARTCircuitCalc is developed with PHP, JavaScript, HTML5 and CSS3. Its home page is presented on Fig.5 and its web address is:

<http://niki.heatdesign.net>

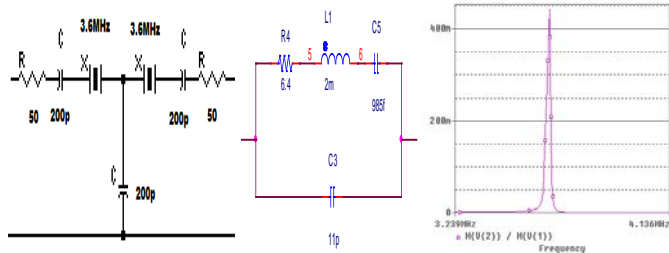


Fig. 4a Filter with 2 quartz crystals entered in AADE filter designer

Fig. 4b. Quartz crystal model with parameters calculated in SMARTCircuitCalc

Fig. 4c. PSpice simulation of the filter gain



Fig. 5. SmartCircuitCalc home page

IV. CONCLUSION

The E-learning Module for Computer-Aided Design was implemented as a part of the individual educational duties of the students in the summer term of the academic year 2013/14 in the Telecommunications faculty. The observations on the students' activity with the E-learning Module show that 165 students have performed Lessons, the Learning tests in the lessons and the Exam tests. The average results for each topic and for the course are shown in Table I.

TABLE I
AVERAGE TEST RESULTS IN THE E-LEARNING MODULE

Topic	Average result for the Learning test	Average result for the Exam test over 10
Topic 1	87,81%	9,12
Topic 2	80.13%	8.99
Topic 3	92.28%	9.75
Topic 4	89.44%	9.42
Topic 5	87.44%	9.26
All topics	87.18%	

All 165 students filled feedback forms at the beginning of the course. At the end of the course 152 students passed all the learning and exam tests successfully, 12 students failed with a score less than 70% to at least one test and 1 student couldn't register until the end of the e-learning course. 160 students filled the feedback forms again at the end of the e-learning

course and all of them declared to be satisfied from their participation in this course. 16 students made comments as follows:

- 6 students wanted a better interface and more friendly environment;
- 2 students wanted more homework and practical work;
- 4 students wanted the correct answers to be given at the end of the Learning test and 1 student wanted no correct answer to be given at the end of the Exam test in order to motivate to study the lessons more deeply.
- 1 student didn't want when failing the Learning test to be driven back to lessons.
- 1 student asked all tests to be open simultaneously from the beginning of the course and during the whole course.
- 1 student reported a special problem with 30 successive low scores on a Learning test.

The average time passed by a student on a test is 1 hour and 40 minutes. These results show that E-learning approach is well accepted by students and they find it useful for improving the quality of their education.

ACKNOWLEDGEMENT

The paper is realized in the framework of the project PROGRESS-FTK. PROJECT BG051PO001-4.3.04-0053 „PROGRES-FTK: Platform for personalized education with guaranties for growth and effective self-improvement in the Telecommunications Faculty”. The project is supported by the Operating program „Human Ressorces development”, cofinanced by the European Social Fund of EU.

REFERENCES

- [1] G. Marinova, “Multitool online assisted design of communication Circuits and systems”, Proc. of ICEST'2012, Veliko Tarnovo, Vol.2, pp.589-592, 28-30 June, 2012.
- [2] J. Bardin, R. Jackson, Electronics I, University of Massachusetts Amherst, http://ece.umass.edu/sites/default/files/ece/ECE323_13_Syllabus.pdf, 2013.
- [3] P. Sankar K. Krishnan, Electronics analysis & Design I, Electronics & Communication Engineering/College of Engineering, Universiti Tenaga Nasional, 2014. <http://lms.uniten.edu.my/moodle/course/index.php?categoryid=101>
- [4] Circuit Analysis I PSpice Exercices, Penn State, Pennsylvania, 2013, <http://www.coursehero.com/file/8537433/PSpice/>
- [5] My VW-Moodle Courses, University of Wisconsin – Madison, 2014, <https://courses.moodle.wisc.edu/prod/>
- [6] Moodle 2.5 Documentation, http://docs.moodle.org/25/en/Main_page
- [7] E-Circuit Center, <http://www.ecircuitcenter.com/>
- [8] AADE Filter Design and Analysis, www.aade.com/filter.htm
- [9] Crystal parameters calculator, <http://www.giangrandi.ch/electronics/crystalfilters/xtaltest.html>
- [10] 555 calculator <http://freespace.virgin.net/matt.waite/resource/handy/pinouts/555/>
- [11] Colpitts Oscillator Calculator http://www.ekswai.com/en_cap3.htm
- [12] Hartley Oscillator Calculator, http://www.ekswai.com/en_ind3.htm

Various Approaches to Learn the Computer Architecture and Organization Course

Goce Armenski¹, Sasko Ristov², Marjan Gusev³, and Magdalena Kostoska⁴

Abstract—Learning the Computer and Organization course is very difficult for computer science students. Apart of the course difficulties, its "hardwaredness" discourages the students to learn the course in depth even more. The computer science students prefer to comprehend the software based courses, where they use the computers only as a black-box tool to run their software programs or web applications or services, rather than to learn how a computer works, especially today's complex multiprocessor architectures, memory hierarchy, pipelining and parallelization, hazards and so on. In this paper, we present several approaches that we have introduced in the Computer Architecture and Organization course. The increased number of students in recent years (from 200 to 1000 per course) motivated us to change the course by introducing several online learning tools and visual simulators to provoke the students' curiosity about the internal organization of the computer. The students are satisfied of these educational tools, which helped them to overcome the required material.

Index Terms—e-Assessment; Hardware; Online Learning Tools; Simulators.

I. INTRODUCTION

Increased number of the computer science students enforced universities to continually improve their programs in order to follow the rapid development of new IT and more globally ICT techniques and technologies. New e-learning trends have changed the traditional way of teaching in the classroom. This concept is excellent for software based courses, where the students can use online tools for debugging and checking the correctness of their programs [25], which also can be used for detecting plagiarism.

However, hardware based courses in computer science curricula cannot be based on e-learning only. The e-learning tools can be used as additional learning tools, but still the students need a lot of practical work, especially in the laboratory.

In this paper we present several different approaches on how to use the e-learning tools in the hardware based Computer Architecture and Organization course. Online e-Assessment system is used both for assessing a student's knowledge and online learning. It is also used for assessing through

¹ G. Armenski is with University Ss Cyril and Methodius, Faculty of Computer Science and Engineering from 2001, Rugjer Boshkovik 16, PO Box 393, 1000 Skopje, Macedonia, Email: goce.armenski@finki.ukim.mk

² S. Ristov is with University Ss Cyril and Methodius, Faculty of Computer Science and Engineering from 2008, Rugjer Boshkovik 16, PO Box 393, 1000 Skopje, Macedonia, Email: sashko.ristov@finki.ukim.mk

³ M. Gusev is with University Ss Cyril and Methodius, Faculty of Computer Science and Engineering from 1989, Rugjer Boshkovik 16, PO Box 393, 1000 Skopje, Macedonia, Email: marjan.gusev@finki.ukim.mk

⁴ M. Kostoska is with University Ss Cyril and Methodius, Faculty of Computer Science and Engineering from 2008, Rugjer Boshkovik 16, PO Box 393, 1000 Skopje, Macedonia, Email: magdalena.kostoska@finki.ukim.mk

learning during the laboratory exercises. Additionally, two visual simulators are used. These educational tools made the course more interesting.

The rest of the paper is organized as follows. Several approaches on how to organize the Computer Architecture and Organization course are presented in Section II. Section III explains the course's organization. In Section IV we present the various learning approaches that we use in the course. The final Section V concludes our work.

II. RELATED WORK

This section presents the related work in the area of learning the hardware based courses, focusing on the Computer Architecture and Organization course.

There are many different pros and cons of using visual simulators or working on real hardware. Nevertheless, the teachers must introduce appropriate hands-on exercises, homework assignments or projects, in addition to the lectures. Liang [14] surveys the proposed hands-on assignments and projects.

Hardware based courses require practical work on real hardware [11], [19], [12]. FPGA-based configurable processors are cheap and can be used in laboratory exercises [26], [13] and the students can develop, implement and monitor both hardware and software of multi-core processor systems.

On the other side, visual simulators together with appropriate hands-on exercises will lighten the learning about the computer architecture and will improve the students' interest in hardware [16], [21]. Although there are many visual simulators, such as [18], [5], [10], [4], [9], [22], [23], none of them can cover all topics in computer architecture and organization.

III. ABOUT THE COMPUTER ARCHITECTURE AND ORGANIZATION COURSE

This section briefly describes the Computer Architecture and Organization course.

A. The Course Organization

The course content is delivered to the students with five classes per week, organized as: 2 classes of theoretical lectures, 2 classes of tutorials and 1 class of practical laboratory tutorials. A student gains 6 ECTS after passing the course.

The course syllabus covers all relevant topics proposed by the ACM/IEEE recommendations [2]. The used textbook [17] covers: Computer abstractions and technology; Control including the MIPS instruction set; Computer arithmetic; Organization of the processor and datapath; Memory and storage organization; and Multi-chip multi-core multi-processors.

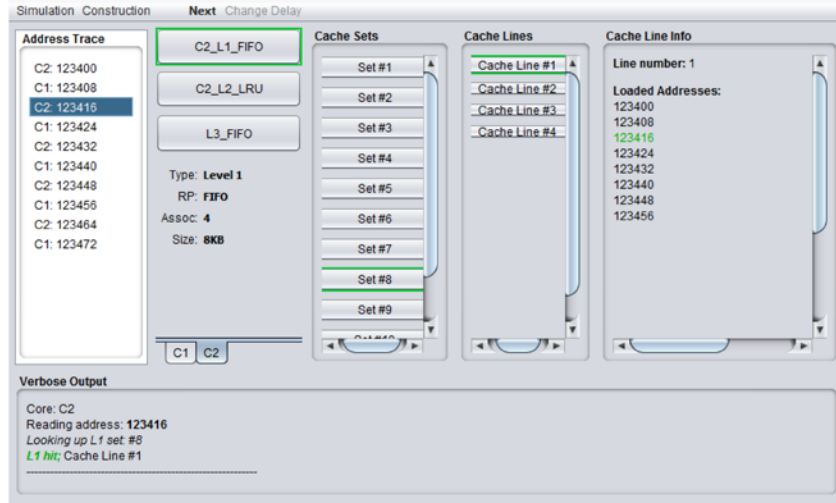


Fig. 1. A snapshot of the EDUCache simulation

The tutorials support these learning topics, including Performance parameters; Data presentation and codes; Computer arithmetic; Digital logic design; Flip-flops and memories; and Essential design of digital logic, including VHDL. Practical laboratory tutorials correspond to the theoretical tutorials.

B. Increased Number of Students

Usually, the lectures and tutorials are organized in larger groups of 80-120 students, while the practical laboratory tutorials are conducted in computer laboratories in groups of up to 20 students. About 200 students were enrolled per course until 2011 and one or two professors with several assistants covered the lectures and tutorials. Starting from 2012, the number of the students has increased even more, i.e., the course enrolled about 1000 students.

Several learning tools were introduced and the course methodology was changed towards the improvement of the course and the student success rate.

IV. LEARNING TOOLS FOR THE COURSE

This section presents the learning tools that are used in the Computer Architecture and Organization course. They are grouped into two groups: Visual simulator tools and online learning tool.

A. Visual Simulators

Since this is the course in the first year of study, we introduced visual simulators, instead of working on a real hardware. We believe that working on a real hardware will discourage even more the computer science students to learn, rather than to awake their curiosity. They prefer more software-based things, instead of hardware-based. This practical approach visualizes the concepts of low level computer digital logic and helps the students learn better and easier how the computer works.

Two visual simulators are used in the course: EDUCache [3] and HADES [8]. The following sections briefly present both visual simulators.

1) *The EDUCache Simulator*: The EDUCache simulator is developed by our students to be used for the Computer Architecture and Organization course. It is JAVA-based tool, which visually explains how a cache memory works, its organization, especially various cache mapping, cache replacement policies, cache positioning, cache lines and blocks, associativities, etc.

The students can design a CPU with an arbitrary number of cache levels, each level with unique parameters: cache size, replacement policy, cache line, and associativity. This yields different number of sets, as well.

ACM/IEEE-CS paid special attention to parallel and distributed computing by adding new knowledge area [1]. EDUCache also supports a simulation of multi-core chips and multilevel cache usage. A processor can have one or several homogeneous cores, each of which has access to a particular cache level of today's L1, L2 and L3. These multi-level caches can be private per core or shared among several or all cores.

A student can design an existing CPU with existing cache hierarchy. But the EDUCache allows the students to design their own cache hierarchy in order to achieve the benefits of different CPU architectures and organizations. For example, AMD CPUs use small cache set associativity of the L1 cache and smaller L3 caches, while Intel's CPUs are designed with higher cache set associativity of the L1 cache and bigger L3 caches.

Afterwards, a student can define a specific data access pattern and visualize its execution presenting each data access as cache hit or miss in each cache level, as depicted in Figure 1. This is the most powerful feature of the EDUCache simulator because the computer science students use their software based skills to learn hardware based courses.

Several predefined hands-on are proposed to use the EDU-

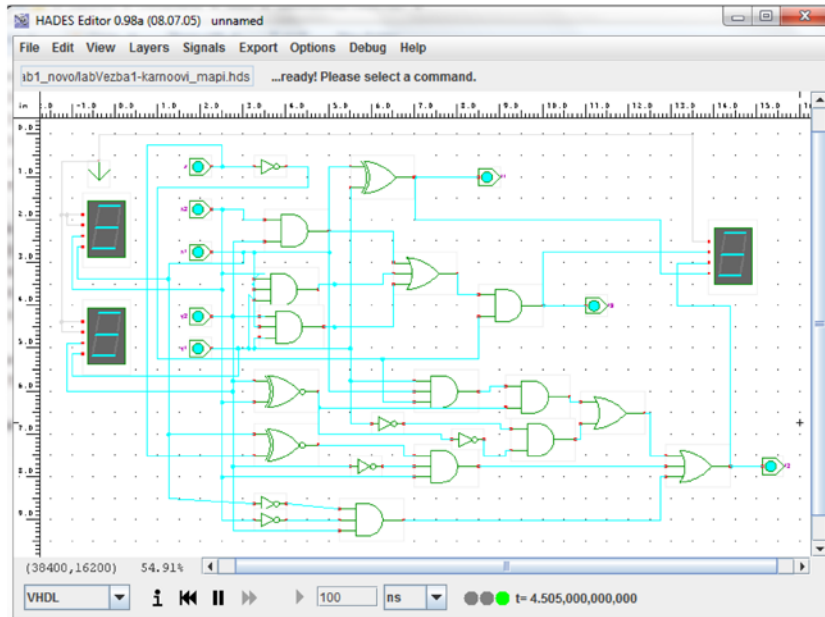


Fig. 2. A snapshot of the HADES simulator

Cache simulator in the Computer Architecture and Organization course [20].

2) *The HADES Simulator:* HADES [24] (Hamburg DEsign System) is also an interactive java based simulation tool, which is also used by the students to design and simulate basic digital systems design, as shown in Figure 2. It is a fully interactive simulator, which consists of graphical editor, discrete-event based simulation engine(s), libraries of simulation components etc.

Hades includes a lot of basic- and complex-gates with up to six inputs, several standard flip-flops, different I/O models, including animated LEDs or seven-segment displays and interactive switches, memories with graphical editors, LC-displays and so on.

The students can simulate three different processor families and architectures:

- The 32-bit R3051 microprocessor (MIPS R3000 family) from IDT;
- The 8-bit PIC16 microcontrollers from Arizona Microchip (namely the PIC16C84 and PIC16F84); and
- The 4-bit Intel MCS4 (i4004) microprocessor chip set; the first microprocessor in history.

B. Online learning and assessment tool

Our e-Assessment system has been used more than 15 years for many courses [6] and several upgrades were introduced during these years. It is used both for online learning and assessment. Additionally, Moodle Learning Management System [15] is used in the course.

1) *e-Assessment:* The e-Assessment system supports four question types:

- Multiple choice questions (MCQ);

- Single choice questions (SCQ);
- single value input questions (SVQ); and
- Essays (EQ).

MCQs are mostly used by the teachers in the question database, in front of SCQs. The other two question types are less used. The experience showed that SVQ produced several problems during the assessments and students are usually revolted. For example, presenting floating points numbers (dot or comma), rounding, writing the units, etc. EQ are not used although they are easy to define, i.e., they also don't need answer options such as SVQs. We believe that the main reasons are the increased number of students per course and possibility of unproper grading.

2) *Online learning:* The e-Assessment system has another module for online learning, which uses its e-Assessment engine to iteratively ask questions, thus enforcing the student to move from one learning objective to another. The online learning tool is organized as follows. The course is divided in several lectures (per week), each of which consists of knowledge items. Each knowledge item contains several learning objectives. Each student has to pass all knowledge items each week by answering the questions.

The system has several strategies in order to motivate the students. The navigation algorithm is the first strategy, which enables the students to move in the knowledge tree in an adaptive manner. The next strategy defines when a given knowledge item is learned. That is, each learning objective is passed after three correct answers in a row [7], while a knowledge area is passed after all learning objectives are passed individually, plus the mixed questions of the whole knowledge area (questions that cover several learning objectives of a single knowledge area).

These strategies enable a unique learning path for a student, that is, better students will move to the next knowledge area faster, while the worse students will need to spend more time on learning.

V. CONCLUSION

Learning the Computer Architecture and Organization course is difficult, especially for computer science students and the universities are making efforts to lighten it. This paper presents how several approaches for learning are used in this direction. We join the use of visual simulators and online learning tool.

Our self-developed EDUCache simulator, which covers the main part of the course material and maybe the hardest one (CPU architecture and organization), and the HADES simulator for digital circuits show the theory in practice. However, they are supplemented with online learning tools for e-Assessment and online Learning through assessment.

REFERENCES

- [1] ACM / IEEE-CS, "Computer science curricula 2013: Curriculum guidelines for undergraduate degree programs in computer science," 2013. [Online]. Available: <http://www.acm.org/education/CS2013-final-report.pdf>
- [2] ACM/IEEE-CS Joint Interim Review Task Force, "Computer science curriculum 2008: An interim revision of cs 2001, report from the interim review task force," 2008. [Online]. Available: <http://www.acm.org/education/curricula/ComputerScience2008.pdf>
- [3] B. Atanasovski, S. Ristov, M. Gusev, and N. Anchev, "Educache simulator for teaching computer architecture and organization," in *Global Engineering Education Conference (EDUCON), 2013 IEEE*, Berlin, Germany, 2013, pp. 1015–1022.
- [4] Y.-T. Chen, J. Cong, and G. Reinman, "Hc-sim: a fast and exact l1 cache simulator with scratchpad memory co-simulation support," in *Proc. of the 7-th IEEE/ACM/FIP Int. conf. on HW/SW codesign and system synthesis (CODES+ISSS '11)*. USA: ACM, 2011, pp. 295–304.
- [5] J. Edler and M. D. Hill, "Dinero iv trace-driven uniprocessor cache simulator," 2012. [Online]. Available: <http://pages.cs.wisc.edu/~markhill/DineroIV/>
- [6] M. Gusev and G. Armenski, "On-line learning and etesting," in *Information Technology Interfaces, 2002. ITI 2002. Proceedings of the 24th International Conference on*. IEEE, 2002, pp. 147–152.
- [7] —, "e-Testing usage in e-Education," in *e-Learning Paradigms and Applications, Agent-based Approach*, M. Ivanovic and L. Jain, Eds. Springer Verlag, 2014, vol. Studies in Computational Intelligence, vol. 528.
- [8] N. Hendrich, "A java-based framework for simulation and teaching: Hades the hamburg design system," in *Microelectronics Education*, B. Courtois, N. Guillemot, G. Kamarinos, and G. Stehelin, Eds. Springer Netherlands, 2000, pp. 285–288.
- [9] E. Herruzo, J. Benavides, R. Quisilant, E. Zapata, and O. Plata, "Simulating a reconfigurable cache system for teaching purposes," in *Micro-electronic Systems Education (MSE '07), IEEE International Conference on*, 2007, pp. 37–38.
- [10] A. Jaleel, R. S. Cohn, C.-K. Luk, and B. Jacob, "Cmpsim: A pin-based on-the-fly multi-core cache simulator," in *The Fourth Annual Workshop MoBS, co-located with ISCA '08*, 2008.
- [11] I. Kastelan, D. Majstorovic, M. Nikolic, J. Eremic, and M. Katona, "Laboratory exercises for embedded engineering learning platform," in *MIPRO, 2012 Proc. of the 35th Int. Conv.*, 2012, pp. 1113–1117.
- [12] D. Kehagias and M. Grivas, "Software-oriented approaches for teaching computer architecture to computer science students," *Journal of Communication and Computer*, vol. 6, no. 12, pp. 1–9, Dec. 2009.
- [13] J. H. Lee, S. E. Lee, H.-C. Yu, and T. Suh, "Pipelined cpu design with fpga in teaching computer architecture," *Education, IEEE Transactions on*, vol. 55, no. 3, pp. 341–348, 2012.
- [14] X. Liang, "A survey of hands-on assignments and projects in undergraduate computer architecture courses," in *Advances in Computer and Information Sciences and Engineering*, T. Sobh, Ed. Springer Netherlands, 2008, pp. 566–570.
- [15] Moodle, "Learning management system," [retrieved: Nov, 2013]. [Online]. Available: <https://moodle.org/>
- [16] B. Nikolic, Z. Radivojevic, J. Djordjevic, and V. Milutinovic, "A survey and evaluation of simulators suitable for teaching courses in computer architecture and organization," *Education, IEEE Transactions on*, vol. 52, no. 4, pp. 449–458, nov. 2009.
- [17] D. A. Patterson and J. L. Hennessy, "Computer organization and design, fourth edition: The hardware/software interface," MA, USA, 2009.
- [18] D. Patti, A. Spadaccini, M. Palesi, F. Fazzino, and V. Catania, "Supporting undergraduate computer architecture students using a visual mips64 cpu simulator," *Education, IEEE Transactions on*, vol. 55, no. 3, pp. 406–411, aug. 2012.
- [19] J. Qian, R. Wang, S. Shi, Y. Zhu, and Z. Xie, "Simplifying and integrating experiments of hardware curriculums," in *Computer Science and Information Technology (ICCSIT), 2010 3rd IEEE International Conference on*, vol. 9, 2010, pp. 610–614.
- [20] S. Ristov, B. Atanasovski, M. Gusev, and N. Anchev, "Hands-on exercises to support computer architecture students using educache simulator," in *Computer Science and Information Systems (FedCSIS), 2013 Federated Conference on*, Sep. 2013, p. 769–776.
- [21] S. Ristov, M. Stolikj, and N. Ackovska, "Awakening curiosity - hardware education for computer science students," in *MIPRO, 2011 Proceedings of the 34th International Convention, IEEE Conference Publications*, Opatija, Croatia, may 2011, pp. 1275–1280.
- [22] SimpleScalar LLC, "SimpleScalar tool set," [retrieved: May, 2013]. [Online]. Available: <http://www.simplescalar.com/>
- [23] University of Extremadura, "Smpcache - simulator for cache memory systems on symmetric multiprocessors," [retrieved: May, 2013]. [Online]. Available: <http://arco.unex.es/smpcache/>
- [24] University of Hamburg, "HADES - Hamburg design system," 2002, [retrieved: Aug., 2013]. [Online]. Available: <http://tams-www.informatik.uni-hamburg.de/applets/hades/html/>
- [25] B. Vogel-Heuser, S. Rehberger, T. Frank, and T. Aicher, "Quality despite quantity teaching large heterogenous classes in c programming and fundamentals in computer science," in *Global Engineering Education Conference (EDUCON), 2014 IEEE*, 2014, pp. 367–372.
- [26] X. Wang, "Multi-core system education through a hands-on project on fpgas," in *Frontiers in Education Conference (FIE), 2011*, 2011, pp. F2G–1–F2G–6.

A Simple Hydraulic System as a Laboratory Equipment for Demonstrating On-Off Control

Milica Ristović¹, Milica B. Naumović², Slobodan Lubura¹

Abstract – This paper deals with a didactic water tank system which is the interesting equipment for demonstration many control problem solutions. In order to stimulate future research, after short description of the system modelling and control strategy, some experimental results are presented. The evaluation of the impact of experimental work on student learning is planned.

Keywords – Industrial automation, Two-position controller, Lab equipment, Engineering education.

I. INTRODUCTION

Many industrial control systems have approximately first order dynamics and are controlled simply by switching an actuator *on* and *off*. Liquid level control systems and heating processes are examples of such systems [1]. The principal advantage of on-off control is that it is a cheap control solution, where the applied controller and the actuator are usually inexpensive. Moreover, on-off control does not even require a controller as the control function can be created with contacts and relays, or other such devices.

The main drawback of the two-position controller implementation is that its normal mode is constant cycling. In addition, the switching rate of two-position controller, as well as the oscillation amplitude of controlled variable is influenced directly by hysteresis present in the real on-off controllers. Therefore, a compromise between the lifetime of the actuator and the accuracy of control is the only possible solution.

The paper is organized as follows. Section 2 introduces some preliminary facts before the experimental setup is presented. The description of the experimental environment is summarized in Section III and illustrated by experimental results. Finally some conclusions of the work are presented in Section IV.

II. A REVISIT TO ON-OFF LIQUID LEVEL CONTROL

In this section, some assumptions are made for the object to

¹Milica Ristović and Slobodan Lubura are with the Faculty of Electrical Engineering, University of East Sarajevo, Vuka Karadžića 30, 71123 East Sarajevo, Bosnia and Herzegovina, E-mail: milica.ristovic@etf.unssa.rs.ba, slobodan.lubura@etf.unssa.rs.ba.

²Milica B. Naumović is with the Faculty of Electronic Engineering, University of Niš, Aleksandra Medvedeva 14, 18000 Niš, Serbia, E-mail: milica.naumovic@elfak.ni.ac.rs.

be modeled, and a control approach is considered.

A. Tank System Model

A cylindrical reservoir shown in Fig. 1, with cross section A and outlet area s , has an influx Q_{in} and an outflux Q_{out} . Note that due to the assumption of an ideal fluid, all forces acting on the fluid are conservative and thus there is an exchange between potential and kinetic energy. Moreover, the outlet area is small in comparison to the cross section of the tank, and as Torricelli's law states, the efflux rate is given by $v_{out} = \sqrt{2gh}$, where g is the acceleration due to gravity and h is the height of liquid in the tank.

Considering mass balance, the liquid volume change is given by

$$A\dot{h} = Q_{in} - Q_{out}, \quad (1)$$

where $Q_{out} = s\sqrt{2gh}$, and the model differential equation becomes

$$\dot{h} + \frac{s}{A}\sqrt{2gh} = \frac{1}{A}Q_{in}. \quad (2)$$

Let the influx be constant $Q_{in} = Q_{in}^0$. Equating fluxes $Q_{out}^0 = Q_{in}^0$, the stationary point h^0 can be calculated by letting $\dot{h} = 0$, which yields

$$h^0 = \frac{1}{2g} \left(\frac{Q_{in}^0}{s} \right)^2 \quad (3)$$

State space representation of the dependence of the influx Q_{in} on the outflux Q_{out} becomes

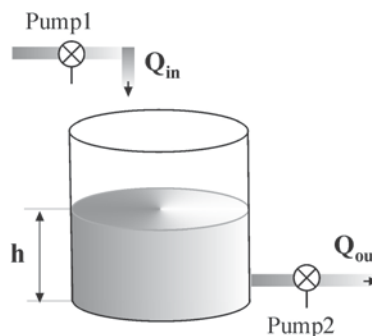


Fig. 1. A cylindrical water tank

$$\begin{aligned} \dot{h} &= -\frac{s}{A}\sqrt{2gh} + \frac{1}{A}Q_{in} = f(h, Q_{in}) \\ Q_{out} &= s\sqrt{2gh} = g(h, Q_{in}) \end{aligned} \quad (4)$$

The behavior of a nonlinear system near an operating (stationary) point can be described by the linear differential equation. Introducing variables which denote deviations from the operating point $\Delta h = h - h^0$, $\Delta Q_{in} = Q_{in} - Q_{in}^0$, and $\Delta Q_{out} = Q_{out} - Q_{out}^0$, the linear differential equation can be found as follows

$$\begin{aligned} \dot{\Delta h} &= -\frac{s}{A}\sqrt{\frac{g}{2h^0}}\Delta h + \frac{1}{A}\Delta Q_{in} \\ \Delta Q_{out} &= s\sqrt{\frac{g}{2h^0}}\Delta h \end{aligned} \quad (5)$$

The linear, time-invariant first order system, given by (5), describes how a perturbation ΔQ_{in} around the nominal input Q_{in}^0 causes a perturbation around the nominal state h^0 .

B. First Order Linear System Subject to On-off Control Input

Fig. 2 shows the block diagram of the closed-loop system configuration with a two-position controller. Recall that a two-position controller recognizes only two states and has only two actions - ON or OFF. To reduce the switching rate, the two-position controller is equipped with hysteresis (dead band) which is a special differential gap between two states. It is well known that the type of controlled object plays an important role [2], [3].

There is no general method of designing control loop with non-linear controller. Configurations with two-position controllers are designed on a case-by-case basis. In this section, the attention will be paid to the behavior of a two-position controller in the system with a first order lag object which is in accordance with the previous analysis.

Let a single-input single-output linear control object in Fig. 2 be described by the differential equation

$$\dot{c}(t) = -ac(t) + K_{ob}au(t), \quad a = 1/T_{ob} \quad (6)$$

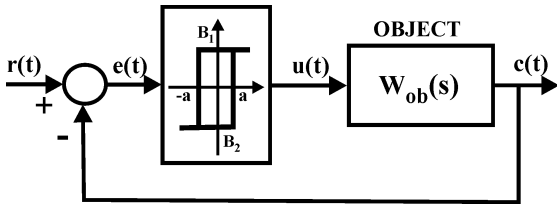


Fig. 2. Block diagram of the closed loop system with a two-position controller

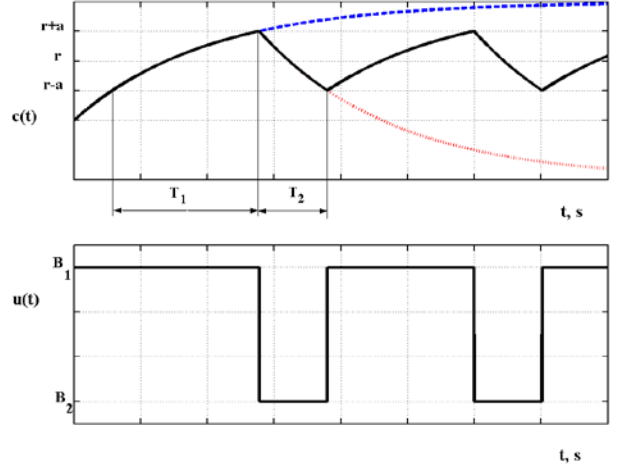


Fig. 3. Step response and object input for system in Fig. 2.

where K_{ob} and T_{ob} are static gain and time constant, respectively, $u(t)$ and $c(t)$ denote the control signal and output signal of the object. If there is switching hysteresis ($\pm a$), two controller states are given by

$$u(t) = \begin{cases} B_1 > 0 & \text{for } e > a \\ B_2 \leq 0 & \text{for } e < -a \\ \text{remains unchanged (} B_1 \text{ or } B_2 \text{)} & \text{for } |e| < a \end{cases} \quad (7)$$

By integrating the differential equation (6) the output of the system $c(t)$ can be find as

$$c(t) = c(0)e^{-t/T_{ob}} + \int_0^t e^{-(t-\tau)/T_{ob}} K_{ob}u(\tau) d\tau, \quad (8)$$

where $c(0)$ is the initial condition.

The essence of on-off control is to apply maximum or minimum control effort depending on the state of the system. The system never reaches a steady state r , but enters the regime of undamped oscillations around it, whose period may be determined by providing two boundary conditions, i.e.

$$c(t = T_1) = r + a = (r - a)e^{-T_1/T_{ob}} + K_{ob}B_1(1 - e^{-T_1/T_{ob}}) \quad (9)$$

and

$$c(t = T_2) = r - a = (r + a)e^{-T_2/T_{ob}} + K_{ob}B_2(1 - e^{-T_2/T_{ob}}). \quad (10)$$

The *on* period T_1 and the *off* period T_2 , which are marked on the responses given in Fig. 3, are determined as follows

$$T_1 = T_{ob} \ln \frac{K_{ob}B_1 - r + a}{K_{ob}B_1 - r - a} \quad (11)$$

and

$$T_2 = T_{ob} \ln \frac{K_{ob}B_2 - r - a}{K_{ob}B_2 - r + a}. \quad (12)$$

Note that the switching rate of two-position controller is influenced directly by hysteresis. From practical point of

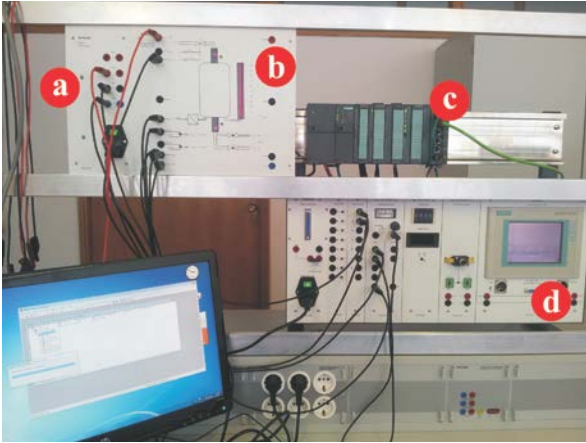


Fig. 4. Layout of the experimental environment

view, requirements for smaller amplitude and a greater period of oscillation are desirable. These are two contradictory requirements, and a compromise is the only possible solution.

III. OVERVIEW OF EXPERIMENTAL SETUP

This section discusses the equipment and experimental procedures used to prove the control strategy presented within this paper.

A. Description of the Experimental Environment

The solution of on-off tank filling control using two-position controller with hysteresis is presented [4], [5]. Experimental environment shown in Fig.4 consists of: (a) WUEKRO power supply unit which supplies the tank filling simulation with $\pm 15\text{VDC}$; (b) WUEKRO tank filling simulator, which has an analogue level sensor that measures actual level and also gives the information on the current level. For better level visualization, it has light indication of the state of liquid in the tank. Besides the sensor, there are two valves used to empty tank at different discharge rates, placed on the pipes with different cross sections. The valve with smaller cross section (V2), and the valve for filling the tank (V1) are used in experimental consideration. These valves are controlled by binary signals, so they can take one of two final positions: opened or closed (0/24 VDC); (c) For the level control, a programmable logic controller (PLC) Siemens S7-300 is used. The CPU of this controller is 314F-2PN/DP, and it is connected with digital input/output module that has 16 digital inputs and 16 outputs, analogue input/output module that has 4 analogue inputs, and 2 analogue outputs, as well as the communication module CP 343-2; (d) The actual fluid level can be shown on the Siemens “Touch panel TP177B 6” which is otherwise used in applications with less complex systems.

The scheme of tank filling level is shown in Fig. 5 [5], [6]. The actual level value is presented with x , which is a process variable, appropriately measured by sensor and converted on a linear basis into a voltage signal U_H in the range from 0 to

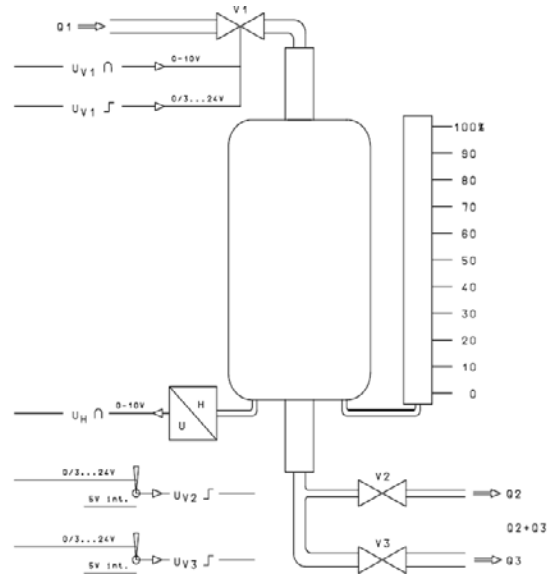


Fig. 5. Schematic representation of the reservoir with liquid [5]

10V. Accordingly, a filling level of 50% corresponds to a voltage of 5V at output U_H .

Setpoint value w is given also as analogue signal, and that is output of potentiometer which can be easily changed during the program execution. The potentiometer output is connected to the analogue input of PLC and it can be scaled during the program execution. It is very important to limit the setpoint value and keep it not to be higher than 10% and lower than 90% of the full scale. Due to the switching hysteresis, process variable x ‘hunts’ between upper response value $X_o = (w+10)\%$ and lower response value $X_u = (w-10)\%$. Difference between the upper response value and lower response value is called the switching difference X_s .

Reading the task, it is clear that PLC gets two analogue signals at its analogue input module. One of them gives the information on the actual fluid level, and the other on the setpoint value (and pursuant to it, the limits within which a fluid can be calculated). These analogue signals x (current level of liquid in the tank) and w (given level) are in the range between 0 and 100%. However, the analogue input module of S7-300 converts these signals into numerical values in the range from 0 to 27648 or from -27648 to 27648,

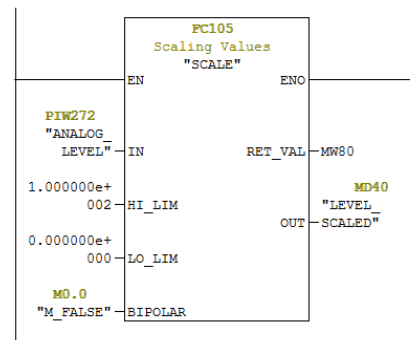


Fig. 6. “SCALE” block in ladder diagram

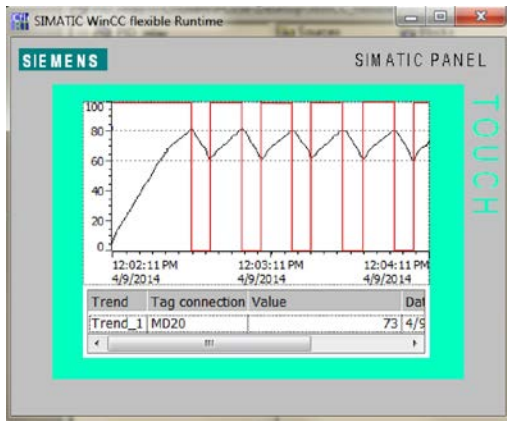


Fig. 7. Changing fluid level if lower and higher response values are 60% i 80% (black line); Valve V1 is opened while level is rising, and closed while level is falling (red line)

depending on binary value of signal at the "BIPOLAR" input of scaling block [7].

Scaling block "SCALE" is SIMATIC function FC 105 from "Standard Library". In this case, the "BIPOLAR" input is set to "0" (logical zero), so the signal is converted in a numerical value in the range from 0 to 27648. The analogue signal x is the input of one "SCALE" block, and w is the input of another "SCALE" block. At the inputs "HI_LIM" and "LO_LIM" of scale blocks limits are written (in the form of a real number) within which the input analogue signal should be observed, in the case the limits are 0 and 100. The scaled value is written in the memory variable of double word type, in this case the address of first "SCALE" block output is MD40, and the address of the other "SCALE" block output is MD48. If programming is performed in the ladder diagram, the "SCALE" block is as shown in Fig. 6.

Having in mind that control signal is digital, or binary (it can only have the values of 0 and 1), the value of memory word MD40 (which is the scaled value of input variable x) is compared to the lower response value. If the valve V1 is open, the corresponding digital output is set and the tank is filled with fluid. When variable x becomes bigger than upper response value, valve V1 closes, and the corresponding digital output is reset. Controlling the valve V2 is similar. If the actual fluid level is lower than lower response value, the valve V2 closes, which means that the corresponding digital output is reset. Likewise, if actual fluid level is higher than upper response value, the valve V2 opens, which means that corresponding digital output is set. Note that lower and upper response values are changed at the same time as analogue input variable w .

B. Results of Experiment

Fig. 7 shows the changes of fluid level if setpoint value is 70%, which means that lower and upper response values are 60% and 80%, respectively. In Fig. 7 also can be seen if valve V1 (fluid inflow) is opened or closed (red line). It is obvious that inflow rate is smaller than discharge rate, while period of filling tank in given range is shorter than period of emptying

tank in same range. The period of filling tank from 60% to 80% is about 12s, while the emptying period is about 7s.

It can be noticed that while the level is rising and falling the line that shows actual value is not smooth, but has some deviations, which is due to the sample time of data acquisition (500ms), and due to fact that actual value of liquid level in the tank is presented in integer format.

C. Evaluation of Student Learning

In addition to the official faculty teaching evaluation for the courses related to the topic, at the end of each semester anonymous student surveys will be conducted to determine whether the learning outcomes have been successfully achieved. A proposal for evaluating the impact of the experimental work on student learning has been prepared.

IV. CONCLUSION

This paper describes the control of fluid level in tank using controller with hysteresis. As tank simulator WUEKRO simulator is used. This is a part of the equipment at the Faculty of Electrical Engineering, University of East Sarajevo. By using the PLC Siemens S7-300 a simple controller structure is realized. The behavior of process is monitored on Siemens Touch panel. Using this simulator, students become familiar with PLC programming, as well as with process control. In this paper the control of fluid level in tank using controller with hysteresis is presented, but this tank can also be controlled with PI/PID controller, which gives space for further work with this simulator and its use in education.

ACKNOWLEDGEMENT

This paper is supported in part by project Grant III44004 (2011-2014) financed by Ministry of Education, Science and Technological Development, Republic of Serbia.

REFERENCES

- [1] F.G. Shinskey, *Process Control Systems: Theory for the User*, Prentice Hall, 1999.
- [2] B. Matić, *Design of Automatic Regulation and Control of Technological Processes*, Svjetlost, OOUR Zavod za udžbenike i nastavna sredstva, Sarajevo, 1989 (in Serbian).
- [3] Č. Milosavljević, *Linear and Nonlinear Automatic Control Continuous-time Systems*, Faculty of Electrical Engineering, East Sarajevo, 2007 (in Serbian). (http://www.etf.unssa.rs.ba/download/TAU_2.pdf)
- [4] M. Ristović, S. Lubura, "Fluid Level Control in Tank using Programmable Logic Controller Siemens S7-300", Infoteh@-Jahorina 2014, Conference Proceedings, pp. 1051-1056, Jahorina, Republic of Srpska, B&H, 2014 (in Serbian). <http://www.infoteh.rs.ba/zbornik/2014/radovi/SUP/SUP-6.pdf>
- [5] "Experimental Manual V174 – Digital Control 1 with SIMATIC S7", WUEKRO GmbH
- [6] "Experimental Manual V175 – Digital Control 2 with SIMATIC S7", WUEKRO GmbH
- [7] "Experimental Manual V173 – Programmable Logic Controllers – SIMATIC S7-300", WUEKRO GmbH

Laboratory Equipment for Hydrogen Energy Education

Silvija Letskovska¹, Kamen Seymenliyski¹ and Pavlik Rahnev²

Abstract – This paper is provided laboratory equipment for experimental work and student laboratory for the study of the production of hydrogen fuel cell type PEMFC.

Keywords - student laboratory, energy system, fuel cells.

I. INTRODUCTION

One of the actual questions today is connected with increasing energy consumption. The nature sources exhaust, the average human life increases, the human population increases. In the front there is the question for environment population using conventional energy sources.

All this wants searching of new possibilities for energy production – more ecology friendly and more economically effective. One of the possibilities in this direction is using hydrogen as a pure fuel.

After burning of hydrogen there is no carbon dioxide (CO₂) or other toxic gases, the only product is water - Table I).

TABLE I

COMPARING CHARACTERISTICS OF AUTO CARS WITH PETROL ENGINES AND ENERGY SYSTEM WITH FUEL CELL

Energy consumption at v = 60 km/h, kWh/100km			
Fuel	Petrol		Hydrogen
		87,2	
Waste products, g/km	CO	2,30	0
	C _n H _m	0,20	0
	NO _x	0,15	0
	CO ₂	213,00	0
	H ₂ O	98,00	117,0

The program for changing of EC countries towards hydrogen energy includes the period 2000÷2050 years. Only in 2003 year 1 million euros are given for hydrogen projects and 1 million euros - for projects, connected with fuel cells. For period 2005÷2015 years - 2.8 billion euros will be invested. The number of the cars using hydrogen should be two million in 2020 year.

As mode of work and laboratory build models exists over 20 types of fuel cells. The most common classification is

¹Silvija Letskovska - Burgas Free University, San Stefano 62, 8000 Burgas, Bulgaria, E-mail: silvia@bfu.bg.

¹Kamen Seimenliyski -Burgas Free University, San Stefano 62, 8000 Burgas, Bulgaria, E-mail: silvia@bfu.bg.

²Pavlik Rahnev – Technical College, As. Zlatarov University, Y. Yakimov 1, Burgas 8010, Bulgaria, E-mail: pavlikrahnev@abv.bg.

according to the type of the used electrolyte (membrane). It dictates the temperature range of the fuel cells as well. On this base there are two types of fuel cells – low temperature and high temperature.

Fuel cell is electrochemical current source, in wish there is direct conversion of the energy of the fuel and oxidizer, passing uninterrupted to the electrodes, into electrical energy (Fig. 1). In the two sides of the membrane powder like electrodes are deposited [1], [2]. The hydrogen comes to the anode and oxygen – to cathode. On every electrode different chemical reactions exist (Fig. 2).

In some fuel cells the electrodes are with catalyzer, usually platinum or other precious metals, stimulating dissociation. The anode and cathode are porous for free passing of hydrogen and oxygen.

The protons pass through the membrane, but the electrons are trapped from external circuit. From the cathode site protons and oxygen produce residual product – water, or clear water.

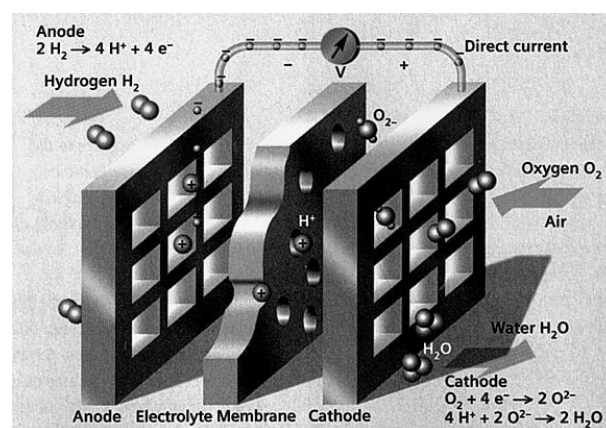


Fig. 1. Fuel cells with polymer electrolytic membrane (PEMFC)

As a difference from galvanic element and the battery, fuel cell do not use electrodes as a spending materials consummated. Hydrogen and oxygen enter in the time of work, but they not charge preliminary. They is way fuel cells can work long time (ten thousand hours).

The additional advantage of the fuel cell are low expense of active materials comparing with conventional electrochemical systems.

The energy from the chemical reaction converts directly in electrical, without forming other types of energy. In this way it could be obtained high values of the yield $\eta - \eta_{\max} = 1 - T(\Delta S/\Delta H)$, where ΔH - enthalpy, ΔS – entropy [3].

For isotherm and reversible process not only chemical energy ($-\Delta H$) convert in the electrical and in the same time the energy from environment heat- $Q = T \cdot \Delta S$, that in why the yield of such source can exceeds 100%.

The real yield η of fuel cell is 40÷60%, under 100% in the same time the heat is produced and could be used. In fuel cell work used gas (H₂, CO, hydrocarbons) and liquid (methanol, formaldehyde) fuels.

Accordingly, a sufficiently high speed can be oxidized only hydrogen in the special fuel cells - the carbon monoxide and methanol.

Fuel cells with polymer electrolytic membrane (PEMFC) effectively produce high density power. PEMFC usually work at low temperatures 60÷80°C, which gives possibility for quick start in comparison with more high-temperature cells [4].

In PEMFC there are not acids and alkalis, that is why for the body construction there is no need of expensive corrosion preventive materials. The sizes are small in the reason of high energy density of the membrane – up to 1A/cm². This makes such type cells compact and suitable for the purpose of this laboratory work.

II. LABORATORY EQUIPMENT WITH POLYMER ELECTROLYTE FUEL CELL H- 20

For creating an educational module for laboratory classes the configuration is proposed, shown in Fig. 2.

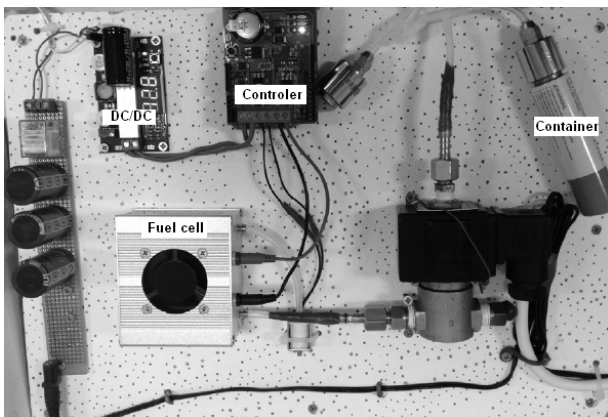
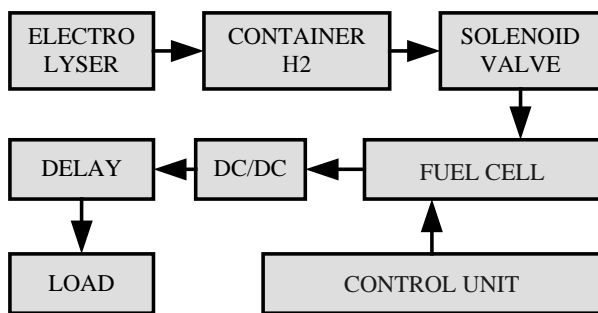


Fig. 2. Block diagram of laboratory equipment

The system uses electrolyser HYDROFILL-FCH-010- "Horizon Fuel Cell Technologies" for hydrogen production. It is a polymer electrolytic reversible fuel cell.

The produced hydrogen is stored in specially designed tanks HYDROSTIK PRO. The body is from aluminum alloy and inside there is an alloy from AB₂ group for hydrogen absorption. There alloys consist titanium, zirconium or hafnium as the base, and metal (nickel, chromium, vanadium) in the lattice structure. They have the possibility to absorb hydrogen, forming hydrides to full saturation, while the process structure expands and releases heat.

Solenoid valve is in the "normally open" and acts as a circuit breaker.

The fuel cell model H-12 (H-20) (FCS-B12) company "Horizon Fuel Cell Technologies" is the main component in the system, it is the source of energy. Furthermore, depending on the type of additional components, and how to configure the system.

Fuel cell is a module of the type of fuel cell PEMFC and contains 13 individual cells connected in series with a total capacity 20W.

Since the output voltage of the fuel cell is not stabilized, the system was added to DC/DC step-up converter (input voltage 3~35V, output DC voltage 3.5V~35V, U_{out}>U_{in}), has stabilized output adjustable output voltage with a potentiometer.

To disconnect the load from the system provided a scheme that is powered by a control voltage from the mains. The scheme has an adapter (9V, 500mA), relay with normally open and normally closed contact and a capacitor connected in parallel to delay the operation of the relay in case of voltage drop.

To make the scheme energy undependable it uses normally closed contact for closing the circuit, i.e. the load will switch the system on loss of control power.

Since after completion of the power control relay must delay the involvement of the load is used in parallel capacitor 10000 μF, which will provide a delay of the order of 8-10 seconds , sufficient for the smooth start of the cell.

To achieve 20W power in this model fuel cell is better to use command system that will provide optimal working conditions. The main functions of the controller are:

- short circuit - to maintain normal operating mode at a higher consumption without disturbing the balance in the fuel cell required operating mode can be divided into cycles. Electrical terminals of the fuel cell should be given a short time X at the end of each cycle, then the beginning of the next cycle time Y. X and Y depend on the model and the nominal capacity of the stack. Fuel cell model H-12, X=100ms, Y=10s.
- purging the water vapor - implemented using attached to the fuel cell valve, which is controlled by the controller. Upon activation, the pressure in the fuel cell decline. Thus, the source of fresh hydrogen enters the exhaust gas with a small amount of water is discharged through the outlet. The valve is activated for the time X at the end of each cycle Y. For fuel cell H-12 (X=100ms, Y=25s) the load is adjustable with the possibility of change of power in the range 1-30 W.

III. TESTING THE LABORATORY EQUIPMENT WITH DIFFERENT LOAD

The work of the proposed equipment was tested using three different values of the consumer – 6, 12 and 20 W. The data obtained are:

- The change of voltage over the load and current through the load;
- The power of the system;
- The change of output voltage of the fuel cell (FC) before DC/DC converter and after that.

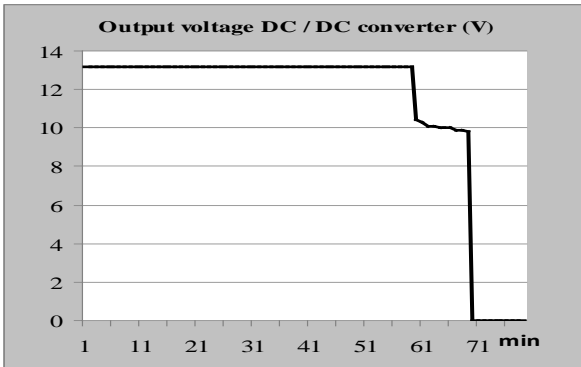


Fig. 3. Change the output voltage(V) DC/DC converter depending on the time

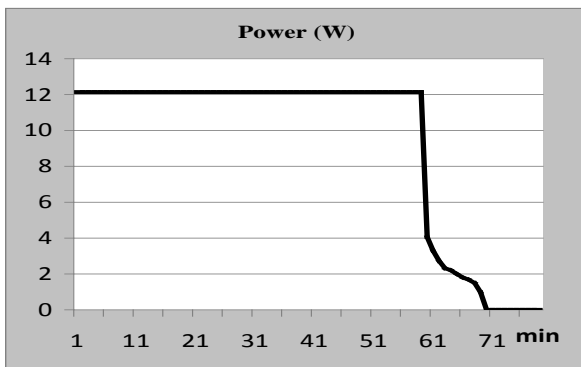


Fig. 4. Change the power (W) depending on the time

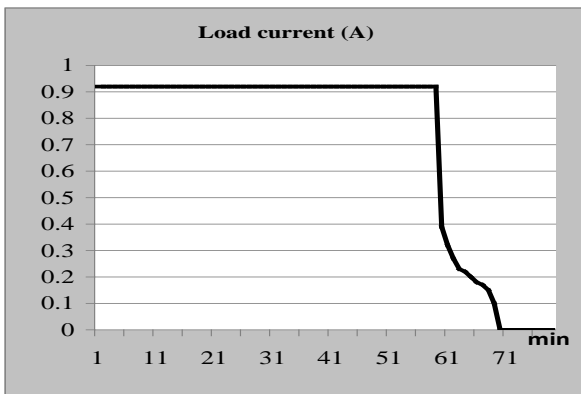


Fig. 5. Change the load current (A) depending on the time

The results obtained from testing the system in continues working cycle in load with power 12 W are shown on Figs. 3-6. The comparable dates for the results in testing the system with consumer power 6, 12 and 20 W are in Table II.

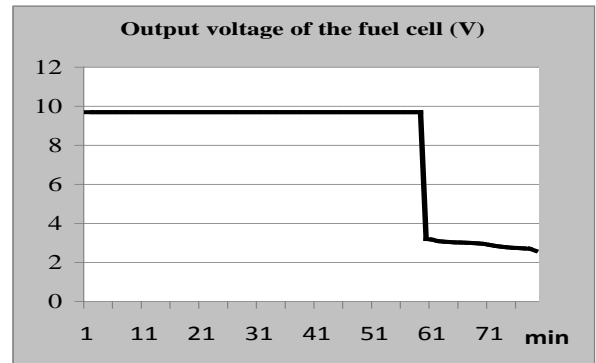


Fig. 6. Change the output voltage of FC depending on the time

TABLE II
TESTING THE SYSTEM WITH CONSUMER POWER 6, 12 AND 20 W

	Power of the consumer (W)		
	6	12	20
Work of nominal power (min)	97	59	26
Inom	0.45	0.92	0.79
Unom	9.9	9.7	9.1
E(Wh)	9.7	11.8	8.6

IV. CONCLUSION

On the base of the obtained results the next conclusions could be done:

- The work of the system with 12 W load gives the highest energy.
- As a variant for developing of the educational equipment it is supposed the connect the photo-voltaic panel into electrolyser and accumulating the energy – hydrogen in suitable for the purpose container.
- The next step is the system to supply energy saving LED illumination in the classroom.

REFERENCES

- [1] Fuel Cells, From Fundamentals to Applications, Springer, 2006.
- [2] M. Mench, *Fuel cell engines*, 2008, ISBN 978-0-471-68958-4 (cloth).
- [3] B.P. Tarasov, M.V. Lototskii, V.A. Yartys, “The problem of hydrogen storage and prospects hydrides for hydrogen storage”, *Ros.him. Well. Islands of Mendeleev*, 2006, t.L, № 6, p.34-48.
- [4] K. Seymenliyski, S. Letskovska, “Hydrogen as a renewable source - industrial production and use”, *BFU-Burgas, Bulgaria, International scientific conference "Knowledge - tradition, innovation, perspectives"*, 14-15 June, 2013.

Session RTE:

**RADIO COMMUNICATIONS,
TELECOMMUNICATIONS
TECHNOLOGY AND
ELECTROMAGNETICS**

Complexity of the McEliece Cryptosystem based on GDBF Decoder for QC-LDPC Codes

Omran Al Rasheed¹, Dejan Drajić², Predrag Ivaniš³ and Goran Đorđević⁴

Abstract – In this paper, we propose the application of Gradient Descent Bit Flipping (GDBF) algorithm in decryption stage of McEliece cryptosystem based on Quasi-Cyclic Low-Density Parity Check (QC-LDPC) codes. Comparing of complexity between GDBF and Gallager B decoders is given by binary operations for each decrypted bit.

Keywords – Low Density Parity Check, Quasi-Cyclic, McEliece cryptosystem.

I. INTRODUCTION

The main purpose of the cryptosystem is to guarantee confidentiality to the message. McEliece cryptosystem is important public key code, derived by Robert J. McEliece in 1978 [1]. It is based on binary Goppa codes [2], it is still unbroken, and worth mentioning that no polynomial-time algorithm is discovered to recover the secret message in the McEliece cryptosystem even using quantum computers. This property is unique from other worldwide implemented solutions for public key cryptosystem and digital signatures as RSA [3], DSA, ECDSA [4].

The McEliece cryptosystem demands the sender to encode the information into a codeword through the receiver's public key, then to introduce a certain number of intentional errors in the encoded word. This allows the receiver that is able to correct those errors through his secret private key, to recover the secret information. The McEliece shows some drawbacks, among of them, the large of the key that prevented its widespread adoption and low transmission rate. There are many ways to overcome these drawbacks of the McEliece cryptosystem, and the most solutions are based on replacing of Goppa codes with other families of codes. However, it is difficult to replace Goppa codes with other codes in the absence incurring into serious security flaws. The families of code must achieve to some conditions to ensure the security, must to be large enough to keep away from the enumeration, a generator matrix of a permutation equivalent code must be

obscure that no permit to appear any construction for the secret code and this code has efficient algorithm to correct the codeword from the errors, this means that receiver can able to read the transmitted ciphertext over the unsecure channel.

On the other hand, it is well known that Low Density Parity Check (LDPC) codes are powerful error correction codes that achieve performance near the Shannon limit [5]. The effective iterative decoding algorithms for LDPC codes make these codes have high attraction comparing with other class of codes. The first supposition to use LDPC codes in the public-key cryptosystem was in [6]. In that paper, it has been clarified that employment of LDPC codes instead of Goppa codes does not allow decreasing the key length. However, it have been presented that QC-LDPC code based cryptosystem is immune to any known attack [7]. The new features are appeared with QC-LDPC code, less key size and higher code rates and keep or respect the original version.

In this paper, we consider the required computational effort for gradient descent bit flipping (GDBF) decoder [8] in BSC with McEliece cryptosystem. Complexity of the decoder is measured by number of needed binary operations for each iteration of GDBF algorithm. We compare the cost of GDBF decoder with Gallager B decoder [5]. In Section II McEliece cryptosystem based on QC-LDPC is described. The GDBF decoder over BSC is described in Section III. In Section IV a calculation cost of GDBF decoder for each iteration. Finally, some concluding remarks and future research directions are given in Section V.

II. DESCRIPTION MCELIECE CRYPTOSYSTEM BASED ON QC-LDPC CODES

In the McEliece cryptosystem, the receiver makes the private key that is created by the sparse parity-check matrix \mathbf{H} , that is selected randomly and has the form

$$\mathbf{H} = [\mathbf{H}_0 | \mathbf{H}_1 | \dots | \mathbf{H}_{n_0-1}], \quad (1)$$

where \mathbf{H}_i is a circulant block, and each row (column) has weight d_v . It is important to avoid short cycles (4-length) in matrix \mathbf{H} . Selecting randomly n_0 vectors h_i (disjoint set of different modulo p), give us huge families of codes with codes identical parameters [11] as a condition to replace Goppa. Systematic generator matrix for the code is $\mathbf{G} = [\mathbf{I} | \mathbf{P}]$, where \mathbf{I} is a $k \times k$ identity matrix and \mathbf{P} is given in form

$$\mathbf{P} = \begin{bmatrix} (\mathbf{H}_{n_0-1}^{-1} \mathbf{H}_0)^T \\ (\mathbf{H}_{n_0-1}^{-1} \mathbf{H}_1)^T \\ \vdots \\ (\mathbf{H}_{n_0-1}^{-1} \mathbf{H}_{n_0-2})^T \end{bmatrix}, \quad (2)$$

¹Omran Al Rasheed is with the School of Electrical Engineering, University of Belgrade, Bul. kralja Aleksandra 73, 11120 Belgrade, Serbia (e-mail: omrano84@hotmail.com).

²Dejan D. Drajić is with IRITEL A.D., Batajnicki drum 23, Belgrade, Serbia. Also, he is with the School of Electrical Engineering, University of Belgrade, Bul. kralja Aleksandra 73, 11120 Belgrade, Serbia (e-mail: dejan.d.drajić@gmail.com).

³Predrag N. Ivaniš is with the School of Electrical Engineering, University of Belgrade, Bul. kralja Aleksandra 73, 11120 Belgrade, Serbia (e-mail: predrag.ivaniš@etf.rs).

⁴Goran T. Đorđević is with the Faculty of Electronic Engineering at University of Niš, Aleksandra Medvedeva 14, Niš 18000, Serbia, E-mail: goran.djordjevic@elfak.ni.ac.rs.

where \mathbf{H}_{n_0-1} is non-singular matrix and operator T denotes transposition.

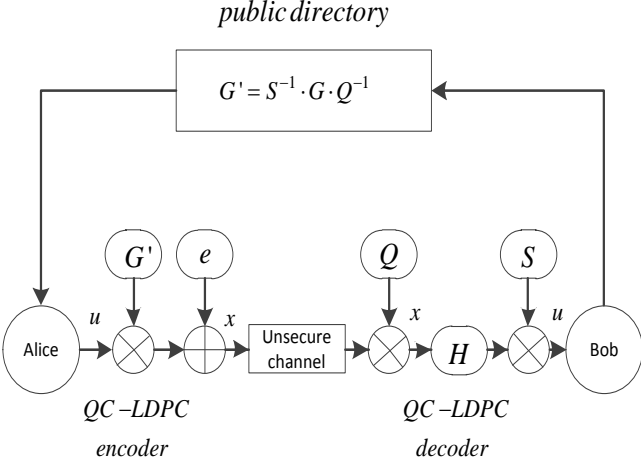


Fig. 1. McEliece cryptosystem with QC-LDPC codes

Procedure of McEliece cryptosystem with QC-LDPC codes is shown in Fig. 1. The receiver (Bob) chooses other two matrices such that increase the code secrecy. The first matrix is $k \times k$ scrambling matrix \mathbf{S} and the second is a $n \times n$ non-singular matrix \mathbf{Q} . Finally the public key is given by

$$\mathbf{G}' = \mathbf{S}^{-1} \times \mathbf{G} \times \mathbf{Q}^{-1}. \quad (3)$$

It should be noticed that low density of matrix \mathbf{G}' helps to avoid attacks to the dual code. Matrix \mathbf{H} can be recognized by one row of each circulant block, so \mathbf{H} is mapped into a new matrix such $\mathbf{H}' = \mathbf{H}\mathbf{Q}^T$. The sender obtains the public key from the public directory, and anyone can get this key. Alice encrypts the cleartext \mathbf{u} to obtain a ciphertext as $\mathbf{x} = \mathbf{u}\mathbf{G}' + \mathbf{e}$. and \mathbf{e} is a random vector of t' intentional errors. The first requirement that Bob does it when the ciphertext is received, is reverse transformation as:

$$\mathbf{x}' = \mathbf{x}\mathbf{Q} = \mathbf{u}\mathbf{S}^{-1}\mathbf{G} + \mathbf{e}\mathbf{Q}, \quad (4)$$

where \mathbf{x}' is a codeword and is affected by the vector error $\mathbf{e}\mathbf{Q}$, with weight less or equal to $t = t' m$, and m is column and row of matrix \mathbf{Q} . Finally, Bob can obtain the cleartext after decoding process using any LDPC decoder and then multiplication by matrix \mathbf{S} .

The capability of the receiver to correct all errors depends on the type of the LDPC decoder and in the other hand on the structure of the private key. The receiver has a lot of chances to select the better structure for private key to avoid the short cycles in the Tanner graph and to avoid any attack. LDPC decoder has an important role to eliminate the intentional error vector. For the decoding algorithm, there are many algorithms based on soft decision and message passing between variable and check nodes, such as Sum Product Algorithm (SPA) [12], SPA algorithm is very complexity and has the best performance. The running time required by each algorithm depends highly on its computational complexity and the processing platform used.

III. GDBF DECODING ALGORITHM FOR BSC

A. LDPC Codes

LDPC codes are linear block codes that are designed by appropriate construction of the corresponding parity check matrix \mathbf{H} , which is characterized by being sparse. LDPC code is denoted as $C(n, k)$ and matrix \mathbf{H} with dimension $m \times n$. Every code vector \mathbf{c} satisfies the condition $\mathbf{H}\mathbf{c} = \mathbf{0}$, where operations are performed over $\text{GF}(2)$. Irregular LDPC code is one with a sparse check matrix \mathbf{H} that has a variable number of '1's per row or per column. The information can be represented by bipartite or Tanner graph. The bipartite graph describes the relationship between two types of nodes, the symbol nodes v_j with column weight d_v and the parity check nodes c_i with row weight d_c . QC-LDPC codes [9] have some advantages compared with other constructions that are constructed by circulant permutation matrices such easier to implement with good performances [10]. Every row of the parity check matrix \mathbf{H} corresponding to a parity check equation, and thus to a parity check node. Each bit of the code vector corresponding to a symbol node. Let v_j a variable node in the Tanner graph and $M(j)$ denotes as a set of parity check nodes connected with v_j , and $N(i)$ is a set of variable nodes connected with parity check node c_i . Let \mathbf{r} is a received codeword and \mathbf{e} is an entry error sequence determined by the probability of the BSC.

B. GDBF Decoder over BSC

GDBF is a class of BF algorithms based on the gradient descent algorithm. This algorithm is designed for transmission is done over additive white Gaussian noise (AWGN) channel and for each iteration an inversion function is calculated as

$$\Delta_j^{(t)}(x, y) = x_j^{(t)} y_j + \sum_{i \in M(j)} \prod_{l \in N(i)} x_l^{(t)}, \quad j = 1, 2, \dots, n, \quad t \geq 0 \quad (5)$$

for AWGN x_j can be considered by polar representation $(-1, +1)$ of the j th bit of the estimated codeword in the t th iteration, and y_j denotes the corresponding symbol of the received signal. For all variable nodes, inversion function is calculated for every particular iteration and only symbols have the minimum value of inversion function are flipped to obtain the new value for the j th bit for the next iteration $x_j^{(t+1)}$. Here we implement GDBF for BSC, where x_j takes binary value (0,1) and inversion function also takes integer value. We can consider an inversion function as a special case for regular LDPC code as:

$$\Delta_{M,j}^{(t)}(v, r) = v_j^{(t)} \oplus r_j + \sum_{i \in M(j)} \sum_{l \in N(i)}^{\oplus} v_l^{(t)}, \quad (6)$$

where summation over modulo 2 is denoted by using \oplus in combination with summation operator. In the above expression, the value of the inversion function is confined to the set of integer values $\Delta_{M,j}^{(t)}(v, r) \in \{0, 1, \dots, d_v + 1\}$, where large value of (6) indicates that the corresponding bit should be probably flipped.

IV. COMPLEXITY OF THE GDBF DECODER OVER BSC

Decryption stage for the McEliece cryptosystem includes LDPC decoder to correct the codeword from the errors. We suppose that receiver performs GDBF decoder. We can apprise the number of binary operation over the Tanner graph for one iteration. We consider some parameters for construction QC-LDPC codes, $n=n_0p$ length of these codes, dimension $k=k_0p$ and redundancy $r=p$, where n_0 is a small integer and $k_0=n_0-1$ with large value for p . In principle, every check node receives d_c binary values from the register which contains all estimated bits for each iteration. Check node XORs all the messages and sends the result to all neighbour variable nodes, so at the check node (d_c-1) binary sums and the total number of operations at the check nodes is $r(d_c-1)$. This process is illustrated in Fig. 2. for parity check matrix

$$\mathbf{H} = \begin{bmatrix} 0 & 1 & 0 & 1 & 1 & 0 & 0 & 1 \\ 1 & 1 & 1 & 0 & 0 & 1 & 0 & 0 \\ 0 & 0 & 1 & 0 & 0 & 1 & 1 & 1 \\ 1 & 0 & 0 & 1 & 1 & 0 & 1 & 0 \end{bmatrix}. \quad (7)$$

Variable node receives messages from XORs, for every variable bit - one XOR between the estimated bit in t th iteration and original received bit, and d_v parity checks. The additional operations are needed for integer values. We can use full adder and for n variable nodes we have about nd_v full adders.

Majority logic (ML) gates is designed to calculate inverse function for every bit, determine the maximum value of Delta, all bits with maximum value and flipping them, so $3n$ binary operations are needed for these tasks. In conclusion, the cost of one iteration of GDBF can be estimated as

$$C_{GDBF}^{(1)} = r(d_c - 1) + 4n + nd_v = n(4 + 2d_v) - r. \quad (8)$$

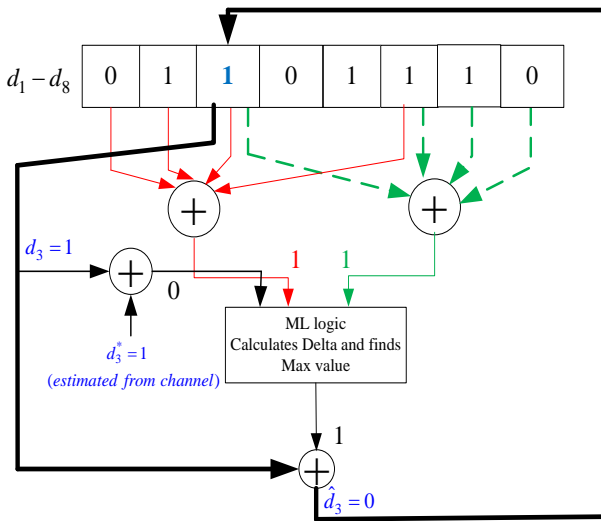


Fig. 2. Structure of GDBF decoder for BSC

To calculate the cost of the decryption process, we also estimate the cost for \mathbf{xQ} and $\mathbf{u'S}$. The traditional multiplication is used for \mathbf{xQ} due to that \mathbf{Q} is a sparse matrix and $n \times m$ binary operations is needed, while \mathbf{S} is a density matrix. Therefore, we must use efficient algorithm as Winograd convolution to reduce the computations [13]. The choice both d_v and m adjusts the computational complexity of the decryption stage. When d_v is increased then cost of \mathbf{xQ} is decreased while cost of the decoding process is increased [14]. In construct, increasing m (matrix \mathbf{Q} must be sparse in order to allow correcting all intentional errors) will increase the cost of \mathbf{xQ} while decrease the cost for decoding process. It is important to choose optimal between all defined parameters for trade-off between security and complexity.

V. NUMERICAL RESULTS

In this section the performance for GDBF will be compared with the typical hard-decision algorithms - bit flipping (BF) and Gallager-B (as simplest possible message passing algorithm). Then, the complexity analysis of the both considered algorithms will be given.

Fig. 3 shows FER performance for simple BF, GDBF and Gallager B decoders for QC732, $R=0.7527$ with maximum number of iterations $t_{max}=100$. It can be observed that the gap between BF and GDBF is very large, and that GDBF decoder has better performance than Gallager B decoder especially for higher values of crossover probability. This characteristic increases immunity of cryptosystem to avoid decoding attacks due to the low weight (t') of the error vector at the sender and it is often more dangerous than structural. Computing both \mathbf{xQ} and $\mathbf{u'S}$ and by using (8), we can estimate the cost (in term of the binary operation) of the decryption process for McEliece cryptosystem. If we consider that $m=7$, the average number of iteration is $t_{av}=10$ for the GBDF decoder. The values in Table I represent the binary operations needed for each decrypted bit using GDBF decoding and Gallager B decoders [15].

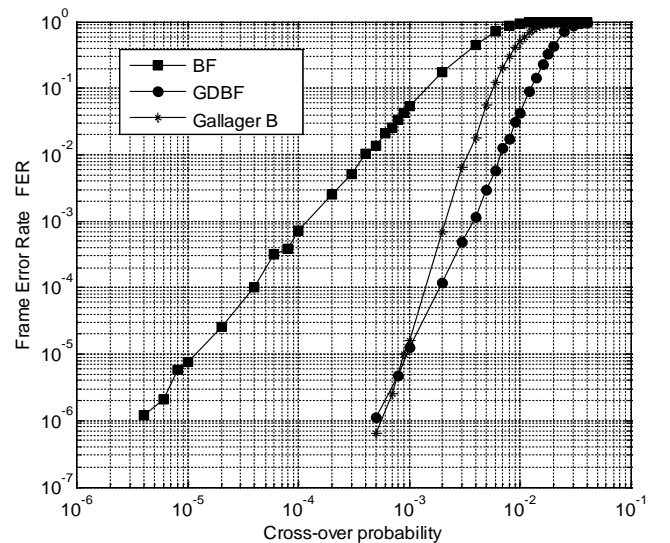


Fig. 3. FER performances for different decoders over BSC for QC732 with code rate $R=0.7527$

TABLE I
COMPARISON BETWEEN GALLAGER B AND GDBF DECODERS USED
IN THE DECRYPTED STAGE

p [bits]	d_v	13	15	13	15
	n_0	3	3	4	4
4096	GDBF	961	1011	1131	1185
	Gallager B	1476	1626	1598	1731
5120	GDBF	1019	1079	1227	1281
	Gallager B	1544	1694	1694	1828
6144	GDBF	1086	1146	1323	1377
	Gallager B	1611	1761	1790	1924
7168	GDBF	1143	1203	1410	1463
	Gallager B	1668	1818	1877	2010
8192	GDBF	1201	1261	1496	1550
	Gallager B	1726	1876	1963	2097
9216	GDBF	1259	1319	1583	1636
	Gallager B	1784	1934	2050	2183
14336	GDBF	1489	1549	1914	1964
	Gallager B	2014	2164	2381	2515
15360	GDBF	1605	1665	2102	2155
	Gallager B	2130	2280	2569	2702
16384	GDBF	1576	1636	2044	2098
	Gallager B	2101	2251	2511	2644

It can be noticed that GDBF decoder has better performance than Gallager B decoder. Furthermore, GDBF decoder has less computational complexity. Increasing length of the clear text and variable degree will increase the cost.

VI. CONCLUSION

In this paper we have described McEliece cryptosystem based on QC-LPDC, with GDBF decoder. We have estimated the cost of the binary operation for each decrypted bit. Although GDBF is hard decision decoder, it has high capability to correct errors for BSC. Also, the complexity of GDBF algorithm is reduced when compared with Gallager B decoder.

ACKNOWLEDGEMENT

This work was supported by the technology development project of the Serbian Ministry of education, science and technology development, under Grant Agreement number TR32007 - "Multiservice optical transport platform OTN10/40/100 Gbps with DWDM/ROADM and CARRIER ETHERNET".

REFERENCES

- [1] R. J. McEliece, "A Public-Key Cryptosystem based on Algebraic Coding Theory." DSN Progress Report, pp.114–116, 1978.
- [2] V. D. Goppa, "A New Class of Linear Error-Correcting Codes," *Probl.Peredachi Inf.*, vol. 6, no. 3, pp. 24–30, Sep. 1970.
- [3] R. L. Rivest, A. Shamir, and L. Adleman, "A Method for Obtaining Digital Signatures and Public-Key Cryptosystems," *Commun. ACM*, vol. 21, no. 2, pp. 120–126, Feb. 1978.
- [4] "Digital Signature Algorithm," 1993. [Online]. Available: http://csrc.nist.gov/publications/fips/fips186-3/fips_186-3.pdf.
- [5] R. G. Gallager, *Low Density Parity Check Codes*, Cambridge, MA: M.I.T Press, 1963.
- [6] C. Monico, J. Rosenthal, and A. Shokrollahi, "Using Low Density Parity Check Codes in the McEliece Cryptosystem," *Proc. IEEE ISIT 2000*, pp. 215, Sorrento, Italy, Jun. 2000.
- [7] M. Baldi, M. Bodrato, and F. Chiaraluca, "A New Analysis of the McEliece Cryptosystem based on QC-LDPC Codes," *Security and Cryptography for Networks*, ser. Lecture Notes in Computer Science. Springer Verlag, vol. 5229, pp. 246–262, 2008.
- [8] T. Wadayama, K. Nakamura, M. Yagita, Y. Funahashi, S. Usami, and I. Takumi, "Gradient Descent Bit Flipping Algorithms for Decoding LDPC Codes," *IEEE Trans. Communications*, vol. 58, no. 6, pp. 1610–1614, Jun. 2010.
- [9] M. Tanner, D. Sridhara, A. Sridharan, T. E. Fuja, and D. J. Costello, "LDPC Block and Convolutional Codes based on Circulant Matrices," *IEEE Transactions on Information Theory*, vol. 50, no. 12, pp. 2966–2984, Dec. 2004.
- [10] L. Chen, J. Xu, I. Djurdjevic, and S. Lin, "Near-Shannon-Limit Quasi-Cyclic Low-Density Parity-Check Codes," *IEEE Trans. Commun.*, vol. 52, no. 7, pp. 1038–1042, Jul. 2004.
- [11] M. Baldi and F. Chiaraluca, "Cryptanalysis of a New Instance of McEliece Cryptosystem based on QC-LDPC Codes", *Proc. IEEE International Symposium on Information Theory (ISIT 2007)*, pp. 2591–2595, Nice, France, Jun. 2007.
- [12] D. J. C. MacKay and R. M. Neal, "Near Shannon Limit Performance of Low Density Parity Check Codes", *Electronics Letters*, vol. 32, no. 18, pp. 1645–1646, Aug. 1996.
- [13] S. Winograd, "Arithmetic Complexity of Computations", ser. CBMS-NSF Regional Conference Series in Mathematics. SIAM, vol. 33, 1980.
- [14] T. J. Richardson and R. L. Urbanke, "The Capacity of Low-Density Parity-Check Codes under Message-Passing Decoding", *IEEE Trans. Inform. Theory*, vol. 47, no. 2, pp. 599–618, Feb. 2001.
- [15] Baldi, Marco, Marco Bianchi, and Franco Chiaraluca, "Security and Complexity of the McEliece Cryptosystem based on Quasi Cyclic Low-Density Parity-Check Codes", *IET Information Security* 7, no.3, pp. 212–220, 2013.

Probability of Collision in a Cooperative Relay Diversity Scheme in Nakagami Fading Channel

Nenad Milošević¹, Bojan Dimitrijević¹, Zorica Nikolić¹

Abstract – In this paper we consider the probability of collision of a cooperative diversity scheme with M relays in Nakagami fading channel. The influence of fading channel parameters, as well as the influence of system's parameters on the probability of collision is investigated. The analytical results obtained in this paper will be compared to the simulation results, and it will be shown that the results match very well.

Keywords – Relaying, Diversity, Cooperative transmission, Nakagami fading.

I. INTRODUCTION

The increasing demand for the capacity of wireless systems, dictate the development of new system configurations and new protocols. Cooperative diversity protocols may significantly improve the performance of wireless communication systems, and such protocols are analyzed in detail during the last decade [1], [2], [3]. Using these protocols it is possible to create additional paths between the source and destination using other users' terminals which serve as intermediate relay nodes. The case of multiple relays is considered in [4] and [5]. Paper [4] studied the case of orthogonal transmission from the source and from the relay. In [5], this orthogonality constraint was relaxed, the source and relay are allowed to transmit simultaneously, and it was shown that in this way a significant performance improvement could be achieved at the cost of higher complexity decoder.

In [6], a simple scheme with multiple relays that selects the best relay between source and destination based on instantaneous channel measurements is proposed. The proposed scheme requires no knowledge of the topology or its estimation. The technique is based on signal strength measurements rather than distance and requires a small fraction of the channel coherence time. Additionally, the algorithm itself provides for the necessary coordination in time and group formation among the cooperating terminals. Also, the simplicity of the technique allows immediate implementation in existing radio hardware. Paper [6] considers the probability of collision, the probability that two or more relays transmit the information from source to destination, in Rayleigh and Rician fading channel.

In this paper we derive the expression for the collision probability in Nakagami channel, for the cooperative diversity scheme given in [6]. Analytical results, from this paper, will be shown to be very close to the simulation results.

¹Nenad Milošević, Bojan Dimitrijević and Zorica Nikolić are with the University of Niš, Faculty of Electronic Engineering, Aleksandra Medvedeva 14, 18000 Niš, Serbia, e-mail: nenad.milosevic@elfak.ni.ac.rs.

II. SYSTEM MODEL

The block diagram of the system, proposed in [6], is shown in Fig. 1. The system selects one relay among a set of M relays, based on a measurement which relay provides the “best” end-to-end path between source and destination. The wireless channel a_{si} between source and each relay i , as well as the channel a_{id} between relay i and destination affect performance. These parameters model the propagation environment between any communicating terminals and change over time, with a rate that macroscopically can be modeled as the Doppler shift, inversely proportional to the channel coherence time. Opportunistic selection of the “best” available relay involves the discovery of the most appropriate relay, in a distributed and “quick” fashion, well before the channel changes again. In that way, topology information at the relays (specifically location coordinates of source and destination at each relay) is not needed.

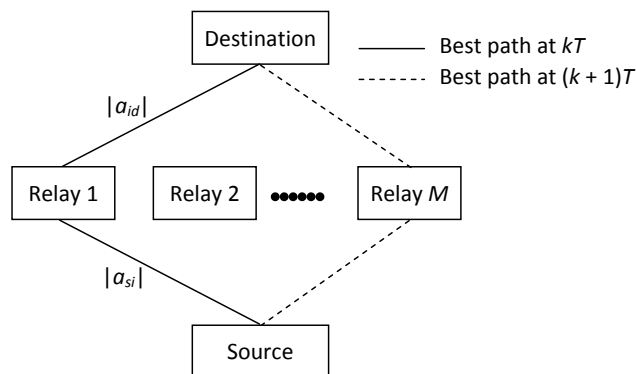


Fig. 1. System model with source, destination, and multiple relays

More specifically, the relays overhear a single transmission of a ready-to-send (RTS) packet and a clear-to-send (CTS) packet from the destination. From these packets, the relays assess how appropriate each of them is for information relaying. The transmission of RTS from the source allows for the estimation of the instantaneous wireless channel a_{si} between source and relay i , at each relay i . Similarly, the transmission of CTS from the destination allows for the estimation of the instantaneous wireless channel a_{id} between relay i and destination at each relay i .

Since communication among all relays should be minimized for reduced overall overhead, a method based on time was selected: as soon as each relay receives the CTS packet, it starts a timer from a parameter h_i based on the instantaneous channel measurements a_{si} , a_{id} . The timer of the relay with the best end-to-end channel conditions will expire first. That relay transmits a short duration flag packet, signaling its presence. All relays, while waiting for their timer to reduce to zero (i.e., to expire), are in listening mode. As

soon as they hear another relay to flag its presence or forward information (the best relay), they back off.

The channel estimates a_{si} , a_{id} at each relay, describe the quality of the wireless path between source-relay-destination, for each relay i . Since the two hops are both important for end-to-end performance, each relay should quantify its appropriateness as an active relay, using a function that involves the link quality of both hops. Two functions are used in [6]: under Policy I, the minimum of the two is selected, while under Policy II, the harmonic mean of the two is used. Policy I selects the ‘‘bottleneck’’ of the two paths while Policy II balances the two link strengths and it is a smoother version of the first one. For Policy I:

$$h_i = \min\{|a_{si}|^2, |a_{id}|^2\} \quad (1)$$

and for Policy II:

$$h_i = \frac{2}{\frac{1}{|a_{si}|^2} + \frac{1}{|a_{id}|^2}} \quad (2)$$

The relay that maximizes function h_i is the one with the ‘‘best’’ end-to-end path between initial source and final destination. After receiving the CTS packet, each relay i will start its own timer with an initial value T_i , inversely proportional to the end-to-end channel quality h_i , according to the following equation:

$$T_i = \frac{\lambda}{h_i}, \quad (3)$$

where λ is a constant and has the units of time.

III. PERFORMANCE ANALYSIS

The probability of having two or more relay timers expire ‘‘at the same time’’ is zero. However, the probability of having two or more relay timers expire within the same time interval c , and therefore cause a collision, is nonzero and was evaluated in [6]. It was shown that the probability of collision is equal to

$$P_c = 1 - M(M-1) \int_c^\infty f(x)[1-F(x)]^{M-2} F(x-c) dx \quad (4)$$

where $f(x)$ is the probability density function (pdf), and $F(x)$ is the cumulative distribution function (cdf) of random variables T_i , $i=1, \dots, M$, where M is the number of relay nodes. The cumulative distribution function and probability density function are related to respective distributions of h_i in the following way:

$$F(t) \equiv \text{cdf}_{T_i}(t) = 1 - \text{cdf}_{h_i}(\lambda/t) \quad (5)$$

$$f(t) \equiv \text{pdf}_{T_i}(t) = \frac{d}{dt} F(t) = \frac{\lambda}{t^2} \text{pdf}_{h_i}(\lambda/t) \quad (6)$$

In case of Nakagami channel, it will be assumed that $|a_{si}|$ and $|a_{id}|$, $i=1, \dots, M$, are independent (but not identically distributed) Nakagami random variables with the following pdfs, respectively:

$$p_1(x) = \frac{2m_1^{m_1} x^{2m_1-1}}{\Gamma(m_1)\Omega_1^{m_1}} e^{-\frac{x^2 m_1}{\Omega_1}} \quad (7)$$

$$p_2(x) = \frac{2m_2^{m_2} x^{2m_2-1}}{\Gamma(m_2)\Omega_2^{m_2}} e^{-\frac{x^2 m_2}{\Omega_2}} \quad (8)$$

where $m_1, m_2, \Omega_1, \Omega_2$ are pdf's parameters, and $\Gamma(\cdot)$ is Gamma function.

The probability density functions of $|a_{si}|^2$ and $|a_{id}|^2$ are given by a Gamma distribution:

$$p_{k,sq}(x) = \frac{m_k^{m_k} x^{m_k-1}}{\Gamma(m_k)\Omega_k^{m_k}} e^{-\frac{x m_k}{\Omega_k}}, \quad k=1,2 \quad (9)$$

A. Policy I

In case of Policy I, the minimum of the variables $|a_{si}|^2$ and $|a_{id}|^2$ is determined. The probability density function of the minimum of variables $|a_{si}|^2$ and $|a_{id}|^2$ is:

$$p_{\min}(x) = p_{1,sq}(x)(1-P_{2,sq}(x)) + p_{2,sq}(x)(1-P_{1,sq}(x)) \quad (10)$$

where $P_{k,sq}$, $k=1,2$ are cumulative distribution functions of $|a_{si}|^2$ and $|a_{id}|^2$:

$$P_{k,sq}(x) = \int_0^x p_{k,sq}(y) dy = \frac{\gamma(m_k, m_k \cdot x / \Omega_k)}{\Gamma(m_k)} \quad (11)$$

where $\gamma(m,x)$ is incomplete Gamma function, defined by

$$\gamma(m,x) = \int_0^x y^{m-1} e^{-y} dy \quad (12)$$

Finally:

$$f(t) = \frac{\lambda}{t^2} P_{\min}\left(\frac{\lambda}{t}\right) \quad (13)$$

$$F(t) = 1 - \int_0^{\lambda/t} p_{\min}(u) du \quad (14)$$

B. Policy II

In case of Policy II, a harmonic mean of random variables $|a_{si}|^2$ and $|a_{id}|^2$ is used. In this case, we will consider that random variables have identical distributions. Probability density function of the harmonic mean of two Gamma random variables with identical distributions

$$p_\gamma(x) = \frac{x^{\alpha-1} e^{-x/\beta}}{\beta^\alpha \Gamma(\alpha)} \quad (15)$$

is derived in [7] and is equal to

$$p_{\gamma_H}(x) = \frac{\sqrt{\pi} \beta^{-\alpha}}{\Gamma^2(\alpha)} \left(\frac{x}{2}\right)^{\alpha-1} e^{-\frac{2x}{\beta}} \Psi\left(\frac{1}{2} - \alpha, 1 - \alpha, \frac{2x}{\beta}\right) \quad (16)$$

where $\Psi(\cdot, \cdot, \cdot)$ is confluent hypergeometric function defined in [8]. The cumulative distribution functions of the harmonic mean of two Gamma random variables is also derived in [7] and is equal to

$$P_{\gamma_H}(x) = \frac{\sqrt{\pi} x}{2^{2\alpha-2} \Gamma^2(\alpha) \beta} G_{23}^{21}\left(\frac{2x}{\beta} \middle| 0, \alpha - 1/2 \atop \alpha - 1, 2\alpha - 1, -1\right) \quad (17)$$

where $G_{pq}^{mn}(\cdot)$ is Meyer G-function defined in [9]. In this case, Gamma distribution (15) is defined by (9), and therefore in (16) and (17) variables are

$$\begin{aligned} \alpha &= m \\ \beta &= \frac{\Omega}{m} \end{aligned} \quad (18)$$

where $\Omega_1 = \Omega_2 = \Omega$, and $m_1 = m_2 = m$.

Now, from equations (5) and (6) we get

$$f(t) = \frac{\lambda}{t^2} p_{\gamma_H}\left(\frac{\lambda}{t}\right) \quad (19)$$

$$F(t) = 1 - P_{\gamma_H}\left(\frac{\lambda}{t}\right) \quad (20)$$

IV. NUMERICAL RESULTS

In this section we will show the probability of collision, determined both analytically using equations (4), (13), (14), (19), and (20), and by computer simulation. Simulation results are determined using Monte-Carlo simulation, and random variable with Nakagami probability density function is generated using a method from [10].

Fig. 2 shows the probability density function (10) and the same pdf obtained by Monte-Carlo simulation. It is clear that there is an excellent match between the analytical result in (10) and the Monte Carlo simulation.

The probability of collision as a function of fading parameter m is shown in Fig. 3. Other fading parameters are $\Omega_1 = \Omega_2 = 1$. The collision probability rises with the increase of fading parameter m . For higher m fading is less severe, and each node's channels are more equal, which results in higher probability of collision. As expected, it can be seen that the higher the number of relay nodes, the higher the probability of collision.

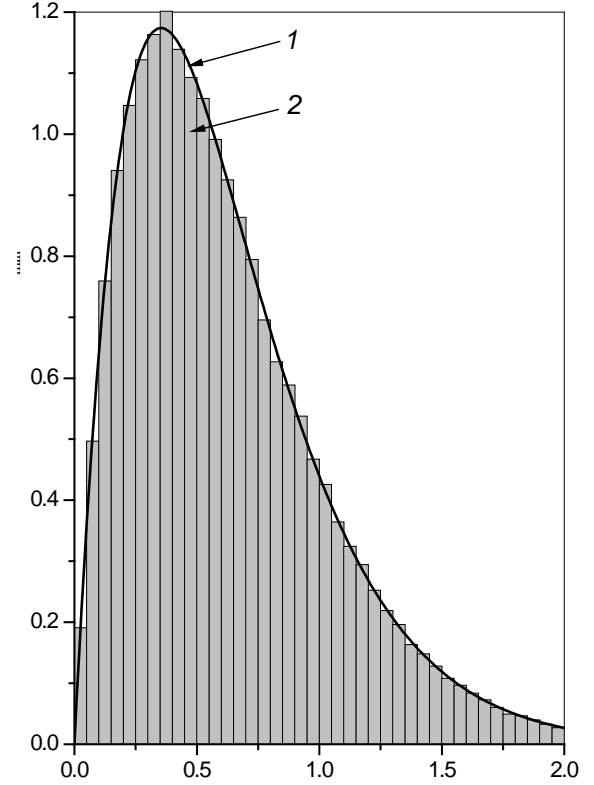


Fig. 2. Comparison between the analytical results (1) and the Monte Carlo simulation (2) for pdf (10), and $\Omega_1 = \Omega_2 = 1$, $m_1 = m_2 = 2$, 200000 iterations

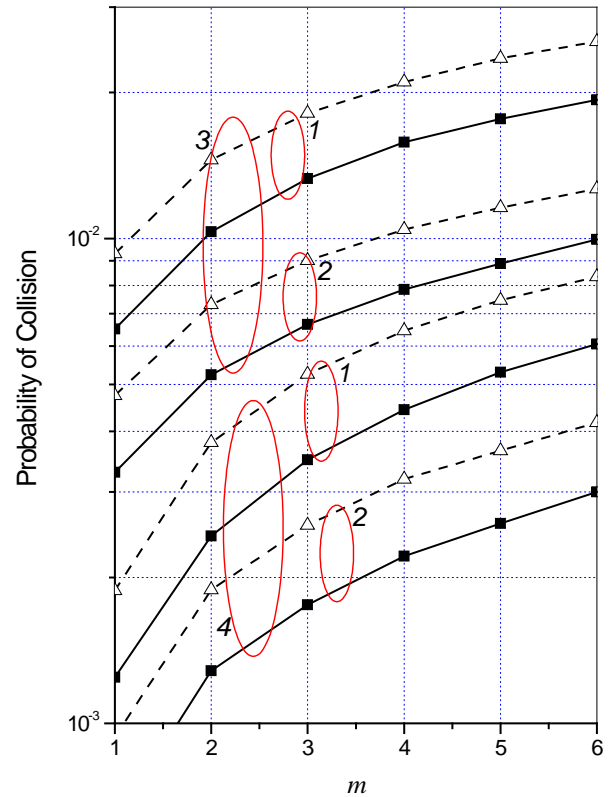


Fig. 3. Probability of collision as a function of m , for $m_1 = m_2 = m$
(1) $\lambda / c = 200$, (2) $\lambda / c = 400$, (3) $M = 6$, (4) $M = 2$
Policy I – Analytic results (solid line), simulation (squares)
Policy II – Analytic results (dashed line), simulation (triangles)

As in paper [6] for Rayleigh and Rician fading, here Fig. 3 confirms that Policy I has better performance than Policy II. It can also be seen that analytic and simulation results are very close to each other.

V. CONCLUSION

An analysis of a cooperative diversity system in the presence of Nakagami fading is considered in this paper. It was shown that the analytical results are in great accordance with the ones obtained by Monte-Carlo simulation. Also, the results show that the probability of collision increases with the number of relay nodes, as well as with parameter m .

ACKNOWLEDGEMENT

This work was supported in part by the Ministry of Science of Serbia within the Project „Development and realization of new generation software, hardware and services based on software radio for specific purpose applications” (TR-11030).

REFERENCES

- [1] J. N. Laneman, D. N. C. Tse, and G.W.Wornell, “Cooperative Diversity in Wireless Networks: Efficient Protocols and Outage Behavior,” *IEEE Trans. Inf. Theory*, vol. 51, no. 12, pp. 3062–3080, Dec. 2004.
- [2] G. Abdelrahman, I. Mahmoud, and M. Hebat-Allah, “Outage Probability Analysis of Cooperative Diversity Networks Over Weibull and Weibull-Lognormal Channels,” *Wireless Personal Communications*, vol. 70, no. 2, pp. 695–708, 2013.
- [3] S. S. Ikki, M. H. Ahmed, “Performance Analysis of Adaptive Decode-and-Forward Cooperative Diversity Networks with Best-Relay Selection,” *IEEE Trans. Comm.*, vol. 58, no. 1, pp. 68-72, January 2010.
- [4] K. Azarian, H. E. Gamal, and P. Schniter, “On the Achievable Diversity-vs-Multiplexing Tradeoff in Cooperative Channels,” *IEEE Trans. Inf. Theory*, vol. 51, pp. 4152–4172, Dec. 2005.
- [5] J. N. Laneman and G. W. Wornell, “Distributed Space-Time Coded Protocols for Exploiting Cooperative Diversity in Wireless Networks,” *IEEE Trans. Inf. Theory*, vol. 49, no. 10, pp. 2415–2525, Oct. 2003.
- [6] A. Bletsas, A. Khisti, D. P. Reed, A. Lippman, “A Simple Cooperative Diversity Method Based on Network Path Selection,” *IEEE Journal on Selected Areas in Communications*, vol. 24, pp. 659–672, Mar. 2006.
- [7] M. O. Hasna and M. S Alouini, “Harmonic Mean and End-to-End Performance of Transmission Systems with Relays,” *IEEE Trans. Commun.*, vol. 52, no. 1, pp. 130–135, 2004.
- [8] M. Abramowitz and I. A. Stegun, *Handbook of Mathematical Functions With Formulas, Graphs, and Mathematical Tables*, 9th ed, Dover, New York, 1970
- [9] Y. D. Yao and A. U. H. Sheikh, “Investigations into Cochannel Interference in Microcellular Mobile Radio Systems,” *IEEE Trans. Veh. Technol.*, vol. 41, pp. 114–123, May 1992.
- [10] L. Jianxia and J. R. Zeidler, “A Statistical Simulation Model for Correlated Nakagami Fading Channels,” in *Proc. WCC-ICCT’00*, pp. 1680–1684, Beijing, China, Aug. 2000.

Level Crossing Rate of Nakagami- m Signal Envelope Subjected to Gamma Shadowing

Danijel Došić¹, Časlav Stefanović¹, Dejan Milić¹, Dragan Radenković¹ and Petar Spalević²

Abstract – In this paper signal envelope subjected simultaneously to Nakagami- m multipath fading and Gamma shadowing is considered. Multipath Nakagami- m fading causes signal envelope variation and Gamma shadowing causes signal envelope power evaluation. Average level crossing rate of considered signal envelope is calculated. Numerical results are presented graphically to show the influence of Nakagami- m fading severity and Gamma shadowing severity on average level crossing rate. Obtained results can be used in performance analysis of wireless communication system in the presence multipath Nakagami- m fading and Gamma shadowing.

Keywords – Level crossing rate (LCR), Nakagami- m , Gamma shadowing.

I. INTRODUCTION

Short term fading and long term fading degrades outage probability of wireless communication system and limits system capacity and spectral efficiency [6]. Received signal suffers simultaneously to long term fading and short term fading, resulting in degradation of system performance of communication system. Short term fading is result of multipath propagation due to reflection, refraction and scattering of radio wave, causing signal envelope variation. Long term fading is result of large obstacles between transmitter and receiver, causing signal envelope power variation [5]. There are more distributions that can be used to describe signal envelope variation in fading channel depend on system nonlinearity, line-of-sight between transmitter and receiver and the number of clusters propagation environment. Rayleigh distribution can be used to describe small scale signal envelope variation in linear, non line-of-sight multipath fading environment with one cluster. In linear line-of-sight

multipath fading environment, small scale signal envelope variation can be described by using the Rician statistical model [8]. Nakagami- m distribution describes small scale signal envelope variation in linear, non line-of-sight multipath fading condition with more clusters. In non linear channels, small scale signal envelope variation can be analyzed by using Weibull and α - μ distributions. The α - μ distribution has two parameters. The parameter α is related to nonlinearity of environment and μ is associated to the number of clusters in environment. Large scale signal envelope power variation in shadowing fading environment can be described by using log-normal distribution or Gamma distribution. The first order statistics or random variable is probability density function, cumulative distribution function, moment generating function and moments. The second order statistics are joint probability density function of random variable and its first derivative, the joint probability density function of random variable at two time instants, average level crossing rate and average fade duration. The average level crossing rate can be calculated as average value of the first derivative of random variable. There are more works considering average level crossing rate of random process and system performance of wireless communication system subjected to long term fading and short term fading.

In paper [1], macrodiversity SC receiver with two microdiversity MRC receivers subjected simultaneously to Nakagami- m multipath fading and Gamma shadowing is considered. Closed form expressions for average level crossing rate of SC receiver output signal envelope and average fade duration of proposed system are evaluated.

In paper [2], macrodiversity system with two microdiversity MRC receivers affected to Rician multipath fading and Gamma shadowing is analyzed. The second order statistics of wireless communication system are calculated in closed form expressions.

In paper [3], level crossing rate and average fade duration of wireless communication system with SC receiver operating over Rician fading channel in the presence of co-channel interference subjected to Rayleigh multipath fading are calculated.

In paper [4], the ratio of product of two random variables and random variable is considered. The product of two random variables can represent desired signal envelope affected to two multipath fading. The random variable in the denominator of the ratio can represent co-channel interference envelope affected to multipath fading. The average level crossing rate of considered ratio is determined.

In this paper the signal envelope subjected to Nakagami- m short-term fading and Gamma long term fading is considered. Joint probability density function of this signal envelope and its first derivative is derived. This expression is used for evaluation of the average level crossing rate of signal

¹Danijel Došić - Faculty of Electrical Engineering at University of Niš, Serbia, Aleksandra Medvedeva 14, 18000 Niš, Serbia, (e-mail: danijeldjosic@gmail.com).

¹Časlav Stefanović - Faculty of Electrical Engineering at University of Niš, Serbia, Aleksandra Medvedeva 14, 18000 Niš, Serbia, (e-mail: caslav.stefanovic@gmail.com).

¹Dejan Milić - Faculty of Electrical Engineering at University of Niš, Serbia, Aleksandra Medvedeva 14, 18000 Niš, Serbia, (e-mail: dejan.milic@elfak.ni.ac.rs).

¹Dragan Radenković - Faculty of Electrical Engineering at University of Niš, Serbia, Aleksandra Medvedeva 14, 18000 Niš, Serbia, (e-mail: dragan.radenkovic@elfak.ni.ac.rs).

²Petar Spalević - Faculty of Technical Sciences, University of Priština, Kneza Miloša 7, 38220 Kosovska Mitrovica, Serbia, (e-mail: petarspalevic@yahoo.com).

envelope affected simultaneously to Nakagami- m multipath fading and Gamma shadowing. The numerical results are presented graphically to show the influence of Nakagami- m severity parameter and Gamma severity parameter on average level crossing rate. To the best of author's knowledge, level crossing rate of signal envelope subjected simultaneously to Nakagami- m short term fading and Gamma long term fading is not reported in open technical literature. Obtained results can be applied in performance analysis and designing of wireless communication system in the presence of Nakagami- m multipath fading and Gamma shadowing fading.

II. LEVEL CROSSING RATE OF GAMMA SHADOWED NAKAGAMI-M MULTIPATH FADING ENVELOPE

Squared Nakagami- m random variable can be written as sum of 2μ independent Gaussian random variables [9]:

$$x^2 = x_1^2 + x_2^2 + \dots + x_{2\mu}^2, \quad (1)$$

where x_i , $i=1, 2, \dots, 2\mu$ independent Gaussian random variables with zero mean and variance σ^2 . The first derivative of Nakagami- m random variables x is:

$$\dot{x} = \frac{1}{x} (x_1 \dot{x}_1 + x_2 \dot{x}_2 + \dots + x_{2\mu} \dot{x}_{2\mu}) \quad (2)$$

The first derivative of Gaussian random variable is Gaussian random variable with zero mean and variance [10]:

$$\sigma_{\dot{x}_i}^2 = 2\sigma^2 \pi^2 f_m^2, i = 1, 2, \dots, 2\mu, \quad (3)$$

where f_m is maximal Doppler frequency. The linear transformation of Gaussian random variables is Gaussian random variable. Therefore, the first derivative of Nakagami- m random variable \dot{x} has conditional Gaussian distribution with mean:

$$\overline{\dot{x}} = \frac{1}{x} (x_1 \overline{\dot{x}_1} + x_2 \overline{\dot{x}_2} + \dots + x_{2\mu} \overline{\dot{x}_{2\mu}}) = 0, \quad (4)$$

since $\overline{\dot{x}_1} = \overline{\dot{x}_2} = \dots = \overline{\dot{x}_{2\mu}} = 0$.

The variance of \dot{x} is:

$$\sigma_{\dot{x}}^2 = \frac{1}{x^2} (x_1^2 \sigma_{\dot{x}_1}^2 + x_2^2 \sigma_{\dot{x}_2}^2 + \dots + x_{2\mu}^2 \sigma_{\dot{x}_{2\mu}}^2). \quad (5)$$

After substituting (3) in (5), the expression for variance of \dot{x} , becomes:

$$\begin{aligned} \sigma_{\dot{x}}^2 &= \frac{2\sigma^2 \pi^2 f_m^2}{x^2} (x_1^2 + x_2^2 + \dots + x_{2\mu}^2) = \\ &= 2\sigma^2 \pi^2 f_m^2 = \pi^2 f_m^2 \frac{\Omega}{m}, \end{aligned} \quad (6)$$

where Ω is power of Nakagami- m random variable and m is Nakagami- m fading severity parameter. Joint probability density function of Nakagami- m random variable and the first derivative of Nakagami- m random variable is:

$$p_{x\dot{x}}(x, \dot{x}/\Omega) = p_x(x/\Omega) p_{\dot{x}}(\dot{x}/\Omega), \quad (7)$$

since random variables x and \dot{x} are independent random variables and Gamma shadowing causes signal envelope power variation. The conditional probability density function of x is:

$$p_x(x/\Omega) = \frac{1}{\Gamma(m)} \left(\frac{m}{\Omega}\right)^m x^{2m-1} e^{-\frac{m}{\Omega}x^2}, \quad (8)$$

where Ω is average square value of x and m is Nakagami- m parameter and $\Gamma(m)$ is Gamma function. The distribution of \dot{x} is:

$$p_{\dot{x}}(\dot{x}/\Omega) = \frac{1}{\sqrt{2\pi}\sigma_{\dot{x}}} e^{-\frac{\dot{x}^2}{2\sigma_{\dot{x}}^2}}. \quad (9)$$

After substituting (8) and (9) in (7), the expression for conditional joint probability density function of x and \dot{x} becomes:

$$p_{x\dot{x}}(x, \dot{x}/\Omega) = \frac{1}{\Gamma(m)} \left(\frac{m}{\Omega}\right)^m x^{2m-1} e^{-\frac{m}{\Omega}x^2} \frac{1}{\sqrt{2\pi}\sigma_{\dot{x}}} e^{-\frac{\dot{x}^2}{2\sigma_{\dot{x}}^2}}. \quad (10)$$

The random variable Ω follows Gamma distribution:

$$p_{\Omega}(\Omega) = \frac{\Omega^{c-1}}{\beta^c \Gamma(c)} e^{-\frac{\Omega}{\beta}}. \quad (11)$$

The joint probability density function of x and \dot{x} can be calculated by averaging the expression (10), over Ω :

$$\begin{aligned} p_{x\dot{x}}(x, \dot{x}) &= \int_0^{\infty} d\Omega p_{x\dot{x}}(x, \dot{x}/\Omega) p_{\Omega}(\Omega) = \int_0^{\infty} d\Omega \frac{1}{\Gamma(m)} \cdot \\ &\cdot \left(\frac{m}{\Omega}\right)^m x^{2m-1} e^{-\frac{m}{\Omega}x^2} \frac{1}{\sqrt{2\pi}\sigma_{\dot{x}}} e^{-\frac{\dot{x}^2}{2\sigma_{\dot{x}}^2}} \frac{\Omega^{c-1}}{\beta^c \Gamma(c)} e^{-\frac{\Omega}{\beta}}. \end{aligned} \quad (12)$$

Average level crossing rate of x can be calculated as average value of the first derivative of x [11]:

$$\begin{aligned} N_x &= \int_0^{\infty} dx p_{x\dot{x}}(x, \dot{x}) \dot{x} = \int_0^{\infty} d\dot{x} \dot{x} \int_0^{\infty} d\Omega \frac{1}{\Gamma(m)} \left(\frac{m}{\Omega}\right)^m \cdot \\ &\cdot x^{2m-1} e^{-\frac{m}{\Omega}x^2} \frac{1}{\sqrt{2\pi}\sigma_{\dot{x}}} e^{-\frac{\dot{x}^2}{2\sigma_{\dot{x}}^2}} \frac{\Omega^{c-1}}{\beta^c \Gamma(c)} e^{-\frac{\Omega}{\beta}} = \end{aligned}$$

$$\begin{aligned}
&= \int_0^{\infty} d\Omega \frac{1}{\Gamma(m)} \left(\frac{m}{\Omega}\right)^m x^{2m-1} e^{-\frac{m}{\Omega} x^2} \frac{\Omega^{c-1}}{\beta^c \Gamma(c)} \\
&\cdot e^{-\frac{\Omega}{\beta} \int_0^{\infty} d\dot{x} \dot{x} \frac{1}{\sqrt{2\pi\sigma_{\dot{x}}}} e^{-\frac{\dot{x}^2}{2\sigma_{\dot{x}}^2}} = \frac{1}{\Gamma(m)} m^m x^{2m-1} \\
&\cdot \frac{1}{\beta^c \Gamma(c)} \int_0^{\infty} d\Omega \Omega^{-m+c-1} e^{-\frac{m x^2}{\Omega} \frac{\Omega}{\beta}} \frac{1}{\sqrt{2\pi}} \sigma_{\dot{x}}, \quad (13)
\end{aligned}$$

since:

$$\int_0^{\infty} d\dot{x} \dot{x} \frac{1}{\sqrt{2\pi\sigma_{\dot{x}}}} e^{-\frac{\dot{x}^2}{2\sigma_{\dot{x}}^2}} = \frac{1}{\sqrt{2\pi}} \sigma_{\dot{x}}. \quad (14)$$

The expression (13), becomes:

$$\begin{aligned}
N_x &= \frac{m^m x^{2m-1}}{\sqrt{2\pi} \Gamma(m) \beta^c \Gamma(c)} \int_0^{\infty} d\Omega \Omega^{-m+c-1} e^{-\frac{m x^2}{\Omega} \frac{\Omega}{\beta}} \\
&\cdot \pi f_m \frac{\Omega^{1/2}}{m^{1/2}} = \frac{m^{m-1/2} x^{2m-1} \pi f_m}{\sqrt{2\pi} \Gamma(m) \beta^c \Gamma(c)} \\
&\cdot \int_0^{\infty} d\Omega \Omega^{-m+c-1} e^{-\frac{m x^2}{\Omega} \frac{\Omega}{\beta}}. \quad (15)
\end{aligned}$$

By using the integral [7]:

$$\int_0^{\infty} dx x^{r-1} e^{-\frac{a}{x} - bx} = \left(\frac{a}{b}\right)^{\frac{r}{2}} K_r(2\sqrt{ab}), \quad (16)$$

where $K_r(y)$ is Bessel function of the second kind, the previously expression becomes:

$$\begin{aligned}
N_x &= \frac{m^m x^{2m-1}}{\sqrt{2\pi} \Gamma(m) \beta^c \Gamma(c)} \left(m x^2 \beta\right)^{\frac{c-m+1/2}{2}} \\
&\cdot K_{c-m+1/2}\left(2\sqrt{\frac{m x^2}{\beta}}\right). \quad (17)
\end{aligned}$$

In figure 1, average level crossing rate is plotted versus signal envelope for several values of Nakagami- m fading severity m , Gamma shadowing severity c and signal envelope power b . For lower values of signal envelope average level crossing rate increases as signal envelope increases. For higher values of signal envelope, average level crossing rate decreases as signal envelope increases. Maximal value of average level crossing rate increases as Gamma shadowing severity decreases. System performances are better for lower

values of average level crossing rate. The influence of signal envelope on average level crossing rate is greater for higher values of Nakagami- m fading several.

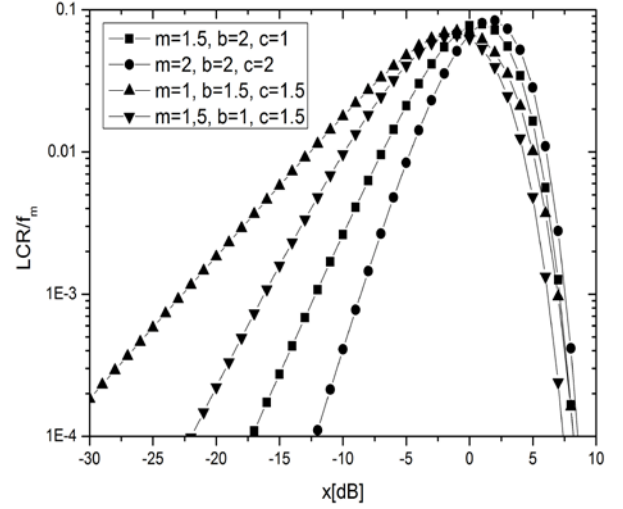


Fig. 1. LCR for different parameters m , c and b

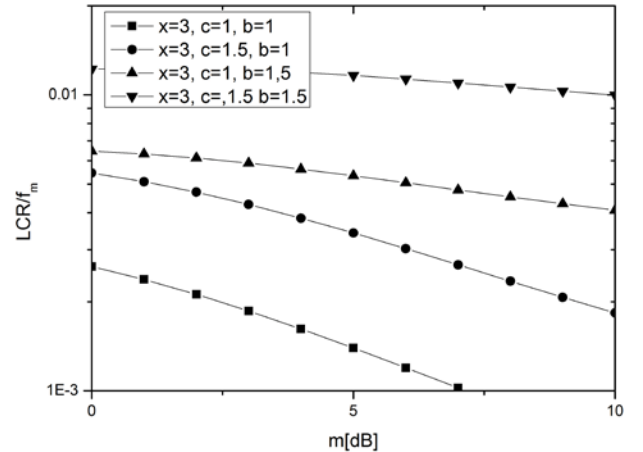


Fig. 2. LCR for different parameters x , c and b

In figure 2, average level crossing rate is shown versus Nakagami- m fading severity for several values of signal envelope x , Gamma shadowing severity c and signal envelope power b . The influence of Nakagami- m fading severity on average level crossing rate is greater for lower values of Gamma shadowing severity c . Average level crossing rate increases as Gamma shadowing severity decreases. System performances are better for higher values of Nakagami- m fading severity and Gamma shadowing severity parameter.

III. CONCLUSION

Obtained results can be used for performance analysis of wireless communication system subjected to multipath fading and shadowing. Received signal experiences Nakagami- m short term fading and Gamma long term fading resulting in

system performance degradation. Small scale Nakagami- m multipath fading causes signal envelope variation and long scale Gamma shadowing causes signal envelope power variation. Received signal envelope has conditional Nakagami- m probability density function. The average square value of received signal envelope follows Gamma distribution. Probability density function of received signal envelope is derived by averaging conditional Nakagami- m described envelope over Gamma distribution. In this paper joint probability density function of received signal envelope and its first derivative is calculated. This expression is used for evaluation of average level crossing rate of received signal envelope in the presence short term fading and long term fading. Average level crossing rate is derived in closed form expression. Average level crossing rate is calculated as average value of the first derivative of signal envelope. Level crossing rate is the second order statistics of random variable envelope. Numerical results are presented graphically to show the influence of short term fading severity parameter and long term fading severity parameter on average level crossing rate. System performances are better for lower values of average level crossing rate of received signal envelope. Average level crossing rate of received signal envelope increases as short term fading severity parameter decreases. Influence of short term fading severity parameter on average level crossing rate is greater for higher values of long term fading severity parameter. The system performances are better for higher values of long term fading severity parameter.

REFERENCES

- [1] D. Stefanovic, S. Panic, P. Spalevic „Second-order Statistics of SC Macrodiversity System Operating over Gamma Shadowed Nakagami- m Fading Channels“, *AEU - International Journal of Electronics and Communications*, Volume 65, Issue 5, pp. 413–418, May 2011.
- [2] N. Sekulović, M. Stefanović, “Performance Analysis of System with Micro- and Macrodiversity Reception in Correlated Gamma Shadowed Rician Fading Channels”, *Wireless Personal Communications*, (publisher: Springer-Verlag New York, Inc.), vol. 65, no. 1, pp. 143-156, 2012.
- [3] A. Panajotovic, N. Sekulovic, M. Stefanovic, D. Draca, “Average Level Crossing Rate of Dual Selection Diversity over Correlated Unbalanced Nakagami- m Fading Channels in the Presence of Cochanel Interference (Article)”, *IEEE Communications letters*, vol. 16, no. 5, pp. 691-693. 2012.
- [4] E. Mekic, N. Sekulovic, M. Bandjur, M. Stefanovic, P. Spalevic, “The Distribution of Ratio of Random Variable and Product of two Random Variables and its Application in Performance Analysis of Multi-Hop Relaying Communications over Fading Channels”, *Przeglad Elektrotechniczny*, vol. 88, no. 7A, pp. 133-137, 2012.
- [5] J. Proakis, *Digital Communications*, 4thed. New York: McGraw-Hill, 2001.
- [6] M. K. Simon, M. S. Alouini, *Digital Communication over Fading Channels*, USA: John Wiley & Sons, 2000.
- [7] I. Gradshteyn, I. Ryzhik, *Tables of Integrals, Series, and Products*, Academic Press, New York 1994.
- [8] G. L. Stüber, *Principles of Mobile Communications*, Norwell, MA Kluwer Academic Publishers, 1996.
- [9] Jr. W. B. Devenport, W. L. Root, *An Introduction to the Theory of Random Signals and Noise*, McGraw-Hill, New York, 1958.
- [10] S. Panic, et al. (2013), *Fading and Interference Mitigation in Wireless Communications*, USA, CRC Press, 2013.
- [11] A. Matovic, E. Mekic, N. Sekulovic, M. Stefanovic, M. Matovic and C. Stefanovic, “The Distribution of the Ratio of the Products of two Independent α - μ Variates and its Application in the Performance Analysis of Relaying Communication Systems”, *Mathematical Problems in Engineering*, 2013.
- [12] A. Panajotovic, M. Stefanovic. D. Draca, N. Sekulovic, “Average Level Crossing Rate of Dual Selection Diversity in Correlated Rician Fading with Rayleigh Cochanel Interference”, *IEEE Communications Letters*, vol. 14, No. 7, July 2010.

Performance Analysis of MADM Algorithms with Different QoS Parameters in Heterogeneous Networks

Raycho Dobrev

Abstract – In current wireless environment the need for an user to be always best connected (ABC) anywhere at anytime leads to execute a vertical handoff decision for guaranteeing service continuity and quality of service (QoS). In Heterogeneous wireless networks main challenge is continual connection among the different networks like WiFi, WiMax, WLAN, WPAN etc. MADM (multiple attribute decision making) is an algorithmic approach suitable to realize a dynamic interface selection with multiple alternatives and attributes. In this paper, we compare the performance of three MADM algorithms e.g. SAW, WP, and TOPSIS. The simulation results show that each algorithm has its own limitations.

Keywords – *Heterogeneous wireless networks, MADM, TOPSIS, SAW, WP, Decision making.*

I. INTRODUCTION

In Heterogeneous Networks are expected to support different access technologies and to integrate multiple networks over a common IP (Internet Protocol) platform. They are managed by different operators like WiMax, WiFi, UMTS, etc. One of the main goal and most challenged area in fourth generation wireless network (4G) was service continuity. Users expect the best connectivity to applications anywhere at anytime, which is most important issue in such environment also known as the Always Best Connected (ABC) concept [1]. ABC requires dynamic selection of the best network and access technologies when multiple options are available simultaneously.

Handover network type has the two types horizontal handover and vertical handover [2]. The homogeneous wireless network performs horizontal handover when the connection just moves from one base station to another within the same network. A vertical handover is the process of changing the mobile connection between different access points belonging to different access technologies. The vertical handover consist mainly in three phases: network discovery, handoff decision and handoff execution. In first step, the mobile terminal (MT) discovers its available neighbouring networks. In the decision phase, the MT determines whether it has to redirect its connection based on comparing the decision factors offered by the available networks and required by mobile user, that is, information gathering in the first phase. The last phase is responsible for the establishment and realise of the connections according to the vertical handoff decision.

MADM (multiple attribute decision making) [3] includes many methods such as SAW (Simple Additive Weighting)

[4], WP (Weighted Product Method) [5] and TOPSIS (Technique for Order Preference by Similarity to Ideal Solution) [6]. Saw calculates the overall score of alternatives by the weighted sum of all attribute values. The overall score in WP is a product of the values made across the attributes. The fundamental premise of TOPSIS is that the best alternatives should have the shortest Euclidean distance from the ideal solution (made up of the best value for each attribute regarding the alternatives) and the farthest distance to the negative ideal solution (made up of the worst value of each attribute regarding the alternatives).

In this paper is proposed a comparative study of three MADM algorithms by means of simulations and performance analysis for a heterogeneous network, integrated by WiFi, UMTS and 4G networks, when the user conducts various applications.

This paper is organised as follows. Section II presents related works. In section, III presents MADM methods. Simulation and results are presented in section IV. Section V consists of conclusion.

II. RELATED WORKS

Many handoff decision algorithms are proposed in the literature so far. In [4] a comparison is done among SAW, TOPSIS, Grey Relational Analysis (GRA) and Multiplicative Exponent Weighting (MEW) for vertical handoff decision. In [7] a comparison analysis done between seven algorithms: SAW, MEW, TOPSIS, ELEKTRE, VIKOR, GRA and WMC for vertical handoff in 4G networks. The aim is to understand its performance for different user applications. Another performance comparison is made in [8]. There is presented study about limitations of three MADM algorithms (SAW, WP, TOPSIS) influencing the decision making for interface selection. Performance evaluation and comparison of MADM algorithms for subjective and objective weights is made in [9]. In [10] their goal is to reduce the overload and the processing delay in the mobile terminal so they proposed novel vertical handoff decision scheme to avoid the processing delay and power consumptions. In [12] is proposed a novel ranking algorithm, which combines multi attribute decision making (MADM) and Mahalanobis distance. The main task of this paper is to deal with limitations like ranking abnormality and number of handovers. Proposed algorithm combines two methods such as Fuzzy AHP and Mahalanobis distance.

III. MADM ALGORITHMS FOR VERTICAL HANDOVER

The most known and used MADM Algorithms for vertical handoff are Simple Additive Weighting (SAW), Technique

Raycho Dobrev, Faculty of Telecommunications at Technical University of Sofia, 8 Kl. Ohridski Blvd, Sofia 1000, Bulgaria, e-mail: r_dobrev@tu-sofia.bg.

for Order Preference by Similarity to Ideal Solution (TOPSIS) and Multiplicative Exponent Weighting (MEW) or still Weight Product Method (WPM). These algorithms have to evaluate and compare the decision factors for each wireless networks, in order to detect and trigger a vertical handover. The factors can be classified as beneficial, i.e. the larger, the better, or cost, i.e. the lower, the better. In this paper, these algorithms are used Euclidian normalization method. We choose this normalization method since it provides the highest-ranking consistency [11].

MADM problem is set out as follows:

$$A = \{A_i, i = 1, 2, \dots, n\} \quad (1)$$

A set of a finite number of alternatives, which represents the possible networks the mobile terminal supports.

$$C = \{C_j, j = 1, 2, \dots, m\} \quad (2)$$

A set of attributes which presented a different criteria as an examples signal strength, bit rate, power consumption, price, delay, security est.

TABLE I
MADM MATRIX

	C_1	C_2	\cdot	\cdot	C_m
	(w_1)	(w_2)	\cdot	\cdot	(w_m)
A_1	x_{11}	x_{12}	\cdot	\cdot	x_{1m}
A_2	x_{21}	x_{22}	\cdot	\cdot	x_{2m}
\cdot	\cdot	\cdot	\cdot	\cdot	\cdot
\cdot	\cdot	\cdot	\cdot	\cdot	\cdot
A_n	x_{n1}	x_{n2}	\cdot	\cdot	x_{nm}

The weight vector $\mathbf{w} = \{w_1, w_2, \dots, w_m\}$ (3) represents the relative importance of these attributes.

MADM problem can be represented by a matrix as shown in Table I.

A. Simple Additive Weighing – SAW

This is the best known and most widely used scoring method, the score of each candidate network i is obtained by adding the contributions from each attribute x_{ij} multiplied by the weight factors w_j . Then the selected network A^*_{SAW} is:

$$A^*_{SAW} = \max_i \sum_{j=1}^m x_{ij} \times w_j \quad (4)$$

The weight vector must satisfy $\sum_{j=1}^N w_j = 1$. (5)

The new from paper [8] is new way to calculate the results with Euclidian normalization method. The formula, which we

used in normalizations for SAW, WP, and TOPSIS, is this:

$$1 - \frac{x_{ij}}{\sqrt{\sum_{i=1}^n x_{ij}^2}} \quad (6)$$

We used that formula in case we have cost parameters. Cost parameters as an example are jitter, delay and lost. Benefit parameter, in our case, is utilization. The new normalization criterion is:

$$r_{ij} = \begin{cases} \frac{x_{ij}}{\sqrt{\sum_{i=1}^n x_{ij}^2}}, & \text{for benefit parameters} \\ 1 - \frac{x_{ij}}{\sqrt{\sum_{i=1}^n x_{ij}^2}}, & \text{for cost parameters} \end{cases} \quad (7)$$

B. Weighted Product Method – WP

This approach is similar to SAW but the scaled property values of each alternative are powered by w_j and the overall score is a product of the values made across the attributes. The selected interface is then:

$$A^*_{wp} = \max_i \prod_{j=1}^m x_{ij}^{w_j} \quad (8)$$

C. Technique for Order Preference by Similarity to Ideal Solution –TOPSIS

TOPSIS is an algorithm widely used for mobile terminal interface selection using multiple attributes. Here, the chosen network is the one, which have the shortest distance to the ideal solution and the longest to the worst-case solution. TOPSIS requests the following steps to compute the network-ranking list.

Step 1: (7) gives construction the normalized decision matrix, which allows comparison across the attributes.

Step 2: Construct the weighted normalized decision matrix.

Step 3: Determine ideal and negative-ideal solutions.

Step 4: Calculate the separation measure between the networks and the positive and negative ideal networks.

Step 5: Calculate the relative closeness to the ideal solution:

$$C_j = \frac{S_j^-}{S_j^- + S_j^+} \quad (9)$$

Step 6: Rank the preference order. A set of alternatives can now be ranked according to the decreasing order of C_j .

IV. SIMULATION RESULTS

Here we present the simulation results and performance analysis of the three MADM algorithms: SAW, WP and TOPSIS. The simulations are carried out using MATLAB.

Two simulations are made. In the simulation, we consider a weight vector in two situations: first situation (10) is when the

utilization is significantly important compared with other QoS parameters and second situation (11) – when the lost is significantly important parameter.

$$W_1 = [0.225 \ 0.225 \ 0.325 \ 0.225] \quad (10)$$

$$W_2 = [0.200 \ 0.220 \ 0.250 \ 0.330] \quad (11)$$

In the simulation, we consider four attributes associated to five network interfaces (UMTS, 802.11b, 802.11a, 802.11n and 4G). The attributes are packet jitter, packet delay, utilization and packet loss for each network. These attributes represent two main criteria: QoS parameters and user's preferences. The attribute list can be expanded depending on the interface selection objectives.

The Packet Jitter (J): is a measure of the average delay variation within the access system. It can be measured in milliseconds.

The Packet delay (D): measures the average delay variation within the access system. It can be measured in milliseconds.

Utilization (U): is a measure of the current utilization of the access network or the wireless link. It can be expressed in percentage.

The Packet Loss (L): is a measure of the average packet loss rate within the access system over a considerable duration of time. It can be expressed in packet losses per million packets.

TABLE II
THE ATTRIBUTE PARAMETERS

	J (ms)	D (ms)	U (%)	L (per10 ⁶)
Net #1 UMTS	50	400	10	100
Net #2 802.11b	25	200	20	20
Net #3 802.11a	15	100	20	15
Net #4 802.11n	30	150	40	20
Net #5 4G	20	100	20	15

A. Simulation

In this section, we calculate the ranking order of the alternatives by using SAW, WP and TOPSIS algorithms. For the first simulation, we calculate with weight vector (10). Table III presents the relative closeness to the ideal solution of TOPSIS and overall score of SAW and WP. The results show the ranking order of the alternatives, which is the same for the three algorithms. The best alternative is with rank #1 (Network 4 in our study).

We measure the difference of ranking values between ranks #1 and #2, #2 and #3, #3 and #4 and so on of all algorithms. Difference allows distinguishing the ranking order and selecting easily the best alternative. In the Figure 1 is shown the difference of ranking values of all algorithms. As it can see, we only received better results for TOPSIS in dif (r1-r2) and dif (r4-r5) but

for WP we received better results in dif(r2-r3) and dif(r3-r4). In the Figure 2 is shown comparison with the results that we received (dif (r1-r2)my_res ...) and the results received in [8] (diff (r1-r2) ...). The result for [8] is made from the table III in [8].

B. Simulation

For the second simulation, we calculate in the same way but with different weight vector (11).

Table IV presents the relative closeness to the ideal solution of TOPSIS and overall score of SAW and WP. The results show the ranking order of the alternatives, which is the same for the three algorithms

TABLE III
THE RANKING ORDER OF SAW,WP AND TOPSIS

	SAW	WP	TOPSIS
Net #1	0.175 Rank #5	0.155 Rank #5	0.070 Rank #5
Net #2	0.579 Rank #4	0.555 Rank #4	0.620 Rank #4
Net #3	0.669 Rank #2	0.629 Rank #2	0.684 Rank #2
Net #4	0.706 Rank #1	0.701 Rank #1	0.835 Rank #1
Net #5	0.652 Rank #3	0.615 Rank #3	0.676 Rank #3

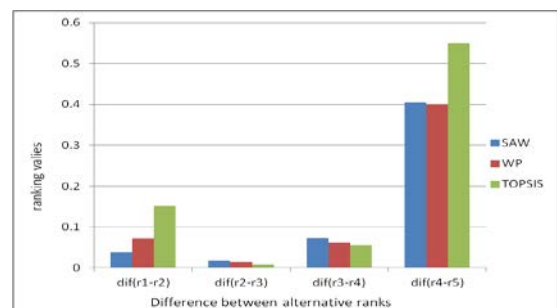


Fig. 1 The difference of ranking values of SAW, WP and TOPSIS

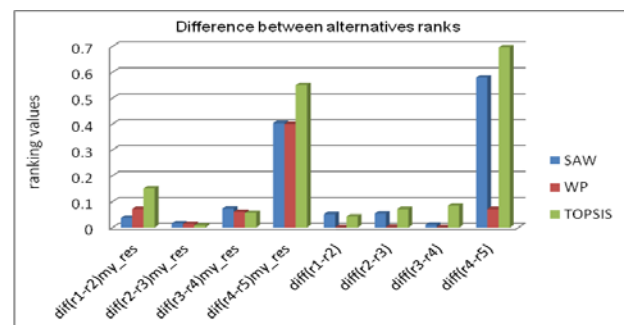


Fig. 2 Comparing the results:
a. on the left on the graphic - our results
b. on the right on the graphic - results in [8]

In the Figure3 is shown the difference of ranking values of all algorithms. As it can see, we again received better results for

TOPSIS in dif (r1-r2) and dif (r4-r5) compared to [8] and better for WP in dif (r2-r3) and dif (r3-r4).

In the Figure 4 is shown the results that we received compared with the results received in [8] in this case based on other condition for weighting vector (11).

TABLE IV
THE RANKING ORDER OF SAW, WP AND TOPSIS

	SAW	WP	TOPSIS
Network #1	0.160 Rank #5	0.135 Rank #5	0.143 Rank #5
Network #2	0.618 Rank #4	0.593 Rank #4	0.720 Rank #4
Network #3	0.708 Rank #2	0.672 Rank #2	0.773 Rank #2
Network #4	0.718 Rank #1	0.712 Rank #1	0.858 Rank #1
Network #5	0.693 Rank #3	0.659 Rank #3	0.769 Rank #3

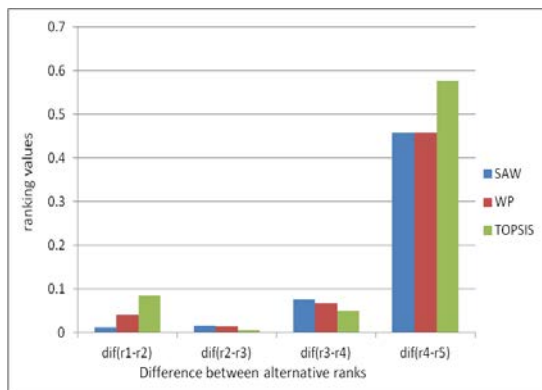


Fig. 3 The difference of ranking values of SAW, WP and TOPSIS

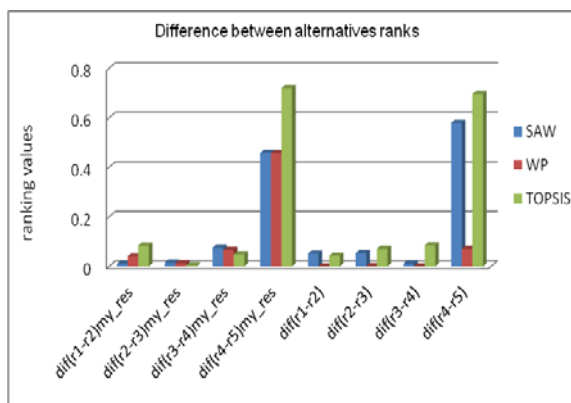


Fig 4. Comparing the results:
a. on the left on the graphic - our results
b. on the right on the graphic - results in [8]

V. CONCLUSION

TOPSIS has the largest difference of ranking values and allows more accuracy in identifying the ranks between the

alternatives compared to SAW and WP but in our simulations the best results is only in dif (r1-r2) and dif (r4-r5). In the network with high rank in dif (r2-r3) and dif (r3-r4) WP has larger ranking values compared TOPSIS.

From the tables III and IV we can see that with increase the values of the weight vector for lost and decrease the value of weighting vector for utilization we received better ranking values.

REFERENCES

- [1] M. Kassar, B. Kervella, and G. Pujolle, "An Overview of Vertical Handover Decision Strategies in Heterogeneous Wireless Networks", *Computer Communications*, vol. 31, pp. 2607-2620, 2008.
- [2] N. Nasser, A. Nasswa, and N. Nassanein, "Handoff in Fourth Generation Heterogeneous Networks", *IEEE Communications Magazine*, Vol. 44, 2006, pp. 96-103.
- [3] K. Yoon and C. Hwang, "Multiple Attribute Decision Making: An Introduction", Sage Publication, 1995.
- [4] A. Memariani, A. Amini, A. Alizehad, "Sensitivity Analysis of Simple Additive Weighting Method (SAW)-The Results of Change in the Weight of One Attribute on the Final Ranking of Alternatives", *Journal of Industrial Engineer.* 4, pp. 13-18, 2009.
- [5] E. Stevens-Navarro and V. W.S Wong, "Comparison between Vertical Handoff Decision Algorithms for Heterogeneous Wireless Networks", *Proc. of IEEE Vehicular Technology Conference*, Melbourne, Australia, May 2006.
- [6] W. Zhang, "Handover Decision Using Fuzzy MADM in Heterogeneous Networks", 2004 *IEEE Wireless Communications and Networking Conference*, Atlanta, USA, March 2004.
- [7] J.D. Matrinez-Moralez, U. Pineda-Pico and E. Stevens-Navarro, "Performance Comparison between MADM Algorithms for Vertical Handoff in 4G Networks", *Electrical Engineering Computing Science and Automatic Control (CCE)*, pp 309-314, Tuxtla Gutierrez, 2010.
- [8] P. Tran and N. Boukhatem, "Comparison of MADM Decision Algorithms for Interface Selection in Heterogeneous Wireless Networks", *Software, Telecommunications and Computer Networks*, pp. 119 -124, Split, 2008.
- [9] N. Baghla, "Performance Evaluation and Comparison of MADM Algorithms for Subjective and Objective Weights", *International Journal of Emerging Trends in Electrical and Electronics (IJETEE)*, Vol. 2, Issue. 2, April-2013.
- [10] R. Tawil, J. Demerjain, G. Pijolle and O. Salazar, "Processing-Delay Reduction During The Vertical Handoff Decision In Heterogeneous Wireless System", *International Conference on Computer Systems and Applications*, pp 381 - 385, 2008.
- [11] S. Chakraborty and C. Yeh, "A Simulation based Comparative Study of Normalization Procedures in Multi-Attribute Decision Making", the 6th *WSEAS Int. Conf. on Artificial Intelligence, Knowledge Engineering and Data Bases*, Corfu Island, Greece, February 16-19, 2007.
- [12] M. Lahby, L. Cherkaoui, A. Adib, "A Novel Ranking Algorithm based Network Selection for Heterogeneous Wireless Access", *Journal of Network*, Vol. 8, NO. 2, February.

Simulation Estimation of Network and Quality Characteristics in Video Transmission over LTE Network

Grigor Mihaylov¹ and Teodor Iliev²

Abstract – In this paper are presented the main technical features of LTE standard. An analysis of LTE physical layer is also given and simulation of video transmission with different resolution and frame rates was conducted.

Keywords – LTE, CQI, video transmission, jitter.

I. INTRODUCTION

The era of new wireless communications is upon us. Telecommunications technologies are evolving at an unbelievable pace, driven by innovation, speed, quality, convenience, and cost. Long-Term Evolution (LTE) is the standard recently specified by the 3GPP on the way towards fourth-generation mobile. LTE leads a big technological improvement as compared with the previous 3G standard.

LTE is designed to increase data rates and cell edge bitrates, improve spectrum efficiency (unicast as well as broadcast) and allow spectrum flexibility (1.25, 2.5, 5, 10, 15 and 20 MHz) for flexible radio planning. LTE has also to reduce packet latency, the main restriction for real-time services, such as VoIP, video-conferencing, stream video, etc., reduce radio access network cost as well as cost-effective migration from earlier 3GPP releases and simplify its network to a flat all-IP packet-based network architecture where all the user plane radio functionalities are terminated at the enhanced Node B (eNB). [1]

II. LTE VERSION 8 MAIN FEATURES

The radio access network of LTE is called E-UTRAN and one of its main features is that all services, including real-time, will be supported over shared packet channels. This approach will achieve increased spectral efficiency which will turn into higher system capacity with respect to current UMTS and HSPA. An important consequence of using packet access for all services is the better integration among all multimedia services and among wireless and fixed services. [2]

The main philosophy behind LTE is minimizing the number of nodes. Therefore the developers opted for a single-node architecture. The new base station is more complicated than the Node B in WCDMA/HSPA radio access networks, and is consequently called eNB (Enhanced Node B). The eNBs have all necessary functionalities for LTE radio access

network including the functions related to radio resource management. The new core network is a radical evolution of the one of third generation systems and it only covers the packet-switched domain. Therefore it has a new name: Evolved Packet Core. Following the same philosophy as for the E-UTRAN, the number of nodes is reduced. Evolved Packet Core (EPC) divides user data flows into the control and the data planes. A specific node is defined for each plane plus the generic gateway that connects the LTE network to the internet and other systems. The EPC comprises several functional entities. [3]

The overall structure of LTE is shown in Fig. 1, where: the Mobility Management Entity (MME) is responsible for the control plane functions related to subscriber and session management; The Serving Gateway is the anchor point of the packet data interface towards E-UTRAN. Moreover, it acts as the routing node towards other 3GPP technologies; The Packet Data Network (PDN Gateway) is the termination point for sessions towards the external packet data network. It is also the router to the Internet; The Policy and Charging Rules Function (PCRF) controls the tariff making and the IP Multimedia Subsystem (IMS) configuration of each user. [4]

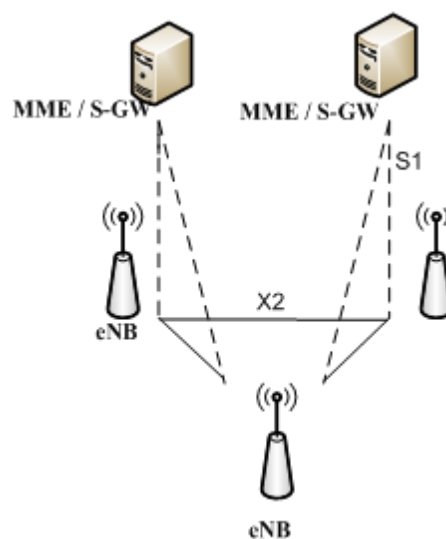


Fig. 1. LTE architecture

III. CHANNEL QUALITY PARAMETERS

In modern wireless networks, the signal quality in wireless channel is estimated based on the channel quality measurements. The measurement results are used to select appropriate modulation and coding scheme for each transmission. In the downlink of Long Term Evolution (LTE) systems, feedback and processing delays cause a mismatch

¹Grigor Mihaylov is with the Department of Telecommunications at University of Ruse, 8 Studentska Str, Ruse 7017, Bulgaria, E-mail: gmihaylov@uni-ruse.bg

²Teodor Iliev is with the Department of Telecommunications at University of Ruse, 8 Studentska Str, Ruse 7017, Bulgaria, E-mail: tiliev@uni-ruse.bg

between the current channel state and the Channel Quality Information (CQI) at the base station. This CQI aging leads to inaccurate channel adaptation and can, thus, highly degrade the cell capacity.[5, 6]

The Channel Quality Indicator (CQI) contains information sent from a UE to the eNode-B to indicate a suitable downlink transmission data rate, i.e., a Modulation and Coding Scheme (MCS) value. CQI is a 4-bit integer and is based on the observed signal-to-interference-plus-noise ratio (SINR) at the UE. The CQI estimation process takes into account the UE capability such as the number of antennas and the type of receiver used for detection. This is important since for the same SINR value the MCS level that can be supported by a UE depends on these various UE capabilities, which needs to be taken into account in order for the eNode-B to select an optimum MCS level for the transmission. The CQI reported values are used by the eNode-B for downlink scheduling and link adaptation, which are important features of LTE.

The supported CQI indices and their interpretations are given in Table 1. In total, there are 16 CQI values, which require a 4-bit CQI feedback. In Table 1, the efficiency for a given CQI index is calculated as:

$$E = Q_m \times R \quad (1)$$

where Q_m is the number of bits in the modulation constellation.

TABLE I
CQI INDEXES

CQI index	Modulation	Code rate R	Efficiency
0	-	-	-
1	QPSK	78	0,1523
2	QPSK	120	0,2344
3	QPSK	193	0,3770
4	QPSK	308	0,6016
5	QPSK	449	0,8770
6	QPSK	602	1,1758
7	16QAM	378	1,4766
8	16QAM	490	1,9141
9	16QAM	616	2,4063
10	64QAM	466	2,7305
11	64QAM	567	3,3223
12	64QAM	666	3,9023
13	64QAM	772	4,5234
14	64QAM	873	5,1152
15	64QAM	948	5,5547

Based on the estimated effective SINR, the UE picks the CQI index that indicates the highest MCS level (modulation and code rate) that can be supported with a 10% BLER on the first H-ARQ transmission. The CQI feedback is used by the eNode-B to select an optimum PDSCH transport block with a combination of modulation scheme and transport block size corresponding to the CQI index that could be received with target block error probability after the first H-ARQ transmission. While this target block error probability is left open as an implementation choice, typical values are in the

range of 10-25%. It should be noted that the target BLER of the transmission is not the same as the BLER of 10% based on which the CQI is computed. Thus, the eNode-B needs to take this into account while selecting the optimum transport block size. If the achieved block error rate is not equal to the target value based on the H-ARQ ACK/NAK ratio, then a fudge factor can be added to the CQI to ensure that the selection of the block size based on the CQI leads to the desired target block error rate. A positive fudge factor implies a more aggressive transport block size selection, whereas a negative fudge factor implies a more conservative transport block size selection. [6]

Figure 2 represents block error rate (BLER) in function of signal-to-noise ratio (SNR) by various CQI indexes.

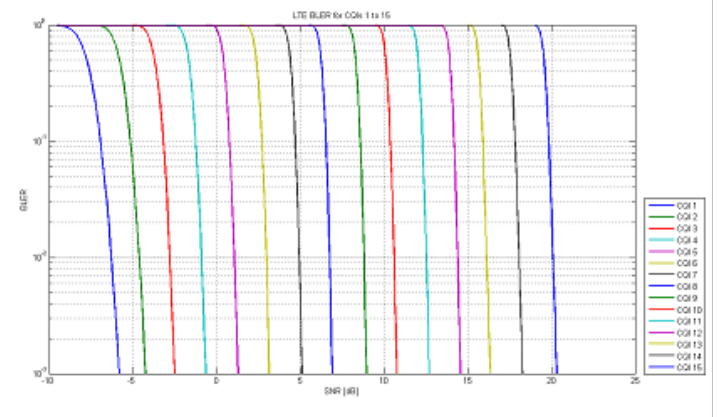


Fig. 2. BLER in various CQI indexes

IV. SIMULATION RESULTS

For transmission simulation we use NS-2 network simulator with two additional modules. The first one is EvalVid – a complete framework and tool-set for evaluation of the quality of video transmitted over a real or simulated communication network. Besides measuring QoS parameters of the underlying network, like loss rates, delays, and jitter, it supports also a subjective video quality evaluation of the received video based on the frame-by-frame PSNR calculation. The tool-set has a modular construction, making it possible to exchange both the network and the codec. The processing of the data takes place in 3 stages. The first stage requires the timestamps from both sides and the packet types. The results of this stage are the frame-type based loss rates and the inter-packet times. Furthermore the erroneous video file from the receiver side is reconstructed using the original encoded video file and the packet loss information. This video can now be decoded yielding the raw video frames which would be displayed to the user. At this point a common problem of video quality evaluation comes up. Video quality metrics always require the comparison of the displayed (possibly distorted) frame with the corresponding original frame. In the case of completely lost frames, the required synchronization cannot be kept up. The second stage of the processing provides a solution to this problem. Based on the loss information, frame synchronization is recovered by inserting the last displayed frame for every lost frame. This

makes further quality assessment possible. The thus fixed raw video file and the original raw video file are used in the last stage to obtain the video quality. [7]

The second additional module we use is Long Term Evolution/System Architecture Evolution (LTE/SAE) module, introduced in [10]. The system model includes LTE/SAE network model, traffic model and flow control model. In the network model, some network configuration parameters can easily be changed, for example it can be defined any number of UEs, bandwidth between the network elements and the usage of the optimization features; others cannot be changed so easily due to the limitation of the implemented model, such as eNB and advanced gateway (aGW) number. In the simulated LTE/SAE network, the following network elements are included – 1 server (provide HTTP, FTP and signaling services), 1 aGW (provide HTTP cache, flow control), 1 eNB (provide flow control information) and many UEs. In this module three types of traffic are provided – Conversational, Streaming and Interactive traffic. The Conversational traffic simulates transmission of Voice over IP, Video conferencing calls and Telephony speech. Interactive traffic simulates Web browsing and e-mail reading/sending. The most important traffic type for us is the Streaming traffic. It's one-way traffic and it is used for Audio and Video streaming. The QoS mechanisms provided in the cellular network have to be robust and capable of providing reasonable QoS resolution. More accurate flow controls, better performance the system can get. However, the system's resource, such as CPU and memory, is limited. Balance between the system performance and resource is needed. Hierarchy Virtual Queue (HVQ) flow control provides the good solution to get the high ratio of performance over resource. The basic principle of the virtual queue based flow control is shown in the following figure.

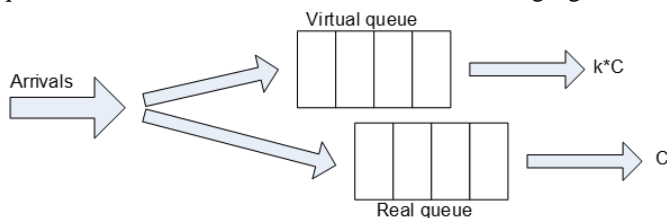


Fig. 3. Virtual queue based flow control

A virtual queue is a fictitious queue with a capacity less than the actually available capacity. The motivation for using the virtual queue is that it provides advance warning of congestion. For each real queue there is a corresponding virtual queue or a set of virtual queues, one for each differently treated traffic class. When packets arrive into the real queue, the virtual queue length is also updated by the length of the received packet. The draining rate of the virtual queue is $k \cdot C$ ($k \leq 1$), where C is the draining rate of the real queue. When the virtual queue length upper threshold reaches, the flow control information is send from air interface to the S1 interface. S1 interface will take the corresponding flow control actions. If the flow control information is about UE, the packets belong to the UE are blocked; if the flow control information is about cell, all the packets belong to the cell where the UE locates are blocked; if the flow control

information is about the eNB, all packets belong to the eNB where the UE locates are blocked. The blocking is cancelled when the lower threshold is triggered. [8]

Fig. 4 shows the architecture of the simulation. During the simulation study, three video clips with different frame rates, resolution and size are used. The parameters of the clips are shown in Table 2.

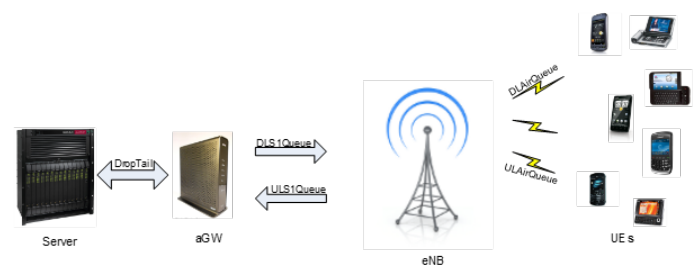


Fig. 4. Architecture of the system

TABLE II
PARAMETERS OF TRANSMITTED VIDEO CLIPS

Clip	Resolution	FPS	Duration, min	Size, Mb
A Bit of a Pickle	1920x1080	24	03:45	90,6
I Nub You	1280x720	24	02:58	39,4
Container	352x288	30	00:10	13,5

The most important parameter in wireless video transmission is the jitter. From the conducted simulation and the graph, shown in Fig. 5, it can be seen, that this parameter has a very low value, which is prerequisite for excellent delivery and play in user side.

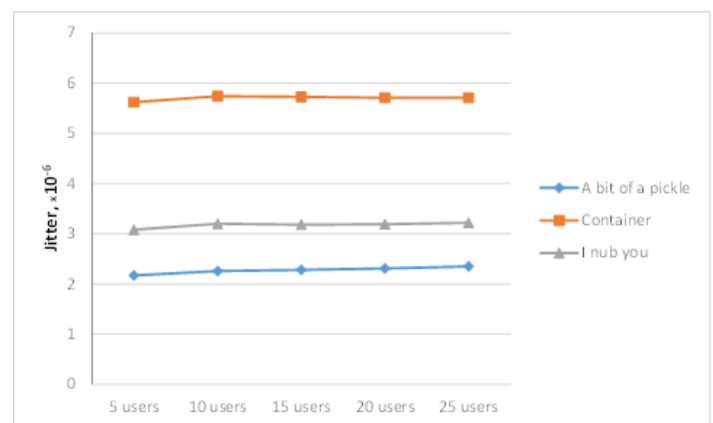


Fig. 5. Jitter of transmitted video clips

V. CONCLUSION

LTE has been designed as a future technology to cope with next user requirements. We have presented a framework for an analytical comparison between the achievable information rate in SC-FDMA and that in OFDMA. Based on the

conducted simulation it can be seen that video files with higher resolution (1920x1080) have lower jitter than the video files with resolution (352x288).

Future work will focus on more detailed analysis, design and simulation of transmission of video information with high resolution to more subscribers (UEs). Finally, combining channel coding influence and channel capacity is an emerging area that will be the subject of future research.

ACKNOWLEDGEMENT

The present paper has been produced with the financial assistance of the European Social Fund under Operational Programme "Human Resources Development". The contents of this document are the sole responsibility of "Angel Kanchev" University of Ruse and can under no circumstances be regarded as reflecting the position of the European Union or the Ministry of Education and Science of Republic of Bulgaria.

Project № BG051PO001-3.3.06-0008 "Supporting Academic Development of Scientific Personnel in Engineering and Information Science and Technologies".

REFERENCES

- [1] A. Gosh, J. Zhang, J. Andrews, R. Muhamed, *Fundamentals of LTE*, Prentice Hall, 2011
- [2] J. Lee, J.-K. Han, and J. Zhang "MIMO Technologies in 3GPP LTE and LTE-Advanced", *EURASIP Journal on Wireless Communications and Networking*, pp. 21, 2009.
- [3] 3GPP TR 25.913, "Requirements for Evolved UTRA (EUTRA) and Evolved UTRAN (E-UTRAN)," v.8.0.0, December 2008.
- [4] "On the Way towards Fourth-Generation Mobile: 3GPP LTE and LTE-Advanced", *EURASIP Journal on Wireless Communications and Networking*, pp.11, 2009.
- [5] M. Kawser, N. Hamid, M. Hasan, M. Alam, M. Rahman, "Downlink SNR to CQI Mapping for Different Multiple Antenna Techniques in LTE", *International Journal of Information and Electronics Engineering*, Vol. 2, No. 5, 2012.
- [6] N. Kolehmainen, J. Puttonen, P. Kela, T. Ristaniemi, T. Henttonen, M. Moision, "Channel Quality Indication Reporting Schemes for UTRAN Long Term Evolution Downlink", *IEEE Magazine*, 2008.
- [7] J. Klaue, B. Rathke, and A. Wolisz, "EvalVid - A Framework for Video Transmission and Quality Evaluation", *13th International Conference on Modelling Techniques and Tools for Computer Performance Evaluation*, pp. 255-272, Urbana, Illinois, USA, September 2003.
- [8] Q. Qiu, J. Chen, L. Ping, Q. Zhang, X. Pan, "LTE/SAE Model and its Implementation in NS 2", *Fifth International Conference on Mobile Ad-hoc and Sensor Networks*, pp. 299-303, 2009.

Indoor Propagation Path Loss Modeling for Wireless Sensor Networks

Sava Savov¹ and Zlatan Ganev¹

Abstract – In this paper path losses during indoor propagation (inside buildings) are considered. Because of serious noisy component, one smart approach is to apply linear regression (obeying “least squares criterion”). Two different scenarios of propagation are considered: a) same floor propagation; b) one floor propagation (here additional losses are due to propagation through a ceiling of one floor).

Keywords – Wireless Sensor Network, Path Losses, Electromagnetic Modeling.

I. INTRODUCTION

Path losses determine the average received power for a given Transmitter – Receiver range. Sometimes shadowing from large obstacles is added in order to improve the accuracy of the model. Fading in the channel represents the short-term effects due to multi-path propagation [1 – 3]. De Friis transmission formula gives the path loss in the case of free-space propagation. Additional losses exist in the feeders of the transmitter and the receiver. All these complicated factors can be taken into account in the “power-loss” model, where the path loss exponent (n) is changing for different scenarios in the interval ($1 < n < 4$) [4 – 5]. Particularly, for the free-space path loss exponent is ($n = 2$). The propagation, that takes into account the slow variations, is called “large scale model”. On the other hand, the fast variations that take into account the fading effect, is so called “small scale model” [6 – 7]. In this paper one method for accurate estimation of path losses for indoor propagation channel) with two important parameters are considered: (n) the best curve-fitting power-law; and σ – the statistical standard deviation. This model can be applied to variety of scenarios, related to WSN (wireless sensor networks).

II. BRIEF THEORY OF THE LINEAR REGRESSION

A. Path loss model:

This is empirical model that try to approximate analytically the results of measurement. The path loss function of the distance can be represented in the following form

$$PL(d) = PL(d_0)(d/d_0)^n \quad (1)$$

or in logarithmic form

$$PL_{dB}(d) = PL_{dB}(d_0) + 10n \log(d/d_0) + X_\sigma \quad (2)$$

where (d) is the distance, (d_0) is the distance from the closest point to the observer, and (X_σ) is a Gaussian noise. Here MMSE (minimum mean square error) estimation about the path-loss exponent (n) is applied and the standard deviation (σ) is found. The sum that should be minimized is

$$S(n) = \sum_{k=1}^N (p_k - q_k n)^2 \quad (3)$$

where

$$q_k = -10 \lg(d_k / d_1) \quad (4)$$

It is assumed that

$$p_1 = 0, p_k = -p(d_k) + p_1 \quad (5)$$

Now for the MMSE $S(n)$ is found the following simple expression

$$S(n) = A - 2Bn + Cn^2 \quad (6)$$

where the coefficients are

$$A = \sum_{k=1}^N p_k^2; B = \sum_{k=1}^N p_k q_k; C = \sum_{k=1}^N q_k^2. \quad (7)$$

The necessary condition for minimum

$$\frac{dS}{dn} = 0 \quad (8)$$

leads to the equation

$$n = B/C \quad (9)$$

It can be shown that appropriate expression for the standard deviation is

$$\sigma[\text{dB}] = \sqrt{S(n)} / 2 \quad (10)$$

¹The authors are with the Department of Electrical Engineering, Technical University of Varna, 9010 Varna, Bulgaria, E-mail: sava.savov12@gmail.com

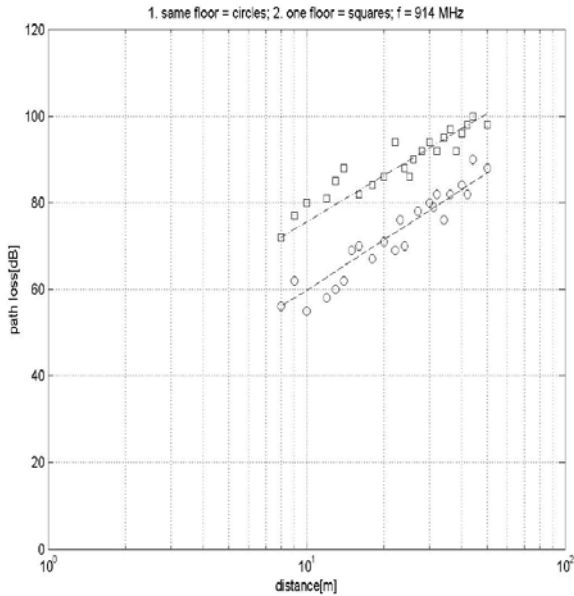


Fig. 1. Best fit linear regressions

III. RESULTS FROM SIMULATIONS

Here we are found two different *best fit lines*: 1) for “the same floor” results of measurements (with circles); 2) for “the one floor” results of measurements (with squares). The range of measurements is $d = [8 - 50 \text{ m}]$. In these experiments the carrier frequency is $f = 914 \text{ MHz}$. Both best fit lines (linear regressions) are shown by dashed lines in Fig.1. More accurate results for the parameters of both linear regression lines are:

- 1) (same floor) $n = 3.87$; $\sigma = 7.36 \text{ dB}$;
- 2) (one floor) $n = 3.60$; $\sigma = 7.27 \text{ dB}$.

We observe one interesting result from this simulation: the two best-fit lines are *almost parallel*, the only difference between them is *offset about 16 dB more* for one-floor case

than for same-floor case. This fact can be explained by “through-ceiling propagation”.

In the near future these approach should be extended for the case of (two floors) and (three floors) measurements.

IV. CONCLUSIONS

Our best-fit model (with linear regression) could be applied to variety of scenarios in the area of WSN: 1) person-to-person interactions (BAN = body-area network, for example); 2) environmental interactions (ESN=environmental sensor network); 3) object-to-object interactions (OSN=object sensor network).

The next step of our research in this field will be an application of the same best-fit algorithm to the case of BAN, where new topic appeared in the last years (RFID = radio-frequency identifications). There is a strong interest here of developing such a system for one hospital environment. There are three different mechanisms of propagation in such an environment: a) in-body propagation; b) on-body propagation; c) off-body propagation.

REFERENCES

- [1] C. Oestges, “Propagation Modeling for Wireless Sensor Networks”, Report, Catholique Universite de Louvain, 2005.
- [2] D. Janvier, «Propagation Models for Wireless Sensor Communications”, Report, Catholique Universite de Louvain, 2006.
- [3] T. Rappaport, “*Wireless Communications (Principles and Practice)*”, 2nd ed., Prentice Hall, 2004.
- [4] A. Molisch, F. Tufvesson, “*Wireless Communications*”, (2nd ed.), Wiley, 2005.
- [5] T. Rappaport et al., “The Renaissance of Wireless Somunicationsin the Massive Broadband Era”, IEEE Veh. Tech. Conference, Sep. 2012.
- [6] T. Rappaport et al., State of the Art in 60 GHz Integrated Circuits and Systems for Wireless Communications”, Proc. IEEE, no. 8, pp. 1390 – 1436, 2011.
- [7] T. Rappaport et al., “Millimetre Wave Mobile Communications for 5 G: It Will Rork!”, IEEE Access, May 2013.

ANN Models for DOA Estimation of Correlated Signals using Circular Antenna Array

Marija Stoilković¹, Zoran Stanković², Nebojša Dončov², Bratislav Milovanović²

Abstract – This article investigates performance of artificial neural networks (ANNs) in detection of correlated signals. In order to cover the whole azimuth plane, circular antenna array is employed at the receiver. Separate ANN configurations are developed for detection of two and three incoming signals, and their results are analysed with regard to distance between sources and degree of correlation. The estimation results are compared with the reference data and the MUSIC algorithm.

Keywords – Artificial neural networks, Circular antenna array, Correlated signals, DOA estimation.

I. INTRODUCTION

Direction of arrival (DOA) estimation of correlated signals is often required in practical applications. Due to the multipath propagation of RF signals, a receiving array collects direct signals from sources as well as fractionally delayed multipath components that have bounced off from some nearby reflective surfaces.

Detection of correlated signals is not always an easy task. Standard algorithms for detection of uncorrelated signals [1], [2] could be modified in order to provide detection of correlated sources as well. The drawback of these algorithms is that they include additional calculations to decorrelate signals. This procedure is useful but, on the other hand, it reduces the effective aperture of the antenna array obtaining the results of lower resolution [3].

In this paper, artificial neural networks (ANNs) are employed to provide DOA estimates of correlated signals. Due to their universal approximation capability and parallel processing of input data, estimation results are provided almost instantaneously. In this way, complex calculations over spatial covariance matrices are avoided. Application of ANNs in detection of correlated signals does not degrade resolution of DOA estimates. In the paper, we analyze detection of two and three EM signals, at different mutual distances, azimuth positions and with various correlation coefficients. Therefore, three levels of generalization of ANN models are achieved. Advantage over MUSIC algorithm is illustrated on several examples of detecting closely spaced and strongly correlated sources.

¹Marija Stoilković is with the Innovation Centre of Advanced Technology, Blvd Nikole Tesle 61/5, 18000 Niš, Serbia, E-mail: marija.stoilkovic@icnt.rs.

²Zoran Stanković, Nebojša Dončov and Bratislav Milovanović are with the Faculty of Electronic Engineering, University of Niš, 18000 Niš, Serbia.

II. DATA MODEL

A uniform circular array (UCA), composed of N equally spaced omnidirectional elements, is illustrated in Fig 1. The radius of the circle is r while the distance between adjacent elements in the array is $d=\lambda/2$ (where λ is the wavelength of impinging signals). The angular position of the n -th element of the array is given by $\gamma_i=2\pi i/N$, $i=0, 1, \dots, N-1$. DOA of the k th incoming signal is determined by the azimuth and elevation angles φ_k and θ_k , respectively. The array manifold vector $\mathbf{a}_k(\varphi_k, \theta_k)$, $k=1, 2, \dots, K$ is given by

$$\mathbf{a}_k(\varphi_k, \theta_k) = [e^{j(2\pi/\lambda)r \sin \theta_k \cos(\varphi_k - \gamma_0)} \ e^{j(2\pi/\lambda)r \sin \theta_k \cos(\varphi_k - \gamma_1)} \ \dots \ \dots \ e^{j(2\pi/\lambda)r \sin \theta_k \cos(\varphi_k - \gamma_{N-1})}]^T \quad (1)$$

Further, a $N \times K$ steering matrix \mathbf{A} and signal model can be defined as follows

$$\mathbf{A}(\varphi, \theta) = [\mathbf{a}(\varphi_1, \theta_1) \ \mathbf{a}(\varphi_2, \theta_2) \ \dots \ \mathbf{a}(\varphi_K, \theta_K)] \quad (2)$$

$$\mathbf{x}(t) = \mathbf{A}\mathbf{s}(t) + \mathbf{n}(t) \quad (3)$$

where $\mathbf{n}(t)$ is the $N \times 1$ noise vector, $\mathbf{x}(t)$ is the $N \times 1$ data vector and $\mathbf{s}(t)$ is the $K \times 1$ signal vector given by

$$\mathbf{s}(t) = [s_1(t) \ s_2(t) \ \dots \ s_k(t)]^T = [\rho_1 \ \rho_2 \ \dots \ \rho_k]^T s_l(t) \quad (4)$$

where ρ_i denotes the relative amplitude and phase between the i -th and l -th source ($\rho_l=1$).

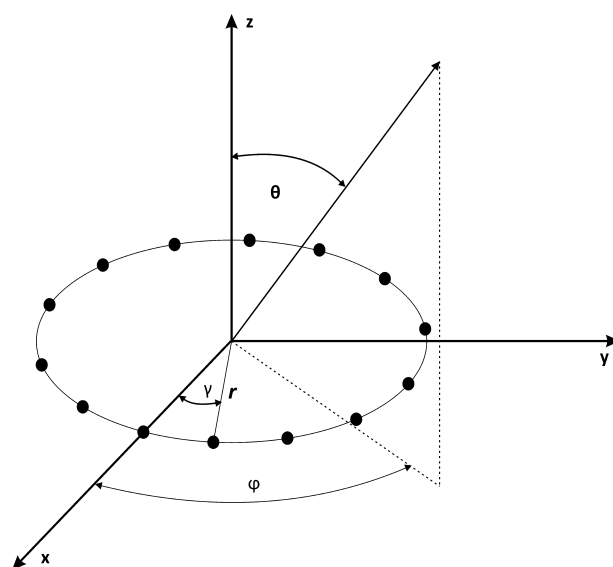


Fig. 1 Uniform circular antenna array (UCA)

The spatial covariance matrix can be estimated as follows

$$\mathbf{R} = E\{\mathbf{x}(t)\mathbf{x}^H(t)\} = \mathbf{A}\mathbf{S}\mathbf{A}^H + \sigma^2\mathbf{I} \quad (5)$$

where $E\{\cdot\}$ is the expectation operator, H denotes the complex conjugate transpose operation, σ^2 is the noise variance, \mathbf{I} is the identity matrix, \mathbf{S} is $K \times K$ signal covariance matrix given by

$$\mathbf{S} = E[\mathbf{s}(t)\mathbf{s}^H(t)] = E[|s_l(t)|^2]\mathbf{c}\mathbf{c}^H \quad (6)$$

where $\mathbf{c} = [\rho_1 \ \rho_2 \ \dots \ \rho_K]^T$. It can be observed that the signal subspace of matrix \mathbf{R} is of rank one instead of K , and the noise subspace is orthogonal to $\mathbf{A}\mathbf{c}$ instead of the columns of \mathbf{A} . This implies the failure of the subspace based method when the matrix \mathbf{R} is used in this form.

III. DOA ESTIMATION BY RBF NEURAL NETWORK

Application of Radial Basis Function Neural Networks (RBF-NN) in the area of DOA estimation is based on the inverse mapping to the one that an antenna array performs. That is the mapping $G: \mathbf{C}^N \rightarrow \mathbf{R}^K$ from the space of antenna array outputs $\{\mathbf{x}(t)=[x_1(t) \ x_2(t) \ \dots \ x_N(t)]^T\}$ to the space of DOAs $\Phi=[\varphi_1 \ \varphi_2 \ \dots \ \varphi_K]^T$. The input data of RBF-NN is the spatial covariance matrix \mathbf{R} of the antenna array outputs, and DOAs of users' signals are neural network responses.

The DOAs from the received signal \mathbf{x} can be estimated as follows

$$\varphi = f(\mathbf{x}) \quad (7)$$

An RBF-NN approximates the reverse mapping function $f(\mathbf{x})$ as a weighted sum of the radial basis function

$$f(\mathbf{x}) = \sum_{j=1}^J \omega_{jm} \exp\left(-\frac{\|\mathbf{x} - \mathbf{c}_j\|^2}{2\sigma_j^2}\right) \quad (8)$$

where \mathbf{c}_j is the central vector of the j th neuron, σ_j^2 is the spread while ω_{jm} is a weight. These parameters are determined through the training process of the RBF-NN. In the equation (8), $\|\cdot\|$ is the Euclidean norm and J denotes the number of hidden neurons [4].

An RBF-NN is composed of input, hidden and output layers. Number of neurons in the input layer of the network depends on the dimensionality of \mathbf{R} matrix. Since \mathbf{R} is an $N \times N$ square matrix and having in mind that ANNs cannot operate with complex numbers, there should be $2N^2$ neurons in the input layer of the network. In the case of correlated signals, upper triangular part of matrix \mathbf{R} is used to represent signals at the array output. Therefore, all inputs are organized into a N^2 -element vector \mathbf{z} . Before it is applied to the input layer of the RBF-NN, the input vector \mathbf{z} is normalized with its norm, $\mathbf{z}_{norm} = \mathbf{z}/\|\mathbf{z}\|$. The j th neuron in the hidden layer has the nonlinear response that can be written as follows

$$h_j(\mathbf{z}_{norm}) = b_{1j} \exp\left(-\frac{\|\mathbf{z}_{norm} - \mathbf{c}_j\|^2}{2\sigma_j^2}\right) \quad (9)$$

where b_{1j} represents a real coefficient. Using this expression the output of the RBF-NN can be calculated by

$$g_k(\mathbf{z}_{norm}) = \sum_{j=1}^J b_{1j} \omega_{kj} \exp\left(-\frac{\|\mathbf{z}_{norm} - \mathbf{c}_j\|^2}{2\sigma_j^2}\right) + b_{2k} \quad (10)$$

where b_{2k} is a bias of the output layer while ω_{kj} is the weight between the k th neuron in the output layer and j th neuron in the hidden layer.

IV. RESULTS

We consider DOA estimation of two and three correlated sources, respectively. Since the number of outputs of an RBF-NN is fixed, separate configurations are developed using the incorporated function provided by the neural network toolbox of MATLAB [5]. The training set is prepared of the training vectors corresponding to different positions of EM sources. The input to the network is the upper triangular part of matrix \mathbf{R} , organized into a vector, while the desired outputs are azimuth positions of sources. Test samples are used to evaluate the performance of the developed neural networks. The test set is formed from data that have not been involved in the training process. However, these data must belong to the same distribution as the training data.

To collect data for the training and test set, it is assumed that a 10-element circular antenna array is positioned at the receiver. Signals that have to be detected are narrowband with SNR of 20 dB. To estimate spatial covariance matrix 1024 signal snapshots are used. The correlation of signals is varied between 0 and 1.

A. Detection of two correlated sources

Let's suppose that two EM sources are located at different azimuth positions from -180° to 180° . Mutual distance between sources is varied as follows: $2^\circ, 5^\circ, 10^\circ, 20^\circ, 30^\circ, 40^\circ, 50^\circ, 60^\circ, 70^\circ, 80^\circ, 90^\circ, 100^\circ, 110^\circ$ and 120° . The starting positions of two sources are -180° and $-180^\circ + dist$, where $dist$ denotes the distance between sources. The sources are further moved towards 180° , in steps of 1° . Correlation between signals is introduced through the correlation coefficient which took values 0, 0.5 and 1, respectively. To validate the performance of trained RBF-NN models, a test set is formed using mutual distances $3^\circ, 15^\circ, 35^\circ, 55^\circ, 75^\circ$ and 95° , and step of 1° . The correlation coefficient is varied as follows 0.1, 0.4 and 0.7. Accordingly, the networks are trained with 6420 samples and tested with 3090 samples.

Following the previously described procedure, a number of neural models are developed and among them, the best model is chosen for further analysis. In our case, the network with correlation coefficient of 0.999 and average error of 0.58% has demonstrated the best performance. The hidden layer of the network is composed of 498 neurons.

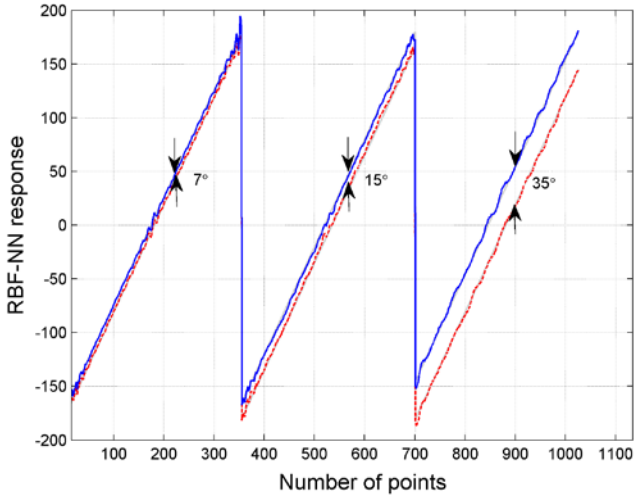


Fig. 2 Response of the RBF-NN model for detection of two signals (- - source 1, - source 2), $\rho=1$

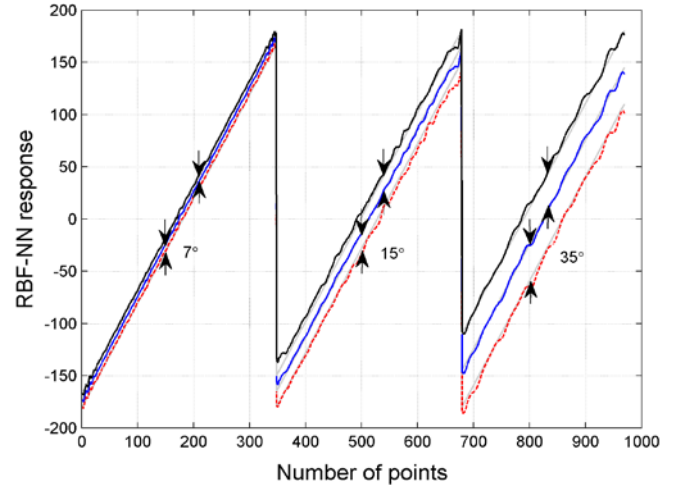


Fig. 4 Response of the RBF-NN model for detection of three sources (- - source 1, - source 2, - source 3), $\rho=1$

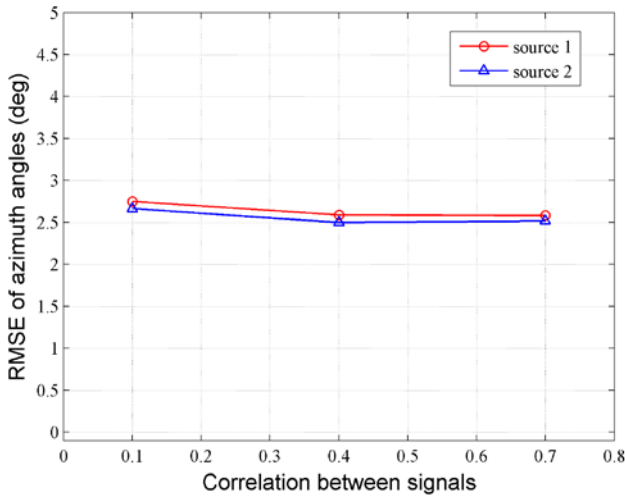


Fig. 3 RMSE versus correlation between signals

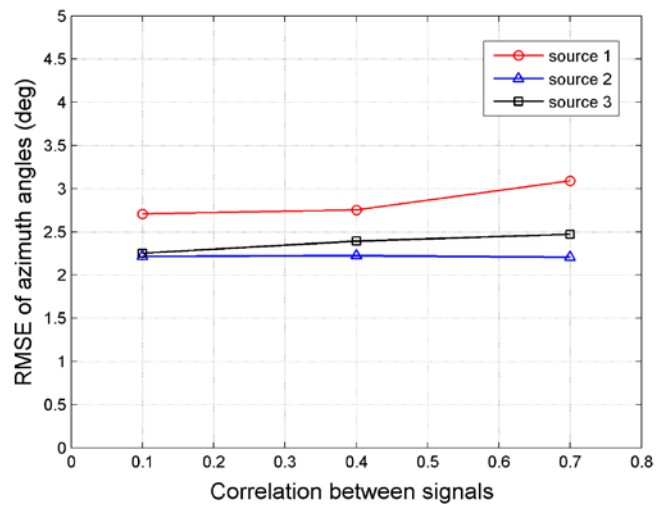


Fig. 5 RMSE versus correlation between signals

The response of the network for test data is presented in Fig. 2. Correlation between signals is 1, and distances are 7° , 15° and 35° , respectively. It can be observed that network has quite good performance for test samples. Even for the separation of 7° , it is able to distinguish two sources. Fig. 3 illustrates dependence of RMSE (Root Mean Square Error) of DOA estimates on the correlation. We can conclude that the network provides almost uniform response for all test values of correlation.

B. Detection of three correlated sources

Similar to the case with two sources, three sources are assumed to be at mutual distances of 2° , 5° , 10° , 20° , 30° , 40° , 50° , 60° , 70° , 80° , 90° , 100° , 110° and 120° . Initially, all sources are positioned at azimuth angles of -180° , $-180^\circ + \text{dist}$ and $-180^\circ + 2 \cdot \text{dist}$, and then moved towards 180° in steps of 1° . The correlation between signals is varied from uncorrelated case, weakly correlated up to fully coherent signals

(coefficients 0, 0.5 and 1, respectively). The test set is formed assuming mutual distances of 12° , 23° , 32° , 64° and 96° . The correlation between signals is 0.1, 0.4 and 0.7. Hence, the network is trained with 10440 and tested with 4053 samples. After the training procedure is finished, the test statistics of the obtained neural models are analysed. The best neural model has 958 hidden neurons, the correlation coefficient of 0.9993 and average error of 0.7%.

In Fig. 4, response of the RBF-NN is illustrated for three mutual distances between sources and correlation coefficient of 1. The response of the network appropriately follows the movement of three sources from -180° to 180° . RMSE of DOA estimates is presented in Fig. 5 for each source separately. The second source is the most accurately detected and almost not dependent on the correlation. Estimation error of the first and the third source is slightly more expressed and rises as the correlation between signals becomes stronger. Also, it can be observed that neural model adequately separates three sources at small mutual distances such as 7° . For instance, the MUSIC algorithm has a problem to separate

closely spaced sources even when the signals are uncorrelated. In the case of correlated signals, the algorithm has problem also with more separated sources. This problem is illustrated in Figs. 6, 7, 8 and 9. Corresponding outputs of RBF-NNs are given in Table 1.

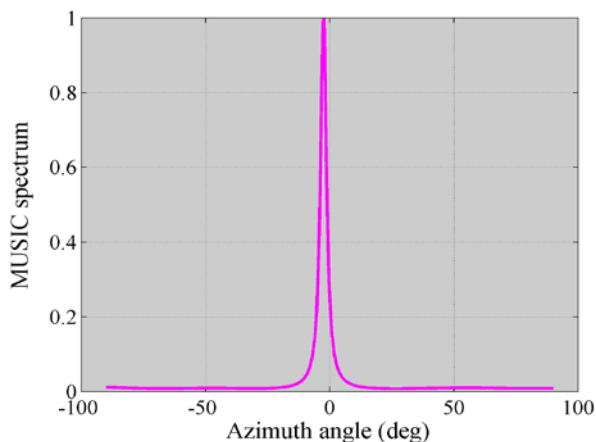


Fig. 6 MUSIC spectrum of two correlated signals ($\rho=1$) at azimuth positions $\varphi_1=-10^\circ$ and $\varphi_2=5^\circ$

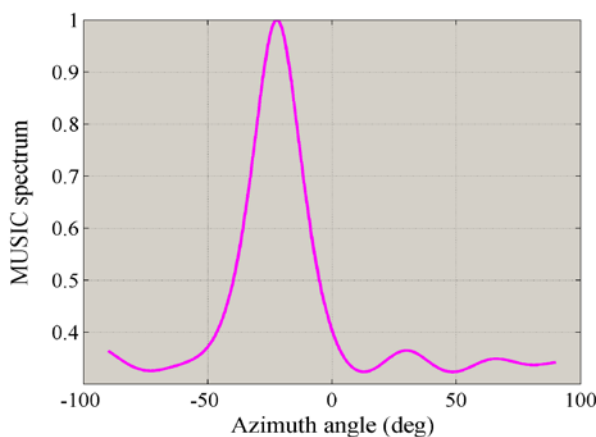


Fig. 7 MUSIC spectrum of two correlated signals ($\rho=1$) at azimuth positions $\varphi_1=-40^\circ$ and $\varphi_2=-5^\circ$

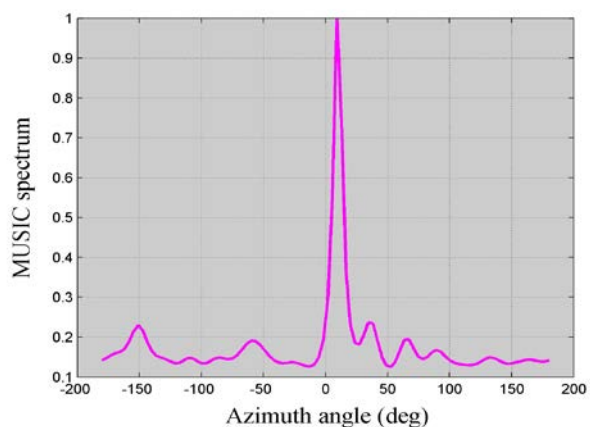


Fig. 8 MUSIC spectrum of three correlated signals ($\rho=1$) at azimuth positions $\varphi_1=-2^\circ$, $\varphi_2=10^\circ$ and $\varphi_3=22^\circ$

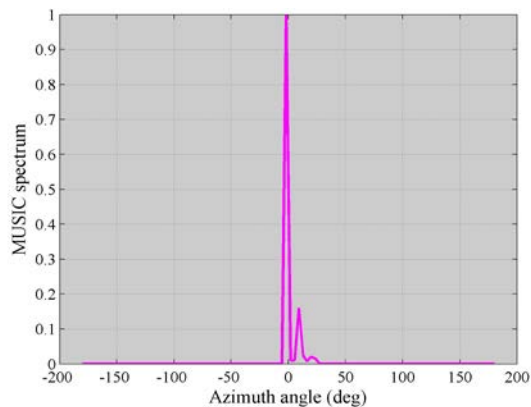


Fig. 9 MUSIC spectrum of three uncorrelated signals ($\rho=0$) at azimuth positions $\varphi_1=-2^\circ$, $\varphi_2=10^\circ$ and $\varphi_3=22^\circ$

TABLE I
DOA ESTIMATES BY RBF-NNs

Actual azimuth angles (deg)			DOA estimates (deg)		
$\varphi_1=-10$	$\varphi_2=5$		$\varphi_{1es}=-8.48$	$\varphi_{2es}=2.25$	
$\varphi_1=-40$	$\varphi_2=-5$		$\varphi_{1es}=-41.47$	$\varphi_{2es}=-2.32$	
$\varphi_1=-2$	$\varphi_2=10$	$\varphi_3=22$	$\varphi_{1es}=-4.97$	$\varphi_{2est}=9.09$	$\varphi_{3es}=23.16$
$\varphi_1=-2$	$\varphi_2=10$	$\varphi_3=22$	$\varphi_{1es}=-3.82$	$\varphi_{2es}=9.64$	$\varphi_{3es}=23.05$

V. CONCLUSION

In this paper, detection of correlated EM signals is presented. Neural networks are used as a tool to extract the information about directions of arrival from the spatial covariance matrix. It is shown that networks are able to deal with differently positioned and correlated signals. Correlated and closely spaced sources are appropriately separated and detected. The accuracy of results could be further improved using more precise data on the positions of sources in the training set.

ACKNOWLEDGEMENT

This work was supported by the project TR-32052 of the Serbian Ministry of Education, Science and Technological Development.

REFERENCES

- [1] R. Schmidt, "Multiple Emitter Location and Signal Parameter Estimation," *IEEE Trans Antennas Propagation*, vol. 34, pp. 276-280, 1986.
- [2] R. Roy and T. Kailath, "ESPRIT-Estimation of Signal Parameters via Rotational Invariance Techniques," *Trans Acoust, Speech, Signal Processing*, vol. 37, pp. 984 - 995, 1989.
- [3] T. J. Shan, M. Wax, and T. Kailath, "On Spatial Smoothing for Estimation of Coherent Signals," *Trans Acoust, Speech, Signal Processing*, vol. 33, 806 - 811, 1985.
- [4] S. Haykin, *Neural Networks*, New York, IEEE Press, 1994.
- [5] H. Demuth, M. Beale, "Neural Network Toolbox", (The Mathworks, Inc., MA, USA, 1998).

Localization of Mobile Users of Stochastic Radiation Nature by using Neural Networks

Zoran Stankovic¹, Nebojsa Doncov¹, Ivan Milovanovic², Bratislav Milovanovic¹, Marija Stoilkovic³

Abstract – Localization of narrow-band electromagnetic sources of stochastic radiation nature in far-field is considered in the paper. Artificial neural networks-based approach is applied here to allow for accurate and efficient direction of arrival (DOA) determination of electromagnetic signals radiated from an arbitrary number of stochastic sources mutually positioned at fixed angle distance or up to two stochastic sources at arbitrary angle distance. Correlation matrix, obtained by signal sampling via antenna array in far-field scan area is used to train an appropriate model based on MLP (Multi-Layer Perceptron) neural network. Proposed approach is validated on the example of neural model performing accurate and fast one-dimensional (1D) DOA estimation of angular position in the azimuth plane of two mobile users at arbitrary angle distance.

Keywords – Source localization, Mobile users, Stochastic radiation, Correlation matrix, Neural networks.

I. INTRODUCTION

Suppression of negative interference impact at the signal reception terminal is one of important tasks to fulfill in the design of modern wireless communication systems. Spatial signal filtering performed by an antenna array and adaptive beamforming algorithms for optimization of radiation pattern of antenna array contribute to this suppression. These techniques are based on a direction-of-arrival (DOA) estimation and spatial localization of numerous sources of electromagnetic (EM) interference of either deterministic or stochastic radiation nature.

There are a number of algorithms in literature developed to deal with the DOA estimation problem. They are mostly based on processing of spatial covariance matrix of received signals by antenna elements. One of these techniques is the subspace-based MUSIC (MULTiple SIGNAL Classification) method, best known for its super-resolution capabilities [1]. MUSIC is able to provide accurate DOA estimation but at the expense of high computational complexity due to demanding spectral search procedure. Artificial neural networks (ANNs) [2] could represent an alternative faster approach to the computationally intensive super-resolution DOA algorithms performing basic mathematical operations and calculating

¹Zoran Stankovic, Nebojsa Doncov and Bratislav Milovanovic are with the Faculty of Electrical Engineering, University of Nis, 18000 Nis, Serbia, E-mails: [zoran.stankovic, nebojsa.doncov, bratislav.milovanovic]@elfak.ni.ac.rs.

²Ivan Milovanovic is with the Singidunum University, DLS Center, 18000 Nis, E-mail: ivanshix@gmail.com.

³Marija Stoilkovic is with the Innovation Centre of Advanced Technology, Blvd. Nikole Tesle 61/5, 18000 Nis, E-mail: marija.stoilkovic@icnt.rs.

elementary functions.

This ability qualifies them as very suitable for determining of angular positions of source signals [3]. In [4] a novel approach combining MLP (Multi-Layer Perceptron) and RBF (Radial Basis Function) ANNs is proposed for DOA estimation in order to detect the presence of deterministic narrow-band EM source and determine its angular coordinates (azimuth and elevation). In [5,6], an ANN approach, realized by MLP neural model, has been presented to provide a high-resolution DOA estimation. However, it was able to provide azimuth position of only few stochastic narrow-band EM sources in far-field.

Neural model for an efficient one-dimensional (1D) DOA estimation of stochastic EM sources, presented in this paper, represents an extension of previously developed models in [5,6] as it is able to provide a solution for cases when there is an arbitrary number of stochastic sources in far-field mutually positioned at fixed angle distance or where there are up to two stochastic sources placed at arbitrary angle distance. Neural model is realized again using MLP ANNs. Its training is based on the correlation matrix of received signals, obtained combining the Green function for electric field in far-field and correlation matrix of feed currents representing stochastic sources. Successfully trained neural model is able to provide accurate and fast DOA of incoming EM signal and determine azimuth coordinates of multiple sources making the model convenient for real-time application.

II. STOCHASTIC SOURCE RADIATION MODEL

We represent a radiation of stochastic source in far-field by linear uniform antenna array with N elements at the mutual distance $d = \lambda/2$ (Fig.1). In this radiation model representing stochastic source, antenna elements feed currents (defined by vector $\mathbf{I}=[I_1, I_2, \dots, I_N]$) are in general mutually correlated. The level of their correlation can be defined by correlation matrix, $\mathbf{c}^I(\omega)$, describing stochastic nature of antenna array radiation [6]:

$$\mathbf{c}^I(\omega) = \lim_{T \rightarrow \infty} \frac{1}{2T} [\mathbf{I}(\omega)\mathbf{I}(\omega)^H] \quad (1)$$

Using Green function to map the domain of radiation source currents into the domain of electric field in far-field, vector \mathbf{M} can be defined as:

$$\mathbf{M}(\theta, \varphi) = jz_0 \frac{F(\theta, \varphi)}{2\pi r_c} [e^{jkr_1} \quad e^{jkr_2} \quad \dots \quad e^{jkr_N}] \quad (2)$$

where z_0 is free-space impedance, $F(\theta, \varphi)$ is the radiation pattern of antenna array elements, r_c is the distance of far-

field point to the centre of array, k is the phase constant ($k=2\pi/\lambda$) and r_1, r_2, \dots, r_N are the distances of far-field point from the first to the N -th element of antenna array. The electric field intensity in sampling point in far-field (sampling point is at the angles θ and φ in azimuth and elevation planes, respectively, defined by the first element of antenna array) can be calculated as:

$$E(\theta, \varphi) = \mathbf{M}(\theta, \varphi) \mathbf{I} \quad (3)$$

If M points are simultaneously observed in far-field, then more general notation can be used to describe the antenna array elements distance from particular points in far-field. In this notation $r_{i,m}$ represents the distance between i -th element ($1 \leq i \leq N$) in the antenna array and m -th point in the far-field ($1 \leq m \leq M$) (see Fig. 1).

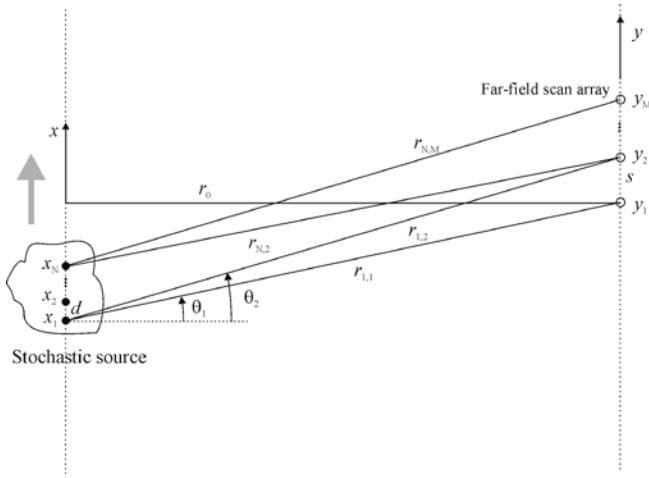


Fig. 1. The position of stochastic source in azimuth plane with respect to the location of EM field sampling points in the far-field scan area.

M points (Y_1, Y_2, \dots, Y_M) in far-field, in which electric field levels are sampled, are at the azimuth and elevation plane angles $(\theta_1, \varphi_1), (\theta_2, \varphi_2), \dots, (\theta_M, \varphi_M)$, determined by the first element of antenna array. The correlation matrix of signals received in these sampling points can be obtained from the correlation matrix of antenna elements feed currents as:

$$\mathbf{C}_E[i, j] = \mathbf{M}(\theta_i, \varphi_i) \mathbf{c}^i \mathbf{M}(\theta_j, \varphi_j)^H \quad (4)$$

$$i = 1, \dots, M \quad j = 1, \dots, M$$

For the case of several stochastic sources in azimuth plane, the radiation of each source can be represented by one antenna array with N elements as previously shown. The level of EM field in far-field sampling point, as well as the elements of correlation matrix are determined by the superposition of radiation from all sources. In accordance with this, when the number of stochastic sources is S , vector \mathbf{M} has a form :

$$\mathbf{M}(\theta, \varphi) = jz_0 \frac{F(\theta, \varphi)}{2\pi r_c} \cdot \begin{bmatrix} e^{jkr_1^{(1)}} & \dots & e^{jkr_N^{(1)}} & e^{jkr_1^{(2)}} & \dots & e^{jkr_N^{(2)}} & \dots & e^{jkr_1^{(S)}} & \dots & e^{jkr_N^{(S)}} \end{bmatrix} \quad (5)$$

where $r_i^{(j)}$ is the distance between i -th element in antenna array, representing j -th stochastic source, and the sampling point in far-field, while the feed currents vector is:

$$\mathbf{I} = [I_1^{(1)} \dots I_N^{(1)} I_1^{(2)} \dots I_N^{(2)} \dots I_1^{(S)} \dots I_N^{(S)}] \quad (6)$$

where $I_i^{(j)}$ is the feed current of i -th element in antenna array representing j -th stochastic source.

Combining Eqs.(3) and (4) with Eqs. (5) and (6) that correspond to the case of several stochastic sources, it is possible to determine the intensity of EM field in the sampling point in far-field, as well as the elements of correlation matrix \mathbf{C}_E . It should be also pointed out that in the case of unknown level of correlation between antenna elements feed currents, its correlation matrix can be obtained by measuring the intensity of electric field in the sampling points in near-field.

III. NEURAL NETWORK MODEL

The neural model based on MLP ANN is developed with the purpose to perform the mapping from the space of signals described by correlation matrix \mathbf{C}_E to the space of DOA in azimuth

$$\boldsymbol{\theta} = f(\mathbf{C}_E) \quad (7)$$

where $\boldsymbol{\theta}$ is azimuthal angles vector of stochastic sources, $\boldsymbol{\theta} = [\theta_1, \theta_2, \dots, \theta_S]$ and S is number of stochastic sources. In the observed case elevation coordinates of radiation sources is neglected. The architecture of developed neural model is shown in Fig.2. Its MLP network can be described by the following function:

$$\mathbf{y}_l = F(\mathbf{w}_l \mathbf{y}_{l-1} + \mathbf{b}_l) \quad l = 1, 2 \quad (8)$$

where \mathbf{y}_{l-1} vector represents the output of $(l-1)$ -th hidden layer, \mathbf{w}_l is a connection weight matrix among $(l-1)$ -th and l -th hidden layer neurons and \mathbf{b}_l is a vector containing biases of l -th hidden layer neurons. F is the activation function of neurons in hidden layers and in this case it is a hyperbolic tangent sigmoid transfer function:

$$F(u) = \frac{e^u - e^{-u}}{e^u + e^{-u}} \quad (9)$$

In order to perform mapping it is sufficient to take only the first column of correlation matrix and therefore $\mathbf{y}_0 = [Re\{\mathbf{C}_E[1,1]\} \quad Im\{\mathbf{C}_E[1,1]\}, \dots, Re\{\mathbf{C}_E[1,M]\} \quad Im\{\mathbf{C}_E[1,M]\}]$. Also, $\boldsymbol{\theta}$ is given as $\boldsymbol{\theta} = \mathbf{w}_3 \mathbf{y}_2$ where \mathbf{w}_3 is a connection weight matrix between neurons of last hidden layer and neurons in output layer. The optimization of weight matrices and biases values during the training allows ANN to approximate the mapping with the desired accuracy.

IV. MODELING RESULTS

The training of ANNs is conducted for the case of four equidistant sampling points in far-field scan area, at the mutual distance $d = \lambda/2$, located 100 m from stochastic

sources (Table I). Angular position in the azimuth plane of two mobile users ($S=2$) at arbitrary angle distance has to be determined. By using Eq.(4) and (5) for $N=4$ and $M=4$, 861 and 276 uniformly distributed samples are generated for training and testing, respectively, in the range $[-80^\circ 80^\circ]$ at the working frequency of 7.5 GHz. Each stochastic source can be described by antenna array with four vertical dipole ($N=4$). The feed currents of two dipoles are mutually uncorrelated so that \mathbf{e}^l is the unit diagonal matrix. Levenberg-Marquardt method with prescribed accuracy of 10^{-4} is used as a training algorithm. The testing results for six MLP models with the lowest average case error are shown in Table II, and MLP2-16-8 is chosen as representative neural model. The neural model simulation of testing samples set shows a very good agreement between the output values of neural model and referent azimuth values for all sources (Fig.3, Fig.4 and Fig.5). In addition, a good agreement with results obtained by MUSIC algorithm can be observed.

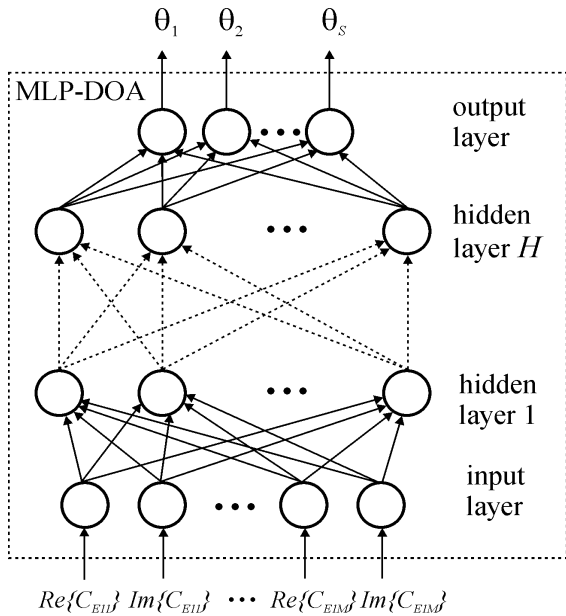


Fig. 2. Architecture of MLP neural model for DOA estimation of stochastic EM source signal in azimuth plane

TABLE I
THE VALUES OF ANTENNA ARRAY PARAMETER WHICH USED IN SAMPLING PROCESS

Frequency	$f = 7.5 \text{ GHz}$
Number of sources	$S = 2$
Number of antenna array elements per one source	$N = 4$
Sampling points distance from source trajectory	$r_0 = 100 \text{ m}$
Number of sampling points	$M = 4$
Mutual distance of the sampling points	$s = \lambda/2 (0.02 \text{ m})$

TABLE II
TESTING RESULTS FOR SIX MLP NEURAL MODELS WITH THE BEST AVERAGE ERRORS STATISTICS

MLP model	WCE [%]	ACE [%]
MLP2-16-8	1.81	0.42
MLP2-14-14	2.26	0.42
MLP2-18-14	2.67	0.39
MLP2-20-10	2.71	0.38
MLP2-16-16	3.27	0.39
MLP2-16-11	3.76	0.41

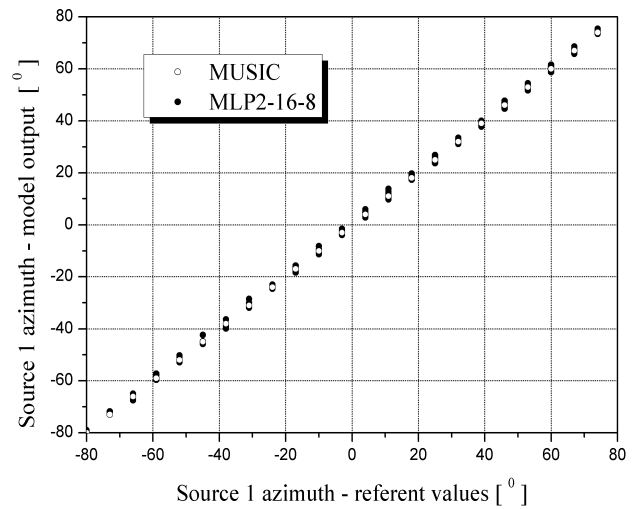


Fig. 3. Comparison of MLP2-16-8 model output 1 (azimuth of source 1) with MUSIC and referent azimuth values

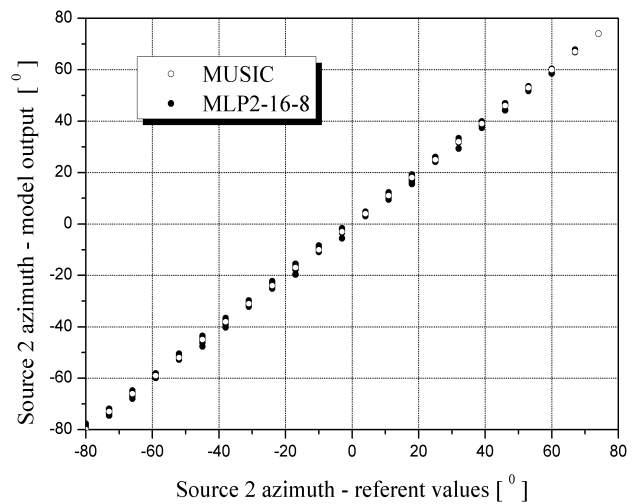


Fig. 4. Comparison of MLP2-16-4 model output 2 (azimuth of source 2) with MUSIC and referent azimuth values

V. CONCLUSION

The neural network-based approach for DOA estimation of electromagnetic radiation of stochastic sources is presented in the paper. Only the first column of correlation matrix obtained by simple signal sampling in far-field scan area by linear uniform antenna array is used as an input of developed neural model. Neural model ability to accurately and efficiently determine the location of the stochastic source is illustrated on one example. As proposed neural model avoids intensive and time-consuming numerical calculations it is more suitable than conventional approaches for real-time applications. At the moment, neural model is capable to determine the location in azimuth plane for up to two stochastic sources placed at arbitrary angle distance. Future research will be focused to the more general DOA estimation of multiple stochastic sources at arbitrary angular distance.

ACKNOWLEDGEMENT

This work has been supported by the Ministry for Education, Science and Technological Development of Serbia, projects number TR32052 and TR32054.

REFERENCES

- [1] R. Schmidt, "Multiple emitter location and signal parameter estimation", *IEEE Transactions on Antennas and Propagation*, vol. 34, no. 3, pp. 276-28, 1986.
- [2] S. Haykin, *Neural Networks*, New York, IEEE, 1994.
- [3] A. H. El Zooghby, C. G. Christodoulou, M. Georgiopoulos, "A neural network based smart antenna for multiple source tracking", *IEEE Transactions on Antennas and Propagation*, Vol. 48, no. 5, pp. 768 – 776, 2000.
- [4] M. Agatonović, Z. Stanković, N. Dončov, L. Sit, B. Milovanović, T. Zwick, "Application of artificial neural networks for efficient high-resolution 2D DOA estimation", *Radioengineering*, Vol. 21, No. 4, pp. 1178-1186, 2012.
- [5] Z. Stanković, N. Dončov, J. Russer, T. Asenov and B. Milovanović, "Efficient DOA estimation of impinging stochastic EM signal using neural networks", *Proceedings of the International Conference on Electromagnetics in Advanced Applications* (15th Edition including EMS), ICEAA 2013, Torino, Italy, September 9-13, 2013, pp.575-578, 2013.
- [6] Z. Stanković, N. Dončov, J. Russer, I. Milovanović, M. Agatonović, "Neural networks based DOA estimation of multiple stochastic narrow-band EM sources", *Proceedings of the 11th IEEE International Conference on Telecommunications in Modern Satellite, Cable and Broadcasting Services, TELSIKS 2013*, Niš, Serbia 16-19 October, Vol.2, pp.526-529, 2013.
- [7] J.A. Russer, T. Asenov and P. Russer, "Sampling of stochastic electromagnetic fields", *IEEE MTT-S International Microwave Symposium Digest*, Montreal, Canada, pp. 1-3, 2012.

Design of a Printed Antenna Array in Rectangular Corner Reflector with Cosecant Square-Shaped Beam Pattern

Marija Milijić¹, Aleksandar Nešić² and Bratislav Milovanović³

Abstract – The preliminary design and simulation results of printed antenna array with cosecant square-shaped beam pattern, using Orchard Elliott’s and genetic algorithm methods, has been presented. The four wideband radiating elements operating at a second resonance are axially placed. The corner reflector is at distance $\lambda_0/4$ from antenna array providing increases in both antenna parameters: gain and side lobe suppression. At the centre frequency of 10 GHz the obtained simulation results clearly show expected advantages of presented antenna.

Keywords – Printed antenna array, Cosecant square radiation pattern, Side lobe suppression.

I. INTRODUCTION

The crucial part of every radar system is antenna. Its main function is to transmit energy to space with the required pattern and to receive intercepted signal by reflecting object. Thus radar antenna enables detection and location of objects.

The coverage of a simple fan beam is usually inadequate for targets at high altitudes close to the radar [1]. The simple fan-beam antenna radiates very little of its energy in this direction. However, there are a few techniques for modifying the antenna pattern to radiate more energy at higher angles. One of them is employing a fan beam with a shape proportional to the square of the cosecant of the elevation angle. Cosecant-squared antenna produces a constant echo-signal power for a target flying at constant altitude, if certain assumptions are satisfied. Search radars generally employ this type of pattern.

There are many algorithms and methods for design cosecant-squared antennas [2-4]. Although the expected radiation pattern is achievable using adequate feeding coefficients for array elements [3], it is recommended to improve the others antenna parameters as gain, side lobe suppression (SLS), bandwidth ... [4].

Cosecant-squared antennas are widely used for radars in lower microwave frequency, especially in L frequency range. This paper will present the antenna array in X range around 10

¹Marija Milijić is with the Faculty of Electronic Engineering, University of Nis, Aleksandra Medvedeva 14, 18000 Nis, Serbia, E-mail: marija.milijic@elfak.ni.ac.yu

²Aleksandar Nešić is with "IMTEL-komunikacije" a.d., Bulevar Mihaila Pupina 165b, 11070 Novi Beograd, Serbia, E-mail: aca@insimtel.com

³Bratislav Milovanović is with the Faculty of Electronic Engineering, University of Nis, Aleksandra Medvedeva 14, 18000 Nis, Serbia, E-mail: bratislav.milovanovic@elfak.ni.ac.yu

GHz. In this range, the functional antenna model will be realized to economize material and space. Certainly, the presented concept can be used in every UHF and microwave frequency ranges, relevant for Cosecant-squared antennas, using dimensions scaling.

II. PENTAGONAL PRINTED DIPOLES

Presented cosecant-squared antenna array is with printed dipoles (Fig. 1) of pentagonal shape [5-7] (one half of them on one side and another half on the opposite side of the substrate).

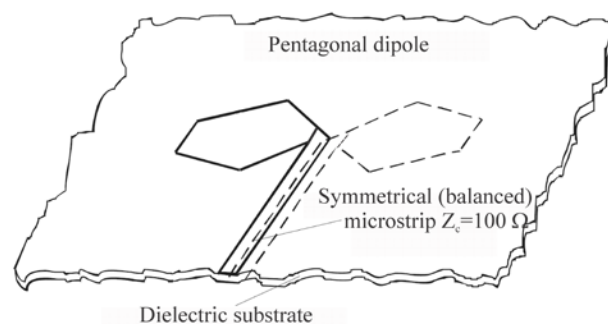


Fig. 1 Pentagonal dipole

They are fed by a symmetrical (balanced) microstrip line. The presented antenna array as well as its radiating element is with rectangular corner reflector at distance $\lambda_0/4$ from antenna array. Differently from conventional dipoles that operate on the first resonance, these dipoles operate on the second resonance [5-7]. The dipole’s impedance varies with frequency very slow (Fig. 2).

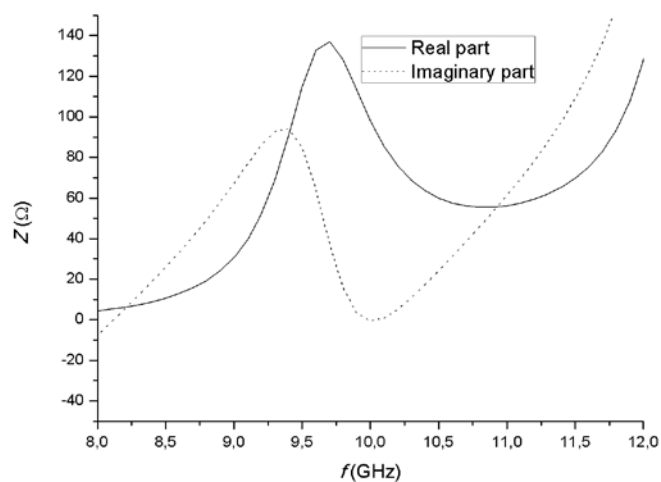


Fig. 2. Real and imaginary part of pentagonal dipole’s impedance

Modification of pentagonal dipole's dimensions enables us to change impedance on the second resonance in a relatively wide range (Fig. 2). In our case, we have adjusted dimensions of pentagonal dipoles in order to obtain dipole impedance of $Z_d=100\Omega$ at the centre frequency (10 GHz) taking into consideration the reflector influence and symmetrical microstrip feeding line of impedance $Z_c=Z_d$.

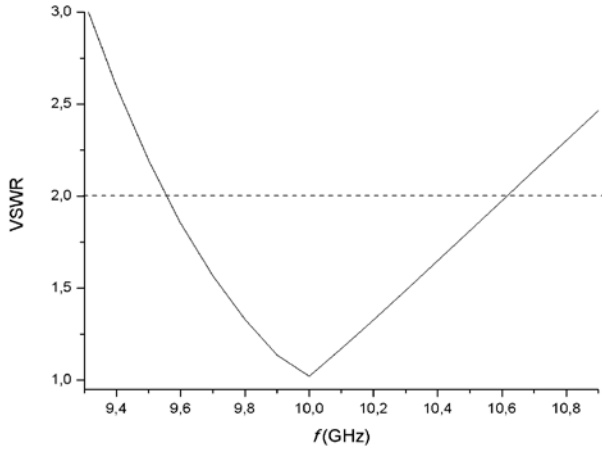


Fig. 3. VSWR of pentagonal dipole

The Fig. 3 presents Voltage Standing Wave Ratio (VSWR) of pentagonal dipole. VSWR is below 2 in the range from 9.6 GHz to 10.6 GHz that is 10% of central frequency. It is certain that the frequency range with VSWR below 2 will be wide if the dielectric substrate is with less height.

III. ANTENNA ARRAY WITH COSECANT SQUARED RADIATION PATTERN

Cosecant function of angle ϕ is defined as:

$$\text{csc } \phi = \frac{1}{\sin \phi}. \quad (1)$$

In the cosecant-squared antenna, the gain as a function of elevation angle is given by [1]:

$$G(\phi) = G(\phi_0) \frac{\text{csc}^2 \phi}{\text{csc}^2 \phi_0} \quad \text{for } \phi_0 < \phi < \phi_m \quad (2)$$

where $G(\phi)$ is the gain at elevation angle ϕ . ϕ_0 and ϕ_m are angular limits between which beam follows cosecant-squared shape.

Antennas with cosecant squared pattern are special designed for the airborne search radar observing ground targets as well as ground-based radars observing aircrafts targets. From $\phi=0$ to $\phi=\phi_0$, the antenna pattern is similar to a normal antenna pattern, but from $\phi=\phi_0$ to $\phi=\phi_m$, the antenna gain varies as $\text{csc}^2 \phi$. Ideally, the upper limit ϕ_0 should be 90° , but it is always much less than this with a single antenna because a practical difficulties. The cosecant-squared pattern may be generated with an array-type antenna.

The presented antenna array consists of four parts (Fig. 4): (1) the axial array of four radiating elements, (2) feeding network and (3) bal-un – part (1), (2) and (3) are printed on the same dielectric substrate and (4) rectangular corner reflector.

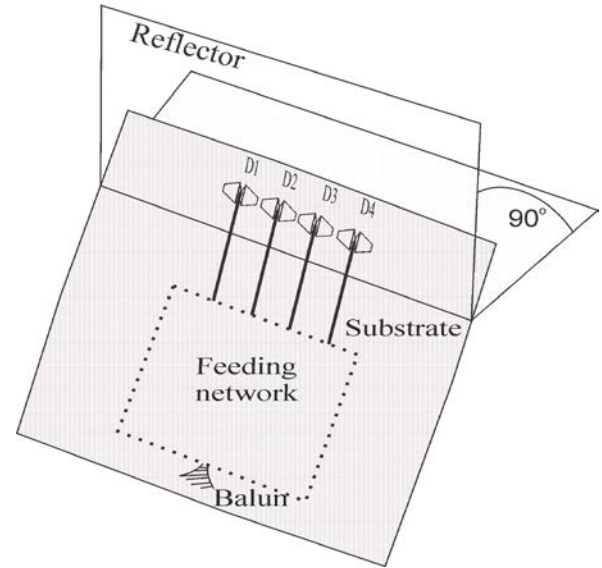


Fig. 4. Antenna array with cosecant squared radiation pattern

Along axis there is an array of four axially placed radiating elements. The dipoles are axially placed decreasing their mutual impedance. Radiating elements are printed on a dielectric substrate of 0.508 mm thickness and $\epsilon_r=2.17$. Symmetrical (balanced) microstrip line is used as a feeding structure, because dipoles are electrically symmetrical elements. Distance between the dipoles is $0.8\lambda_0=24$ mm (at the centre frequency).

The normalized amplitude, u_i and phase shifts ϕ_i , $i=1,2,3,4$ for four radiating elements are shown in Table I [2,3].

TABLE I
THE DISTRIBUTION COEFFICIENTS FOR ANTENNA ARRAY WITH COSECANT SQUARED RADIATION PATTERN

Dipoles number	1	2	3	4
Normalized amplitude u_i	0.4038	0.567	1	0.725
Phase shifts ϕ_i [°]	0	14	0	-36

IV. SIMULATION RESULTS

The simulation model [8] of antennas with cosecant squared pattern is shown in Fig. 5.

The gain is 17 dBi that is significantly improved than in antenna array with U-slot rectangular patch element [3] where gain is around 10 dBi. Further, the SLS is also better and it is equal 19.35 dB that is greater than 13 dB corresponding SLS from antenna array with U-slot rectangular patch element [3].

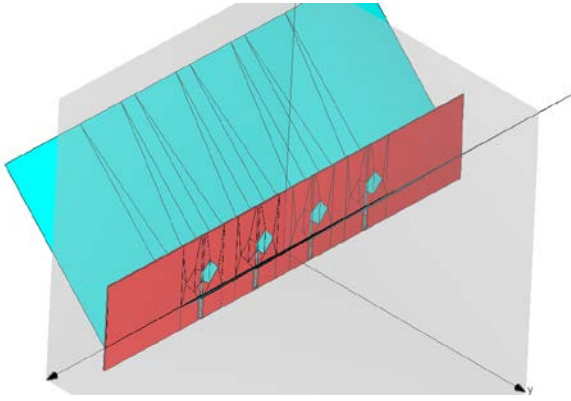


Fig. 5. The simulation model of antennas with cosecant squared pattern

The most important is that radiation pattern in E-plane does not vary a lot from theoretically simulated cosecant square radiation pattern for a four-element linear array [3] (Fig. 6).

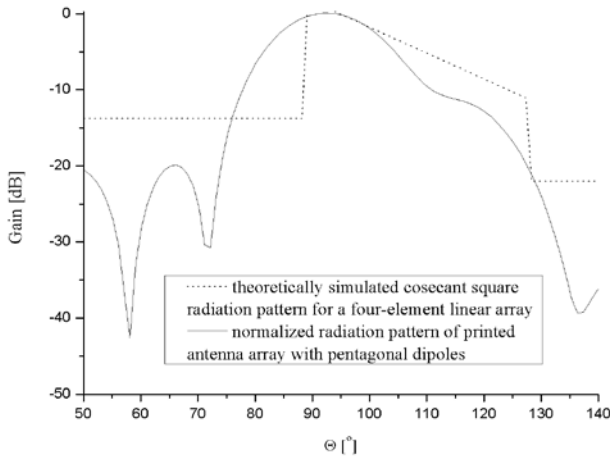


Fig. 6. The normalized radiation pattern of printed antenna array with pentagonal dipoles versus theoretically simulated cosecant square radiation pattern

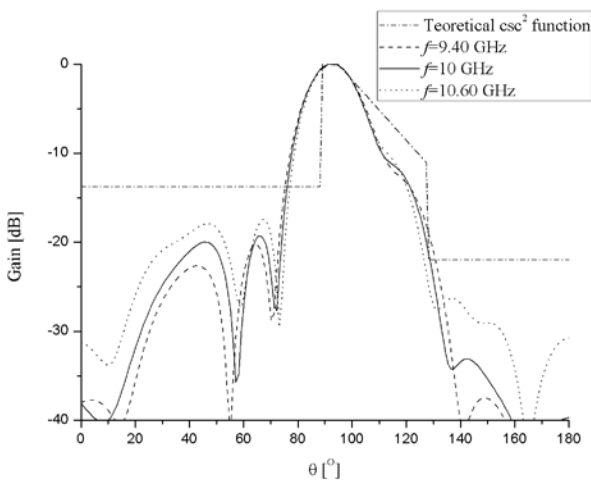


Fig. 7. The normalized radiation pattern of printed antenna array with cosecant squared pattern at 9.4 GHz, 10 GHz and 10.6 GHz

The Fig. 7 presents the normalized radiation pattern of proposed antenna array in wide frequency range. Considering results shown in Fig. 7, it can conclude that the antenna array with csc^2 radiation pattern can be applied in frequency range 0.6 GHz from the central frequency of 10 GHz.

Also, the radiation pattern of presented antenna array in H-plane depends considerably on parameters of corner reflector: its angle, its dimensions and the distance of radiating elements from its apex. For rectangular corner reflector that is at distance $\lambda_0/4$ from antenna array, the radiation pattern in H-plane is shown in Fig. 8. The adjusting the parameters of corner reflector, the wide frequency range of antenna array can be obtained.

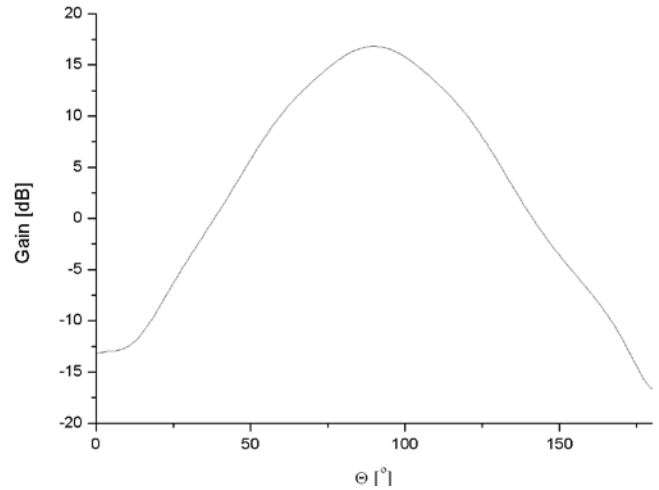


Fig. 8. The radiation pattern in H-plane of antenna array with rectangular corner reflector's apex at distance $\lambda_0/4$ from antenna array

V. CONCLUSION

The paper presents the printed antenna array with four radiating elements in corner reflector whose radiation pattern in E-plane has shape of cosecant square function. The pentagonal dipoles fed by a symmetrical (balanced) microstrip line are used as radiating elements. They have a few advantages over recently used radiating elements of antenna with cosecant square-shaped radiation pattern. Besides their simple structure, they have significantly wide frequency range (for $VSWR < 2$, $BW = 10\%$).

The simulation model consists of dipoles fed by generators with distribution coefficients calculated by Orchard Elliot's and genetic algorithm methods. The obtained radiation pattern very little varies from theoretical radiation pattern. Further, it is possible to adjust the of antenna beam width in H-plane changing parameters of corner reflector. Antenna gain is 17 dBi. The central frequency of simulation models is 10 GHz. The further research will be modeling feeding network that enables required distribution, in the same dielectric substrate as antenna array, as well as complete realization of antenna.

ACKNOWLEDGEMENT

This work was supported by the Ministry of Education, Science and Technological Development of Republic Serbia within the projects No. III44009.

REFERENCES

- [1] M. Skolnik, *Introduction to Radar Systems*, Tokyo, McGraw-Hill, 1981.
- [2] H.J. Orchard, R.S. Elliott, and G.J. Stern, Optimizing the synthesis of shaped beam antenna patterns, *IEE Proc H* 132 (1985), 63–69.
- [3] A. Kedar, P. N. S. Kutiyal, M. Garg, and U. K. Revankar, “Wide band low profile linear microstrip antenna array with cosecant square-shaped beam pattern”, *Microwave and optical technology letters*, vol. 49, no. 4, pp. 963-965, April 2007.
- [4] O. Yurduseven, O. Yurduseven, “Compact Parabolic Reflector Antenna Design with Cosecant-Squared Radiation Pattern”, *Microwaves, Radar and Remote Sensing Symposium*, pp. 382 – 385, Kiev, Ukraine, August 25 – 27, 2011.
- [5] A. Nestic, I. Radnovic, “New Type of Millimeter Wave Antenna with High Gain and High Side Lobe Suppression”, *Optoelectronics and Advanced Materials – Rapid Communications* Vol. 3, No.10, October 2009, pp. 1060-1064.
- [6] A. Nestic, Z. Micic, S. Jovanovic, I. Radnovic, D. Nestic, “Millimeter Wave Printed Antenna Arrays for Covering Various Sector Width”, *IEEE Antennas and Propagation Magazine*, Vol.49, No.1, Feb. 2007, pp. 113-118.
- [7] A. Nešić, I. Radnović, Z. Mičić, S. Jovanović, “Side Lobe Suppression of Printed Antenna Arrays for Integration with Microwave Circuits”, *Microwave Journal*, Vol. 53 No. 10, October 2010, pp. 72-80.
- [8] WIPL-D Pro v10.0, WIPL-D Team.

Electromagnetic Modeling in Combination with Wave Digital Approach for Efficient Analysis of Microstrip Bandpass Filters with a Dual-Passband Response

Biljana P. Stošić and Nebojša S. Dončov

Abstract – In this paper, an efficient technique, combining an electromagnetic (EM) modeling with a wave digital approach, is used for analysis of a 2.4/5.2 GHz dual-band microstrip bandpass filter (BPF). The studied BPF with dual passbands is composed of two parallel coupled microstrip lines and stepped-impedance-resonator. Step in width discontinuities and coupled-line sections, present in this filter layout, make analysis of this filter computationally very demanding and run-time consuming if only EM modeling is used. The described technique first uses a full-wave EM approach to generate equivalent circuit parameters of mentioned discontinuities from its S -parameters. The wave digital models of the equivalent circuits are then developed and incorporated into an equivalent wave digital network efficiently representing the complete microstrip structure. Three cases of BPF with different parallel coupled line dimension (varied dual-passband widths), are considered here in order to validate the presented combined wave digital/EM technique.

Keywords – Bandpass filter, dual-passbands, wave digital approach, electromagnetic modeling.

I. INTRODUCTION

Nowadays, the trend is to take advantage of the accessible and powerful full-wave electromagnetic (EM) simulators, which can provide numerical calculation of the structure characteristics. The circuit designers use these EM modeling tools to simulate and test their designs before major expenses are committed to circuit construction and experimental verification. The numerical calculation of the structure characteristics must be fast and of high accuracy because the realistic and real-time simulations are essential for proper and timely design.

Filters are important and essential components in modern wireless and mobile communication systems for several decades [1-3]. In a case of microstrip circuit design one can commonly encounter many different types of discontinuities in the filter topology such as steps, open-ends, and gaps [4]. Conventional modeling of discontinuities by full-wave numerical techniques, especially differential ones based on space and time discretization, can be computationally very demanding and time-consuming. It usually requires a very fine numerical mesh to accurately describe EM field distribution around discontinuities and calculate the real

characteristics of the complete circuit. Therefore, efficient discontinuity representation in the form of equivalent circuit suitable to be easily integrated into the otherwise coarse numerical mesh is of key importance for accurate and fast circuit simulation by full-wave EM modeling tools.

In recent years a wave digital approach has become a useful tool for efficient modeling and analysis of different physical systems. The entry point, for any study of numerical methods based on wave and scattering ideas, must necessarily be a review of wave digital filters (WDFs) [5-6]. The term “Wave digital filters” was first reported in the early 1970s by A. Fettweis [5]. He proposed a class of digital filters of particular interest. Some numerical simulation techniques, as well as WDF theory are listed in [7-8].

A novel technique combining one-dimensional wave digital approach [8] with an equivalent discontinuity model, obtained from a full-wave EM tool, has been presented in [9-11] to accurately and efficiently describe microstrip structures with different discontinuities but only of one type. In the proposed technique, the presence of discontinuity has been described by appropriate equivalent circuit, derived from scattering matrix calculated by full-wave EM modeling. These equivalent circuits are then represented by their corresponding wave digital models in order to be further incorporated into an equivalent wave digital network (WDN) used to model the complete structure with considered discontinuity. This combined approach has showed a great potential in terms of computing time compared to the full-wave EM modeling of complete circuits and in terms of accuracy compared to existing discontinuity closed-form expressions formulations. Also, WDF concept, consisting of network with the wave digital elements such as unit delay elements and adaptors, is therefore very suitable for easy and efficient integration of equivalent circuits of discontinuities. In addition, as it deals with signal flow graphs, it is much closer to the software implementation of the considered EM problem model compared to some classical full-wave EM modeling techniques.

The efficient modeling and analysis of different types of microstrip filters (low-pass and band-pass) with step discontinuities have been done in [9-10]. An equivalent circuit is generated in the form of lossless transmission line capable to account for different line width ratio cases for which errors, when existing closed-form expressions are used [12], are more than 10%.

The conventional design method of the parallel-coupled bandpass filter (BPF) that uses several quarter-wavelength ($\lambda/4$) coupled-line sections was well documented in [1]. The parallel-coupled BPF consisting of series of half-wavelength line resonators that are positioned so that

Biljana P. Stošić and Nebojša S. Dončov are with University of Niš, Faculty of Electronic Engineering, Department of Telecommunications, Aleksandra Medvedeva 14, P.O. Box 73, 18000 Niš, Serbia, E-mails: biljana.stosic@elfak.ni.ac.rs, nebojsa.doncov@elfak.ni.ac.rs.

adjacent resonators are parallel to each other along one-half of their lengths has been considered in [13]. Equivalent circuits of these gaps are represented in the form of admittance (J)-inverters and half-wavelength resonators.

Admittance inverters ($J, -90^\circ$) are used to transform a filter layout into an equivalent circuit which is modeled and analyzed by use of wave digital approach. The resulting wave digital network is represented as a cascade connection of frequency-independent two-port network model of admittance inverter based on parallel adaptor network and frequency-dependent two-port unit elements.

This paper presents the application of combined EM modeling/wave digital filter technique for an efficient analysis of a dual-band microstrip BPF whose design is presented in [15]. A 2.4/5.2 GHz dual-band microstrip BPF is composed of two parallel coupled microstrip lines (PCML) and one stepped-impedance-resonator (SIR), so in its layout it has two different types of discontinuities: step discontinuity and gap discontinuity. Each discontinuity type is represented by its corresponding wave digital model as described in [9] and [11], respectively. Three cases of BPF with different parallel coupled line dimension (varied dual-passband widths), are considered here in order to validate the presented technique.

II. MODELING APPROACH FOR DUAL-BAND BPF

A. PCML Model

In order to model coupled-line sections, an equivalent circuit described in [11], is used. According to this, a single coupled-line section from Fig. 1a is approximately modeled by the equivalent circuit consisting of one J -inverter and two $\lambda/4$ resonators shown in Fig. 1b. It is done by calculating the $ABCD$ matrix of the coupled-line section and showing that it is equal to the $ABCD$ matrix of the equivalent circuit for electrical length $\theta = \pi/2$.

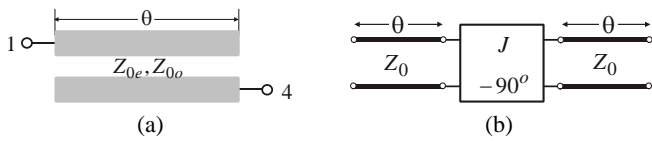


Fig. 1. (a) A single coupled-line section (two coupled $\lambda/4$ open lines), (b) Equivalent circuit of the coupled line section

The admittance inverter constant J is determined by

$$J = \frac{Y_0}{2} \cdot (Z_{0e} - Z_{0o}), \quad (1)$$

where Z_{0e} and Z_{0o} are even- and odd-mode characteristic impedances of a single coupled-line section of electrical length θ , and Y_0 is its characteristic admittance.

Synthesis of wave digital network model of admittance inverter with characteristic impedance $1/J$ that transforms its load admittance by -90° is described in [13]. Obtained

model, based on two-port parallel adaptor network, allows for an easy integration into equivalent wave digital network.

Wave digital networks of admittance inverters that transform their load admittances J by $+90^\circ$ assigned as $(J, +90^\circ)$ and by -90° assigned as $(J, -90^\circ)$, are described in details and developed in [14] based on scattering parameter formalism and two-port networks of parallel or series adaptors.

B. Dual-band BPF Model

Development of an equivalent wave digital model of a dual-band BPF from [15] is shown in Fig. 2. Fig. 2a shows the physical layout of the studied BPF with dual passbands composed of two PCMLs and one SIR. A network representation with several cascaded two-port subnetworks of half a symmetrical structure is shown in Fig. 2b. The next step in development of an equivalence is to replace each PCML (Fig. 1a), assigned as C -line in Fig. 2b, with its equivalent circuit shown in Fig. 1b, as well as subnetworks corresponding to SIR with uniform transmission lines. A half of the resultant equivalent circuit is shown in Fig. 2c. It contains J -inverters and uniform transmission lines. Final step is to form wave digital network given in Fig. 2d from resultant circuit given in Fig. 2c. To do this, blocks of the J -inverters (ADP-Inv) are modeled by their wave digital models based on two-port parallel adaptor network [11]. Each of the blocks corresponding to uniform transmission lines is modeled by several cascaded unit elements (UEs) [8]. The resultant wave digital network is then analyzed using earlier developed one-dimensional wave digital approach [8].

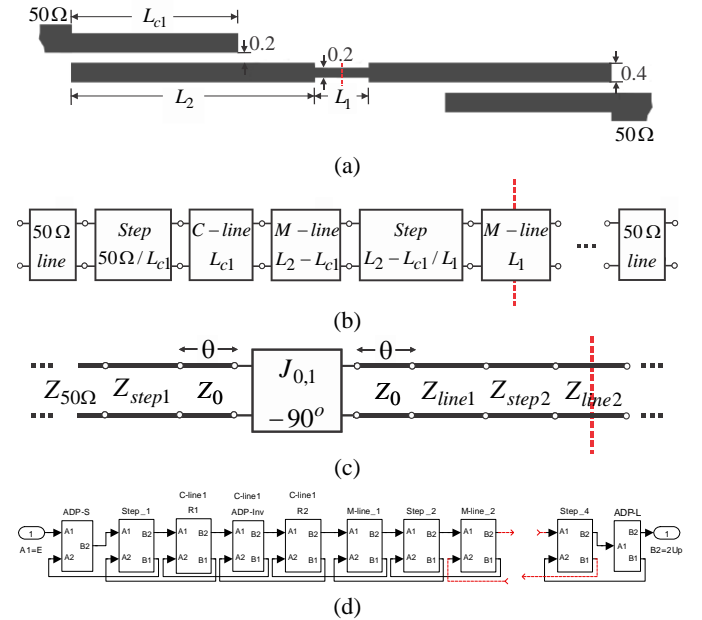


Fig. 2. Development of an equivalent wave digital network model for a dual-band BPF, (a) Physical layout of BPF (top view), (b) Network representation with cascaded subnetworks of half a symmetrical structure, (c) Resultant circuit using equivalent circuits for each subnetwork of half a symmetrical structure, (d) Wave digital network

III. ANALYSIS REMARKS

A BPF is designed in [15] on the substrate Rogers 6010, with a relative dielectric constant of 10.8, and thickness of 0.635 mm . The design parameter dimensions are chosen as following: $L_2 = 10.5\text{ mm}$ and $L_1 = 1.4\text{ mm}$. BPF with varied dual-passband widths obtained by varying length of coupled-line sections L_{c1} is analyzed here using the proposed combined technique.

A. PCML Characterization

Two-port PCML from Fig. 3, for three different physical lengths $L_{c1} = 9\text{ mm}$, $L_{c1} = 7.3\text{ mm}$ and $L_{c1} = 5.6\text{ mm}$, is characterized.

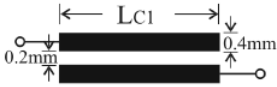


Fig. 3. Two-port PCML

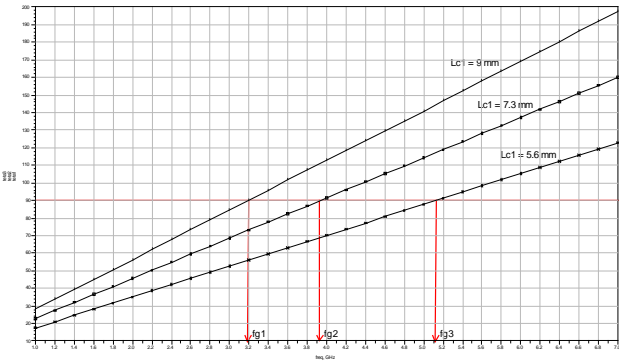


Fig. 4. Electrical line lengths for different L_{c1}

Fig. 4 illustrates the equivalent electrical line lengths versus frequency for different physical line lengths L_{c1} . These graphs are used to find frequencies on which these PCMLs are quarter-wavelength long. For PCML of physical length $L_{c1} = 9\text{ mm}$, the frequency is $f_{g1} = 3.2\text{ GHz}$, for PCML of $L_{c1} = 7.3\text{ mm}$ it is $f_{g2} = 3.925\text{ GHz}$, and for the third case of PCML of $L_{c1} = 5.6\text{ mm}$ it is $f_{g3} = 5.125\text{ GHz}$.

B. Simulink-based Model of Microstrip BPF Structure

In Figs. 5-9, Simulink-based blocks of the microstrip BPF (shown in Fig. 2a) are given. Individual blocks shown in Figs. 6-9 are putted together to represent BPF in block diagram form as shown in Fig. 5.

Each of the blocks in Fig. 5 represented by uniform transmission line (Step_1 to 4, M-line_1 to 3, C-line1 to 2) is modeled by several cascaded UEs. Simulink-based model of block represented by eight cascaded UEs is shown in Fig. 9.

Complete WDN is analyzed based on its Simulink model and MATLAB code.

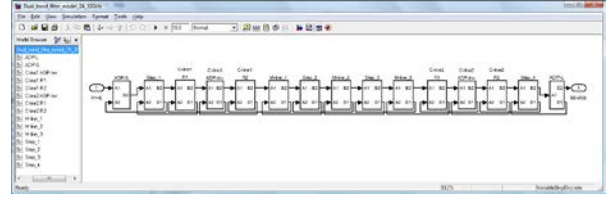


Fig. 5. Simulink-based WDN model of microstrip BPF structure

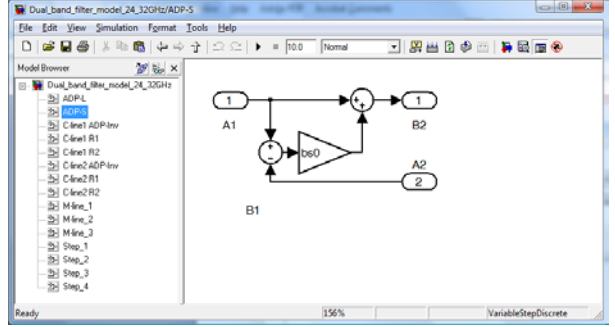


Fig. 6. Simulink-based model of two-port adaptor ADP-S

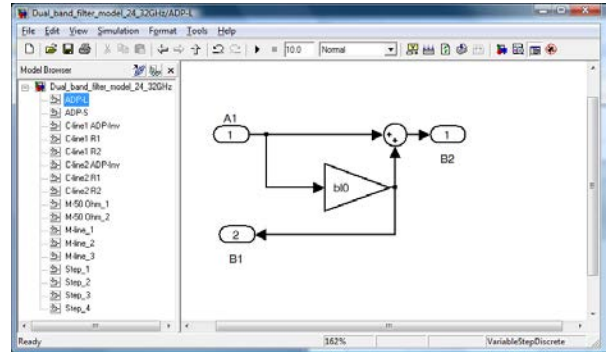


Fig. 7. Simulink-based model of two-port adaptor ADP-L

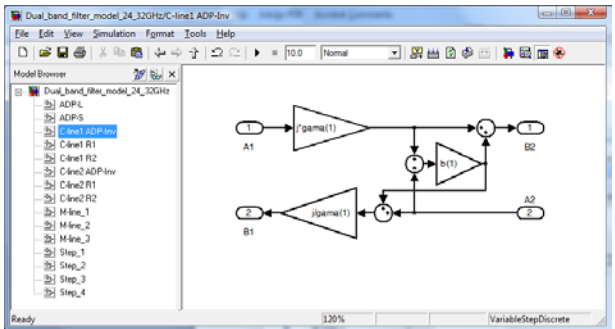


Fig. 8. Simulink-based model of two-port adaptor C-line1 ADP-Inv

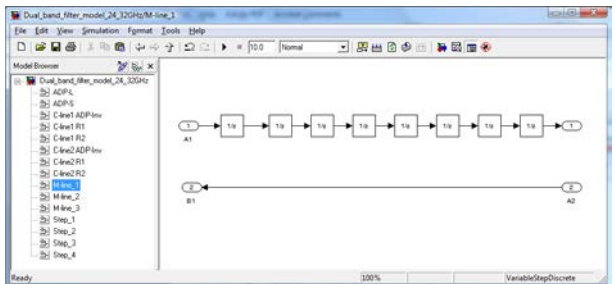


Fig. 9. Simulink-based model of block contains eight cascaded UEs

C. Modeling and Analysis Results

Layout of the structure under investigation shown in Fig. 2a contains two types of step discontinuity: symmetrical (composed of lines of lengths L_2 and L_1) and asymmetrical (composed of 50Ω -lines and lines of lengths L_{c1}). They are analyzed by use of EM tool in the frequency range (1-7) GHz, and S -parameters are obtained in Touchstone file format. Then, S -parameter data are taken to generate an equivalent model in the form of lossless transmission line. Equivalent model parameters characteristic impedance and delay are $Z_{cstep} = 128.9557\Omega$ and $T_{step} = 0.0020\text{ ns}$ for symmetrical step, as well as $Z_{cstep} = 91.7216\Omega$ and $T_{step} = 0.0016\text{ ns}$ for asymmetrical step discontinuity.

Applying the full-wave EM modeling tool, the characteristic impedances of the even- and odd-modes in the PCLM are calculated. They are used to obtain J -inverter network parameter given by (1) of two PCMLs. For each equivalent PCML model, J -inverter constants are: $J_{9mm} = 0.005535$, $J_{7.3mm} = 0.005541$, $J_{5.6mm} = 0.005459$. The other parameters are calculated according to equations given in [12]. For chosen port resistance $R_1 = Z_0$ the parameters for J -inverter multipliers shown in [13] are: $\gamma_{9mm} = 3.088$, $\gamma_{7.3mm} = 3.072$, $\gamma_{5.6mm} = 3.101$ and $\beta_{9mm} = -0.85768$, $\beta_{7.3mm} = -0.85741$, $\beta_{5.6mm} = -0.86131$. Analysis results are:

- **BPF with PCMLs of length $L_{c1} = 9\text{ mm}$** : For the given error of 1%, a multiple factor is $q=1$ and a total minimal number of sections in WDN is $n_t = \sum_{k=1}^{13} n_k = 280$. The numbers of sections in individual uniform segments $n_k = \text{round}[q \cdot T_k / T_{\min}]$ are 28, 1, 49, 49, 8, 1, 8, 1, 8, 49, 49, 1 and 28, respectively. A minimum delay is $T_{\min} = \min\{T_1, T_2, \dots, T_{13}, T_{step}\} = T_{step}$. A real delay of the structure is $T_{\Sigma} = \sum_{k=1}^{11} T_k = 448.2232\text{ ps}$. A total delay for the digital model of the structure is $T_t = n_t \cdot T_{\min} / q = 448.7969\text{ ps}$. A sampling frequency of the digital model is found as $F_s = n_t / T_t = 623.8901\text{ GHz}$. A relative error of delay is $er = [(T_{\Sigma} - T_t) / T_{\Sigma}] \cdot 100\% = -0.12801\%$.

- **BPF with PCMLs of length $L_{c1} = 7.3\text{ mm}$** : A total minimal number of sections in WDN is 264. The numbers of sections in individual uniform segments are 28, 1, 40, 40, 18, 1, 8, 1, 18, 40, 40, 1 and 28, respectively. A real delay of the structure is $T_{\Sigma} = 422.2704\text{ ps}$. A total delay for the digital model of the structure is $T_t = 423.1513\text{ ps}$. A sampling frequency of the digital model is $F_s = 623.8901\text{ GHz}$. A relative error of delay is $er = -0.20862\%$.

- **BPF with PCMLs of length $L_{c1} = 5.6\text{ mm}$** : A total minimal number of sections in WDN is 246. The numbers of sections in individual uniform segments are 28, 1, 31, 31, 27,

1, 8, 1, 27, 31, 31, 1 and 28, respectively. A real delay of the structure is $T_{\Sigma} = 395.9972\text{ ps}$. A total delay for the digital model of the structure is $T_t = 394.3002\text{ ps}$. A sampling frequency of the digital model is $F_s = 623.8901\text{ GHz}$. A relative error of delay is $er = 0.42854\%$.

The two-port parallel adaptor coefficients [13] in WDF network from Fig. 5 are $\beta_{Source} = -\beta_{Load} = -0.07085$.

In Fig. 10, the magnitude of transmission coefficients in dB versus frequency for all three studied BPF cases are shown. Zooms of passband regions are shown in Figs. 11 and 12.

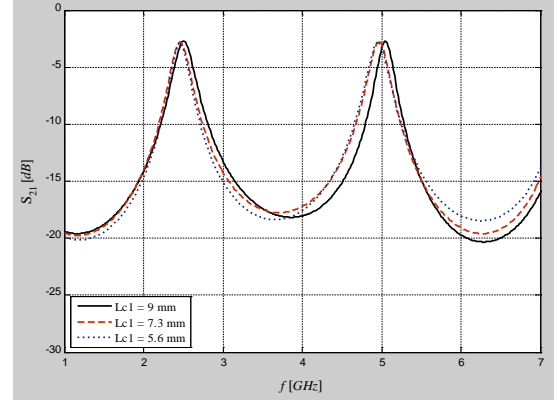


Fig. 10. The magnitudes of the transmission coefficients in dBs for all analyzed cases

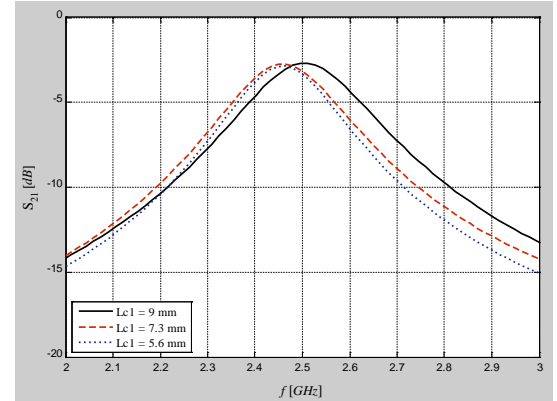


Fig. 11. The magnitudes of the transmission coefficients in dBs for all analyzed cases in the first passband region

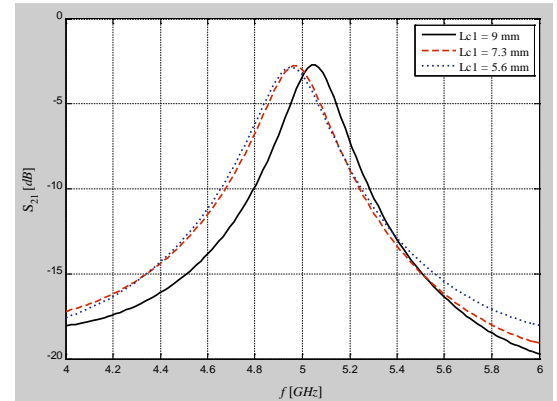


Fig. 12. The magnitudes of the transmission coefficients in dBs for all analyzed cases in the second passband region

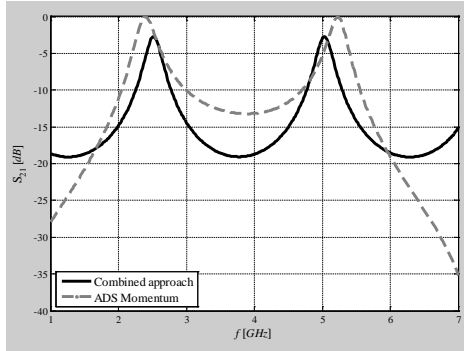


Fig. 13. Comparison of the magnitudes of the transmission coefficients in dBs for BPF with PCMLs of length $L_{c1} = 9 \text{ mm}$

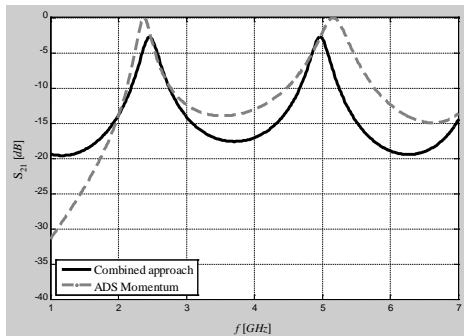


Fig. 14. Comparison of the magnitudes of the transmission coefficients in dBs for BPF with PCMLs of length $L_{c1} = 7.3 \text{ mm}$

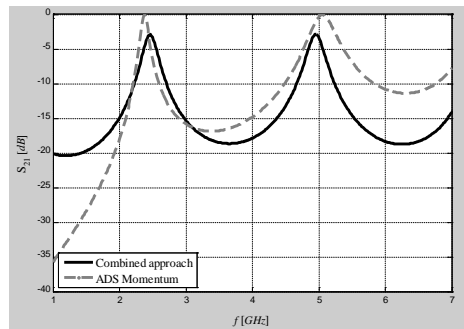


Fig. 15. Comparison of the magnitudes of the transmission coefficients in dBs for BPF with PCMLs of length $L_{c1} = 5.6 \text{ mm}$

Results calculated by proposed combined approach for all three studied BPF cases are compared with results obtained by the EM modeling simulator in Figs. 13-15, respectively. The curves are slightly shifted one from another and it is still an open issue and will be the subject of further researches of the authors.

IV. CONCLUSION

A model has been presented for calculating the scattering parameters of a dual-band BPF. Comprehensive comparisons between the results which are obtained by using the created model on one side, and those obtained by analysis in some other EM simulator on the other side, are shown for all analyzed cases and practical ranges of physical dimensions.

This example together with other BPF examples considered in [10-11] confirms that BPFs with freedom in layout

implementation can be accurately and fast simulated by proposed technique. The discontinuity model is capable to represent it without any restriction in its dimensions and substrate permittivity.

ACKNOWLEDGEMENT

This work has been supported by the Ministry of Education, Science and Technological Development of Serbia, project number TR32052.

REFERENCES

- [1] D. M. Pozar, *Microwave Engineering*, New York, Wiley, 1998.
- [2] R. J. Cameron, Ch. M. Kudsia, R. R. Mansour, *Microwave Filters for Communication Systems – Fundamentals, Design and Applications*, New Jersey, John Wiley and Sons, 2007.
- [3] J.-Sh. Hong, *Microstrip Filters for RF/Microwave Applications*, New Jersey, John Wiley & Sons, 2011.
- [4] K. C. Gupta, R. Garg, I. Bahl, P. Bhartia, *Microstrip Lines and Slotlines*, Artech House, Boston-London, pp. 190-198, 1987.
- [5] A. Fettweis, "Digital circuits and systems", *IEEE Transactions on Circuits and Systems*, vol. CAS-31, no. 1, pp. 31-48, 1984.
- [6] A. Fettweis, "Wave Digital Filters: Theory and Practice", *Proc. IEEE*, vol. 74, pp. 270-327, 1986.
- [7] S. Bilbao, *Wave and Scattering Methods for Numerical Simulation*, Hoboken, New Jersey: Wiley, 2004.
- [8] B. P. Stošić, M. V. Gmitrović, "Implementation of Wave Digital Model in Analysis of Arbitrary Nonuniform Transmission Lines", *Microwave and Optical Technology Letters*, vol. 49, no. 9, pp. 2150-2153, 2007.
- [9] B. P. Stošić, N. S. Dončov, T. Asenov, "Solving Step Discontinuities in Microstrip Circuits with a Combined Wave Digital – Full Wave Electromagnetic Approach", *Proceedings of 56th ETRAN Conference*, pp. MT2.1-1-4, Zlatibor, June 11-14, 2012.
- [10] B. P. Stošić, N. S. Dončov, J. A. Russer, B. D. Milovanović, "A Combined Wave Digital/Full-wave Electromagnetic Approach used for Response Calculation in Equivalent Networks of Microwave Circuits", *2013 International Conference on Electromagnetics in Advanced Applications (ICEAA)*, pp. 569-572, Torino, Italy, September 9-13, 2013.
- [11] B. P. Stošić, N. S. Dončov, A. S. Atanasković, "Response Calculation of Parallel-coupled Resonator Filters by use of Synthesized Wave Digital Network", *2013 11th International Conference on Telecommunications in Modern Cable, Satellite and Broadcasting Services (TELSIKS)*, Serbia, Niš, October 16-19, pp. 253-256, 2013.
- [12] A. K. Verma, H. Singh, "Circuit Model of Microstrip Step Discontinuity", *International Journal of Microwave and Optical Technology*, vol. 4, no. 2, pp. 76-82, March 2009.
- [13] B. P. Stošić, "Wave Digital Network of Parallel-coupled Microstrip based on Admittance Inverter Model", *2013 11th Int. Conf. on Telecommunications in Modern Cable, Satellite and Broadcasting Services (TELSIKS)*, pp. 249-252, Serbia, Niš, October 16-19, 2013.
- [14] B. P. Stošić, N. S. Dončov, "Synthesis and Use of Wave Digital Networks of Admittance Inverters", *Microwave Review*, vol. 19, no.2, pp. 89-95, December 2013.
- [15] S. Sun, L. Zhu, "Coupling Dispersion of Parallel-coupled Microstrip Lines for Dual-band Filters with Controllable Fractional Pass Bandwidths", *2005 IEEE MTT-S International Microwave Symposium Digest*, pp. 2195-2198, 12-17 June 2005.

Three-Wire Star-Shaped Grounding Electrode in the Vicinity of the Semi-Cylindrically Shaped Ground Inhomogeneity

Nenad N. Cvetković¹, Dragan D. Vučković¹, Miodrag S. Stojanović¹ and Aleksa S. Ristić¹

Abstract –The influence of the road, treated as a ground inhomogeneity, on the grounding system in its vicinity is analyzed in the paper. Using an estimation method, the road is approximated by a domain having semi-circular cross-section. The analysis includes using of quasi-stationary image theory and the Green's function for the point source in the vicinity of the cylinder of circularly shaped cross-section, which is for the first time explicitly given in this paper. The leakage current distributions are obtained applying the Method of Moments. Afterwards, the grounding system characteristics are determined.

Keywords – Green's function methods, grounding, nonhomogeneous media.

modeled as a homogeneous domain of rectangular cross-section, and afterwards approximated by a semi-circular cross-section cylinder using the estimation method [1]. That resulted in a need to use the quasi-stationary Green's function of the point source in the vicinity of such domain given in [2].

The rest of the analysis is performed applying the Method of Moments (MoM) [3] in a usual way. The geometrical parameters of analyzed grounding systems, as well as used conductivity values of the surrounding ground, and the road (the inhomogeneity) have been taken from the official publications, [4]-[5], and from [6]. The resistance and potential distribution in the vicinity of the grounding system are determined.

I. INTRODUCTION

Different technological systems like power facilities, telecommunication systems, or lightning protection systems include a grounding system as a necessary part. Very often, the road is located in the vicinity of such objects. If the road was treated as a ground inhomogeneity, one can expect that there is a certain influence on the grounding system characteristics placed in their vicinity.

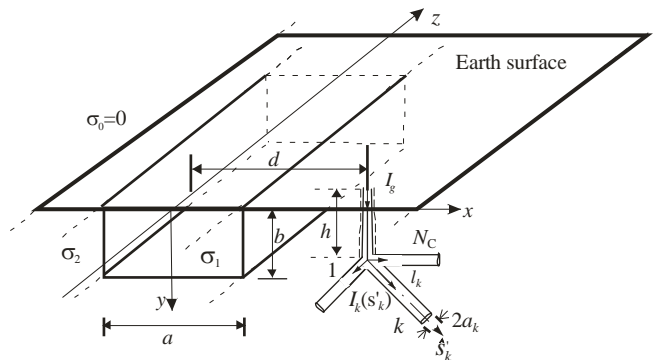


Fig. 1. The star-shaped grounding system in the vicinity of the road

In this paper, a semi-analytical approach to the quasi-stationary analysis of this influence is proposed. The road is

¹Nenad N. Cvetković, Dragan D. Vučković, Miodrag S. Stojanović and Aleksa S. Ristić are with the University of Niš, Faculty of Electronic Engineering, Aleksandra Medvedeva 14, P.O. Box 73, 18000 Niš, Serbia, E-mails: [nenad.cvetkovic, dragan.vuckovic, miodrag.stojanovic, aleksa.ristic]@elfak.ni.ac.rs.

²Ivo Dochev is with the Faculty of Telecommunications at Technical University of Sofia, 8 Kl. Ohridski Blvd, Sofia 1000, Bulgaria.

II. THEORETICAL BACKGROUND

A. Description of the Problem

The wire star-shaped grounding system placed in the vicinity of the road, Fig. 1, is analyzed. It is fed by an isolated earthing conductor with current I_g .

Although the domain of the road usually consists of a few sub-domains made of different materials [6], in this case it is modeled as a homogeneous cylindrical domain having rectangular ($a \times b$) cross-section of specific conductivity σ_1 .

The road is surrounded by the homogeneous ground of known conductivity σ_2 where the grounding system is placed. Corresponding Cartesian coordinate system is assigned.

Star-shaped electrode is formed of N_C mutually connected wires, having length l_k and circle cross-section of radii a_k , $a_k \ll l_k$, $k = 1, 2, \dots, N_C$. Conductors' axis and corresponding ords are labeled by s'_k , while longitudinal current distributions are denoted by $I_k(s'_k)$, $k = 1, 2, \dots, N_C$.

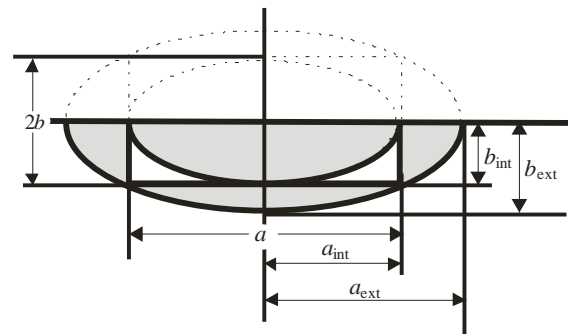


Fig. 2. Approximation of the rectangular cross-section using an equivalent semi-circular one.

B. Approximating the Road with a Domain of Semi-Circular Cross-Section using the Estimation Method

The estimation method allows approximation of the road domain (modeled as an infinitely long domain of rectangular cross-section), by a cylinder of semi-circular cross-section having equivalent radius a_{eq} . This is carried following the approach described in [1].

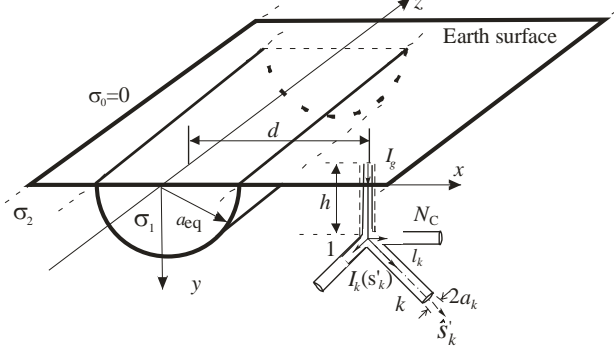


Fig. 3. The star-shaped wire grounding system in the vicinity of the infinitely long cylinder of semi-circular cross-section.

The interval that includes the value of the equivalent radius a_{eq} (Fig. 3) can be estimated using additional domains (Fig. 2) whose cross-sections are confocal ellipses of semi-axis

$$a_{int} = a/2 \text{ and } b_{int} = b \text{ for the interior ellipse,} \quad (1)$$

$$\text{i.e. } a_{ext} = \sqrt{a(a+2b)}/2 \text{ and } b_{ext} = \sqrt{2b(a+2b)}/2 \quad (2)$$

for the exterior one. The interval is defined by values

$$a_{eq \min} = (a_{int} + b_{int})/2 = (a + 2b)/4 \text{ and} \quad (3)$$

$$a_{eq \max} = (a_{ext} + b_{ext})/2 = \sqrt{a+2b}(\sqrt{a} + \sqrt{2b})/4. \quad (4)$$

Finally, the approximate value of the equivalent radius is

$$a_{eq} = \frac{a_{eq \min} + a_{eq \max}}{2} = \frac{a + 2b + \sqrt{a+2b}(\sqrt{a} + \sqrt{2b})}{8}. \quad (5)$$

This way, the problem is reduced to the case of the grounding system in the vicinity of a cylinder of semi-circular cross-section, Fig. 3.

C. Green's Functions

In order to obtain potential of the system from Fig. 3 the Green's function for the point source in the vicinity of the infinitely long cylinder having circular cross-section of radii a_{eq} is applied, Fig. 4. This was carried out following the procedure for the internal point source given in [2]. The corresponding Cartesian (x, y, z) and cylindrical coordinate systems (r, θ, z) are assigned, where is

$$x = r \cos \theta, y = r \sin \theta, z = z. \quad (6)$$

The source position (point M) is defined by the field vector $\vec{R}_0 = x_0\hat{x} + y_0\hat{y} + z_0\hat{z} = r_0\hat{r} + z_0\hat{z}$ and the field vector of the image source placed at the point M' is

$$\vec{R}'_0 = x_0\hat{x} - y_0\hat{y} + z_0\hat{z}. \quad (7)$$

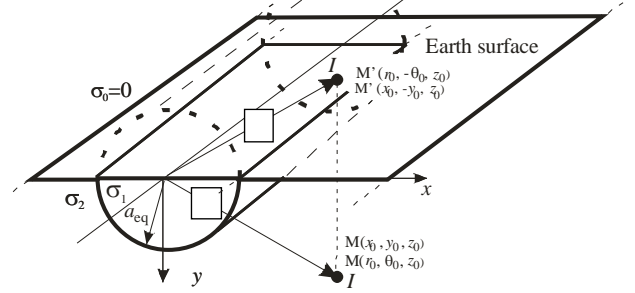


Fig. 4. The point current source near the semi-cylinder

The potential of the point source near a semi-cylinder (Fig. 4) can be expressed as

$$\begin{aligned} \varphi_1 = \frac{I}{\pi^2 \sigma_2} \sum_{m=0}^{\infty} \{ \xi_m \cos m\theta \cos m\theta_0 \times \\ \times \int_0^{\infty} A_m(\lambda) I_m(\lambda r) I_m(\lambda r_0) \cos[\lambda(z - z_0)] d\lambda \}, r < a_{eq}, \quad (8) \end{aligned}$$

$$\xi_0 = 1, \xi_m = 2, m = 1, 2, \dots$$

and

$$\begin{aligned} \varphi_2 = \frac{I}{4\pi\sigma_2} \left(\frac{1}{|\vec{R} - \vec{R}_0|} + \frac{1}{|\vec{R} - \vec{R}'_0|} \right) + \\ + \frac{I}{\pi^2 \sigma_2} \sum_{m=0}^{\infty} \{ \xi_m \cos m\theta \cos m\theta_0 \times \\ \times \int_0^{\infty} B_m(\lambda) I_m(\lambda r_0) K_m(\lambda r) \cos[\lambda(z - z_0)] d\lambda \}, r > a_{eq}, \quad (9) \end{aligned}$$

$$\xi_0 = 1, \xi_m = 2, m = 1, 2, \dots$$

In the previous expression, I_m and K_m denote the modified Bessel functions of the first and second kind, respectively.

The coefficients $A_m(\lambda)$ and $B_m(\lambda)$, $m = 0, 1, 2, \dots$ in expressions (8), i.e. (9), are given by following relation:

$$A_m = \Delta_{A_m} / \Delta_m, B_m = \Delta_{B_m} / \Delta_m, m = 0, 1, 2, \dots \quad (10)$$

Labels Δ_A , Δ_B and Δ in (10) are defined as

$$\Delta_{A_m} = K_m(\lambda r_0) I_m(\lambda r_0) / (\lambda a_{eq}), \quad (11)$$

$$\Delta_{B_m} = I_m(\lambda a_{eq}) I_m(\lambda r_0) I'_m(\lambda a_{eq}) K_m(\lambda r_0) \left(1 - \frac{\sigma_1}{\sigma_2} \right) \quad (12)$$

and

$$\Delta_m = [I_m(\lambda r_0)]^2 \left[(\sigma_1 / \sigma_2) I'_m(\lambda a_{\text{eq}}) K_m(\lambda a_{\text{eq}}) - I_m(\lambda a_{\text{eq}}) K'_m(\lambda a_{\text{eq}}) \right] \quad (13)$$

The corresponding Green's functions for the point source from Fig. 4 can be defined as

$$G_1(\vec{R}, \vec{R}_0) = \varphi_1 / I \text{ and } G_2(\vec{R}, \vec{R}_0) = \varphi_2 / I. \quad (14)$$

where φ_1 and φ_2 are given by (8), i.e. (9).

D. Application to the Star-Shaped Grounding System

The longitudinal currents along the wires of the grounding system from Fig. 3 are $I_k(s'_k)$, $k=1, \dots, N_C$. Electrical scalar potential at an arbitrary point of the grounding system's surroundings can be expressed as

$$\varphi_{1/2}(\vec{R}) = \sum_{k=1}^{N_C} \int_{l_k} G_{1/2}(\vec{R}, \vec{s}'_k) I_{\text{leak}}(s'_k) ds'_k \quad (15)$$

where index "1" denotes the potential inside the semi-cylinder ($r < a_{\text{eq}}$) and "2" the potential in the surrounding domain ($r > a_{\text{eq}}$). Also, \vec{s}'_k in (16) presents the position of the element of the k -th conductor ds'_k , $k=1, \dots, N_C$. The current that leaks from the wire element ds'_k , $k=1, \dots, N_C$ is labeled by $dI = I_{\text{leak}}(s'_k) ds'_k$, where

$$I_{\text{leak}}(s'_k) = -\partial I_k(s'_k) / \partial s'_k = -I'_k(s'_k), \quad (16)$$

is density of the leakage current per unit length.

Based on the analysis described in the previous text, the Method of Moments is applied for characterization of the system from Fig. 3. Each conductor of the star-shaped electrode is uniformly divided into finite number of segments M_k , $k=1, \dots, N_C$. Assuming that the star-shaped electrode surface is approximately equipotential, it is possible to match potential value $\varphi = U$ at the surface point in the middle of the segments on the k -th conductor, defined by field vector \vec{R}_{ni} , $n=1, \dots, N_C$, $i=1, \dots, M_n$. Previously described procedure results in a system of linear equations

$$\varphi(\vec{R} = \vec{R}_{ni}) \cong U = \left[\sum_{k=1}^{N_C} \sum_{j=1}^{M_k} \frac{I_{kj}}{\Delta_{kj}} \int G_2(\vec{R}_{ni}, \vec{s}'_k) ds'_k \right], \quad (17)$$

$$n=1, \dots, N_C, \quad i=1, \dots, M_n.$$

In (17), Δ_{kj} and I_{kj} , $k=1, \dots, N_C$, $j=1, \dots, M_k$ are lengths and leakage currents of the segments on the conductors of the star-shaped electrodes' system, respectively. The solution of the system of equations (17) are total leakage currents of the segments, I_{kj} , $k=1, \dots, N_C$, $j=1, \dots, M_k$. The feeding current is equal to the sum of leakage currents, i.e.

$$I_g = \sum_{k=1}^{N_C} \sum_{j=1}^{M_k} I_{kj}. \quad (18)$$

The resistance of the grounding system is now

$$R_g = U / I_g. \quad (19)$$

After determining the unknown leakage currents I_{kj} , $k=1, \dots, N_C$, $j=1, \dots, M_k$, the potential distribution of the system from Fig. 3, has the form

$$\varphi_{1/2}(\vec{R}) = \left[\sum_{k=1}^{N_C} \sum_{j=1}^{M_k} \frac{I_{kj}}{\Delta_{kj}} \int G_{1/2}(\vec{R}, \vec{s}'_k) ds'_k \right]. \quad (20)$$

As in (20), indexes "1" and "2" correspond to the semi-cylinder, and the surrounding domain, respectively.

III. NUMERICAL RESULTS

The proposed procedure is applied on the road and grounding systems realized in practice. The values of the geometrical and electrical parameters of the road, surrounding ground, and the grounding are chosen based on the ones from [4]-[6].

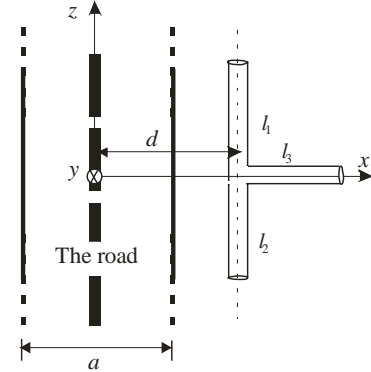


Fig.5. Three-wire grounding system

The grounding system formed of $N_C = 3$ conductors of length $l_1 = l_2 = l_3 = 5$ m, and wires' cross-sections radii $a_1 = a_2 = a_3 = 5$ mm, is analyzed in this part of the paper. Conductors are buried at depth $h = 0.8$ m, parallel to the ground surface, and along the road, Fig. 5. The dimensions of the road domain are $a = 10$ m and $b = 4.75$ m. Using (5), we get $a_{\text{eq}} = 5.88$ m for the equivalent radius. The system is placed at distance 3 m from the boundary of the equivalent semi-cylinder, so the distance from the road axis is $d = a_{\text{eq}} + 3$ m = 8.88 m. The described procedure is applied for $M_1 = M_2 = 25$ segments.

The normalized resistance of the grounding system from Fig. 5 versus ratio σ_2 / σ_1 is shown in Fig. 6. The

normalization factor is ρ_2/d_{nor} , where $\rho_2 = 1/\sigma_2$ is the specific resistivity of the surrounding ground and $d_{\text{nor}} = 1\text{ m}$.

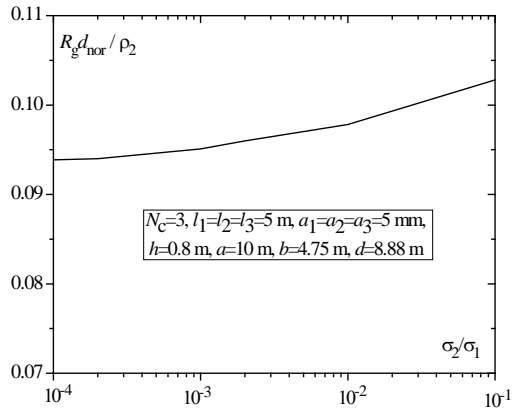


Fig.6. The normalized resistance of the grounding system from Fig. 5 versus ratio σ_2/σ_1

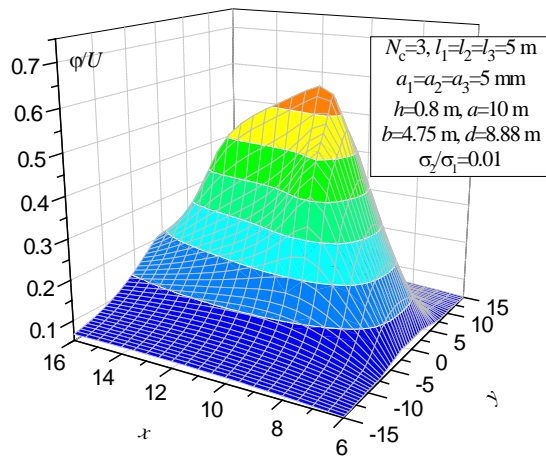


Fig.7. The normalized potential distribution on the ground surface above the electrode from Fig. 5.

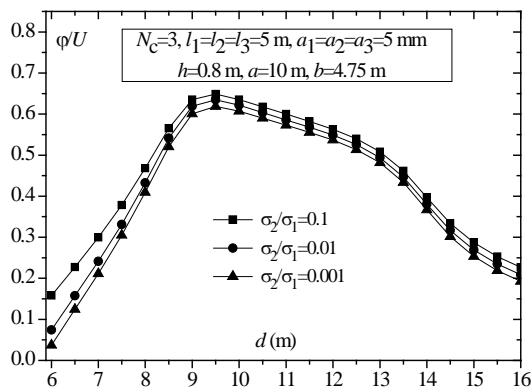


Fig.8. The normalized potential distribution of the grounding system from Fig. 5 along x -axis with ratio σ_2/σ_1 as a parameter.

The normalized potential distribution on the ground surface above the ground electrode from Fig. 5 is shown in Fig. 7. The potential is normalized by the potential of the grounding system U . Values of $\sigma_1 = 0.1\text{ S/m}$ and $\sigma_2 = 0.01\text{ S/m}$ are adopted for conductivities, and the rest of the parameters are the same as in Fig. 6.

In Fig. 8, the normalized potential distribution along x -axis, i.e. for $y=0$ and $z=0$, with ratio σ_2/σ_1 as a parameter, is presented. The rest of the parameters is the same as in Fig. 7.

The shape of the obtained functions from Figures 6-8 was expected. It is noteworthy that conductivities ratio σ_2/σ_1 has noticeable influence on potential distribution, especially in the space between the road and the grounding system. Actually, the step-voltage is decreasing with the increase of the ratio σ_2/σ_1 .

IV. CONCLUSIONS

Asemi-analytical procedure for modeling influence of the road on the characteristics of grounding system in its vicinity is presented in this paper. It is based on the modeling of the road with a semi-cylindrical domain. The obtained results show that this influence exists for real geometrical and electrical parameters of the analyzed system, especially when the grounding system is placed close to the road, which was expected.

Proposed method considers application of the quasi-stationary Green's function for the point source placed near the infinitely long homogenous cylinder.

The method can be applied to analysis of other types of ground inhomogeneities that can be modeled as horizontally placed cylinders or semi-cylinders (riverbeds, different kinds of ducts, etc.)

ACKNOWLEDGEMENT

This research was partially supported by the funds from the Serbian Ministry of Education and Science in the frame of the project TR 33008.

REFERENCES

- [1] N. N. Cvetković and P. D. Rančić, "Model for analyzing a pillar grounding system with cylindrically-shaped concrete foundation", *Electromagnetics*, Taylor & Francis. vol. 29, no 2, pp. 151–164, 2009; DOI: 10.1080/02726340802676154.
- [2] D. D. Vučković, N. N. Cvetković, D. Krstić, M. Stojanović, "Modeling of the Road Influence on the Grounding System in its Vicinity", *The 15th International IGTE Symposium*, CD Proceedings, pp. 294-299, Graz, Austria, 2012, ISBN: 978-3-85125-258-3.
- [3] R. F. Harrington, *Field computation by Moment Methods*, The Macmillan Company, New York, 1969.
- [4] Technical Recommendation of Electric Power Industry of Serbia: Grounding of the Power Network Pillars, TR No. 9, Belgrade 2000. [in Serbian]. Available at: <http://bit.ly/jrcrpd>.
- [5] Ordinance on conditions in terms of traffic safety which must be fulfilled by meet travel facilities and other elements of the public road, Ministry for infrastructure of Republic of Serbia, 2011. [in Serbian]. Available at: <http://bit.ly/QPJLEQ>.
- [6] T. Saarenketo, "Electrical Properties of Road Materials and subgrade Soils and the Use of Ground Penetrating Radar in Traffic Infrastructure Surveys", *Acta Universitatis Ouluensis, Series A-Scientiae Rerum Naturalium*, University of Oulu Finland, ISBN: 951-42-8222-1 (PDF); Available at: <http://bit.ly/1k7XdPP>.

Session DSP:

DIGITAL SIGNAL PROCESSING

Research and Analysis of Methods for Localization of Audio Sources

Viktor Hristov¹ and Snejana Pleshkova²

Abstract – In this paper was done research and deep analysis of existing methods for localization of audio sources. After the precise mathematical description of microphone arrays, are prepared simulations of some chosen types of microphone arrays, for example with three microphones, using the Matlab resource and it was applied the Time Delay Of Arrival method for localization of the audio source. Therefore, the goal of this article is to present the microphone array description as mathematical model and to use this model for simulation in Matlab environments.

Keywords – microphone array, beamforming, simulation, time delay of arrival.

I. INTRODUCTION

Discussing and researching of microphone array processing is one of the most interesting topics nowadays. The main problem in simulating and constructing following devices is localization of audio source and define angel at which sound wave has arrived. It has many important applications including systems for extracting voice input from ambient noise (speech recognition systems, hearing aids and telephones), mobile robots [1, 2], video-conferencing systems [3], surround sound and locating objects for police and military purposes [4].

Methods for localization of sound sources can be defined in three main groups: dependent from time of arrival, fixed beamforming and adaptive (hybrid) beamforming using correlation functions.

The most popular and investigated method for sound source localization (SSL) is based on measurement of the time of delay of arrival (TDOA) [5].

Beamforming is spatial filtering based on microphone characteristics and microphone array configuration. It can be classified in two groups: fixed (classical) and adaptive (hybrid) depending of the input data [6].

There are two scenarios dependent of the distance from source to the microphone: far-field and near-field. In first one situation, the destination from source to the each microphone in microphone array is many times bigger than the distance between microphones and it can assume that waves are planar. In near-field, wave fronts are spherical. It is included attenuation of the signals [7].

¹Viktor Hristov is with the Faculty of Telecommunications at Technical University of Sofia, 8 Kl. Ohridski Blvd, Sofia 1000, Bulgaria, E-mail: hristov.viktor@gmail.com.

²Snejana Pleshkova is with the Faculty of Telecommunications at Technical University of Sofia, 8 Kl. Ohridski Blvd, Sofia 1000, Bulgaria, E-mail: snejpl@tu-sofia.bg.

There are two scenarios dependent of the place, were experiment was done – open space, without any reflections and in closed space, also called multipath propagation, because each reflection from the wall or object can be treated as a separate source [6].

The goal of this article is to present the microphone array description as mathematical model and to use this model for simulation in Matlab environments. As an example to prepare experimental tests of the proposed simulation model is chosen the most popular method for sound source localization (SSL) based on measurement of the time of delay of arrival (TDOA).

II. METHODS OF INVESTIGATION

A. Mathematical model of sound localization method using time delay of arrival

On Fig. 1 is shown the general microphone array processing block scheme suitable for sound localization. Sound reaches the microphone array in form of plane wave. It was made an assumption that the sound source is at reasonable distance from microphone sensors, therefore a flat sound wave falls in the place of linear arranged microphone array. Each microphone receives sound waves in different moment. Output signals from all microphones are processed with appropriate filters $w_1(f) \dots w_N(f)$ necessary to adjust time delay of microphones from M_2 to M_N according to first microphone M_1 . After that all from filters output sound signals are summed to obtain final output signal of the microphone array $y(f)$.

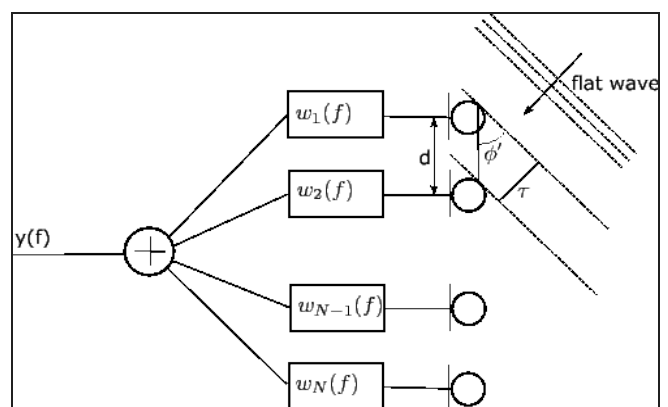


Fig. 1. Microphone array processing

Shown on Fig. 1 block scheme can be used to describe the mathematical model of a linear microphone array. This model can be used to analyze different types of structures in situation of linear microphone array, choosing and changing M as

number of microphones in microphone array, which can be situated on a distance d from each other. The choice of this distance d also can be subject of changes to investigate the sound localization capabilities of microphone array from values of distance d .

Localization of the sound source can be done using the hypothesis that it should be found the point in the space where energy is the highest one.

From the microphone array structure presented on Fig.1 is can be determined the mathematical equations described the work of a linear microphone array.

If M is the number of microphones in an array, then the signal received at the microphone m , where $m=1\dots M$ at the moment n is Eq. (1):

$$x_m(n) = h_m(n)s(n) + n_m(n) \quad (1)$$

where, $n_m(n)$ is additive noise and $h_m(n)$ is a room impulse response.

It is possible to assign $E(l)$ in Eq. (3) as sound energy in point l and $p(l)$ in Eq. (2) as an arbitrary space location. These two microphone array characteristics are presented with the following equations:

$$p^*(l) = \arg \max \{E(l)\} \quad (2)$$

$$E(l) = \left| \sum_{m=1}^M x_m(n - t_m) \right|^2 \quad (3)$$

where, t_m is the time that takes sound to travel from the signal source to the microphone m .

When use microphone array with only two microphones, it is applicable one-step TDOA. The main advantage of that method is the fact that calculation can be done in one step and there are no need of approximations and loss of information. The disadvantage of this method is in the complicated calculations.

When the array has more than two microphones, the conventional TDOA sound source localization is in two steps. In first step calculation is done for each pair of the microphones. The weighting function is added to improve the quality in process of estimation for localization. In the second step, results from the first one are taken and summed in order to obtain the final localization of the sound source. The main advantage of that method is that this well-known domain has a lot of weight functions, which can be used. This is the reason for easier calculations on the second step.

The basic disadvantages are the approximations for the average time of delay in arrival, which leads to loss of information.

B. Mathematical model of sound localization method using classical beamforming

Classical beamforming is data-independent technique. Some of the fixed beamforming methods are Filter-and-Sum beamformer design, superdirective beamforming, matched filtering as white noise gain maximization, Delay-and-Sum beamforming and Delay-and- Subtract algorithm.

The simplest configuration of all microphone arrays is Filter-and-Sum beamformer design. It is so named because the sensors' inputs are first delayed by time τ_n in time domain on Eq. (4), and then summed to give a single array output.

$$\tau_n = \frac{(n-1)d \cos \phi}{c} \quad (4)$$

Usually, each channel is given equal amplitude weighting in the summation. That means the directivity pattern demonstrates unity gain in the desired direction. This leads to the complex channel weights on Eq. (5):

$$\omega_n(f) = \frac{1}{N} e^{j \frac{-2\pi f}{c} (n-1)d \cos \phi} \quad (5)$$

The delay-sum beamformer belongs to a more general class known as filter sum beamformers, in which both the amplitude and phase weights are frequency dependent. In practice, most beamformers are a class of filter-sum beamformer.

One simple method of covering broadband signals is to implement the array as a series of sub-arrays, which are by themselves linear arrays with uniform spacing. These sub-arrays are designed to give desired response characteristics for a given frequency range [8].

Super directive beamforming method has the highest directivity (DI) but very poor white noise gain (WNG). This is the reason for the problems with robustness (sensor noise) [9].

C. Mathematical model of sound localization method using adaptive (hybrid) beamforming

In previous point [II.B] were described most popular fixed beamforming techniques and now we continue with adaptive beamforming, which is data dependent.

We will focus in LSMV beamforming, Frost beamforming and Generalized sidelobe canceller.

Linearly Constrained Minimum Variance (LCMV) beamforming. The main purpose is to minimize noise output power, while maintaining a chosen response in a given look direction which is closer to the operations of superdirective array or delay-and-sum, but now noise field is unknown.

Frost beamforming is the adaptive version of LCMV. It is a long standing (1970's) beamforming technique that reduces noise whilst maintaining the look direction signal. It is an adaptive system that aims to minimal noise energy by adjusting the beamformer filter weights. Although it was investigated and published a while ago, a great deal of current work builds upon and references this work, so it's well worth looking at.

Generalized sidelobe canceler (GSC) is alternative adaptive filter formulation of the LCMV-problem: constrained optimisation is reformulated as a constraint pre-processing, followed by an unconstrained optimisation, leading to a simpler adaptation scheme [10]. GSC consists of three parts: fixed beamformer, which satisfying constraints but not yet minimum variance, creating 'speech reference'; blocking

matrix, placing spatial nulls in the direction of the speech source (at sampling frequencies), creating 'noise references' and multi-channel adaptive filter (linear combiner) LSM. GSC is an algorithm shown on Fig.2 is with complex mathematics calculations in Eq. (6).

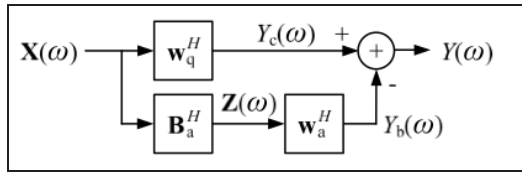


Fig. 2. Microphone array processing

The main problem is the fact of impossibility to reduce noise from look-direction.

$$Y = (w_q - B_a w_a)^H X \quad (6)$$

In this situation reverberation effects cause signal leakage in noise reference adaptive filter should only be updated when no speech is present.

III. MATLAB SIMULATION OF TIME OF DELAY OF ARRIVAL (TDOA) METHOD FOR SOUND LOCALIZATION

The simulation model based on the mathematical description (equations 1-5) is prepared and is shown on Fig. 3. It is a special case of Fig.1 with constant distance d between each element. We used a real microphone to record an audio file and apply this sound record as test signal simulating the sound signal from first microphone in microphone array (assuming relative zero time delay for this microphone).

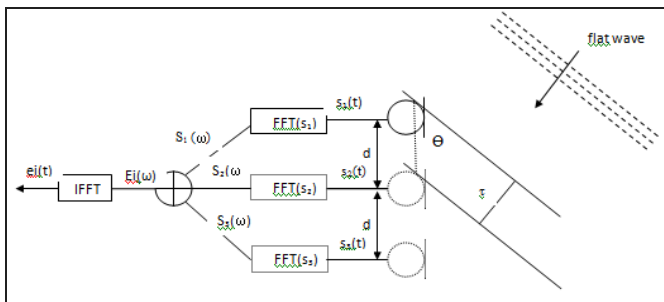


Fig. 3. The simulation model based on the mathematical description (equations 1-5)

Then we simulated microphone array with following initial conditions, which are input parameters in simulation of microphone array example:

- $M = 3$ microphones (1 real and 2 simulated)
- $c = 330$ m/s – propagation speed of voice
- $d = 0.03$ m – distance between microphones
- $\theta = 30$ deg - angel from which sound reaches microphone.
- $F_{sig} = 4000$ Hz –signal frequency

The simulation model is arranged as an appropriate algorithm shown in Fig. 4 and applying the mathematical description (equations 1-5).

In block 1 we received sound signal in first microphone of array. In block 2 we set microphone array parameters to simulate it. After that we define time delay of arrival of the signals for the different microphones in block 3. We apply Fourier transform for signals in different microphones in block 4 to make possible sum them in block 5.

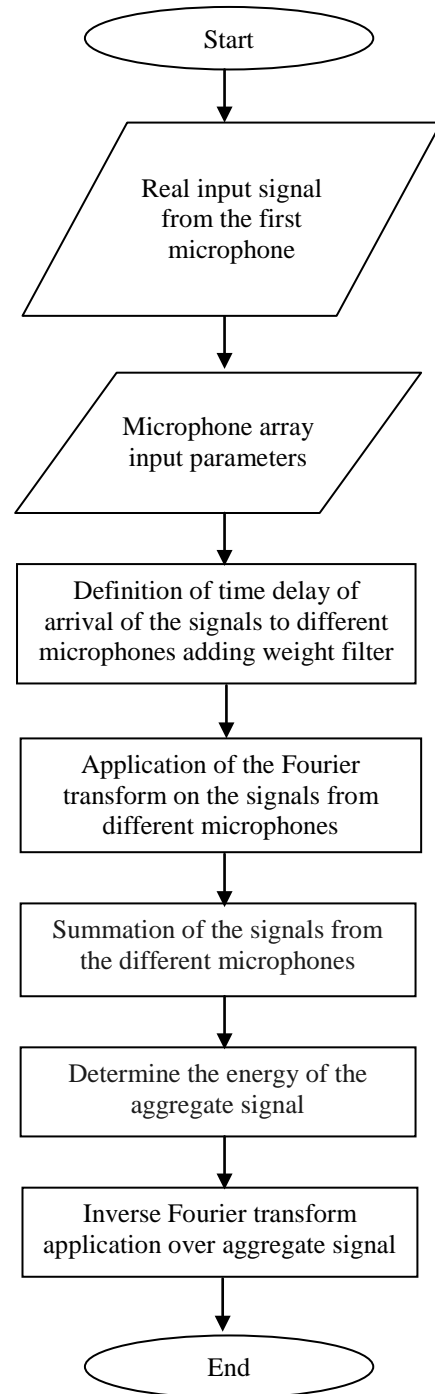


Fig. 4. The simulation model is arranged as an appropriate algorithm

In the next block we determine the energy of the aggregate signal to apply the hypothesis for localization in point of the space where it is the highest one. Finally in last block we apply Inverse FFT over the aggregate signal to find time of delay and following the Eq. (7) to calculate the angel of arrival.

The results from execution of the described algorithm above are used to calculate time delay in each sound waves arrival situation and after that the desired direction of arrival indicating sound source localization.

The results from simulation as values of the parameters in the following equations to calculate time of delay of the signal to each microphone:

$$\tau = abs\left\{\frac{d \cos(\theta) t_{sig}}{c}\right\}. \quad (7)$$

Sampling period can be calculated from sampling rate:

$$T_{sig} = \frac{1}{f_{sig}}. \quad (8)$$

Number of bits delay on the graphic is:

$$N = \frac{\tau}{T_{sig}}. \quad (9)$$

The experiment was carried out in far-field zone therefore we can make the assumption that angle for all microphones in the array is the same. The algorithm of Fig.3 for Time Delay Of Arrival and simulation of microphone array was implemented by Matlab.

First we get a real signal from microphone and record it in audio file. Then we load this file and input the array parameters. We calculate the time of delay and using it we simulated the second and third signal from microphone array. Using a Fast Fourier Transformation (FFT) we receive spectrum of all signals. Following the physical diagram next step is to summarize them in one signal and find the point where the amplitude is maximal. After that using the Inverse FFT we transfer the received signal spectrum in time domain.

IV. EXPERIMENTAL RESULTS

The simulation model arranged as an appropriate algorithm shown in Fig. 3 is used in experiment carried out in this article. The experiments are performed and experimental results are presented below.

On Fig.5 are shown three sound signals, received in microphone array. The first one is real sound signal from microphone and the other two below are simulated with proper delay, described in previous section.

On the next Fig. 6 are presented three signals on one graphic to be clear shown their delay. Graphic in blue shows the original signal, received from microphone, green – shows the simulated signal with delay τ and with red – simulated signal with delay 2τ .

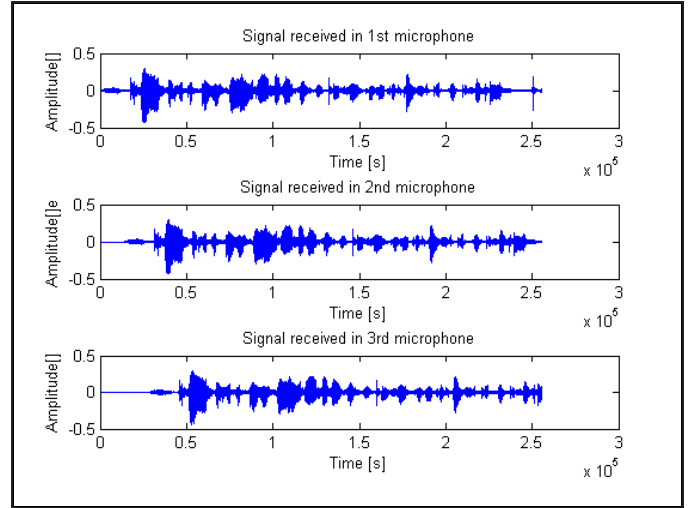


Fig. 5. Sound signals received from microphone array

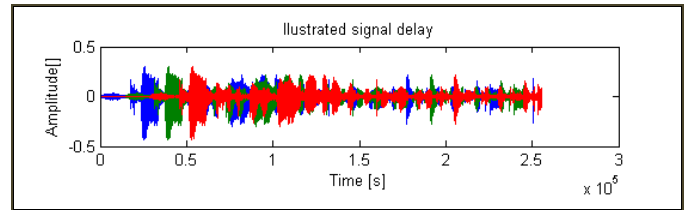


Fig. 6. Sound signals received from microphone array on one graphic

According to the algorithm in Fig. 7 and in Fig. 8 are shown spectra of the individual and aggregate microphone signals after Fast Fourier Transformation and their Inverse Fast Fourier Transformation (Fig. 9), respectively.

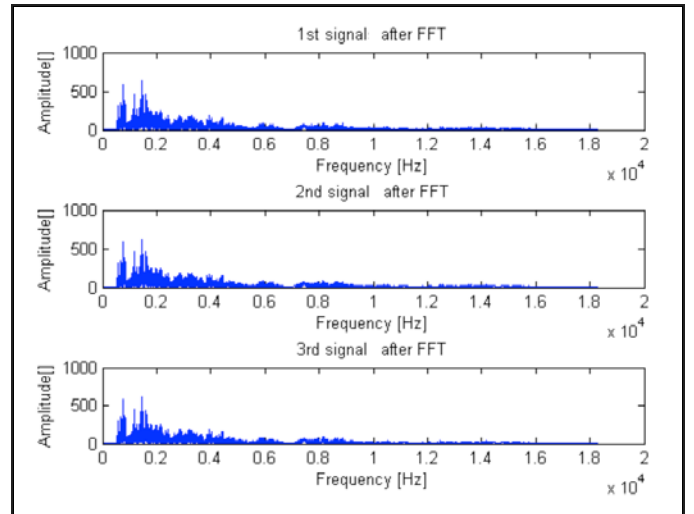


Fig.7. Sound signals spectrum applying Fast Fourier Transformation

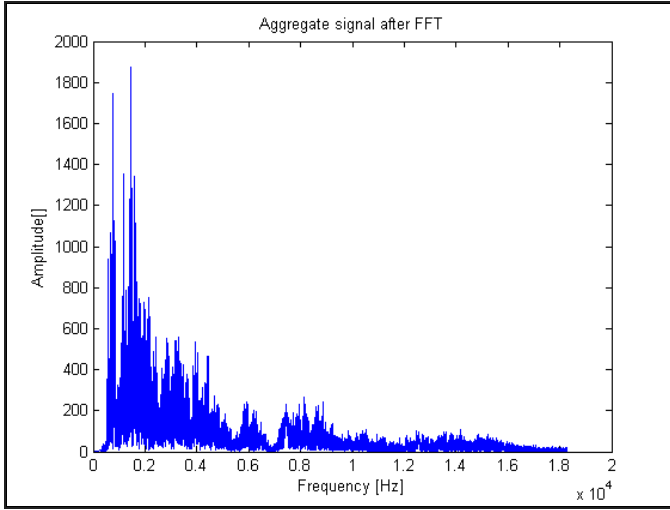


Fig. 8. Spectrum of aggregate signal after Fast Fourier Transformation

We can see that the maximum amplitude of the signal is observed between 2-4 kHz. Also it is possible to conclude that in the spectral domain there isn't exist an important information, which can be used to sound direction of arrival calculation applying the used in this and investigated in this article time of delay of arrival (TDOA) method.

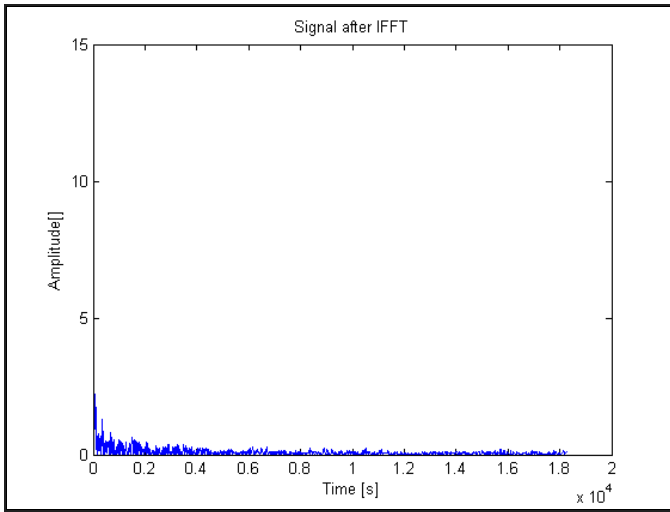


Fig. 9. Inverse Fast Fourier Transformation from microphone signals spectrum

The results from experiments with algorithm are used to calculate time delay in each sound waves arrival situation and after that the desired direction of arrival indicating sound source localization.

These calculations are explained below for a chosen example of simulations.

Following the MatLab workspace we use discrete values

$$N = 1.389 \cdot 10^4 ,$$

which will be different for the real microphone array and setted sample frequency 44100 kHz.

Using the Eq. (7), we can calculate the T_s :

$$T_{sig} = \frac{1}{f_{sig}} = 2,268 \cdot 10^{-5} s .$$

After that using the Eq. (8) we can calculate time of delay:

$$\tau = NT_{sig} = 0,315 s .$$

Finally applying the Eq. (6), we received:

$$\theta = \arcsin\left(\frac{\tau \cdot c}{f_{sig} d}\right) = 29,974 \text{ deg} .$$

Name	Value	Min	Max
N	1.3890e+04	1.3890e+...	1.3890e+04
S1	<255744x1 double>	1.3055e-04	633.3511
S2	<255744x1 double>	2.0398e-04	619.2827
S3	<255744x1 double>	5.3830e-05	619.7611
Ts	2.2676e-05	2.2676e-05	2.2676e-05
W1	0.0019	0.0019	0.0019
c	330	330	330
d	0.0300	0.0300	0.0300
fd	'proba1_25.02201...		
fs	44100	44100	44100
fsig	4000	4000	4000
l1	255744	255744	255744
l2	255744	255744	255744
l3	255744	255744	255744
lsigin	255744	255744	255744
sigin	<255744x1 double>	-0.4346	0.2961
sigt1	<255744x1 double>	-0.4346	0.2961
sigt2	<255744x1 double>	-0.4346	0.2961
tau	0.3150	0.3150	0.3150

Fig. 10. Values in Matlab Workspace after execution of one simulation example to use in angle of sound arrival θ calculations

The presented values above are delivered from Matlab Workspace after execution of one simulation example (Fig. 10) and are used in angle of sound arrival θ calculations.

The values of calculate angle θ represent direction of sound waves arrival from source of the sound. This means that the sound localization is done properly.

V. CONCLUSION

In this paper was described microphone array simulation and its realization in Matlab framework. They are based on presented here mathematical equation as models of more important sound localization methods. After an analysis carried out it is chosen to simulate in Matlab environments Time Delay Of Arrival method. An block algorithm is prepared first to describe the necessary operations in Matlab simulation program, which is executed for some defined as

concrete values microphone array parameters. The results from execution of Matlab simulation program are used to calculate time delay of sound waves arrival and from this calculated time delay determined direction of arrival indicating sound source localization. The results of these calculations show the ability of the proposed in this article algorithm and Matlab simulation program to properly determine direction of arrival of sound waves from sound source solving the problem of sound source localization, when applying the investigated in this article Time Delay Of Arrival method and algorithm.

ACKNOWLEDGEMENT

This paper was supported by Technical University – Sofia inner program to support PhD research projects under Contract 142 PD 0018-07: “Development of methods and tools to locate audio sources in information and communication networks”.

REFERENCES

- [1] J.M. Valin, J. Rouat, F. Michaud, “Enhanced Robot Audition Based on Microphone Array Source Separation with Post-Filter”, Université de Sherbrooke, Sherbrooke (Quebec) CANADA, 2004.
- [2] A. Bekiarski, S. Pleshkova, “Microphone array beamforming for mobile robot”, CSECS'09 Proceedings of the 8th WSEAS International Conference on Circuits, systems, electronics, control & signal processing, 2009, p. 146-149.
- [3] Powerful microphone for the Polycom Group and HDX Series , <http://www.polycom.com> .
- [4] M. Okandan, E.P. Parker, N.A. Hall, K. Peterson, P. Resick, D. Serkland, “Ultrasensitive Directional Microphone Arrays for Military Operations in Urban Terrain”, 2007.
- [5] Y. Rui, D. Florencio, “New direct approaches to robust sound source localization”, January, 2004.
- [6] I. McCowan, Microphone Array, April 2001.
- [7] I. McCowan, “Multi-channel sub-band speech recognition”, Speech Research Laboratory, RCSAVT, School of EESE, Queensland University of Technology, GPO Box 2434, Brisbane QLD 4001, Australia, Feb 2001.
- [8] E. Fisher, B. Rafaely, Near-field spherical microphone array for speech, France, May 2010.
- [9] S. Doclo, M. Moonen, “Superdirective beamforming robust against microphone mismatch”, Katholieke Universiteit Leuven, Dept. of Electrical Engineering (ESAT-SCD), Kasteelpark Arenberg 10, 3001 Leuven, Belgium.
- [10] J. McDonough, “Generalized Sidelobe Canceller”, Spoken Language Systems Saarland University, Jan 2009.

MIPFD Algorithm for Image Fire Detection

Bojan Prlinčević¹, Zoran Milivojević², Darko Brodić³

Abstract – Image Processing Fire detection (IPFD algorithm) and its modification in the part of detection of fire pixel is described in the first part of the paper. The second part of the paper presents the testing of MIPFD algorithm efficiency during the detection of fire pixels. The results of testing are presented both in tables and graphics. Finally, the comparative analysis with IPFD algorithm was conducted.

Keywords – Fire detection, RGB model, Test image, Image processing, Chromatic feature.

I. INTRODUCTION

Fire is a hazard inflicting enormous damage in all spheres of the society, ecological systems (a significant factor in environmental protection because it causes great ecological damage), infrastructure and human lives [1]. Therefore, an early detection of fire and fast reaction for its extinguishing is very important. Due to rapid development of technology of digital cameras and digital image processing and video content, there is a strong tendency to conventional systems (fire detection sensors, thermometers etc.) be replaced by computer system of fire detection by digital image processing [2].

Success of fire detection greatly depends on implemented algorithm. There is a large number of proposed algorithms for fire detection in which in detection process the analysis of color image is performed. Fire detection process implies value analysis of luminance and chrominance characteristics of each pixel and accordingly the classification of fire pixels. During the classification an errors can occur (positive and negative errors), which in final balance determines the performances of the algorithm. Errors imply the following decisions: a) there is fire-detection says there is no fire and b) there is no fire-detection says there is fire, (while correct detection implies fire detection when there is really a fire). The quality of the algorithm can be described by percentage success of properly detected fire pixels.

During the analysis of color images a few systems are used; presentation of images, RGB (Red, Green, Blue), YUV and YCrCb. In the paper [3] for fire detection the YUV model is used for presentation of video content, where Y component is used for identification of potential fire pixel, while final decision is made according to U and V components. In the paper [4] normalized RGB values for formation of generic model of flame are used. Generic model is obtained by usage of statistic analysis conducted in R-G, R-B and G-B region.

Pixel is qualified as fire pixel if found in the area of triangle

¹Bojan Prlinčević, Polytechnic School for vocational studies, Nušićeva 6, Zvečan, Serbia, E-mail: b.prlincevic@vts-zvecan.edu.rs.

²Zoran Milivojević, College of Applied Technical Sciences, A. Medvedeva 20, 18000 Nis, Serbia, zoran.milivojevic@vtsnis.edu.rs.

³Darko Brodić, University of Belgrade, Tehnicka faculty Bor, V. Jugoslavije 2, 19210 Bor, Serbia, E-mail: d.brodic@tf.bor.ac.rs.

defined by three lines R-G, R-B and G-B. In regard to YUV algorithm from [3], RGB algorithm from [4] provides mitigation of the effect in the changes of luminance component Y. In the paper [5] was proposed algorithm for fire and smoke detection by analyzing YC_bC_r components of the image. This algorithm has a very high success rate of detection fire pixels.

In this paper is proposed an algorithm for image fire detection that was created by modifying the Image Processing Fire Detection (IPFD) algorithm [6]. Modified, MIPFD (*Modified Image Processing Fire Detection*) algorithm has been tested by images processing from the image database [7]. Also, for the needs of comparison with IPFD algorithm, the original Test image was created. For the purpose of efficiency of proposed MIPFD algorithm, the Test image was created, which consists of 36 fields grouped in three units: a) 12 fire segments, b) 12 smoke segments and c) 12 segments with no fire and smoke. Obtained results are compared with results obtained in the paper [6].

The paper is organized in the following way: section II describes algorithms IPFD and MIPFD; section III describes testing results and comparative analysis. Conclusion is given in section IV.

II. ALGORITHMS

A. IPFD algorithm

Analyzed IPFD algorithm for detection of fire pixels in image can be executed in the following steps:

Input: RGB image $X_{M \times N}$.

Output: Fire_Flag (1 fire, 0 no fire).

Step 1:

```

FOR x=1:M
  FOR y=1:N
    IF (R(x,y)>G(x,y)>B(x,y)) & (R(x,y)>Sr1 & ...
      R(x,y)<Sr2 & G(x,y)>Sg1 & G(x,y)<Sg2 & ...
      B(x,y)>Sb1 & B(x,y)<Sb2);
      R1(x,y)=1;
    IF R(x,y)>=Cb(x,y)&(Cr(x,y)>=Cb(x,y)) ...
      & (Y(x,y)>=Ymean) & Cb(x,y)<=Cbmean & ...
      Cr(x,y)>=Crmean & (|Cb(x,y)-r(x,y)|>=Th) ...
      & (Cb(x,y)<=Scb & Cr(x,y)>=Scr);
      R2(x,y)=1;
    ELSE
      R2(x,y)=0;
    END
  ELSE
    R1(x,y)=0;
  END
ENDy
ENDx
    
```

Step 2:

```

Fire_Flag=0;
FOR x=1:M
  FOR y=1:N
    IF R1(x,y)==1 & R2(x,y)==1;
      Fire_Flag=1;
    END
  END
END.

```

Y, C_b and C_r components are generated from RGB components by transformation:

$$\begin{bmatrix} Y \\ C_b \\ C_r \end{bmatrix} = \begin{bmatrix} 0.2568 & 0.5041 & 0.0979 \\ -0.1482 & -0.2910 & 0.4392 \\ 0.4392 & -0.3678 & -0.0714 \end{bmatrix} \begin{bmatrix} R \\ G \\ B \end{bmatrix} + \begin{bmatrix} 16 \\ 128 \\ 128 \end{bmatrix}, \quad (1)$$

where Y luminance, C_b Chrominance Blue and C_r Chrominance Red components.

Values S_{r1}, S_{r2}, S_{g1}, S_{g2}, S_{b1}, S_{b2}, S_{cb} and S_{cr} are determined by using histograms of R, G, B, Cr and Cb components. Value Th was experimentally determined and presents the value in which the relation of correctly detected and false detected fires the highest.

Mean values of components Y, C_b, C_r designated as Y_{mean}, C_{b_mean} and C_{r_mean} have been calculated in the following way:

$$Y_{mean} = \frac{1}{M \times N} \sum_{x=1}^M \sum_{y=1}^N Y(x, y), \quad (2)$$

$$C_{b_mean} = \frac{1}{M \times N} \sum_{x=1}^M \sum_{y=1}^N C_b(x, y), \quad (3)$$

$$C_{r_mean} = \frac{1}{M \times N} \sum_{x=1}^M \sum_{y=1}^N C_r(x, y). \quad (4)$$

B. MIPFD algorithm

Applied IPFD algorithm has been modified in the part of decision making and detecting of fire pixels. First step is detecting of fire, it is detected if value of difference Cb and Cr is greather then Th. If conditions in step two are fulfil the fire is confirmed. Modified algorithm is executed in the following steps:

Input: RGB image X_{MxN}.

Output: Fire_Flag (1 fire, 0 no fire).

Step 1:

```

R1(1:M,1:N)=0;
FOR x=1:M
  FOR y=1:N
    IF (|Cb(x,y) - Cr(x,y)|>=Th);
      R1(x,y)=1;

```

```

ELSEIF (R(x,y)<1.3*G(x,y) | (Cr(x,y)>Scr2) | ...
(Cb(x,y)>Scb2));
  R1(x,y)=0;

```

```

END
END
ENDy

```

END_x

step 2:

```

Fire_Flag=0;
FOR x=1:M
  FOR y=1:N
    IF R1(x,y)==1;
      Fire_Flag=1;
    END
  END

```

END

END.

III. EXPERIMENTAL RESULTS AND ANALYSIS

A. Experiment

For the purpose of determination of IPFD (section II.A) and MIPFD (section II.B) algorithms, the experiment has been conducted within which the image processing from image database and purposefully created Test image was executed. Comparison of Test image and processing results of Test image, in accordance with hypothesis (fire, no fire) and outcomes of the tests, the following is determined: TP (True Positive), FP (False Positive), TN (True Negative) and FN (False Negative) (Table I). By comparative analysis of TP, FP, TN, FN the decision on efficiency of algorithm has been made. The processing has been made for different values of Th.

TABLE I
THE PRINCIPLE OF ERROR CLASSIFICATION

		Real	
		Fire	No fire
Detected	Fire	(TP) True Positive	(FN) False Negative Negative
	No fire	(FP) False Positive	(TN) True Negative

B. Image database

The following is used in experiment a) image database [7] and b) Test image containing 36 fields grouped in three units: a) 12 fire segments, b) 12 smoke segments and c) 12 segments with no fire and smoke.

C. Results

Fig. 1 displays Test image and testing results of Test image for: a) Th=30, b) Th=65 i c) Th=90. Fig. 2 displays visual results of detection efficiency of fire pixels, image X1, by algorithms IPFD and MIPFD and R, G, B, Y, C_b and C_r components.

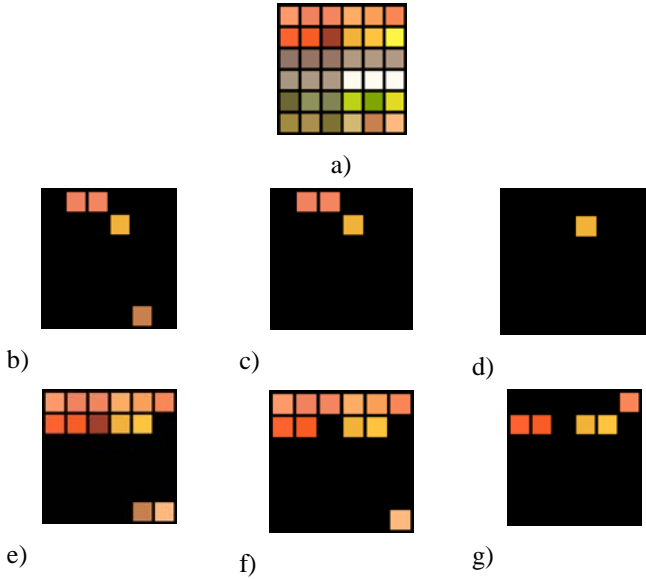


Fig. 1. a) Test image and results of processing of Test image: b) for Th=30 (IPFD), c) for Th=65 (IPFD), d) for Th=90 (IPFD), e) for Th=30 (MIPFD), f) for Th=65 (MIPFD), g) for Th=90 (MIPFD)

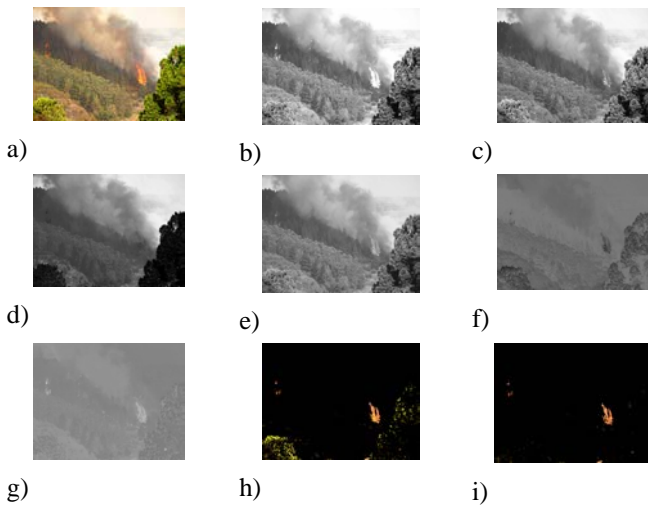


Fig. 2. Results of processing of fire image X1: a) original image, b) R-component, c) G-component, d) B-component, e) Y- component, f) C_b- component, g) C_r- component, h) fire image (IPFD) and i) fire image (MIPFD) for Th=65

Fig. 3 displays visual results of detection efficiency of fire pixels, image X2 and X3, by algorithms IPFD and MIPFD.

Results of TP, FP, TN and FN depending on Th for both algorithms are graphically presented on Fig. 4. Diagrams displayed on Fig. 5. are presented FP, TP, FN, TN of applied algorithms depending on Th. Percentage values of TP, FP, TN and FN depending on Th for algorithms IPFD and MIPFD are given in Table II.

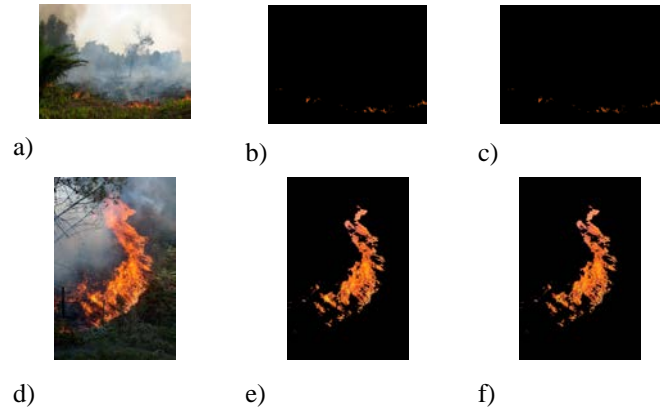


Fig. 3. Results of fire image processing X2 and X3: a) original image-X2, b) fire image-X2 (IPFD), c) fire image-X2 (MIPFD), d) original image-X3, e) fire image-X3 (IPFD) and f) fire image-X3 (MIPFD), for Th=70

TABLE II
PERCENTAGE VALUES OF TP, FP, TN AND FN DEPENDING ON TH FOR IPFD AND MIPFD ALGORITHMS

Algorithm	Error	Th							
		0	10	20	30	40	50	55	60
IPFD	TP	25	25	25	25	25	25	25	25
	FP	75	75	75	75	75	75	75	75
	FN	4,2	4,2	4,2	4,2	4,2	4,2	4,2	4,2
	TN	95,8	95,8	95,8	95,8	95,8	95,8	95,8	95,8
MIPFD	TP	91,7	91,7	91,7	91,7	91,7	91,7	91,7	91,7
	FP	8,3	8,3	8,3	8,3	8,3	8,3	8,3	8,3
	FN	16,7	16,7	16,7	8,3	8,3	8,3	8,3	8,3
	TN	83,3	83,3	83,3	91,7	91,7	91,7	91,7	91,7
		65	70	75	80	85	90	95	100
IPFD	TP	25	25	25	25	8,3	8,3	8,3	0
	FP	75	75	75	75	91,7	91,7	91,7	100
	FN	4,2	0	0	0	0	0	0	0
	TN	95,8	100	100	100	100	100	100	100
MIPFD	TP	91,7	83,3	83,3	83,3	58,3	41,7	33,3	25
	FP	8,3	16,7	16,7	16,7	41,7	58,3	66,7	75
	FN	8,3	4,2	0	0	0	0	0	0
	TN	91,7	95,8	100	100	100	100	100	100

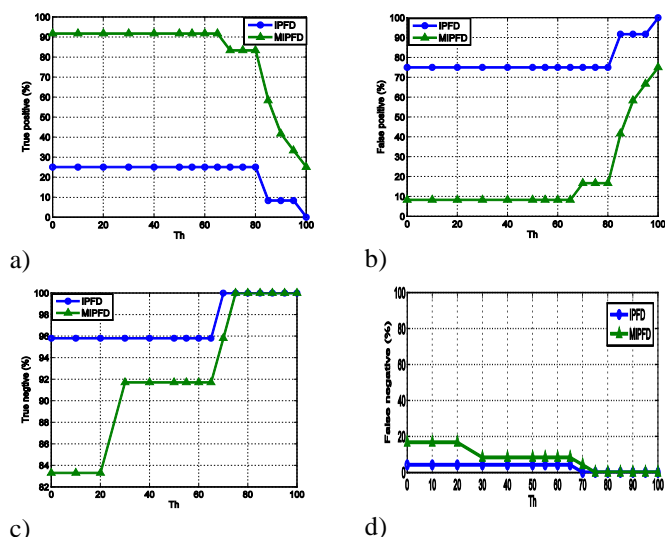


Fig. 4. Dependence diagram of TP, FP, TN, FN parameters of applied algorithms depending on Th: a) True Positive, b) False Positive, c) True Negative i d) False Negative

D. Analysis of results

According to results presented on Figs 1-4 and Table II, the following can be concluded:

a) optimal value is $Th=65$, which can be concluded according to Table II,

b) the percentage of successfully detected fire pixels (TP) is significantly better at MIPFD algorithm. At $Th=65$, the percentage of successfully detected fire pixels is 91.7%, and in analyzed IPFD algorithm the percentage of successfully detected fire pixels is 25%.

c) the percentage of false detected fire pixels (FP) in MIPFD algorithm at $Th=65$ is 8.3%, and in IPFD algorithm the percentage of false detected pixels is 75%.

d) the percentage of successfully detected pixel (TN) of environment in MIPFD algorithm at $Th=65$ is 91.7%, and in IPFD algorithm 95.8%, and with the increase of $Th=75$ the percentage of successfully detected pixels of the environment increases up to 100%.

e) percent of false detected pixels (FN) of the environment in MIPFD algorithm at $Th=65$ is 8.3%, and in IPFD algorithm is 4.2% and with the increase of $Th=75$ the percentage of false detected pixels of the environment decreases to 0% in MIPFD algorithm.

According to previous analysis it can be concluded that MIPFD algorithm is more efficient than IPFD algorithm. In addition, its numerical complexity is significantly smaller, and therefore is suitable for implementation into systems for real time operation.

IV. CONCLUSION

The efficiency of the proposed MIPFD algorithm for detection of fire pixels in the image was analyzed in the paper. Analysis was conducted for Test image at varying $Th=0-100$. The optimal value for $Th=65$ has been determined. Thorough analysis of the parameters for detection of fire pixels in the image has shown an extreme efficiency of MIPFD algorithm. In analyzed Test image, at $Th=65$ (optimal value) the fire pixel (TP) was successfully detected in 91.7%, of the cases, which is for 66.7%, better result comparing to analyzed IPFD algorithm. Also, MIPFD algorithm demonstrated extreme efficiency in detecting environment (TN) and false fire pixels (FP), the efficiency of MIPFD algorithm has been significantly improved in detecting of false fire pixels (FP) compared to IPFD algorithm. Due to its efficiency and small numerical complexity MIPFD algorithm is suitable for implementation into systems for real time operation.

REFERENCES

- [1] J.R. Gonzalez, M. Palahi, A. Trasebores, T. Pukkala, "a fire probability model for forest stands in Cataonia (north-east Spain)", *Annals of Forest Science*, pp.169-176, 2006.
- [2] E. Kuhrt, J. Knollenberg, V. Mertens. "An Automatic Early Warning System for Forest Fires", *Annals of Burns and Fire Disasters*, vol. XIV, pp. 151-154, 2001.
- [3] G. Marbach, M. Leopfe, T. Brupbacher, "An image processing technique for fire detection in video images", *Fire Saf. J.* 41 (4), pp 285-289,2006.
- [4] T. Celik, H. Demirel, H. Ozkaramanli, "Automatic Fire detection in video sequences", *Proceedings of European Signal Processing Conference*, September 2006.
- [5] T. Celik, H. Demirel, H. Ozkaramanli, "Fire and smoke Detection without Sensors: Image Processing Based Approach", *Proceedings of 15th European Signal Processing Conference*, Poland, September 3-7, 2007.
- [6] V. Vipin, "Image Processing Bassed Forest Fire Detection", *International Journal of Emeging Technology and Advanced Engineering*, ISSN 2250-2459, Vol.2, Issue 2, February 2012.
- [7] Forest fire images: <http://www.flickr.com>.

Image Edge Detection as Part of the Feature Extraction for Neural Network Realized with LabVIEW Application

Liljana Docheva¹

Abstract – Edge detection is often used in the areas of machine vision, intelligent systems, object recognition etc. This article presents a short introduction to convolution implementation for edge detection using Labview. Labview block diagram for implementation of different two-dimensional convolution kernels, applied to test images, is given. The behaviour of the kernels is investigated in case of the coefficients value in order to improve the quality of edge detection. The obtained results are presented and discussed.

Keywords – Image processing, Local operators, Edge detectors, Convolution kernels, Convolution matrix, Labview.

I. INTRODUCTION

Image data are very high dimensional. For this reason, feature extraction is often a necessary step before neural network training for successful object recognition. The goal of feature extraction is to find a subset of variables based on image data. One can present to the neural network inputs for learning speed increasing. When it's used neural network for object recognition it's necessary to extract those features that preserve the class separability well [1], [8]. Edges are very important feature in image recognition problem and often are used like one of the relevant features.

There are various program applications that provide an environment for implementation of different digital signal processing tools. Each of them has their own characteristics and advantages. LabVIEW is measurement and automation programming language that allows construction of different architectures by building different virtual instruments. Because of ability to develop data flow that are highly parallel in structure LabVIEW can be successfully used for building neural networks [3].

In this article is described image edge detection with different two-dimensional convolution kernels. The aim of this research is to explore the most appropriate operators for realization by means of LabVIEW. These operators will be applied in neural network realized for image processing with LabVIEW [3].

II. CONVOLUTION BASED OPERATORS FOR EDGE DETECTION

There are too many ways to perform edge detection: fuzzy logic based algorithms, local operators, wavelet based

algorithms and other. Wavelet based techniques characterize the nature of the transition for each edge in order to distinguish different types of edges. Local operators are applied to the input image to create the output image with pixels, obtained as weighted combination of the input pixels in the neighborhood. This article describes the most common methods - gradient and Laplacian. The gradient method searches for maximum and minimum in the first derivative of the image. The Laplacian method is looking for zerocrossings in the second derivative of the image [5], [7].

This article describes the most common methods - gradient and Laplacian. The gradient method searches for maximum and minimum in the first derivative of the image. The Laplacian method is looking for zerocrossings in the second derivative of the image [5], [7].

Convolution is an important operation that is used to decide various image processing problems. Two dimensional convolution is defined as follows [6]:

$$R(i, j) = \sum_{m=-N}^N \sum_{n=-N}^N I(m, n)K(i - m, j - n), \quad (1)$$

where $I(m, n)$ is a pixel of the input image with coordinates (m, n) . Correspondingly $R(i, j)$ is a pixel of the resulting image with coordinates (i, j) and $K(i-m, j-n)$ is the convolution kernel.

The Laplacian $L(i, j)$ of an image is given by [4]:

$$L(i, j) = \frac{\partial^2 I}{\partial i^2} + \frac{\partial^2 I}{\partial j^2}, \quad (2)$$

where $I(i, j)$ are the pixel intensity values.

III. EDGE DETECTION WITH LABVIEW

Fig. 1 depicts one way to build block diagram of edge detector, realized with LabVIEW.

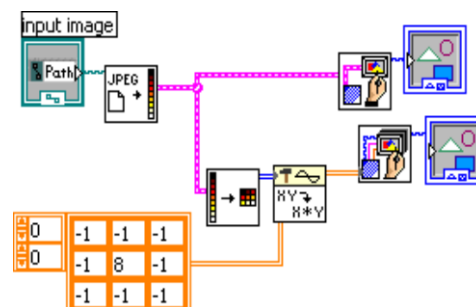


Fig. 1. Block diagram of edge detector realized with LabVIEW

¹Liljana Docheva is with the Faculty of Telecommunications at Technical University of Sofia, 8 Kl. Ohridski Blvd, Sofia 1000, Bulgaria.

In order to realize the kernel, the convolution virtual instrument is used. For edge detection implementation the following virtual instruments are still required:

- Read JPEG File to read a JPEG file,
- Unflatten Pixmap to converts a cluster of image data into a 2D array,
- Draw Flattened Pixmap to draw a 24-bit RGB pixmap into a picture,
- Draw Unflattened Pixmap to convert a pixmap into a picture image.

For edge detector testing the image with inhomogeneous background and with noise is used. One is shown in Fig. 2. Two-dimensional convolution kernels are applied.



Fig. 2. Input image for edge detector

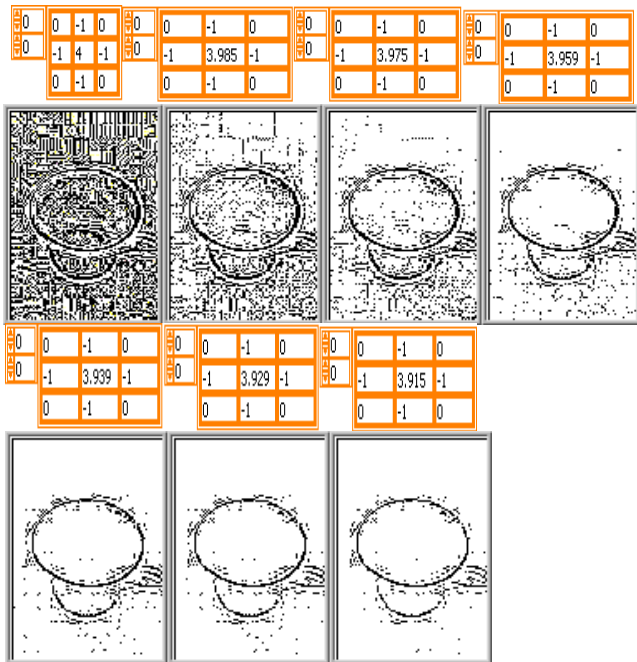


Fig. 3. The results of the Labview realization of the first Laplacian operator application for edge detection.

Laplacian operator application for edge detection.

The results of the first edge operator application are presented in Fig. 3. From the Fig. 3 first picture can be seen the LabView implementation of Laplacian filter don't give satisfactory results, when the image is with added noise. With modified filter coefficients the resulting image edge detection is improved. From the next six Fig. 3 pictures can be seen the relationship between the filter coefficients decrease and edge detection improvement. When filter coefficients decrease (Fig. 3 from left to right), reducing of false edges is observed.

Further reduction of the coefficients would cause the contours rupture. From the seven operators shown in Fig. 3, the last is best suited for neural netlork application, because of reducing of false edges.

The second Laplacian operator application to the test image is shown in Fig. 4. In this case the more filter coefficients decrease is required for the false edges decrease (Fig. 4 from left to right). It can be seen that the seventh operator is best suited for neural netlork application.

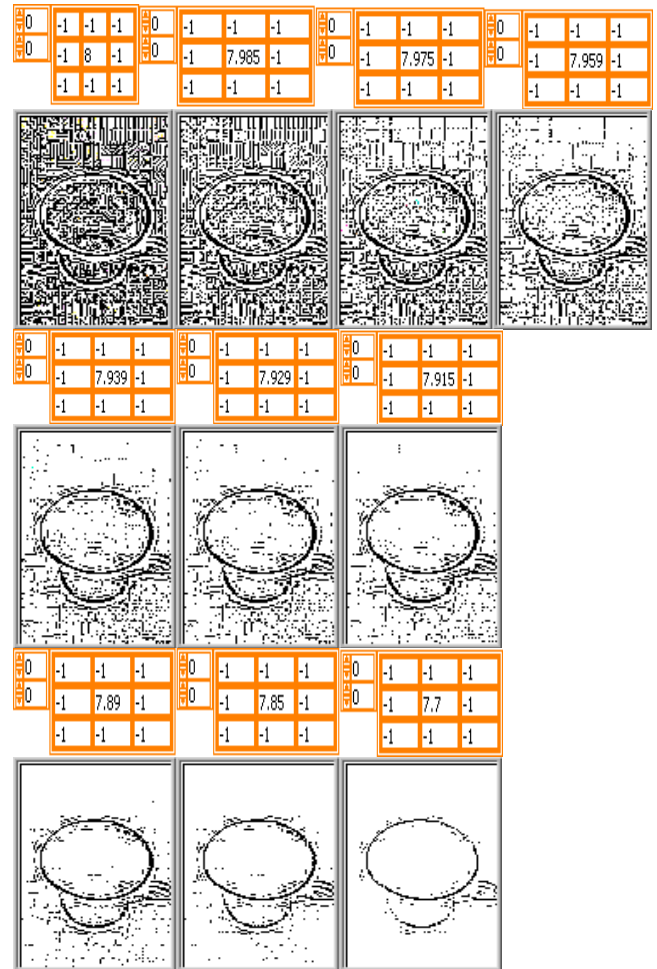


Fig. 4. The results of the Labview realization of the second Laplacian operator for edge detection

The third Laplacian operator application to the test image is shown in Fig. 5. It is easy to see that the decreasing of the coefficients causes the contours rupture. Therefore, these operators are not appropriate for neural netlork application.

These results can be compared with those obtained with the Sobel operator. Fig. 6 depicts the results of the Sobel operator and the modified Sobel operator edge detection. The first two pictures (from left to right) show the effect of the horizontal and vertical lines separation respectively. The third picture presents the combined image. It can be seen from the next six pictures that application of experimentally obtained modified Sobel operator results in false edges reduction, but in the last modified operator contours rupture is observed. Therefore one is not quite suitable for neural network application.

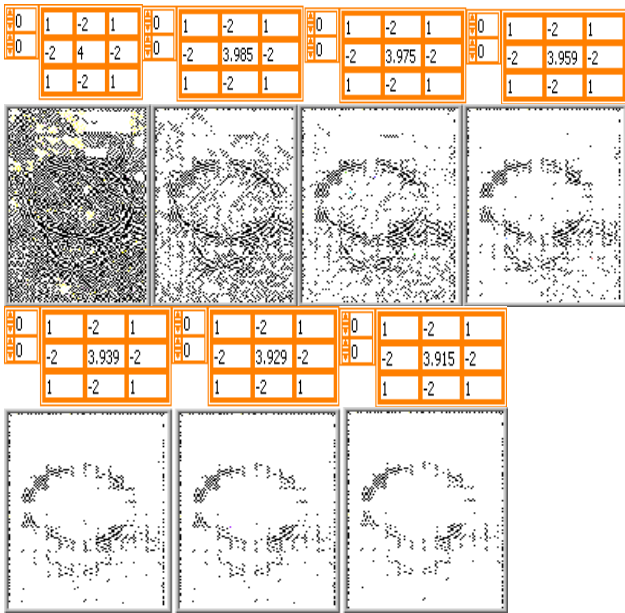


Fig. 5. The results of the Labview realization of the third Laplacian operator for edge detection

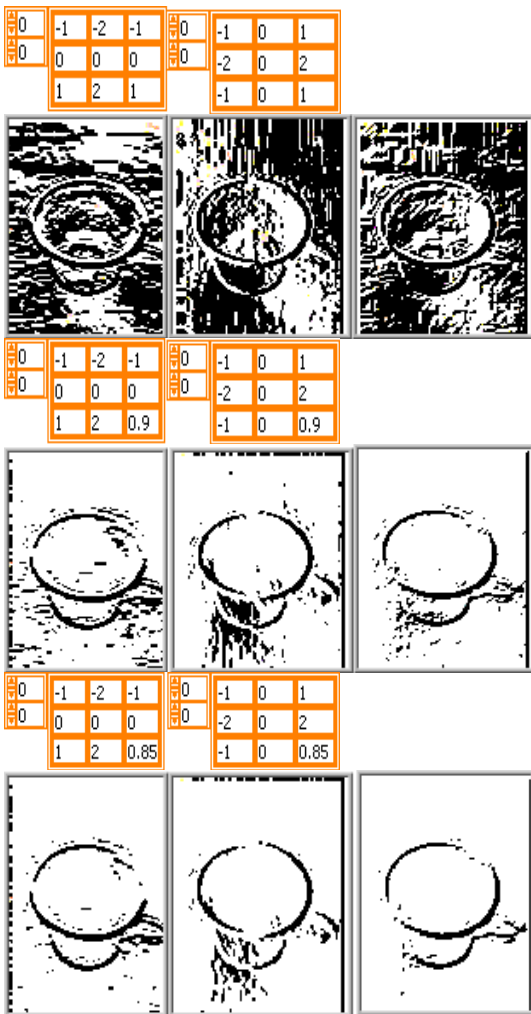


Fig. 6. The results of the Labview realization of the Sobel operator for edge detection

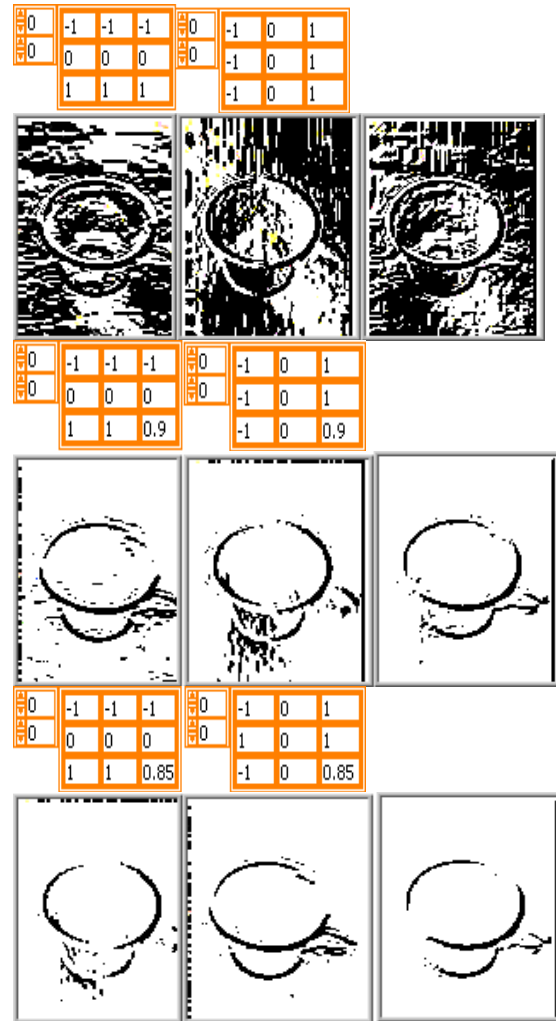


Fig. 7. The results of the Labview realization of the Prewitt operator for edge detection

The separated edges with the Prewitt operator and the modified Prewitt operator are shown in Fig. 7. The results are similar to that obtained by the Sobel operator. Modified Prewitt operator is not quite suitable for neural network application because of contours rupture is observed.

From Figs. 6 and 7 comparison is observed more visible contours rupture for modified Prewitt operator.

From the results shown above can be seen that LabView implementation of the first two Laplacian filters after modification (Fig. 3 and Fig. 4) are most appropriate to be applied to the neural network, realized with LabVIEW. They can be used for feature detection or other image processing purpose.

IV. CONCLUSION

In this article LabView implementation of two-dimensional convolution kernels is presented. There are detected edges of image with inhomogeneous background and added noise. The first case the Laplacian filter detects edges better than the others considered local operators. But the presence of noise

and inhomogeneity in image background strongly affects the quality of edge detection.

It is shown that, a little modification of the LabView implemented convolution kernels coefficients is sufficient to improve the quality of the edge detection. But for the third Laplacian operator (Fig. 5) the decreasing of the coefficients causes the contours rupture. Contours rupture is observed in modified Prewitt operator (Fig. 7) and modified Sobel operator (Fig. 6) too. Therefore, these operators are not appropriate for neural network application.

The most appropriate operators for neural network, realized with LabVIEW application are the first two Laplacian filters after modification (Fig. 3 and Fig. 4). Ones will be applied to the neural network realized with LabVIEW for image recognition purpose.

REFERENCES

- [1] M. Egmont-Petersen, D. de Ridder, H. Handels, "Image processing with neural networks—a review", *Pattern Recognition* 35 (2002), pp. 2279–2301.
- [2] Ch. Relf (2003), *Image acquisition and processing with LabVIEW*, CRC Press, 2004
- [3] L. Docheva, A. Bekjarski, "Implementation of Analog Neural Networks with Labview", XLVII International Scientific Conference Information, Communication And Energy Systems And Technologies, vol: 2, pp. 367 – 370, June 28-30, Veliko Tarnovo, Bulgaria, 2012.
- [4] R. Maini, H. Aggarwal, "Study and Comparison of Various Image Edge Detection Techniques", *International Journal of Image Processing (IJIP)*, Volume (3) : Issue (1).
- [5] D. Rao, S. Patil, N. Babu, V. Muthukumar, "Implementation and Evaluation of Image Processing Algorithms on Reconfigurable Architecture using C-based Hardware Descriptive Languages", *International Journal of Theoretical and Applied Computer Sciences*, GBS Publishers and Distributors (India) Volume 1 Number 1, 2006, pp. 9–34.
- [6] R. Ingold, *Image Processing: Local Operators*, 2004.
- [7] G.T. Shrivakshan, C. Chandrasekar, "A Comparison of various Edge Detection Techniques used in Image Processing", *IJCSI International Journal of Computer Science Issues*, Vol. 9, Issue 5, No 1, September 2012, pp. 269-276.
- [8] I. Draganov, A. Popova, "Handwritten word segmentation combining self-organizing neural networks and heuristic rules", In *Proceedings of the Technical University – Sofia, Bulgaria*, Vol. 57, No. 1, pp. 148-153, 2007.

Digital Image Filtering with LabVIEW

Liljana Docheva¹

Abstract – Digital filters are indispensable tools for image processing. In this article an implementation of some local operators using Labview is considered. The local operators are used to perform image filtering. The results of the noise reducing and sharpening of the image are presented. Labview block diagram of different two-dimensional convolution kernels implementation that are applied to the test image is given. For the filter effect illustration the histograms of the resulting images are presented.

Keywords – image processing, local operators, digital filters, convolution kernel, convolution matrix, Labview.

I. INTRODUCTION

Image Filtering is an important operation for improving the image quality. Thus enables further image processing. For example in the cases of neural network image processing, it is desirable to filter the input image before neural network application to improve the recognition capability of the neural network. After processing the image have to present to the network. There are several ways to do this. Extracting features from the image (e.g. edges) is commonly used approach. These features present to the neural network inputs. On this way incorporating prior knowledge before neural network training is made. This leads to neural network learning speed increasing, but only if extracted features are correctly selected. One of the relevant features for image recognition are the edges. Image filtering can be used before edge detection to obtain reducing of false edges.

In this article is introduced implementation of digital filters for image processing with LabVIEW. These filters will be applied in neural network realized for image processing with LabVIEW. The filters are experimentally obtained. The investigation purpose is to find most appropriate filter for application to neural network realized with LabVIEW. From the one hand, this filter have to reduce image noise, from the other - essentially affect to the image is undesirable.

Two-dimensional convolution is used to implement local filters. The resulting image histograms are given to illustrate the filter effects in the output image.

II. IMAGE FILTERING

There are many methods for image filtering. Most important of them are based on operations convolution and correlation. With convolution a number of filtering operations using local kernels can be implemented. Correlation uses matching the image neighborhood with pattern or mask [1].

¹Liljana Docheva is with the Faculty of Telecommunications at Technical University of Sofia, 8 Kl. Ohridski Blvd, Sofia 1000, Bulgaria.

Image filtering, using local operators is used to perform smoothing, noise reducing, edge detection or sharpening. In this article is presented sharpening of the edges of image and noise reducing. Sharpening consists in isolating the edges and amplifying them and adding amplified edges back to the original image [2].

Image filtering, using local operators can be presented in Eq. (1).

$$R(x, y) = F\{I(x \pm \Delta x, y \pm \Delta y)\} , \quad (1)$$

where $I(x \pm \Delta x, y \pm \Delta y)$ is a pixel of the input image with coordinates $(x \pm \Delta x, y \pm \Delta y)$, correspondingly $R(x, y)$ is a pixel of the resulting image with coordinates (x, y) and F is an appropriate function. The output pixel is weighted combination of the gray values of pixels in the neighborhood of the input pixel. The size of the neighborhood and the pixel weights determine the action of the operator.

III. IMPLEMENTATION OF IMAGE FILTERING WITH LABVIEW

Fig. 1 depicts one way of block diagram building for image filtering, realized with LabVIEW.

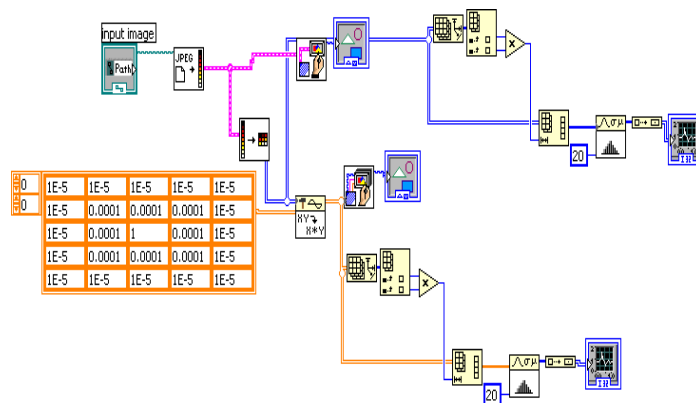


Fig.1. Block diagram of an image filtering implementation using LabVIEW

In order to realize the kernel, the convolution virtual instrument is used. For edge detection implementation the following virtual instruments are required:

- Read JPEG File to read a JPEG file,
- Unflatten Pixmap to converts a cluster of image data into a 2D array,
- Draw Flattened Pixmap to draw a 24-bit RGB pixmap into a picture,
- Draw Unflattened Pixmap to convert a pixmap into a picture image.

- Histogram to find the discrete histogram of the input sequence.

- Waveform Graph to display the histogram.

The histogram is created in order to point out the filter effect of the resulting images.

The test picture and image histogram are presented in Fig. 2. In purpose to perform noise reducing the local operators, shown in Figs. 3, 4 and 5 are used. Ones are experimentally obtained in order to find most appropriate filter for application to neural network realized with LabVIEW. The results can be seen too. The LabVIEW implemented filters coefficients increasing lead to image quality decreasing.

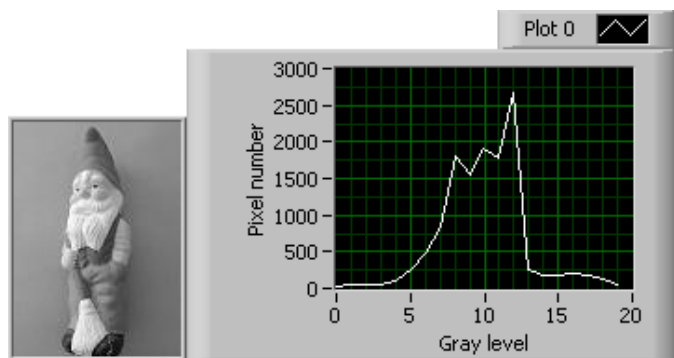


Fig. 2. Input image for image filtering and the corresponding histogram

0	1E-7	1E-7	1E-7	1E-7	1E-7
0	1E-7	1E-5	1E-5	1E-5	1E-7
	1E-7	1E-5	1	1E-5	1E-7
	1E-7	1E-5	1E-5	1E-5	1E-7
	1E-7	1E-7	1E-7	1E-7	1E-7

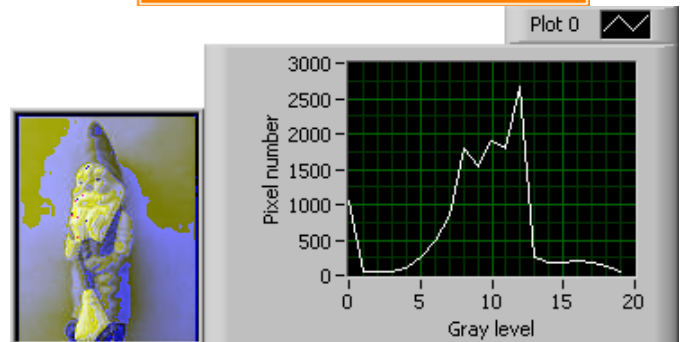


Fig. 4. Noise reducing

0	1E-6	1E-6	1E-6	1E-6	1E-6
0	1E-6	1E-5	1E-5	1E-5	1E-6
	1E-6	1E-5	1	1E-5	1E-6
	1E-6	1E-5	1E-5	1E-5	1E-6
	1E-6	1E-6	1E-6	1E-6	1E-6

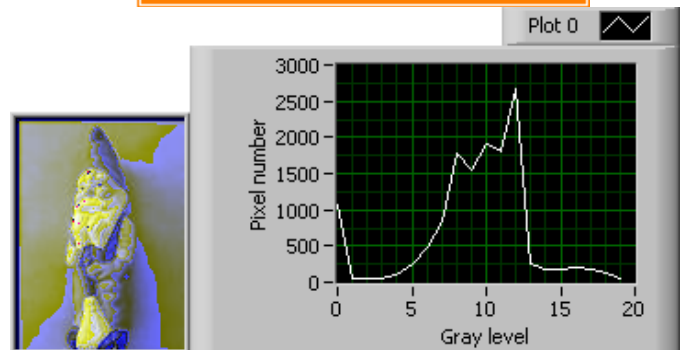


Fig. 5. Noise reducing

0	1E-9	1E-9	1E-9	1E-9	1E-9
0	1E-9	1E-7	1E-7	1E-7	1E-9
	1E-9	1E-7	1	1E-7	1E-9
	1E-9	1E-7	1E-7	1E-7	1E-9
	1E-9	1E-9	1E-9	1E-9	1E-9

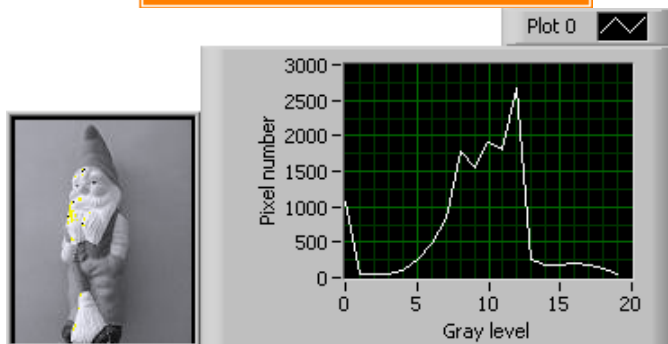


Fig. 3. Noise reducing

It can be seen from Fig. 4 that the LabVIEW implemented filters coefficients increasing lead to undesirable effects in the resulting image. Accordingly, Fig. 6 shows that very little increasing coefficients enhances this effect. Therefore, the filters shown in the Figs. 4 and 5 are not suitable for neural network application.

After image filtration the edges can be detected. The aim is to reduce the noises first and then to detect the edges. Fig. 6 depicts one way of block diagram building for edge detection after image filtering, realized with LabVIEW. For digital image filtering the first filter (Fig. 3) is used. It can be seen from Fig. 3 that this filter blur an image and so reduces noise. The results are presented in Figs. 7 and 8 for two different modified Laplas operators. The modification is made in order edge detection implemented with LabVIEW to give better results. The left picture is the result of the image filtering, the right one is the result of edge detection.

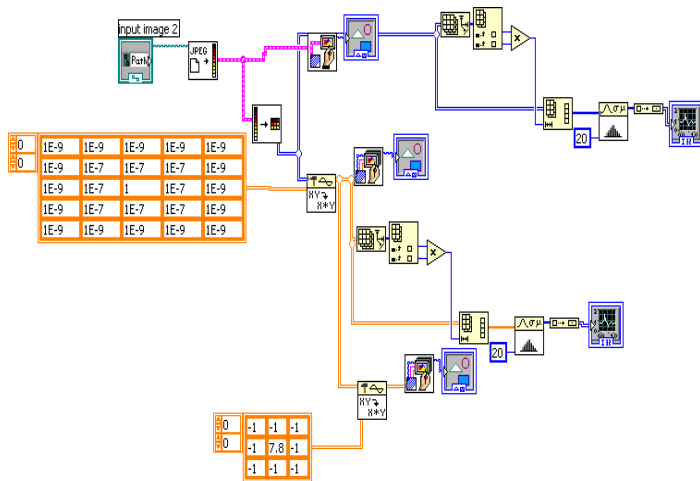


Fig. 6. Block diagram for edge detection after image filtering, realized with LabVIEW

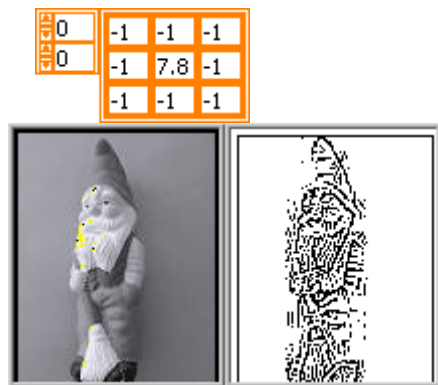


Fig. 7. Edge detection application after image filtering, realized with LabVIEW. The Laplas operator is shown at the top

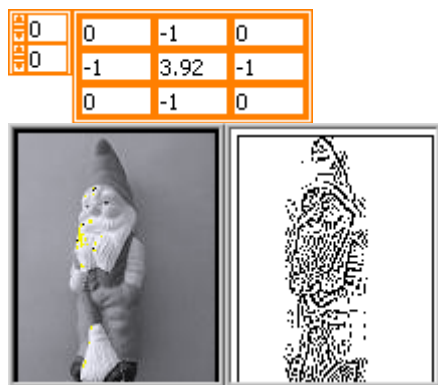


Fig. 7. Edge detection application after image filtering, realized with LabVIEW

The left picture from Figs. 7 and 8 is the result of image filtering, the right one is the result of edge detection.

The Block diagram of an image filtering implementation, using LabVIEW from Fig. 1 can be used for sharpening the edges of the image. One is obtained by means of the filters, presented in Figs. 8, 9 and 10. The results can be seen too.

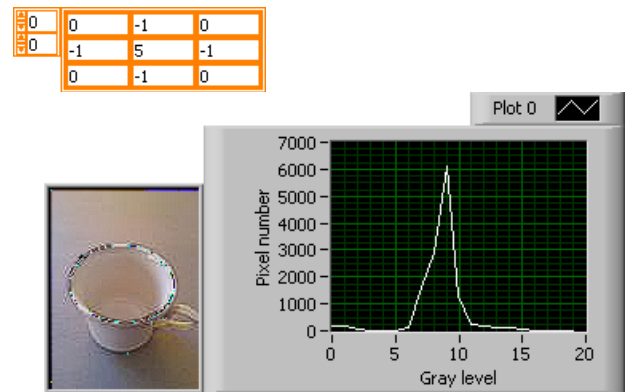


Fig. 8. Sharpening the edges of the image

Filters sharpen an image by enhancing the color contrast around edges in the image. Figs. 8, 9 and 10 show that increasing the LabVIEW implemented sharpen filters coefficients lead to image quality decreasing. From the figures can be seen the presence of the noiselements which are highly visible in Fig. 10.

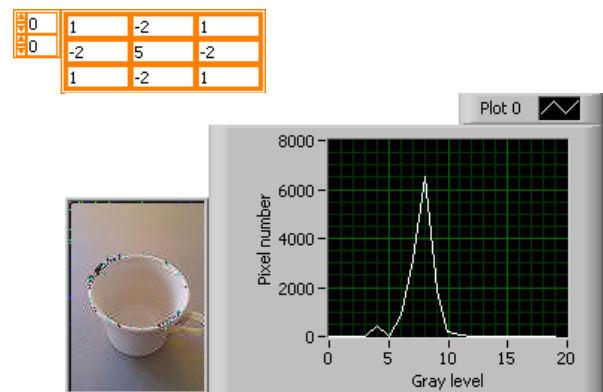


Fig. 9. Sharpening the edges of the image

From the filters investigated in this paper, most appropriate for application in neural network, realized for image processing with LabVIEW is the shown in Fig. 3 one.

This will be investigated in further research.

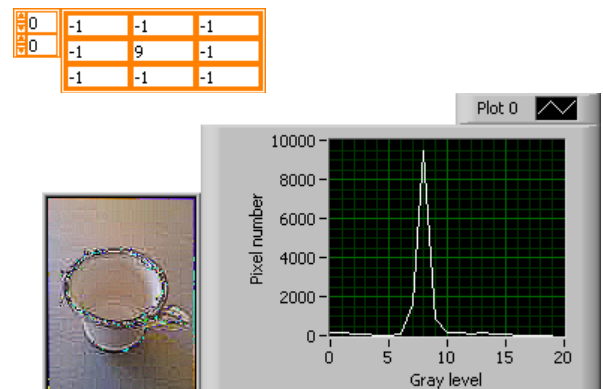


Fig. 10. Sharpening the edges of the image

IV. DIGITAL FILTER APPLICATION TO NEURAL NETWORK REALIZED WITH LABVIEW

In some articles have been successfully used LABVIEW for building neural networks [7], [8] because one has the ability to develop data flow that are highly parallel in structure. Therefore LABVIEW seems to be a very effective approach for building and investigating neural networks.

The first experimentally obtained filter (Fig. 3) will be applied in neural network realized for image processing with LabVIEW [6]. After processing the image can be presented to the network. The image values can be put into input vector and feed this vector into the network. Another way for neural network image presentation is by extracting features from the image and using them for neural network inputs. The presented in [6] neural network can be used in both cases. This will be the subject of further research.

V. CONCLUSION

In this article LabVIEW implementation of two-dimensional convolution kernels for image filtering is presented. With local operators sharpening of the edges of an image and noise reducing are performed. There can be seen the effects of the input image filtering by means of LabVIEW.

Two-dimensional convolution is used to implement local filters. The resulting image histograms are given to illustrate the filter effects in the output image.

It's studied which of these filters are appropriate to be applied in the neural network realized for image processing with LabVIEW. The first three filters are experimentally obtained. The investigation purpose is to find most appropriate filter for application to neural network realized with LabVIEW. It's shown that very little increasing

coefficients leads to undesirable effects in the resulting image (Fig. 4) and (Fig. 5). Therefore only the first of the presented three filters (Fig. 3) is suitable for neural network application.

Presence of the noise elements in the image can be seen in the Sharpening filters (Fig. 8), (Fig. 9), (Fig. 10). Therefore ones are not suitable for neural network application.

REFERENCES

- [1] Ch. Relf (2003), *Image acquisition and processing with LabVIEW*, CRC Press, 2004.
- [2] R. Maini, H. Aggarwal, "Study and Comparison of Various Image Edge Detection Techniques", *International Journal of Image Processing (IJIP)*, Volume (3) : Issue (1).
- [3] D. Rao, S. Patil, N. Babu, V. Muthukumar, "Implementation and Evaluation of Image Processing Algorithms on Reconfigurable Architecture using C-based Hardware Descriptive Languages", *International Journal of Theoretical and Applied Computer Sciences*, GBS Publishers and Distributors (India) Volume 1 Number 1, 2006, pp. 9-34.
- [4] R. Ingold, *Image Processing: Local Operators*, 2004.
- [5] G.T. Shrivakshan, C. Chandrasekar, "A Comparison of various Edge Detection Techniques used in Image Processing", *IJCSI International Journal of Computer Science Issues*, Vol. 9, Issue 5, No 1, September 2012, pp. 269-276.
- [6] L. Docheva, A. Bekjarski, "Implementation of Analog Neural Networks with Labview", *XLVII International Scientific Conference Information, Communication And Energy Systems And Technologies*, vol: 2, pp. 367 - 370, June 28-30, Veliko Tarnovo, Bulgaria, 2012.
- [7] J. Fernandez de Canete, S. Gonzalez-Perez, P. del Saz-Orozco, "Artificial Neural Networks for Identification and Control of a Lab-Scale Distillation Column using LABVIEW", *World Academy of Science, Engineering and Technology*, 2008.
- [8] M.A. Panait, T. Tudorache, "A Simple Neural Network Solar Tracker for Optimizing Conversion Efficiency in Off-Grid Solar Generators", *International conference on renewable energies and power quality (ICREPQ'08)*.2008.

Robustness of SVD Watermarks in Video Sequences Encoded with H.264/AVC

Zoran Milivojević¹ and Zoran Veličković²

Abstract – This paper analyzes the robustness of watermarks based on SVD transformation in order to protect the copyright of H.264 encoded video. The robustness of the CSP watermark has been tested with algorithm which performs extracting and thresholding of the watermark. A comparative results analysis, using the PSNR as a measure of quality, has been shown that robustness increase in the function of the number sampled bits in video sequence. The results indicate that the CSP algorithm can be successfully applied in professional video profiles defined H.264/AVC standard.

Keywords – Singular value decomposition, Digital watermark, H.264/AVC codec, Multimedia.

I. INTRODUCTION

The development of modern digital telecommunications networks and systems has led to a dramatic increase of the volume multimedia traffic [1]. Today's customers are particularly interested for new multimedia services such as VoIP (Voice over Internet Protocol), VoD (Video on Demand), IPTV (Internet Protocol Television), videoconferencing, etc. Viewing and sharing of digital video content in a wireless environment is extremely demanding services and require significant network resources [2]. For efficient use of video on the network, as well as its storage, it is necessary to apply specialized compression algorithms [3]. The latest ITU-T recommendations relating to the use of H.264 compression standards include both current as well as future video applications [4]. Recent application of this standard include HD video resolution and different sampling format. For professional application uses a larger number of bits per samples as well as higher resolution of sampling color. For the purposes of this, standard H.264/AVC has been expanded with new coding tools that are called the FRExt [5].

The global availability of multimedia contents over the Internet is resulted in the increase of their illegal use. Protection from illegal use that are based on hardware or software techniques have not bring satisfactory results. Many companies that are owners of video materials giving up on technical ways to protect and turning to legislation which regulates copyrights. In order to prove copyright over the video material, owners use algorithms to inserting invisible marks (watermarks) in video [6]. Algorithm for inserting the watermark should not cause visible degradation of the image, and it should be allow extracting of the watermark satisfactory

quality. The most common in use are the algorithms based on the transformation techniques such as DCT (Discrete Cosine Transform), FFT (Fast Fourier Transform) or SVD (Singular Value Decomposition). SVD is a transformation technique for inserting a watermark in the video, which is often used. This paper analyzes the robustness of CSP algorithms, [7] which belongs to the class of very robust SVD algorithms. Pursuant to the advanced capabilities H.264/AVC standard, is analyzed the robustness of encoded video sequences in function of number of bits per samples. The analysis was conducted with the video content which is sampled with 8 and 10-bits per samples and coded in accordance with the H.264/AVC standard. Extracted watermark and his binarized (thresholded) version are analyzed. The robustness of extracted and binarized watermark are evaluated by objective PSNR parameters. Higher PSNR value means that extracted watermark is a better quality, and the greater robustness of the CSP algorithm.

This paper is organized as follows. In Section II describes FRExt profiles of H.264 standard. In Section III is presented an algorithm for testing of the robustness of the watermark, while in section IV presents the results of experiments and comparative analysis of the results. In Section V, some conclusions about the robustness of CSP algorithm and avenues for further research are done.

II. FREXT PROFILES OF H.264/AVC STANDARD

H.264 video compression algorithms are based on removing redundant information from the videos, with the methods of prediction in time (temporal, inter) and space (spatial, intra). Powerful mechanism for research redundancy in the current picture and/or images that precede, or follow, is the basis of superior compression characteristics of H.264 encoder [3], [4]. Anticipating the content of some parts of the image based on the observed similarity, it is possible to form a residual frame with much less data. The consequence of this approach may be the neglecting of fine detail in the image, which will have a negative effect on the video quality. In addition to the negative effect on the video, neglecting fine detail reflects negatively on the quality of the injected watermark. In addition to the standard application of H.264/AVC encoder on the Internet, for professional applications this standard provides profiles that support more than 8 bits for sampling (10-14 bits). Also, this standard supports higher resolution for color representation (4:2:2 or 4:4:4). These profiles are known as FRExt. The influence of the number of bits in a video sample on the quality of the extracted and binarized watermark is discussed. On Fig. 1 is presented relationship between profiles of the H.264/AVC standard.

¹Zoran Milivojević is with College of Applied Technical Sciences, Nis, Serbia, A. Medvedeva 20, 18000 Niš, Serbia, E-mail: zoran.milivojevic@vtsnis.edu.rs

²Zoran Veličković is with College of Applied Technical Sciences, Nis, Serbia, Niš, A. Medvedeva 20, 18000 Niš, Serbia, E-mail: zoran.velickovic@vtsnis.edu.rs

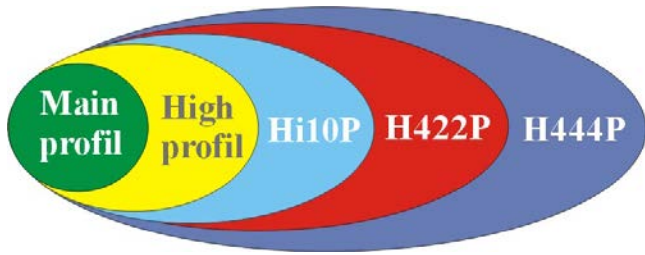


Fig. 1. FRExt expansion H.264/AVC standard

III. ALGORITHM FOR TESTING OF ROBUSTNESS

In this chapter is proposed algorithm for testing of the robustness of the watermark that is inserted in the video. Input, and output parameters of this algorithm are:

Input: Uncoded video sequence (A), watermark (W) and inserting factor α .

Output: Decoded video sequence (A_w^*), extracted watermark W^* , binarized watermark (W_b^*) and PSNR.

Algorithm for testing of the robustness consists of the following steps:

Step 1: Insertion of the watermark W in uncoded video sequence A with CSP algorithm and inserting factor α , thereby forming a video sequence A_w [8].

Step 2: Coding video sequences A_w with H.264/AVC coder and forming sequence $A_{w_H264}^*$.

Step 3: Decoding of sequence $A_{w_H264}^*$ with H.264/AVC decoder and forming video sequence A_w^* .

Step 4: Extract the watermark W^* from video sequence A_w^* with CSP algorithm.

Step 5: Forming watermark W_b^* with binarization algorithm.

Step 6: Calculation PSNR for W^* and W_b^* watermarks.

IV. EXPERIMENTAL RESULTS AND DISCUSSIONS

A. Experimental setup

For the purposes of assessing the robustness of CSP watermark is applied the algorithm described in Section III. The first frame of the test sequence is shown in Fig. 2a, while the mark is shown in Fig. 2.b. For comparison of the quality inserted watermark in the function of the number of bits in the sample, the test video sequence is used at the two sampling formats, as follows: 4:2:0 and 4:2:2. Format 4:2:0 is sampled with 8-bits, while the 4:2:2 format is sampled with 10 bits. In the video sequence (Fig 2a) is inserted the mark (Fig 2b), and after that is done encoding with H.264/AVC encoder. The watermark is inserted in each frame of uncompressed video



Fig. 2. Test sequence with resolution of 384x216 pixels: a) First frame of video-sequence and b) watermark

test sequences with the constant value of the inserting factor α . In the process of encoding/decoding is used Reference Software JM 18.4 software [9], [10] is running in MATLAB. This JM software represents an official version of ITU-T and support FRExt profiles. Coding of the protected video was done for a group of code parameters that define the code profile. The chosen parameters of H.264 coder in relation to had the following values:

- **8-bits:**

- ProfileIDC = 100* (FRExt Profile, *LevelIDC = 40*)
- IntraPeriod = 1,*
- NumberReferenceFrames = 1,*
- RateControlEnable = 0,*
- InitialQP = 28.*

- **10-bits:**

- ProfileIDC = 122* (FRExt Profile, *LevelIDC = 42*),
- IntraPeriod = 1,*
- NumberReferenceFrames = 1,*
- RateControlEnable = 0,*
- InitialQP = 28.*

After decoding video sequences, watermark is extracted and binarization algorithm is applied on him. In the process of extracting the watermark is coming to rounding errors that negatively affect the appearance of the extracted mark. This is reason to apply the binarization process. Binarization process of watermark is performed on the basis statistical analysis of the distribution of values of pixels, which are displayed with the histogram. The decision threshold in the binarization process is located midway between the maximum values of the intensity in the histogram. Examples of histograms obtained for each value of the parameter α are shown in Tab. III. From accuracy of determining the threshold depends the quality of the binarized watermark. The quality of extracted mark is evaluated by PSNR which gives an objective assessment of the quality of the mark, i.e., the robustness of the CSP algorithm.

B. Test sequences

In the video sequence of resolution 384x216 pixels (Fig. 2a) is inserted the mark with the same resolution (Fig. 2b). Uncompressed video sequence with inserted watermark is encoded using the H.264/AVC codec. The video-sequence which is used in the algorithm for testing the robustness of the CSP watermark is part of *Kimono1.yuv*. This sequence is sampled in both formats (4:2:0 and 4:2:2) and can be found at the URL: <ftp://hvc:US88Hula@ftp.tnt.uni-hannover.de/testsequences>.

TABLE I
EXTRACTED AN BINARIZED WATERMARKS, 8-BITS

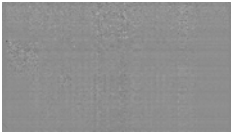
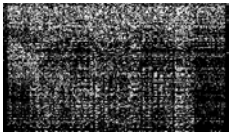






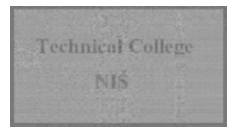
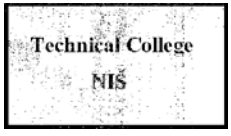
α	Extracted watermark W^*	Binarized watermark W_b^*
0.01		
0.02		
0.03		
0.04		
0.05		

TABLE II
EXTRACTED AN BINARIZED WATERMARKS, 10-BITS


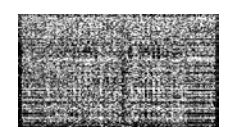



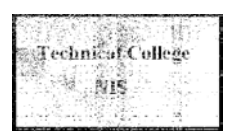

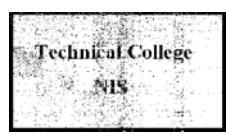
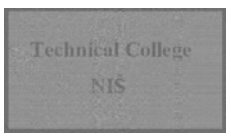
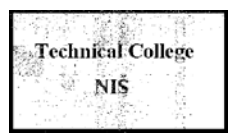
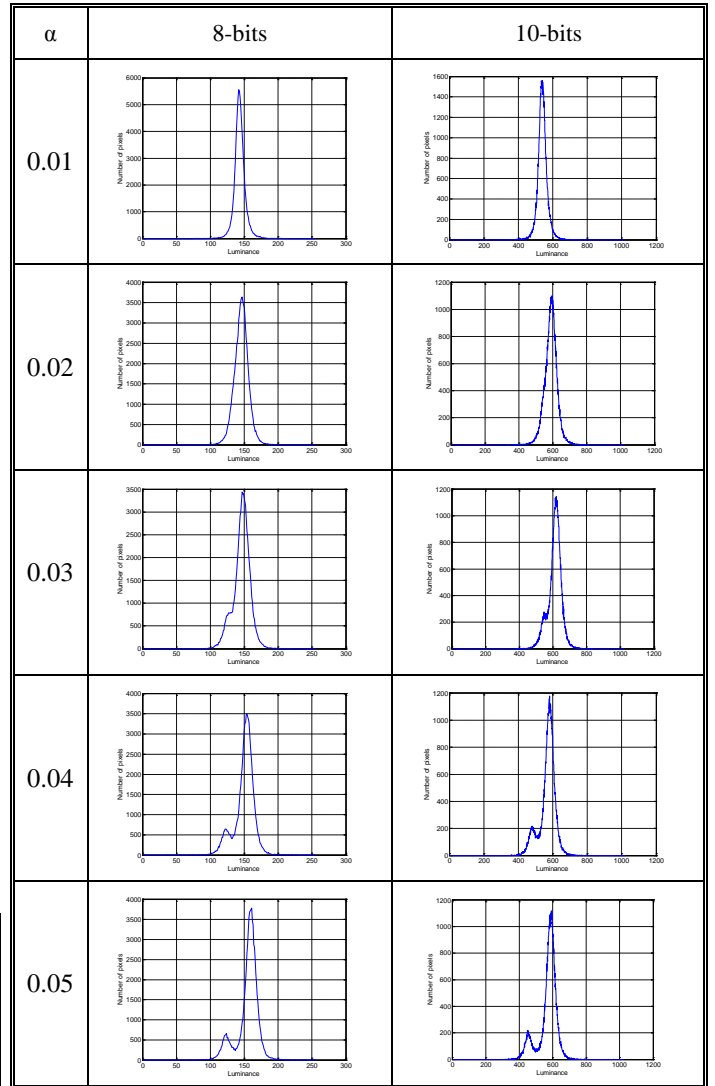
α	Extracted watermark W^*	Binarized watermark W_b^*
0.01		
0.02		
0.03		
0.04		
0.05		

TABLE III
HISTOGRAMS FOR EXTRACTED WATERMARKS FOR 8 AND 10 BITS



C. Results

Visual representation of extracted (W^*) and binarized (W_b^*) watermark are shown in Table I, for the video sequences encoded with 8 bits, and in Table II, for video sequences encoded with 10-bits. Histograms of extracted watermarks for 8-bits and 10-bits encoded sequence are shown in Table III. In cases where the histogram does not have a clear expressed peaks, binarization process has no significant effect on the quality of the watermark. PSNR values in function of insertig factor α , for the original and binarized watermark version when the video sequence is sampled with 8-bits, are shown in Fig. 3, while the PSNR values in function of insertig factor α , for the original and binarized watermark version when the video sequence is sampled with 10 bits, are shown in Fig. 4.

Based on the results shown in Tables I-III and Figures 3 and 4, it can be concluded that:

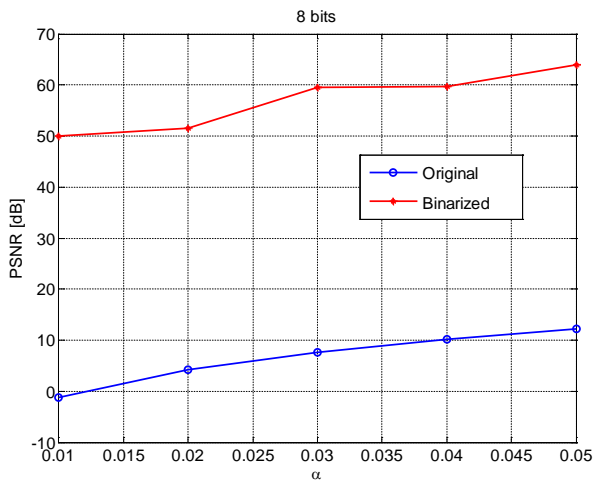


Fig. 3. PSNR as a function of inserting factors α for a) an original and b) binarized version of watermarks for 8-bits coding video-sequence

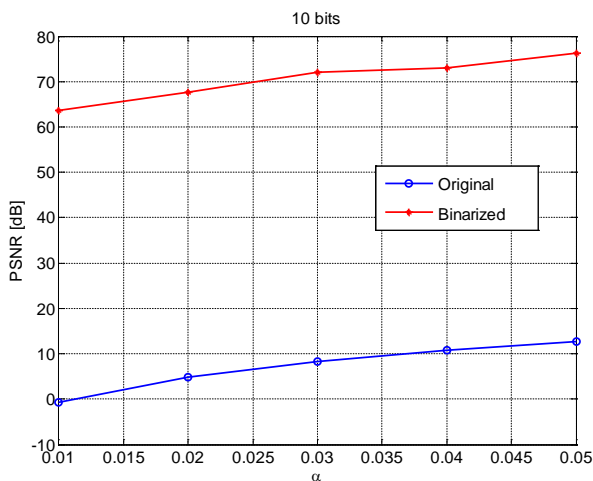


Fig. 4. PSNR as a function of inserting factors α for a) an original and b) binarized version of watermarks for 10-bits coding video-sequence

- With increasing inserting factor α , the quality of separated watermark leads to an increase in both analyzed length of codewords.
- The lower limit of visibility of the watermark for 8-bits is $\alpha=0.03$, and for 10-bits the boundaries is $\alpha=0.02$ (Tables I and II).
- With respect to PSNR, binarized version of the watermark is approximately 10dB higher in the sequence of 10-bits, than sequence compared to one with a 8-bits for all of the analyzed parameter α (Fig. 3 and 4).
- Binarized watermark gives a higher quality in the 8-bits (extracted watermark: from PSNR=0dB to 12dB; binarized watermark: from 50dB to 64dB) and 10-bits sequence (extracted watermark: PSNR=0dB to 12.5 dB, binarized watermark: from 62dB to 76dB).
- PSNR for binarized watermark in 10-bits is an average of 12dB higher than watermark by 8-bits.

- The upper limit of the inserting factor is set to $\alpha=0.05$ and represents the limit of significant degradation of the video.
- The quality of the watermark represented by means of a PSNR (Fig. 3 and 4), separated from the video sequence sampled with 10-bits, is increased compared to the watermark extracted from the sampled sequence of 8-bits.

V. CONCLUSION

Based on the experimental results presented in this study it can be concluded that the resistance of the watermark in H.264 encoding depends on the number of bits which is sampled video. This is the consequence of rounding which is done by CSP algorithm when inserting and extraction of the watermark. It is clear that the fault of rounding error have smaller values in the video sampled with 10-bits of those sampled with 8-bits. As an objective measure of quality was used PSNR, where the higher value of PSNR means higher the quality watermark, i.e., a greater robustness. Based on a detailed analysis of PSNR, it can be concluded that the robustness of the watermark inserted in video sequences sampled with 10-bits is larger than the one sampled with 8-bits on average by about 0.5 dB for a extracted, to 12dB for binarized watermark. Based on these results it can be concluded that robustness of watermarking based on SVD transformation increases with the number of sampling bits of video sequence and can be recommended for its use in FExt profile of H.264 encoder.

REFERENCES

- [1] M. Jevtović, Z. Veličković, "Komunikacioni protokoli prepletenih slojeva", Akademska misao, Beograd, 2013.
- [2] Z. Velickovic, M. Jevtovic, V. Pavlovic, "Cross-layer Throughput Optimization in Slow Fading Wireless Channel", International Journal Elektronika Ir Electrotehnika, Vol. 19, No. 6, pp. 131-137, 2013.
- [3] I. E. Richardson, *The H.264 advanced video compression standard*, 2nd ed., John Wiley & Sons, Ltd, 2010.
- [4] ITU-T, Recommendation H.264, Advanced Video Coding for Generic Audiovisual Services. Technical report, ITU-T, 2011.
- [5] D. Marpe, T. Wiegand, S. Gordon, "H.264/MPEG4-AVC fidelity range extensions: tools, profiles, performance, and application areas", ICIP 2005, pp. 593-596, 2005.
- [6] R. Run, S. Horng, J. Lai, T. Kao, R. Chen, "An Improved SVD-based watermarking technique for copyright protection", Expert Systems with Applications 39, pp. 673-689, 2012.
- [7] C. Jain, S. Arora, P. Panigrahi, "A Reliable AVD based Watermarking Scheme", Journal CoRR, vol. abs/0808.0309, 2008. <http://dbpl.uni-trier.de>.
- [8] Z. Veličković, Z. Milivojević, "Coding of a Video with the Inserted Watermark using H.264/AVC Coder", ICEST 2013, Proceedings Vol. 2, pp. 589-592, Ohrid 2013.
- [9] JM reference software version 18.4, <http://iphome.hhi.de/suehring/tml/> May, 2013.
- [10] A. M. Tourapis, A. Leontaris, K. Suehring, G. Sullivan, "H.264/MPEG-4AVC Reference Software Manual", Joint Video Team Document JVT-AD010, January 2009.

Session ESE:

**ENERGY SYSTEMS AND
EFFICIENCY**

The Influence of the Power Systems from the Neighboring Countries, on the Fault Currents in the Macedonian Power System

Ljupco Trpezanovski¹, Metodija Atanasovski² and Mile Miloshevski³

Abstract – In this paper is presented the influence of the each neighboring power system and all together on the value of the fault currents in the power system of the Republic of Macedonia. All 400 kV connection lines among power systems are taken into account. The mathematical models of the power system elements and methodology for calculation of three and one phase fault currents are shortly described. The power systems of the neighboring countries Serbia, Bulgaria and Greece are modelled with the Ward's equivalents which are adequately connected in the connection nodes of the power system of the Republic of Macedonia. A way for Ward's equivalent obtaining with rearranging the admittance matrix of the regional power system is explained. With application of the software package Neplan 5.3.5, calculations are performed for five cases and obtained results for three and one phase fault currents in important nodes of the power system of the Republic of Macedonia are given.

Keywords – Power system connections, Fault currents, Ward's equivalent.

I. INTRODUCTION

The values of the fault currents in the power system nodes are very important data for choosing the electrical equipment and their performances. The circuit breakers, disconnectors, measuring current transformers and lighting protection bare conductors should be chosen according to the maximum fault current in the sub-transient period. Also, the fault current data are necessary for setting the protection devices and designing the grounding systems. The degree of safety, reliable and stable function of the power systems depends of the type and duration of the fault currents. Liberalization of the electricity market enable the consumers to provide the electricity not only from the power plants in the Republic of Macedonia but from the power systems of the neighboring countries and wider. For these reasons to obtain the better transfer capacities the power system of the Republic of Macedonia (PSM) is connected with 400 kV lines with the power systems of the neighboring countries. With Serbia there is line between TS Skopje 5 – TS Kosovo B, with Bulgaria exist line between TS

Shtip – TS Chervena Mogila and with Greece there are two connection lines: TS Bitola 2 – TS Lerin and TS Dubrovo – TS Solun. The new 400 kV lines which are planned in the future are with Serbia TS Shtip – TS Nish and with Albania TS Bitola 2 – TS Ohrid – TS Elbasan [1]. The connections among power systems with 220 kV and 110 kV lines are not taken in the analysis because of small transfer capacities or because some of them are not in function.

The regional connections among the power systems of different countries increase the degree of safety, reliable and stable working of the each power system. On the other hand, these connections influence on the fault currents increasing in each of the power systems separately. That's just the point to take into account mutually connections among the power systems when fault currents analysis are performed.

With application of the software package Neplan 5.3.5 [2], calculation of three phase fault currents (3pfc) and one phase fault currents (1pfc) for five state cases are performed for the PSM. The power systems of the neighboring countries are modeled with Ward's equivalents obtained on the data base of the regional South-East Europe power systems [3]. All data for the power systems are taken for the state in year 2012 [1].

II. POWER SYSTEM ELEMENTS MODELLING AND METHOD FOR FAULT CURRENTS CALCULATION

In the Macedonian power system there are overhead lines with total length of 507 km for 400 kV, 103 km for 220 kV and 1480 km for 110 kV voltage level. The total number of transformer stations is five for 400/110 kV/kV, two for 220/110 kV/kV and sixty for 110/x kV/kV voltage levels [1]. One line diagram of the Macedonian power system is shown on Fig. 1 (state in 2012). All 400, 220 and 110 kV transmission lines and all 400/110, 220/110 and 110/x kV/kV transformer stations are taken into account in the power system model for fault current calculation. The overhead transmission lines are modelled with “ π ”-equivalent scheme for the positive and negative-sequence systems with serial impedance $\underline{Z}_v = (R_v + jX_v)$ and shunt jB_v branches. The impedance for the zero-sequence system is greater than positive-sequence system and depends of earth conductivity, disposition of phase conductors and presence (and number) of lighting protection conductors. These impedances are obtained by multiplying the values of positive-sequence system impedances with proper coefficients [4]. The transformers are modelled with “G”-equivalent scheme for the positive and negative-sequence systems with impedance serial branch $\underline{Z}_t = (R_t + jX_t)$ and shunt admittances $\underline{Y}_t = (G_t - jB_t)$.

¹Ljupco Trpezanovski is with the Faculty of Technical Sciences at University St. Kliment Ohridski – Bitola, I. L. Ribar bb. 7000 Bitola, Republic of Macedonia, E-mail: ljupco.trpezanovski@uklo.edu.mk.

²Metodija Atanasovski is with the Faculty of Technical Sciences at University St. Kliment Ohridski – Bitola, I. L. Ribar bb. 7000 Bitola, Republic of Macedonia.

³Mile Miloshevski is the postgraduate student on the Faculty of Technical Sciences at University St. Kliment Ohridski – Bitola.

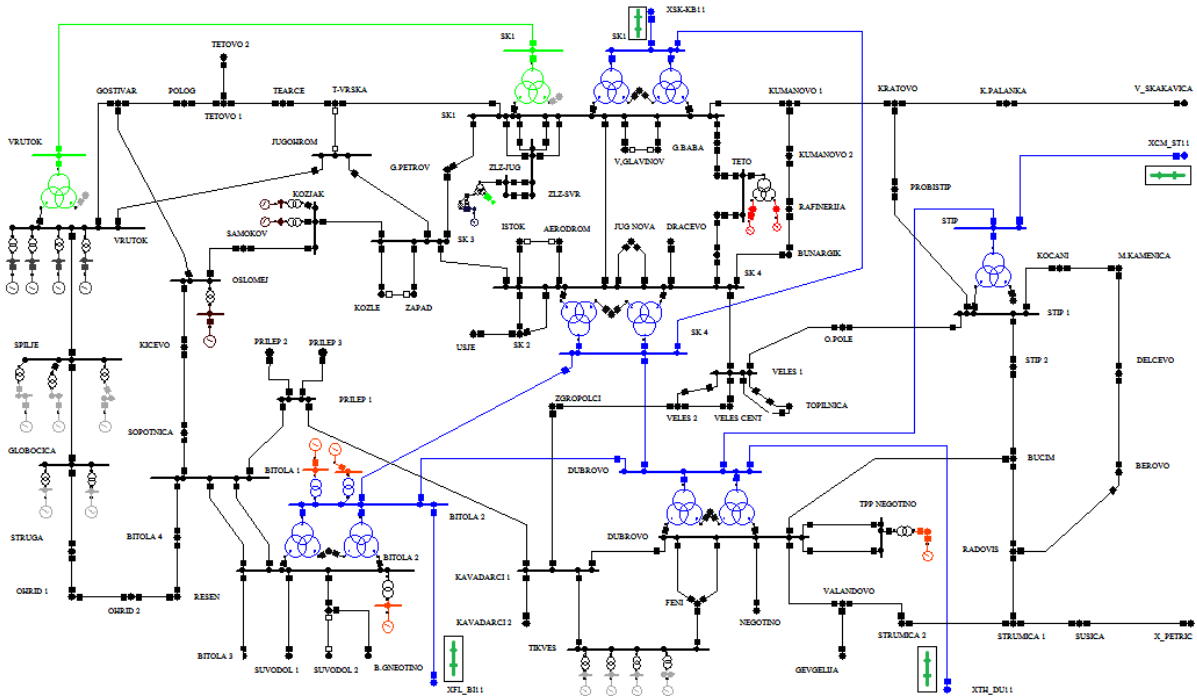


Fig. 1. One line diagram of the power system of the Republic of Macedonia (state in year 2012).

The equivalent scheme and impedance value for the zero-sequence system depends of the transformer windings connection, grounding of the winding neutral point(s) (if they exist) and transformer construction (3, 4 or 5 iron cores) [4]. During the fault duration, the synchronous generators change their reactance. In the sub-transient period the positive-sequence reactance is X_+'' , negative-sequence reactance is $X_-'' \approx X_+''$. The zero-sequence reactance depends of the generator neutral point treatment [4].

Calculations of fault currents are performed according to the IEC 60909 standard proposed by the IEC technical committee 73 [5]. This standard consists of a base document and five additional parts in which are defined all necessary steps for fault currents calculation in low and high voltage three phase power systems with rated frequency of 50 or 60 Hz. With this standard is established a general and precise procedure which gives the results with acceptable accuracy. The calculating method in the standard is based on theory for calculating the equivalent voltage generator and equivalent impedance on the fault point for positive, negative and zero-sequence circuits. Main assumptions which are taken into account during the calculations are:

- all shunt admittances and loads which haven't rotation parts (except one for the zero-sequence) are neglected;
- voltage of the equivalent voltage generator during the fault duration is with the value of $1,1 \cdot U_n$ (where U_n is rated voltage on the fault point);
- topology structure of the power system is that one which has maximum fault current in the fault point;
- maximum 3pfc and 1pfc are calculated only for the sub-transient period;
- voltage and power regulators are not activated.

III. OBTAINING OF WARD'S EQUIVALENTS

The Ward's equivalents of the power systems of the neighboring countries are obtained according to the data for the regional transmission network of the South-East Europe shown on Fig 2. These models are taken from the Department of strategic planning and power system analysis in AD MEPSO - Skopje.

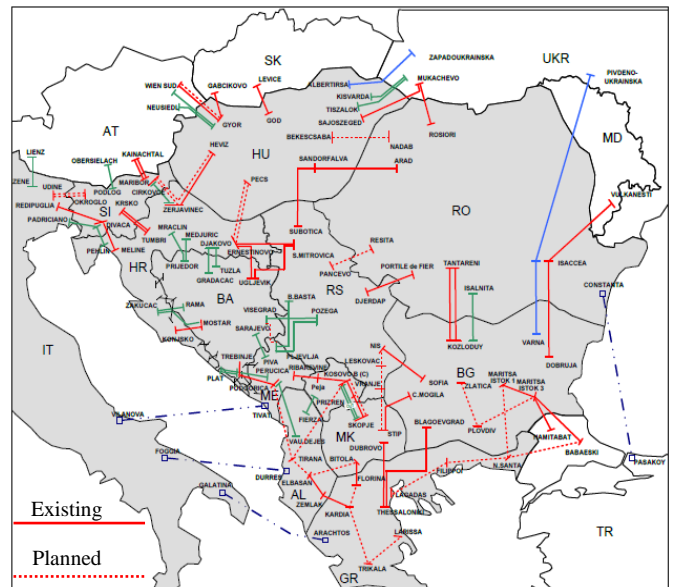


Fig 2. Regional transmission lines in South-East Europe.

The final models of the Ward's equivalents are consisted of the ending nodes of transmission lines which connect the neighboring power systems. These nodes are signed as terminal nodes. All terminal nodes are connected with

equivalent transmission lines and in each node exists an equivalent generator. The connecting transmission lines among PSM and neighboring countries, equivalent transmission lines among terminal nodes and equivalent generators of the Ward's equivalents are shown on Fig 3.

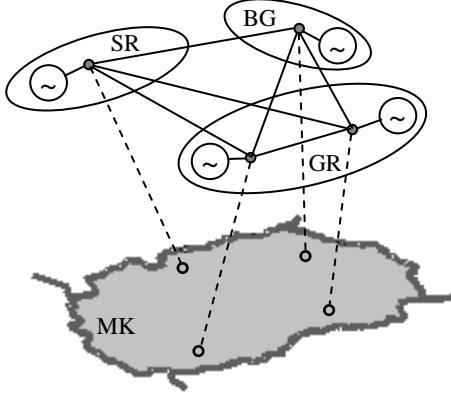


Fig. 3. Network model for fault currents calculation in the PSM.

The parameters of the equivalent transmission lines and generators are obtaining with simple procedure for regional power system admittance matrix $\mathbf{Y}^{externo}$ rearrangement. This matrix is concerned on external (neighboring) power systems which influence should be taken into account. If neighboring power systems have n nodes and if the procedure for obtaining Ward's equivalent results with nt terminal nodes, than parameters for equivalent transmission lines and generators are implemented in sub-matrix signed as \mathbf{Y}^{ward} . These parameters are obtaining through the elements of the $\mathbf{Y}^{externo}$ matrix [6]. At first, the elements of $\mathbf{Y}^{externo}$ which correspond to terminal nodes nt should be displaced in the last rows and columns with scripts from $(n-nt+1)$ to n and group in sub-matrix \mathbf{W} , as it is shown on Fig. 4.

$$\mathbf{Y}^{externo} = \begin{matrix} & \begin{matrix} 1 & 2 & \dots & (n-nt) & (n-nt+1) & \dots & n \end{matrix} \\ \begin{matrix} 1 \\ 2 \\ \vdots \\ (n-nt) \\ (n-nt+1) \\ \vdots \\ n \end{matrix} & \left[\begin{array}{cccccc} & & & & & \\ & & & & & \\ & & & & & \\ & & & & & \\ & & & & & \\ \hline & & & & & & \mathbf{W}_{nt \times nt} \\ & & & & & & \end{array} \right] \end{matrix}$$

Fig. 4. Admittance matrix structure for the neighboring power systems.

It is necessary to update the values of the $\mathbf{Y}^{externo}$ matrix applying Eq. 1:

$$Y_{jk} = Y_{jk} - \frac{Y_{ji}}{Y_{ii}} \cdot Y_{ik}; \quad (1)$$

$$i=1, \dots, (n-nt); j=(i+1), \dots, n; k=(i+1), \dots, n.$$

Using the elements from sub-matrix \mathbf{W} and applying Eqs. 2, the elements of sub-matrix \mathbf{Y}^{ward} can be calculated as:

$$\begin{aligned} & \text{for } i=1, \dots, nt; j=1, \dots, nt \Rightarrow \\ pom &= \sum W_{ij}; \quad i \neq j; \quad Y_{ij}^{ward} = -W_{ij}; \quad i \neq j \\ & \text{and } Y_{ij}^{ward} = W_{ij} + pom; \quad i = j. \end{aligned} \quad (2)$$

For the Ward's equivalents, the impedances of the equivalent generators are obtained by the reciprocal values of the diagonal elements and the serial impedances of the equivalent transmission lines are obtained by the reciprocal values of the off-diagonal elements of \mathbf{Y}^{ward} .

IV. FAULT CURRENT CALCULATION IN THE PSM

The purpose of this paper is to show the influence of the 400 kV connections with neighboring power systems (all together and separately) on the increasing of the fault currents in the PSM. Therefore, applying the software package Neplan 5.3.5, calculations of 3pfc and 1pfc for the following five state cases are performed for the PSM [7]:

1. The system works with all 400 kV connections to the power systems of the neighboring countries (results in Table I).
 2. The system works with connection only with the power system of the Republic of Serbia (results in Table II).
 3. The system works with connection only with the power system of the Republic of Bulgaria (results in Table II).
 4. The system works with connection only with the power system of the Greece (results in Table II).
 5. The system works independently (without any connection with other power system, results in Tables I and II).
- The fault currents comparison is given in Tables I and II.

TABLE I
FAULT CURRENTS COMPARISON BETWEEN CASE 1 AND CASE 5.

Node	U [kV]	Case 5-alone		Case 1-all		Δ_{pfc}	
		3pfc [kA]	1pfc [kA]	3pfc [kA]	1pfc [kA]	3pfc [%]	1pfc [%]
BITOLA2	400	6,6	7,8	18,5	18,2	180,0	134,0
DUBRVO	400	6,1	6,8	16,7	15,3	176,2	123,1
SKOPJE1	400	5,6	6,4	13,2	14,2	135,6	121,9
SK 4	400	6,2	7,2	14,4	14,6	133,1	104,5
STIP	400	4,8	4,9	11,7	9,9	145,5	99,4
BITOLA2	110	16,0	20,5	23,5	29,0	46,8	41,5
DUBRVO	110	16,5	19,8	25,3	28,5	53,1	43,9
SKOPJE1	110	17,6	21,7	27,2	32,4	54,7	49,2
SK 4	110	17,7	21,7	27,6	32,0	55,5	47,4
STIP 1	110	10,3	11,7	14,2	15,2	38,0	30,3
TIKVES	110	11,1	11,1	13,9	12,9	24,9	16,5
TETO	110	15,8	16,0	21,0	19,7	33,0	22,9

TABLE II
FAULT CURRENTS COMPARISON AMONG CASE 5, CASE 2, CASE 3 AND CASE 4.

Node	U [kV]	Case 5-alone		Case 2-Serbia		Case 3-Bulgaria		Case 4-Greece		Δ_{2-5}		Δ_{3-5}		Δ_{4-5}	
		3pfc [kA]	1pfc [kA]	3pfc [kA]	1pfc [kA]	3pfc [kA]	1pfc [kA]	3pfc [kA]	1pfc [kA]	3pfc [%]	1pfc [%]	3pfc [%]	1pfc [%]	3pfc [%]	1pfc [%]
BITOLA2	400	6,6	7,8	8,3	9,7	8,1	9,3	16,4	16,6	25,8	24,3	23,1	18,7	148,1	113,5
DUBRVO	400	6,1	6,8	7,8	8,6	8,9	9,3	12,9	12,5	29,1	25,6	46,8	36,6	112,4	82,0
SKOPJE1	400	5,6	6,4	10,1	11,9	6,7	7,3	8,4	8,7	79,5	86,7	19,9	15,1	49,8	35,6
SK 4	400	6,2	7,2	9,9	11,4	7,7	8,5	10,1	10,5	60,2	59,2	24,2	18,7	64,0	46,7
STIP	400	4,8	4,9	5,8	5,8	8,3	7,8	7,9	7,1	20,8	16,6	74,8	58,3	65,6	43,1
BITOLA2	110	16,0	20,5	17,9	23,0	17,7	22,5	22,6	28,0	11,8	12,3	10,7	9,7	41,6	36,8
DUBRVO	110	16,5	19,8	18,9	22,6	20,1	23,4	23,1	26,3	14,3	13,9	21,5	18,1	39,7	32,8
SKOPJE1	110	17,6	21,7	23,6	29,3	19,8	24,0	22,5	26,7	34,4	35,2	12,6	10,7	28,1	23,2
SK 4	110	17,7	21,7	23,3	28,4	20,2	24,3	23,3	27,3	31,3	30,8	14,1	11,8	31,3	25,5
STIP1	110	10,3	11,7	11,4	12,8	12,6	13,8	12,8	13,7	10,3	9,3	22,1	18,2	24,2	18,7
TIKVES	110	11,1	11,1	12,0	11,8	12,3	11,9	13,2	12,5	7,9	6,3	11,2	7,7	19,4	13,0
TETO	110	15,8	16,0	19,0	18,6	17,2	17,0	18,8	18,1	20,7	16,3	9,1	6,3	19,2	13,0

The fault currents when the PSM works without (case 5) and with all connections with neighboring countries (case 1) and percentage of 3pfc and 1pfc increasing, signed as Δ_{pfc} are shown for five 400 kV nodes and seven 110 kV nodes in which the increasing are the biggest (Table I). It is obvious that in 400 kV nodes (on which voltage level are connections with neighboring countries) the increasing of the fault currents are bigger, than in the nodes with lower voltage levels, dipper in the PSM. The increasing of the fault currents in the PSM, when exist connection with only one of the neighboring countries power systems are shown in the same nodes as in case 1. The percentage of fault currents increasing when PSM is connected only with the power system of: Serbia is signed as Δ_{2-5} , Bulgaria as Δ_{3-5} and Greece as Δ_{4-5} . Comparing the results in Table II we can conclude that the biggest influences of the fault currents increasing are in the nodes where exist 400 kV transmission lines which connect PSM and neighboring countries power systems.

V. CONCLUSION

Knowing the values of the fault currents in the power system nodes is very important for choosing the equipment performances, relay protection setting, stability analysis, designing the grounding systems, etc. The connections with high voltage transmission lines among the neighboring countries power systems influence on the fault currents increasing in each of the systems separately. Because of the above mentioned reasons it is very important to take into account this influence and calculate correct fault currents. In this paper is shown a way how to calculate the influence of the neighboring countries power systems on the fault currents

increasing in the power system of the Republic of Macedonia.

With real data for the power systems of the countries in South - East Europe obtained from [3] and software package [2], the fault currents in the nodes of the power system of the Republic of Macedonia are calculated. Five cases for different connections with neighboring countries are analyzed [7]. The results of obtained fault currents values and percentage of current increasing for each case are shown in proper tables. The obtained results are verified with their comparison with results presented in [1] which are obtained with software package PSS/E v.32.0.

REFERENCES

- [1] AD MEP SO-Skopje, *Study for Transmission Network Development in the Republic of Macedonia for the period 2010-2020*.
- [2] NEPLAN User's Guide V5.3.5, BCP Bussarelo+Cott+Partner, www.neplan.ch.
- [3] Power System Operator in AD MEP SO-Skopje, Department for Strategic Planning and Power System Analysis, 2011.
- [4] R. Achkovski, *Transmission and Distribution Systems*, Faculty of Electrical Engineering, Skopje, 1995.
- [5] IEC 60909-0, Short Circuit Currents in three-phase a.c. systems- Calculation of currents, Standard IEC technical committee 73.
- [6] R. Achkovski, K. Naumoski, "Assessment of Fault Currents After Starting in Operation of New Constructions in the Power System of the Republic of Macedonia", IV Conference MAKOCIGRE, September 26-29, Ohrid, C4-11, 2004.
- [7] M. Miloshevski, *The Influence of the Power Systems from the Neighboring Countries, on the Fault Currents in the Power System of the Republic of Macedonia*, seminar work on postgraduate studies, Faculty of Technical Sciences – Bitola, 2013.

Station for Emulation of Load and Electrical Motors Testing

Marko Rosić¹, Miloš Božić² and Miroslav Bjekić³

Abstract – This paper presents realized station for testing of electrical motors. Station has two main parts: Emulator of load and part for control and monitoring of the whole system. Emulator is a calibrated electromagnetic brake. Emulator can emulate different types of load, like gravitational, linear, fan and compound load, which is combination of first three. Control of emulator and monitoring of motor parameters during testing is realized with Compact RIO controller. Graphical user interface is realized in LabVIEW. Results obtained during motor testing, are shown at the end, and compared with the MATLAB simulated results.

Keywords – Electromagnetic brake, Emulator, Compact RIO, motor, LabVIEW, electrical motor.

I. INTRODUCTION

Testing of electrical induction motors (IM) in laboratory environment requires different types of tests. Crucial tests for testing the IM in laboratory are no load and short circuit load tests in accordance with standard EN 60034-2-1. These tests provide parameters of equivalent circuit of IM, losses and efficiency [1] [2]. No load and full load tests present only two limit points of work regime of IM. It would be very useful if IM could be tested in whole working range, thus we would have real state of IM in its normal work regime. For testing the operation of IM in work environment there are two methods. First one is to test machine on the site, and second one is testing machine in test station. IM drives pumps, fans, cranes and many other working machines, so it is a common case that IM cannot be tested on the site. If we want to test IM like it was in real industrial surrounding we need to connect it to a working machine, which is complicated and expensive process. In order to overcome these problems we can emulate load, so the IM “sees” the load like fan, pump or some other type of work machine. With emulator we have different types of loads in one machine.

In Laboratory for electrical machines and drives on Faculty of Technical Sciences in Čačak, this type of emulator for electrical motors was realised for powers up to 7,5kW [3].

II. MAIN PARTS OF THE EMULATOR SYSTEM

In the next figure (Fig. 1) is shown complete system with all components.

¹Marko Rosić, Faculty of Technical Sciences Čačak, University of Kragujevac, Srbija, e-mail: marko.rosic@ftn.kg.ac.rs

²Miloš Božić, Faculty of Technical Sciences Čačak, University of Kragujevac, Srbija, e-mail: milos.bozic@ftn.kg.ac.rs

³Miroslav Bjekić, Faculty of Technical Sciences Čačak, University of Kragujevac, Srbija, e-mail: miroslav.bjekic@ftn.kg.ac.rs

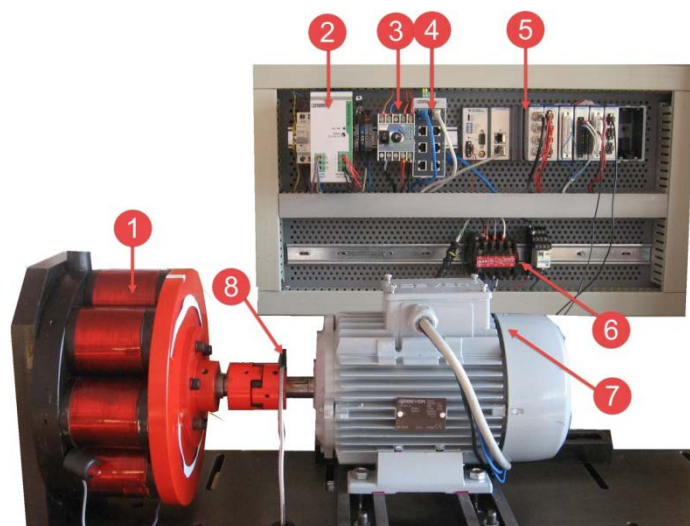


Fig. 1. Emulator system

1. Electromagnetic brake
2. DC power supply
3. Amplifier for Pulse Width Modulated (PWM) signal
4. Ethernet switch, for remote access
5. Compact RIO controller (cRIO)
6. Contactors equipment
7. Motor under the test, induction motor, 1.1kW, 920 rpm
8. Speed sensor

A. Electromagnetic brake

The main parts of the electromagnetic brake are: stator and rotor. There are eight electromagnets on the stator. Each electromagnet has 700 turns of Cu wire for currents up to 10 amperes. Air gap between stator and rotor is about 0.8 mm. There are two types of disk for the rotor, one of iron and one of aluminum. Electromagnetic brake is projected for torque up to 100Nm. In the Fig. 1 on the left side, electromagnetic brake with its main components is shown.

Electromagnetic brake is calibrated with a DC motor whose torque diagram is known [3]. Equations, which are obtained during process of calibration, are implemented in real time controller [4]. Desired torque is achieved by measuring speed of shaft rotation, and with PID controlled current through windings. The required current for actual speed is calculated from implemented equations. Desired torque is achieved with current feedback, and there is no need for using an expensive torque sensor.

B. Compact RIO controller

Control of electromagnetic brake is realized with National Instruments controller cRIO 9074. This integrated system

combines a real-time processor and a reconfigurable field-programmable gate array (FPGA) within the same chassis for embedded machine control and monitoring applications. It integrates a 400 MHz industrial real-time processor with a 2M gate FPGA and has eight slots for I/O modules [5-7].



Fig. 2. cRIO controller with modules

The system is commonly programmed by using LabVIEW software and can be used in a wide variety of applications for monitoring and control in real-time [8]. Controller with modules is shown in Fig. 2.

C. I/O modules

cRIO provides direct hardware access to the input/output circuitry of each I/O module using LabVIEW FPGA elemental I/O functions. Each I/O module contains built-in signal conditioning which are ready for direct connection to industrial sensors and actuators. Following modules are used for emulator:

- NI 9402 – fast 100ns, 8 channel bidirectional module for generation of PWM 5V/TTL level signal.
- NI 9403 – fast 55ns, 4 channel bidirectional module is used for acquisition of 5V digital signals from speed sensor.
- NI 9225 – 3 channel analog input module, measurement range of 300V RMS, 24 bit resolution, 50kS/s is used for measuring motor voltage
- NI 9227 – 4 channel analog input module, measurement range of 5A RMS, 24 bit resolution, 50kS/s in combination with current transformers is used for measuring motor current.
- NI 9211 – 4-Channel, 14 S/s, 24-Bit, ± 80 mV thermocouple input module is used for measuring of motor and brake temperature.
- NI 9476 – 32 channel, 500 μ s digital output, 6 to 36 V output range (based on supplied voltage), sourcing 250 mA/ch is used to turn on/off motor and brake power supply.

D. Sensor for speed measuring

Digital unipolar HALL sensor is used for measuring the speed of motor – emulator shaft. The magnet ring is placed on the motor shaft. In this way, problems with encoder - motor shaft coupling were overcome. HALL sensor TLE 4905L [9] is a cheap solution.

E. PWM amplifier

Control of brake current is realized with pulse width modulation. Connection between module 9402 and brake is made with PWM amplifier. PWM amplifier is a simple module with a FET transistor which works in a switching regime. Signal from module 9402 directly turns on and off current throw windings. Frequency of PWM is set to 1 kHz but it can be changed easily.

F. Emulator software

Complete software part of Emulator is realized in LabVIEW. Graphical user interface consists of four tabs. These tabs are shown in Fig. 3. Name of the first tab is *PID current* and in this tab user can tune PID parameters of brake current and watch response in time chart diagram Fig. 3.a. In second tab *PID speed*, the user can tune speed loop. Third tab *Load Emulator* is the main part of application and the user can choose between different types of load here. Forth tab is a monitoring tab in which user can watch and record motor and emulator parameters, like voltage, current, temperature etc.

III. LOAD EMULATOR

After the user sets up PID parameters for current control, the user can access the tab called Load Emulator which is presented in the Fig. 3. C. This tab consist of two parts, block with parameters for emulation of load on the left side and torque speed diagram on the right side. Emulation of load is realized with equation (1) [3]:

$$M_k = k_1 n^2 + k_2 n + k_3 \quad (1)$$

Between four options, of types of loads, from dropdown menu: the user has to choose one: gravitational, linear, fan or compound. When the user chooses gravitational type of load coefficients k_1 and k_2 are automatically set to zero so the torque is equivalent to coefficient k_3 . If user chooses fan type of load than torque changes with square of the speed with coefficients k_2 and k_3 set to zero. Compound type of load is combination of gravity, linear and fan type.

IV. INDUCTION MACHINE IN “UNSTABLE” PART OF TORQUE-SPEED DIAGRAM

System, induction motor – load, usually defines operating point on linear, stable, part of the torque-speed characteristic. Due to load variations, which may occur during operation with induction machine, it is very important to know maximum available torque (breakdown torque) and overload coefficient. For loads greater than maximum available torque motor enters the unstable, nonlinear part of torque-speed characteristic. In this part of the characteristic it is usually impossible to achieve a stable operating point and motor slows down.

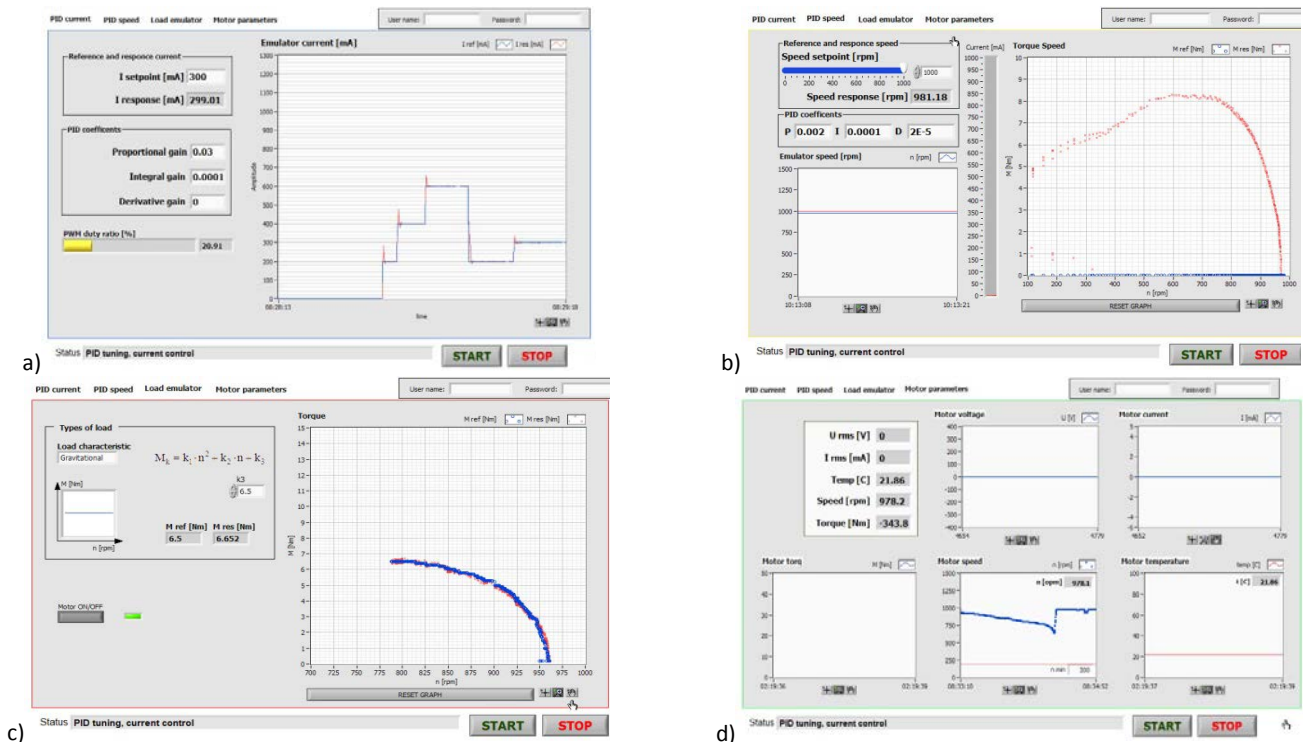


Fig. 3. Graphical User Interface tabs: a) PID current, b) PID speed, c) Load Emulator, d) Monitoring

The analysis and examination of this unstable part of the characteristic (where the slip is greater than the breakdown slip) is usually based on mathematical simulations. However, with this testing platform (with load emulator) testing induction motor in the “unstable” part of torque-speed characteristic can be achieved. The software’s speed loop allows us to define the motor speed and the load required to meet the required speed. In this way it is possible to define the motor speed corresponding to the unstable part of the characteristic, which will define operating point of the machine. In this case, load emulator acts as an adaptive load that allows stable operating point on unstable part of the characteristic. This enables analysis of the induction motor at speed range from zero to breakdown speed and validation of mathematical simulation models of the motor. Results of testing induction motor of 1.1kW as well as simulation results are shown in following.

Induction motor parameters obtained from short circuit and no load test are shown in TABLE I [10].

TABLE I – 3 phase AC 1.1 kW Motor ATB SEVER parameters obtained from short circuit and no-load test

U_{01} (V)	R_1 (Ω)	R_m (Ω)	$X_1=X_{2(1)}$ (Ω)	X_m (Ω)	$R_{2k(1)}$ (Ω)
100	7.1	11.76	5.9723	94.64	5.7001
200	7.1	8.209	5.9723	93.88	5.7001
300	7.1	5.97	5.9723	84.1	5.7001
400	7.1	3.833	5.9723	60.96	5.7001
380	7.1	4.455	5.9723	63.76	5.7001

Software for plotting torque-speed curves of induction machines [11] is used to simulate characteristics of the motor (Fig. 4)

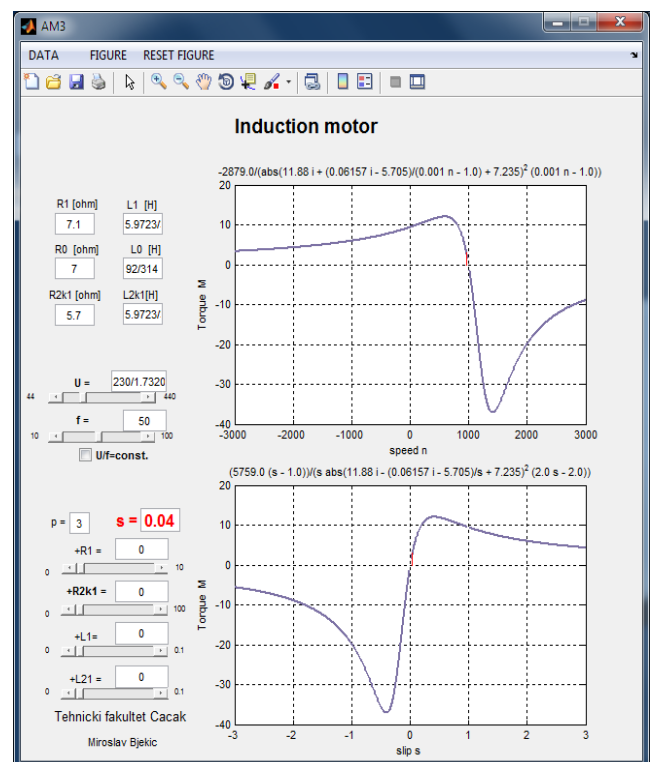


Fig. 4. Software for plotting static torque-speed curves $M=f(n)$

Simulated torque-speed characteristics of three phase induction motor (with nominal values given in TABLE II in the Appendix) are given in Fig. 5 with respect to the values given in TABLE I.

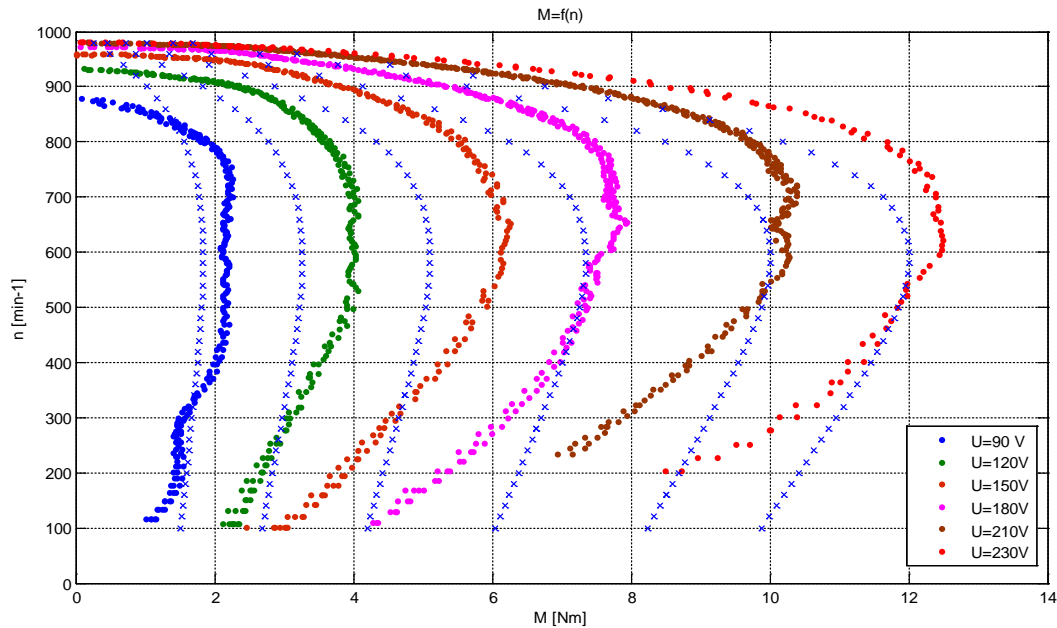


Fig. 5 – Simulated and measured results of static torque-speed characteristic.

Fig. 5 shows simulated and measured results of static torque-speed characteristic. It can be noted that measured values are not completely match with simulated values. Differences are the result of idealized conditions and omissions in the mathematical simulation model on one side, and calibration accuracy of electromagnetic emulator on the other side. Accurate results for torque-speed characteristics can be expected with electromagnetic brake calibrated with torque sensor

V. CONCLUSION

This paper presents a platform for load emulation of electric motors up to 7.5kW. Main part of the platform is electromagnetic emulator of load that can ensure application of the continuous load to the motor. Graphical user interface is realized in LabVIEW and allows easier control and setting the load reference and visualization of measured motor quantities. Motor can be tested and examined in unstable part of torque-speed characteristic due to implemented speed loop. The simulation results and measured results are close, which makes basis for further work and development on the platform for testing electric motors.

VI. APENDIX

TABLE II – 3 phase AC Motor ATB SEVER nominal values

U_n (V)	I_n (A)	f_n (Hz)	n_n (rpm)	P_n (kW)	n_s (rpm)	$\cos\varphi$
380	3.5	50	920	1.1	1000	0.7

VII. ACKNOWLEDGEMENT

This paper is a result within the project TR33016 which is

supported by Ministry of Education, Science and Technological Development of the Republic of Serbia.

REFERENCES

- [1] Koprivica, B., Božić, M., Rosić, M., Bjekić, M., "Application of Standard and Modified Eh-Star Test Method for Induction Motor Stray Load Losses and Efficiency Measurement", Serbian Journal of Electrical Engineering, Vol. 9, No. 3, October 2012, 277-391 ISSN 1451-4869
- [2] Božić, M., Rosić, M., Koprivica, B., Bjekić, M., Antić, S., "Efficiency classes of three-phase, cage-induction motors (IE-code) software", INDEL2012, IX International Symposium Industrial Electronics, November 1-3, Banja Luka, Bosna i Hercegovina, 2012
- [3] Bjekic, M., Bozic, M., Rosic, M. et al., "Design, Construction, Calibration and Use of A New Type of Electromagnetic Brake", XLVIII International Scientific Conference on Information, Communication and Energy Systems and Technologies, ICEST 2013, 26-29 June 2013 Ohrid, Macedonia, Vol. 2 pp. 727-730
- [4] <http://www.empr.ftn.kg.ac.rs/DiplRad/Strujno%20upravljanje%20elmag%20kocnicom%20cRIO%20-%20Asanin%20Njegos.pps>
- [5] National Instruments, www.ni.com
- [6] CompactRIO Part I Programming with LabVIEW Real-Time
- [7] CompactRIO Part II Programming with LabVIEW Real-Time
- [8] Božić, M., Rosić, M., „Razvoj platforme za ispitivanje algoritama upravljanja motorima naizmenične struje“, ETRAN 2013. Zbornik radova 57. Konferencije za ETRAN, Zlatibor, EE 1.7, 3-6 juna 2013
- [9] TLE 4905, Infineon technology, datasheet
- [10] <http://www.empr.ftn.kg.ac.rs/DiplRad/Indirektan%20postupak%20odredjivanja%20mehanicke%20k-ke%20asinronih%20motora-Slavisia%20Puzovic.pps>
- [11] <http://www.empr.ftn.kg.ac.rs/5%20AM/am05/Mehanicke%20k-ke%20i%20kruzni%20dijagram%20asinhrone%20masine.zip>

Modelling Self-Excitation Overvoltage in an Induction Motor With Individual Compensation of Reactive Power

Milan M. Radić¹, Zoran P. Stajić²

Abstract – In this paper we have studied the problem of overvoltage appearance occurring after an induction motor with individual compensation of reactive power was disconnected from the power supply. Phenomenon of self-excitation and overvoltage appearance have been described by the appropriate system of differential equations, including important nonlinearities of machine's parameters. Mathematical model was implemented on the computer and the simulation was performed using parameters of the laboratory 1.5 kW induction motor. Experimentally obtained data are in good agreement with simulation results, thus proving that developed model can be utilized as a tool in situations when it is necessary to determine the maximum capacitance allowed for individual compensation of reactive power. Results have confirmed the opinion that for the modern design of induction motors, characterized with highly saturated magnetic core, established limits of maximum capacitance for individual compensation could be exceeded.

Keywords – self-excitation, overvoltage, induction motor, individual compensation, reactive power.

I. INTRODUCTION

Individual compensation of reactive power is performed by connecting the capacitor bank directly to the terminals of a device that demands reactive power from the electrical grid. The application of this method is primarily focused on induction motors, as major consumers of reactive power. The method is very effective and inexpensive, because it does not require the use of additional equipment (contactors, fuses, units for reactive power control) which is necessary if central or group compensation is utilized. The cost of the compensation is significantly reduced in this manner, and its reliability is increased. Reactive power of the capacitor bank is usually selected to be approximately equal to the Q_0 , which is the value of reactive power consumed by the induction motor at no load. This limit had been defined by the recommendations established during mid 20th century [1], and was frequently cited later in the relevant literature [2]. Limitation of the capacitor's reactive power has been primarily established in order to avoid possible problems during transient regimes. Two most dangerous phenomena described in the literature are appearance of excessive dynamic torques during re-establishment of power supply after the short interruptions, and appearance of overvoltage caused by self-excitation.

¹Milan M. Radić is with the Faculty of Electronic Engineering, University of Niš, Aleksandra Medvedeva 14, 18000 Niš, Serbia
E-mail: milan.radic@elfak.ni.ac.rs

²Zoran P. Stajić is with the Faculty of Electronic Engineering, University of Niš, Aleksandra Medvedeva 14, 18000 Niš, Serbia
E-mail: zoran.stajic@elfak.ni.ac.rs

In large systems, where great number of different induction motors operate in different time intervals, analysis of the economic feasibility of individual compensation becomes a complex problem. If compensation is performed on each of the existing machines, large amount of the installed reactive power will be out of effective use, during periods when some machines are not working. On the other hand, if individual compensation is performed only on certain machines, it will inevitably result in low cumulative power factor when uncompensated motors operate in parallel.

Recently, the method of "improved individual compensation of reactive power" appeared in the literature ([3]). It is essentially based on utilization of oversized capacitor banks for individual compensation, on a number of selected machines that are in continuous (or at least long-lasting) operation. Generated excess reactive power is spent on compensation of reactive power in machines that are not provided with their own capacitor banks. It has been shown that an appropriate choice of machines to be compensated and values of capacitors to be used, led to the cumulative effect approximately the same as if there was a regulated central compensation. In the same time, the level of investment was much lower than if regulated central compensation had been really made. This approach demands violation of recommendations for the maximum permissible reactive power of capacitor bank for individual compensation.

The experience of the authors who carried out individual compensation with oversized capacitor banks ($Q_C > Q_0$) is that the aforementioned problems almost do not exist in practice [3]. They have tried to explain such situation by the fact that magnetic core of the contemporary induction machines is far more saturated, compared to the usual design from mid 20th century. However, they have used relatively simple, graphical method, suitable for analysis of steady state conditions.

In [4], we have analysed conditions that are necessary for existence of self-excitation in an induction machine. We have also developed and experimentally verified mathematical model of voltage build-up process in a self-excited induction generator [5], considering that machine was not loaded and that there was no external voltage supply. However, the proposed model is not suitable for analysis of overvoltage that could appear as a result of disconnecting from the power grid.

In this paper, we go one step further, developing the more accurate model of the self-excitation overvoltage in an individually compensated induction motor, caused by disconnection from the power grid. The main goal of the work presented here is to help solving dilemma whether it is allowed, or not, to perform individual compensation of reactive power using capacitor bank whose reactive power exceeds the value of Q_0 .

II. MATHEMATICAL MODEL

The process of self-excitation and overvoltage appearance is quite complex, and can not be fully depicted without solving mathematical model consisted of several nonlinear differential equations.

The mathematical model developed for this occasion is based on the theory of arbitrary reference frame [6]. Equivalent circuits for two orthogonal axes, q and d , are shown in Figs. 1 and 2, indicating that stationary reference frame is used. For simpler dynamic models of transient phenomena in induction machine, the most common approach is to neglect core losses, and also to consider magnetization inductivity L_m as constant. Bearing in mind that the actual goal of this model is to realistically describe the change of voltage at the terminals of the stator during the period after disconnection from the network, it is necessary to take into account the changes of mutual inductivity caused by variation of magnetization current [7]. This is done by using a nonlinear inductive element $L_m = f(I_m)$ in magnetization branches of equivalent circuits shown on Figs. 1 and 2. Also, the accuracy of voltage waveform prediction is increased by accurate modeling of iron core losses. This is performed by adding a nonlinear resistor $R_c = f(E)$ in parallel with magnetization inductivity, where E is effective value of emf induced in stator.

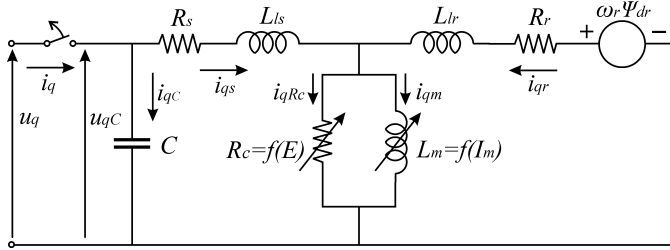


Fig. 1. Equivalent circuit for q axis

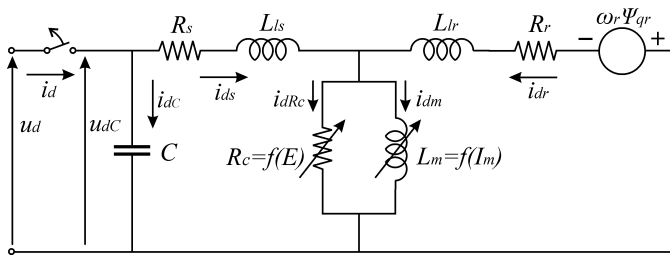


Fig. 2. Equivalent circuit for d axis

Regarding the circuits shown on Figs. 1 and 2, the following set of differential equations for currents can be written:

$$p i_{qs} = \frac{1}{L_{ls}} (u_{qC} - R_s \cdot i_{qs} - R_c \cdot i_{qRc}) \quad (1)$$

$$p i_{qr} = \frac{1}{L_{lr}} (-R_r \cdot i_{qr} - R_c \cdot i_{qRc} + \omega_r \cdot \psi_{dr}) \quad (2)$$

$$p i_{qRc} = \frac{1}{L_m} (-u_{qC} + R_s \cdot i_{qs} + L_s \cdot p i_{qs} + L_m \cdot p i_{qr}) \quad (3)$$

$$p i_{ds} = \frac{1}{L_{ls}} (u_{dC} - R_s \cdot i_{ds} - R_c \cdot i_{dRc}) \quad (4)$$

$$p i_{dr} = \frac{1}{L_{lr}} (-R_r \cdot i_{dr} - R_c \cdot i_{dRc} - \omega_r \cdot \psi_{qr}) \quad (5)$$

$$p i_{dRc} = \frac{1}{L_m} (-u_{dC} + R_s \cdot i_{ds} + L_s \cdot p i_{ds} + L_m \cdot p i_{dr}) \quad (6)$$

where $p = \frac{d}{dt}$.

One should notice that by substituting the Eqs. (1) and (2) into the Eq. (3), and also by substituting the Eqs. (4) and (5) into the Eq. (6), time derivatives of currents i_{qs} , i_{qr} , i_{ds} and i_{dr} at the right sides of Eqs. (3) and (6) can be eliminated.

The necessary flux linkages are calculated as:

$$\psi_{qr} = L_{lr} \cdot i_{qr} + L_m \cdot (i_{qs} + i_{qr} - i_{qRc}) \quad (7)$$

$$\psi_{dr} = L_{lr} \cdot i_{dr} + L_m \cdot (i_{ds} + i_{dr} - i_{dRc}) \quad (8)$$

and the electromagnetic torque is defined by:

$$T_e = \frac{3}{2} \cdot P \cdot (\psi_{qr} \cdot i_{dr} - \psi_{dr} \cdot i_{qr}) \quad (9)$$

where P represents the number of machine's pole pairs.

The electrical speed of the rotor is given as:

$$\omega_r = P \cdot \omega_m \quad (10)$$

and the mechanical speed is defined by Newton's equation:

$$p \omega_m = \frac{1}{J} (T_e - K_t \cdot \omega_m) \quad (11)$$

where K_t is constant representing friction coefficient and J is the moment of inertia.

While the machine is connected to the power supply (circuit breaker is closed), the voltage across capacitor is equal to the voltage applied to the stator, i.e. $u_{qC} = u_q$ and $u_{dC} = u_d$. After the circuit breaker is opened, the capacitor's voltage becomes an independent variable whose components along q and d axis can be calculated as:

$$u_{qC} = \frac{1}{C} \cdot \int i_{qC} \cdot dt = -\frac{1}{C} \cdot \int i_{qs} \cdot dt \quad (12)$$

$$u_{dC} = \frac{1}{C} \cdot \int i_{dC} \cdot dt = -\frac{1}{C} \cdot \int i_{ds} \cdot dt \quad (13)$$

In order to solve system of Eqs. (1)-(13), it is necessary to know actual values of parameters L_m and R_c . During each

discrete time interval of the simulation, it is possible to calculate effective value of magnetization current as:

$$I_m = \frac{\sqrt{i_{qm}^2 + i_{dm}^2}}{\sqrt{2}}$$

$$= \frac{\sqrt{(i_{qs} + i_{qr} - i_{qRc})^2 + (i_{ds} + i_{dr} - i_{dRc})^2}}{\sqrt{2}} \quad (14)$$

and effective value of *emf* induced in stator as:

$$E = L_m \cdot \frac{\sqrt{pi_{qm}^2 + pi_{dm}^2}}{\sqrt{2}} \quad (15)$$

After that, it is easy to calculate actual values of L_m and R_c , assuming that functional dependencies $L_m = f(I_m)$ and $R_c = f(E)$ have been previously determined.

Presented system of equations can be successfully solved using *MATLAB/Simulink* solver *ode23tb*, which is designed for stiff problems.

III. EXPERIMENTAL VERIFICATION

The proposed mathematical model was tested using three-phase, squirrel cage, Y-connected induction machine, with rated data of 1.5kW, 380V, 50Hz, 3.2A, 2860 rpm. Parameters of the machine's equivalent circuit have been obtained from standard no-load and locked rotor tests, while the moment of inertia and friction coefficient have been calculated regarding the results of retardation test at no load conditions. Values are given in Table I.

TABLE I
VALUES OF THE MACHINE'S PARAMETERS

Stator resistance, R_s	4.05 [Ω]
Rotor resistance, R_r	2.75 [Ω]
Stator leakage inductivity, L_{ls}	0.0138 [H]
Rotor leakage inductivity, L_{lr}	0.0088 [H]
Friction coefficient, K_t	0.0017 [$Nm \cdot s \cdot rad^{-1}$]
Moment of inertia, J	0.023 [$kg \cdot m^2$]

Nonlinear function $L_m = f(I_m)$ was identified using the data obtained from no-load test that was performed for several different values of the applied voltages. It is represented as two-segment curve (see Fig. 3), defined by:

$$L_m = \begin{cases} 0.722 & \text{I} \\ 0.808 - 0.35I_m + 0.073I_m^2 - 0.007I_m^3 + 2.6 \cdot 10^{-4} I_m^4 & \text{II} \end{cases} \quad (16)$$

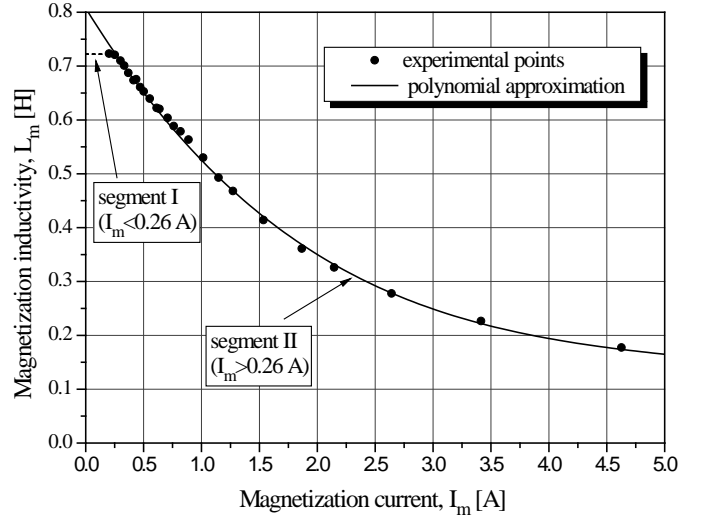


Fig. 3. Magnetization inductivity versus magnetization current

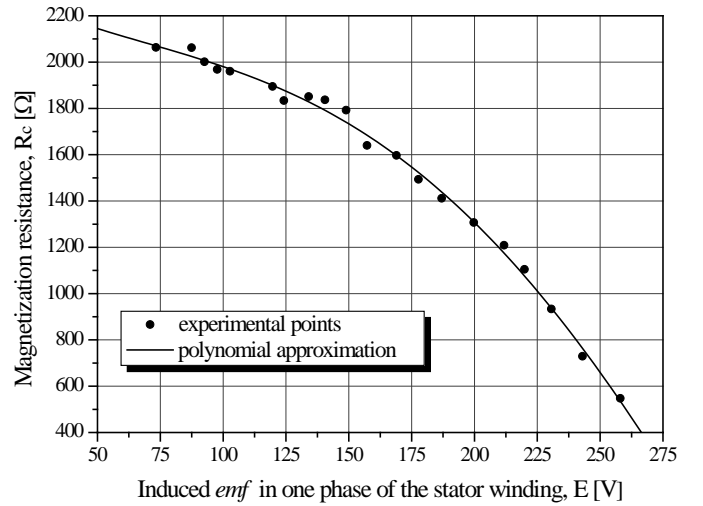


Fig. 4. Magnetization resistance versus induced *emf*

Value of variable resistor $R_c = f(E)$, placed in the magnetization branch, is defined using the 4th degree polynomial approximation (see Fig. 4) defined as:

$$R_c = 2379 - 6.7E + 0.055E^2 - 0.00031E^3 + 3.7 \cdot 10^{-7} E^4 \quad (17)$$

Model was experimentally tested using the symmetrical three-phase capacitor bank with rated capacitance of $C = 35 \mu F$ per phase, connected directly to the stator's terminals. The test machine demands reactive power of $Q_0 = 1210 \text{VAR}$ when it operates at no load and with rated voltage applied on the stator. It is clear that the power of the used capacitor bank, $Q_C = 3 \cdot \omega \cdot C \cdot U_f^2 = 1588 \text{VAR}$, exceeded the limit defined in the literature, because the ratio of $Q_C / Q_0 = 1.31$ was obtained. Machine was at no load operation, and the waveform of stator's voltage was recorded before, and shortly after disconnection from the power supply. Recorded waveform is shown in Fig. 5.

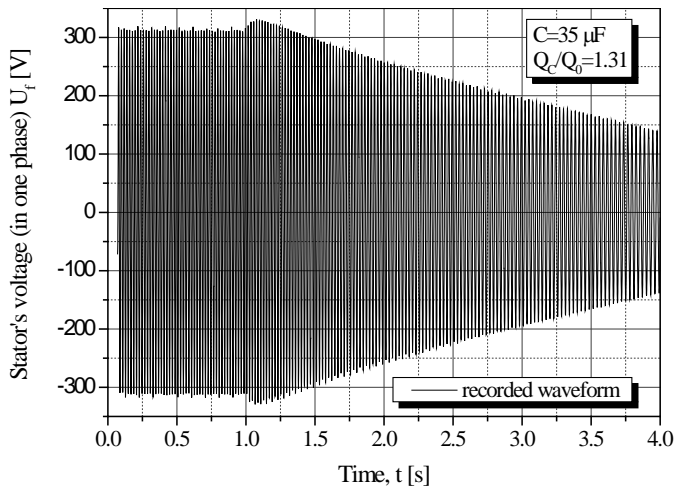


Fig. 5. Recorded waveform of stator's voltage after disconnection

The developed mathematical model was used for computer simulation of stator's voltage behavior after machine was disconnected from the grid. Calculated waveform is presented in Fig. 6, and it is in good agreement with experimental result.

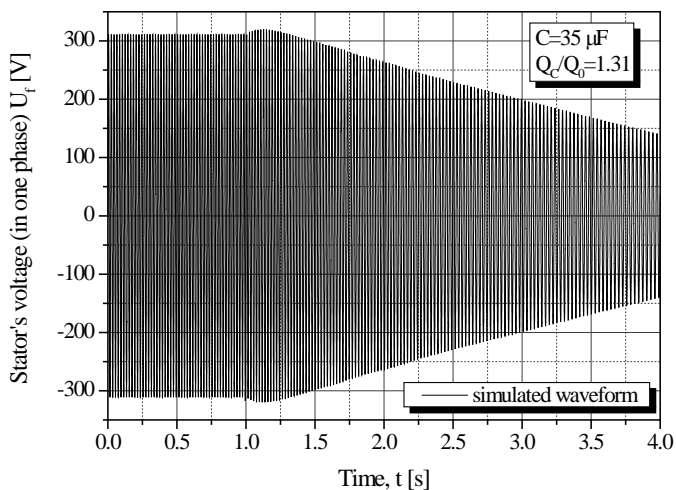


Fig. 6. Simulated waveform of stator's voltage after disconnection

Observing the results shown in Figs. 5 and 6, one can see that the maximum value of the self-excitation overvoltage is only about 7 % higher than the stator's rated voltage, although the capacitor bank with $Q_C/Q_0 = 1.31$ was used. This result should not be generalized, because the overvoltage may vary from one induction machine to another. However, if the motor parameters are known, and if the main nonlinearities describing magnetic circuit have been successfully identified, it is possible to make better choice of capacitors for individual compensation, using this model. It is very important to accurately represent functional dependence of mutual

inductivity between stator and rotor (magnetization inductivity) versus magnetizing current, otherwise the obtained results will not be realistic. Considering the fact that magnetic circuits of modern induction machines usually have heavily saturated magnetization characteristics, results justify the view that nowadays individual compensation can be performed using capacitor bank whose power exceeds value of Q_0 , as it has been suggested in [3].

IV. CONCLUSION

Developed model gives realistic image of self-excitation overvoltage occurring at the stator of an induction machine with individual compensation of reactive power. Simulation results are in good agreement with experimentally recorded values. Therefore, the model can be exploited as a useful additional tool during the selection of the capacitors for individual compensation of reactive power. Although the model was tested on the example of the small induction motor with rated power of 1.5 kW, it has a universal character and can be also used for prediction of overvoltages in large induction motors.

ACKNOWLEDGMENT

The work presented here has been supported by the Ministry of Education and Science of the Republic of Serbia, as a part of projects III44006 and TR35005, financed for the period 2011-2014.

REFERENCES

- [1] W. C. Bloomquist, W. K. Boice, "Application of Capacitors for Power-factor Improvement of Induction Motor", AIEE Trans. El. Eng., vol. 64, iss. 5, pp 274-278, 1945.
- [2] T. Longland, *Power Capacitor Handbook*, London-Boston, Butterworth, 1984.
- [3] M. Kostić, "Najveće dozvoljene snage kondenzatora za pojedinačnu kompenzaciju asinhronih motora" *Elektroprivreda*, broj 4, pp 26-34, 2005. (in Serbian)
- [4] M. Radić, Z. P. Stajić, "Self-excitation of an Induction Generator – Mathematical Model and Experimental Verification", ICEST 2008, Conference Proceedings, vol. 2, pp. 674-677, Niš, Serbia, 2008.
- [5] M. Radić, Z. P. Stajić, "Critical Speed-Capacitance Requirements for Self-Excited Induction Generator", ICEST 2010, Conference Proceedings, vol. 1, pp. 435-438, Ohrid, Macedonia, 2010.
- [6] P. C. Krause, *Analysis of Electric Machinery*, New York, McGraw-Hill Book Company, 1986.
- [7] I. Boldea, S. Nasar, *The Induction Machine Handbook*, London - New York - Washington D.C., CRC Press, 2002.

Multicriteria Analysis of the Smart Grid Project Efficiency

Aleksandar Janjić¹, Lazar Velimirović², Suzana Savić³ and Miomir Stanković⁴

Abstract – In this paper, the key performance indicators related to the smart grid efficiency have been analyzed. The authors are proposing multicriteria fuzzy AHP methodology for the determination of overall smart grid efficiency. After this evaluation, the ranking of different development alternatives including costs has been enabled. The methodology is illustrated on the choice of smart grid development strategy for the medium size power distribution company.

Keywords –AHP, Multicriteria analysis, Smart Grid

I. INTRODUCTION

With the development of the Smart grid architecture, the perspective of the traditional energy indicators has changed, introducing new goals and objectives. Smart Grid generally refers to an electricity network that can intelligently integrate the actions of all users connected to it – in order to efficiently deliver sustainable, economic and secure electricity supplies. These systems are made possible by two-way communication technology and computer processing that has been used for decades in other industries. According to [1] main objectives of smart grids are: increased use of renewable electricity sources, grid security, energy conservation and energy efficiency, and deregulated energy market. Therefore, the strategy for sustainable, competitive, and safe energy primarily implies: competitiveness, use of different energy sources, sustainability, innovation, and technological improvement [2], while possible benefits brought by any smart grid initiative have to be evaluated by the degree of the approach to the ideal smart grid.

A measure of the contribution of projects to the ideal Smart Grid is quantified in terms of benefits, via a set of KPIs. The European Electricity Grid Initiative [3] has divided the ideal Smart Grid system into thematic areas (clusters) and is currently mapping Smart Grid projects into clusters. In USA, the ideal characteristics of the Smart Grid and a set of metrics to measure progresses toward the ideal Smart Grids has been defined [4]: build metrics that describe attributes that are built in support of a Smart Grid (e.g. percentage of substations using automation) and value or impact metrics that describe the value that may derive from achieving a Smart Grid (e.g. percentage of energy consumed to generate electricity that is not lost, or quantity of electricity delivered to consumer

compared to electricity generated expressed as a percentage).

Due to the presence of both quantitative and qualitative criteria, and many uncertainties related to the smart grid operation environment, the paper proposes a new algorithm for the assessment of renewable energy integration in the smart grid, which uses the fuzzy AHP method for multicriteria decision making. Based on fuzzy matching of alternatives, the method determines the optimal set of activities concerning smart grid projects. We proved that the method is highly successful in the evaluation of alternatives in the presence of heterogeneous criteria. After the brief overview of key performance indicators for the smart grid evaluation, the fuzzy AHP methodology has been presented. Finally, the methodology is illustrated on the choice of four different alternatives (of different size, location and technology) of distributed generator insertion in the IEEE 33 bus test radial distribution feeder.

II. SMART GRID ASSESSMENT

A. Smart grid evaluation metrics

The implementation of a Smart Grid is useful to achieve strategic policy goals, such as the smooth integration of renewable energy sources, a more secure and sustainable electricity supply, full inclusion of consumers in the electricity market, helping them to better understand their own energy use, which in turn allows consumers to identify energy saving opportunities. Smart grid and Advanced Metering Infrastructure (AMI) systems also could open up opportunities for energy management companies, hired by consumers, to use data from consumers' smart meters to identify opportunities for energy savings or to measure the success of energy savings measures after they are undertaken. For utilities, a better understanding of the electrical grid's status at a second-by-second level allows the grid to be operated at much tighter tolerances, resulting in greater efficiencies and reliability.

The characteristics of the ideal Smart Grids and defined metrics to measure progresses and outcomes resulting from the implementation of Smart Grid projects have been defined in [5]-[7]. The ideal Smart Grid has been defined in terms of characteristics in the US and in terms of services in the European Union, including:

- Enabling the network to integrate users with new requirements;
- Enabling and encouraging stronger and more direct involvement of consumers in their energy usage and management;

¹Aleksandar Janjić is with the Faculty of Electronic Engineering at University of Niš, 14 Aleksandra Medvedeva, Niš 18000, Serbia, E-mail: aleksandar.janjić@elfak.ni.ac.rs.

²Lazar Velimirović is with the Mathematical Institute of SASA

^{3,4}Suzana Savić and Miomir Stanković are with the Faculty of Occupational Safety at University of Niš,

- Improving market functioning and customer service;
- Enhancing efficiency in day-to-day grid operation;
- Enabling better planning of future network investment;
- Ensuring network security, system control and quality of supply

Together with the list of these services, the list of benefits has been identified deriving from the implementation of a Smart Grid. Smart Grid services and benefits are strongly linked to the policy goals that are driving the Smart Grid deployment (sustainability, competitiveness and security of supply), and consequently, they can be considered as useful indicators to evaluate the contribution of projects toward the achievement of these policy goals. A clearly defined framework can concretize where exactly the project contributed to a smart electricity grid. The mixture of quantitative and qualitative indicators is one of the major reasons for introducing the multi-criteria decision analysis techniques.

B. Multi-criteria assessment model

Starting from the list of main services and corresponding benefits (section A) in order to get a thorough understanding of the status of smart grid development, an adapted list of main criteria can be defined, including:

- Technology, covering all aspects of advanced services and new requirements imposed to the distribution and transmission network;
- Optimized asset utilization, including the costs reduction, enhanced efficiency and better planning of future investment;
- Customer satisfaction, encompassing different options of customer choice, new energy services and market participation;
- Environmental impact.

After the first level of benefits defined, the second set of performance indicators has been chosen, for the particular assessment aspects, out of the complete indicator list. For instance, the indicators that can be measured are: the quantified reduction of carbon emissions, voltage quality performance of electricity grids (e.g. voltage dips, voltage and frequency deviations and the level of losses in distribution networks (absolute or percentage). If new projects are evaluated, the net present value of the investment can be added. Qualitative indicators are the evaluated environmental impact and societal benefits of the project.

All indicators (quantitative and qualitative) are influencing all of four main criteria, according to the decision maker preferences. For instance, reduced voltage deviation and stable voltage profile in the network will enable the usage of advanced technologies and services; they will reduce the costs of low power quality, increasing the customer satisfaction.

The assessment framework proposed by [5] is based on a merit deployment matrix, where benefits and corresponding KPIs are reported in the rows, whereas functionalities (which are univocally linked to a service) are reported on the

columns. For each project, the matrix is filled in two main steps:

- a) Identify links benefits/KPI and functionalities. Select the corresponding cell.
- b) For each cell, explain how the link between benefits/KPI and functionalities is achieved in the project. Assign a weight (in the range 0-1) to quantify how strong and relevant the link is.

However, the described method doesn't offer the tradeoffs between different criteria, which is the main reason of introducing advanced multicriteria methodology for the smart grid evaluation.

III. SMART GRID EVALUATION METHOD

In this paper fuzzy AHP method is used for the evaluation of efficiency of smart grid projects. Mathematical basis for fuzzy AHP method is based on fuzzy sets, fuzzy numbers and fuzzy arithmetic.

A. Fuzzy AHP method

The fuzzy AHP method involves the following steps:

- Step 1. The overall goal (objective) is identified and clearly defined;
- Step 2. The criteria, sub-criteria, and alternatives are identified;
- Step 3. The hierarchical structure is formed;
- Step 4. Pair-wise comparison is made using fuzzified Saaty's evaluation scale;
- Step 5. The priority weighting vectors are evaluated using the Row Geometric Mean Method (RGMM);
- Step 6. Consistency of the judgments is checked by Geometric Consistency Index (GCI);
- Step 7. The defuzzification and the final ranking of alternatives are defined.

In this study the fuzzy AHP method is applied to the ranking smart grid projects, as presented in the following text.

1. Goal identification. The goal is to evaluate the efficiency of the renewable energy plant integration in the smart grid context.

2. Identification of criteria, sub-criteria, and alternatives. Criteria for smart grid projects selection are: Technology, Costs reduction, Customer satisfaction, encompassing different options of customer choice, and Environmental impact reduction. Finally, the different smart grid projects are identified as alternatives.

3. Hierarchical structure formation. The Fuzzy AHP method presents a problem in the form of hierarchy: the first level represents the goal; the second level considers relevant criteria (four identified criteria); the third level considers relevant sub-criteria; and the fourth level defines smart grid project alternatives.

4. Pair-wise comparison. Pairs of elements at each level are compared according to their relative contribution to the

elements at the hierarchical level above, using fuzzified Saaty's scale, as shown in Table I.

TABLE I
CRISP AND FUZZIFIED SCALE FOR PAIRWISE COMPARISONS [8]

Crisp values (x)	Judgment description	Fuzzy values
1	Equal importance	(1, 1, 1+δ)
3	Weak dominance	(3-δ, 3, 3+δ)
5	Strong dominance	(5-δ, 5, 5+δ)
7	Demonstrated dominance	(7-δ, 7, 7+δ)
9	Absolute dominance	(9-δ, 9, 9)
2, 4, 6, 8	Intermediate values	(x-1, x, x+1)

In this paper fuzzification is implemented by triangular fuzzy numbers, and the value of fuzzy distance of 2 is used, as recommended in [8], because the most consistent results can be expected.

5. Priority weights vectors evaluation. The priority weighting vectors on each level are evaluated using the RGMM. The ranking procedure starts with the determination of criteria weighting vector:

$$W_c = (w_{c1}, w_{c2}, w_{c3}, w_{c4})^T \quad (1)$$

where w_{ci} is the fuzzy weight of i -th criterion:

$$w_{ci} = \frac{\left(\prod_{j=1}^4 a_{ij} \right)^{\frac{1}{4}}}{\sum_{i=1}^4 \left(\prod_{j=1}^4 a_{ij} \right)^{\frac{1}{4}}}, \quad i = \overline{1, 4} \quad (2)$$

Sub-criteria weighting vectors are defined by pairwise comparison of performance indicators according to each criterion. Appropriate elements of these vectors are calculated as follows:

$$w_{sci}^p = \frac{\left(\prod_{j=1}^6 a_{ij} \right)^{\frac{1}{6}}}{\sum_{i=1}^6 \left(\prod_{j=1}^6 a_{ij} \right)^{\frac{1}{6}}}, \quad i = \overline{1, 6}, \quad p = \overline{1, 4} \quad (3)$$

where w_{sci}^p represents the fuzzy weight of the i -th performance indicator with respect to the p -th criterion. The final sub-criteria weighting vector is obtained by multiplying the matrix of the sub-criteria weights according to all criteria (W_1) and the matrix of the criteria weights (W_c):

$$W_{sc} = W_1 \otimes W_c \quad (4)$$

Finally, the projects are compared according to the each performance indicator. Proper weights of projects, i.e. alternatives with respect to the individual performance indicator are determined as follows:

$$w_{ai}^r = \frac{\left(\prod_{j=1}^4 a_{ij} \right)^{\frac{1}{4}}}{\sum_{i=1}^4 \left(\prod_{j=1}^4 a_{ij} \right)^{\frac{1}{4}}}, \quad i = \overline{1, 4}, \quad r = \overline{1, 6} \quad (5)$$

where w_{ai}^r represents the fuzzy weight of the i -th project with respect to the r -th performance indicator. Final projects weights are obtained by multiplying the matrix of the projects weights according to all alternatives (W_2) and the matrix of sub-criteria weights:

$$W_a = W_2 \otimes W_{sc} = (w_{a1}, w_{a2}, w_{a3}, w_{a4})^T \quad (6)$$

6. Consistency control. Consistency in this case means that the decision procedure is producing coherent judgments in specifying the pairwise comparison of the criteria, sub-criteria or alternatives. When the RGMM is employed as the prioritization procedure, the geometric consistency index (GCI) is used for consistency control [9].

7. Defuzzification and the final ranking of alternatives. In this paper triangular fuzzy numbers are ranked by applying the mean value method. For the given triangular fuzzy number $M=(a,b,c)$, the mean value method for defuzzification is defined crisp number value as follows:

$$m = \frac{a + b + c}{3} \quad (7)$$

The highest rank has the alternative with the highest value m .

IV. CASE STUDY

The proposed methodology is illustrated on the choice of the technology, size and location of one distributed renewable generator. Four possible alternatives are evaluated on IEEE radial 33 bus test feeder, with parameters, including the nominal active power (P_{nom}), the node the generator is connected to ($Bus\ No$), type of renewable source (RS) and expected annual energy production of generator (W), represented in table II.

TABLE II
PROJECT SCENARIOS

Project	P_{nom}	Bus N°	RS	W (GWh)
Project 1	1.8MW	6	Wind	5, 2
Project 2	1 MW	10	Biomass	7,0
Project 3	2 MW	17	Hydro	4,0
Project 4	1 MW	17	Biomass	5,00

Sub-criteria that are aggregated for this particular smart grid project including the renewable source integration, and their calculated values are presented in table III. The columns

in the table are representing: (1) – project number, (2) - net present value of the project in millions of Euros, (3) – total voltage drop in percents, (4) – power losses in kW, (5) – reduction in CO₂ emission in tons per year, (6) – environmental impact and (7) – social benefits.

TABLE III
QUANTITATIVE AND QUALITATIVE PROJECT EFFICIENCY INDICATORS

(1)	(2)	(3)	(4)	(5)	(6)	(7)
Pr. 1	4,2	29,6	156,4	5 148	Moderate	High
Pr. 2	5,1	30,5	176,8	6 930	Moderate	Moderate
Pr. 3	2,7	22,0	265,3	3 960	Low	Very high
Pr. 4	3,8	26,3	190	4 950	Very low	Moderate

These four smart grid projects (Project 1, Project 2, Project 3 and Project 4) are compared in relation to four criteria presented in section B, and six sub-criteria (SC) presented in Table III. The pairwise comparison of alternatives in relation to performance indicators is presented in table IV with following abbreviations (BS-Basis of comparison; EI – Equal importance; WD Week dominance; SD – Strong dominance.)

TABLE III
QUANTITATIVE AND QUALITATIVE PROJECT EFFICIENCY INDICATORS

	SC1	SC2	SC3	SC4	SC5	SC6
A1	WD	EI	SD	WD	BC	WD
A2	BC	BC	WD	SD	EI	BC
A3	SD	SD	BC	BC	WD	SD
A4	WD	WD	WD	WD	SD	EI

The final fuzzy weights for smart grid projects, according to Equation(6) and the results of pairwise comparison of alternatives in relation to all performance indicators calculated from values given in Table II, are:

$$W_a = \begin{bmatrix} (0.0140, 0.2067, 3.3081) \\ (0.0121, 0.1589, 2.5160) \\ (0.0251, 0.3982, 5.0638) \\ (0.0176, 0.2363, 3.7016) \end{bmatrix} \quad (8)$$

The Project 1 is dominant in relation to the power losses, Project 2 – in relation to the carbon emission reduction, Project 3 – in relation to net present value of investment, voltage deviation and the societal benefits (however, it is the worst in relation to the power losses and the carbon emission reduction), Project 4 – in relation to environmental impact.

The final rank of the projects indicates that the highest rank has the Project 3, followed by the Project 4 and the Project 1; the lowest priority has the Project 2 (Equation 8). This means

that for the implementation of the smart grid Project 3 should be selected.

V. CONCLUSION

To evaluate to what extent the smart grid projects are contributing to progresses toward the “ideal smart grid” and its expected outcomes (e.g. sustainability, efficiency, consumer inclusion), the new approach has to be adopted. In this paper, starting from a general set of smart grid performance indicators, a new assessment framework for the evaluation of smart grid project efficiency has been established, based on fuzzy AHP methodology.

The proposed methodology is illustrated on the choice of the optimal size, location and technology of renewable resources planned for the integration in the existing distribution network. Using four main criteria and six sub-criteria derived from the adopted set of smart grid benefits, we proved that the method is highly successful in the evaluation of alternatives in the presence of heterogeneous criteria. This method allows the decision makers to incorporate unquantifiable information, incomplete information, non-obtainable information and partially ignorant facts into decision model.

ACKNOWLEDGEMENT

This work was supported by the Ministry of Education, Science and Technological Development of the Republic of Serbia under Grant III 42006 and Grant III 44006.

REFERENCES

- [1] European Commission Task Force for Smart Grids, 2010. “Expert Group 3: Roles and responsibilities”
- [2] European Network for the Security of Control and Real time systems, 2011. *R&D and standardization Road Map, final deliverable 3.2.*
- [3] European Electricity Grid Initiative (EEGI) 2010. “Roadmap 2010-18 and Detailed Implementation Plan 2010-12”
- [4] U.S. Department of Energy (DOE), 2010. “Guidebook for ARRA SGDP/RDSI Metrics and Benefits”, DOE Report
- [5] European Commission Task Force for Smart Grids, 2010a. “Expert Group 2: Regulatory Recommendations For Data Safety, Data Handling And Data Protection”
- [6] B. Dupont, L. Meeus, R. Belmans “Measuring the “smartness” of the electricity grid”. *7th International Conference on the Energy Market (EEM)*, 1-6.2010
- [7] EPRI (Electric Power Research Institute), 2010. Methodological Approach for Estimating the Benefits and Costs of Smart Grid Demonstration Projects. Palo Alto, CA: EPRI. 1020342.
- [8] B. Srdjevic, Y. Medeiros “Fuzzy AHP assessment of water management plans”. *Water Resources Management* 2008; 22: 877-894.

Session MST:

**MEASUREMENT SCIENCE AND
TECHNOLOGY**

Acquisition System for Generation of the Test Signals with Standard Harmonic Disturbances

Milan Simić¹, Dragan Živanović², Dragan Denić³ and Goran Miljković⁴

Abstract – Data acquisition system, developed for generation of the reference voltage test waveforms with standard high-order signal harmonic disturbances, is presented in this paper. This software supported acquisition system, functionally based on the LabVIEW application software, includes standard computer and acquisition card NI PCIe 6343. The basic purpose of this system is to provide standard voltage waveforms applicable for testing of instruments for measurement of basic electrical power quality parameters and high-order signal harmonics, according to the European power quality standard EN 50160. Specific level of the high-order harmonics in test signals can be individually defined and generated. Continuous variation of the percentage amplitude level in input control segment can be performed separately for each individual signal harmonic or at the same time for all levels of the high-order signal harmonics. Developed solution is verified using the sophisticated instrument for measurement and analysis of the standard power quality parameters - Fluke 435 Series II. Some obtained measurement results are presented in the paper.

Keywords – Acquisition system, Voltage test signals, Standard harmonic disturbances, LabVIEW software support.

I. INTRODUCTION

Signal disturbances, present in the form of the RMS voltage value variations or high-order signal harmonics, directly cause decreasing of the energy efficiency level in electrical power production, distribution and consumption process. Increased concern for problems of electrical power quality distribution, indicated in the recent years, primarily is caused by limitation of the natural resources used for energy production, followed by widespread using of the alternative energy resources. In order to reduce possibilities for potential power distribution network disturbances and to prevent failures of the customer equipment, highly sensitive to various quality degradation and problems, companies for electrical power delivery are forced to assure efficient monitoring of the power delivery networks. Such monitoring process involves measurement and detailed analysis of the basic power quality parameters and network

disturbances, defined by the relevant international documents and quality standards [1,2]. Relevant information necessary for providing optimal power quality level can be obtained by measurement and detailed analysis of the basic power quality parameters at specific locations in power distribution network. Various types of instruments and equipment for measurement and software processing of the standard quality parameters are commercially available at the market. These instruments are developed for continuous monitoring of the voltage supply quality in power distribution networks. By measurement of the relevant quality parameters and by performing software supported analysis in single or three-phase power distribution networks, these instruments are capable to verify compliance of the measured quality parameters with relevant standards, such as the European power quality standard EN 50160 [3,4].

Solution of the data acquisition system described in this paper is developed using LabVIEW [5] software package for generation of the reference voltage test waveforms, including special functions for simulation of the various signal harmonic disturbances, typical for real power distribution networks. Procedure for signal generation is functionally based on the virtual instrumentation concept, which includes application software developed in LabVIEW environment and acquisition card NI PCIe 6343. Software support of the generation system provides definition and presentation of the reference voltage signal waveforms. Number of control functions and switches, implemented on front panel of developed virtual instrument, provides adjustment of the basic parameters for definition, presentation and signal generation. Complex test waveforms, defined directly from control block diagram of the virtual instrument, according to requirements of the quality standard EN 50160, can be used for generation of the various voltage test sequences. Generally, using this data acquisition system is possible to generate various voltage test sequences. For this specific purpose are generated voltage waveforms with some typical combinations of the high-order harmonic disturbances. Generated voltage test waveforms are used for testing of the three-phase power quality analyzer Fluke 435 Series II [6].

II. SOFTWARE SUPPORT OF THE SYSTEM

Developed acquisition system includes standard computer, supported by control application in LabVIEW programming environment and data acquisition card NI 6343, equipped with the standard connector block SCB-68A. Complete procedure includes two connected functional segments. First segment of this process provides definition and simulation of the standard voltage signal waveforms, with specified amplitude levels of the signal harmonic disturbances for generation. Definition of the basic signal parameters for various classes of individual disturbances can be performed during programming process, directly inside front panel and block diagram of the LabVIEW

¹Milan Simić is with the University of Niš, Faculty of Electronic Engineering, Aleksandra Medvedeva 14, 18000 Niš, Serbia, E-mail: milan.simic@elfak.ni.ac.rs.

²Dragan Živanović is with the University of Niš, Faculty of Electronic Engineering, Aleksandra Medvedeva 14, 18000 Niš, Serbia, E-mail: dragan.zivanovic@elfak.ni.ac.rs.

³Dragan Denić is with the University of Niš, Faculty of Electronic Engineering, Aleksandra Medvedeva 14, 18000 Niš, Serbia, E-mail: dragan.denic@elfak.ni.ac.rs.

⁴Goran Miljković is with the University of Niš, Faculty of Electronic Engineering, Aleksandra Medvedeva 14, 18000 Niš, Serbia, E-mail: goran.miljkovic@elfak.ni.ac.rs.

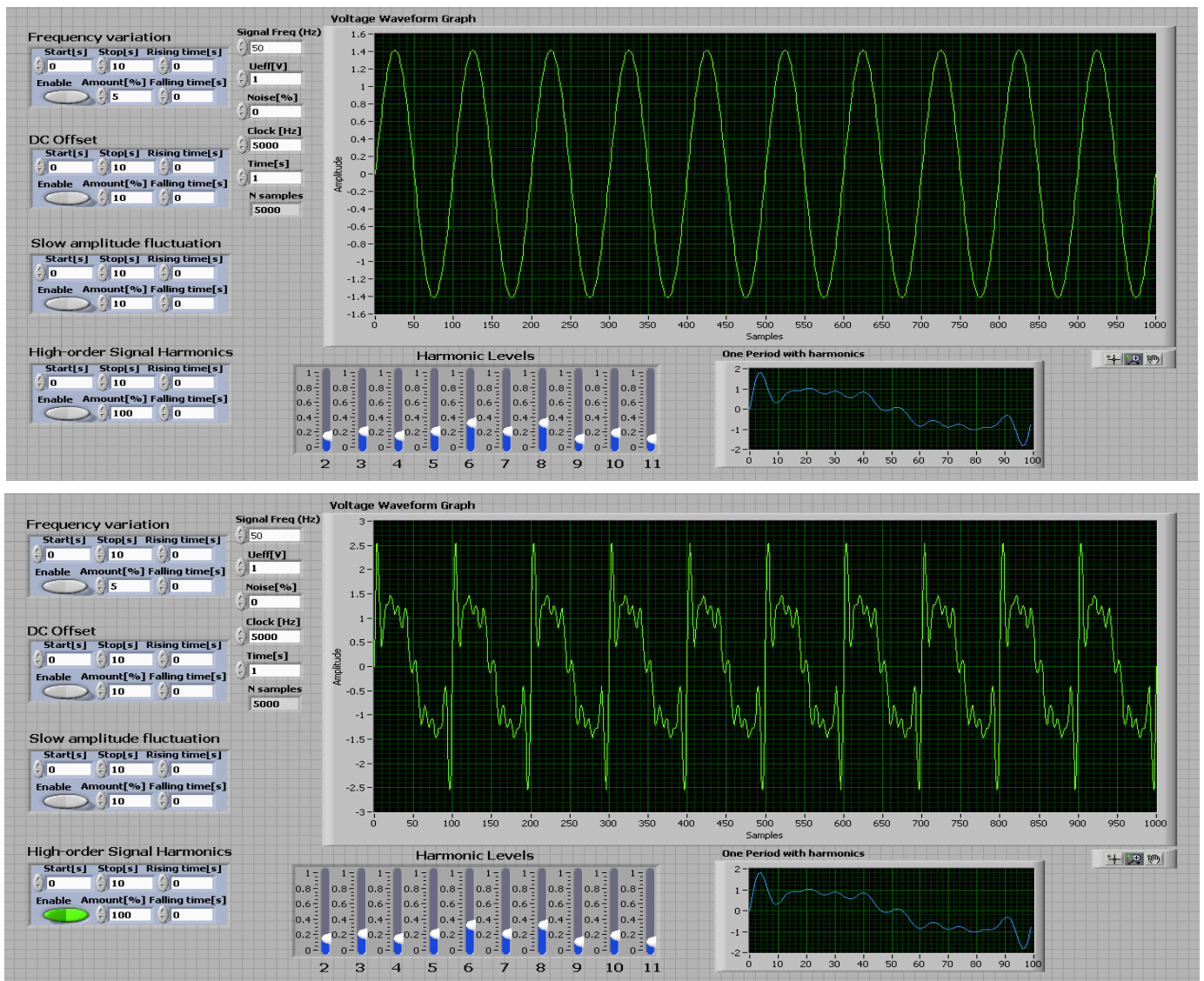


Fig. 1. LabVIEW panel for generation of the voltage waveform: undisturbed signal (above) and signal with harmonic disturbances (below)

virtual instrument [7]. Control front panel gives possibility for fast and simple correction of the basic waveform parameters, according to specific user requirements and purposes. Second functional segment of this procedure is focused on real-time generation of the previously defined and selected waveforms with harmonic disturbances, using analog outputs of the data acquisition card NI 6343. This is 32-channel PCIe acquisition card, capable for digital to analog signal conversion, designed for output voltage range of $\pm 10V$ and with 16-bit resolution.

Virtual instrumentation is based on the standard computers, hardware components for acquisition and software packages for graphical presentation and software processing of obtained results [5]. Front panel of the virtual instrument in LabVIEW software environment, developed for generation and graphical presentation of the standard voltage waveform, is presented in Fig. 1. Shown control panel of the virtual instrument provides selection and adjustment of the basic waveform parameters, by number of the control functions and knobs, implemented in block diagram of the virtual instrument. Presented voltage waveform is generated with nominal frequency value of 50Hz

and normalized RMS voltage level of 1V. Separated segment of the control functions on front panel is used for selection and adjustment of the specific maximum levels regarding to the individual high-order voltage harmonics. Content of the specific high-order signal harmonics can be precisely defined by number of the control knobs used for regulation of the harmonic amplitude levels. In Fig. 1. are presented two cases of the generated voltage waveform. Above picture shows undisturbed voltage waveform without signal disturbances, while below picture presents standard voltage waveform generated with certain levels of the high-order harmonic disturbances. In order to be more realistic in generation of the signal waveforms, for particular disturbances is enabled separate definition of the nominal frequency variations, signal DC offset, amplitude fluctuations, start and stop times of the disturbances, rising and falling times and percentage amounts of the disturbance amplitude levels. Specified precise levels of the individual high-order signal harmonics, from 2nd to 11th voltage harmonic orders, are indicated on separate segment of the control front panel, which is in detail shown in Fig. 2.

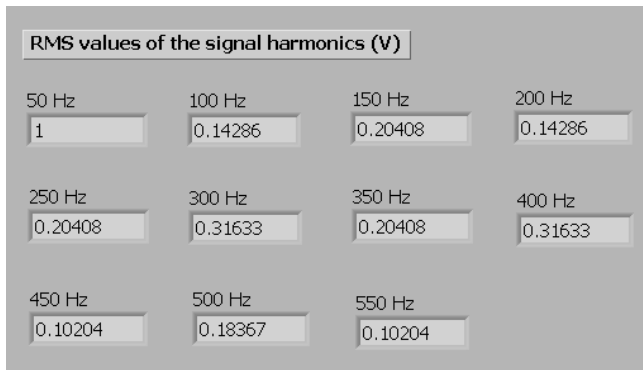


Fig. 2. Front panel for indication of the selected signal harmonics (RMS voltage values from 2nd to 11th high-order harmonics)

III. USING OF THE SYSTEM

Presented solution of the data acquisition system can be used for generation of the reference signals, applicable in testing of instruments for measurement and analysis of the standard power quality parameters and high-order harmonic disturbances. As an example, in this specific case generated voltage waveforms with harmonic disturbances are used for testing of three-phase power quality analyzer Fluke 435 Series II. Hardware block configuration of this testing procedure is presented in Fig. 3. Reference voltage waveforms, generated with desired level of the harmonic disturbances, from analog output channels of the data acquisition card NI 6343 are sent directly to voltage inputs of the tested instrument Fluke 435, using standard connector block SCB 68A (line 1). Instrument is set to work in mode for measurement of the high-order signal harmonic components. Direct communication from instrument output to computer is provided using standard USB communication interface (line 2), so measurement data

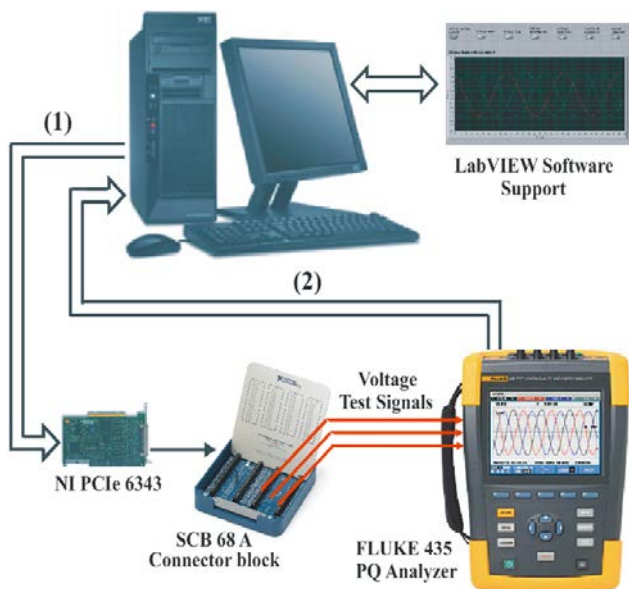


Fig. 3. Hardware configuration of the software supported procedure for testing of the power quality (PQ) analyzer Fluke 435

obtained during testing process can be easily transferred to computer, recorded and processed for graphical presentation. Some characteristic results obtained from described testing procedure are presented in following section of this paper.

Software supported testing process includes three basic segments. First segment is recording of the three-phase test voltage waveforms on graphical display of the tested device. Second part is recording of the high-order signal harmonic graphs. Third part of the process involves measurement of the high-order harmonic RMS values for generated test voltage waveforms. Voltage signal waveforms for all three phases, recorded on graphical display of the tested instrument, power quality (PQ) analyzer Fluke 435 Series II, are shown in Fig. 4. Presented voltage waveforms correspond to the test signal with harmonic disturbances, previously illustrated in Fig. 1.

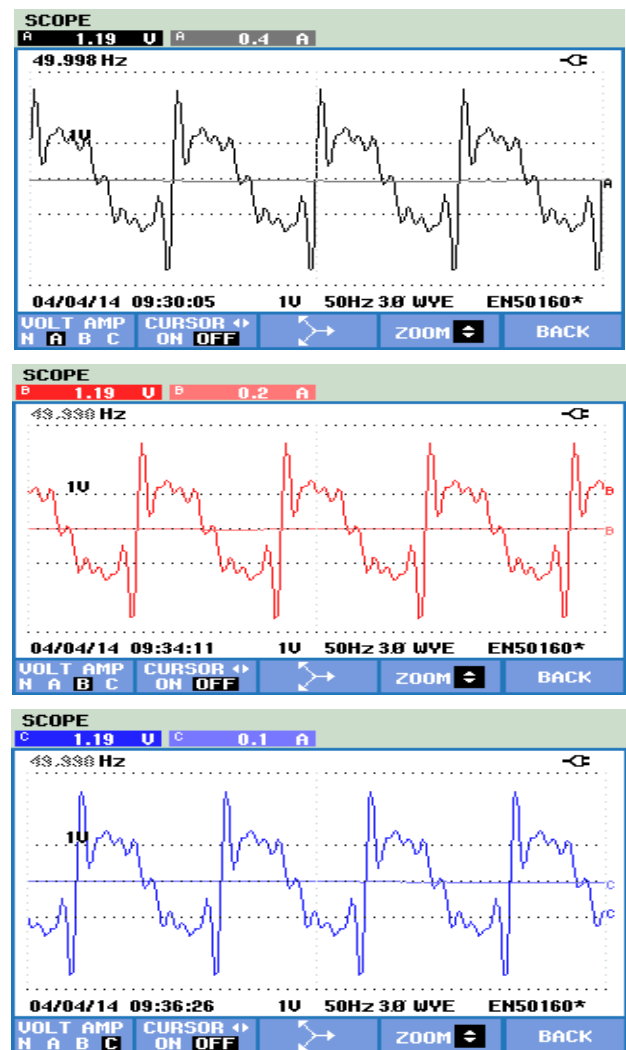


Fig. 4. Three-phase voltage waveforms recorded on display of the tested instrument - power quality analyzer Fluke 435

Graphs of the measured high-order harmonics, recorded on graphical display of the tested instrument for all three phases of the test signals, are presented in Fig. 5. Shown harmonic graphs indicate maximum measured percentage values of individual high-order voltage harmonics in test waveforms. Obtained harmonic levels, shown on instrument display, fully

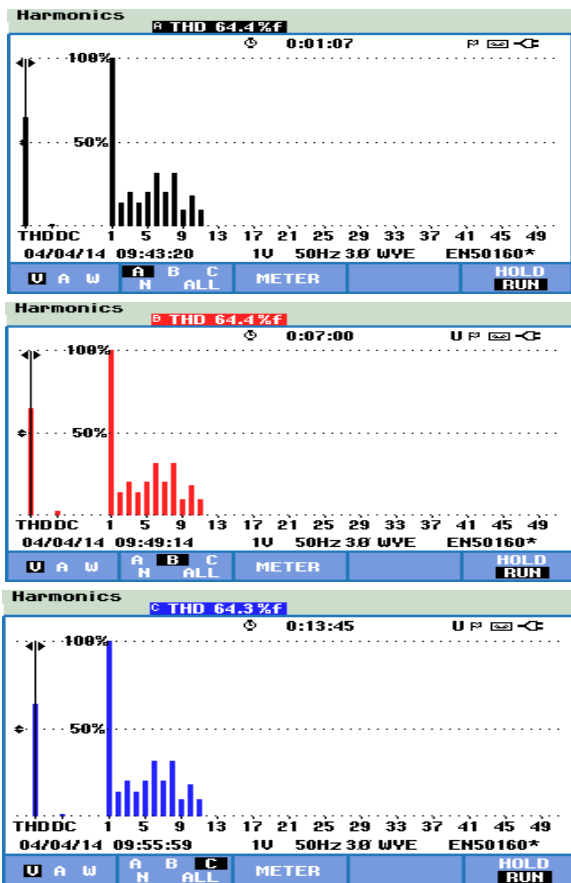


Fig. 5. Recorded graphs of the high-order signal harmonics

HARMONICS TABLE				
	A	B	C	N
Volt	100.0	100.0	100.0	100.0
H1% _f	14.2	14.3	14.3	58.3
Volt	20.4	20.4	20.3	72.4
H3% _f	14.3	14.3	14.2	69.8
04/04/14 10:20:02 1U 50Hz 3Ø WVE EN50160*				
HARMONICS TABLE				
	A	B	C	N
Volt	20.4	20.3	20.2	110.7
Volt	31.5	31.5	31.4	183.2
H7% _f	20.2	20.2	20.2	145.9
Volt	31.3	31.4	31.3	246.2
04/04/14 10:20:44 1U 50Hz 3Ø WVE EN50160*				
HARMONICS TABLE				
	A	B	C	N
Volt	10.1	10.1	10.1	84.1
Volt	18.1	18.1	18.0	144.9
H11% _f	10.0	10.0	10.0	95.8
Volt	0.0	0.1	0.1	44.1
04/04/14 10:21:31 1U 50Hz 3Ø WVE EN50160*				

Fig. 6. Measured percentage values of the signal harmonics

correspond to the previously selected harmonic values in test waveforms, from 2nd to 11th harmonic orders, given in Fig. 2.

Finally, measurement results related to percentage values of the high-order signal harmonic components in test signals, obtained using tested instrument Fluke 435, are presented in Fig. 6. Shown measurement results, obtained during testing process, are completely matching to previously defined values of the high-order harmonic components in test waveforms.

IV. CONCLUSION

Software supported procedure, applied for generation of the test voltage signals with certain level of the standard harmonic disturbances, is described in this paper. Generation process is functionally based on the virtual instrumentation concept, which includes control application developed in LabVIEW software environment and data acquisition card NI PCIe 6343. Variation of the basic parameters for definition, presentation and signal generation is provided by various control functions and switches, implemented on front panel of developed virtual instrument. For specific harmonic disturbances is possible to define percentage amounts of the harmonic amplitude levels, nominal frequency variations, amplitude fluctuations, start and stop times, rising and falling times of the disturbances. Presented data acquisition system is verified by means of the software controlled procedure used for testing of the power quality analyzer Fluke 435 Series II. Using described solution of the acquisition system, can be provided various voltage test sequences with standard harmonic disturbances. In this case for testing purposes are used some characteristic voltage test waveforms with harmonic disturbances. Basic measurement results and recorded three-phase voltage waveforms, obtained from testing process, are presented and analyzed in this paper.

ACKNOWLEDGEMENT

This work was supported by national scientific project, with reference number TR 32019, sponsored by Serbian Ministry of Education, Science and Technological Development.

REFERENCES

- [1] E.F. Fuchs, M.A.S. Masoum, *Power Quality in Power Systems and Electrical Machines*, Academic Press, USA, February 2008.
- [2] J.C. Whitaker, *AC Power Systems Handbook, Third edition*, Taylor & Francis Group, New York, 2007.
- [3] B. D'Apice, C. Landi, A. Pelvio, N. Rignano, "A Multi-DSP based Instrument for Real-time Energy and PQ Measurements", *Metrology and Measurement Systems*, vol. 14, no. 4, pp. 495–506, 2007.
- [4] *Power Quality Application Guide, Voltage Disturbances, Stand. EN 50160*, Copper Development Association, 2004.
- [5] *LabVIEW Users Manual*, National Instruments, 2012.
- [6] *Fluke 435 Series II - Three-phase Energy and Power Quality Analyzer Users Manual*, Fluke Corporation, January 2012.
- [7] M. Simić, D. Denić, D. Živanović, D. Taskovski, V. Dimcevic, "Development of a Data Acquisition System for the Testing and Verification of Electrical Power Quality Meters", *JPE – Journal of Power Electronics*, vol. 12, no. 5, pp. 813-820, 2012.

Using Multifunction DAQ and LabVIEW for the Development of a Single-Channel EEG for Multiple Sclerosis Detection

Viktor Mihaylov¹, Kalin Dimitrov², Yuliyana Velchev³, Tsvetan Mitsev⁴

Abstract – In this paper is presented a single-channel EEG acquisition system using a multifunction DAQ. This is done in order to provide a presentation to students of the application of an EEG measurement setup for detecting symptomatic epilepsy-induced seizures in patients with multiple sclerosis.

Keywords – single channel EEG, multiple sclerosis, engineering education.

I. INTRODUCTION

Electroencephalography (EEG) is the recording of electrical activity of the human brain along the scalp. EEG measures voltage fluctuations resulting from ionic current flows within the neurons of the brain. In clinical contexts, EEG refers to the recording of the brain's spontaneous electrical activity over a period of time, as recorded from multiple electrodes placed on the scalp. Diagnostic applications generally focus on the spectral content of EEG, that is, the type of neural oscillations that can be observed in EEG signals.

EEG examination is a crucial precursor for the evaluation of a Multiple sclerosis (MS) patient. Diagnosing multiple sclerosis is a complicated task. There is no specific test for multiple sclerosis and, anyway, it is not even certain that it is only one disease. To an extent, getting an MS diagnosis is a process of eliminating all other causes of EEG abnormalities. Typically, people who have finally been diagnosed with definite MS have been passed through several diagnostic stages. This process is often drawn out over months or years.

As a chronic inflammatory disease of the immune system MS affects the brain central and central nervous system, spinal cord and optic nerves. More specific consequences subside to epilepsy seizures. Although not often manifested, they are more frequent than in the general population [1], with the average 2-2.5% [2]. Symptomatic seizures are the main

differentiator when conducting EEG studies. EEG findings contribute to the multi-axial diagnosis of epilepsy [3], in terms of whether the seizure disorder is focal or generalised, idiopathic or symptomatic, or part of a specific epilepsy syndrome.

There are three main types of evoked potential test:

Visually Evoked Potential (VEP)-This test measures the speed of the optic nerve. The patient has to focus on the centre of a "TV" screen on which there is a black and white chequered pattern. Each square in the pattern alternates between black and white at measured intervals. The patient wears a patch on one eye for a while and then on the other, so that the speed of both optic nerves can be measured. 85-90% of people with definite MS and 58% of people with probable MS will have abnormal VEP test results [4,5].

Brainstem Auditory Evoked Response (BAER) test measures the speed of impulses along the auditory portion of Cranial Nerve VIII. This nerve arises in the Pons area of the Brainstem and therefore this test may be indicative of lesions in that area. The patient lies down in a darkened room to prevent visual signals from interfering with measurements. A series of clicks and beeps are played back to the patient. 67% of people with definite MS and 41% of people with probable MS will have abnormal BAER test results [6].

Somatosensory Evoked Potential (SSEP) test involves strapping an electrical stimulus around an arm or leg. The current is switched on for 5 seconds and electrodes on the back and skull measure the response at particular junctions. The current is very low indeed and completely painless. The speed of various nerves can be measured in this way and the points of slow-down (i.e. demyelinated lesions) approximated to because of the sampling at several places. 77% of people with definite MS and 67% of people with probable MS will have abnormal SSEP test results [7].

Slow nerve responses in any of these tests are not necessarily indicative of MS but can be used in conjunction with a neurological examination, medical history, an MRI and a spinal tap to deduce some kind of diagnosis.

A large variety of specialized EEG devices have been developed for all those different clinical approaches. But for experimenting with new methods for signal processing and to be able to reach a better educational effect it is feasible to utilize a Multifunction DAQ with a proper software [8]. National Instruments' LabView presents such a solution.

With recent bandwidth improvements and new innovations from NI, USB has evolved into a core bus of choice for measurement and automation applications. Devices for USB deliver high-performance data acquisition in an easy-to-use and portable form factor through USB ports on laptop computers and other portable computing platforms. National

¹Viktor Mihaylov is with the Faculty of Telecommunications at Technical University of Sofia, 8 Kl. Ohridski Blvd, Sofia 1000, Bulgaria, E-mail: vvmihaylov@abv.bg.

²Kalin Dimitrov is with the Faculty of Telecommunications at Technical University of Sofia, 8 Kl. Ohridski Blvd, Sofia 1000, Bulgaria, E-mail: kld@abv.bg.

³Yuliyana Velchev is with the Faculty of Telecommunications at Technical University of Sofia, 8 Kl. Ohridski Blvd, Sofia 1000, Bulgaria, E-mail: julian_s_velchev@abv.bg.

⁴Tsvetan Mitsev is with the Faculty of Telecommunications at Technical University of Sofia, 8 Kl. Ohridski Blvd, Sofia 1000, Bulgaria, E-mail: mitsev@tu-sofia.bg.

Instruments designed the new and innovative patent-pending NI signal streaming technology that enables sustained bidirectional high-speed data streams on USB. The new technology, combined with advanced external synchronization and isolation, helps engineers and scientists achieve high-performance applications on USB.

NI M Series bus-powered multifunction data acquisition devices for USB are optimized for superior accuracy in a small form factor. They provide an onboard NI-PGIA 2 amplifier designed for fast settling times at high scanning rates, ensuring 16-bit accuracy even when measuring all available channels at maximum speed.

All bus-powered devices have a minimum of 16 analog inputs, digital triggering, and two counter/timers. USB M Series devices are ideal for test, control, and design applications including portable data logging, field monitoring, embedded OEM, in-vehicle data acquisition and academic.

II. METHODOLOGY

A. EEG recording

EEG signals have highly non-Gaussian and nonstationary characteristics. In order to extract any beneficial information signal processing has to be employed. The postsynaptic potentials sum is the range of about 5 μ V to 100 μ V and frequency range 3Hz to 70Hz [4]. This narrows down to a few of the shelf solutions as the one chosen for the project – National Instruments USB-6211 data acquisition module along side the LabView graphical programming language. LabView allows a fast paced and low cost development of smart algorithms for signal processing.

An important matter is the ability for denoising the acquired signal. A common drawback in evaluating patients with MS is that the measurements are conducted in intensive care units which have the disadvantage of the low preparation time and exposure to a variety of electrical equipment [2]. In this case there are many sources of noise, to most of which the available EEG equipment is highly susceptible to. EMI artefacts are seen more frequently. An important matter is to obtain the main characteristics of the measurement device in these conditions. Recording methodology and is crucial for minimizing noise.

Instead of doing a single conversion, the ADC performs the conversions ("samples" the input) periodically. Resulting in a sequence of digital values that have converted a continuous-time and continuous-amplitude analog signal to a discrete-time and discrete-amplitude digital signal. This greatly reduces and simplifies the medical and engineering analysis. The estimated levels of the signals in such a small range (± 0.2 to ± 10 V per channel) as specified previously can be calculated from the main characteristics of the DAQ. Most important being the Minimum Voltage Range (from -200 mV to -200 mV) and Minimum Voltage Range Sensitivity - 4.8 μ V, well in the limits of normal EEG signals. Input impedance for the analog input is >10 G Ω in parallel with 100 pF. Analog input are 16-bits and sampling rate 250ks/s, so within the range the best resolution will be about 6 μ V. In

order to improve the resolution we perform a suitable amplification of the EEG signal with gain of 100. Also, the sampling rate is reduced down to 250S/s.

C. Amplification

The EEG Amplifier plays a vital role in the field of education and research. The EEG amplifier has served many different uses in a variety of different fields, and even with more recent advancements in high-tech machines. EEG Amplifier system may combine data acquisition hardware and software to allow researchers and educators to perform unipolar and bipolar measurements. Output can be switched between normal EEG output and Alpha wave detection, and software can then automatically filter the raw EEG signals for Alpha, Beta, Theta, and Gamma wave activity, providing a full frequency analysis of the data.

D. Single channel EEG

One of the holy grails of EEG, along with dry electrodes, is the idea of single-channel EEG. System solely dependent . Or rather, useful single-channel EEG. It's very easy to record EEG from a single channel but making sense of the data and building a useful application around it is not. The reason that single-channel EEG is so attractive is not just ease-of-use but the relationship between ease-of-use and the amount of data that can be reasonably recorded.

When it comes to EEG, more channels (electrodes) are always better, having a dense network of electrodes allows us to create spatial maps of activity which brings EEG into the realm of brain imaging. See Michel and Murray for a nice overview of this topic. As we know EEG (along with MEG) has far and above the best temporal resolution of all techniques used to study the brain. If we add full-head dense electrode arrays we also have decent spatial resolution.

This is an extremely powerful and as yet underexploited tool in neuroscience but it has a major drawback, by increasing spatial resolution we decrease ease-of-use and comfort while increasing the cost. The beauty of EEG is that, of all possibilities for measuring brain activity, it is currently the only one that can conceivably be packaged in a miniaturised, light, comfortable and low cost package. This directly addresses one of the major obstacles in neuroscience today, lack of data. We typically only have data for patients who have already presented with serious symptoms (because brain imaging is expensive and difficult). We don't know very well what "normal" brains look like and how they evolve over the life time.

The solution for us is obvious, cheap, medical grade EEG on a massive scale but to make this happen we need to reduce the number of electrodes to make the process user friendly and robust. The end point of this is single channel EEG.

Consumer grade products already exist such as Neurosky and iBrain. With these devices the emphasis is on making it easy to use and cheap enough for consumer apps.

E. Multiple sclerosis detection

Three main types of evoked potential tests are used in the diagnosis of MS. Each of these tests requires that electrodes are attached to the scalp and connected to an electroencephalograph (EEG) to record brainwaves in response to different stimuli. The different tests are:

Brainstem Auditory Evoked Potentials (BAEP): A series of clicks are played in each ear through headphones.

Visual Evoked Potentials (VEP): A series of checkerboard patterns are displayed on a screen.

Sensory Evoked Potentials (SEP): Mild electrical shocks are administered to an arm or leg.

The doctor is looking for both the size of the response and the speed in which the brain receives the signal. Weaker or slow signals may indicate that demyelination has occurred and that MS is a possibility. However, this test is also not specific to MS; abnormalities could indicate another problem. A series of all three tests could take up to two hours to complete.

III. EXPERIMENTS

A. Setup

A setup was prepared to closely resemble an EEG acquisition room – away from active electronics and with reduced electromagnetic interference. Signal recordings were made with differentiation in the electrode to electrode comparison. NRSE (detect the ground voltage provided by the signal for all EEG leads) and differential voltage between the electrodes. 3 leads are chosen for the measurement – Z (for ground - ear), Cz, C4, T4. All are placed on the EEG cap and linked to bridge electrodes.

B. Real recorded data

In Fig. 1 two notable noise components are observed. One is a low frequency component "pushing" the whole envelope below the zero and the second is dominant 50 Hz mains one. Fig.2 on the other hand exhibits a steady low frequency amplitude change due to heart rate/ pulse interference. In Fig.3 a multiple electrode NRSE measurement was set up graphically depicting the 50 Hz induced component from the power supply.

IV. RESULTS

A working setup was created for testing.

Due to the high susceptibility of the set up to noise a good step would be the inclusion of a better pre-amplifier, post processing, low and notch filters, as well.

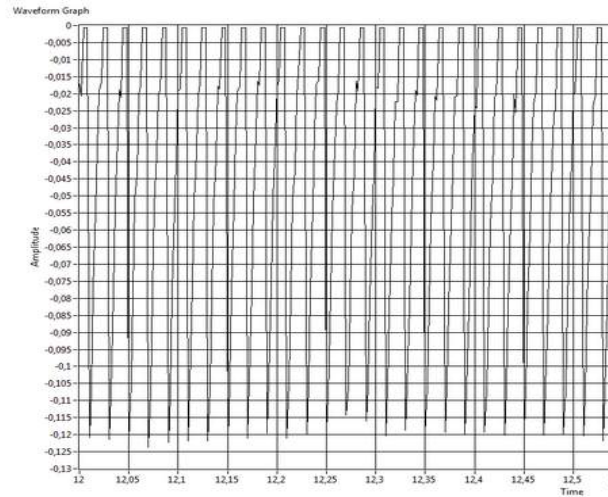


Fig. 1. Sample measurement Cz-Z. Amplitude is mV [Y axis], Time is in seconds [X axis]

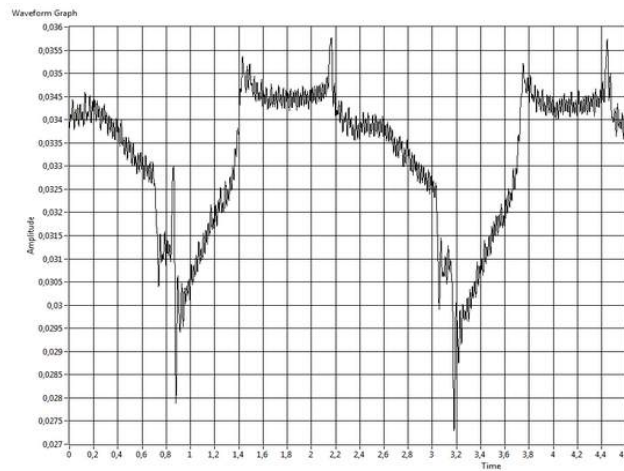


Fig. 2. Sample measurement C4-Z. Amplitude is mV [Y axis], Time is in seconds [X axis]

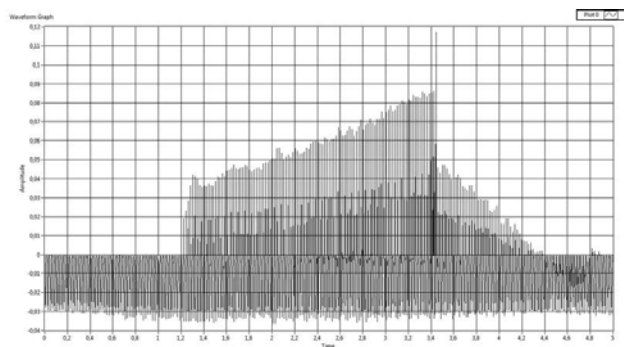


Fig. 3. Sample measurement Cz, C4, T4-Z. NRSE Measurement. Amplitude is mV [Y axis], Time is in seconds [X axis]

ACKNOWLEDGEMENT

The research in this paper is supported by PhD grant 132PD0053-07, R&D Sector, Technical University of Sofia.

REFERENCES

- [1] A. Ghezzi, et al. "Epilepsy in multiple sclerosis", *Eur Neurol*, 30(4), pp.218-23, 1990.
- [2] H. Catenox, et al., "Multiple sclerosis and epileptic seizures" *Mult Scler*, 17(1), pp.96-102, 2011.
- [3] L. Greenfield, J. Geyer, P. Carney, "Reading EEGs: A Practical Approach", Lippincott Williams & Wilkins, 2012.
- [4] M.M. Christoph, "Electrical Neuroimaging", Cambridge University Press, New York, 2009.
- [5] P. Fuhr, A. Borggreffe-Chappuis, C. Schindler, L. Kappos "Visual and motor evoked potentials in the course of multiple sclerosis", *Brain*, 124, Oxford University Press, pp.2162–2168, 2001 .
- [6] A. Rae-Grant, R. Fox, F. Bethoux, *Multiple Sclerosis and Related Disorders: Diagnosis, Medical Management, and Rehabilitation*, Demos Medical Publishing, 2013.
- [7] K.H. Chiappa, *Evoked Potentials in Clinical Medicine*, Lippincott Williams & Wilkins, 1997.
- [8] J. Kasarwala, J. Warriar, S. Sanghvi, "Development of Single Channel EEG using LabVIEW", *International Journal on Advanced Electrical and Electronics Engineering*, (IJAEED), ISSN (Print) 2278-8948, Vol.1, 1, pp.94-96, 2012.

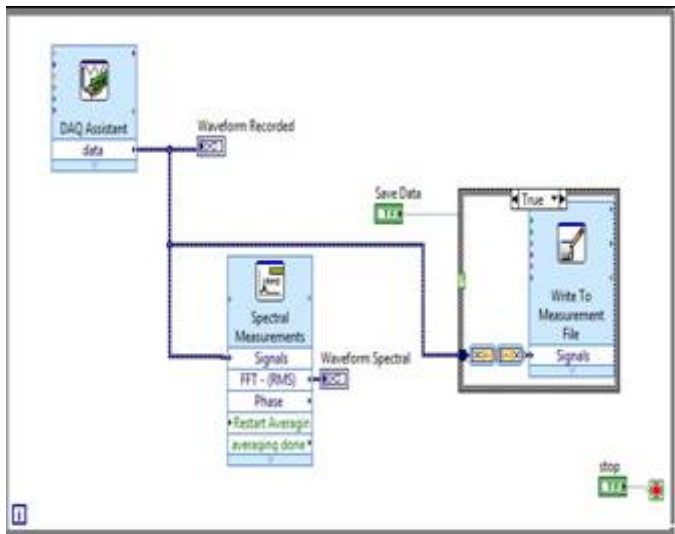


Fig. 4. An overview of the LabView measurement recording without any post signal processing. All data is recorded to a TDMS file format

V. CONCLUSION

It is convenient to use Multifunction DAQ and LabVIEW when it comes to experimentation. It is also suitable for students training. In real task is better to think for specialized FPGA solution.

Model Development for Digital Stochastic Measurement of Noised EOG Signals

Jelena Djordjevic-Kozarov¹, Platon Sovilj², Dejan Mitic³, Vladimir Vujcic⁴,
Dragan Radenkovic⁵

Abstract –The paper presents simulation model development for an example of digital stochastic measurement method (DSMM) for measurement of nonstationary signals. This method is based on stochastic analog-to-digital (A/D) conversion, with a low-resolution analog-to-digital converters (ADCs), and accumulation. The simulation has been realised using the Matlab program, and electrooculography (EOG) signal is used as an example of a real low nonstationary signal. Tests are done with adding a noise-varying signal-to-noise ratio (SNR) from 10 to –10 dB.

Keywords –Digital stochastic measurement, electrooculography (EOG), signal processing, simulation model, measurement errors.

I. INTRODUCTION

The method for digital stochastic measurement (DSM) of stationary signals has been developed and described in [1-6]. Few prototypes of instruments based on these methods has been developed. This instruments were named digital stochastic instruments.

Then, a question appears - whether it is possible to apply the stochastic digital measurement methods for measurement of nonstationary signals, such as biomedical signals, audio and video signals, etc. The DSM of electroencephalography (EEG) signals has been discussed in [7, 8], where EEG signal has been taken as an example of nonstationary signals.

This paper discusses further application of DSM for nonstationary signals. An electrooculography (EOG) signal is used as an example of biomedical nonstationary signal for DSM model developed simulation tests.

Electrooculography is the standard method by which eye movements are recorded in the clinical eye movement laboratory [9]. The resulting signal is called the

electrooculogram.

EOG signal presents the corresponding record in the function of time for each kind of eyeballs movements, such as up, down, left, right, and eye blinking. Obtained signals can be used for external devices control, such as virtual keyboards, electric wheelchairs, artificial arms and robots. Also, in ophthalmology the recording of eye movements is necessary for a detailed description and analysis of the eye motoric functioning. Various changes in the eye can be detected by analyzing EOG signals. In that way, the condition of the eye can be determined.

II. STOCHASTIC DIGITAL MEASUREMENT METHOD

Digital stochastic measurement (DSM) method is based on measurement over an interval [1]. Measurements are carried out by low-resolution ADCs. In order to eliminate the influence of the quantization error, which is significant here, an uniform random noise with average value equal to 0 is added to the input signal in the range of quant of the applied ADC.

If needed to measure the RMS value of the signal, than measurement block is extended by another ADC, another uniform random noise generator and multiplier-accumulator. If the uniform noises on the inputs of both ADCs are not in correlation and the same signal at the input of both channels, the mean value of the accumulator contents is then equal to the square of the effective value on interval.

If the input of the second channel multiplier-accumulator is a basis function from the orthonormal function set, such as Fourier, then the mean value of the accumulator is equal to the value of the corresponding signal coefficient in the orthonormal set. In this way, the coefficients can be measured very accurately.

The problem appears because the correct presentation of the signal over an interval, in the case of Fourier, requires a huge number of coefficients (defined by the sampling theorem). In that case, the measurement hardware would be very complicated and impractical.

Since the function of the second channel is known, as well as noise, it is possible to generate basis function values over the interval, and stores them in memory. The memory output is the second input of multiplier-accumulator. This structure is shown in Fig. 1.

¹Jelena Djordjevic-Kozarov is with the Faculty of Electronic Engineering at University of Niš, Aleksandra Medvedeva 14, 18000 Niš, Serbia, E-mail: jelena.djordjevic@elfak.ni.ac.rs.

²Platon Sovilj is with the Faculty of Technical Sciences at University of Novi Sad, Trg Dositeja Obradovića 6, 21000 Novi Sad, Serbia.

³Dejan Mitic is with the Faculty of Electronic Engineering at University of Niš, Aleksandra Medvedeva 14, 18000 Niš, Serbia.

⁴Vladimir Vujcic is with the Faculty of Technical Sciences at University of Novi Sad, Trg Dositeja Obradovića 6, 21000 Novi Sad, Serbia.

⁵Dragan Radenkovic is with the Faculty of Electronic Engineering at University of Niš, Aleksandra Medvedeva 14, 18000 Niš, Serbia.

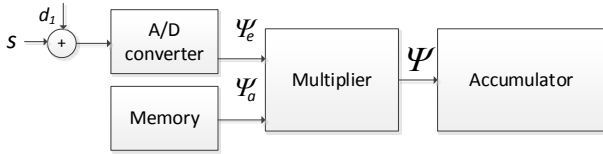


Fig. 1. Block diagram of digital stochastic measurement of one Fourier coefficient of conditioned input signal

III. SIMULATION AND RESULTS

The DSM system consists of three blocks: a signal conditioning block (amplification, linearization, filtering, scrolling levels, noise suppression, electrical isolation), a DSM block, and a block for data processing, recording, and presenting. The signal at the input of the DSM block is the conditioned signal. The system has been realized using software package Matlab.

A. Input Signal

As the input signal of DSM block is taken conditioned EOG signal. Typical EOG signals have amplitudes in the millivolts range with frequencies of DC - 100 Hz [10]. EOG signal is one of the standard biopotentials measured during a deep sleep, so called REM (Rapid-Eye-Movement) phase of sleep. REM involves very quick and random eye movements. In a normal night sleep, REM occurs every 90 minutes and lasts for approximately 5 to 30 minutes at a time.

An input signal of DSM block is 10 s of signal extracted from a real measurement session of the EOG signal. These values of signal are amplified and adapted to a range [-0.5 V, 0.5 V]. therefore, the conditioned signal is the input of the DSM block.

In the real measurement, which was a typical digital measurement procedure, the EOG signal was stored with 250 samples per second (S/s). For obtaining a smooth input for simulation, these 250 S/s records were transformed into 5000 S/s data. This was achieved by using the Matlab function 'interp', for resampling input signal by integer factor, with a given value of 20. Each sample of conditioned signals is stored as a value in a simulation lookup table.

For obtaining correct simulation results, each simulation included measuring the same EOG signal. Repeatability of EOG signals could not be achieved with a humane subject and "live" measurement for each experiment. Therefore, the source of the EOG signal in simulation measurements was not a humane subject, but an data source of conditioned signals was made.

B. System Properties and Results

The DSM block in simulation was configured according to the data presented in Table I. Three sets of simulations were run, with adding white noise to the input signal. The noise has

a uniform probability density function, and the signal-to-noise ratio (SNR) was 10, 0, and -10 dB. There is no antialiasing filter before the DSM block, which would limit noise bandwidth.

At the output of each set of simulation is obtained the reproduced signal. As a result of simulation, errors in frequency and time domain are obtained, as well as corresponding graphics of the input and the reproduced signal. The results of one measurement series, i.e. measurement errors in the time domain, are shown in Table II.

TABLE I
DSM BLOCK PROPERTIES IN SIMULATION SETS

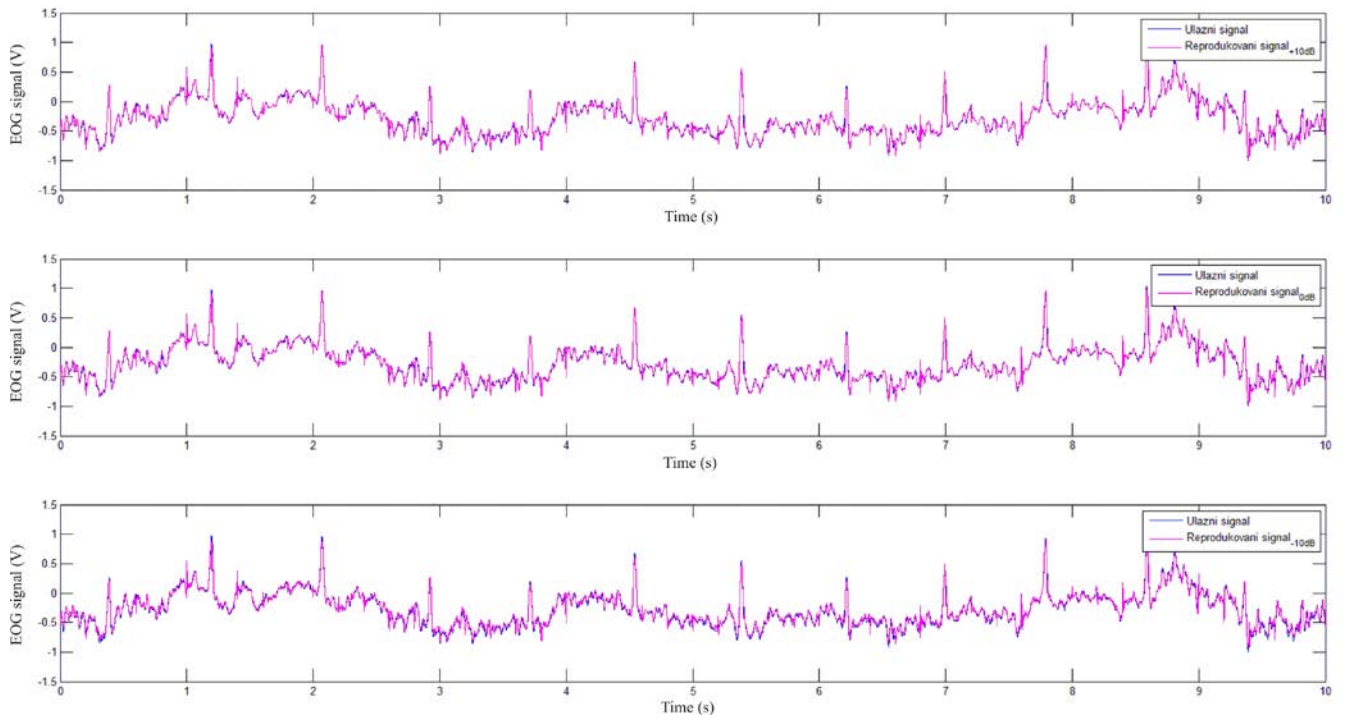
Number of simulations	3 x100 (for each SNR level)
SNR level	10 dB, 0 dB, -10 dB
A/D converter	Resolution: $m_1 = 6$ bits Input range: $\pm R$ and $R = 2.5$ V Sampling frequency: $f_{ADC} = 250$ kHz
Measurement Interval	$[0, T]$ and $T = 0.2$ s
Fundamental frequency	$f_0 = 5$ Hz
Number of samples per measurement interval	$N = f_{ADC} T = 50\ 000$
Digital dithered base functions	Stored in memory simulating an A/D converter with following properties: Resolution: $m_2 = 8$ bits Range: $\pm R$ and $R = 2.5$ V Sampling frequency: $f_{ADC} = 250$ kHz
Number of measured Fourier coefficients	DC component + 15 sine coefficients + 15 cosine coefficients

TABLE II
MEASUREMENT ERRORS IN TIME DOMAIN

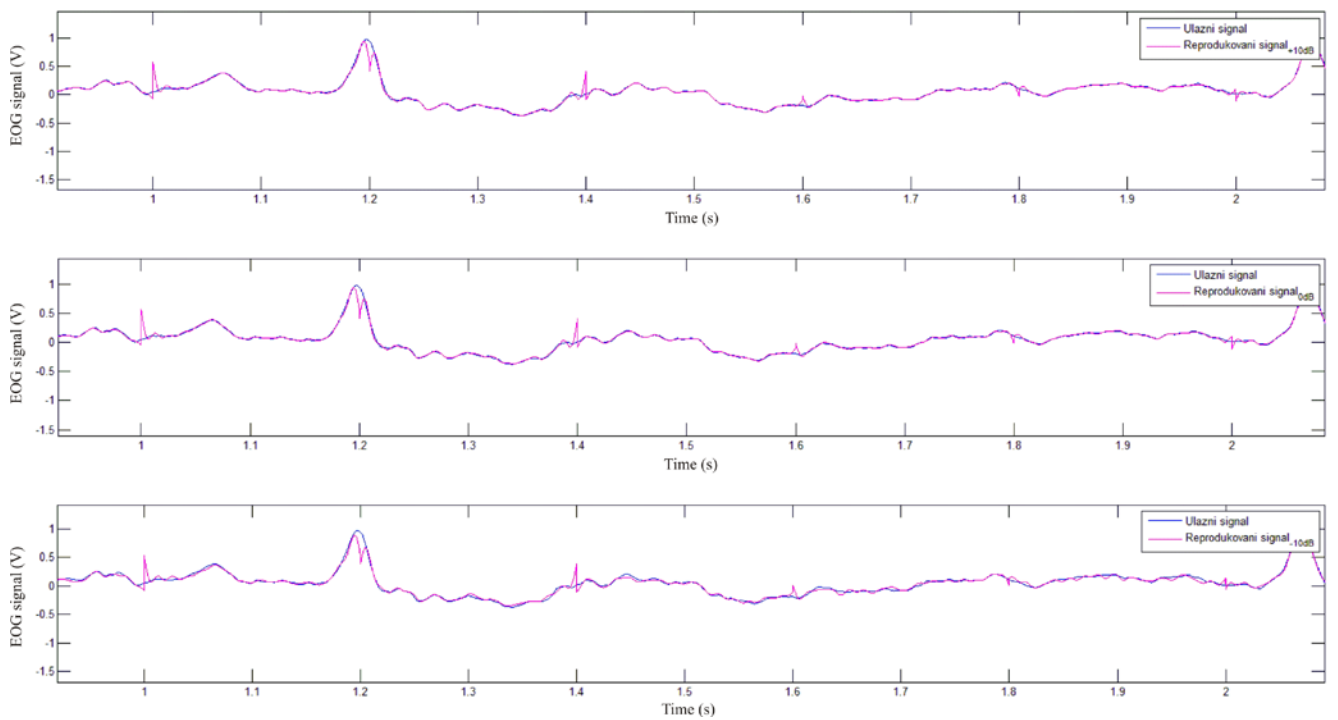
Measurement interval: 0.2 s			
Number of harmonics: 15			
ERRORS	SNR = 10 dB	SNR = 0 dB	SNR = -10 dB
Max absolute	0.551834	0.557231	0.539366
Max relative (%)	27.2716	27.5384	26.6555
Average absolute	0.015895	0.017386	0.030128
Average relative (%)	0.7856	0.8592	1.4889

In Fig. 2a is a graph showing the input and of reproduced signals.

In Fig. 2b can be observed significant deviations of reproduced signal from the input signal.



a)



b)

Fig. 1. Measurement results for Digital Stochastic Measurement of noisy EOG signals, for measurement interval 0.2 s: a) comparison of input signal and noised signals for the series of 100 measurements, b) zoomed panel a)

These deviation occur at the beginning and at the end of each measurement interval, i.e. every 0.2s, and they are the consequence of occurrence of Gibb's phenomenon. This phenomenon significantly increases the total measurement error, so that the maximum relative error of measurement (for SNR 0dB) reaches 27.5384%.

IV. CONCLUSION

This paper presents a model for digital stochastic measurement of EOG signals where the realization of DSM block is carried out by 6-bit and 8-bit ADCs. The entire system has been implemented using Matlab. Based on analysis of results, can be concluded that the greatest influence on the total measurement error is appearance of the Gibb's phenomenon at the ends of measurement interval.

The idea of further model development is to eliminate the Gibb's phenomenon, in order to improve the model and to decrease the measurement error. It would be interesting to explore what will be the results if an identical measurement sequence had been realized, where measurement starts delayed by a certain Δt . In that way, an overlap of the measurement intervals on the places where the Gibb's phenomenon occurs is achieved.

REFERENCES

- [1] V.V. Vujicic, I. Župunski, Z. Mitrovic, M.A. Sokola, "Measurement in a point versus measurement over an interval," Proc. of the IMEKO XIX World Congress; Lisbon, Portugal, no. 480, pp. 1128-1132, Sep. 6–11, 2009.
- [2] V. Vujčić, S. Milovančev, M. Pešaljević, D. Pejić, I. Župunski, "Low frequency stochastic true RMS instrument," *IEEE Trans. Instrum. & Measurement*, vol. 48, no. 2, pp. 467–470, Apr. 1999.
- [3] D. Pejic, V. Vujicic, "Accuracy limit of high-precision stochastic Watt-hour meter," *IEEE Trans. Instrum. & Measurement*, vol. 49, no. 3, pp. 617–620, Jun. 2000.
- [4] V. Vujčić, "Generalized low frequency stochastic true RMS instrument," *IEEE Trans. Instrum. & Measurement*, vol. 50, no. 5, pp. 1089–1092, Oct. 2001.
- [5] B. Santrač, M.A. Sokola, Z. Mitrović, I. Župunski, V. Vujčić, "A novel method for stochastic measurement of harmonics at low signal-to-noise ratio," *IEEE Trans. Instrum. & Measurement*, vol. 58, no. 10, pp. 3434–3441, Oct. 2009.
- [6] V. Pjevalica, V. Vujčić, "Further generalization of the low-frequency true-RMS instrument," *IEEE Trans. Instrum. & Measurement*, vol. 59, no. 3, pp. 736–744, Mar. 2010.
- [7] P.V. Sovilj, S.S. Milovancev, V. Vujicic, "Digital Stochastic Measurement of a Nonstationary Signal With an Example of EEG Signal Measurement", *IEEE Trans. Instrum. & Measurement*, vol. 60, no. 9, pp. 3230–3232, September 2011.
- [8] P.V. Sovilj, "Stohastičko digitalno merenje EEG signala," doktorska disertacija, Fakultet tehničkih nauka, Univerzitet u Novom Sadu, Novi Sad, Srbija, 2010.
- [9] J.R. Carl, "Principles and Techniques of Electro-oculography," in *Handbook of Balance Function Testing*, ch. 4, pp. 69–82, San Diego, US: Singular Publishing Group, Inc., 1997.
- [10] CleveLabs Laboratory Course System – Student Edition, "Electro-Oculography I Laboratory," Cleveland Medical Devices Inc., Cleveland, OH, USA.
- [11] <http://www.physionet.org/cgi-bin/atm/ATM?tool>

Based on CPLD Programmable Counter for Experimental Digital Electrical Energy Meter Part 2

Nikola Draganov¹ and Totka Angelova²

Abstract – A creating of digital electrical energy meter conduces to its correctly measurement and to a price fixing of each electronic setup. Each measuring device effectiveness increases considerably with a introducing in them of modern programmable setup. The article presents a module depicting a electrical energy measurement information received by developed digital three-phase electrical energy meter. The block diagram of the device, the principle circuit diagram display and programmable logic have been presented. The schematic diagram of the counter programmed into the programmable block has been presented. The timing diagrams describing the operation of the device have been presented. The described module has real application in different digital electricity meters. The counter allows flexibility in the programming of reading programme.

Keywords – Programmable logic device, CPLD, FPGA, Digital measuring device.

I. INTRODUCTION

A modern measuring device improvement increases an accuracy, reliability decreases operator participation and measuring and indication time leads to automatic adjustment, self test, lower production and market prices. This all is possible with a modern programmable integrated circuit introduction based on CPLD and FPGA structures. Almost each up-to-day electronic device has reprogrammable module permitting not only flexible fulfilling of a measuring algorithm but also and a possibility to renovate managing software with an aim to get bigger efficiency and functioning. Reprogrammable logical set or more accurate programmable logical matrixes are more applied in an industry, motor-car and medical electronics, telecommunications, instrumentation etc. Their application in devices for consumption and generation measurement for instant of water, electrical energy increases a device reliability and a measured parameters keeping for a longer time [1-6].

An experimental development of electronic counter for three-phase electrical energy meter is described in the article. It is realized on the base of produced by Xilinx[®] integrated device CPLD and rules six digit seven segments LCD.

¹Nikola Draganov is with the Department of Electronics at Technical University of Gabrovo, Hadgi Dimitar, str.4, Gabrovo 5300, Bulgaria, E-mail: niko_draganov@mail.bg.

²Totka Angelova is with the Department of Electronics at Technical University of Gabrovo, Hadgi Dimitar, str.4, Gabrovo 5300, Bulgaria.

II. PRESENTATION

The created programmable counter block schematic diagram is shown in Fig. 1.

Its main component is a programmable unit PLU. It is built by a produced by Xilinx programmable logical device CPLD of the family XC9572. The logical device program is ushered by an external personal computer by means of IEEE1149.1 interface, known as JTAG. The described further software arranges input-output pins in such manner so and the information about enumerated units have to come energy measuring device in a strictly determined by a clock generator (G) time. In the same time the information about enumerated pulses is depicted in six digit seven segments LCD ruled by six CMOS decoders (D1-D6). The signals from EM get across input buffer in order to protect the matrix inputs. The measured information is preserved by means of transmission through communication port (CP) to an additional memory.

The unit for information displaying DU is another big module. It is consist of six decoders D1-D6 and six digit LCD. The circuit power supply is by a unit PU giving electrical voltages for separate blocks – logical matrix, decoders and pulse generator ($U_{DD} = 5V$) and negative voltage ($U_{EE} = -5V$) applied to a decoder for display control.

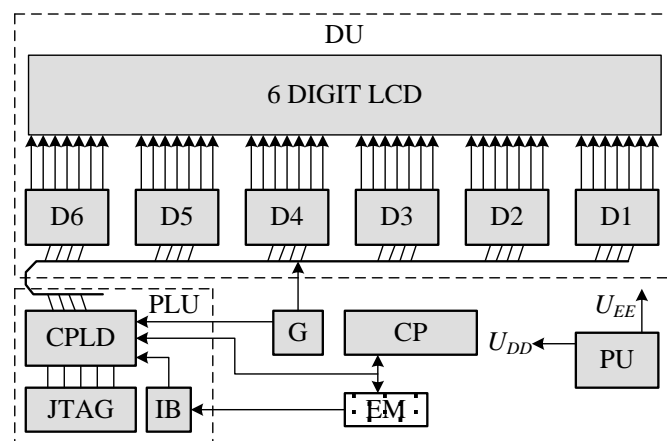


Fig. 1. Functional block diagram of programmable counter

A display module schematic circuit diagram is depicted in Fig. 2.

It is realized on base of six CMOS decoders (IC4 ÷ IC9) of the type CD4055. They control six digit seven segments LCD indicator. To each of decoders a negative $U_{EE} = -5V$ voltage to pin 7 is applied and alternating with 200Hz frequency signal to pin 6 for correct display control. All unused pins are switched to ground. It is not depicted in Fig. 2.

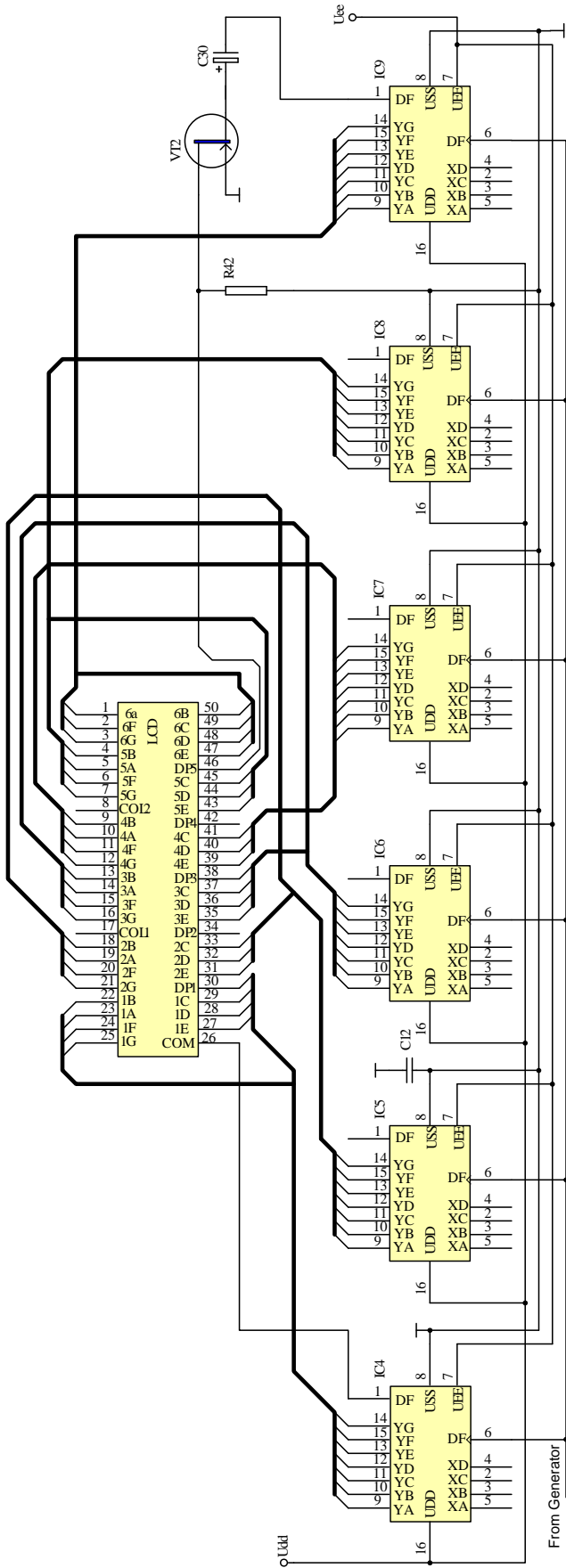


Fig. 2. Display module schematic circuit diagram

A schematic circuit diagram of programmable logical unit PL is shown in Fig. 4. It is created on the base of a produced by Xilinx programmable logical matrix. The matrix IC3 is produced in case PQFP-84 and is of the type XC9572 and enables programming according to conventional IEEE1149.1 interface. The circuit IC3 more leads are taken out to connectors.

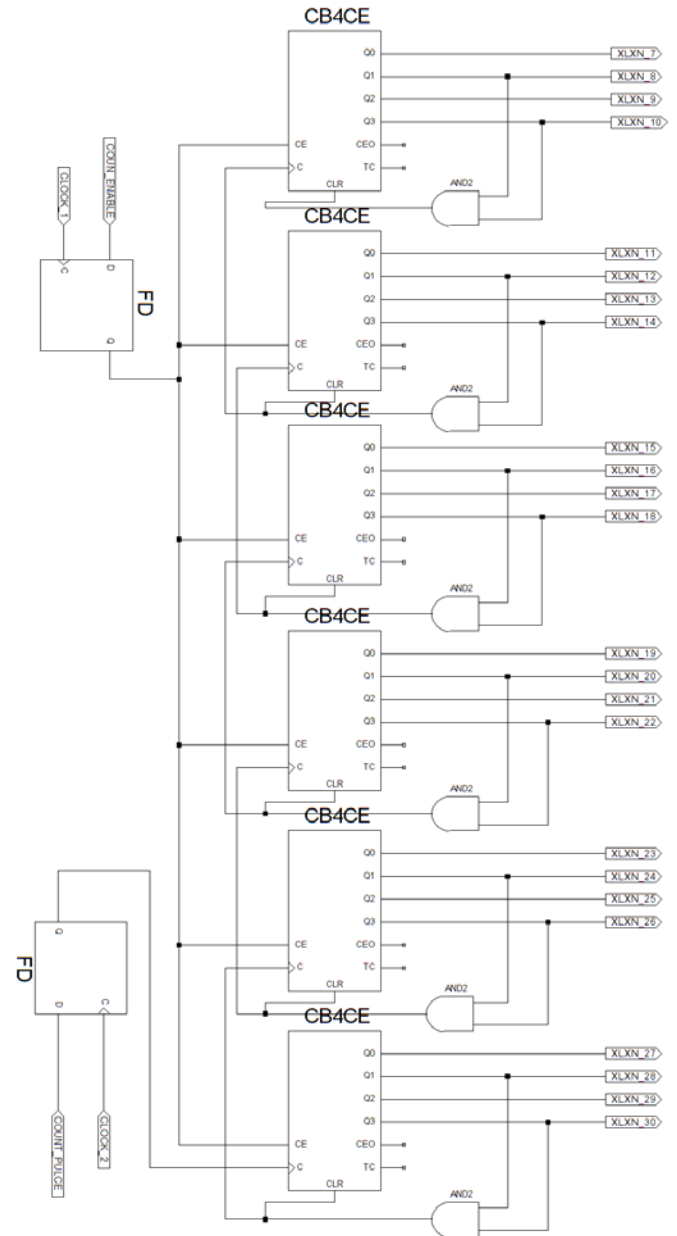


Fig. 3. Schematic circuit diagram of counter

It enables additional modules switching and device functional possibility extension. Another leads receive signal extra amortized by a logical element NAND with ordinary input (IC2 – CD4011 from port CON B) and with Schmitt trigger on an input (IC11 – CD4093 from CON 4). By means of connector CON 1 a personal computer makes a device program. A schematic circuit diagram of a unit G is realized on the base of integrated generator of the type LM555

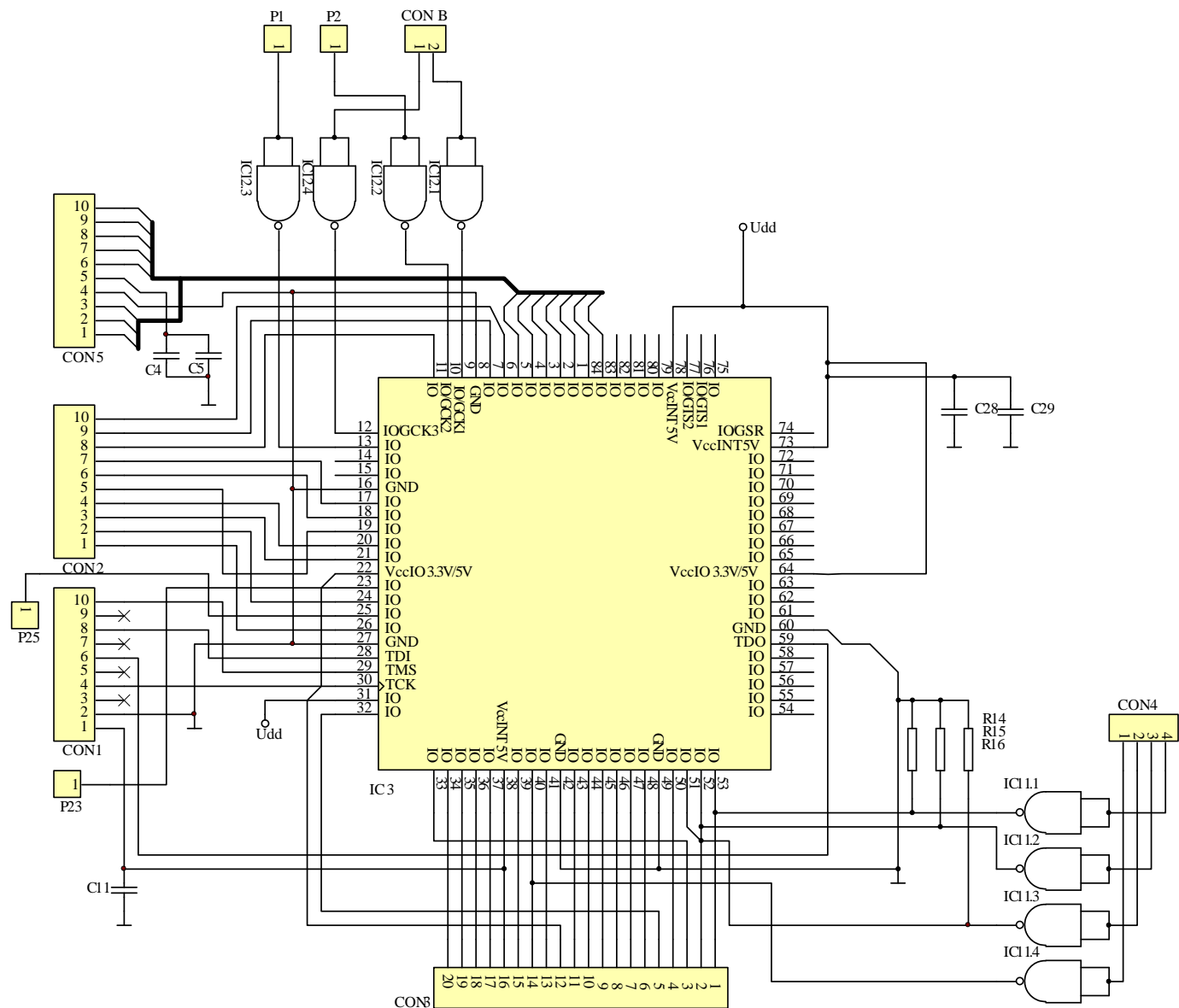


Fig. 4. Schematic circuit diagram of programmable logical unit

switched as a mono-stable multivibrator. The generated by this circuit pulses are used only for LCD control and are fed to pins 6 of the decoders (IC4÷IC9). This signal is too used by unit PLU for a noise stability increase of a circuit work. These circuit elements are so selected and output frequency is 200Hz. In Fig. 5 is shown a schematic diagram of generation circuit, realized by integrated generator of the type LM555.

The soft ware is realized by program product Xilinx ISE10.1. The used in the device program schematic circuit diagram is as for an ordinary counter but it is possible to create more complex one with more functions. The complete circuit diagram consisted of 6 switched in series binary-decimal counters is depicted in Fig. 3.

By means of a logical element AND they are connected. So they receive a high level (logical "1") at a passage from 9 to 10 and a lower digit gets to zero, The generated by integrated circuit EM pulses with alternating duration are fed to D-

trigger through a terminal COUNT PULSE configured to pin 9 of EM. A high frequency signal from a configured as an input pin 10 of circuit IC3 is fed to a clock input C of a D-trigger of EM through a terminal CLOCK2. This signal is received from a generator unit. After this manner a noise perception is avoided and it can not be counted as useful signal.

A permissive circuit configuration created by another D-trigger is the same.

The measuring electrical energy unit has time at a working setting up by a first switching or by a power supply temporarily interruption indicated by the light of LED RP. The programmed in a matrix IC3 counter starts to count upon the permuting signal receipt (logical "1") from integrated circuit IC2 (electrical energy meter) lead REVP. This signal is applied to terminal COUNT ENABLE through integrated

circuit IC3 pin 13. A high frequency signal from a pulse generator is applied to terminal CLOCK 1.

Timing diagrams describing the operation of the module are shown in Fig. 6. They indicate the status of the output ports of the programmable matrix at the time of the input signal. Fig. 7 shows a waveforms of display depolarizing signal and the main generator signal.

When the device is switched off or the power supply is interrupted the accumulated up to this time values do not keep. If the power supply is restored the counter will begin to count from zero. It can be avoid by means of an additional in program diagram block which sends data to an externally memory. The connectors CON 2, CON 3 and CON 5 of the printed circuit board are provided for an external switching of EEPROM or other device for control and data acquisition. The last is not described in this paper.

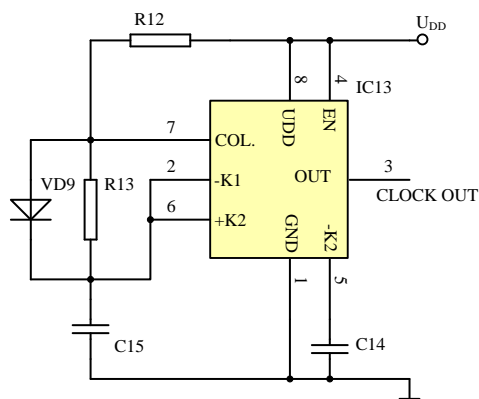


Fig. 5. Schematic circuit diagram of pulse generator

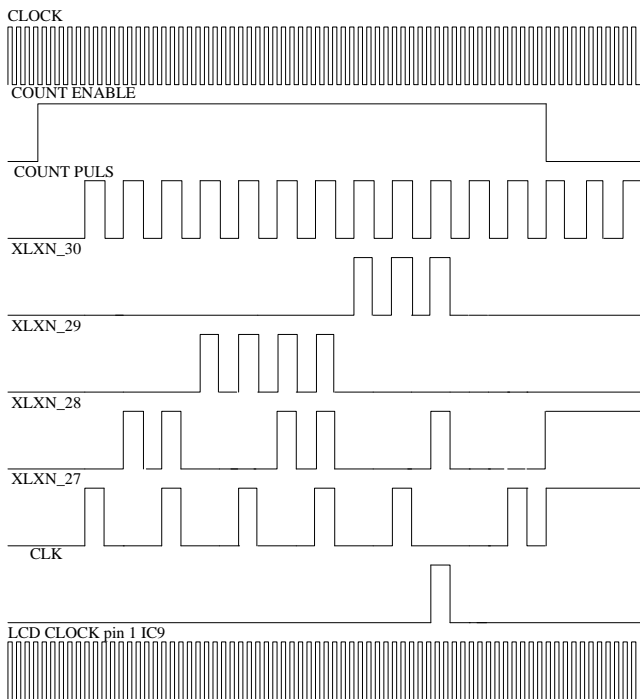


Fig. 6. Timing diagrams describing the operation of the module

III. CONCLUSION

A functional block schematic diagram and a schematic circuit diagram of a programmable counter on the base of a programmable logical matrix XC9572 is synthesized.

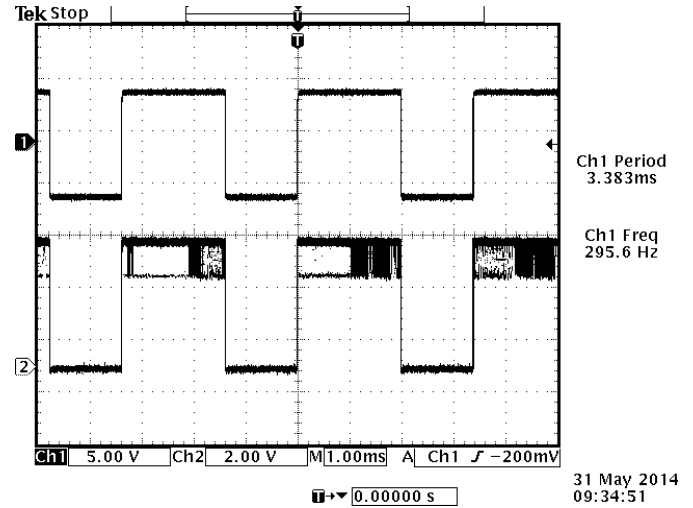


Fig. 7. Waveforms of depolarizing LCD signal versus clock signal

The described module is expected to be further developed with the addition of memory and design of different tariffs for reading.

The realized elaboration application is to count pulses generated by a three-phase electrical energy meter but it can be use in another similar cases.

The developed module for counting pulses from a digital electricity meter offers flexibility in designing. Using the capabilities of the produced by company Xilinx programme environment ISE10 the programme has can be made by program language C or by schematic editor. This enables designers with a bad programming experience, but knowing better circuitry to cope with such task.

The realized circuit decision priority is accessible and cheap elements embedding which do not require an electrical energy big consumption and special software knowledge.

REFERENCES

- [1] T. Angelova, "Experimental Device for Automation Reeding of Galvanomagnetic Elements Transducer Characteristics", Journal of the Technical University of Gabrovo, Vol. 44, 2014.
- [2] N. Draganov, "Based of AMR Sensor Device for Contact less Measuring of AC Current", Journal of the Technical University of Ruse, Vol. 52, series 3.1, Ruse, 2012, pp. 66-70.
- [3] N. Draganov, "Contactless protection of induction motor", Scientific Works Volume LX, Food Science, Engineering and Technologies – 2013, 18-19 October 2013, Plovdiv.
- [4] Analog Device, Application notes and part information, www.analog.com, Jan. 2014.
- [5] N. Draganov, "Integrated Evolution Sistem for Programmable Sensors Signals Conditioner of ZMDI Company", Journal of the Technical University of Gabrovo, Vol. 44, 2012, pp. 42-47.
- [6] Xilinx, Application notes and part information, www.xilinx.com, Jan. 2014.

Artificial Neural Network-Based Classification of Volatile Organic Compounds for Indoor Air Quality Control

Georgi Georgiev¹, Zvezditzia Nenova² and Stefan Ivanov³

Abstract – The volatile organic compounds (VOCs) are chemical contaminants which are subject to indoor air quality control. The results of measurement of VOCs concentration in test chamber by metal-oxide gas sensors are presented. An artificial neural network (ANN) approach for the classification of acetone, ethanol, trichloroethylene, dibutyl phthalate, xylene-o and benzene is proposed.

Keywords – volatile organic compounds, artificial neural network.

I. INTRODUCTION

The levels of many biological, chemical, and particulate contaminants are monitored at indoor air quality control. According to a scores laboratory centers and organization which regulate eligible and dangerous for human health pollution levels, the indoors, in which the problem of air quality is considered, are offices, schools, industrial and commercial buildings and hospital facilities [1-5]. The volatile organic compounds are some of the most common chemical pollutions. The levels of specific contaminant are controlled in offices, schools and homes. The total volatile organic compounds (TVOCs) are monitored in indoors with industrial and commercial activities. These compounds are not subject to measurement in hospitals. There are different sources of VOCs as adhesives, varnishes, cosmetics, cleaners, furniture, carpets, curtains, floor and ceiling coverings, office machines, etc. [5-7]. The effect of the volatile organic compounds on the people can cause a variety of health problems and illnesses [8, 9].

The problem of identification of gases is solved by using of different types of discriminant analysis as Kernel Discriminant method [10], the method of k-nearest neighbors [11], ANN methods, etc. An ANNs are widely used because of the achieving of higher classification accuracy [12-14].

The paper presents ANN-based classification of some of the most common volatile organic compounds – acetone (A),

ethanol (E), trichloroethylene (T), dibutyl phthalate (D), xylene-o (X) and benzene (B), which are subject of control in at least two types of indoors.

II. EXPERIMENTAL PROCEDURE

The experimental equipment, shown in Fig. 1, consists of test gas chamber, measuring module AS-ML of AppliedSensor company and three types of gas sensors – AS-MLV for detection of substance of VOCs, AS-MLC for carbon monoxide (CO) and AS-MLN for nitrogen dioxide (NO₂) [15]. The sensor module control, data acquisition and communication are realized by personal computer (PC) and serial interface RS-232. The parameters which are subject of measurement are resistances R_s of the sensing elements as marked with R_{sV} , R_{sC} and R_{sN} , respectively. The variation of gas concentration leads to change of these parameters. The injecting of the tested compounds in the chamber is performed

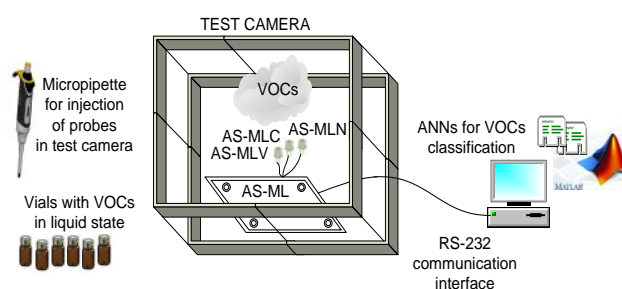


Fig. 1. Experimental equipment

by micropipette SVA – 100 model of Accumax company [16].

In Table I are given the measurement ranges of the investigated gases.

TABLE I
MEASUREMENT RANGES OF VOCs

Gas	Measurement ranges, ppm
acetone (A)	5 - 25
ethanol (E)	3 - 19
trichloroethylene (T)	1.2 – 7.2
dibutyl phthalate (D)	0.4 – 2.4
xylene-o (X)	0.88 – 5.28
benzene (B)	1.17 – 7.02

¹Georgi Georgiev is with the Faculty of Electrical Engineering and Electronics at Technical University of Gabrovo, 4 H. Dimitar Str., Gabrovo 5300, Bulgaria, E-mail: givanow@abv.bg.

²Zvezditzia Nenova is with the Faculty of Electrical Engineering and Electronics at Technical University of Gabrovo, 4 H. Dimitar Str., Gabrovo 5300, Bulgaria, E-mail: z_nenova@yahoo.com.

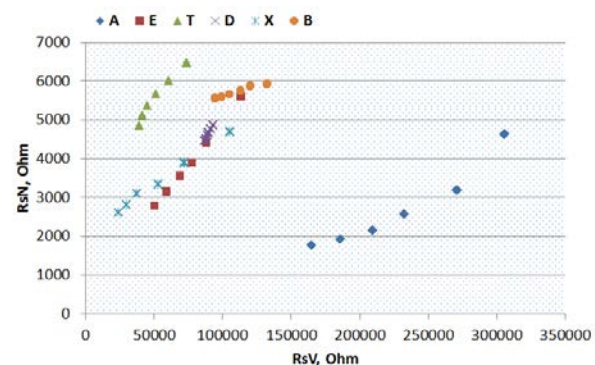
³Stefan Ivanov is with the Faculty of Electrical Engineering and Electronics at Technical University of Gabrovo, 4 H. Dimitar Str., Gabrovo 5300, Bulgaria, E-mail: st_ivanov@abv.bg.

Each compound is injected separately in the test chamber as the obtaining of a wanted gas concentration in ppm is based on the evaporation of a pre-calculated amount of a liquid compound in μl [17]. The minimum and the maximum values of the measurement ranges correspond to the lowest and the highest gas concentrations which are created into the chamber.

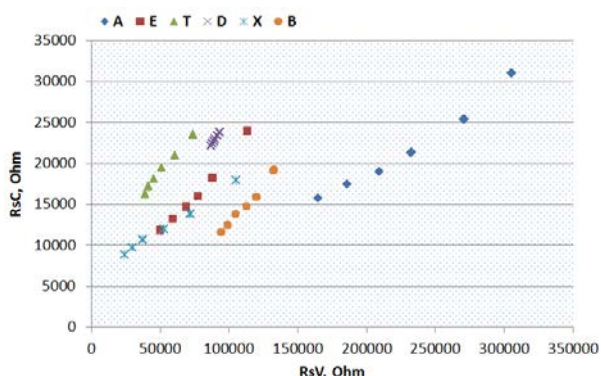
III. RESULTS AND DISCUSSION

3.1. R_s measurements

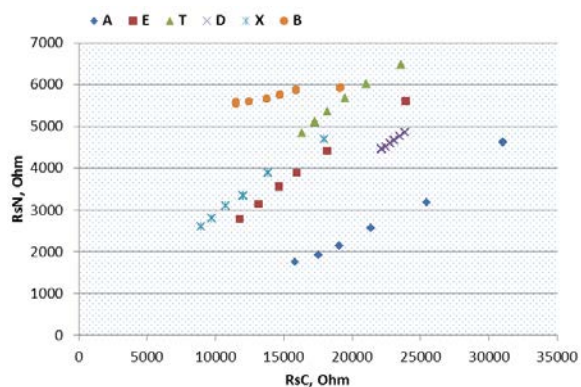
Two-dimensional (2D) and three-dimensional (3D) presentations of the measured resistance of the sensors are shown in Fig. 2 and Fig. 3.



a)



b)



c)

Fig. 2. 2D presentation of: a) $R_{sN}=f(R_{sV})$, b) $R_{sC}=f(R_{sV})$ and c) $R_{sN}=f(R_{sC})$

The 2D representation shows overlap between the groups B with E, D with E for sensors AS-MLN and AS-MLV and E with X for AS-MLC and AS-MLV. Although in use of the sensors AS-MLC and AS-MLN overlap of groups doesn't observe, the samples are closely located for groups as B and T, X and E. Therefore for the VOCs classification the parameters R_{sV} , R_{sC} and R_{sN} of the three sensors are used.

3.2. ANN classification

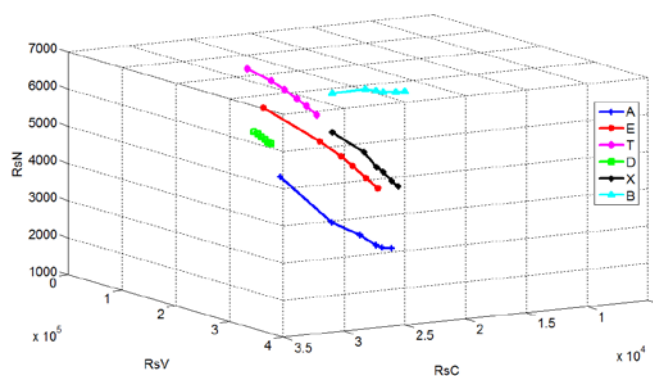


Fig. 3. 3D presentation of R_{sV} , R_{sC} and R_{sN}

The instrumentation of artificial neural networks is widely used for the processing of tasks with varying grades of complexity and dimension of the input and output parameters [18-21]. The advantage of back-propagation learning algorithm is in the process of updating the network weights during each iteration to minimize the error between the expected and the calculated result of the network output [22, 23].

To process the recognition task of the analyzed compounds neural network with one input layer, one hidden layer and output layer is proposed. ANN is built using Matlab R2009b.

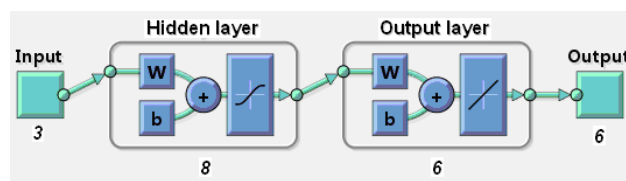


Fig. 4. Artificial neural network architecture

The neural network architecture is presented in Fig. 4. In the hidden layer tangent-sigmoid function is used, and in the output layer - a linear activation function. The input data comprises a group of 90 samples for each gas, i.e. total 540 samples. The dataset is normalized in range of $[-1, +1]$ and divided into training set (60%), validation set (20%) and test set (20%). In Table II are presented the network input parameters, the target output parameters and the parameters of network training. For each of the examined VOCs a definite code combination of the output parameters having 0 and only one 1 is assigned. The group presence is marked by the position of 1.

Tests with different number of hidden neurons are conducted during the training of the network. Optimal network architecture is achieved with eight neurons when a minimum mean squared error from 0.0033 is obtained. In Fig. 5 the change of the mean squared error depending on the number of epochs for ANN training is shown. The validation and test curves have a very similar nature of amendment. There is not an increasing amendment of the mean squared error in respect to the process of ANN testing, which indicates that an overfitting of neural network has not occurred [24]. The minimum gradient magnitude is reached at epoch 8.

TABLE II
INPUT, TARGET AND LEARNING NETWORK PARAMETERS

Input parameters	
Sensor	Resistance
AS-MLV	RsV
AS-MLC	RsC
AS-MLV	RsN
Target parameters	
VOCs	Code combination
acetone	1 0 0 0 0
ethanol	0 1 0 0 0
trichloroethylene	0 0 1 0 0
dibutyl phthalate	0 0 0 1 0
xylene-o	0 0 0 0 1
benzene	0 0 0 0 1
Learning network parameters	
show	25
epoch	1000
lr (learning rate)	0.05
goal	0.01
min_grad	1e-05

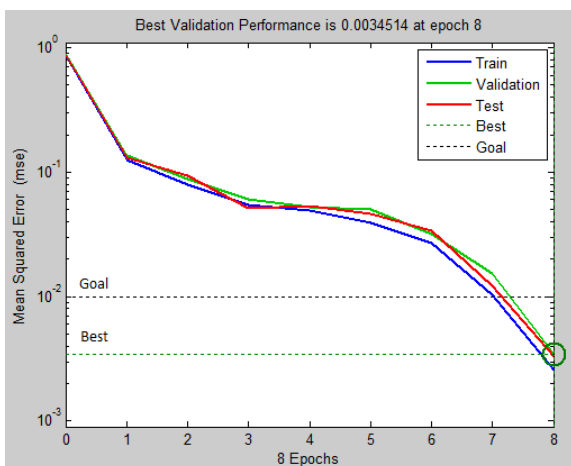


Fig. 5. Change of the mean squared error

In Table III the parameters of linear regression relations between network and target outputs – the slope m and y-intercept b of the best linear regression and the correlation coefficients R are presented.

TABLE III
REGRESSION PARAMETERS RELATING TARGETS TO NETWORK OUTPUTS

Output	Slope of the best linear regression m	Y-intercept of the best linear regression b	Correlation coefficient R
1	0.9875	-0.0086	0.9986
2	0.9266	0.0406	0.9879
3	0.9473	0.0384	0.9894
4	1.0047	-0.0079	0.9981
5	0.8891	-0.0060	0.9886
6	0.8914	0.0018	0.9953

The confusion matrix, which defines the correct and incorrect classifications, is given in Fig. 6. The matrix is formed on the base of the test set from 108 samples and shows a correct classification of all considered groups (classes) by ANN proposed.

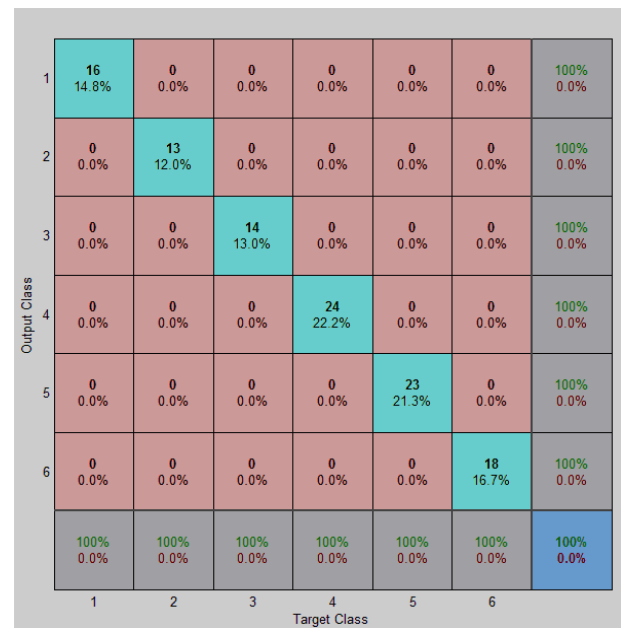


Fig. 6. Confusion matrix for the classes 1-A, 2-E, 3-T, 4-D, 5-X and 6-B

The absolute network error for the samples of the test set for each output group (class) is shown in Fig. 7. The error is calculated as a difference between the network output values and the target values for each of the test samples and varies in the range from -0.2349 to 0.2446. The smallest errors are observed for the fourth group (D) and the greatest – for the fifth group (X).

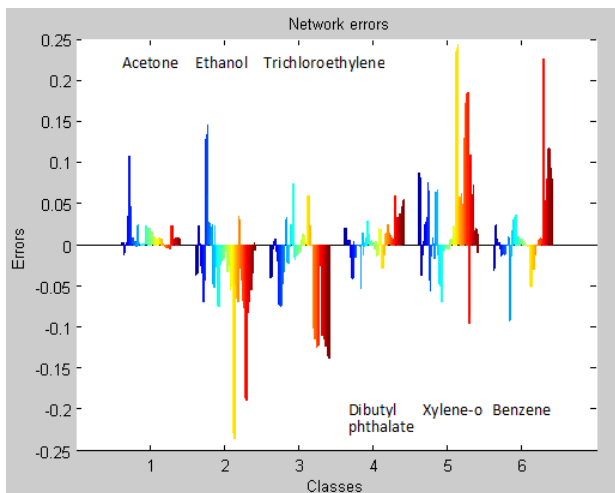


Fig. 7. Change of the network error

The obtained results confirm the possibility of using the specified sensors and ANN for classification of VOCs at indoor air quality control.

IV. CONCLUSION

The identification of volatile organic compounds at indoor air quality control is a major step to ensure a health environment with minimum contamination levels, to improve the quality of study at schools, to provide a comfortable environment at homes. The trained ANN and the relevant gas sensors could be successfully used in the computer based systems for monitoring of VOCs contamination in a different category of indoors.

REFERENCES

- [1] World Health Organization – Regional Office for Europe, “WHO Guidelines for Indoor Air Quality: Selected Pollutants”, 2010. <http://www.euro.who.int>.
- [2] Air Quality Sciences, “The Office Equipment Industry’s Guide to Managing Product Emissions”, 2003. <http://www.aqs.com>.
- [3] M. Freitas, et al.*, “Indoor Air Quality in Primary Schools”, Environmental Health and Air Pollution Case Studies, DOI: 10.5772/17609, pp.361-384, 2011.
- [4] California Environmental Protection Agency, Ventilation and Indoor Air Quality in New Homes. California Energy Commission, PIER Collaborative Report, CEC-500-2009-085, 2009. <http://www.calepa.ca.gov>.
- [5] G. Georgiev, Z. Nenova, “Control of Indoor Air Pollutions”, International Scientific Conference “UNITECH’12”, Gabrovo, Bulgaria, vol. II, pp.371-376, 2012.
- [6] International Association of Certified Home Inspectors, “Air Quality in the Home”, 2012. <http://www.nachi.org>.
- [7] A. Pickett, M. Bell, “Assessment of Indoor Air Pollutions in Homes with Infants”, International Journal of Environmental Research and Public Health, 8, pp.4502-4520, 2011.
- [8] United States Environmental Protection Agency, “An Introduction to Indoor Air Quality”, 2012. <http://www.epa.gov>.
- [9] California Environmental Protection Agency, “Indoor Air Quality and Personal Exposure Assessment Program”, 2003. <http://www.arb.ca.gov>.
- [10] L. Zhang, F. Tian, “A new kernel discriminant analysis framework electronic nose recognition”, National Center for Biotechnology Information, Anal. Chim. Acta, 833, pp.48-55, 2014.
- [11] S. Belhaouari, R. Abaza, “Gas Identification by Using of a Cluster-K-Nearest Neighbor”, International Conference of Machine Learning and Computing, vol.3, pp.123-127, 2011.
- [12] P. Chang, J. Shih, “The Application of Back Propagation Neural Network of Multi-channel Piezoelectric Quartz Crystal Sensor for Mixed Organic Vapours”, Tamkang Journal of Science and Engineering, vol. 5, No. 4, pp. 209-217, 2002.
- [13] J. Shih, H. Hsu, “Multi-Channel Surface Acoustic Wave (SAW) Sensor Based on Artificial Back Propagation Neural (BNP) Network and Multivariable Linear Regression Analysis (MLR) for Organic Vapours”, Journal of Chinese Chemical Society, 2007, 54, p.401-410, 2007.
- [14] C. Chen, J. Shih, “Multi-Channel Piezoelectric Quartz Crystal Sensor with Principal Component Analysis and Back-Propagation Neural Network for Organic Pollutant from Petrochemical Plants”, Journal of the Chinese Chemical Society, 55, pp.979-993, 2008.
- [15] AppliedSensor, “Quick Reference Manual – Test Kit AS-ML Sensor Components”, 2009. <http://www.appliedsensor.com>.
- [16] Accumax, “Accumax SMART series of pipette”. <http://www.accumax.com>.
- [17] A. Uyanik, N. Tinkilic, “Preparing Accurate Standard Gas Mixtures of Volatile Substances at Low Concentration Levels”, Chem. Educator, 4, pp.141-143, 1999.
- [18] A. Srivastava, “Detection of volatile organic compounds (VOCs) using SnO₂ gas-sensor array and artificial neural network”, ELSEVIER Sensors and Actuators B 96, pp.24-37, 2003.
- [19] S. Benedetti, S. Mannino, A. Sabatini, G. Marazzan, “Electronic nose and neural network use for classification of honey”, INRA/DIB-AGIB/ EDP Sciences, Apidologie 35, pp.1-6, 2004.
- [20] A. Yamazaki, T. Ludermit, “Classification of Vintages of Wine by an Artificial Nose with Neural Networks”, Centre of Informatics Federal University of Pernambuco, Brazil, 2001.
- [21] S. Sharma, “Implementation of artificial neural network for odor identification using e-nose”, National Conference of Computational Instrumentation “NCCI 2010”, CSIO Grandigarh, India, 2010.
- [22] R. David, L. Sovan, D. Ioannis, J. Jean, L. Jacques, S. Aulagnier, Artificial neural networks as classification method in the behavioural sciences, ELSEVIER Behavioural Processes 40, pp.35-43, 1997.
- [23] G. Zhang, “Neural Network for Classification: A Survey”, IEEE Transactions on Systems, Man, and Cybernetics – Part C: Applications and Reviews”, vol.30, No.4, pp.451-462, 2009.
- [24] Mathworks, “Analyze Neural Network Performance After Training”, 2014. <http://www.mathworks.com>.

Experimental Digital Three-Phase Check Electrical Energy Meter Part 1

Nikola Draganov

Abstract – A creating of digital electrical energy meter conduces to its correct measurement and to a price fixing of any electrical device. The article presents a digital three-phase test electrical energy meter realized on the base of especial integrated circuit manufactured by Analog Device®. The presented device has as a measuring as well an advanced application.

Keywords – Energy measuring, Digital measuring device, Energy measuring resources.

I. INTRODUCTION

The electrical energy measurement is very important for a people being and an industry. On its correct measurement depends a price of any electrical product and its effective use. Therefore the precise electrical energy measurement is important and necessary.

The direct electrical energy measurement is fulfilled by an especial meter. The first types of these meters work on induction principle and are well known in practice and theory. Nevertheless their constructive feature and metrology do not enable to report on others energy system parameters except a consumed power. Now when alternative electrical energy sources are in use applied until recently bi-quadrant to the power induction meters are already not suitable because it is now necessary to measure the energy sent back to the energy network. So the induction electrical energy meters use is reduced but the interest in an elaboration of new electronic circuitry and technological decisions for electrical energy measurement is increased. The modern microelectronic technologies improvement enables combining on one chip a great number of functional unite which permits a construction of digital electrical energy meter only by one integrated circuit. It increases measuring apparatus reliability and a precision of data treatment and indication.

The purpose of the present working is to realize and investigate a three-phase check electrical energy meter created on the base of produced by Analog Device for such measurements especial integrated circuit [1-3].

II. PRESENTATION

The digital three-phase electrical energy meter block schematic diagram is shown in Fig. 1. The all phases (A, B, C) of the supply network are synchronously and absolutely

Nikola Draganov is with the Department of Electronics at Technical University of Gabrovo, Hadgi Dimitar, str.4, Gabrovo 5300, Bulgaria, E-mail: niko_draganov@mail.bg.

independently watched by three identical current channels (CCA, CCB, CCC) and three also equal voltage channels (VCA, VSB, VCC). The current channels transform the consumed by phases electrical current to electrical voltages fed to respective inputs of special for electrical energy measurement integrated circuit. The voltage channels measure uninterruptedly voltages of all phases and after suitable amplitude reduction they are fed to measuring circuit EMC voltage inputs. The modes operation control is fulfilled by giving modes unit MU which defines a transformation coefficient of calculated energy to frequency signal. The device working state, phase existence or absence, output signal and running consumed electrical energy are watched by indication I. EMC disposed of precise analog-to-digital converter (ADC) and computing block. Their correct processing is guaranteed by an added block generating pulses PG. EMC enables to deliver measured data suitable to a treatment by diverse schemes. To this aim the output signals are applied through output circuit OC. It must not ignore the power supply stability. This primary task is entrusted on the power supply unit PU. The produced by Analog Device especial integrated circuit ADE7756 is precise three-phase electrical energy meter provided with serial delivering data interface SPI with leads for control of electromechanical or electronic counter. There are embedded two precise Σ - Δ analog-to-digital converters, digital integrator, regulated power supply, thermal sensor and all necessary for a treatment of active, reactive effective electrical energy and a calculator for effective value. This circuit is suitable for a measurement and of active, reactive and effective electrical energy generated by different three-phase connection (delta or wye) with three or four wires network. The integrated circuit ensures anyone adjustment – power factor correction, phase and power adjustment. An embedded phase register notes down an information of input signal form.

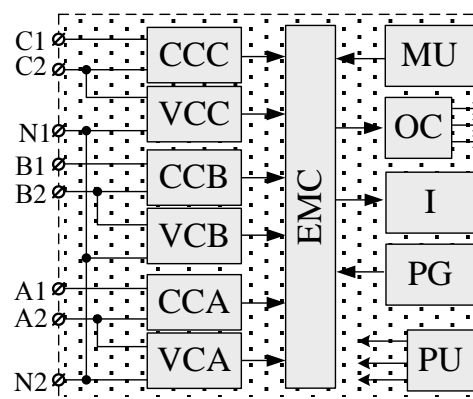


Fig. 1. Digital three-phase electrical energy meter functional block diagram

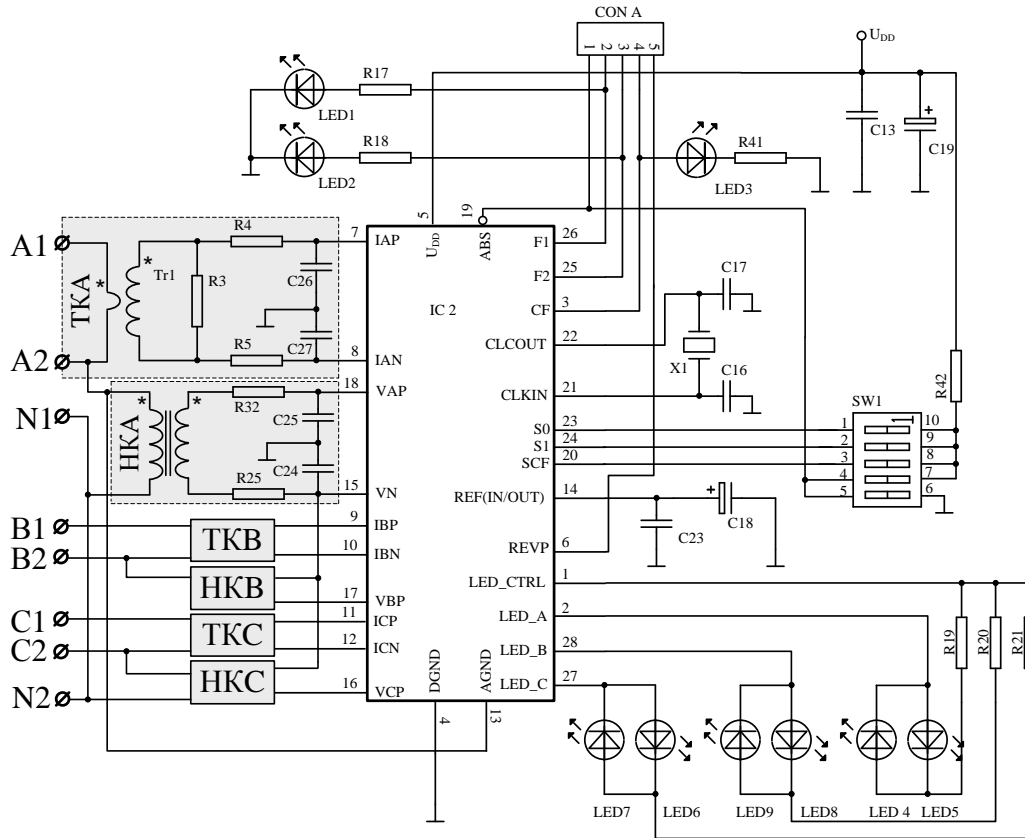


Fig. 2. Simplified schematic circuit diagram

It has taken out output leads of integrated circuit. A scheme for short connections and voltage small changes detection is embedded too. A zero watching circuit is synchronized against all phases voltages. A measurement is fulfilled on the base of input voltages periods of any phase [3]. Simplified schematic circuit diagram of a device for three-phase electrical energy measurement is depicted in Fig. 2.

A phase A current and voltage channels are shown. The other phases B and C channels are identical. The phase A current channel is built by elements R3, R4, R5, C26, C27 and current transformer Tr1. The task of Tr1 is to transform a flowing through primary coil current of phase A in voltage with a transmission factor 1:1000. This voltage is fed with suitable amplitude to current inputs IAP and IAN of integrated circuit IC2. The resistors R3, R4 and R5 define the parameters of delivered to integrated circuit inputs signals. According to the producer specification the amplitude of a delivered to pin IAP and IAN (and also to IBP, IBN, ICP, ICN) input signals must not be over ± 500 mV.

The phase A voltage channel VCA is built by elements R32, R25, C25, C24 and transformer Tr2. This transformer ensures a signal giving an information for phase and amplitude of a voltage delivered to a consumer. It is a step down transformer and reduces 230V primary voltage to 5V secondary one. The amplitude of a signal delivered to inputs for measurement of the all phases voltage (VAP, VBP, VCP) must be not over ± 500 mV.

The peculiarity during the voltage switching on to the active inputs (VAP, VBP, VCP) for integrated circuit IC2 voltage measurement and common input to voltage channels VN is to observe the transformers coil terminals (Fig. 2). The primary winding beginning (marked with a dot *) is turned on to respective phase but the end is to zero conductor N. The secondary winding end is turned on to respective active input of IC2 (for example VAP) but the end to the passive one (VN).

An indication about correct switched current and voltage transformers gives the embedded in integrated circuit IC2 phasic monitor which by means of pins 1, 2, 27 and 28 can control six light emitting diodes (LED4 – LED9) switched as antiparallel pairs as is depicted in Fig. 2. The indicators LED4, LED9 and LED7 are in operating when anyone phase is fallen away. LED5, LED8 and LED6 are in operating when the phases with necessary voltage and current channels are correct switched to measuring leads. Then and with application of a third (neutral) conductor towards that the signals are measured the voltage lines will be dephased at 120° each to other,

$$\begin{aligned}
 U_{A(t)} &= \sqrt{2} \cdot U_A \cdot \cos(\omega_t \cdot t) \\
 U_{B(t)} &= \sqrt{2} \cdot U_B \cdot \cos(\omega_t \cdot t + \frac{2\pi}{3}) \\
 U_{C(t)} &= \sqrt{2} \cdot U_C \cdot \cos(\omega_t \cdot t + \frac{4\pi}{3})
 \end{aligned}
 \tag{1}$$

where: U_A, U_B, U_C are RMS voltage values.

The signals received at the current inputs are computed by the equations,

$$\begin{aligned} I_A(t) &= \sqrt{2} \cdot I_A \cdot \cos(\omega_i t + \varphi_A) \\ I_B(t) &= \sqrt{2} \cdot I_B \cdot \cos(\omega_i t + \frac{2\pi}{3} + \varphi_B) \\ I_C(t) &= \sqrt{2} \cdot I_C \cdot \cos(\omega_i t + \frac{4\pi}{3} + \varphi_C) \end{aligned} \quad (2)$$

where: I_A, I_B, I_C are RMS values of the current in the phases, $\varphi_A, \varphi_B, \varphi_C$ – phasic difference between current and voltage on each phase.

For the power momentary values can be written:

$$\begin{aligned} P_A(t) &= U_A(t) \cdot I_A(t) \\ P_B(t) &= U_B(t) \cdot I_B(t) \\ P_C(t) &= U_C(t) \cdot I_C(t) \end{aligned} \quad (3)$$

After substitution of (1) and (2) in (3) the active power in each phase will be:

$$\begin{aligned} P_A(t) &= U_A(t) \cdot I_A(t) \cdot \cos(\varphi_A) - U_A(t) \cdot I_A(t) \cdot \cos(2\omega_i t + \varphi_A) \\ P_B(t) &= U_B(t) \cdot I_B(t) \cdot \cos(\varphi_B) - U_B(t) \cdot I_B(t) \cdot \cos(2\omega_i t + \frac{4\pi}{3} + \varphi_B) \\ P_C(t) &= U_C(t) \cdot I_C(t) \cdot \cos(\varphi_C) - U_C(t) \cdot I_C(t) \cdot \cos(2\omega_i t + \frac{8\pi}{3} + \varphi_C) \end{aligned} \quad (4)$$

The total power is defined as a sum:

$$P_{(t)} = P_{A(t)} + P_{B(t)} + P_{C(t)} \quad (5)$$

The connector CON A leads are directly connected to the integrated circuit IC2 leads F1, F2, CF. By means of CON A the measurement information is applied to the treatment block. The process status is watched by indicators connected to some leads (F1, F2, CF).

A block MU is built by five microswitches SW1 and a resistor R24. Microswitch SW1 rules the integrated circuit IC2 leads S0, S1 SCF. By means of SW1 the frequency of received from leads F1, F2 and CF output signals is tuned according to a measured electrical energy. By means of them the analog-to-digital converter working frequency and adjusting frequency are tuned. Their status and their influence on output signals are shown in Table I. The output frequency values (leads F1 and F2) at different currents by 100 pulses per 1kW are shown in Table II.

By measurement of three-phase electrical energy the developed test device makes errors defined by next formula,

$$\varepsilon = \left(\frac{E_M - E_T}{E_T} \right) \cdot 100 \quad (6)$$

where: E_M – measured by developed device electrical energy, E_T – measured by certificated device electrical energy.

TABLE I

SCF (J6)	S1 (J7)	S0 (J8)	F1 и F2 f, Hz
0	0	0	0,92
1	0	0	1,84
0	0	1	0,46
1	0	1	1,84
0	1	0	2,09
1	1	0	0,46
0	1	1	0,23
1	1	1	0,23

TABLE II

I, A	F1 и F2 f, Hz
10	0,18
25	1,46
40	0,73
60	1,1
80	1,47
100	1,83

This error appears as a result of others errors depended on an elements selection and on printed circuit board construction. Some of they are:

- Difference between channels. It appears if there are faulty or unequal elements in filter group of current and voltage channels. As a result phasic difference appears between channels and phase correcting circuit (elements R4, R5, C26, C27 of current channel and R25, R32, C24, C25 of voltage channel). A phase correcting circuit compensates phases between current and voltage channels with $\pm 0,1^\circ$ at network frequency change from 45Hz to 65Hz and with $\pm 0,2^\circ$ at 40Hz to 1kHz;

- Unregulated power supply;

- Level replacement of analog ground against continuous current one, leads AGND and DGND.

In Fig.4 is shown the experimental characteristic of input voltage versus current channel $U_{IN} = f(I_{TEST})$. This is applied to pins 7 and 8 of IC2 (for phase A). Another characteristic describes an output signal frequency versus a test load current $F_{F1} = f(I_{TEST})$.

The analysis shows that the function $U_{IN} = f(I_{TEST})$ by a change in current from 0 to 50A input voltage is changed from 0 to 250mV almost linear and the output signal frequency is increased $F_{F1}=0 \div 1,25\text{Hz}$.

According to catalog data of the measurement circuit the experimental results obtained for the function of the frequency F_{F1} are overlapped with a minimum difference. In Fig. 3 with dotted line function is depicted according to catalog data whereas by means of points it is depicted with experimental values.

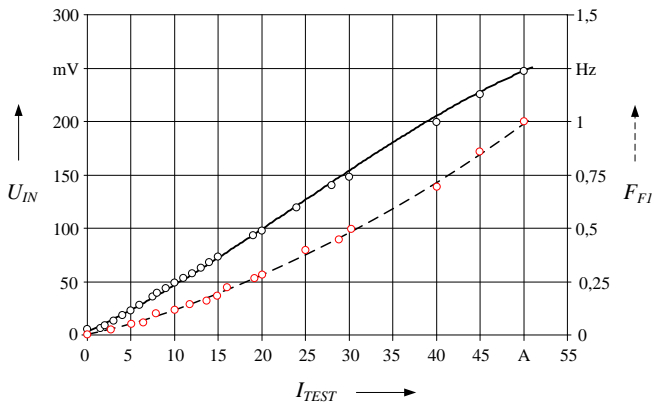
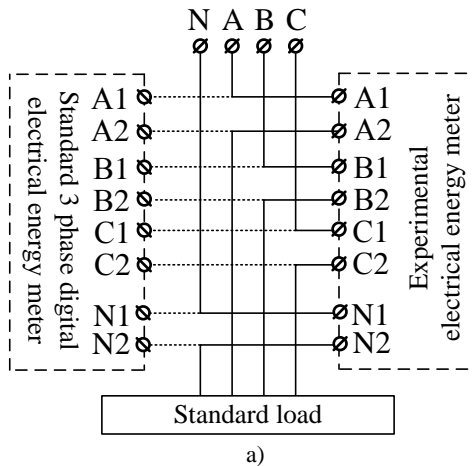
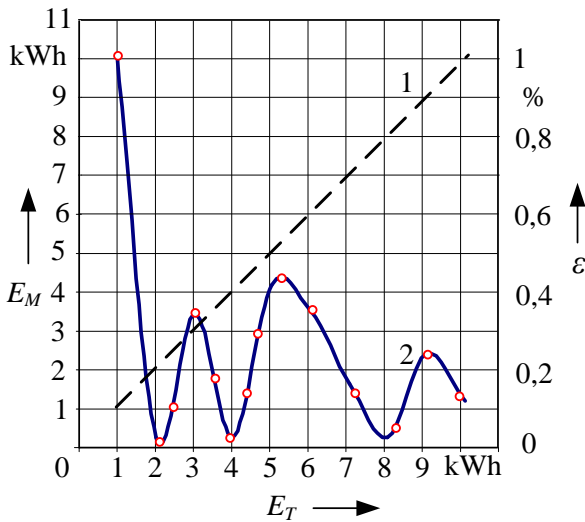


Fig. 3. Experimental characteristics $U_{IN}=f(I_{TEST})$ and $F_{FI}=f(I_{TEST})$



a)



b)

Fig. 4. (a) Experimental setup, (b) experimental characteristics $E_M=f(E_T)$ and $\epsilon=f(E_T)$

The developed device has been tested with standard three-phase load. Fig.4(a) shows a scheme of the experimental setup. It consists of standard meter and experimental

developed one. The results for the electricity measured by an developed electrometer are compared with those obtained with standard one. Measurements were performed sequentially, first with standard device then with developed (experimental) energy meter. The obtained results are presented in Fig.4(b). They give the dependence of the measured with experimental device energy between measured by standard energy meter $E_M=f(E_T)$ – graph 1. Another graph 2 $\epsilon=f(E_T)$ shows the error obtained from the experimental device in accordance with Eq. (6).

The analysis of the obtained characteristics shows that the developed experimental electrical energy meter measures consumed energy with accuracy similar to that of a standard meter. The greatest error $\epsilon=0,45\%$ occurs when there is a load about 5,2 kWh.

III. CONCLUSION

A block schematic diagram of developed and investigated three-phase digital test electrical energy meter has been submitted. It enables to control the transmission characteristic, the phase status monitoring and a treatment of received from electromechanical or microcontroller signals.

The experimental device is tested with a standard load. The characteristics of input voltage and frequency of the output signal versus the current through the load $U_{IN}=f(I_{Test})$, $F_{FI}=f(I_{Test})$ have been obtained. Approximately an error of the device is established by means of the constructed characteristics $\epsilon=f(E_T)$.

Based on produced by Analog Device especial integrated circuit ADE7762 a schematic circuit diagram is developed. The described experimental device is characterized with simple realization and a possibility of easy adjustment and measurement data processing. The added LED indicators give a real notion of the measured signals momentary status.

This device for digital measurement of three-phase electrical energy can be used as in instrumentation as well in engineering investigations. An input channels schematic configuration and a transmission characteristic flexible control by means of MU enable this development to have measuring and advanced application.

A developed device is put to a more detailed studies in different $\cos\phi$, different phase voltages and others. This will be describe in the others article.

REFERENCES

- [1] T. Angelova, "Experimental Device for Automation Reeding of Galvanomagnetic Elements Transducer Characteristics", Journal of the Technical University of Gabrovo, Vol. 44, 2014.
- [2] N. Draganov, "Contactless protection of induction motor", Scientific Works Volume LX, Food Science, Engineering and Technologies – 2013, 18-19 October 2013, Plovdiv.
- [3] Analog Device, Application notes and part information, www.analog.com, Jan. 2014.

Research of Transmission Loss Properties of Thin Layered Sound Reduction Systems for Building Partition Elements

Tsvetan Nedkov¹, Snejana Pleshkova-Bekjarska²

Abstract – In this document are studied the properties of different combinations of thin layered materials for increasing the index of sound insulation of separating walls built from bricks with holes that are most commonly used in the contemporary building constructions. In the research are combined thin porous elastic elements laminated with thin plates with medium and high density.

Keywords – sound reduction systems, transmission loss properties, building partition elements.

I. INTRODUCTION

In the contemporary building constructions the need of thin layered noise reduction system for airborne sound becomes more common to use for application on partition walls, floors and ceilings. The “classical” systems are built from metal or wood frame, porous absorbers and gypsum boards, but they take away from the useful space of the room at least 70 to 150 mm from every surface. Moreover to be high efficient the systems must be suspended on expensive rubber hangers. For this reason in this document are studied the properties of different combinations of thin layered systems, directly laminated to the existing brick wall, combining elastic polyurethane absorbing layer with solid plates with different properties.

II. INSTRUCTIONS FOR THE AUTHORS

For this research Sharp’s prediction model [1] will be used to calculate the sound reduction curve, describing the lost of energy when sound transmits trough double partition wall. The sound reduction curve owns a few characteristic points [2,3] (Fig. 1). Point *A* from the graphic (Fig.1) defines the resonant, frequency of the system f_0 and its value of sound pressure TL_A :

$$f_0 = 80\sqrt{(m_1 + m_2) / dm_1 m_2} \text{ (Hz)} \quad (1)$$

$$TL_A = 20\log_{10}(m_1 + m_2) + 20\log_{10} f_0 - 48 \text{ (dB)} \quad (2)$$

¹Tsvetan Nedkov is with the Faculty of Telecommunications at Technical University of Sofia, 8 Kl. Ohridski Blvd, Sofia 1000, Bulgaria, E-mail: tsvetan_nedkov@abv.bg.

²Snejana Pleshkova-Bekjarska is with the Faculty of Telecommunications at Technical University of Sofia, Kl. Ohridski 8, Sofia 1000, Bulgaria. E-mail: snegpl@tu-sofia.bg.

m_1 and m_2 – masses of the first and second partition,
 d – distance between the partitions.

Point *B* defines the beginning of the coincidence region closed between the values of the critical frequencies of the partitions $0.5 f_{c1}$ and f_{c2} :

$$f_{c1} = 0.55c^2 / c_{L1} h_1 \text{ (Hz)} \quad (3)$$

$$c_{L1} = \frac{\sqrt{12}}{h} \sqrt{\frac{B}{m}} \quad (4)$$

c_{L1} – speed of sound propagation in the first partition,
 h_1 – thickness of the first partition,
 c – speed of sound in the air 332 m/s,
 B – bending stiffness of the first partition.

The type of connection between the partitions defines the value (dB) of point B and is line-line [1] [2] [3] described with the following equation:

$$TL_{B2} = 20\log_{10} m_1 + 10\log_{10} b + 20\log_{10} f_{c1} + 10\log_{10} f_{c2} + 20\log_{10} \left[1 + \frac{m_2 f_{c1}^{1/2}}{m_1 f_{c2}^{1/2}} \right] - 78 \text{ (dB)} \quad (5)$$

where f_{c2} is the critical frequency of the second partition; b is the spacing between line supports.

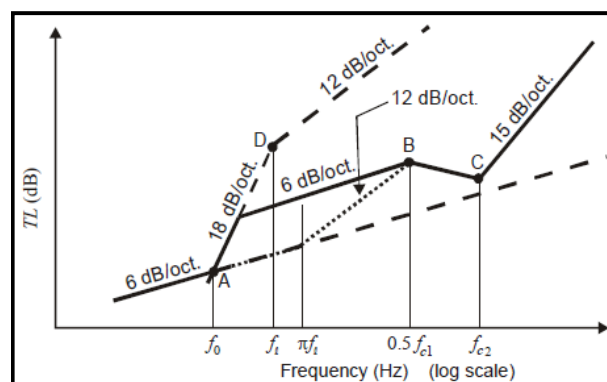


Fig. 1. A design chart for estimating the transmission loss of a double panel wall, based on Sharp’s analysis

Defining point *C*: this point marks the end of the well expressed region of coincidence, after that the curve mounts with 15 dB/octave [5]. When the partitions have a different density and thickness this means that f_{c2} is not equal to f_{c1} and the equation that describes the value (dB) of point C is:

$$TL_C = TL_{B2} + 6 + 10 \log_{10} \eta_2 + 20 \log_{10} \frac{fc_2}{fc_1} \text{ (dB)}. \quad (6)$$

Coefficient η_2 defines the internal loss of the second partition.

Point [5,6] describes the increase of the noise reduction curve when there is absorption material in the cavity, defining the specific frequency f_i :

$$f_i = \frac{55}{d} \text{ (Hz)}. \quad (7)$$

III. EXPERIMENTAL PART

The source room is a soundproofed reverberation chamber with dimensions 332 x 200 x 150 cm and with an opening for the tested specimens of 182 x 135 cm. The receiver room is 1220 x 680 x 320 cm. The testing chamber did not match ISO standart 140 – 1 and 140 – 3 but it's parameters are satisfying the needs of the experiment [4]. In the testing opening is built a partition wall from a ceramic brick with holes, thickness of 120 mm, plastered from one side with cement based mortar 15 mm thick. This type of wall is one of the commonly used in the contemporary building process. Tested specimens are separated from the other elements with a 10 mm rubber pad. In the source chamber is placed a dodecahedron sound source connected with a generator of "pink noise". One microphone is placed in the source chamber, connected with a sound level meter and frequency analyzer. In the source room at distance 40 cm from the specimen is placed a condenser microphone, connected with a sound level meter and a frequency Pulsar Instruments 106. The generated sound pressure in the source room is SPL = 94 dB.

The first part of the experiment is the measurement of sound reduction index of the brick wall without insulation. This sound reduction curve exists in all of the figures in order to facilitate the comparison of all applied systems.

TABLE I
PARAMETERS OF TESTED MATERIALS

Type of material	Density	E Modulus	Coeff. of Poisson	Coeff. of internal loss
---	kg./m ³	GPa	v	η
Ceramic brick with holes	655	6,85	0,12	0,013
Gypsum fiber board (GF)	1130	3,9	0,3	0,012
Gypsum board (GB)	680	2,1	0,24	0,01
PU elastic absorber (Ab)	150	0,7	0,35	0,15

In the second part are prepared 4 different combinations with 3 sub combinations of each one:

Set I. The absorbing elastic layer with thickness of 10 mm is laminated to gypsum fiber board (the elastic layer is glued

to the wall and to the fiber board with polyurethane glue) and is measured. After that are added 6 point connections (PVC nails) and the measurement is done again. In the third combination is added second mass to the fiber board with 12.5 mm thick gypsum board by screws (linear connection) and it is measured as well (Fig. 3).

Set II. The absorbing elastic layer is doubled (20 mm) and the other elements are the same as in Set I. (Fig. 4).

Set III. Here, again the elastic layer is 20 mm, but the thickness of the fiber board (GF) is increased to 15 mm. The other elements are the same as Set I (Fig. 5).

Set IV. Successively are connected 10 mm elastic layer with 10 mm fiber board plus 10 mm elastic layer and 10 mm fiber board – combination of two elastic and two solid plates with final layer of gypsum board (Fig. 6).

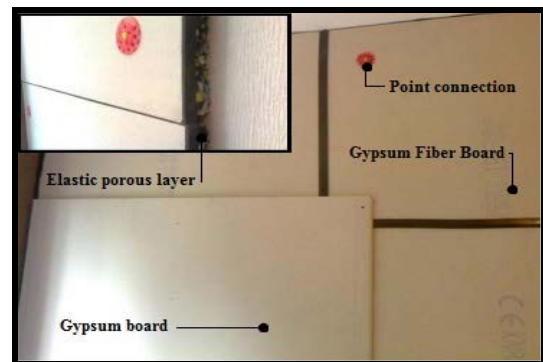


Fig. 2. Thin layered noise reduction system (Set II, measurement 5)

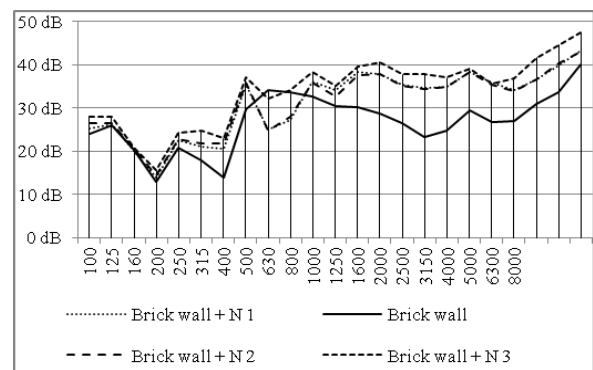


Fig. 3. Experimental results of noise reduction to Set I, measurement 1, 2 and 3

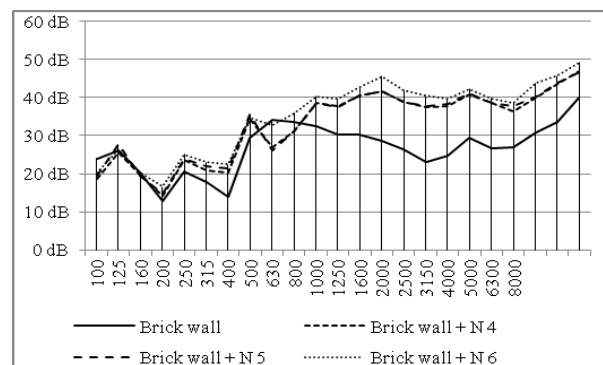


Fig. 4. Experimental results of noise reduction to Set II, measurements 4, 5 and 6

TABLE II
COMBINATIONS WITH EXAMINED MATERIAL

Set	N Measurement	Elastic porous layer	Point connect.	1-st added mass	Elastic porous layer	2-nd added mass	3-rd added mass
I	1	10 mm + Ab	-	10 mm GF	-	-	-
	2	10 mm + Ab	6 pcs.	10 mm GF	-	-	-
	3	10 mm + 3Π	6 pcs.	10 mm GF	-	12.5 mm GB	-
II	4	20 mm + Ab	-	10 mm GF	-	-	-
	5	20 mm + Ab	6 pcs.	10 mm GF	-	-	-
	6	20 mm + Ab	6 pcs.	10 mm GF	-	12.5 mm GB	-
III	7	20 mm + Ab	-	15 mm ΓΦ	-	-	-
	8	20 mm + Ab	6 pcs.	15 mm ΓΦ	-	-	-
	9	20 mm + Ab	6 pcs.	15 mm ΓΦ	-	12.5 mm GB	-
IV	10	10 mm + Ab	-	10 mm GF	10 mm + Ab	10 mm GF	-
	11	10 mm + Ab	6 pcs.	10 mm GF	10 mm + Ab	10 mm GF	-
	12	10 mm + Ab	6 pcs.	10 mm GF	10 mm + Ab	10 mm GF	12.5 mm GB

Ab – elastic absorbing material from polyurethane foam
GF – gypsum fiber board;

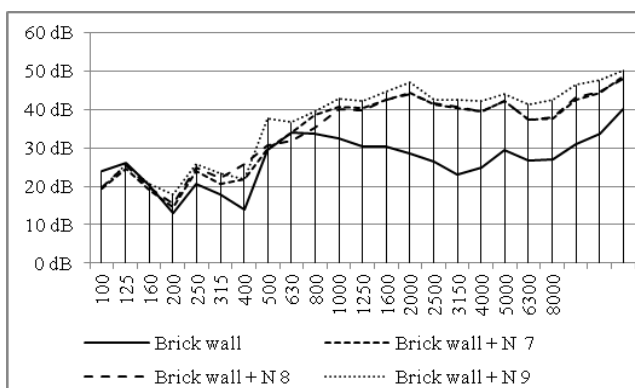


Fig. 5. Experimental results of noise reduction to Set III, measurements 7, 8 and 9

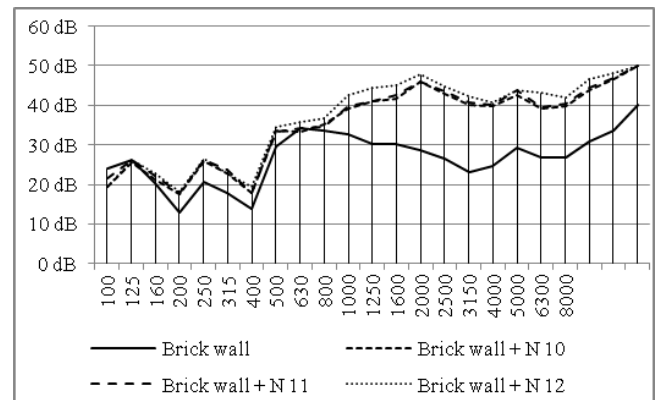


Fig. 6. Experimental results of noise reduction to Set IV, measurements 10, 11 and 12

GB – gypsum board;
Point connection – realised from 6 peaces of PVC nails

IV. ANALYSIS OF RESULTS

In Set I the increase of sound insulation is mainly in the high frequency region. The resonance frequency is observed at 200 Hz and there is insignificant decrease at 630 Hz. Differences between the calculated and measured results (Fig. 7) are caused from that Sharp's model [1] which does not give satisfactory results for cavities below 25 mm and the second reason is the flanking transmission between the chambers. In Set II the thickness of the porous elastic layer is doubled to 20 mm. The result is increasing sound insulation in frequency region from 630 to 1250 Hz with an average of 5 dB. Again there is an insignificant decrease at 630 Hz.

In Set III the thickness of the first mass is increased from 10 to 15 mm and the elastic layer is 20 mm. The sound insulation in the mid frequency region is increased with an average of 6 dB.

In Set IV the resonance frequency is moved to 400 Hz and

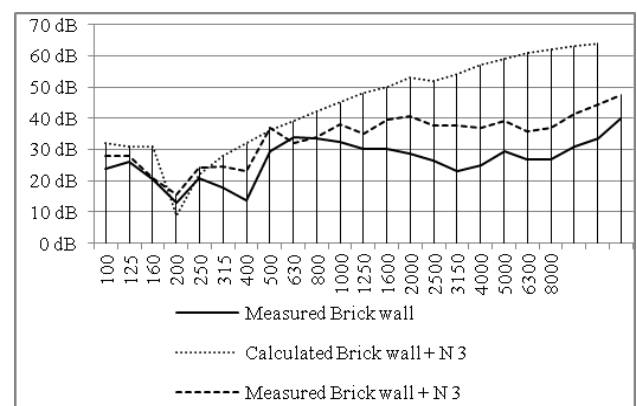


Fig. 7. Comparison between measured and calculated results of sound reduction index of Set I, N3:brick wall + 10mm elastic layer (Ab) + 10 mm fiber board (GF) + 6 point connections

the average sound insulation in mid frequencies is 4 dB (Fig. 8).

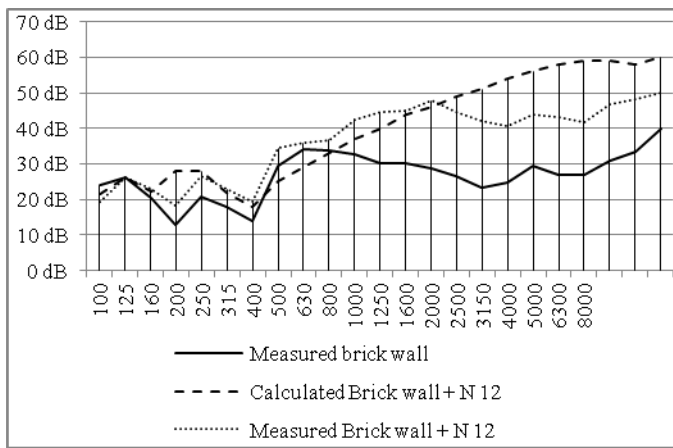


Fig. 8. Comparison between measured and calculated results of sound reduction index of Set IV, N12: brick wall + 10 mm elastic payer (Ab) + 10 mm fiber board (GF) + 6 point connections + 12.5 mm gypsum board (GB)

In all the sets the increase of sound insulation for the range of 125 to 250 Hz is an average of 3 dB compared with the brick wall. The resonance frequency is well predicted from the theoretical model, but there is a big differences for the coincidence region. The influence of point connections is measured - it is beneficial for sound insulation with 1 to 2 dB for low frequencies and declines it with 1 to 2 dB for mid frequencies. For high frequencies there is no change in the behavior. Point connections are necessary for the mechanical strong connection for the added layers because only with glue equal strength cannot be guaranteed. The addition of second mass (gypsum board) gives results up to 500 Hz.

V. CONCLUSION

From the measured combinations the optimal balance between noise reduction properties and low price can be appointed the system with 20 mm elastic layer plus fiber board 15 mm and final layer of gypsum board (Set III, Measurement 9).

With total thickness of 47.5 mm is achieved increase of natural sound insulation of the brick wall with 12 dB. In contrary of the expectations the use of two added masses with two elastic layers by 10 mm (Set IV, Measurement 12) does not show significantly improved results than Set III - the natural sound insulation index is again 12 dB, but the thicknes is increased to 52.5 mm and the cost increases with almost 30 %. In Set I the achieved natural sound insulation index is 7 dB and the total thickness is 32.5 mm. In Set II the total thickness is 42.5 mm and that natural sound insulation index is 9 dB. All the systems are highly efficient for high frequencies and poorly efficient for mid and low frequencies. On other hand they are various methods of mountage and have a wide range of application in a building constructions.

ACKNOWLEDGMENT

This paper was supported by Technical University - Sofia inner program to support PhD research projects under Contract 145 PD0017-07: "Development of algorithms to study the acoustical characteristics of covering materials for recording studios and concert halls".

REFERENCES

- [1] B.H. Sharp, "A Study of Techniques to Increase the Sound Installation of Building Elements", Washington, DC, 1973.
- [2] D. Bies, C. Hansen, "Engineering noise control Theory and practice", *Engineering noise control Theory and practice*, 2009.
- [3] R.S. Smith, *Sound Transmission trough Lightweight Parallel Plates*, Edinburgh: Heriot-Watt University, 1997.
- [4] *ISO 140-3*, 1995. Acoustics - Measurement of sound insulation in buildings and of building elements - Part 3: Laboratory measurements of airborne sound insulation of building elements.
- [5] A. London, 1950, "Transmission of reverberant sound through double walls", *Journal of the Acoustical Society of America* 22, pp. 270-279.
- [6] L.L. Beranek, G.A. Work, 1949, "Sound transmission through multiple structures containing flexible blankets", *Journal of the Acoustical Society of America* 21, pp. 419-428.

The Acoustic Analysis of a Single Room

Violeta Stojanović¹, Zoran Milivojević², and Staniša Dimitrijević³

Abstract – This paper describes the acoustic analysis of the parameters for a single room intended for meetings. In the first part of this paper both objective and subjective acoustic parameters are described in accordance with ISO 3382 standard. In the second part of the paper an experiment was done in which the acoustic impulse responses were practically measured. Then the graphical and tabular presentation of both subjective and objective parameters results set out of the acoustic impulse response was shown. Finally, the comparative analysis of acoustic parameters values along with the recommended values of ISO 3382 standard was done, and based on that, the acoustic quality of the room was evaluated in terms of its application.

Keywords – Room Impulse Response (RIR), Acoustic parameters, Reverberation.

I. INTRODUCTION

The beginning of any acoustic measurements is attributed to Sabine, who was first to measure the reverberation time in 1900 [1]. Since then, we have reached significant discoveries which allow to obtain good acoustic of a certain space, whether it was speech intelligibility or music quality.

The analysis *Acoustic Impulse Response* (AIR) of rooms is an important part in mere acoustic interpretation of rooms. Room impulse response contains all the information about the acoustic characteristics of a room between the source position and the receiver position. During the transmission of a sound from a source to a certain receiving point within a room, the main characteristic of the room as an acoustic transmission system is the existence of reflected sound energy.

An impulse response can be obtain in several ways. One of them is using a diagram of waveform signal from the output of the measuring microphone at room impulse using several acoustic sources which produce a shot signal (Dirac impulse which is subjectively sensated as a shot, a gun, firecracker, piercing of the inflated balloon, electric spark etc.) [1]. Other ways are based on more sophisticated methods of measuring impulse response which are more precise and fully meet the requirements of the ISO 3382 standard [2]. These are methods which are based on the emission of complex incentive signals. Most frequently these are [3]: broadband, deterministic and recurring signal, eg *Maximum Length Sequence MLS* for system impulse which is believed to be linear and time invariable and sinusoidal signal with frequency which changes exponen-

tially, logarithmic sweep signal, *SineSwap*, for system impulse which is not linear and also for time variable systems.

Measuring of acoustic impulse response using *MLS* technique was first introduced by Schroeder in 1979 [4]. In 1995 Suzuki established „Optimum computer generated impulse signal“ [5]. In 2000 Farina introduced logarithmic SineSweep technique wit which he managed to overcome most of the limitations which at that time existed in the other techniques [6].

This paper analyzes the acoustic quality of a single room so that, based on impulse responses observed at multiple position of a microphone, following objective and subjective acoustic parameters are determined: *Reverberation Time: T_{R20} , T_{R30} and T_{R60} ; Early Decay Time EDT; Centre Time T_s ; Clarity: C_{50} and C_{80} ; Definition: D_{50} and D_{80}* and rating of speech intelligibility: *Articulation Loss of Consonants AL_{cons} , Speech Transmission Index STI and Rapid Speech Transmission Index RASTI*. Diffusivity of a room is also tested using *EDT/ T_{30}* ratio [7]. Obtained parameters values are analyzed compared to standard value and certain conclusions are given.

The organization of work is as follows. In section II the acoustic parameters of the room obtained from the acoustic impulse response are defined. In section III the experimental results and the analyses of the results for the acoustically treated room are shown. Section IV is the conclusion.

II. ACOUSTIC PARAMETERS OF A ROOM

Following acoustic parameters are defined by ISO 3382 [2] i IEC 60268-16 standards [8]:

1) *Reverberation Time T_{R60}* (s), is the time necessary for decreasing of the sonic energy of a room, after turning off the sound source, to one millionth of its value compared to the steady state. Respectively, it is the time necessary for decreasing of the sound level, after turning off the sound source to 60dB compared to the sound level in steady state. T_{R60} is the same at all points of the room and it doesn't depend on either sound source or room geometry, but it is frequency dependant value.

Reverberation time T_{R60} (s), is defined in accordance to Sabine equation [1]:

$$T_R = \frac{0.16V}{A}, \quad (1)$$

and Eyring's equation [2]:

$$T_R = \frac{0.16V}{-S \ln(1 - \bar{\alpha})}, \quad (2)$$

where: $V [m^3]$ is the total volume of a room; $A [m^2] = \bar{\alpha} S$ is the equivalent absorption area in a room; $S [m^2]$ is the sum of all areas in a room; $\bar{\alpha}$ is the mean coefficient of the absorption. Sabine's formula is applicable for the rooms with the ap-

¹ Violeta Stojanović is with the College of Applied Technical Sciences of Niš, 20. Aleksandra Medvedeva, St, 18000 Niš, Serbia, e-mail: violeta.stojanovic@vtsnis.edu.rs

² Zoran Milivojević is with the College of Applied Technical Sciences of Niš, 20. Aleksandra Medvedeva, St, 18000 Niš, Serbia.

³ Staniša Dimitrijević is with the College of Applied Technical Sciences of Niš, 20. Aleksandra Medvedeva, St, 18000 Niš, Serbia.

proximate diffuse sound field where $T_R > 0.8s$, while Eyring's formula states more precision results for the rooms with $T_R < 0.8s$.

During the measuring procedure it is not possible to achieve the dynamics of decline of the sound level in a room to 60dB, so that the reverberation is determined according to the decline of the sound level at 20dB, (T_{R20}), 25dB, (T_{R25}), 30dB, (T_{R30}).

Duration of the impulse response must be longer than the reverberation time. The dynamics of the measured impulse response must be at least 20dB, but it is recommended, for the sake of objectivity, that the dynamic range is at least 30dB [9].

2) *Early Decay Time, EDT*, is [10] defined as the time necessary for the sound level to decrease by 10dB, starting from -5dB compared to the maximum level. It depends on a room geometry. If *EDT* significantly deviates from the reverberation time, it is shown that it is most important for the subjective perception of a room reverberation.

3) *Centre Time T_s* , is a dimension which shows the discretely divides the impulse response into an early and a late period [7]. Along the timeline of the impulse response the values of this dimension give the information about equal energy of the initial part of the impulse response and the energy of the rest of the impulse response:

$$T_s = \int_0^{\infty} t h^2(t) dt \bigg/ \int_0^{\infty} h^2(t) dt . \quad (3)$$

4) *Clarity* is the parameter which characterizes the time distinguishing tones which appear simultaneously despite the existing reverberation. The objective measure of the clarity is clarity index C [dB]. The parameters C_{50} and C_{80} are defined as logarithmic relation of the early acoustic energy (the one which reaches the certain spot in the room for the first 50ms or 80ms of impulse response) to the remaining subsequent acoustic energy (the energy which appears after a defined moment in time):

$$C_{t_e} = 10 \log \left(\frac{\int_0^{t_e} h^2(t) dt}{\int_{t_e}^{\infty} h^2(t) dt} \right) . \quad (4)$$

t_e is 50ms or 80ms. The parameter C_{50} is used for speech, and a C_{80} for music.

5) *Definition, D_{50} , or D_{80}* , represents the relation between the early acoustic energy (first 50ms or 80 ms of the impulse response) and the total acoustic energy ranging (0 - ∞):

$$D_{t_e} = \frac{\int_0^{t_e} h^2(t) dt}{\int_0^{\infty} h^2(t) dt} . \quad (5)$$

D_{t_e} also measures the share of the energy of a direct wave and early reflections within the total signal. It can be also shown as a percentage. The definition of the higher percentages provides better listening conditions, and significantly influences the intelligibility. The connection between the parameters D_{t_e} and C_{t_e} is achieved by the following relation:

$$C_{t_e} = 10 \log \frac{D_{t_e}}{1 - D_{t_e}} . \quad (6)$$

6) Speech intelligibility is performed using the objective parameters AL_{cons} (*Articulation Loss of Consonants*), STI (*Speech Transmission Index*) and $RASTI$ (*Rapid Speech Transmission Index*) which qualify the subjective feeling of speech intelligibility. Peutz [10] explained that the percentage of indistinct consonants AL_{cons} . AL_{cons} depends on relation between the direct and the reflected sound, reverberation time, and the relation signal/noise in a room.

$RASTI$ and $STIPA$ (*Speech Transmission Index for Public address*) methods represent the condensed STI methods [8]. They are obtain by reducing the number of modulation frequencies and the number of octaves in which STI is calculated i.e. measured. $STIPA$ is sensitive to the distortion in the system, and $RASTI$ is focused on direct speech communication and it includes the impact of the environment.

III. EXPERIMENTAL RESULTS AND ANALYSIS

A. The Experiment

The objective of the experiment is to establish the acoustic parameters of a room (teachers' office in the School of Mechanical Engineering '12. Februar' in Nis). Primarily the acoustic impulse responses are recorded, and then, using the software package Matlab both objective and subjective acoustic parameters are calculated. The decision on the suitability of a room is made using the comparative analysis of parameters values determined by ISO 3382 standard.

B. The Basis of the Acoustic Impulse Response

The recording of the acoustic impulse responses is carried out in the room shown in Fig. 1.

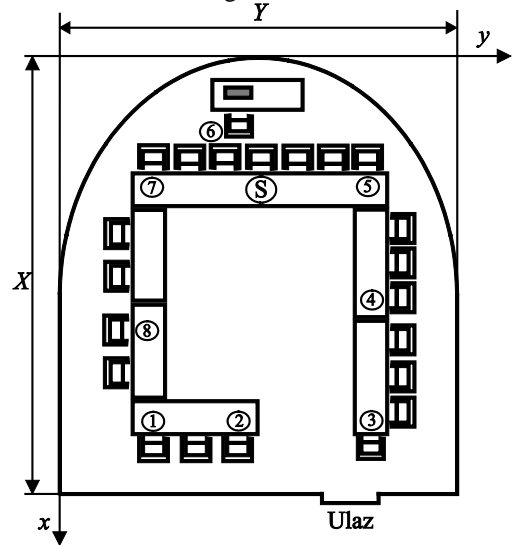


Fig. 1. The shew of the room where the impulse response is measured: S-the location of the sound source, 1 - 8 –the location of the receiver

Room dimensions are $9.9\text{m} \times 9.8\text{m} \times 3.6\text{m}$. Room volume is $V = 312,1\text{m}^3$. A room may have up to 40 seats. The measuring of the impulse response is carried out using sweep incentive signal lasting 5s. The sampling frequency is $f_s = 44.1\text{kHz}$. The location of a sound source is S (2.64, 4.9, 1.3). The measurements are carried out at 8 measurement points: M1 (7.2,2.6, 1.3); M2 (7.2, 3.9, 1.3); M3 (7.2, 7.1, 1.3); M4 (4.84, 7.3, 1.3); M5 (2.64, 7.3, 1.3); M6 (1.55, 5.2, 1.3); M7 (2.64, 2.6, 1.3); M8 (4.57, 2.6,1.3). The reflective coefficients of the floor and ceiling walls are: 0.95, 0.95, 0.95, 0.95, 0.85 and 0.88.

C. The Results

The show of the acoustic impulse responses of a room and the show of Schroeder's curve (on the basis of which the reverboration time is determined) for 8 measured locations, are shown in Fig. 2 to 8. The obtained values of the acoustic parameters are shown in Table I (t is the arrival time of direct sound to the receiver).

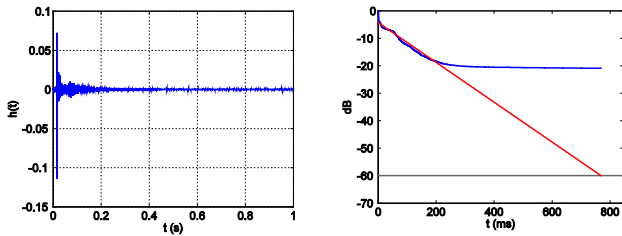


Fig. 2. The acoustic impulse response of a room and Schroeder's curve for the measured location 1

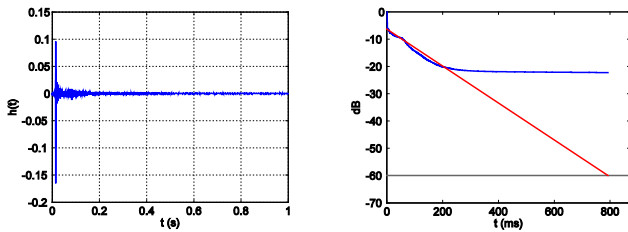


Fig. 3. The acoustic impulse response of a room and Schroeder's curve for the measured location 2

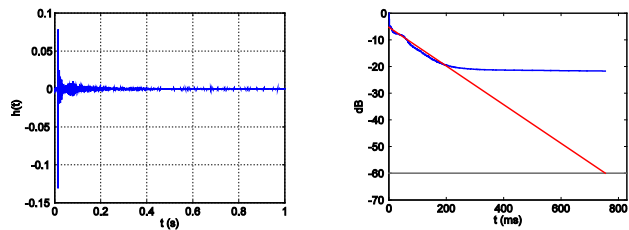


Fig. 4. The acoustic impulse response of a room and Schroeder's curve for the measured location 3

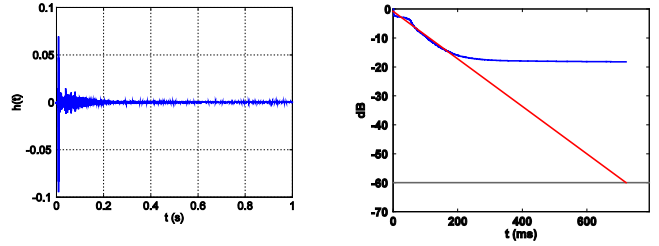


Fig. 5. The acoustic impulse response of a room and Schroeder's curve for the measured location 4

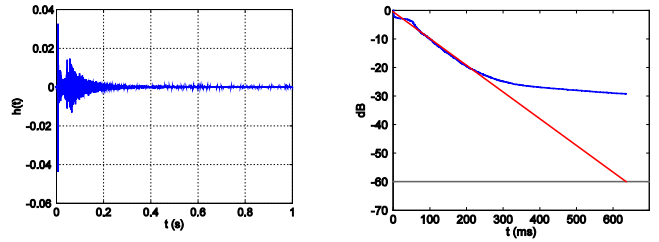


Fig. 6. The acoustic impulse response of a room and Schroeder's curve for the measured location 5

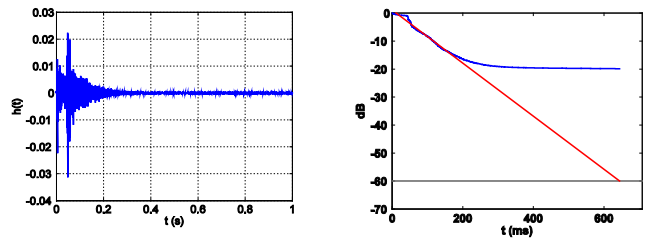


Fig. 7. The acoustic impulse response of a room and Schroeder's curve for the measured location 6

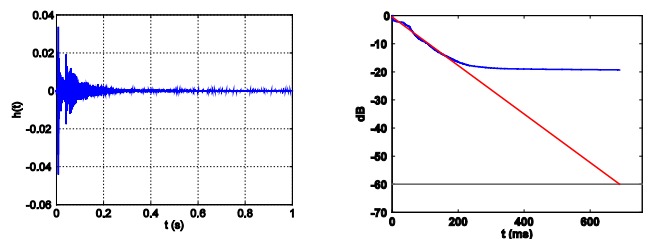


Fig. 8. The acoustic impulse response of a room and Schroeder's curve for the measured location 7

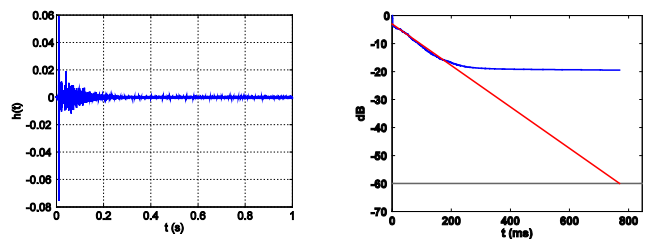


Fig. 9. The acoustic impulse response of a room and Schroeder's curve for the measured location 8

TABLE I
THE VALUES OF THE ACOUSTIC PARAMETERS OF THE ROOM.

Pos.	1	2	3	4	5	6	7	8
t (ms)	15.3	13.9	14.5	8.6	5.7	3.9	7.4	9.5
EDT (s)	0.87	0.86	0.82	0.82	0.69	0.6	0.62	0.76
T_{20} (s)	0.22	0.2	0.2	0.23	0.27	0.22	0.23	0.23
T_{30} (s)	0.36	0.35	0.33	0.35	0.36	0.33	0.34	0.35
T_{60} (s)	0.77	0.79	0.75	0.76	0.72	0.64	0.69	0.77
$\frac{EDT}{T_{30}}$	2.42	2.49	2.48	2.31	1.92	1.82	1.82	2.17
T_c (ms)	43.6	30.1	35.2	50.2	83	87.3	76.5	59.1
C_{50} (dB)	6.49	9.0	7.96	6.17	1.27	0.24	1.57	5.53
C_{80} (dB)	10.7	12.5	12	9.57	7.16	5.87	7.38	8.76
D_{50} (%)	81.7	88.8	86.2	80.6	57.3	48.6	58.9	78.1
D_{80} (%)	92.2	94.7	94	90	83.8	79.4	84.6	88.3
STI	0.74	0.77	0.75	0.7	0.7	0.69	0.69	0.72
$RASTI$	0.75	0.81	0.78	0.71	0.68	0.63	0.7	0.72
AL_{cons} (%)	3.11	2.67	2.92	3.81	3.95	4.12	4.07	3.52

D. The Results Analysis

Based on the results shown in Fig. 2. to 9. and the Table I we can conclude the following:

1) The values during the reverberation time are within the following range $T_{R60} = (0.64 - 0.79)s$. The mean values of the reverberation time is $\bar{T}_{R60} = 0.74s$. Considering that the optimal reverberation time for the rooms where speech prevails, with their volumes greater than $300m^3$, with the range $T_{R60} = (0.4 - 0.8)s$, the measured reverberation time entirely meets the criteria. While measuring the reverberation time, using Sabin's model, $T_{R60} = 0.6s$ is obtained, which is also within at above mentioned limits.

2) The relation EDT/T_{30} at medium frequencies is within the plan range $EDT/T_{30} = 1.82 - 2.49$. As the obtained values are not within the plan range $EDT/T_{30} = 0.8 - 1.1$, it means that the measurements have been carried out in the space which is not diffusive.

3) The values of the definitions, D_{50} , and D_{80} , are higher than 50%. It confirms the excellent clarity of speech and bad clarity for the music in the room. Minimal deviation is for the measured location 6, $D_{50} = 48.6\%$.

4) The centre time is $T_s = (30-87.3)ms$. Only the measured location 4, 7 and 8 meet the demands of $T_s = (50-80)ms$, which represent the integration constants for speech and music. Low values of the centre time for the measured locations 1, 2 and 3 indicate that most of the energy arrives in the initial part of the impulse response, which is related to the subjective feeling of the reverberation.

5) The value ranges for the speech transmission index STI and $RASTI$ are $STI = 0.69 - 0.77$ and $RASTI = 0.63 - 0.81$. These values are within the range of determined values which represent good speech intelligibility: $0.6 - 0.75$, and excellent speech intelligibility: values higher than 0.75 .

6) The articulation loss of consonants, AL_{cons} , has values within the range of (2.67% - 4.12%) which belong to this pa-

rameter categorization $AL_{cons} < 10\%$ and indicate very good intelligibility (the ideal). The highest expected articulation loss of consonants, i.e. the weakest intelligibility (4.12%) is obtained for the measured location 6.

According to the conducted analyses of the results, we can draw the conclusion that the acoustic parameters of the analyzed room meet the conditions required by ISO 3382 standard for good speech intelligibility.

IV. CONCLUSION

The results of the measured acoustic parameters for the room which is used as teachers' office are shown in this study. Both objective and subjective parameters for rating of the room acoustics are defined. Based on the measured impulse responses of the room, both objective and subjective acoustic parameters are determined. The parameters are analysed in relation to the standard values determined by ISO 3382 standard for good speech intelligibility which concludes that: the mean values of reverberation time $0.4s \leq \bar{T}_{R60} = 0.74s \leq 0.8s$, the mean value of speech clarity index $\bar{C}_{50} = 4.72dB \geq -0.2dB$, articulation loss of consonants index $\bar{AL}_{cons} = 3.52\% \leq 10\%$. According to the above shown results and their comparison to the standard values for the rooms intended for speech, we can draw the conclusion that the analyzed room is acoustically suitable for meetings.

REFERENCES

- [1] H. Kuttruff, "Room acoustics", fifth edition, Spoon Press, 2009.
- [2] ISO 3382: Measurement of the Reverberation Time of Rooms with Reference to Other Acoustical Parameters.
- [3] D. Čirić, "Doprinos razvoju postupka merenja i obrade impulsnog odziva prostorije pri određivanju akustičkih karakteristika", Doktorska disertacija, Katedra za telekomunikacije, Elektronski fakultet, Univerzitet u Nišu, Niš, Srbija, 2006.
- [4] M. R. Schroeder, "Integrated - impulse method for measuring sound decay without using impulses", vol. 66, no. 2, pp. 497–500, 1979.
- [5] A. Farina, "Simultaneous measurement of impulse response and distortion with a swept-sine technique", 108th AES Convention, Paris, France, February 19-22 2000.
- [6] A. Farina, "Impulse response measurements by exponential sine sweeps", Industrial Engineering Dept. University of Parma, Italy, 2008.
- [7] M. Topa, N. Toma, B. Kirei, I. Homana, M. Neag, G. Mey: Comparison of different experimental methods for the assessment of the room's acoustics, Acoustical Physics, 2011, Vol. 57, No. 2, pp. 199–207.
- [8] International electrotechnical commission IEC 60268 Sound system equipment Part 16: Objective rating of speech intelligibility by speech transmission index, IEC, 2002.
- [9] G. B. Stan, J.-J. Embrechts and D. Archambeau, Comparison of different impulse response measurement techniques, Journal of Audio Engineering Society, vol. 50, No.4, pp.249-262, 2002.
- [10] T. Houtgast, M. Steeneken, A review of the MTF concept in room acoustics and its for estimating speech intelligibility in auditoria, J. Acoust. Soc. Am. 77, 1069 – 77, 1985.

Session ELT:

**ELECTRONIC MATERIALS,
COMPONENTS, SYSTEMS AND
TECHNOLOGIES**

Synthesis of Zeolite NaA with Facets through the Sol-Gel Technology

Dimitar Georgiev¹, Ivan Petrov², Todor Michalev³ and Ivan Pejchev⁴

Abstract – We examined the possibility of obtaining pure synthetic crystals of zeolite NaA with the chemical composition $\text{Na}_{12}[(\text{AlO}_2)_{12}(\text{SiO}_2)_{12} \cdot 27\text{H}_2\text{O}]$ by sol-gel methods. What we received was a product with the proven structure of zeolite NaA, confirmed by studies conducted using the methods of XRD, IR spectroscopy and SEM. The technology for the preparation of zeolite NaA was developed using the method of the sol-gel process comprised of preparation of two sol-gel solutions (at temperature up to 90°C for the reflux), and synthesis of the final product (washing, drying and activation of the zeolite).

Using the methods of IR, XRD and SEM was studied the structure of the obtained synthetic product, and the results were compared to those of zeolite NaA, prepared through hydrothermal synthesis. It was found that the synthetic product obtained by sol-gel technology is in its pure crystalline phase, the obtained crystalline entities are 2-3µm in dimension; single crystals are cubes with symmetrical facet form.

Keywords – Zeolite NaA, Synthetic zeolite, Sol-gel technology, Structure of zeolite.

I. INTRODUCTION

Zeolites are materials, which have many applications, such as in household products, aquacultures, agriculture, water treatment, etc., due to their absorption abilities, ion exchange and size selectivity properties. Zeolite NaA has also been used in gas separation membranes to enhance the selectivity of the support. Commercial Zeolite NaA is synthesized through conventional techniques and silicates and aluminates are mostly used as starting materials [1-4].

Convenient synthesis procedures for pure Zeolite NaA by sol-gel methods were developed so that microcrystals of high chemical quality, good crystalline and size homogeneity can be obtained.

This method for the preparation of Zeolite NaA is preferred by many authors [5-11], because it uses pure raw materials, the obtained products are homogeneous and the synthesis is performed at lower temperatures.

¹Dimitar Geotgiev is with the Technical Faculty of Assen Zlatarov University in Burgas, 1 Prof. Iakimov str., Bourgas 8010, Bulgaria, E-mail: dgeorgiev@btu.bg.

²Ivan Petrov Ph.D. is a student at the Technical Faculty of Assen Zlatarov University in Burgas, 1 Prof. Iakimov str., Bourgas 8010, Bulgaria, E-mail: bulmarine@abv.bg.

³Todor Michalev Ph.D. is a student at the Technical Faculty of Assen Zlatarov University in Burgas, 1 Prof. Iakimov str., Bourgas 8010, Bulgaria, E-mail: rl_burgas@abv.bg.

⁴Ivan Pejchev Ph.D. is a student at the Technical Faculty of Assen Zlatarov University in Burgas, 1 Prof. Iakimov str., Bourgas 8010, Bulgaria, E-mail: peichev.ivan@gmail.com.

II. EXPERIMENTALS

The synthesis procedure leads to crystals with the chemical composition of $\text{Na}_{12}[(\text{AlO}_2)_{12}(\text{SiO}_2)_{12} \cdot 27\text{H}_2\text{O}]$.

Used raw materials: Tetraethoxysilane $\text{Si}(\text{OC}_2\text{H}_5)_4$, Aldrich, purity > 99%, Aluminum powder, purity 99.9%, Sodium Hydroxide (NaOH), pellets, Merck, purity > 99%, Deionized water.

In Figure 1 is the projects scheme for the preparation of zeolite NaA using the sol-gel technology.

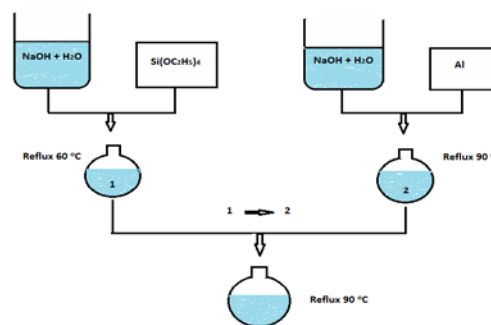


Fig. 1. Scheme of the synthesis procedure for zeolite NaA

For this purpose we prepared a starting gel, which was a combination of two working solutions. The starting compositions are prepared in a suitable vessel with constant stirring at a temperature of 60 to 90°C, and then refluxed. The solutions and the gel are prepared in the following sequence, which is shown in Table 1.

TABLE I
SEQUENCE OF PREPARATION OF THE BASIC COMPOUNDS

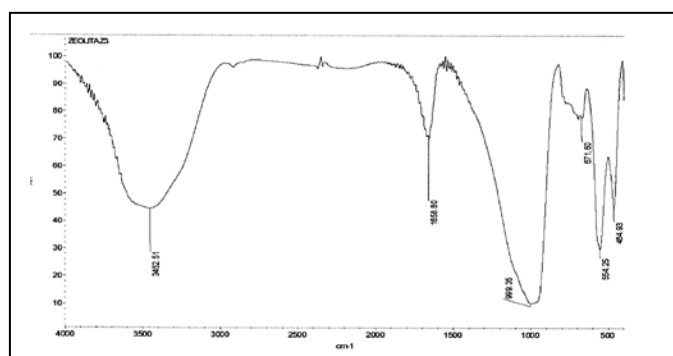
Comp osition	Procedures	Specifications
A.	1. [150 ml H_2O + 5.97 g NaOH]; 2. [(1) + 7.85 g $\text{Si}(\text{OC}_2\text{H}_5)_4$].	Temperature - 60°C, 60 min, reflux.
B.	3. [150 ml H_2O + 5.97 g NaOH]; 4. [(3) + 2.15 g Al.	Temperature - 90°C, 120 min, reflux.
Total	5. [A → B].	1. Temperature - room, 30 min, reflux. 2. Temperature - 90°C, 12 h, shear, reflux.

The next stage is the finalization of the synthesis of the zeolite. This stage is very important and includes washing, drying and activation of the final product. The washing was performed with water, and is done to eliminate the excess of soluble sodium compounds. Practically this is done by repeated subsequent washing with deionized water heated at 90°C and with continuous stirring of the slurry. After each wash centrifugation should be done (4500 rpm, 10 min). This continues until the system reaches a pH of 7-8. The drying is done in vacuum at 100°C for 120 min. The activation of the zeolite is performed by a heat treatment in a muffle furnace at a temperature of 550-600°C for 3 hours.

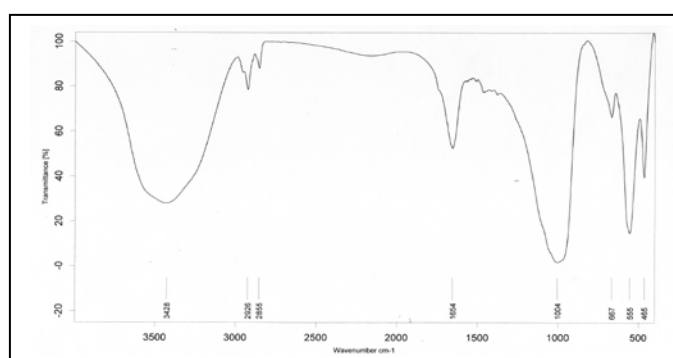
III. RESULTS AND DISCUSSIONS

The obtained product was tested using the methods XRD, IR spectroscopy and SEM. This was done in order for the structural features of the synthetic zeolite, that was received as a product, to be identified and compared with similar data obtained from the zeolite received through the hydrothermal method [12-14].

In Figure 2 are compared the IR studies of the NaA zeolite prepared by hydrothermal method and the one prepared by a sol-gel technology.



(a)



(b)

Fig. 2. IR specter of the Zeolite NaA prepared by: (a)- hydrothermal method, (b) - sol-gel technology

In Table 2 is shown the comparative data on the IR vibrational frequencies of the experimental results for the

zeolite synthesized by the method of the sol-gel technology and the one prepared through the hydrothermal method.

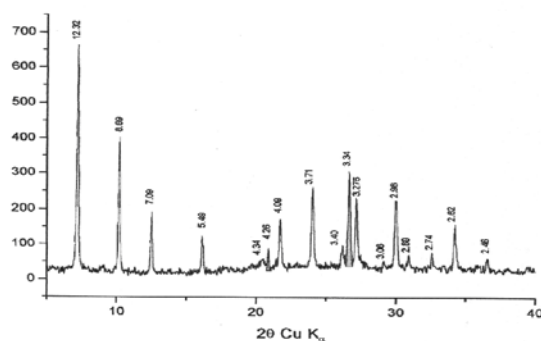
TABLE II
Most intense bands

Zeolite NaA- (sol-gel), Frequency, cm ⁻¹	Zeolite NaA -(hydrothermal), Frequency, cm ⁻¹
3228	3452
1654	1658
1004	999
667	671
555	554
465	464

It is clear from the data shown that the synthesized zeolite has intense groups of IR vibrational frequencies comparable to those of the zeolite prepared by the Hydrothermal Method, and to the literature values for the same zeolite. The vibrational frequencies of the Al-O groups are observed up to 667 cm⁻¹. And after 1000 cm⁻¹ are observed the ones that show the Si-O-Al relationship in the TO₄ tetrahedra (T = Si or Al). On the left side of the IR spectrum there are clearly shaped peaks at around 3428 cm⁻¹ and 1654 cm⁻¹ which characterize the zeolitic water. The experimentally obtained IR spectrum proves that the formed product is zeolite NaA, as there is coincidence in the IR waves at 1004, 667, 555 and 465 cm⁻¹ in the IR spectrum of zeolite NaA with the data from the literature consulted [15].

Figure 3 shows the diffractograms of Zeolite NaA obtained by sol-gel technology (a) and the one produced through the hydrothermal method (b). It is obvious that the zeolite prepared by the sol-gel process does not contain additional crystalline phases. This results from the fact that it is produced from pure starting materials. The products received from kaolin through the hydrothermal method [12-14], are displayed below:

Major phases: Zeol-A = Zeolite A (NaAlSi₃O₈);
Q = Quartz (SiO₂).
Minor phases: Hid = Hydroxycancrinite -
(Na₈(Al₆Si₆O₂₄)(OH)_{2,04}(H₂O)_{2,66});
Par = Paragonite -(NaAl₂(Si,Al)₄O₁₀(OH)₂);
And = Andalusite (Al₂(SiO₄)O).



(a)

IV. CONCLUSION

The studies conducted through scientific work give reason for the following important conclusions:

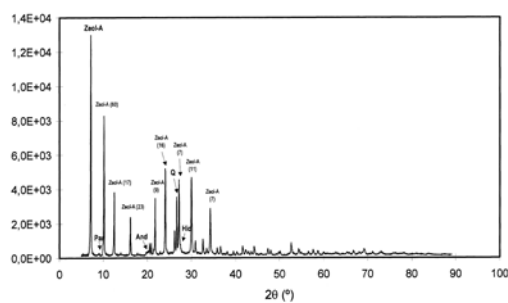
- We examined the possibility of obtaining a synthetic Zeolite NaA with the chemical composition of $\text{Na}_{12}[(\text{AlO}_2)_{12}(\text{SiO}_2)_{12} \cdot 27\text{H}_2\text{O}]$ through the method of sol-gel technology and we received a product with the proven structure of Zeolite NaA, which was confirmed by studies conducted through the methods of XRD, IR and SEM.

- The technology that has been developed for the preparation of Zeolite NaA under the method of sol-gel technology comprises of the following stages: obtaining two compositions (at temperature of 60-90 °C, with continuous vigorous stirring and reflux), and final treatment (washing, drying and activation) of the zeolite.

- Using the methods of IR, XRD and SEM was studied the structure of the obtained synthetic product, and the results were compared to those from Zeolite NaA, prepared by hydrothermal synthesis. It was found that: the synthetic product obtained by sol-gel technology is in pure crystalline phase, it was compared with the one obtained through hydrothermal method from natural Bulgarian kaolin, and the resulting crystalline entities are of the same size (2-3 μm); the single crystal is a regular cube with facet edges.

REFERENCES

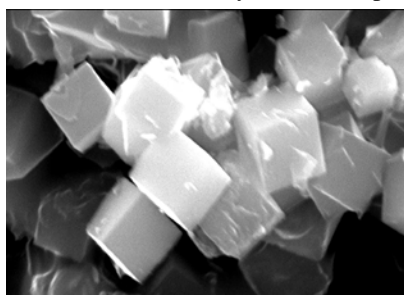
- [1] D. W. Breck: *Zeolite Molecular Sieves: Structure, Chemistry and Use*. John Wiley and Sons, London, UK, 1974.
- [2] R.M. Barrer: *Hydrothermal Chemistry of Zeolites*. Academic Press, London, UK, 360 p. 1982.
- [3] S. P. Jdanov, E. N. Egorova: *Chemistry of zeolites*. Science, Leningrad, Russia, 1968.
- [4] V. H. Bekkum, E.M.Flanigen, P.A. Jacobs, J.C. Jansen: *Introduction to Zeolite Science and Practice*. 2nd. Revised Edn., Elsevier, Amsterdam, 1991.
- [5] J. Weitkamp, A. Raiuhle, Y. Traa, *Appl. Cat. A* 2001, 222, 277.
- [6] G. Schulz-Ekloff, D. Wdhrle, B. van Duffel, R. A. Schoonheydt, *Microporous Mesoporous Mater.* 2002, 51, 91.
- [7] D. Bruhwiler, G. Calzaferri, *Microporous Mesoporous Mater.* 2004, 72. 1.
- [8] W. Sachtler, *Ace. Chem. Res.*, 1993, 26, 383.
- [9] M. Wark. G. Schulz-Ekloff, N. I. Jaeger. *Bulg. Chem. Comm.* 1998, 30, 129.
- [10] A. A. Demkov, O. F. Sankey, *J. Phys.: Cond. Matter* 2001, 13, 10433.
- [11] K. Kuge, G. Calzaferri, *Microporous Mesoporous Mater.* 2003. 66. 15.
- [12] D. Georgiev, B. Bogdanov, Y. Hristov, I. Markovska, I. Petrov, "Synthesis of NaA zeolite from natural kaolinite", *Book of Zeolite 2010*, 8th international conference, July 2010 Sofia, Bulgaria, 95-97, 2010.
- [13] D. Georgiev, B. Bogdanov, Y. Hristov, I. Markovska, K. Angelova, "Synthesis of NaA zeolite", *Proc. of 12th Int. Conf. on Mechanics and Technology of Composite Materials*, 22-24 Sept. 2009, Varna, Bulgaria, p. 41-46.
- [14] D. Georgiev, B. Bogdanov, Y. Hristov, I. Markovska, "Synthesis of NaA Zeolite from Natural Kaolinite", *Oxidation Communications* 34, No 4, 812-819 (2011).
- [15] Markovic S., V. Dondur, R. Dimitrijevic, "Journal of Molecular Structure", 654, 2003, 223-234.



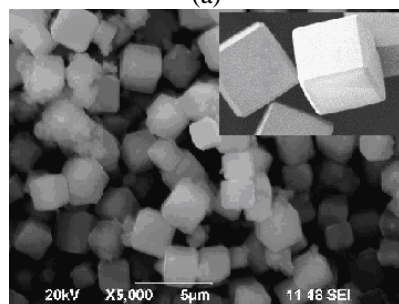
(b)

Fig. 3. XRD of Zeolite NaA: (a) - sol-gel technology, (b) - hydrothermal method

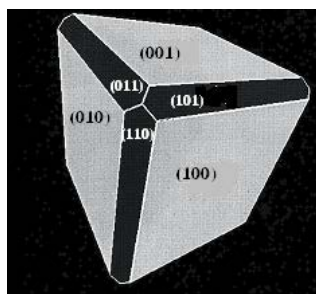
In Figure 4 are shown photographs from scanning electron microscopy of Zeolite NaA - synthesized by hydrothermal method (a), synthesized by sol-gel technology (b), and a single crystal of zeolite NaA, synthesized by sol-gel technology. The resulting crystal formations synthesized by the both methods are clear cubes measuring about 2-3 μm. You can see the cube's facet edges of Zeolite NaA synthesized by sol-gel technology. This is probably due to the use of optimal conditions in the crystallization process.



(a)



(b)



(c)

Fig.4. SEM of Zeolite NaA: (a) - synthesized through hydrothermal method, (b)- synthesized through sol-gel technology, (c)- scheme of a single crystal, received through sol-gel technology

The removal of Cu(II) Ions from Aqueous Solutions on Synthetic Zeolite NaA

Todor Michalev¹, Ivan Petrov² and Ivan Pejchev³

Abstract – In this study the adsorption of Cu (II) ions from aqueous solutions on synthetic zeolite NaA was evaluated. Determination of the effects of the temperature of the solution and the kinetic parameters of adsorption of Cu(II) from aqueous solution on zeolite NaA is important for the understanding of the mechanism of the adsorption. Variables of the system include the adsorption time, the temperature (293-328K), the initial concentration of the solution and pH of the system. The kinetic model of sorption of the copper ions was found to be strongly dependent on pH (the optimum pH 3-5), the concentration of ions in the solution and the temperature (293 – 328 K). It was found that the pseudo-second-order model was the best choice among all the kinetic models to describe the adsorption behaviour of Cu(II) onto zeolite NaA, suggesting that the adsorption mechanism might be a process of chemisorption. The activation energy of adsorption (E_a) of Cu(II) was determined as 13.5 kJ mol⁻¹. The low value of E_a shows that the process of adsorption of Cu(II) process on zeolite NaA may be an activated chemical adsorption. The thermodynamic parameters (ΔG^0 , ΔH^0 , and ΔS^0) were also determined from the temperature dependence. The results show that the process of adsorption of Cu(II) is spontaneous and endothermic process and higher temperature favours the adsorption.

Keywords – Zeolite NaA, adsorption, adsorption capacity, kinetic sorption.

chemical compounds like nitrates, phosphates, heavy metals, etc. One method for removal of heavy metals from drinking water is the treatment with synthetic zeolites [3,4].

Using zeolites as sorbents is preferred due to their specific structure, which allows selectivity of the processes involved (adsorption and ion-exchange), simple operation and effectiveness. This is a result from the main properties of the synthetic zeolites like highly developed porous surface, phase purity and resistance to chemical reagents.

The present paper deals with issues referring to the studies on the opportunity of purifying aqueous solutions containing copper ions using synthetic zeolite NaA together with the methods of adsorption and ion-exchange. Higher levels of Cu(II), as well as other heavy metals, in water facilities poses great risk to human health. Therefore, it is of major importance to find ways of lowering the concentration or removing such contaminants from basins used for drinking water [5,6].

For this purpose, the paper discusses the adsorption kinetics of synthetic zeolite L in model aqueous solutions containing Cu(II) ions, as well as the various factors affecting the process of adsorption. The results obtained are further adapted in the kinetic models and an assessment of the adsorption processes is made.

I. INTRODUCTION

Zeolites are aluminosilicate minerals containing exchangeable alkaline and alkaline earth metal cations (normally Na, K, Ca and Mg) as well as water in their structural framework. The physical structure is porous, enclosing interconnected cavities in which the metal ions and water molecules are contained [1,2]. Zeolites are appropriate material for the removing heavy metal ions from wastewater because of their relatively low price, together with the fact that their exchangeable ions (Na⁺, Ca²⁺ and K⁺) are relatively harmless.

The properties of drinking waters and these used in food industry, as well as waters packed for retail selling should conform to certain requirements regarding their contents of

¹Todor Michalev Ph.D. is a student at the Technical Faculty of Assen Zlatarov University in Burgas, 1 Prof. Iakimov str., Bourgas 8010, Bulgaria, E-mail: rl_burgas@abv.bg.

²Ivan Petrov Ph.D. is a student at the Technical Faculty of Assen Zlatarov University in Burgas, 1 Prof. Iakimov str., Bourgas 8010, Bulgaria, E-mail: bulmarine@abv.bg.

³Ivan Pejchev Ph.D. is a student at the Technical Faculty of Assen Zlatarov University in Burgas, 1 Prof. Iakimov str., Bourgas 8010, Bulgaria, E-mail: peichev.ivan@gmail.com.

II. EXPERIMENTALS

A. Adsorbate

All the compounds used to prepare the reagent solutions were of analytic reagent grade. The initial copper solutions were prepared from deionized water and Cu(NO₃)₂·3H₂O (Merck). To maintain certain values of pH during the process of adsorption, various buffer solutions were added to the total model solution studied in quantities up to 25%.

B. Adsorbent

The adsorbent used for the studies was synthetic zeolite NaA produced through a technology described earlier [7,8].

C. Batch Adsorption Experiments

The adsorption kinetics was studied through the method of volt-ampometric, a volt-ampere meter ECOTEST-VA (ECONIX-EXSPERT) was used. This method allows direct registration of the amount of Cu(II) in the adsorbate monitored at every moment of contact with the adsorbent (zeolite NaA) [9].

The measuring system was specially designed for the experiments to allow constant homogenization (through

varied velocities of a propeller) for better contact between the adsorbent and the adsorbate, as well as to provide the possibility of isothermal periods in thermostatic cell. The experiments were carried out at constant temperatures of 293, 313 and 328 K and two initial Cu(II) concentrations of the model solution.

To study the kinetics of adsorption, 100 ml of model solution of Cu(II) with initial concentration of 60 or 100 mg/L was placed in a flat-bottomed flask (under continuous agitation and the selected constant temperature). From the moment of the mixing with the adsorbent, the decrease of the amount of the studied ions was monitored and recorded for a period of 60 min. Simultaneously, the change of pH in the adsorbate was also measured.

The adsorption capacity of the sorbent (q_e , mg/g) was calculated by an equation (1).

$$q_e = \frac{(C_o - C_e)}{m} \cdot V \quad (1)$$

Where C_o and C_e are respectively the initial and the final sample concentrations (mg/L), V (L) – the volume of the sample solution and m (g) is the weight of the added adsorbent.

III. RESULTS AND DISCUSSION

A. Theory

The models of kinetics of the adsorption were correlated to the solution uptake rate, hence these models are important in the design of the water treatment process. In order to elucidate the adsorption mechanism and the potential rate controlling step, four kinetic models including the pseudo-first-order equation [10], the pseudo-second-order equation, the Elovich equation, and the intraparticle diffusion model were tested to fit the experimental data obtained from the batch of experiments on the removal of metal ions.

1. Pseudo-first-order Model

The adsorption kinetic data was described by the Lagergren pseudo-first-order model, which is the first known equation that describes the adsorption rate based on the adsorption capacity. The equation in its linear form looks this way:

$$\log(q_e - q_t) = \log q_e - \frac{k_1}{2.303} t \quad (2)$$

where q_e and q_t are, respectively, the adsorption capacity at equilibrium and at time t (mg g⁻¹), k_1 is the rate constant in the pseudo-first-order adsorption (L min⁻¹).

2. Pseudo-second-order Model

The kinetics of the adsorption may be described by the pseudo-second-order model.

The equation in its linear form is:

$$\frac{t}{q_t} = \frac{1}{K_2 q_e^2} + \frac{t}{q_e} \quad (3)$$

Where q_e and q_t are the ions of heavy metals per mass unit of the adsorbent (mg/g) at equilibrium and at specific time, K_2 (g/mg min) is the rate constant in the second order kinetics.

The initial sorption rate, h , can be defined as

$$h = K_2 q_e^2 \quad (4)$$

so (4) can be represented in the following way:

$$q_t = \frac{t}{((1/h) + (t/q_e))} \quad (5)$$

The initial sorption rate, h (mmol g⁻¹ min⁻¹), the equilibrium sorption capacity, q_e , and the pseudo-second-order rate constant, K_2 , can be determined experimentally through slope-intercept plotting of t/q_t against t .

3. The Elovich equation

The Elovich equation is given as follows:

$$q_t = \frac{\ln(\alpha\beta)}{\beta} + \frac{\ln t}{\beta} \quad (6)$$

where q_t is the sorption capacity at time t , α is the initial sorption rate of the Elovich equation (mmol g⁻¹ min⁻¹), and the parameter β is related to the extent of surface coverage and the activation energy for chemisorption (g mmol⁻¹). The constants can be obtained from the slope and intercept equation form of a straight line of q_t versus $\ln t$.

4. Intraparticle diffusion model

The intraparticle diffusion model is:

$$q_t = k_p t^{1/2} + C \quad (7)$$

where k_p is the intraparticle diffusion rate constant (mmol g⁻¹ min^{-1/2}), C is the intercept.

The activation energy for the adsorption of metal ions was calculated using the Arrhenius equation:

$$k = k_o \exp\left[\frac{-E_a}{RT}\right] \quad (8)$$

where k_o is the temperature independent factor in g mmol⁻¹ min⁻¹, E_a is the activation energy of the reaction of adsorption in kJ mol⁻¹, R is the gas constant, 8.314 J mol⁻¹ K⁻¹ and T is the adsorption absolute temperature, K.

The linear form is:

$$\ln k = \frac{-E_a}{RT} + \ln k_o \quad (9)$$

When $\ln k$ is plotted versus $1/T$, a straight line with slope $-E_a/R$ is obtained.

To calculate the thermodynamic activation parameters such as enthalpy of activation (ΔH^0), entropy of activation (ΔS^0), and free energy of activation (ΔG^0), the Eyring equation was applied:

$$\lg K_D = -\frac{\Delta H^0}{2.303RT} + \frac{\Delta S^0}{2.303R} \quad (10)$$

$$\Delta G^0 = \Delta H^0 - \Delta S^0 T \quad (11)$$

where $K_D = q_e/C_e$.

B. Parameters of adsorption

The experimental results of adsorption of Cu(II) onto the Zeolite NaA at various temperature 293–328K, (initial concentrations 60 mg/L) are shown in Figure 1.

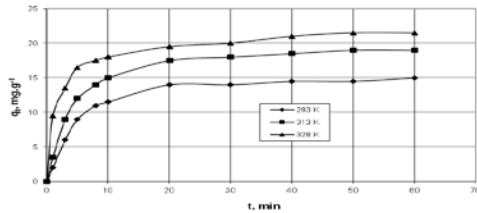


Fig. 1. The effect of contact time and temperature to adsorption of Cu(II) onto the Zeolite NaA (initial concentrations 60 mg/L)

Figure 1 illustrates that the equilibrium time of sorption was obviously shortened with the increase of the temperature from 293 to 328K. The equilibrium sorption was attained after about 60 min of solute-sorbent contact at temperature ranging from 293 to 328K, and there wasn't any remarkable removal of Cu(II) in case of elongated contact time. The increase of Cu(II) adsorption capacity with the increase of the temperature indicates that higher temperature promotes Cu(II) adsorption onto the Zeolite NaA, and the adsorption is controlled by an endothermic process.

The preliminary studies show that the aqueous solutions of Cu(II) are quite unstable due to the susceptibility of the copper ions to hydrolyzation. This process depends on the ion concentration in the solution and mainly on the medium pH. Copper ions in aqueous solution are most stable at medium pH from 2 to 4.5. Studies have shown that there is probability for hydrolyzation at pH of the solution above 4.5–5.0. Thus, copper hydroxide precipitate was observed in the adsorbate at pH higher than 5.0, the amount of copper ions sharply decreased and could not be registered by the ionometer (especially at low concentrations). Therefore, up to 25% buffer solution was added to the model aqueous solution for its stabilization.

The selection of proper buffer solution and its amount is an important issue in the studies on the kinetics of sorption of copper ions from aqueous solutions since the process is accompanied by ion exchange with the zeolite. It should also be taken into account that, as a result from the ion exchange, sodium ions are released into the solution from the zeolite NaA which increases the medium pH. This is registered directly by the pH measuring gauge.

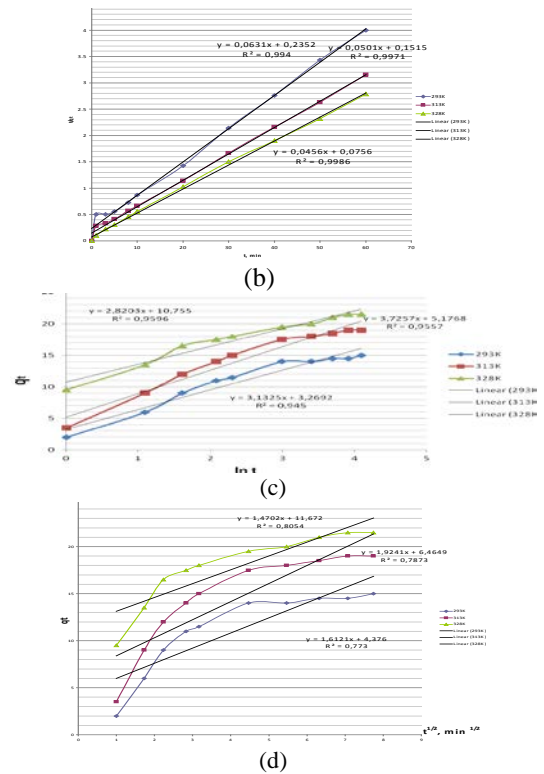
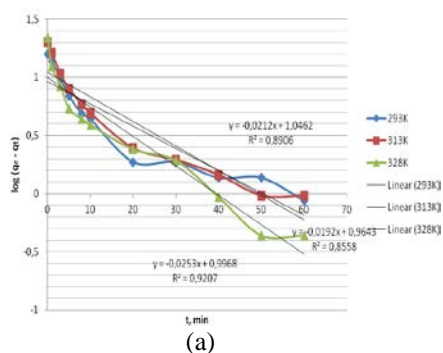


Fig.2. Plots of the four kinetic models for Cu(II) adsorption onto Zeolite NaA at various temperature

The plots of the four kinetic models for Cu (II) adsorption onto the Zeolite NaA at various temperature were given in Figure 2. The values of the kinetic parameters of the four kinetic models were calculated according to Figure 1. The kinetic parameter (k_2) measured from the pseudo-second order model shows very high correlation coefficient. The equilibrium adsorption capacity of Cu (II) measured from the pseudo-second order model agrees with the experimental data. The value of the kinetic parameter (k_2) increases from 0.00187 to 0.00345 kg/mg-min with the increase of the temperature from 293 to 328K. The above features explain why the adsorption of Cu (II) onto the synthetic Zeolite NaA might be a chemical reaction, and can be expressed by the pseudo-second order model.

C. Thermodynamic parameters of adsorption

A plot of $\ln k_2$ against $1/T$ is shown in Figure 3. The activation energy (E_a) was determined according to the characteristics of the linear plot. The magnitude of the activation energy may give an idea about the type of sorption. There are two main types of adsorption: physical and chemical. The activation energy for the physical adsorption is usually no more than 4.2 kJ mol^{-1} , since the forces involved in the physical adsorption are weak.

The chemical adsorption is specific and involves forces much stronger than those in the physical adsorption. There are two kinds of chemical adsorption which include activated and nonactivated chemical adsorption. The term activated chemical adsorption means that the rate varies with the

temperature according to the finite activation energy (8.4–83.7 kJ mol⁻¹) in the Arrhenius equation. In nonactivated chemical adsorption, the activation energy is close to zero.

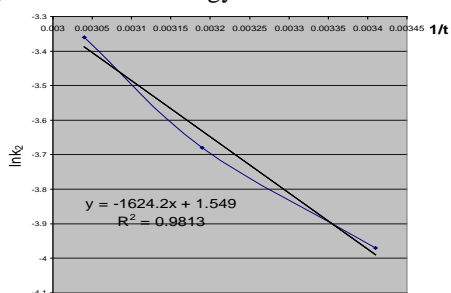


Fig. 3. Linear plot of $\ln K_2$ versus $1/T$

The values of the rate constant from the pseudo-second-order can be used in the calculation of the activation energy of the sorption process. The energy of activation (E_a) was determined from the slope of the Arrhenius plot of $\ln k_2$ versus $1/T$ according to Eq. (10) and was found to be 13.5 kJ mol⁻¹ for Cu(II). This value is of the same magnitude as the activation energy of the activated chemical sorption. The positive values of E_a suggest that the rise in temperature favors the adsorption and that the adsorption process is an endothermic.

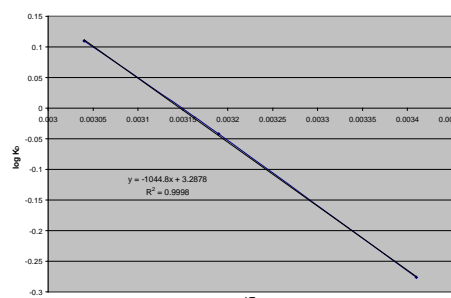


Fig. 4. The linear plot of $\log K_D$ versus $1/T$

To calculate the thermodynamic activation parameters such as ΔH^0 , ΔS^0 , and ΔG^0 , the Eyring equation Eq (10,11) was applied and the results are listed in Table 1.

TABLE I
THE ACTIVATION ENERGY AND THERMODYNAMIC ACTIVATION PARAMETERS OF Cu(II) ADSORPTION ONTO ZEOLITE NaA

THERMODYNAMIC PARAMETERS	VALUE
1. Activation energy – E_a , kJ mol ⁻¹	13.5
2. Enthalpy of activation – ΔH^0 , kJ mol ⁻¹	20.0
3. Entropy of activation - ΔS^0 , kJ mol ⁻¹ K ⁻¹	0.062
4. Free energy of activation - ΔG^0 , kJ mol ⁻¹	
- for 293 K	1.84
- for 313 K	0.61
- for 328 K	-0.33

The positive ΔS^0 indicates that no significant change occurs in the internal structure of the Zeolite NaA, during the

adsorption of copper ions. The positive values of ΔH^0 indicate the endothermic nature of the process. The negative ΔG^0 values of Cu(II) ions at temperature 328 K are due to the fact that the adsorption processes are spontaneous and the negative value of ΔG^0 decrease with the increase of temperature, indicating that the spontaneous nature of adsorption of Cu(II) is inversely proportional to the temperature. It is obvious from the results reported in Table 1 that temperature affects the adsorption process of the metal ion adsorption, as the higher the temperature the more the energy to enhance the adsorption rate.

IV. CONCLUSION

In this study was investigated the kinetic sorption of Cu(II) and can be obtained the following conclusions:

The adsorption capacity of the sorbent (Zeolite NaA) strongly depends on the pH and the temperature of the sorbate.

The adsorption of Cu(II) is best described at different physical and chemical conditions in accordance with the pseudo-second order kinetic model.

The measured E_a value (E_a , 13.5 kJ mol⁻¹) suggests that the adsorption may be a chemical reaction.

The values of the thermodynamic parameters indicate that the adsorption is endothermic reaction in its nature.

REFERENCES

- [1] M. J. Yabe, E. Oliveira “Heavy metals removal in industrial effluents by sequential adsorbent treatment”, *Adv. Env. Res.*, 7, 2003, pp. 263-272.
- [2] K. K. Panday, G. Prasad, V. N. Singh “Copper (II) removal from aqueous solutions by fly ash”, *Wat. Res.* Vol.19, 1985, pp.869.
- [3] G. Blanchard, M. Maunaye, G. Martin “Removal of heavy metals from waters by means of natural zeolites”, *Water Res.* 18,1984, pp.1501–1507.
- [4] Y.S.Ho “Second-order kinetic model for the sorption of cadmium onto tree fern: A comparison of linear and non-linear methods”, *Water Res.* 40(1), 2006, pp. 119–125.
- [5] H.J.M. Bowen, “Environmental Chemistry of the Elements”, Academic Press, London, 1979, pp 109-111.
- [6] S. Curkovic; “Metal ion exchange by natural and modified zeolites”; *Wat. Res.*, vol.31, 1997, pp.1379-1382.
- [7] K. A. Stancheva, B. I. Bogdanov, D. P. Georgiev, “Synthetic Zeolites. Structures, Classification, Properties, Synthesis, Industrial and Environmental Applications”, *Oxidation Communications* 34, No 4, 792–811 (2011).
- [8] D. Georgiev, B. Bogdanov, Y. Hristov, I. Markovska, “Synthesis of NaA Zeolite from Natural Kaolinite”, *Oxidation Communications* 34, No 4, 2011, 812–819.
- [9] F. Scholz, *Electroanalytical Methods, Guide to Experiments and Applications*, Springer, Moskow, 2006.
- [10] B. Biskup, B. Suboti “Kinetic analysis of the exchange processes between sodium ions from zeolite A and cadmium, copper and nickel ions from solutions”, *Separation and Purification Technology*, vol. 37, 2004, pp. 17-31.

Electrical Properties of Piezo Organic Materials and Application

Lyudmila Borisova¹, Dimitrina Kiryakova¹ and Atanas Atanassov¹

Abstract – Nanocomposite materials on the basis of vinylidene fluoride–hexafluoropropylene copolymer with organically modified nanoclays were obtained by co-precipitation method from its solution in dimethylsulfoxide. The addition of nanoclays was found to facilitate the transformation of the polymer crystals from α - to β - phase. The increase of the tensile strength and elongation at break of the nanocomposites, containing Cloisite®15A was higher at lower content of nanoclays, compared to that of the initial VDF–HFP copolymer, thus disclosing that the clay layers were better exfoliated. The results obtained showed that the nanocomposites prepared could be promising for the application as new piezo materials.

Key words - Electrical properties, Nanoclay, Nanocomposites, Vinylidene fluoride-hexafluoropropylene copolymer, Co-precipitation, Piezo effect, Organic piezo materials.

I. INTRODUCTION

There are four basic methods for synthesis of polymer/silicate materials: from melt, from solution, by in-situ polymerization and sol-gel techniques. Every polymer system requires selection of proper method and treatment conditions to obtain the product wanted at highest efficiency. In the present paper, the experiments were limited to mixing from solution based on consideration on simplifying the technological procedures aiming at further implementation of the method directly in the industry.

The mixing from solution is based on a system where the polymer is soluble and silicate layers swell. Layered silicates swell in the solvent while polymer is dissolved.

The layered silicate suspension and the polymer solution are mixed, so polymer chains penetrate and substitute the solvent in the intermediate silicate layers. After the removal of the solvent, polymer nanocomposite is obtained [1].

Special attention should be paid to the proper selection of solvent. It should be suitable for the polymer and considered against the layered silicate and its organic modifier.

There is certain risk of solvent intercalation in the polymer which is unwanted process.

¹Lyudmila Borisova – Department of Materials Science, Assen Zlatarov University, Y. Yakimov Str. 1, Burgas 8010, Bulgaria, e-mail: liusiila1976@gmail.com

¹Dimitrina Kiryakova – Department of Materials Science, Assen Zlatarov University, Y. Yakimov Str. 1, Burgas 8010, Bulgaria, e-mail: dskiryakova@abv.bg

¹Atanas Atanassov – Department of Materials Science, Assen Zlatarov University, Y. Yakimov Str. 1, Burgas 8010, Bulgaria, e-mail: aatanassov@btu.bg

The dimethyl sulfoxide (DMSO) is a common solvent for many polymers, suitable for the preparation of nanocomposites by co-precipitation method.

It is well known that films of vinylidene fluoride hexafluoropropylene copolymer (VDF–HFP) with different HFP contents indicate prominent piezo-, pyro-, and ferroelectricity comparable to that in PVDF [4-11].

It was found also that these properties are highly dependent on the crystal structure and polymer chain orientation of the VDF–HFP copolymer [12].

Casting from dimethylformamide solution [9, 10] or stretching of VDF–HFP films [8] leads to chain conformations that are similar to those of polar β - PVDF.

The addition of nanoclays is a prerequisite for the improvement of the mechanical, barrier, piezo-, pyro- and ferroelectric properties [13-15].

It was reported in ref. [14] that the addition of organically modified nanoclays to the VDF–HFP copolymer facilitated the transformation of the polymer crystals from α - to β -.

The nanocomposite materials obtained showed increased values of elongation at break compared to the initial copolymer, as well as high dielectric permeability in wide temperature interval.

The piezoelectric β - phase in VDF–HFP nanocomposites with layered silicate was retained after swift heavy ion irradiation, indicating that the nanocomposites can be used as radiation-resistant materials at high temperature [15].

The aim of the present work is to obtain nanocomposite materials on the basis of vinylidene fluoride–hexafluoropropylene copolymer with organically modified nanoclays Cloisite®15A and Cloisite®30B by co-precipitation method from solution in dimethylsulfoxide and study the tensile, dielectric and piezoelectric properties of the nanocomposites obtained.

II. EXPERIMENTS

A. Materials

Vinylidene fluoride–hexafluoropropylene copolymer referred to as VDF–HFP is a copolymer (15 mol% HFP comonomer) with melting temperature 117°C and melt index 6.52 g/10 min (220°C, load 98 N) in the form of powder, kindly supplied from Arkema, France.

Cloisite®15A and Cloisite®30B, organically modified montmorillonite nanoclays from Southern Clay Products Inc. were used. Cloisite®15A is Na⁺ montmorillonite clay modified with dimethyl, dehydrogenated tallow, quaternary ammonium (2M2HT) with d_{001} spacing – 31.5 Å and density – 1.66 g/cm³. HT stands for a tallow-based compound (~65% C18, ~30%

C16, ~5% C14) in which the majority of the double bonds have been hydrogenated.

The modifier concentration of Cloisite®15A was 125 meq/100 g. Cloisite®30B is montmorillonite clay modified with methyl, bis-2-hydroxyethyl tallow, quaternary ammonium (MT2EtOH) with d_{001} spacing – 18.5 Å and density – 1.98 g/cm³.

The modifier concentration of Cloisite®30B was 90 meq/100 g. The solvent used for the compositions was dimethylsulfoxide (DMSO), Sigma Aldrich.

All the materials described above were used directly without any further modification or treatment.

B. Sample Preparation

The co-precipitation method was used to prepare VDF–HFP copolymer nanocomposites containing 1, 2 and 3 mass% of Cloisite®15A or Cloisite®30B.

To obtain the nanoclay contents in the VDF–HFP copolymer mentioned, two premixes were made: one for the nanoclay and the other for the VDF–HFP, using DMSO as solvent. The two premixes were sonicated using a Branson 8510 ultrasonication bath at 30–40°C for approximately 5 min.

The final 10% solution was prepared by adding the contents of the nanoclay premix to the VDF–HFP copolymer premix and the product was sonicated again for 20 min.

The mixture obtained, 150 ml of deionized water were added. A stringy, white, translucent precipitate formed immediately. Then, the precipitate was removed and dried in a vacuum oven until constant weight.

For most physical testing, the precipitated samples were pressed into films on a laboratory press PHI (England) between aluminum foils under the following conditions: samples thickness about 0.3 mm, temperature 200°C, melting period at 200°C – 3 min, pressing pressure – 12 MPa; cooling rate – 40°C/min.

C. Tensile Properties

The tensile strength, elongation at break and the other characteristics of the initial VDF–HFP copolymer and the nanocomposite materials based on it were measured on a dynamometer INSTRON 4203 (England) at speed of 100 mm/min and room temperature.

D. Electrical properties

Before studying the electrical parameters the samples should be metalized for ohmic contacts.

The electrodes could be made using two methods:

- Film deposition in vacuum of conductive materials (e.g. Al Al–Ni, Ag, Au);
- Printing of conductive layer (epoxy+Ag-powder).

The first method of vacuum deposition is sputtering [2, 3, 17], because is low temperature, not destructive with good adhesion.

In these experiments conductive silver glue is used for easy preparation of the electrodes.

The process is screen printing and polymerization at 60–80°C for 20 minutes.

The shape of samples is shown in Fig. 1.

The next very important step for preparation of the samples is thermal and electrical polarization.

The electric field is applied (100 to 500 kV/cm) to align the dipoles at a temperature in the range of 90–100°C.

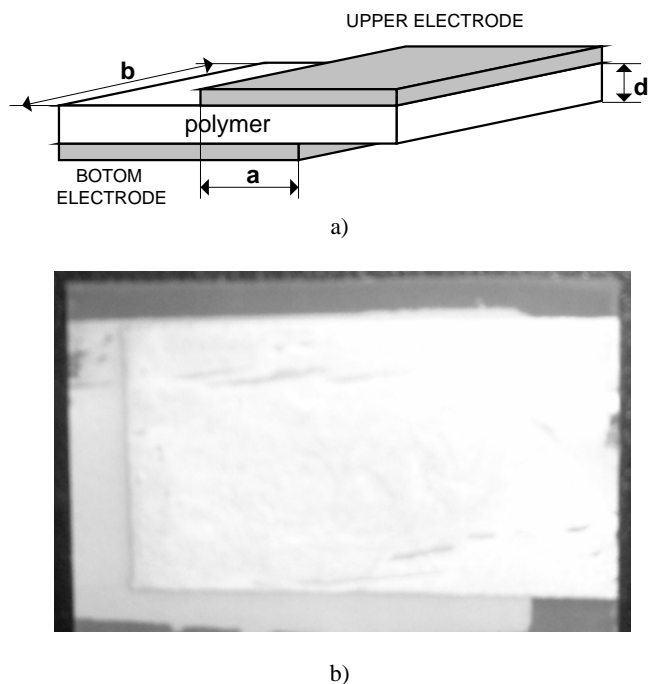


Fig. 1. a) The shape and dimension of samples.
 $S=a \times b$ – common surface between upper and bottom electrodes (Ag); d – thickness of samples
 b) Physical model

The next is cooling of the sample with electrical field thus freezing the polar alignment.

Before electrical testing the samples are numbered as follows:

1. Initial VDF–HFP copolymer;
2. VDF–HFP + 1 mass% Cloisite®15A;
3. VDF–HFP + 2 mass% Cloisite®15A;
4. VDF–HFP + 3 mass% Cloisite®15A.

TABLE I
 DIELECTRIC CONSTANTS AND CRITICAL ELECTRICAL FIELD OF THE SAMPLES

PARAMETER	NUMBER OF SAMPLES			
	1	2	3	4
C(pF)	212	70	110	190
ϵ_r	9	15	22	25
$U_{BR}(KV)$	5.1	5.2	5.8	5.7
$E(V/m) \times 10^7$	6.0	5.7	3.0	-

The main electrical parameters such as dielectric constant ϵ_r , breakdown voltage of resistively are shown in Table I.

The experiments showed that the specific resistance (total ohmic resistance) rapidly drops after 50°C. At room temperature (20°C) the resistance of all samples is over the measuring range 200 MΩ. After temperatures between 70 - 80°C the resistance is in the range between 9 - 30 MΩ. It could be seen that after the initial rapid changes there are stabilization of total resistance. It means that over temperature 55 - 60°C there are saturation of current thermogeneration.

The conclusion is that these materials have semiconductor behavior with clear negative temperature coefficient of resistivity.

III. RESULTS AND DISCUSSION

The initial VDF-HFP copolymer obtained by co-precipitation method contains mainly α - phase. With the addition of organically modified nanoclays (Cloisite®15A, Cloisite®30B) to the copolymer, α - phase was transformed into β - phase.

The presence of polar electroactive β - phase is the reason for the ferro-, pyro-, and piezoelectric properties of the materials based on this copolymer which makes possible to use them in control and measuring gauges, in microelectronics and other specific fields.

Because of the rigid structure of clay layers and their high aspect ratio, they have proven to be very effective in the improvements of the nanocomposites mechanical properties even at very lower nanoclay additions [16] in well dispersed state.

The tensile strength, elongation at break and Young modulus of the materials based on VDF-HFP copolymer with Cloisite®15A and Cloisite®30B are shown in Table III.

It can be seen that the increase of the values of tensile strength (to 38.7 and 34.3 MPa, respectively) and elongation at break (to 848 and 835%, respectively) was higher at lower content of the nanoclays used (0.75, 1.0 mass%), compared to that of initial VDF-HFP copolymer. It means that the clay layers are better dispersed in the polymer matrix. The reinforcing effect was lower for the nanocomposites with higher clay content (up to 3.0 mass%) owing to some clay platelets being agglomerated and stacked.

The formation of β - phase in the compositions studied is also beneficial to the improvements of mechanical properties of the materials obtained.

The Young modulus of the composite materials prepared by the co-precipitation method showed higher values, compared to that of initial copolymer.

IV. APPLICATION AND CONCLUSION

Polymer nanocomposite materials containing up to 3.0 mass% organically modified montmorillonite nanoclays Cloisite®15A and Cloisite®30B were prepared by co-precipitation method. The nanocomposites obtained were characterized by their tensile, dielectric and piezoelectric properties.

TABLE III
TENSILE PARAMETERS OF THE INITIAL VDF-HFP COPOLYMER AND ITS NANOCOMPOSITES

NUMBER OF SAMPLES	TENSILE STRENGTH, MPa		ELONGATION AT BREAK, %		YOUNG MODULUS, MPa	
	Cloisite®15A	Cloisite®30B	Cloisite®15A	Cloisite®30B	Cloisite®15A	Cloisite®30B
1	27.2	27.2	795	795	125	125
2	38.7	34.3	823	835	215	184
3	35.2	32.9	805	770	156	165
4	33.6	30.7	750	700	154	155

The main application is transforming mechanical effect into an electric signal.

There are many variation of this effect but in two main configuration – bending and pressing – Fig. 2.

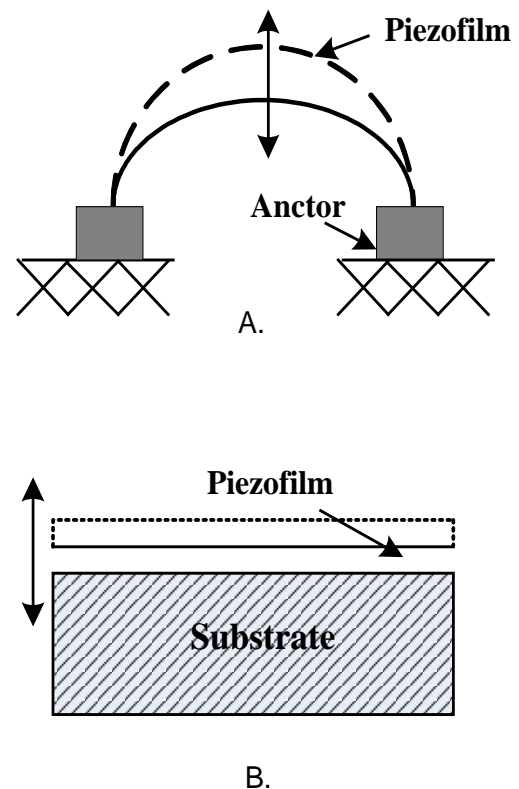


Fig. 2. Bending (A) and pressing (B) of piezomaterials.

REFERENCES

- [1] S. S. Ray and M. Okamoto, "Polymer/layered silicate nanocomposites: a review from preparation to processing", *Progr. Polym. Sci.*, vol. 28, pp. 1539-1641, 2003.
- [2] P. Rahnev, D. Kiryakova, L. Borisova and A. Atanassov, "Electrical Properties of Poly (Vinylidene Fluoride-co-Hexafluoropropylene) Nanocomposites with Nanoclays", XLVIII International Scientific Conference On Information, Communication And Energy Systems And Technologies, ICEST 2013-Ohrid, Macedonia.
- [3] P. Rahnev, S. Letskovska, D. Parachkevov and K. Seymenliyski, "Sputtering of Thin Films on Flexible Substrates", XLVIII International Scientific Conference On Information, Communication And Energy Systems And Technologies, ICEST 2013-Ohrid, Macedonia.
- [4] X. Lu, A. Schirokauer and J. Scheinbeim, "Giant electrostrictive response in poly(vinylidene fluoride-hexafluoropropylene) copolymers", *IEEE Trans. Ultrason. Ferroelectr. Freq. Contr.*, vol. 47, pp. 1291-1295, 2000.
- [5] W. K nstler, M. Wegener, M. Sei  and R. Gerhard-Multhaupt, "Preparation and assessment of piezo- and pyroelectric poly (vinylidene fluoride-hexafluoropropylene) copolymer films", *Appl. Phys. A.*, vol. 73, pp. 641-645, 2001.
- [6] A. C. Jayasuriya, A. Schirokauer and J. I. Scheinbeim, "Crystal-structure dependence of electroactive properties in differently prepared poly(vinylidene fluoride/hexafluoropropylene) copolymer films", *J. Pol. Sci. B: Polym. Phys.*, vol. 39, pp. 2793-2799, 2001.
- [7] M. Wegener, W. K nstler, K. Richter and R. Gerhard-Multhaupt, "Ferroelectric polarization in stretched piezo- and pyroelectric poly(vinylidene fluoride-hexafluoropropylene) copolymer films", *J. Appl. Phys.*, vol. 92, pp. 7442-7447, 2002.
- [8] F. Wang, Z. Xia, X. Qiu, J. Shen, X. Zhang and Z. An, "Piezoelectric properties and charge dynamics in poly(vinylidene fluoride hexafluoropropylene) copolymer films with different content of HFP", *IEEE Trans. Dielectr. Electr. Insul.*, Vol. 13, pp.1132-1139, 2006.
- [9] A. C. Jayasuriya and J. I. Scheinbeim, "Ferroelectric behavior in solvent cast poly(vinylidene fluoride/hexafluoropropylene) copolymer films", *Appl. Surf. Sci.*, vol. 175, pp. 386-390, 2001.
- [10] M. Wegener, W. K nstler and R. Gerhard-Multhaupt, "Piezo-, pyro- and ferroelectricity in poly (vinylidene fluoridehexafluoropropylene) copolymer films", *Integr. Ferroelectr.*, vol. 60, pp. 111 - 116, 2004.
- [11] F. Wang, P. Fr bing, W. Wirges, R. Gerhard and M. Wegener, "Enhanced Polarization in Melt-quenched and Stretched Poly(vinylidene Fluoride - Hexafluoropropylene) Films", *IEEE Trans. Dielectr. Electr. Insul.*, vol. 17, no. 4, pp. 1088-1095, 2010.
- [12] X. He, K. Yao and B. K. Gan, "Phase transition and properties of a ferroelectric polyvinylidene fluoride-hexafluoropropylene Copolymer", *J. Appl. Phys.*, vol. 97, pp. 084101-084101-5, 2005.
- [13] L. Priya and J. P. Jog, "Intercalated poly (vinylidene fluoride)/clay nanocomposites: structure and properties", *J. Polym. Sci. B Polym. Phys.*, vol. 41, pp. 31-38, 2003.
- [14] A. Kellarakis, S. Hayrapetyan, S. Ansari, J. Fang, L. Estevez and E. P. Giannelis, "Clay nanocomposites based on poly (vinylidene fluoride-co-hexafluoropropylene): Structure and properties", *Polymer*, vol. 51, pp. 469-474, 2010.
- [15] Vimal K. Tiwari, Pawan K. Kulriya, Devesh K. Avasthi and Pralay Maiti, "Poly (Vinylidene fluoride-co-hexafluoro propylene)/Layered Silikate Nanocomposites: The Effect of Swif Heavy Ion", *J. Phys. Chem. B*, vol. 113, no. 34, pp. 11632-11641, 2009.
- [16] P. C. LeBaron, Z.Wang and T. J. Pinnavaia, "Polymer-layered silicate nanocomposites: an overview", *Appl. Clay Sci.*, vol. 15, pp. 11-29, 1999.
- [17] S. Letskovska, P. Rahnev, "Material science for electronics", Burgas Free University - Bulgaria, Informa print, ISBN-978-954-8468-04-6, 2008.

Impact of the Isolation Gap Position on the Voltage Gain Characteristics of Disc-Shaped Piezoelectric Transformers

Nedyu Nedev¹, Zvezditzia Nenova², Toshko Nenov³

Abstract – Piezoelectric transformers have various areas of application as electronic components. This paper presents the investigations of the voltage gain characteristics of disk-shaped piezoelectric transformers with a chord oriented isolation gap between the electrodes. It shows the impact of the isolation gap position and of the load resistance on the frequency characteristics and on the maximum voltage gain.

Keywords – piezoelectric transformer, piezoelectric disk, isolation gap, voltage gain

I. INTRODUCTION

The development of technologies and of new ceramic materials leads to widening of the application fields of piezoelectric transformers (PTs) not only as an alternative to magnetic transformers in portable devices - laptops, PDA, etc., but also in medical devices, instrumentation, even in the field of space technology [1]. PTs have a lot of advantages compared to electromagnetic transformers [2]: high efficiency at resonance, possibility of miniaturization, insensibility to the electromagnetic fields, operation in a wide frequency range, simple production technology, etc.

The piezoelectric transformer is a solid state element from a piezoelectric material (often piezoceramics) with applied electrodes of different configuration. PTs can be formed in various shapes. Most often they are rectangular, disk or ring-shaped [1, 3, 4]. Disc-shaped PTs convert mechanical energy into electrical energy more effectively [5].

The operation principle of PT is based on the direct and inverse piezoelectric effect [6, 7]. The electrodes to which the source of the electrical signal is connected create the excitation section of the PT and the electrodes to which the load is connected – the generator section. In the excitation section the sine wave electrical signal is converted into mechanical vibrations as a result of the inverse piezoelectric effect. These oscillations are formed on the border of the electrodes and they spread through the whole volume of the piezoelectric elements. Reflecting from the areas with different acoustic impedance, they form direct and backward

waves. Their collection results in a standing wave. The amplitude of the standing wave reaches a peak when the direct and reflected waves are in phase. This occurs when the frequency of the excitation source is near to one of the resonance frequencies of the mechanical oscillations of the piezoelectric element. In the generator section of the PT the mechanical vibrations resulting from direct piezoelectric effect are converted into an electrical signal. Since the mechanical tension in the standing wave has maximum at the resonance frequency, then the voltage gain has a maximum value of this frequency.

On this principle operate all structures of piezoelectric transformers. Since the energy from the excitation to the generator section is transmitted only mechanically, the PT gives the opportunity for galvanic separation of the input from the output circuit [6, 8-10]. Depending on the shape and dimensions of the piezoelectric element, the resonance mode is obtained at different frequencies of the input signal.

When the volumes of excitation and generator sections are equal (symmetrical design) the voltage gain of the PT is determined only by the resonance properties of the piezoelectric element. When the design is unsymmetrical, the transformation ratio depends not only on the resonance properties of a piezoelectric element, but also on the design parameters [11].

In the literature known, various monolayer and multilayer PTs and the possibility of their application to different devices were studied [3,12-14]. There are few investigations of the influence of the geometric dimensions and the shape of the electrodes of the PTs on their voltage gain characteristics [15].

This paper presents the results of the studies of the impact of the isolation gap position between the electrodes of the disk-shaped piezoelectric transformers on their voltage gain characteristics.

II. EXPERIMENTAL PROCEDURE

A. Studied samples

Piezoelectric transformers as well as electromagnetic transformers can amplify the signal voltage and current, to divide galvanically the electric circuit, to invert the phase of the input signal, etc. The investigated samples were prepared as disk-shaped piezoelectric transformers with a diameter of 30mm and a thickness of 2.5mm from SPZT-8 piezoceramic, with a set of chord oriented isolating gaps. The design of the studied samples is shown in Fig. 1.

¹Nedyu Nedev is with the Faculty of Electrical Engineering and Electronics at Technical University of Gabrovo, 4 H. Dimitar Str., Gabrovo 5300, Bulgaria, E-mail: nedyu.nedev@gmail.com.

²Zvezditzia Nenova is with the Faculty of Electrical Engineering and Electronics at Technical University of Gabrovo, 4 H. Dimitar Str., Gabrovo 5300, Bulgaria, E-mail: z_nenova@yahoo.com.

³Toshko Nenov is with the Faculty of Electrical Engineering and Electronics at Technical University of Gabrovo, 4 H. Dimitar Str., Gabrovo 5300, Bulgaria, E-mail: tgnenov@gmail.com.

The design includes excitation and generator electrodes and a common electrode which form two sections of electrodes – an excitation and a generator section.

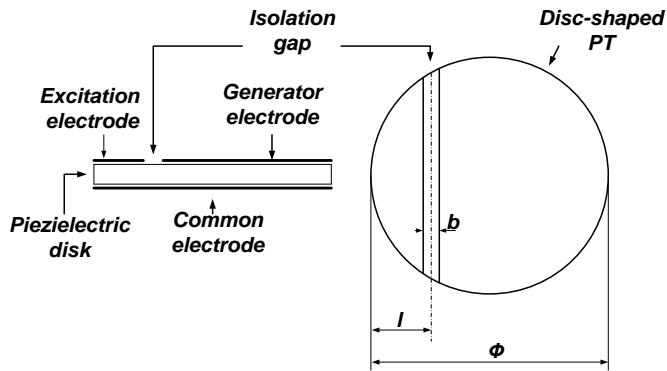


Fig. 1. Design of the samples

The isolating gap with a width $b=1,5$ mm separates the excitation and generator electrodes. The position of the isolation gap is marked by l . For the different samples this parameter is 7.5, 15.0 and 22.5mm, respectively. The studied samples are presented in Fig. 2.



Fig. 2. Studied samples

B. Measurement system

The study of the piezoelectric transformer elements is performed according to the measurement system shown in Fig. 3.

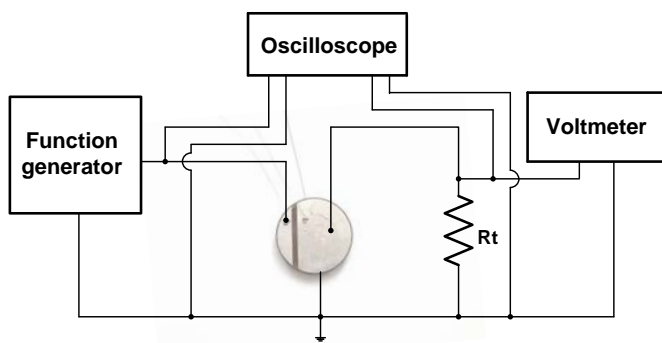


Fig. 3. Measurement system

The system comprises HAMEG HM8150 functional generator with a voltage range from 20mV to 20V and a frequency range from 10mHz to 12,5 MHz, B3-57 voltmeter with a voltage range from 0,03mV to 300V and a frequency range from 40Hz to 10GHz. To control the form of the input and output signals a Philips PM3212 oscilloscope with a

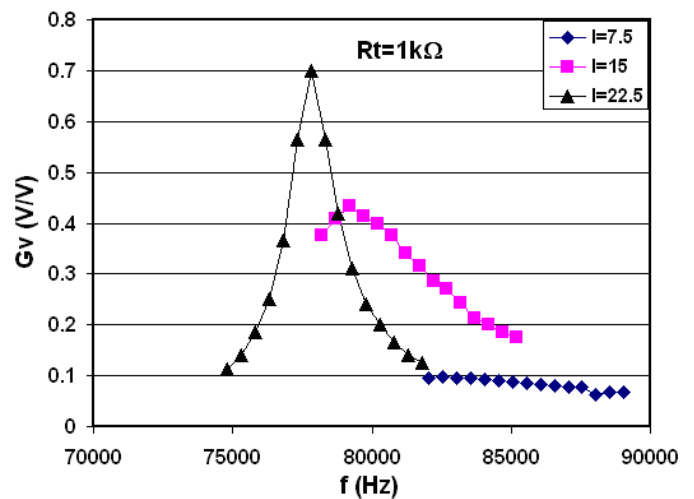
frequency range of 25MHz is used. As load of PT standard resistors R331 with values 1kΩ, 100kΩ with accuracy of 0.01, R4010 with 1MΩ value and accuracy of 0.02 are used. Measurements are taken also in an open circuit ($R_t = \infty$).

III. RESULTS AND DISCUSSION

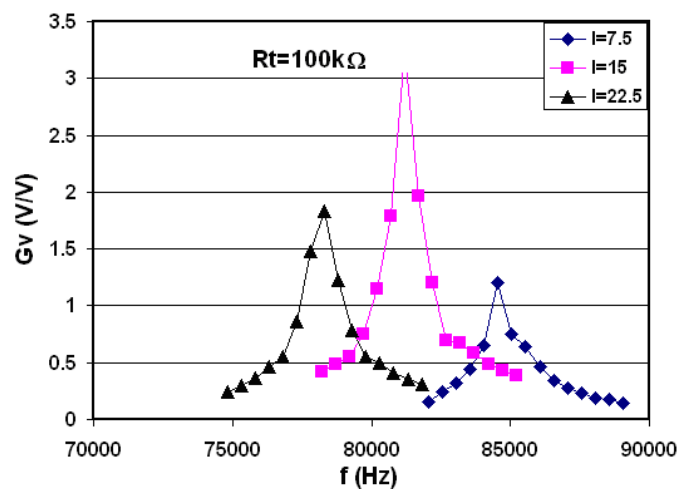
The frequency responses for three values of the parameter l of the piezoelectric transformers at the input sinusoidal signal with amplitude of 2V in the frequency range from 71 to 93kHz are studied. Based on them, the voltage gain characteristics $G_v = U_o/U_i$ as a function of frequency f and the maximum voltage gain G_{vm} as a function of R_t and the position l of the insulation gap are obtained.

The frequency characteristics of the voltage gain $G_v = F(f)$ for different values of parameter l and load resistance R_t are shown in Fig. 4.

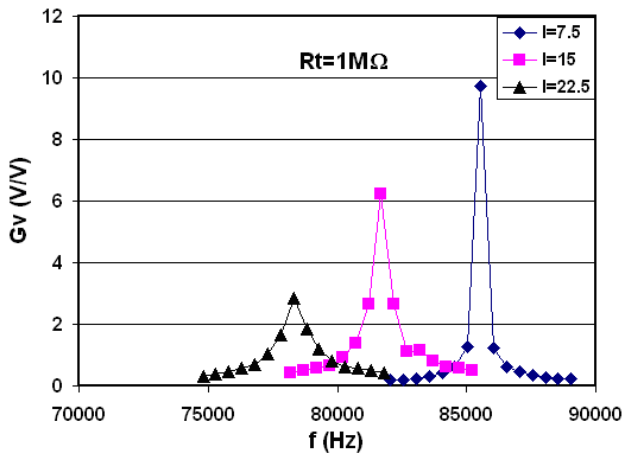
On the basis of the results shown in Fig. 4, the characteristics of the maximum voltage gain frequency f_m as a function of the load resistance R_t and the position l of the isolating gap are obtained and presented in Fig. 5.



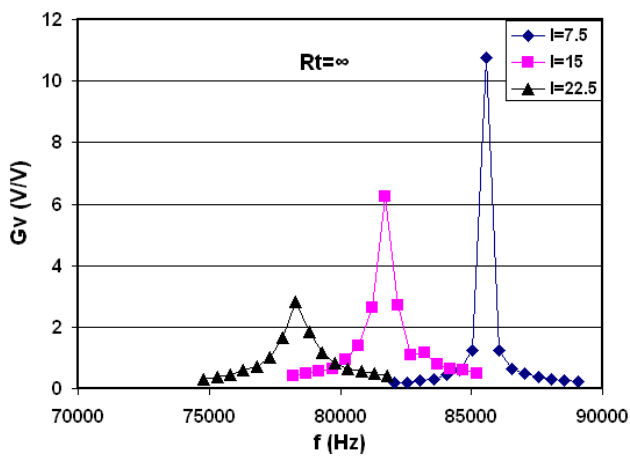
a)



b)



c)



d)

Fig. 4. Frequency characteristics $Gv = F(f)$ for various values of position l and of load resistance R_t : a) $R_t = 1\text{k}\Omega$; b) $R_t = 100\text{k}\Omega$; c) $R_t = 1\text{M}\Omega$; d) $R_t = \infty$

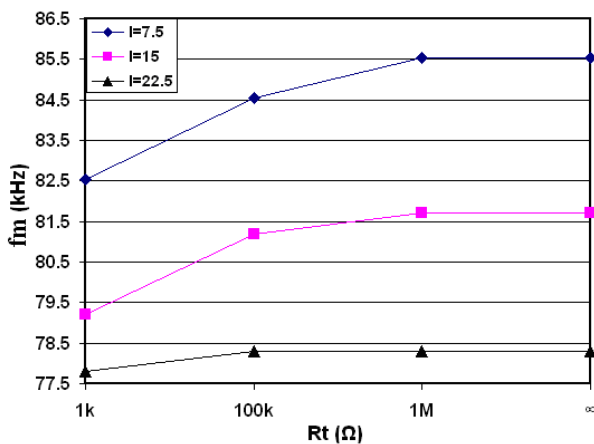
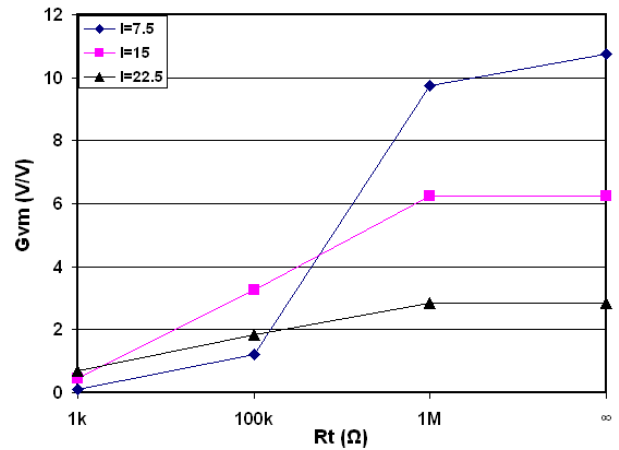


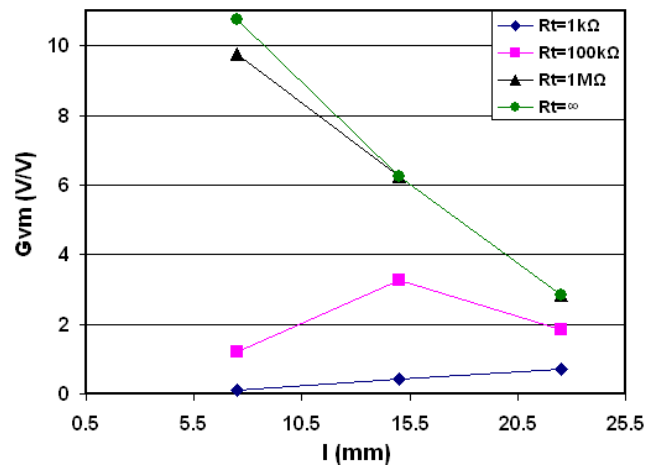
Fig. 5. Characteristics $f_m = F(R_t)$ for different values of parameter l

The increase in R_t leads to an increase in frequency f_m for different values of parameter l . The impact of l on G_{vm} is bigger than the one of R_t . Frequency f_m increases with the decrease in l and has a maximum value at $l = 7.5\text{mm}$. For all samples tested at various load resistances frequency f_m varies within the range 77.6 - 85.6kHz.

The impact of R_t and l on G_{vm} for the studied samples is shown in Fig. 6.



a)



b)

Fig.6 Impact of: a) the load resistance R_t and b) the position l of the isolation gap on the maximum voltage gain G_{vm}

On the basis of these characteristics it is found, that for values of $R_t > 1\text{M}\Omega$ the highest value is observed when $l = 7.5\text{mm}$. When $R_t = 100\text{k}\Omega$ the function G_{vm} has a maximum at $l = 15\text{mm}$ as for smaller values of R_t the characteristic is changed and when $R_t = 1\text{k}\Omega$, G_{vm} increases with the increase in l . It has a maximum value at $l = 22.5\text{mm}$. For all values of parameter l investigated the increase in R_t leads to an increase in the voltage gain G_{vm} , i.e. the increase in the value of load resistance leads to improved performance of the PTs. For samples and parameters investigated the highest value of G_{vm} is observed at $R_t = \infty$ and $l = 7.5\text{mm}$.

IV. CONCLUSION

Piezoelectric transformers with a different position l of a chord oriented isolation gap with a fixed width b have been investigated. Measurements have been taken to establish the influence of the position l and the load resistance R_t on the frequency characteristics and on the maximum voltage gain of piezoelectric transformers. The frequency f_m of piezoelectric transformers depends on both parameters. For large values of R_t a decrease in l leads to an increase in f_m .

From the measurements taken it has been found, that the increase in the load resistance R_t leads to an increase in the maximum voltage gain G_{vm} . The position l of the isolation gap has a significant impact on G_{vm} . At high load resistance the decrease in l , i.e. a decrease in the area of the excitation and the increase in the area of the generator electrode, results in an increase in maximum gain voltage G_{vm} . This makes it possible to control its value depending on the design position of the electrodes.

ACKNOWLEDGEMENTS

The present paper has been produced with the financial assistance of the European Social Fund under Operational Programme "Human Resources Development", Project № BG051PO001-3.3.06-0008 "Supporting Academic Development of Scientific Personnel in Engineering and Information Science and Technologies". The contents of this paper are the sole responsibility of "Angel Kanchev" University of Russe and can under no circumstances be regarded as reflecting the position of the European Union or the Ministry of Education and Science of Republic of Bulgaria.

REFERENCES

- [1] A. V. Carazo, "50 Years of Piezoelectric Transformers, Trends In The Technology", Materials Research Society Symposium, vol. 785, pp. D1.7.1-D1.7.10, 2004.
- [2] S.Priya, H. Kim and K. Uchino, "Design Consideration for Nonlead Piezoelectric Transformers", International Conference on Intelligent Materials (5th) (Smart Systems & Nanotechnology) JUN 2003.
- [3] M.Day, B.Lee, „Understanding piezoelectric transformers in CCFL backlight applications“, Texas Instruments Incorporated, www.ti.com/sc/analogapps Analog Applications Journal 4Q 2002.
- [4] C. Panya-Isara, T. Kulworawanichpong, and P. Pao-La-Or, „Study of Characteristics of Multi-Layer Piezoelectric Transformers by using 3-D Finite Element Method“, World Academy of Science, Engineering and Technology 60, 2011.
- [5] Shine-Tzong Ho „Electromechanical Analysis of a Ring-type Piezoelectric Transformer“, Mechatronic Systems Simulation Modeling and Control, InTech, March, ISBN 978-953-307-041-4, 2010.
- [6] Lavrinenko V.V, *Piezoelectric Transformers*, Moskva, 1975. (in Russian).
- [7] N.Nedev, Z. Nenova, T.Nenov, "Humidity sensing element on the basis of piezotransformer", International scientific conference UNITEH'12, proceedings vol.1, pp.583 - 586, 16-17 November 2012 (in Bulgarian) .
- [8] A.A.Erofeev, *Piezoelectronic devices in automation*, L:Mashinostroenie,212p. , 1982. (in Russian)
- [9] R.G.Dzagupov, A.A.Erofeev, *Piezoceramic elements in instrumentation and automation*, L:Mashinostroenie, 256p., 1986. (in Russian)
- [10] V.M.Pluznikov, V.S.Semenov, *Piezoelectric solid schemes*, Moskva, 1971. (in Russian)
- [11] H. Katz, *Solid state magnetic and dielectric devices..* Wiley, New York, 1959.
- [12] P.C.Y. Lee, R. Huang, X. Li, W.-H. Shih, "Vibrations and static response of asymmetric bimorph disks of piezoelectric ceramics", IEEE Transactions on Ultrasonics, Ferroelectrics, and Frequency Control 47(3), pp.706–715, 2000.
- [13] Yong-Wook Park Electrical Properties of a Piezoelectric Transformer for an AC-DC Converter, Journal of the Korean Physical Society, Vol. 57, No. 4, pp. 1131_1133, October 2010.
- [14] V.M.Sharapov, Z.M.Sotula, "Bimorph piezo transformers for sensors of mechanical parameters", Newspaper of Cherkasy State Technological University, no.2, pp.77-80, 2008.(in Russian)
- [15] Kuo-Tsai Chang, Hsiang-Chang Chiang, Kuo-Sheng Lyu, "Effects of electrode layouts on voltage gain characteristics for ring-shaped piezoelectric transformer", Sensors and Actuators, A141, pp.166-172, 2008.

High Frequency Inductive Power Transfer Device for Ultrasonic Applications

Nikolay Dimitrov Madzharov

Abstract-High Frequency Inductive Power Transfer (HFIPT) device is inherently a transformer, which transfers high frequency electrical energy from the primary to the secondary without direct contact between the two components. The difference between the HFIPT device and standard transformers is in the fact that the secondary of the transformer moves at a relatively high speed. This paper contains the development results of linear HFIPT for ultrasonic applications. There are several significant factors that make design of HFIPT more challenging. Due to complicated circuit of different ultrasonic applications where the compact transducer (CT) impedance could be change strongly in the technological process, there must be compensating capacitors installed in the primary and secondary circuit.

Keywords - HFIPT, MDM, CT, Matching circuit, Air gap.

I. INTRODUCTION

HFIPT to a moving recipient is not common in the field of electrical engineering; however, some systems have been developed in the past for special situations. An early example of this was an HFIPT system invented in St. Petersburg, Russia around 1940 for a vehicle receiving energy inductively from two cables. The vehicle had an “antenna” on the bottom with a rectifier and DC motor. Later, similar devices were used in coal mines with explosive atmosphere. The frequency of the current used in these systems was several kilohertz. Contactless power transfer allows avoiding problems caused by currently used sliding contacts. Sliding contacts have insufficient life time due to mechanical wearing and electrochemical degradation in the process of service [1-5].

The HFIPT device is inherently a transformer, which transfers electrical energy from the primary to the secondary without direct contact between the two components. The difference between the HFIPT device and standard transformers is in the fact that at least the secondary of the transformer must move at a relatively high velocity. In order to have good operating mode of the US generator and sufficient technological results a special matching circuit has to be developed.

II. MAGNETIC MATERIALS FOR HFIPT CORES

There are two families of materials for the HFIPT primary and secondary magnetic core, ferrites and Magneto-Dielectric Materials (MDM). Selection of material must be based on mechanical properties, permeability, electric conductivity, losses and electrical strength. Ferrites of Mn-Zn type can't be used for HFIPT because of low resistivity and electric strength. Ni-Zn or special ferrites may be theoretically used for these applications. However the inverted E shape of the primary magnetic core used for the HFIPT device is not a standard shape available for ferrites. Therefore, in order to make the core using ferrites, ferrite plates must be machined, custom manufactured in net shape or the cross-section must be made by combination of several pieces. “Net-shape” manufacturing of large ferrite cores is expensive and anyway they must be machined to the final tolerances; machining of ferrites is very difficult and expensive requiring special tools. It is almost impossible to make technological holes in the core for HFIPT assembling. If the ferrite cores were made from multiple pieces, then a support structure would be required requiring additional costs and space. Plus, multiple assembling gaps in the core will result in reduction of equivalent permeability of the core. Results of a search for magnetic materials that could be used for HFIPT core are presented in table 1.

TABLE I
MAGNETIC MATERIALS FOR HFIPT

Material	Permeability	El. Resistivity Ohm.cm	El. Strength Vrms/mm (300kHz)	Availability in sizes and shapes	Curie temp. °C	Thermal conduct. W/cm ²
Mn-Zn Ferrite	750-15000	Low 10-1000	Low	TBD	100-300	0.03
Ni-Zn Ferrites	10-2000	High	High TBD	TBD	150-450	0.03
Fer. 559	18-20	High >15000	Medium ≤100	Any when machined	>300	0.04
Fer.119	7	Very High	> 300 Vrms/mm	Any when machined	>300	0.02
Fluxtrol 50	50	Low	< 100 Vrms/mm	Any when machined	>300	0.05
Fluxtrol HF	5	Very High	>> 300 Vrms/mm	Any when machined	>300	TBD

MDMs are manufactured in large standard sizes and are easily machinable with standard tools. Because of that, it is possible to make the primary magnetic core out of 1 piece of material, eliminating the need for any joining or support structures. Therefore, MDMs are the preferred material for constructing the geometry. Four MDMs are presented in Table 1 – Ferrotron 559, Ferrotron 119, Fluxtrol 50 and new HF material Fluxtrol HF. Fluxtrol HF has excellent

¹Nikolay Dimitrov Madzharov is with the Faculty of Electrical Engineering and Electronics at Technical University of Gabrovo, H. Dimitar Str. 4, 5300 Gabrovo Bulgaria, E-mail: madjarov@tugab.bg

mechanical properties, good electrical strength and low losses but its permeability is insufficient for effective use in HFIPT [6].

For HFIPT cores material Fluxtrol 50 was chosen and tested. It has relatively high permeability, excellent mechanical and electrical properties and may be machined into any shape with high precision.

III. HFIPT DESIGN

Two major criteria must govern optimal HFIPT design:

A. Good controllability based on relation between primary and secondary currents;

B. Minimal apparent power on HFIPT input resulting in less losses, smaller step-down transformer (SDT) and smaller capacitor battery at the generator output [3,4].

For criterion A. Impedance Z_{p0} (see fig. 4) of coupling must be as small as possible. With a very small Z_{p0} , the same current will flow in the load and at the HFIPT input.

For criterion B. There are optimal values of HFIPT components, that must be defined with account of restrictions set by the device size and material properties. It is clear that optimal design depends on parameters of the load. CT is a complex resonant load and its equivalent impedance depends strongly on frequency and to a certain degree on a signal level. For these reasons it is difficult to rely on calculation of CT impedance starting from its equivalent resonant scheme.

Additionally, it was found from calculations and open circuit tests that the HFIPT magnetization current has a significantly high value (about 120 A). There are three options to reduce the magnetization current:

1. Increase the number of primary turns.
2. Make the active zone (length of the secondary block) longer.
3. Provide larger area for magnetic flux to cross the gap using deeper grooves or multiple grooves, which might be easily accomplished using MDM materials.

In order to reduce HFIPT losses, the following methods are possible:

- use litz for the primary. However, this will lead to more complicated design. At frequency 28 kHz the penetration depth in copper equals to 0.4 mm and litz AWG 38 may be used.
- optimal design of primary with wider current carrying surface.
- core design optimization to improve magnetic coupling and therefore to reduce magnetization current.

The developed design (see figure 1) is similar to the Flat Core to E-shaped Core, except that the secondary E-shaped Core poles are “dropped into” the primary magnetic circuit. The main advantage of this design compared to the Flat Core to E-shaped Core is that the magnetization current should be less, because there is a longer magnetic coupling zone between the primary and the secondary magnetic circuits. Another advantage is that the sensitivity to the gap variation is much lower than with the Flat core for the primary. The disadvantage of this style is that there is less space available for copper if there is a limit on the height of the secondary.

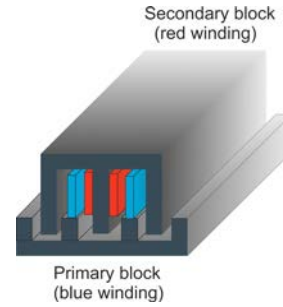


Fig. 1. HFIPT design of an Inverted E-shaped Core to E-shaped Core

Specifications the designed HFIPT are: input power 3 kW; work frequency 25 – 35 kHz; max. output voltage, amplitude - 1000 V ; stable operation with gap variation in a range 3 +/- 0.5 mm; efficiency > 90 % ; air natural cooling.

Figure 2 shows dimensions of the HFIPT device mock-up. The secondary core width is 62 mm, height is 42 mm and the length is 50.8 mm according to standard thickness of Fluxtrol blocks. The primary core width is 80 mm and the overall HFIPT length is 220 mm.

Primary winding W_1 has only one turn according to construction considerations and it is made of copper thickness 2.5 mm and height 15 mm.

Secondary winding must be multiturn with W_2 more than 40 turns, which may be made of Litz AWG 38 (0.1 mm x 60, total cross section 0.47 mm²).

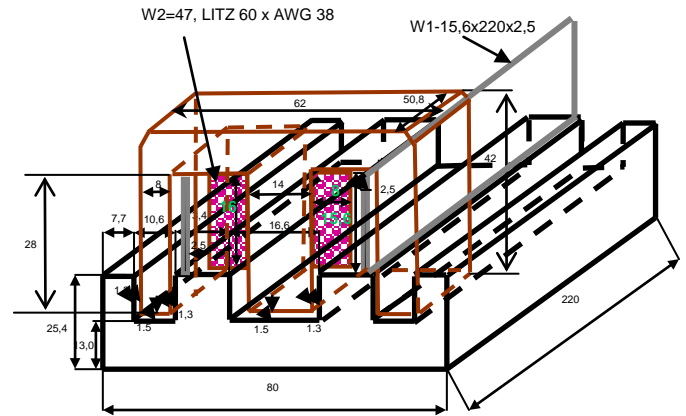


Fig. 2. Dimensions of HFIPT prototype with a multi-turn secondary winding.

The HFIPT magnetization current is equal to:

$$I_{MAG} = \frac{B \cdot S_F}{n} (R_F + R_G) \quad (1)$$

$$R_G = \frac{l_G}{\mu_0 \cdot S_G} \quad (2)$$

$$R_F = \frac{l_F}{\mu \cdot S_G} \quad (3)$$

where S_F , S_G – cross-sectional core and air gap area ; n – turn number; R_F and R_G – core and air gap reluctance; l_F and l_G – magnetic path and air gap length.

Voltage per turn is equal to

$$U = 2 \cdot \pi \cdot f \cdot B \cdot S_F \quad (4)$$

For selected induction of 0.25T (RMS) the voltage per turn is 21V (RMS).

IV. DESIGN OF HFIPT MATCHING CIRCUITRY

An initial configuration of the circuitry is shown in Fig.3. It contains a US load with parallel capacitor battery in the secondary circuit - CT, HFIPT and matching block on the primary side. Matching block, contained matching transformer and parallel capacitor battery. It is essential to select an optimal scheme for the reactive power compensation. Number of turns of the secondary winding must be defined according to a CT parameters. Profound study of HFIPT and component performance was made using computer simulation, experimental study and combination of both [1,7,8].

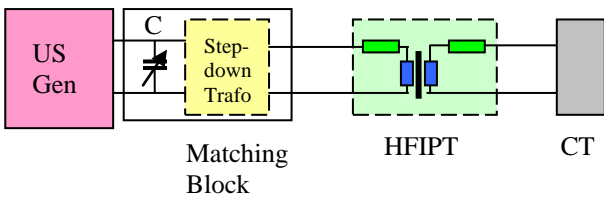


Fig. 3. Initial configuration of HF IPT and matching circuitry

The studied circuit is shown in Fig.4. As mentioned earlier, a SDT may be made with a good magnetic circuit and relatively low stray inductance. In the first approach it may be considered as ideal and therefore excluded from consideration. HFIPT must be considered as a “bad” transformer with a gap in magnetic circuit and big stray inductance of windings especially of the primary one due to significant inductance of rails.

A. Π -parameters of HFIPT and “IDEAL” Compensation Capacitances

The whole circuit “HFIPT + SDT” with linear parameters may be accurately described as a passive 4-pole and represented in the form of T or Π schemes. These parameters are very important for the HFIPT design and performance evaluation. If the ratio of SDT is the same as of HFIPT, it is not necessary to “transfer” the CT parameters on the generator side and all the differences in values are due to the influence of SDT and HFIPT. Parameters of SDT + UIPT are given below for winding ratio 47:1:1:47 for HFIPT gaps from 0,5mm to 3mm as well as the capacitor values necessary for complete compensation (Fig. 4).

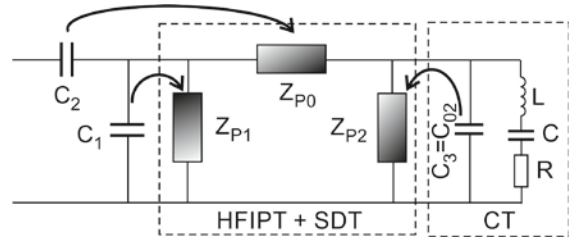


Fig. 4. “ Π ” parameters of “HFIPT + SDT” and their compensation elements

B. Determining the “ Π ” Parameters

The parameters of these schemes may be found from 3 independent measurements on output and input of the 4-pole. In turn these measurements may be performed using AC impedance meter such as LCR or method of voltmeter and ampermeter. In the last case a phase angle must be also found for accurate calculation. The HFIPT + SDT circuit has high quality factor and for matching purposes it is sufficient to measure U and I only.

The procedure for determining the “ Π ” parameters includes measuring the following impedances:

Z_{OC1} – impedance measured on primary with open circuit(OC) secondary

Z_{OC2} – impedance measured on secondary with OC primary

Z_{SC1} – impedance measured on primary with short circuit (SC) secondary

Z_{SC2} – impedance measured on secondary with SC primary

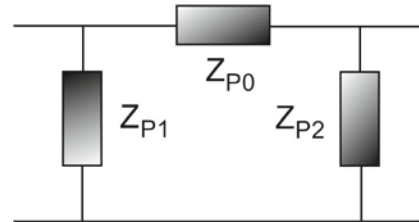


Fig. 5. “ Π ” parameters of “UIPT + SDT”

As mentioned, it is enough to measure three regimes. The fourth measurement may be used for control of the measurement accuracy.

1. OC on the secondary

Z_{OC1} – impedance measured on primary with OC secondary

$$Z_{OC1} = U_{11} / I_{11} \quad (5)$$

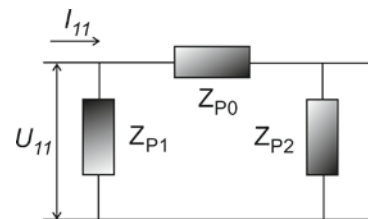


Fig. 6. Test on primary with OC secondary

2. Short circuit on the secondary.

Z_{SC1} - impedance measured on primary with SC secondary

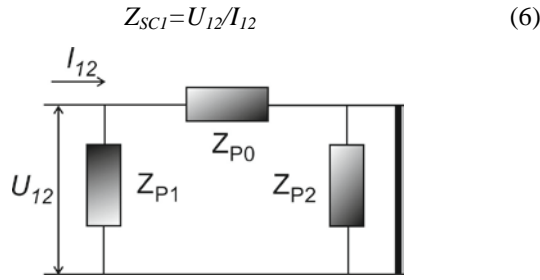


Fig. 7. Short circuit on the secondary

3. Open circuit on the primary

Z_{OC2} - impedance measured on the secondary with OC primary

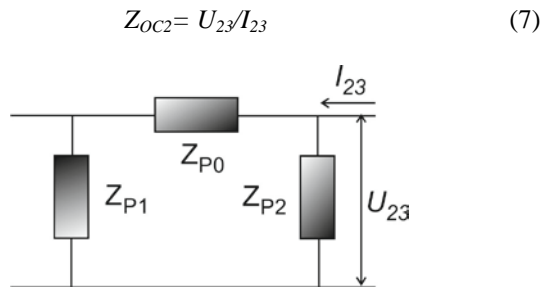


Fig. 8. Open circuit on the secondary

4. Short circuit on the primary

Z_{SC2} - impedance measured on the secondary with SC primary

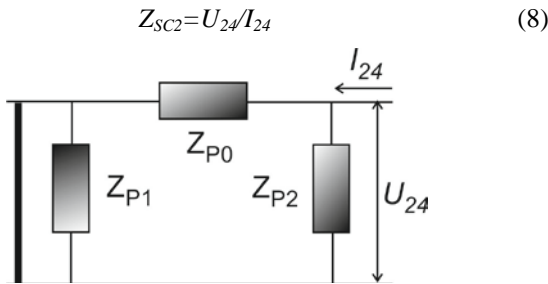


Fig. 9. Short circuit on the primary

Formulae for Z_{P1} , Z_{P0} and Z_{P2} :

$$(Z_{P0})^2 = Z_{OC1} \cdot (Z_{SC2})^2 / (Z_{OC2} - Z_{SC2}) \quad (9)$$

$$Z_{P1} = Z_{P0} \cdot Z_{SC1} / (Z_2 - Z_{SC1}) \quad (10)$$

$$Z_{P2} = Z_{P0} \cdot Z_{SC2} / (Z_2 - Z_{SC2}) \quad (11)$$

Table 2 contains "II" parameters of SDT+HFIPT with ratio 47:1:1:47 air gap from 0,5 mm to 3 mm and capacitors values necessary for their "ideal" compensation at frequency 28 kHz.

TABLE II
"II" PARAMETERS OF THE SD+HFIPT 47:1:1:47 AND COMPENSATING CAPACITORS

Gap, mm	Z_{P1} , Ohm	L_1 , mH	C_1 , nF	Z_{P2} , Ohm	L_2 , mH	C_2 , nF	Z_{P3} , Ohm	L_3 , mH	C_3 , nF
0,5	1522	8.65	3,7	137.3	0.78	40	283.6	1.61	19,4
1	1508	8.57	3,67	134.2	0.76	41	278.0	1.58	19,7
1,5	1603	9.12	3,4	133.7	0.76	41	270.9	1.54	20,2
2	1614	9.18	3,4	130.8	0.74	42	251.3	1.42	21,8
2,5	1652	9.40	3,3	130.6	0.74	42	246.5	1.40	22,2
3	1659	9.43	3,3	130.5	0.74	42	237.5	1.35	23,1

Analysis:

1. Values of capacitance C_3 resonant with L_3 at 28 kHz is close to the natural value of the CT parallel capacitance C_0 for turn numbers 47.
2. Variation of the resonant C_3 is about $-4/+10\%$ when the coupling gap changes in a range 1.5 ± 1.0 mm
3. It follows from the table that HFIPT scheme parameters change around $\pm 10\%$ when the gap varies in the range from 0 to 3 mm. Besides of parallel capacitor C_1 , this scheme contains an additional series capacitor C_2 in the primary side, which may be also used for matching or regime stability adjustment if required.
4. Analyzing the "II" equivalent parameters of the HFIPT (Figure 4) it was found that the value of Z_{P0} was small. Hence, the capacitor C_2 must be big and does not influence matching essentially.

V. EVALUATION OF HFIPT LOSSES

In order to make a full evaluation of the HFIPT losses, a temperature test was implemented. Figure 10 shows the temperature of the HFIPT secondary core vs time. During the tests HFIPT secondary was covered with thermal insulation. 47:1:1:47 U uipout max= 1100V P = 3 kW

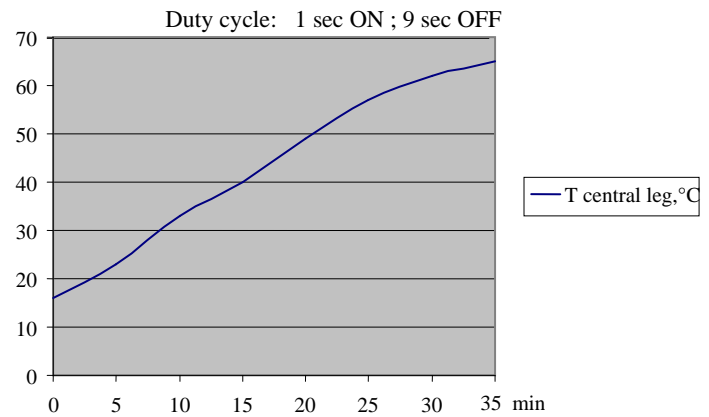


Fig. 10. HFIPT secondary core temperature vs time at ratio

Value of ratio ($\Delta\text{Temp}/\Delta\text{time}$) and losses ΔP have been determined from Figure10 by the following formula:

$$\Delta P = \frac{c \cdot G \cdot \Delta T}{\Delta t} \quad (12)$$

c – specific heat of Fluxtrol, $0.444 \text{ J/g}^\circ\text{C}$
 G – component mass, g
 ΔT – temperature differential
 Δt – heating time differential.

The tests and calculations for power losses in HFIPT secondary core : $G = 500 \text{ g}$; $\Delta t = 2100 \text{ sec}$ at duty cycle 10 %,

showed for 47:1:1:47 - $\Delta P = 51,8 \text{ W}$;

The total power losses in primary and secondary FL core + losses in primary and secondary winding are close to 136 W at input power of 3 kW. The obtained results give an efficiency of 93 % - 95 %.

VI. CONCLUSION

The presented a profound theoretical and experimental study of the most prospective geometrical solutions and designs for an HFIPT established a basis for development of HFIPT. The analysis showed that the most favorable solution is an inverted E-shaped primary magnetic circuit with popped-up single-turn winding and an E-shaped secondary magnetic circuit with multi-turn Litz winding.

A method for predicting the HFIPT matching performance with any load has been developed. Using this method, it is possible to determine the parameters of an electrical circuit (losses, apparent power, currents and voltages) as well as parameters of the resonant circuit composed of capacitor battery, transformer and HFIPT. The HFIPT was able to be matched to the US generator at rated power without changing the ratio of the trafo or the value of capacitance for gaps

between 0 and 3 mm. The stability of electrical parameters was very good in this range of gaps.

The final electrical and thermal tests showed that the efficiency of HFIPT with ratio 47:1:1:47 is 93-95% which is good for such system. After 35 min at full power and duty cycle of 10% the temperature of HFIPT secondary core reached 70°C , which is acceptable for the used materials.

REFERENCES

- [1] N. D. Madzharov, "Autonomous inverters with energy dosing for ultrasonic application", ICEST 2013, 26-29 June 2013, Ohrid, Macedonia, pp.647-651.
- [2] N.D. Madzharov, A.T. Tonchev, "Contactless Charging System For Electric Vehicles", International Scientific Conference PCIM2012, Nuremberg, Germany, pp.1400-1408.
- [3] Colonel Wm. T. McLyman, "Transformer and Inductor Design Handbook", Kg Magnetics Inc. Idillwild, California, USA
- [4] Patent WO 2006/048441, Sealing Device For Producing Sealed Packages of a Pourable Food Product, Valentin Nemkov (Fluxtrol, USA), Nikolay Madzharov (TU, BG)
- [5] K. Throngnumchai, T. Kai and Y. Minagawa "A Study on Reciever Circuit Topology of a Cordless Battery Charger for Electric Vehicles", Nissan Research Center, Nissan Motor Company.
- [6] www.fluxtro.com
- [7] G. Kraev, N. Hinov, L. Okoliyski, "Analysis and Design of Serial ZVS Resonant Inverter", Annual Journal of Electronics, V5, B1, TU Sofia, Faculty of Electronic Engineering and Technologies, ISSN1313-1842, pp.169-172, 2011.
- [8] N. Bankov, Al. Vuchev, G. Terziyski. "Operating modes of a series-parallel resonant DC/DC converter". – Annual Journal of Electronics, Sofia, 2009, Volume 3, Number 2, ISSN 1313-1842, pp.129-132.

Efficiency Investigations of DC-DC Converter Supplying Power Amplifiers

Tihomir Brusev¹, Boyanka Nikolova², Georgi Kunov³ and Stoyan Vuchev⁴

Abstract – In the modern battery powered mobile communication devices output transmitted power is changed in wide range. Most of the energy in such electronic systems is consumed from power amplifier (PA). By increasing of power amplifier's efficiency significantly could be increased the overall efficiency of those portable devices. The widespread used method is modulation of collector voltage (V_{cc}) of PA. Using switching-mode dc-dc converter the operated voltage of power amplifier could be dynamically changed. In this paper are presented investigation results of dc-dc converter, which can be used for dynamically regulation of collector voltage of PA.

Keywords – dc-dc converter, efficiency, Cadence, CMOS technology.

I. INTRODUCTION

The modern mobile communication electronic devices transfer data in the wide frequency range. One of the most critical parameter is their efficiency because of the limited battery resources [1]. Therefore power consumption of the system's building blocks has to be minimized. Most of the energy is consumed from power amplifier. Improving of transmitted power efficiency of this single component can help to increase the battery run time.

Power amplifiers (PAs) used in the portable communication devices have to be linear because the distortions have to be minimized. In order to fulfill this requirement class-A PAs are usually used. They are linear, but the maximum possible theoretical efficiency of those circuits is only 50 %. Their best efficiency can be achieved when the output signal of power amplifier swings from rail to rail [2]. Therefore results closed to 50 % could be reached if collector voltage (V_{cc}) is changed dynamically as a function of output signal's amplitude.

The regulations of power amplifier's collector voltage V_{cc} can be performed by high frequency voltage regulators. The optimal choice is switching-mode dc-dc converters because

they are high efficient circuits. Collector voltage (V_{cc}) of power amplifier is smaller than battery voltage during most of the operation time of portable electronic devices. The focus of that paper is switching-mode buck dc-dc converter, suitable for dynamic output voltage regulation.

In Section II are presented the challenges and problems connected with efficiency improvement of power amplifiers used in the new mobile communication devices. Theory information about dc-dc converters is given also in the same section. Received investigation results of buck dc-dc converter, which can dynamically adjust V_{cc} voltage of PA, are presented in Section III. The whole switching-mode regulator system is designed for integrated circuits (IC) applications in CMOS technology.

II. POWER AMPLIFIER AND DC-DC CONVERTER IN MOBILE ELECTRONIC DEVICES

The new cellular technology is 3rd Generation Partnership Project (3GPP) Long Term Evolution (LTE). High data rate and high quality is ensured for mobile communications devices [3]. Therefore the increased customer requirements for more function of the portable electronic devices at low cost can be satisfied. For example nowadays online gaming, mobile television, multimedia streaming is available in the cellular phones.

LTE supports several channel bandwidths, which are: 1.4MHz, 3MHz, 5MHz, 10MHz, 15MHz, and 20MHz. Long Term Evolution maintain earlier 3GPP technology such as code division multiple access CDMA, wide-band code division multiple access/high-speed packet access WCDMA/HSPA, time division synchronous code division multiple access TD-SCDMA.

The most important parameters for modern generation mobile electronic devices are liner output power and high efficiency. Low energy consuming building blocks is challenge to the overall system design in order to be achieved longer battery run time [4].

A. Power Amplifier

Power amplifiers can work as a linear circuit with poor efficiency or as a circuit with better efficiency, but with distortion. Obviously trade-off between linearity and efficiency is needed when appropriate class of PA is selected from the designers [5]. Usually for RF power amplifiers in the new generation portable electronic devices is used class-A PA.

The easiest way is PA to be powered directly from battery. This is not efficient method because the mobile electronic devices work at different output powers level. The voltage

¹Tihomir Brusev is with the Faculty of Telecommunications, Technical University of Sofia, Kl. Ohridski 8, 1797 Sofia, Bulgaria, E-mail: brusev@ecad.tu-sofia.bg.

²Boyanka Nikolova is with the Faculty of Telecommunications, Technical University of Sofia, Kl. Ohridski 8, 1797 Sofia, Bulgaria, E-mail: bnikol@tu-sofia.bg.

³Georgi Kunov is with the Faculty of Electronic Engineering and Technologies, Technical University of Sofia, Kl. Ohridski 8, 1797 Sofia, Bulgaria, E-mail: gkunov@tu-sofia.bg.

⁴Stoyan Vuchev is with the Faculty of Electronic Engineering and Technologies, Technical University of Sofia, Kl. Ohridski 8, 1797 Sofia, Bulgaria, E-mail: vu4ev_100yan@abv.bg.

regulators, which change their outputs according to the required signal being transmitted, are used. The efficiency of power amplifier is increased if collector voltage is adjusted.

The power added efficiency (PAE) is a parameter which describes the RF power amplifier efficiency:

$$PAE = \frac{P_{out} - P_{in}}{P_{DC}}, \quad (1)$$

where P_{out} is a output power of PA, P_{in} is a input power of PA and P_{DC} is a dc power which is delivered to PA. These parameters express how dc power is transformed to the RF power.

Different techniques are used for improving the efficiency and linearity of power amplifier [2]. The average power tracking and envelope tracking are different method used to adjust collector voltage V_{cc} as function of the transmitted output power. In the Fig. 1 are shown the principle of operation of those two techniques.

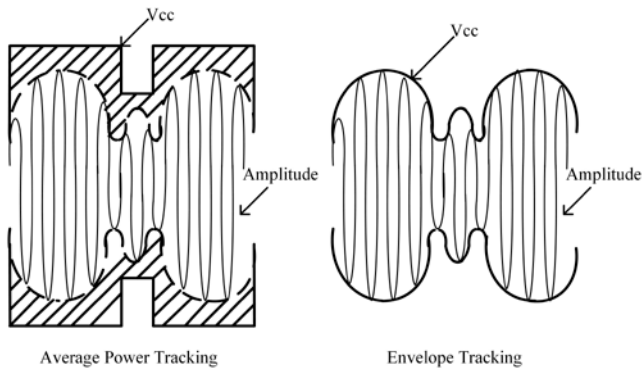


Fig. 1. Average power tracking and envelope tracking techniques.

Envelope tracking method is faster than average power tracking. The shaded area in average power tracking techniques is proportional to the power dissipation. As can be seen from the picture in Fig. 1 consumed energy in average power tracking is bigger compare to envelope tracking. Dissipated power is smaller if V_{cc} is closed to the output voltage amplitude. Envelope tracking mechanism is more efficient than average power tracking.

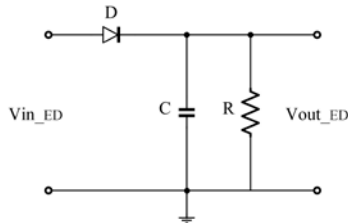


Fig. 2. Envelope detector.

For amplitude detection of the transmitted signal are used envelope detectors. The control system of dc-dc converter receives information from those circuit's blocks and adjust the output voltage of the regulator to the desired level [6]. One of

the circuits, which can be used for the envelop detectors (ED), is shown in Fig. 2.

The circuit is simple and includes a diode and a RC (resistor-capacitor) filter. The designers have to choose values of R and C to satisfy the condition:

$$f_{signal} < \frac{1}{2\pi RC} \ll f_{carrier}, \quad (2)$$

where $f_{carrier}$ is a carrier frequency and f_{signal} is a base band signal frequency.

Linear voltage regulators have low efficiency when output voltage is not close to the input voltage. Because of the different powers of the transmitted signal, collector voltage V_{cc} of PA has to vary in order to be increase the efficiency. Therefore switching-mode dc-dc converter is better choice for voltage regulator's circuit.

B. DC-DC Converter

The efficiency of PA, which is the most energy consumed circuits in the modern portable electronic devices, can be increased by decreasing of power dissipation. Voltage regulator, which can control V_{cc} , is used.

High efficient voltage regulator is needed to improve the overall efficiency of the mobile devices. Linear regulators have simple structure and occupied small silicon area, but they have great energy dissipation, which is transformed in heat.

During most of the time collector voltage of power amplifier is less than battery voltage. Therefore switching-mode buck dc-dc converter is considered as a circuit, which can ensure dynamic regulation of collector voltage of power amplifier. Theoretically they have very high efficiency. The switching frequency f_s of the dc-dc converter should be much higher than base band signal frequency. In Fig. 3 is shown schematic of synchronous buck dc-dc converter.

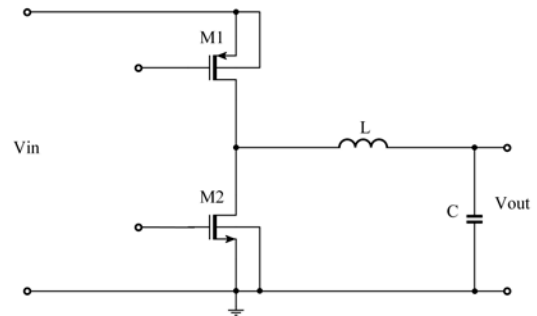


Fig. 3. Synchronous buck dc-dc converter.

Higher switching frequency f_s leads to increasing of switching power losses and decreasing of efficiency of the buck converter. The dc-dc converter efficiency is equal to:

$$\eta = \frac{P_{out}}{P_{in}}, \quad (3)$$

where P_{out} is a average output power of the regulator (output voltage of synchronous buck dc-dc converter in Fig. 3 is applied to collector of PA); P_{in} is a average input power of the regulator (input voltage of synchronous buck dc-dc converter in Fig. 3 is battery voltage of the mobile electronic devices).

The conducting losses in the MOS transistors are proportional to the switching frequency f_s and the rms-value of the current flowing through the device [7]. This relationship is given below:

$$P_{MOS} = k_1 i_{rms}^2 + k_2 f_s, \quad (4)$$

where k_1 and k_2 is are technology dependent coefficient, which are taking into account the size of the power MOS transistors, as well as the resistive and the capacitive losses associated with the MOS structure. Small inductor ripple current will result in smaller rms-value of the current through the MOS structure, and it will respectively lead to better efficiency.

III. INVESTIGATIONS RESULTS OF DESIGNED BUCK DC-DC CONVERTER

Buck dc-dc converter is designed with Cadence on CMOS process for low voltage integrated circuits applications. The switching frequency f_s of the circuit should be much higher than 20 MHz, which is larger base band supported from LTE. A Pulse-Width Modulation (PWM) control technique is used to regulate the two transistors in power stage of synchronous buck dc-dc converter. The schematic of designed switching-mode regulator is shown in Fig. 4.

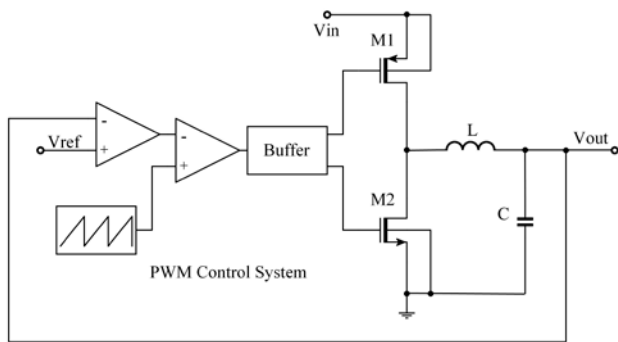


Fig. 4. Schematic of buck converter system designed on CMOS process.

The switching frequency f_s determined from ramp generator is equal to 76.2 MHz. Output voltage of the regulator has to be dynamically adjusted as function of transmitted signal from power amplifier.

The ability of designed buck converter to react at fast changes of reference voltage V_{ref} is examined. In Fig. 5 are presented received simulations results when voltage reference jumps from 0.5 V to 1.3 V. As can be seen from the picture output voltage of the buck converter is stabilized at the new desire level for approximately 1.5 μ s.

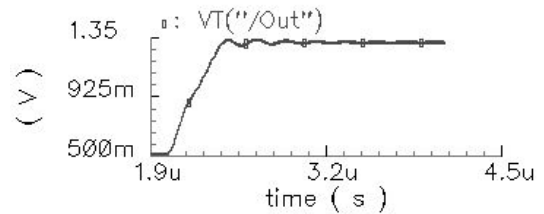
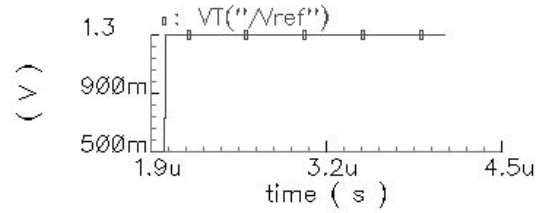


Fig. 5. Reaction of buck converter when voltage reference V_{ref} jumps from 0.5 V to 1.3 V.

In Fig. 6 are shown waveforms of ramp generator's signal and output voltage V_{out} of dc-dc converter, when V_{out} is stabilized. The reaction of the regulator when V_{ref} is changed from 1.3 V to 2.8 V is investigated. The received simulations results are presented in Fig. 7.

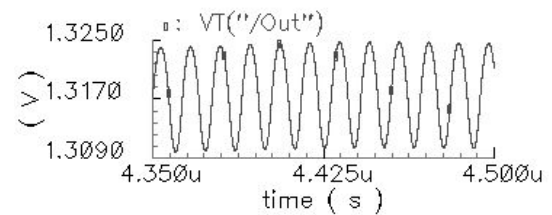
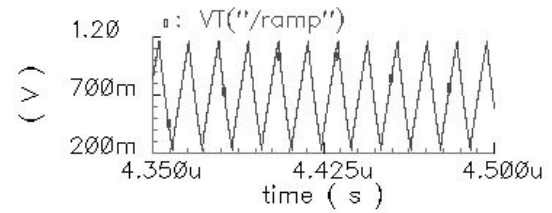


Fig. 6. Waveforms of V_{ramp} and V_{out} and when V_{ref} jumps from 0.5 V to 1.3 V.

As can be seen from the picture presented in Fig. 7 output voltage V_{out} is stabilized for approximately 1.5 μ s.

High switching frequency f_s is key parameter for dc-dc converters, which have to change dynamically their output voltages according to the transmitted power level of mobile devices. On the other hand switching power losses of the voltage regulators are proportional to f_s . High switching frequency of buck converter can helps also for fully integration of whole regulator system together with other circuit's block of the mobile electronic devices.

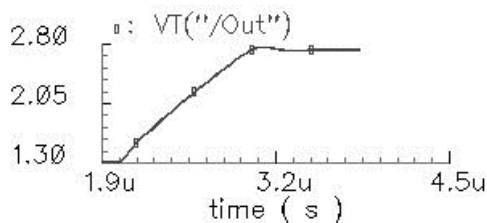
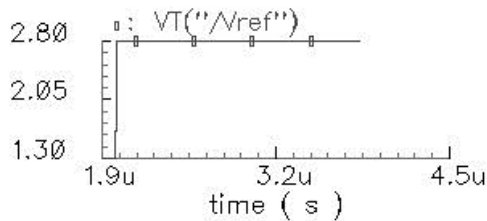


Fig. 7. Reaction of buck converter when voltage reference V_{ref} jumps from 1.3 V to 2.8 V.

The efficiency investigations of the designed buck converter system at different output voltages are performed. The received results are presented in Table 1.

TABLE I
EFFICIENCY RESULTS OF BUCK CONVERTER AT DIFFERENT OUTPUT VOLTAGES

Vout [V]	Efficiency [%]
0.5	52.4
1.3	77.2
2.8	85

As can be seen from the Table 1, the efficiency of the buck converter is equal to 77.2 %, when output voltage V_{out} is controlled to be 1.3 V. Decreasing of the transmitted power level, which required smaller collector voltage V_{cc} of PA, leads to decreasing of the overall efficiency of the dc-dc converter.

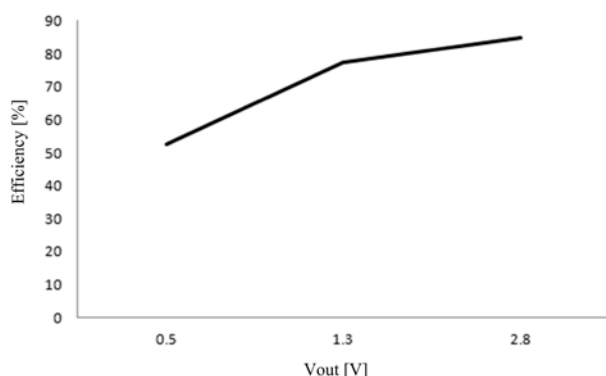


Fig. 8. Efficiency of buck converter as a function of output voltage V_{out} .

In Fig. 8 is presented graphically efficiency of the investigated circuit as a function of output voltage. When V_{out} of buck converter is controlled to be 0.5 V efficiency is 52.4 %, as well as for V_{out} equal to 2.8 V efficiency is equal to 85 %.

IV. CONCLUSION

In this paper are presented investigations results of buck dc-dc converter, which can be used for dynamic regulation of power amplifier's collector voltage in mobile portable electronic devices. The problems connected with efficiency improvement of power amplifier are discussed. The reaction of regulator's output voltage as function of reference voltage of PWM control system is examined. The switching frequency f_s of the buck converter designed with Cadence on CMOS technology is equal to 76.2 MHz. The output voltage V_{out} of investigated circuit is stabilized for approximately 1.5 μ s, when reference voltage jumps from 0.5 V to 1.3 V and from 1.3 V to 2.8 V. The efficiency of the buck converter varies from 52.4 % to 85 %, when V_{out} is respectively 0.5 V and 2.8 V.

ACKNOWLEDGEMENT

The research described in this paper was carried out within the framework of Project DUNK – 01/03 – 12.2009.

REFERENCES

- [1] T. Tuovila, T. Rahkonen, "Characterization of an envelope tracking system for mobile devices", University of Oulu, 2013.
- [2] B. Sahu and Rincón-Mora G. A., "System-Level Requirements of DC-DC Converters for Dynamic Power Supplies of Power Amplifiers", IEEE Asia-Pacific Conference on ASIC, 2002.
- [3] Y. Li, Zhu R., Prikhodko D. and Tkachenko Y., "LTE Power Amplifier Module Design: Challenges and Trends", Skyworks Solutions, Inc., 20 Sylvan Road, Woburn, MA 01801, USA.
- [4] R. Krysteva, I. Cholakova, G. Angelov, R. Rusev, T. Takov, "Simulation of a Radio-Frequency Single-Electron Transistor (RF-SET) in Cadence Spectre", Proc. of the 9th International Scientific Conference Advanced Materials and Operations 2009 (AMO '09), Vol. 2, pp. 385-388, Kranevo, Bulgaria, June 25-27, 2009.
- [5] Ó. Sverrisson, Moller P., Andersen M. and Thomsen O., "A DC-DC Converter for RF PA in WCDMA Mobile Phones", Denmark, 2006.
- [6] F. H. Raab, B. E. Sigmon, R. G. Myers, and R. M. Jackson, "L-band transmitter using Kahn EER technique," IEEE Trans. on Microwave Theory and Techniques, Vol. 46, No.12, pp. 2220-2225, 1998.
- [7] V. Kursun, "Analysis of Buck Converter for On-Chip Integration With a Dual Supply Voltage Microprocessor", IEEE Trans. on VLSI Systems, Vol. 11, No.3, pp. 514-522, 2003.

Two-Parametrical Control of Series Resonant DC-DC Converters that Operate with Common Load

Aleksandar Vuchev¹ and Nikolay Bankov²

Abstract – A control technique is investigated for two series resonant DC-DC converters that operate with common load. In order to reduce the inverter currents a change of both operating frequency and phase shifting together is used. On the base of existing analyses output and control characteristics are built. The obtained results are confirmed by computer simulations.

Keywords – Series Resonant DC-DC Converters, Frequency Control, Phase Shift Control.

I. INTRODUCTION

Series resonant DC-DC converters working above resonant frequency have been widely used recently. A well-known method for the output power control is the phase shift control technique [1-4]. Constant operating frequency is the main advantage of it. This control technique is based on the simultaneous operation of two inverters the output voltages or currents of which are phase-shifted. Therefore, two converter topologies are available: a series and a parallel one.

When the series topology is in use, the two inverters are connected in series to a common load [3, 4]. As a result, the converter output voltage equals the sum of the output voltages of the inverters. The inverter currents are equal and depend on the load. A main disadvantage of this topology is the inability of no-load mode. It is well-known that the output current decrease causes the resonant inverter to stop working.

The parallel topology requires both the inverters to be connected in parallel to the load [2]. In this case the load current equals the sum of the inverter output currents. The main advantage is that the load resistance increase does not cause compulsory work stop. It is well-known that as the phase-shift angle increases, the inverters begin sharing energy to each other, remaining their output current values high enough. Therefore, at certain conditions the converter work is preserved even in no-load mode. At very big phase-shift angles, however, the output currents of the inverters have significant values. Violating the condition the operating frequency to be constant is one of the ways of elimination of this drawback.

Purpose of this paper is a DC-DC converter based on series

¹Aleksandar Vuchev is with the Department of Electrical Engineering and Electronics, Technical Faculty, University of Food Technologies, 26 Maritza Blvd., 4002 Plovdiv, Bulgaria, E-mail: avuchev@yahoo.com

²Nikolay Bankov is with the Department of Electrical Engineering and Electronics, Technical Faculty, University of Food Technologies, 26 Maritza Blvd., 4002 Plovdiv, Bulgaria, E-mail: nikolay_bankov@yahoo.com

resonant inverters connected in parallel to a common load to be examined at change of both phase-shifting and operating frequency change together. The investigation is based on the results of existing analyses of series resonant converters operating above the resonant frequency at phase-shift control.

II. CONVERTER EQUIVALENT CIRCUITS

The circuit of the examined converter is presented in fig.1. Two half-bridge resonant inverters and an uncontrollable rectifier are its main modules.

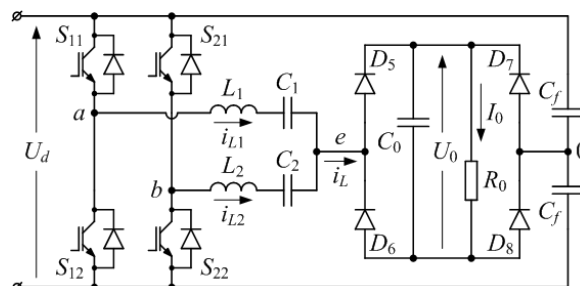


Fig.1. Circuit of the resonant DC-DC converter

With the conventional phase-shift control of the output power the switches of the first inverter (S_{11} , S_{12}) conduct in opposite at an operating frequency f_s . The switches of the second inverter (S_{21} , S_{22}) work in the same way. The control impulses applied to S_{11} and S_{21} (respectively S_{12} and S_{22}) are phase-shifted to an angle α . The two half-bridge inverters have one common node (node 0). Hereby, two square-wave voltages, shifted one towards another at angle α , are generated between point 0 and points a and b respectively. Their amplitude equals half of the supply voltage ($U_d/2$).

As the two resonant inverters work at the same frequency f_s , it is necessary that $L_1 = L_2 = L$ и $C_1 = C_2 = C$. Thus, the resonant frequency, the characteristic impedance and the frequency detuning for the two resonant circuits are:

$$\omega_0 = 1/\sqrt{LC}; \quad Z_0 = \sqrt{L/C}; \quad \nu = 2\pi f_s / \omega_0 = \omega_s / \omega_0 \quad (1)$$

In [5] it is shown, that the operation of the converter can be examined on the basis of the equivalent circuit shown in fig.2a. Because of the parallel connection between the two inverters the resonant frequency does not change but the characteristic impedance is reduced twice:

$$Z_{0PAR} = \sqrt{L_{EQ}/C_{EQ}} = 0,5\sqrt{L/C} = 0,5Z_0 \quad (2)$$

The circuit in fig.2a corresponds to a converter, realized with the series topology. The voltage u_{SW} is as a result of the operation of the inverter switches. It has a quasi-square wave-

form and amplitude equal to $U_d/2$. On the other hand, the voltage u_0 corresponds to the commutations in the rectifier. It has a square wave-form, switching between $\pm U_0$, and is phase-locked with the inductor current i_L .

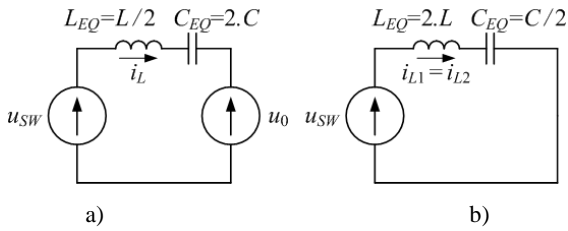


Fig.2. Equivalent Circuits

In no-load mode, current to the input of the rectifier does not flow. In this case, the energy is exchanged only between the inverters and the examination can be conducted on the base of the equivalent circuit shown in fig.2b. The characteristic impedance for this circuit increases twice:

$$Z_{0SER} = \sqrt{L_{EQ} / C_{EQ}} = 2\sqrt{L / C} = 2Z_0 \quad (3)$$

This circuit corresponds to a converter realized with a series topology in short circuit mode. In this case, the voltage u_{SW} has amplitude that equals the supply voltage U_d .

III. CONVERTER OPERATING MODES

In order to simplify the analysis and the obtaining of generalized results, all the parameters related to the examined converter are normalized:

- voltages towards $U_d/2$;
- currents towards $U_d/2Z_0$;
- resistances towards Z_0 .

As the equivalent circuits (fig.2) correspond to a converter realized with a series topology, results from existing analyses of series resonant DC-DC converters with phase-shift control can be applied. Thus, in [3] two main operating modes of the converter are defined. They are determined according to the commutation mechanisms of the inverter switches – with zero-voltage switching or with zero-current and zero-voltage switching. The analysis presented in [4] shows, however, that the second of these modes is divided to two sub-modes, which is related to the appearance of current pauses (discontinued current mode) in the operation of the rectifier. For the so determined modes, the operation of the converter is illustrated in fig.3. It presents normalized wave-forms of the inverter voltage u_{SW} , the rectifier input voltage u_0 , the voltage u_C across the capacitor C_{EQ} and the current i_L through the inductor L_{EQ} .

In **MODE I**, both the inverters deliver energy to the rectifier. This case can be observed at small values of the load resistor R_0 .

In **MODE II** and **MODE III**, as one of the inverters delivers energy to the rectifier, the other returns part of this energy back to the supply. This case can be obtained with increase of the value of R_0 . At significant values of the load resistor (**MODE III**), discontinued current mode is available.

Regardless of the operating mode, three commutations can be observed during a half-period – two for the voltage u_{SW} and one for the voltage u_0 . In this way, three working intervals are formed, at the time of which a voltage u_{EQ} is applied to the resonant circuit.

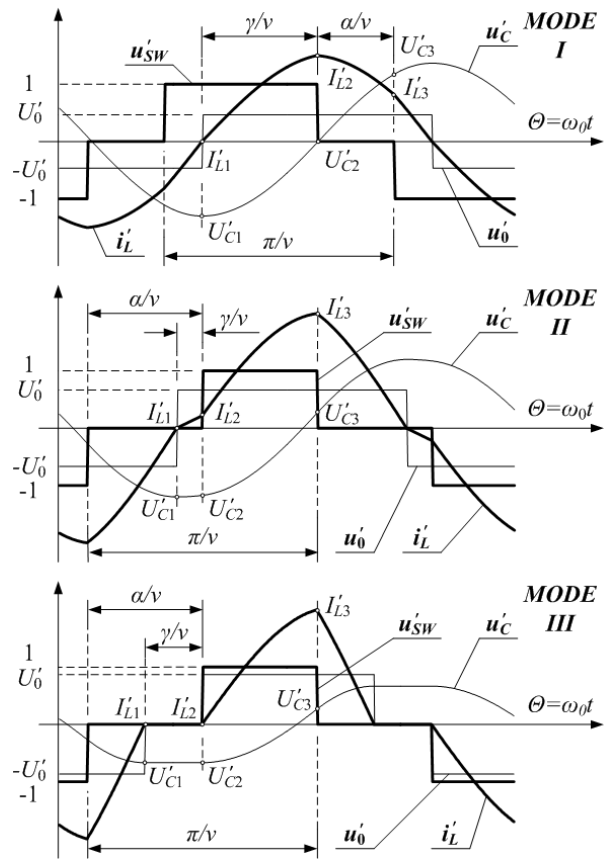


Fig.3. Waveforms for different operating modes

For the operating frequency ω_S in fig.3, the angle of the first interval is labeled with γ . At the beginning of this interval, the inductor current i'_L equals zero ($I'_{L1}=0$), and the capacitor voltage u'_C – negative peak value ($U'_{C1}=-U'_{CM}$). The normalized values of the voltages U'_{EQ} and the interval angles Θ_W for the resonant frequency ω_0 are presented for the different modes in Table I.

TABLE I
OPERATING INTERVAL'S PARAMETER DESCRIPTION

Case	Parameter	Interval		
		1	2	3
MODE I	Θ_W	γ/v	α/v	$(\pi-\alpha-\gamma)/v$
	U'_{EQ}	$1-U'_0$	$-U'_0$	$-1-U'_0$
MODE II	Θ_W	γ/v	$(\pi-\alpha)/v$	$(\alpha-\gamma)/v$
	U'_{EQ}	$-U'_0$	$1-U'_0$	$-U'_0$
MODE III	Θ_W	γ/v	$(\pi-\alpha)/v$	$(\alpha-\gamma)/v$
	U'_{EQ}	$-U'_{CM}$	$1-U'_0$	$-U'_0$

From the presented in [5] analysis and in accordance with the equivalent circuit in fig.2a, for the j -numbered interval the

inductor current i'_L and the capacitor voltage u'_C are expressed as follows:

$$i'_L(\Theta) = I'_{Lj} \cos \Theta - (U'_{Cj} - U'_{EQj}) \sin \Theta / 0,5 \quad (4)$$

$$u'_C(\Theta) = 0,5 I'_{Lj} \sin \Theta + (U'_{Cj} - U'_{EQj}) \cos \Theta + U'_{EQj} \quad (5)$$

In the above expressions j is the interval number; I'_{Lj} and U'_{Cj} are the initial values of the current i'_L and the voltage u'_C ; U'_{EQj} - the equivalent voltage acting upon the resonant circuit during the interval; $\Theta=0 \div \Theta_{Wj}$; Θ_{Wj} - angle corresponding to the interval duration.

In fig.3 it can be seen that the value of i'_L at the end of the examined interval appears to be the initial value of the next one. The same thing is valid for the voltage u'_C . Then:

$$I'_{Lj+1} = I'_{Lj} \cos \Theta_{Wj} - (U'_{Cj} - U'_{EQj}) \sin \Theta_{Wj} / 0,5 \quad (6)$$

$$U'_{Cj+1} = 0,5 I'_{Lj} \sin \Theta_{Wj} + (U'_{Cj} - U'_{EQj}) \cos \Theta_{Wj} + U'_{EQj} \quad (7)$$

Baring in mind that at the end of the third interval the inductor current equals zero again, and the capacitor voltage reaches positive peak value, on the base of (6) and (7) the following expressions are obtained:

$$-U'_{CM} = \frac{\sum_{j=1}^3 U'_{EQj} \left[\sin \left(\frac{\pi}{\nu} - \sum_{i=1}^j \Theta_{Wi} \right) - \sin \left(\sum_{i=j}^3 \Theta_{Wi} \right) \right]}{\sin \frac{\pi}{\nu}} \quad (8)$$

$$U'_{CM} = \frac{\sum_{j=1}^3 U'_{EQj} \left[\cos \left(\sum_{i=j}^3 \Theta_{Wi} \right) - \cos \left(\frac{\pi}{\nu} - \sum_{i=1}^j \Theta_{Wi} \right) \right]}{1 + \cos \frac{\pi}{\nu}} \quad (9)$$

Equations for normalized values of both the capacitor peak voltage U'_{CM} and the output voltage U'_0 are obtained from these expressions. Thereafter, the initial values I'_{Lj} and U'_{Cj} can be calculated by means of (6) and (7). On the base of expression (4), an equation for the average output current I'_0 is obtained:

$$I'_0 = \frac{\nu}{0,5\pi} \sum_{j=1}^3 \frac{I'_{Lj} \sin \Theta_{Wj}}{2} - \frac{\nu}{0,5\pi} \sum_{j=1}^3 (U'_{Cj} - U'_{EQj}) (1 - \cos \Theta_{Wj}) \quad (10)$$

By proper integration, expressions for the average and root means square (RMS) values of the currents through the different circuit elements can also be obtained on the base of equation (4).

IV. CONTROL TECHNIQUE

In accordance with the equivalent circuit in fig.2b and on the base of the results from the analyses, presented in [4, 5],

expressions for the RMS values of the inverter inductor

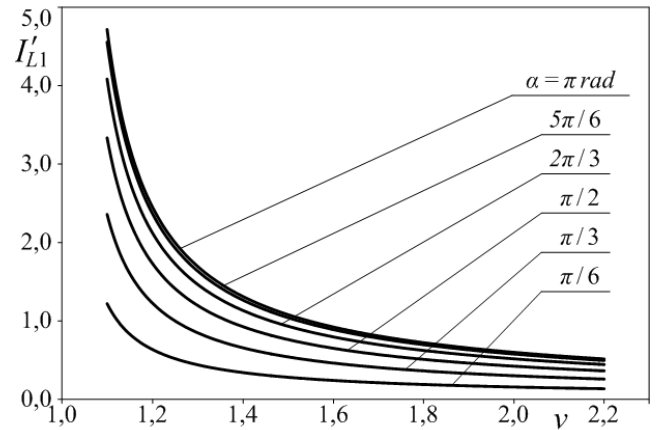


Fig.4. Normalized RMS value of the inductor current I'_{L1} as function of frequency detuning ν

currents are obtained.

Fig.4 presents the normalized dependencies of the inductor current RMS value of the first inverter on the frequency detuning ν , when the converter operates in no-load mode. These dependencies are obtained for different values of the phase-shift angle α . The characteristics for the second inverter are analogous. Fig.4 shows that when the converter works in no-load mode at low frequency, the stresses over the circuit elements may be significant. A solution to this problem is increase of the operating frequency. It can be observed that increasing the operating frequency only twice results in significant decrease of the coil currents. However, this causes reduction of the converter efficiency.

In order to maintain the efficiency of the converter at high output power and to reduce the stresses over the elements at small loading, a normalized control variable CP is introduced to change simultaneously two parameters - the phase-shift angle α and the working frequency f_s :

$$\alpha = (1 - CP)\pi, \quad f_s = f_L + (1 - CP)(f_H - f_L) \quad (11)$$

When CP is changed from 0 to 1, α changes from π to 0 and f_s changes from a minimum value f_L to a maximum value f_H .

On the base of equations (1) and (12), a minimum ν_L and a maximum value ν_H for the frequency detune can be defined.

V. OUTPUT AND CONTROL CHARACTERISTICS

As a result of the presented analysis and in accordance with the proposed control strategy, the output and control characteristics are drawn for the examined converter. It is assumed for the range of the frequency detuning that $\nu_L=1,1$ и $\nu_H=2,2$. From the analysis presented in [5], it can be proved that at $\nu_H > 2$ only two of the mentioned operating modes are possible - **MODE I** and **MODE II**.

Fig.5 presents the normalized output characteristics (with thick curves) obtained for several values of the control parameter $CP=[0,2; 0,4; 0,6; 0,8; 0,9; 0,95]$. The boundary between the operating modes is drawn with dotted curve. The

characteristics are similar to those at conventional phase-shift control.

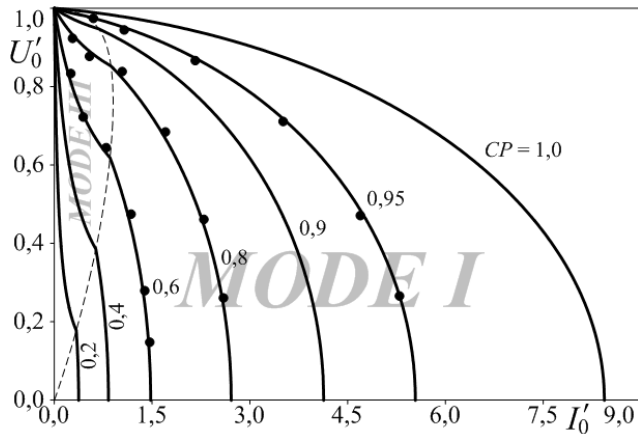


Fig.5. Load characteristics of the converter

Fig.6 presents the normalized control characteristics (with thick curves). They are obtained for several values of the load resistor ($R'_0=U'_0/I'_0$). The boundary between the working modes is drawn with dotted curve. At high values of the load resistor ($R'_0 \geq 1$) the characteristics are similar to those at conventional phase control. At low values ($R'_0 < 1$), however, their shape is different.

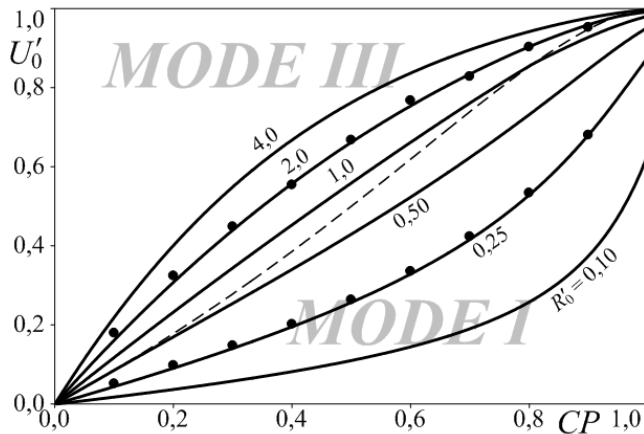


Fig.6. Control characteristics of the converter

The analysis of the two figures shows several main differences compared to the conventional phase-shift control [3, 4]:

1. The range of **MODE I** is increased (fig.5), which is a premise for improvement of the converter efficiency;
2. At low values of the control parameter CP , the more significant influence is that of the operating frequency, while at high values it is the phase-shift angle α that influences more.
3. At low values of the load resistor ($R'_0 < 1$), increase of the control parameter CP results an increased gradient of the control characteristics.

In order to verify the theoretically obtained results, simulations with OrCAD PSpice are done. A converter based on parallel topology is modeled for this purpose. The main specifications of this prototype are: $U_d=300V$; $f_L=50kHz$; $f_H=100kHz$; $L_1=L_2=204,223\mu H$; $C_1=C_2=60nF$; $Z_0=58,357\Omega$; $CP=0 \div 1$ ($\alpha=\pi \div 0$; $v=1,1 \div 2,2$).

On the base of operation in steady state mode, normalized values of the output voltage U'_0 and current I'_0 are obtained. The results obtained at $CP=[0,6; 0,8; 0,95]$ and $R'_0=[0,1; 0,2; 0,4; 0,8; 1,6; 3,2]$ are entered as dots in the area of the output characteristics. Analogically, normalized values of the voltage U'_0 are obtained at $R'_0=[0,25; 2,00]$ and $CP=[0,1; 0,2; 0,3; 0,4; 0,5; 0,6; 0,7; 0,8; 0,9]$. They are entered as dots in the area of the control characteristics.

The comparison done in this way shows very good match between the results from the theoretical analysis and those from the simulation examinations.

VI. CONCLUSION

A DC-DC converter consisting of two series resonant inverters connected in parallel to a common load (a rectifier) is examined. In order to maintain its efficiency at high output power, as well as, to reduce the stresses over the elements at lower loading, the control is realized by the simultaneous change of two parameters – the phase-shift between the currents of the two inverters and their operating frequency.

On the base of results from existing analyses, the converter work above the resonant frequency is examined. As a result, output and control characteristics are drawn. The comparison between these characteristics and those at conventional phase-shift control shows several essential differences. The authenticity of the theoretical examination is confirmed by computer simulations.

The obtained results can be used for design of DC-DC converters similar to the examined one.

REFERENCES

- [1] Y. Cheron, H. Foch, J. Roux, *Power Transfer Control Methods in High Frequency Resonant Converters*, PCI Proceedings, Munich, 1986, pp 92-103.
- [2] P. Savary, M. Nakaoka, T. Maruhashi, "Novel Type of High-Frequency Link Inverter for Photovoltaic Residential Applications", Vol. 133, Pt. B, No. 4, pp. 279-284, July 1986.
- [3] Sabate J.A., F.C. Lee, *Zero-Voltage Switching with Fixed Frequency Clamped-Mode Resonant Converters*, Proceedings of Virginia Power Center Seminar, 25-27 September 1989, pp.83-91.
- [4] B. S. Nathan, V. Ramanarayanan. "Analysis, Simulation and Design of Series Resonant Converter for High Voltage Applications", Industrial Technology 2000. Proceedings of IEEE International Conference, Vol. 1, pp. 688-693, 19-22 Jan. 2000.
- [5] A. Vuchev, N. Bankov, "Analytical Modeling and Investigation of Phase Shift Controlled Resonant DC-DC Converter", Engineering Sciences, Journal of the Bulgarian Academy of Sciences, 2010, № 2, pp. 36-50.

Control Characteristics of High-Voltage Resonant DC/DC Converter

Nikolay Bankov¹, Yassen Madankov² and Aleksandar Vuchev³

Abstract – A state plane analysis of high-voltage resonant DC/DC converter, operating above the resonant frequency, is presented. The parasitic parameters of the matching transformer are taken into account during the study. The possible operating modes of the converter are defined, according to the commutation time of the rectifier diodes. The control characteristics are obtained. In the plane of these characteristics the boundary curve between the particular modes is shown, as well as the area of soft commutation of the transistors. The results from the analysis are compared with these from computer simulations of the converter with OrCAD PSpice.

Keywords – High-voltage resonant DC/DC converter, Control characteristics

I. INTRODUCTION

The resonant DC/DC converters have been proved as a proper choice in the high-voltage power supplies design [1], [2]. The LCC topology is one of the most suitable for these applications [2]–[4]. One of the reasons is the possibility of operation in the whole loading range – from no-load to short circuit, preserving the soft commutation conditions of the switching devices. Another important advantage of these converters is the opportunity to implement the high-voltage matching transformer parasitic parameters (leakage inductance and winding capacitance) in the resonant tank [4].

The rectifier diodes commutations are not instantaneous, because of the capacitance which is parallel to the input of the rectifier. Usually this circumstance is neglected [5]. A study of the possible operating modes of LCC resonant DC/DC converter is proposed in [6] and [7], where the transformer's parasitic parameters are taken into account. As a result the output characteristics of the converter are obtained.

The aim of the present paper is to extend the analysis for the control characteristics area of the LCC resonant DC/DC converter. The boundary curve between the operating modes and the region of soft commutation of the transistors are obtained as an addition. An OrCAD PSpice simulation is used

to achieve accuracy verification of the proposed analysis.

II. CONVERTER OPERATING MODES

The circuit of the considered resonant converter is shown on Fig. 1. It consists of full-bridge inverter (transistors Q_1 – Q_4 with freewheeling diodes D_1 – D_4), resonant circuit (L , L_T , C and C_T), high-voltage transformer (Tr) and uncontrollable full-bridge rectifier (D_5 – D_8). Snubber capacitors (C_1 – C_4), which provide zero voltage switching (ZVS), are connected in parallel with the transistors. Filter capacitors (C_{F1} and C_{F2}) are connected to both the input and output of the converter.

The output power control is achieved by a change of the operating frequency, which is higher than the resonant one.

All circuit elements (without the matching transformer) are assumed to be ideal; the input and output voltage ripples are neglected, as well as the influence of the snubbers.

The transformer is shown on Fig. 1 with its simplified equivalent circuit, provided that the magnetizing current of each transformer is negligible to the resonant tank current. In such case Tr is comprised by its full leakage inductance L_T and the windings capacitance C_T , referred to the primary side, as well as an ideal transformer with turns ratio k .

The leakage inductance L_T is connected in series with the inductance of the resonant circuit L and can be regarded as part of it. With the capacitances C_T the resonant tank becomes of third order (L , C and C_T).

The inverter's output voltage (u_a) polarity changes immediately, because the snubber capacitors are not taken into account. But the presence of capacitance C_T makes the commutations in the input voltage of the rectifier (u_b) non-instantaneous. They start when a diode pair (D_5/D_7 or D_6/D_8) stops conducting at the moments of zeroing the current through the resonant circuit (i) and end up when the other diode pair (D_6/D_8 or D_5/D_7) starts conducting, while the capacitor C_T recharges from $+U_0/k$ to $-U_0/k$ or backwards. During these commutations none of the rectifier diodes conducts and the resonant current flows through the capacitance C_T .

When the load and/or the switching frequency are deeply changed, two different operating modes of the converter could be observed.

Characteristic of the first one is that the commutations in the rectifier occur entirely in the conducting intervals of the transistors. This is the *main* operating mode of the converter and is observed at comparatively small values of the load resistor R_0 .

We have the second case when the converter is very close to no-load regime. Than the commutations in the rectifier complete after these of the inverter, i.e. the rectifier diodes

¹Nikolay Bankov is with the Department of Electrical Engineering and Electronics, Technical Faculty, University of Food Technologies, 26 Maritza Blvd., 4002 Plovdiv, Bulgaria, E-mail: nikolay_bankov@yahoo.com

²Yassen Madankov is with the Department of Electrical Engineering and Electronics, Technical Faculty, University of Food Technologies, 26 Maritza Blvd., 4002 Plovdiv, Bulgaria, E-mail: yassen.madankov@gmail.com

³Aleksandar Vuchev is with the Department of Electrical Engineering and Electronics, Technical Faculty, University of Food Technologies, 26 Maritza Blvd., 4002 Plovdiv, Bulgaria, E-mail: avuchev@yahoo.com

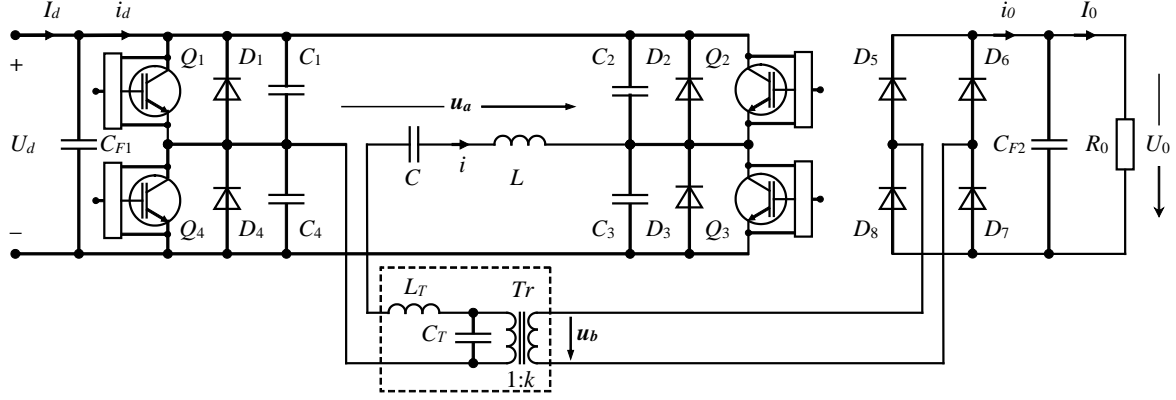


Fig. 1. Scheme of the high-voltage resonant DC/DC converter

start conducting after the corresponding inverter diodes are forward-biased. This mode is called *boundary*.

III. STATE PLANE ANALYSIS

All parameters are presented in relative units, as follow:

$U'_{Cm} = U_{Cm}/U_d$ - peak value of the voltage drop across the capacitor C ;

$U'_0 = \frac{U_0}{k \cdot U_d}$ - output voltage;

$I'_0 = \frac{k \cdot Z_0}{U_d} \cdot I_0$ - output current;

$\nu = \omega/\omega_0$ - normalized switching frequency

where ω is the operating frequency of the converter, $\omega_0 = 1/\sqrt{LC}$ is the resonant frequency and $Z_0 = \sqrt{L/C}$ is the characteristic impedance of the resonant tank L - C . Coefficients $a = C_T/C$ and $n = \sqrt{(a+1)/a}$ are also used.

The normalized load resistance is expressed as:

$$R'_0 = U'_0/I'_0 = R_0/k^2 Z_0 \quad (1)$$

As proposed in [6], the work of the converter in the *main* operating mode could be illustrated by a state plane trajectory with axes ($x = U'_C$; $y = I'$), shown on Fig. 2. Each operating period is divided into six consecutive intervals: **1**, **3**, **4** and **6** – conduction of transistors, **2** and **5** – conduction of the inverter reverse diodes, **3** and **6** – rectifier diodes commutation.

The times of these intervals for half a period could be expressed using the coordinates of points M_1 , M_2 and the resonant frequency ω_0 , by Eqs. (2)÷(7). Note that for t_3 (commutation time of the rectifier diodes) C and C_T are connected in series. Thus the resonant frequency is $\omega'_0 = n \omega_0 = 1/\sqrt{LC_E}$, where $C_E = C \cdot C_T / (C + C_T)$.

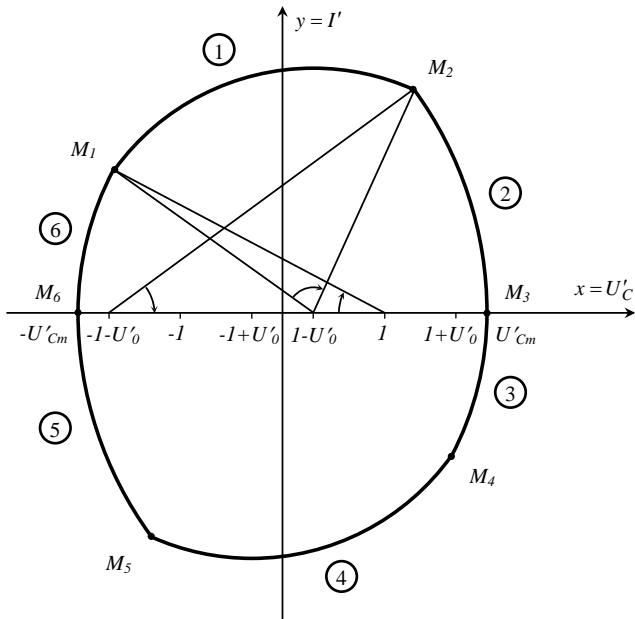


Fig. 2. State plane trajectory for the *main* operating mode

$$t_1 = \frac{1}{\omega_0} \left(\arctg \frac{y_2}{-x_2 + 1 - U'_0} - \arctg \frac{y_1}{-x_1 + 1 - U'_0} \right) \quad (2)$$

for $x_2 \leq 1 - U'_0$ and $x_1 \leq 1 - U'_0$

$$t_1 = \frac{1}{\omega_0} \left(\pi - \arctg \frac{y_2}{x_2 - 1 + U'_0} - \arctg \frac{y_1}{-x_1 + 1 - U'_0} \right) \quad (3)$$

for $x_2 > 1 - U'_0$ and $x_1 \leq 1 - U'_0$

$$t_1 = \frac{1}{\omega_0} \left(\arctg \frac{y_2}{-x_2 + 1 - U'_0} + \arctg \frac{y_1}{x_1 - 1 + U'_0} \right) \quad (4)$$

for $x_2 > 1 - U'_0$ and $x_1 > 1 - U'_0$

$$t_2 = \frac{1}{\omega_0} \arctg \frac{y_2}{x_2 + 1 + U'_0} \quad (5)$$

$$t_3 = \frac{1}{n \omega_0} \left(\arctg \frac{ny_1}{-x_1 + 1 - U'_0} \right) \quad \text{for } x_1 \leq 1 - U'_0 \quad (6)$$

$$t_3 = \frac{1}{n \omega_0} \left(\pi - \arctg \frac{ny_1}{x_1 - 1 + U'_0} \right) \quad \text{for } x_1 \geq 1 - U'_0 \quad (7)$$

The used coordinates represent the initial values of the resonant current (y_i) and the voltage drop across the capacitor C (x_i) for the particular interval (in relative units):

$$x_1 = -U'_{Cm} + 2aU'_0 \quad (8)$$

$$y_1 = \sqrt{4aU'_0(U'_{Cm} - aU'_0 + 1)} \quad (9)$$

$$x_2 = U'_0U'_{Cm} - aU'^2_0 \quad (10)$$

$$y_2 = \sqrt{U'_{Cm}(U'_{Cm} + 2)(1 - U'^2_0) + aU'^2_0(2 + 2U'_0 + 2U'_0U'_{Cm} - aU'^2_0)} \quad (11)$$

The equation for the output current of series resonant converter is known [8]: $I'_0 = 2vU'_{Cm}/\pi$. But in this case, $I'_0 = 0$ during the commutations in the rectifier, because of the persistence of the parallel capacitance C_T , so the value is:

$$I'_0 = 2vU'_{Cm}/\pi - \Delta I'_0 = 2v(U'_{Cm} - aU'_0)/\pi \quad (12)$$

The way for determination of the coordinates of the points M_i and the time intervals ($t_1 \div t_3$) for the *boundary* operating mode of the converter is quite similar. Detailed analysis for this case is given in [7].

IV. CONTROL CHARACTERISTICS AND BOUNDARY CURVES

Using Eqs. (1) and (12), U'_{Cm} can be submitted in function of U'_0 , v , R'_0 и a :

$$U'_{Cm} = \frac{\pi}{2v} \cdot \frac{U'_0}{R'_0} + aU'_0 \quad (13)$$

By Eq. (13) U'_{Cm} is eliminated from Eqs. (8)÷(11). Next steps are consecutive substitution of Eqs. (8)÷(11) in Eqs. (2) ÷(7) and after that Eqs. (2)÷(7) in:

$$\frac{\pi}{v} = \omega_0(t_1 + t_2 + t_3) \quad (14)$$

Solving Eq. (14), a function $U'_0 = f(a, v, R'_0)$, which represents the control characteristics of the converter for the *main* operating mode, could be obtained. The procedure for the *boundary* mode is the same, only the equations for (x_i ; y_i) and t_i have to be used from [7].

The control characteristics of LCC resonant DC/DC converter with capacitors ratio $a = 1,0$, for different values of R'_0 , are shown on Fig. 3. Dashed curves correspond to the *boundary* mode and continuous – for the *main* mode.

In the *main* operating mode the rectifier commutations (intervals **3** and **6**) have to complete before the inverter commutations begin. This is true if the statement $x_1 \leq x_2$ is fulfilled. Expressed by Eqs. (8), (10) and (13), the next inequality is received:

$$v \leq \frac{\pi}{2a} \cdot \frac{U'_0 + 1}{R'_0} \quad (15)$$

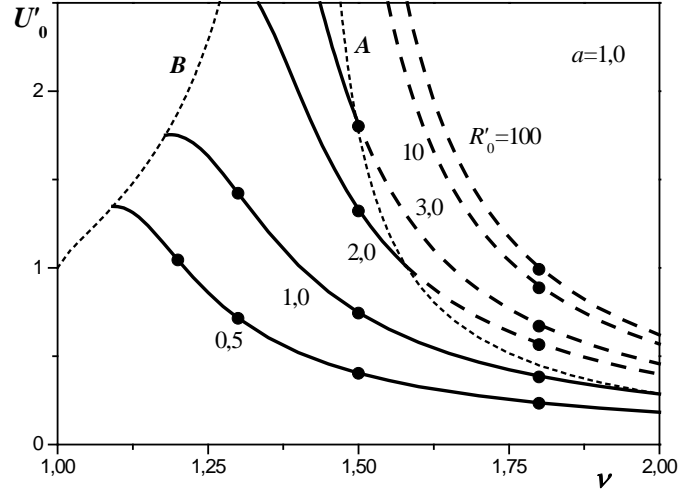


Fig. 3. Control characteristics of LCC resonant DC/DC converter

To ensure the soft switch-on of the transistors at zero voltage (ZVS), the inverter commutations (points M_2 and M_5) have to complete before zero crossing of the resonant current. If this is not fulfilled, the switching-off of one the transistor pairs doesn't lead to soft switch-on of the other pair at zero voltage and the converter stops working. This is covered by the statement $x_2 < U'_{Cm}$, which expressed by Eqs. (10) and (13) leads to the inequality:

$$v \leq \frac{\pi}{2a} \cdot \frac{U'_0 - 1}{R'_0} \quad (16)$$

Eqs. (15) and (16) provide the possibility to plot the boundary curve between the *main* and the *boundary* modes (curve **A**) in the control characteristics plane (Fig. 3), as well as the curve of the soft commutation (curve **B**). These curves define the area of each operating mode of the converter.

V. SIMULATING RESULTS

In order to prove the obtained theoretical results a transistor LCC resonant DC/DC converter, operating above the resonant frequency, was designed using the methodology proposed in [9]. Its input parameters are:

- output power $P_0 = 3 \text{ kW}$;
- output voltage $U_0 = 150 \text{ V}$;
- operating frequency $f = 100 \text{ kHz}$;
- supply voltage $U_d = 300 \text{ V}$;
- $a = 1,0$; $k = 1$.

The chosen nominal operating point is at $v = 1,15$. Than the following values for the elements of the resonant tank are obtained: $L = 72,577 \mu\text{H}$; $C = 46,157 \text{ nF}$; $C_T = 46,157 \text{ nF}$.

A PSpice simulation of the designed converter was made for different combinations of $v = [1,2; 1,3; 1,5; 1,8]$ and $R'_0 = [0,5; 1,0; 2,0; 3,0; 10; 100]$ (in real units corresponds to $R_0 = [19,83; 39,65; 79,31; 118,96; 396,53; 3965,32] \Omega$). The PSpice model circuit is shown on Fig. 4.

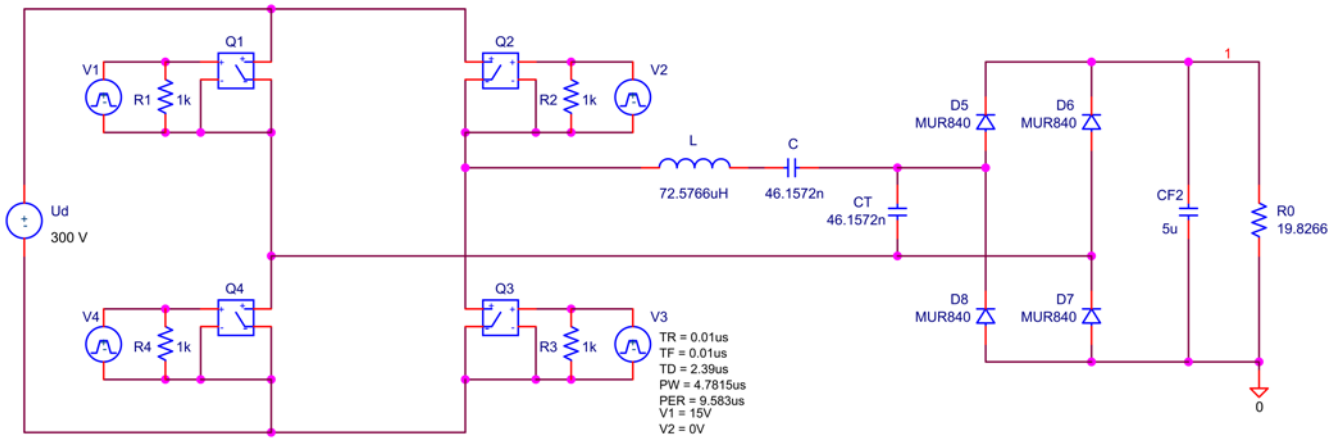


Fig. 4. PSpice simulation circuit of the designed LCC resonant DC/DC converter

The measured values of the output voltage (converted in relative units) are shown with points on Fig. 3. The results from the simulation together with these, obtained following the suggested methodology, are presented in Table I. The correspondence between the results is very good – the relative error is below 2%. It can be noticed that the error increases with the increase of the load resistor or the normalized switching frequency.

TABLE I
COMPARISON BETWEEN THE THEORETICAL AND SIMULATION RESULTS

		Simulation	Theory	Error
R'_0	v	U'_0	U'_0	$\delta, [\%]$
0,5	1,2	1,044	1,044	0,049
	1,3	0,715	0,715	-0,026
	1,5	0,402	0,404	-0,434
	1,8	0,233	0,236	-1,214
1,0	1,3	1,422	1,422	-0,008
	1,5	0,743	0,746	-0,505
	1,8	0,383	0,388	-1,303
2,0	1,5	1,322	1,331	-0,671
	1,8	0,564	0,573	-1,443
3,0	1,5	1,800	1,815	-0,808
	1,8	0,669	0,679	-1,513
10	1,8	0,886	0,900	-1,577
100	1,8	0,992	1,004	-1,204

VI. CONCLUSION

A high-voltage LCC resonant DC/DC converter with capacitive output filter have been studied. It operates above the resonant frequency. In the proposed analysis the parasitic parameters of the matching transformer are taken into account. Typical operating modes of the converter are considered, according to the commutation time of the rectifier diodes. The control characteristics for each operating mode are obtained. The boundary curve between the modes, as well as the area of soft commutation of the transistors are presented in the plane of these characteristics.

The results of the theoretical study are compared with these of computer simulation using the software product OrCAD PSpice. The error between the obtained results is very small, less than 2%, which confirms the accuracy of the proposed methodology.

The described investigation can be used for designing LCC converter power supplies for microwave magnetrons, laser tubes, fluorescent lamps, etc. It is suitable especially for applications where a wide range of load changing is needed.

REFERENCES

- [1] N. D. Madzharov, M. S. Gardevski, "A DC/DC High Voltage Power Supply", PCIM'10, Conference Proceeding, Nurnberg, Germany, 2010.
- [2] N. D. Madzharov, "Autonomous Inverters with Energy Dosing for Ultrasonic Application", ICEST 2013, pp. 647-650, Ohrid, Macedonia, 2013.
- [3] M. Rentzsch, F. Gleisberg, H. Guldner, F. Benecke and C. Ditmanson, "Closed Analytical Model of a 20 kV Output Voltage, 800 W Output Power Series-Parallel-Resonant Converter with Walton Cockroft Multiplier", PESC 2008. IEEE, pp. 1923-1929, 2008.
- [4] J. Liu, L. Sheng, J. Shi, Z. Zhang and X. He, "Design of High Voltage, High Power and High Frequency Transformer in LCC Resonant Converter", APEC 2009, Twenty-Fourth Annual IEEE, pp. 1034-1038, Washington, USA, 2009.
- [5] R. W. Erickson, D. Maksimovic, *Fundamentals of Power Electronics*, New York, Boston, Dordrecht, London, Moscow, Kluwer Academic Publishers, 2004.
- [6] N. Bankov, A. Vuchev, Y. Madankov, "Analysis of High Voltage Resonance DC/DC Converter in Main Operating Mode", EICS 2013, pp. 224-229, Sofia, Bulgaria, 2013 (in Bulgarian).
- [7] N. Bankov, A. Vuchev, Y. Madankov, "Analysis of High Voltage Resonance DC/DC Converter in Boundary Operating Mode", EICS 2013, pp. 230-235, Sofia, Bulgaria, 2013 (in Bulgarian).
- [8] L. Rossetto, "A Simple Control Technique for Series Resonant Converters", IEEE Trans., Power Electronics, vol. 11, no. 44, pp. 554-560, 1996.
- [9] N. D. Bankov, A. S. Vuchev, Y. K. Madankov, "Design Methodology for High Voltage Resonant DC/DC Converter for CO₂ Laser Power Supply", Annual Journal of Electronics, vol. 7, pp. 152-155, 2013.

Three-Phase Soft-Switched Quasi Resonant DC Link Inverter for Induction Motor Drive Application

Dimitar Spirov¹ and Nikolay Komitov²

Abstract – A zero-voltage transition soft-switching inverter for an induction motor drive is developed. The proposed soft-switching inverter is formed from the traditional pulse-width modulated (PWM) inverter by simply augmenting with auxiliary resonant circuits, and the soft switching is achieved through applying PWM switching control signals with suitable delays for the switches. The designed soft-switching inverter is used for powering an induction motor drive to test its effectiveness. The proposed drive system is modelled and its performance is simulated in PSpice. The simulation results show that a smaller switching loss and higher conversion efficiency are obtained by the proposed soft-switching inverter.

Keywords – Induction motor drive, Soft-switching inverter, Zero-voltage transition.

I. INTRODUCTION

Inverters have many applications in power electronic devices. The performance of a pulse-width modulated inverter-fed system can be much improved by increasing the switching frequency. In hard switching inverters, a higher switching frequency leads to increased switching losses which consequently increases the size of the snubber circuits [1, 2]. This will suffer by giving large switching stresses of the power devices. In addition, electromagnetic interference increases and efficiency decreases. To overcome these problems, the application of soft switching techniques is essential [1-5].

The resonant DC-link inverter is the most commonly used one for induction motor drives, owing to its simplicity, but it possesses the disadvantage of having a high resonant link voltage, which is equal to or greater than twice the supply voltage [1].

Quasi-resonant (QR) inverters offer several advantages compared with resonant DC-link inverters with regard to resonant link design and control, device rating requirements and use of pulse width modulation (PWM) [6]. The QR inverter schemes generate zero-voltage instants in the DC link at controllable instants that can be synchronised with any PWM transition command, thus ensuring a zero-voltage switching condition of inverter devices. As a result, these inverters can be operated at high switching frequencies with high efficiency [6].

The passively clamped QR inverter is reported in [7]. This

topology satisfying most of the essential requirements, such as low clamp factor, simple resonance control, guaranteed zero-link voltage condition, PWM capability, use of only one auxiliary switch and recycling of resonant energy. The only drawback of this scheme was the high reverse voltage requirement of the clamp diode. This problem can be solved by use of a separate, low-voltage DC source [5, 6]. Another possible solution could be to use a simple R-C parallel circuit to maintain low voltage [6].

One of the main QR inverter research goals is to achieve soft switching conditions with a minimum number of auxiliary circuit elements [2]. Reducing the number of auxiliary switches simplifies the control circuit and decreases the inverter cost.

The object of this work is to develop and simulated in PSpice a three-phase induction motor drive fed by a PWM voltage source soft-switching inverter. It is necessary to investigate a performance of proposed drive system for the dynamic and steady-state modes.

II. SIMULATION MODEL

The circuit diagram of the QR inverter is illustrated in Fig. 1. This topology is similar to the classic converter, plus an auxiliary circuit consists of switch S_a , antiparallel diode D_a and the coupled inductors L_{r1} and L_{r2} . The dc-link switch is S_L and the dc-link resonant capacitor is C_r .

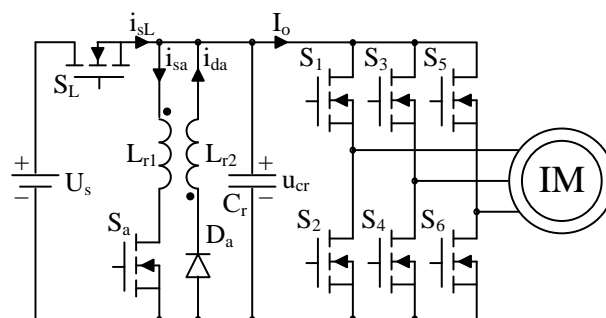


Fig. 1. QR DC-link inverter

The circuit operates by setting up a resonating dc link that periodically returns the dc bus voltage to zero. During the interval that the diodes in antiparallel with the main inverter devices are conducting, all inverter devices may be turned off, if desired, with minimal turn-off losses. At the same time, all incoming devices may be turned on with zero turn-on losses.

Six operating intervals can be identified. Before the first operating interval, it is assumed that S_L is on and S_a is off. This regime corresponds to the pseudo steady state conditions with link voltage equal to U_s . The output current I_o flows through S_L .

¹Dimitar Spirov is with the Department of Electrical Engineering, University of Food Technologies - Plovdiv, 26, Maritza Blvd., 4002 Plovdiv, Bulgaria, e-mail: dimitar_spirov@abv.bg

²Nikolai Komitov is with the Department of Electrical Engineering, University of Food Technologies - Plovdiv, 26, Maritza Blvd., 4002 Plovdiv, Bulgaria, e-mail: nikkomitov@abv.bg

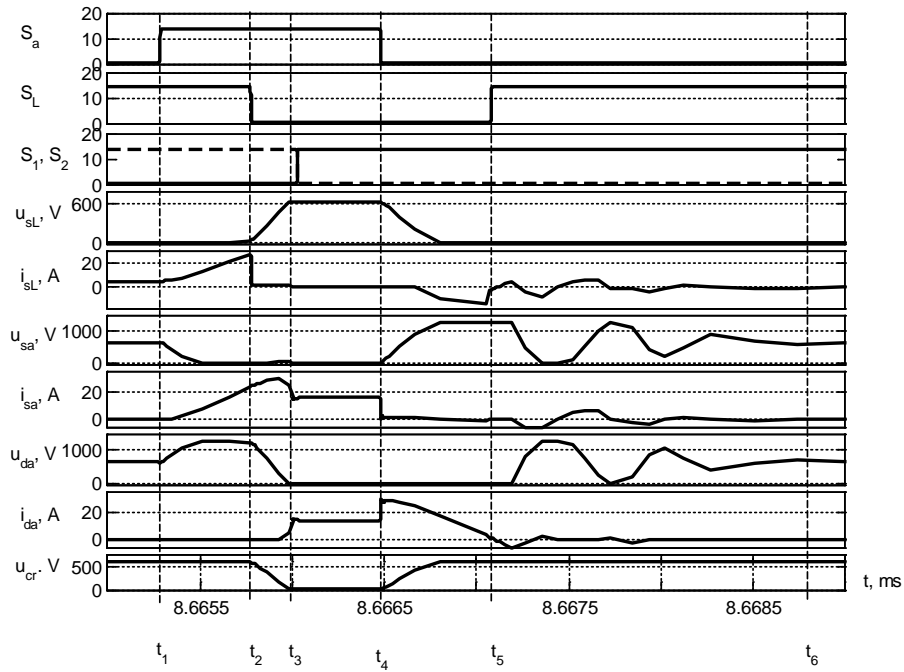


Fig. 2. Resonant link waveforms

Whenever a change in the state of the inverter main switches is desired, S_a is turned on (t_1). Due to existence of L_{r1} , the turn on of S_a is under zero-current switching condition and i_{sa} increases linearly ($t_1 \div t_2$) until it reaches I_{min} which is defined as the minimum required current of L_{r1} that guarantees the charging of C_r in interval ($t_4 \div t_5$). The design procedure of I_{min} is illustrated in [2].

When i_{sa} reaches I_{min} , switch S_L must be turned off (t_2). S_L is turned off under zero-current switching condition due to the existence of C_r . In this interval, a resonance starts between C_r and L_{r1} which decreases the dc-link voltage ($t_2 \div t_3$).

When u_{cr} reaches zero the diode D_a turns on (t_3). Thus, a fraction of the flux linkage of L_{r1} , moves to L_{r2} . In order to operate at zero-voltage switching condition, the state of the inverter switches must be changed in this interval ($t_3 \div t_4$). After the inverter switches change state, switch S_a then turned off in a zero-voltage switching manner (t_4). Thus, i_{da} current increases and begins to charge C_r ($t_4 \div t_5$).

When C_r reaches U_s , antiparallel diode of the switch S_L turns on under zero-voltage switching condition (t_5). Thus, switch S_L can be turned on under zero-voltage-zero-current switching condition. i_{da} current decreases to I_0 . When the antiparallel diode of the switch S_L current reaches zero and turns off under zero-voltage-zero-current switching condition, the S_L current begins to increase until it reaches I_0 and i_{da} current reaches zero (t_6).

After this interval, the link returns to the pseudo steady state and the cycle repeats for the next switching command.

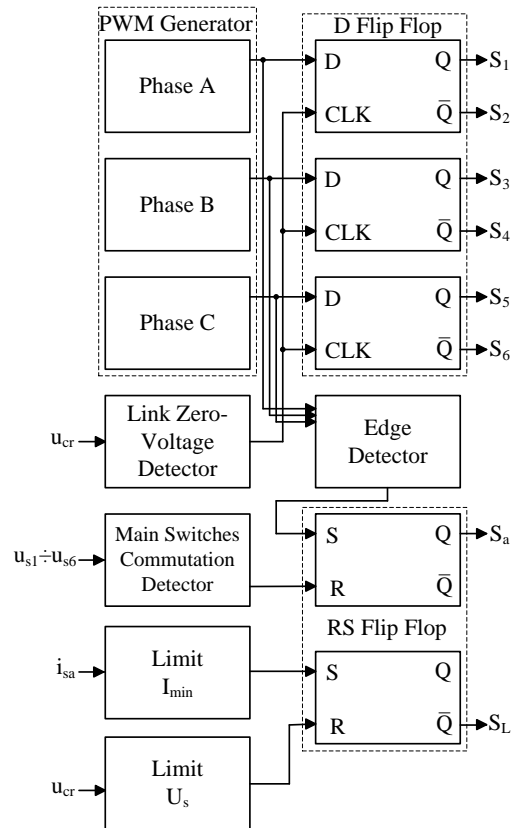


Fig. 3. Control circuit diagram for soft-switched PWM modulation

III. RECEIVED RESULTS

Simulation is done on a three phase induction motor fed by a PWM inverter developed in PSpice. The basic circuit of the proposed scheme consists of a three phase induction motor type AO-90S-4 having ratings as 1,1kW, 380V, 50 Hz which is connected to drive the constant nominal load. The PSpice model of three phase induction motor inverter drive has been developed in [7]. The technical data of the electric motor are given in Appendix.

The design of the proposed inverter involves the selection of parameters C_r , L_{r1} , L_{r2} to satisfy the desired link waveform specifications such as du/dt , di/dt and peak currents [6]. The design expressions are derived from the differential equations of each mode of the resonant cycle [1-7]. A set of parameters has been chosen as $L_{r1}=10\mu\text{H}$, $L_{r2}=10\mu\text{H}$, $C_r=10\text{nF}$. The magnetic coupling between L_{r1} and L_{r2} is designed as 0.9.

A three-phase sine-triangle PWM command generator was implemented to control the six inverter switches. The frequency of the carrier wave is maintained at 2 kHz.

Inverter control is implemented based on the link operation requirements, whenever a switching signal is generate, the auxiliary circuit must first be turned on to initiate a resonant transient. The inverter switches, when the link voltage reaches zero. A block diagram for a control scheme is shown in fig. 3. The edge detector locates the desired state change before the switching command is passed to the inverter switches. The detected edges are used as an input of a RS-flip flop to turn on of the auxiliary circuit. The auxiliary switch turns off, when the state of the inverter switches was changed. When i_{sa} reaches I_{\min} , the pulse is used as an input of a RS-flip flop to turn off of the link circuit. The link switch turns on, when the C_r reaches U_s .

Fig. 4 shows the link voltage u_{DC} , inverter line-line voltage and phase current. It is seen that there is some distortion in the motor current. The reason for the distortion has to be attributed to the minimum link pulse requirement in the resonant inverter.

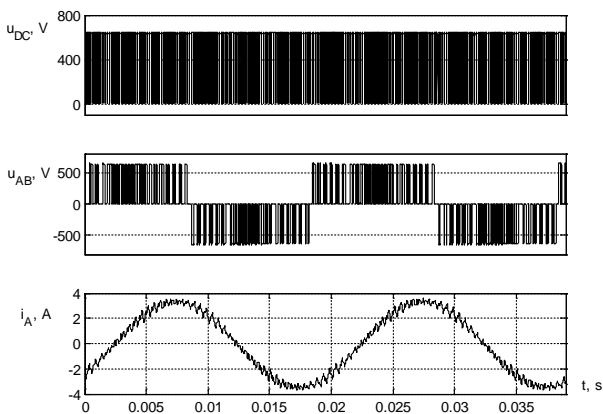


Fig. 4. Dependences u_{DC} , u_{AB} , $i_A=f(t)$

From the basic waveforms shown, it is seen that some limitations still exist. The control circuit must drive the auxiliary switch and the dc-link switch at the proper time. It

can be observed from Fig. 2, that the state of the inverter switches can be changed $1\mu\text{s}$ after turning S_L off. When the control circuit decides to change the state of inverter switches, this action should be performed with a delay $0.6\mu\text{s}$ in order to have enough time to reduce the dc-link voltage to zero. Thus, switch S_a is turned on first and i_{sa} current increases until it reaches I_{\min} . This current must be large enough ($I_{\min}=26.8\text{A}$) to guarantee charging C_r . A larger I_{\min} causes greater current stresses on S_L and S_a [2].

The fall time for the link voltage is about 990ns. The zero link voltage condition maintained for about $1.3\mu\text{s}$. The rise time for the link voltage is more than $1.7\mu\text{s}$.

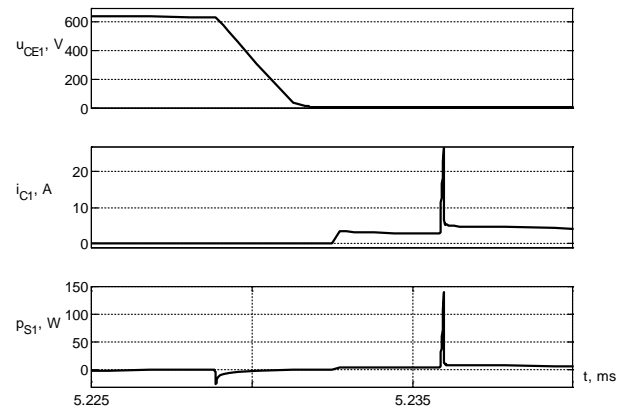


Fig. 5. Dependences u_{CE1} , i_{C1} , $p_{S1}=f(t)$ with "soft switching" control scheme

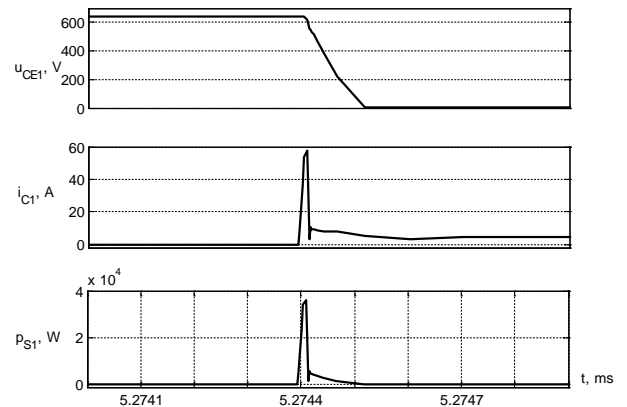


Fig. 6. Dependences u_{CE1} , i_{C1} , $p_{S1}=f(t)$ without "soft switching" control scheme

Management of inverter drives attached proposed control algorithm for "soft switching" voltage of the keys. Fig. 5 shows the shapes of the current, voltage and power losses in the switches of the test circuit. For comparison are shown in scheme losses without "soft switching" control scheme (Fig. 6).

From fig. 5 and fig. 6 is seen that the current through transistor S_1 begins to flow in the reset voltage on it. This led to a significant reduction in switching losses - in the case of pulses presented in the figure of 8730 W when dealing with

"hard switching" to 8.127 W when using "soft switching", i.e. 8722 W reduce the emitted power. Amplitude value of current through the transistor S_1 at work "hard switching" is 59.37 A, when using "soft switching" is 3.15 A, i.e. with 56.22 A reducing the amplitude value.

IV. CONCLUSION

A three-phase induction motor drive fed by a PWM voltage source soft-switching QR inverter is presented. The proposed circuit uses two additional switches to create zero-voltage instants in the DC link.

The proposed drive system is modeled and its performance is simulated in PSpice. Simulation results show that the proposed scheme for the "soft switching" is obtained a significant reduction of the power losses in the power switches and the reduction of the amplitude values of the current through the transistors as compared with the scheme of "hard switching".

APPENDIX

Induction motor type AO-90S-4

$P_N=1,1\text{kW}$; $U_N=380\text{V}$; $I_N=2,8\text{A}$; $f=50\text{Hz}$; $p_p=2$;
 $n_N=1410\text{min}^{-1}$; $M_N=7,45\text{Nm}$; $\cos\varphi=0,8$; $J_m=0,001\text{kgm}^2$.

Parameters for $s=s_N$

$R_s=7.45\Omega$; $R_r=5.00255\Omega$; $L_{os}=0.01839\text{H}$; $L_{or}=0.01839\text{H}$;
 $L_m=0.33475\text{H}$.

REFERENCES

- [1] K. H. Chao, C. M. Liaw, "Three-phase soft-switching inverter for induction motor drives", IEE Proc-Electr. Power Appl, vol 148, no. 1, pp. 8-20, 2001.
- [2] M. R. Amini, H. Farzanehfard, "Quasi Resonant DC Link Inverter with a Simple Auxiliary Circuit", Journal of Power Electronics, vol. 11, no. 1, pp. 10-15, 2011.
- [3] W. Yi, H. L. Liu, Y. C. Jung, J. G. Cho, and G. H. Cho, "Program-Controlled Soft Switching PRDCL Inverter with New Space Vector PWM Algorithm", IEEE, pp. 313-319, 1992.
- [4] S. Chen, B. J. C. Filho and T. Lipo, "Design and Implementation of a Passively Clamped Quasi Resonant DC Link Inverter", IEEE, pp. 2387-2392, 1995.
- [5] S. Chen and T. Lipo, "A Novel Soft-Switched PWM Inverter for AC Motor Drives", IEEE Trans. On Power Electr, vol. 11, no. 4, pp. 653-659, 1996.
- [6] J. Shukla and B.G. Fernandes, "Three-phase soft-switched PWM inverter for motor drive application", IET Electr. Power Appl., vol. 1, no. 1, pp. 93-104, 2007.
- [7] D. Spirov, N. Komitov and N. Bozukov. PSpice Modeling of Inverter Induction Machine Drive. TECHSYS'13, pp. 73-76, 2013.

Matlab-Simulink Model of Three-Phase BUCK Rectifier with Sinusoidal PWM

Georgi Kunov and Stoyan Vuchev

Abstract – A three-phase BUCK rectifier with sinusoidal PWM is considered in the present paper. An algorithm for control is synthesized and Matlab-Simulink model is constructed based on this algorithm. The simulation results are presented illustrating the mode of operation of the functional blocks, as well as the shape of the voltage on the load.

Keywords – Power Electronics, Three Phase Rectifiers, PFC Rectifiers, Sinusoidal PWM BUCK Rectifiers, Matlab-Simulink Simulation.

I. INTRODUCTION

The rectifiers are components of many electro-technological and energetic devices. A key requirement to them is the high power factor. The first circuit solutions for improving the power factor are used in non-adjustable diode rectifiers. These are circuits of single-phase and three-phase Power Factor Correction (PFC) Rectifiers. According to the principle of operation, they are step-up (BOOST) rectifiers [1, 2].

Often it is necessary in the practice to adjust the rectified voltage from 0V to the nominal voltage. In such cases an additional step-down (BUCK) DC-DC converter is used in BOOST PFC rectifiers. This approach leads to an increase in size and to more expensive device.

The above-mentioned problem is solved by BUCK rectifiers operating under sinusoidal pulse width modulation (PWM). A review of the circuit variants of this type of rectifiers, as well as of BOOST PFC rectifiers is performed in [3, 4, 5].

In the present paper, a three-phase rectifier with sinusoidal BUCK PWM is considered and corresponding Matlab-Simulink model is synthesized. This model is valid for both active and inductive load.

II. MATLAB-SIMULINK MODEL OF THREE-PHASE BUCK RECTIFIER WITH SINUSOIDAL PWM

The power circuit of the Simulink simulation model of the rectifier is shown in Fig.1. It is realized by six unidirectional

Georgi Kunov is with the Faculty of Electronic Engineering and Technologies, Technical University of Sofia, Kl. Ohridski 8, 1000 Sofia, Bulgaria, E-mail: gkunov@tu-sofia.bg.

Stoyan Vuchev is with the Faculty of Electronic Engineering and Technologies, Technical University of Sofia, Kl. Ohridski 8, 1000 Sofia, Bulgaria, E-mail: vu4ev_100yan@abv.bg.

switches (DR1, Sw1 ÷ DR6, Sw6) and Control Unit (Subsystem CU-BUCK PWM Rectifier).

The block diagram of the Subsystems of the Control Unit is shown in Fig. 2. It, in turn, is built of of six blocks: Subsystem positive/negative High Voltage; Subsystem positive/negative Phases; Subsystem Pulse Width Modulation and three blocks with the same internal configuration - Subsystem Gate Pulses.

The purpose of each of the blocks of the Control Unit is considered separately.

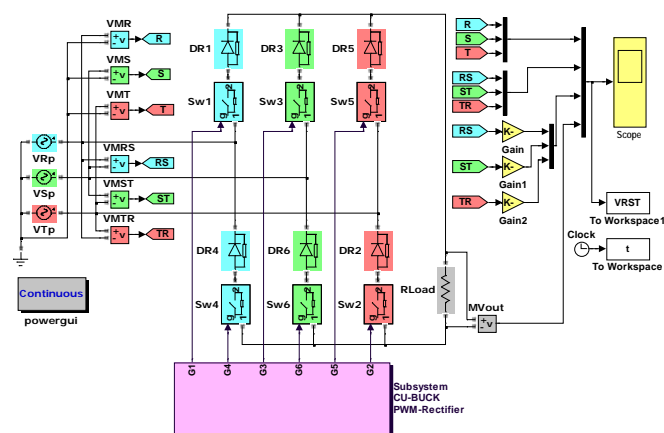


Fig. 1. Power circuit of the three-phase rectifier

A. Subsystems positive/negative High Voltage and positive/negative Phases

The circuit realizing the Subsystem positive/negative High Voltage is shown in Fig. 3. Its purpose is to produce signal “logical 1” for the intervals, where each of the three phases is the most positive (most negative). This is realized by three-phase diode rectifier, by controlling the current through each of the diodes.

As it is seen from the waveforms shown in Fig. 5, the phase R is most positive when the diode D1 is conducting (VCD1=1; in the interval from $\pi/6$ to $\pi/6$) and is the most negative when the diode D4 is conducting (VCD4=1; in the interval from $7\pi/6$ to $9\pi/6$).

The purpose of the Subsystem positive/negative Phases is to produce signal “logical 1” for the intervals, where each of the phases is positive (negative). Its circuit realization is shown in Fig. 4. As it is seen from the waveforms shown in Fig. 5, in the interval where phase R is positive, VRp=1 (from 0 to π) and in the interval where it is negative VRn=1 (from π to 2π)

The signals *Positive/negative High Voltage* and *positive/negative Phases* for the phases S and T are also shown in Fig. 5 and are obtained similarly.

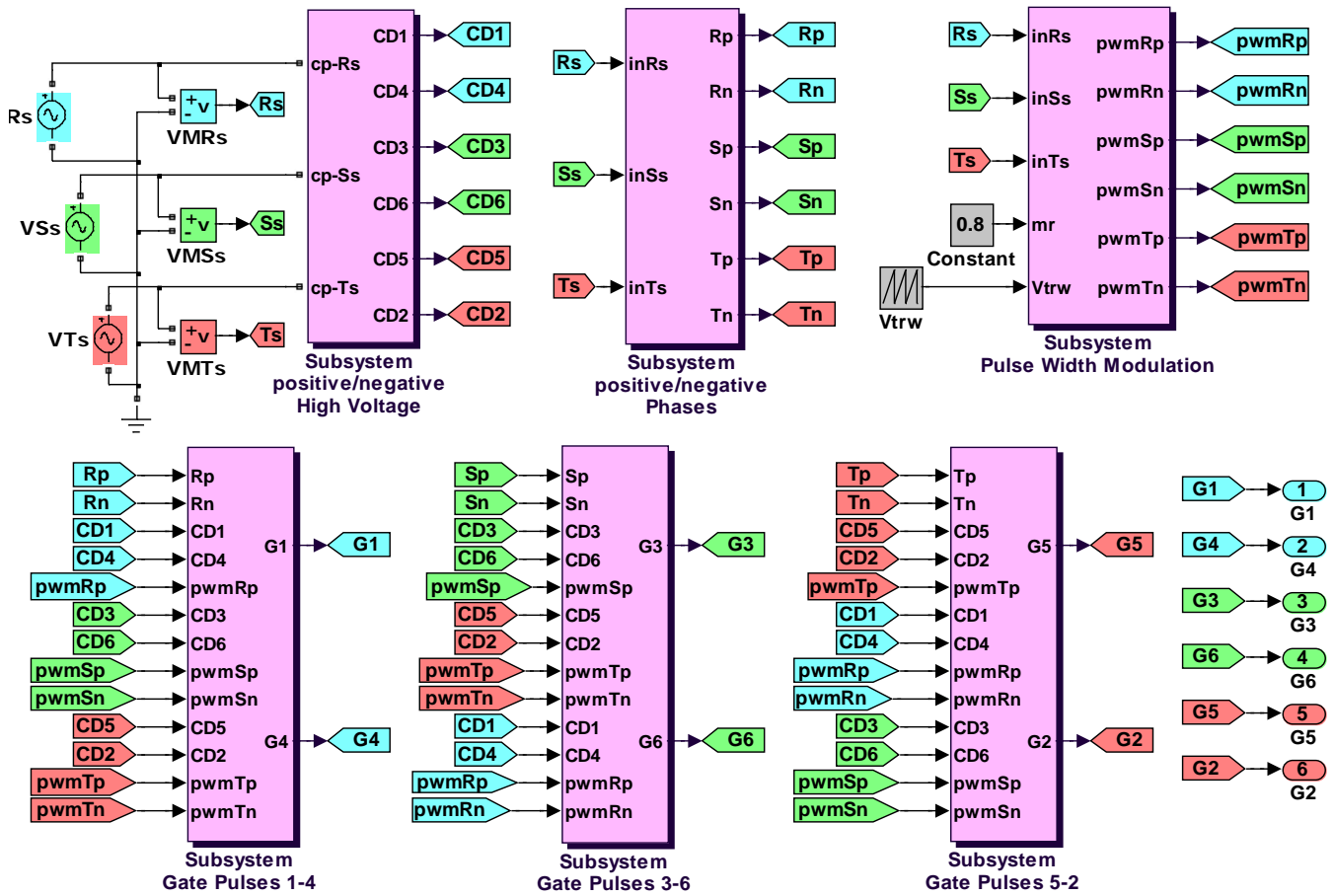


Fig. 2. Subsystems of the Control Unit

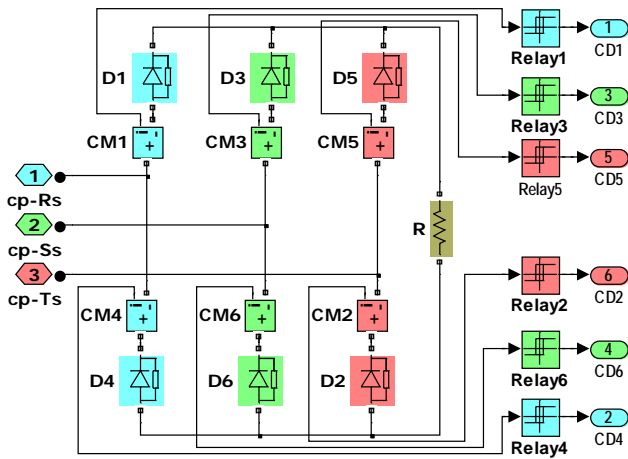


Fig. 3. Subsystem positive/negative High Voltage

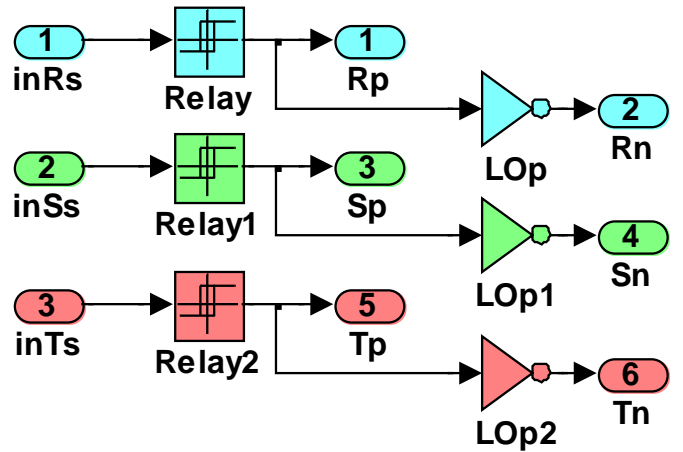


Fig. 4. Subsystem positive/negative Phases

B. Subsystem Pulse Width Modulation

The circuit realizing the Subsystem Pulse Width Modulation is shown in Fig. 6. The waveforms, illustrating its principle of operation, are shown in Fig. 7.

The sinusoidal PWM for each of the phases, is obtained by comparing the corresponding phase voltage ($|V_{R1}|$; $|V_{S1}|$; $|V_{T1}|$) with a sawtooth voltage (V_{trw}). The obtained in such a way three PWM signals (pwm_{Rp} , pwm_{Sp} and pwm_{Tp}) are supposed positive.

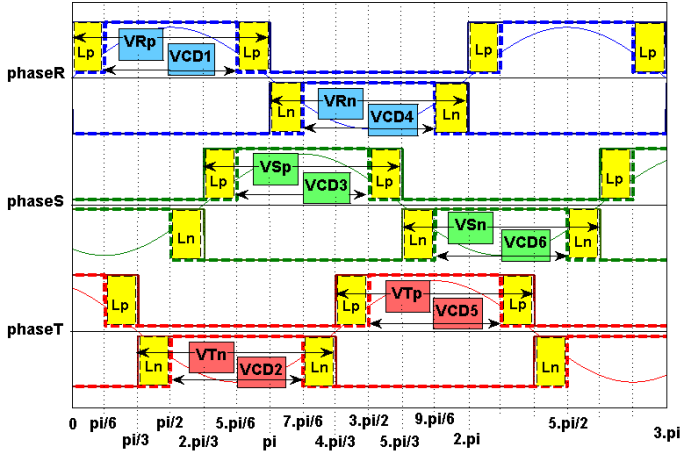


Fig. 5. Waveform of Subsystems positive/negative High Voltage and positive/negative Phases

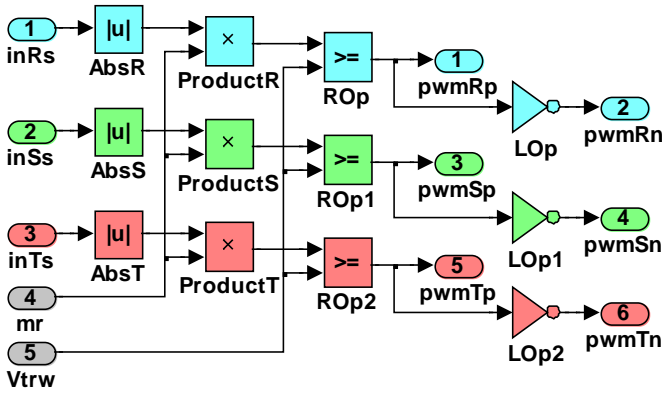


Fig. 6. Subsystem Pulse Width Modulation

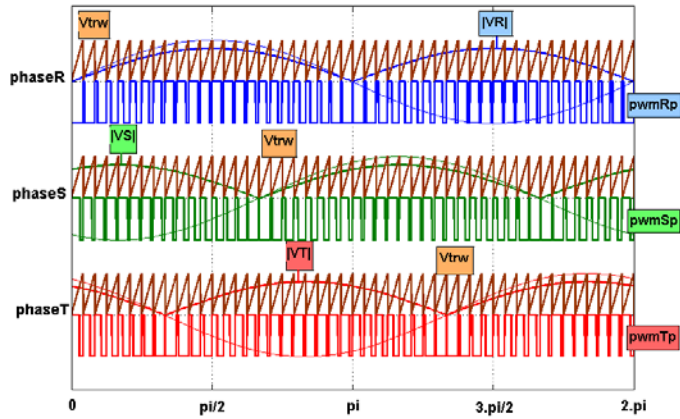


Fig. 7. Waveform of Subsystem Pulse Width Modulation

Their corresponding inverse logical values are denoted as negative values (pwmRn, pwmSn and pwmTn). Only positive PWM logical signals are presented in Fig. 7. The modulation coefficient can be varied by the signal mr ($0 < mr < 1$).

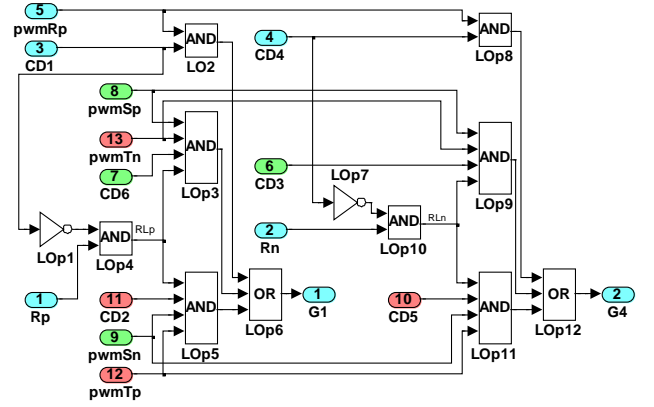


Fig. 8. Subsystem Gate Pulses 1-4

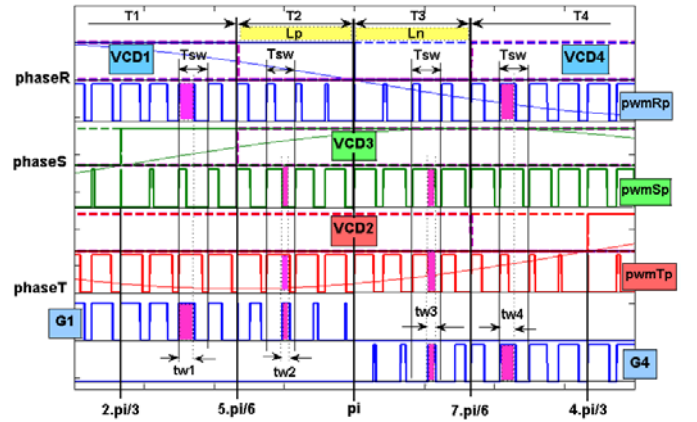


Fig. 9. Waveform of Subsystem Gate Pulses 1-4

C. Subsystem Gate Pulses 1-4

The circuit realizing the Subsystem Gate Pulses 1-4 is shown in Fig. 8. The modulated according sinusoidal law signals $G1$ and $G4$ are created using this logical circuit. The signals $G1$ and $G4$ commute the switches $Sw1$ and $Sw4$ correspondingly (Fig.1), which are connected to power phase R (VRp).

The operation of the circuit is illustrated by the waveforms, presented in Fig. 9.

For the intervals, where the phase R is the most positive ($VCD1=1$; interval $T1$), Gate Pulses $G1$ coincide with those of $pwmRp$.

For the intervals, where the phase R is the most negative ($VCD4=1$; interval $T4$), Gate Pulses $G4$ also coincide with those of $pwmRp$.

The elements ($LOp1, LOp4$) and ($LOp7, LOp10$) realize the corresponding functions:

$$RLp = \overline{VCD1} \cdot VRp \quad \text{and} \quad RLn = \overline{VCD4} \cdot VRn$$

It is seen from Fig. 5, that those are the intervals where $VRp=1$ and $VCD1=0$ (denoted in Fig. 5 as Lp) and the intervals where $VRn=1$ and $VCD4=0$ (denoted in Fig. 5 as Ln).

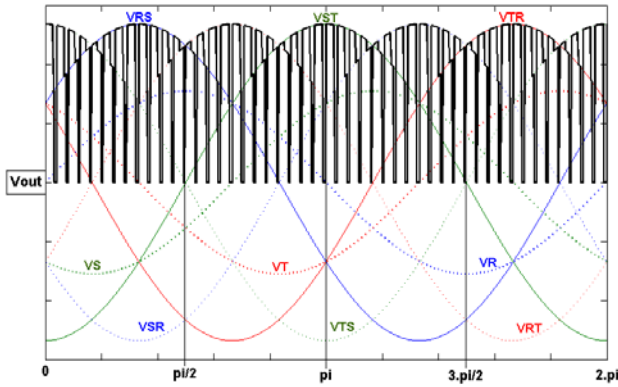


Fig. 10. Waveform of PWM output voltage

For the intervals L_p , Gate Pulses $G1$ are generated corresponding to the logical function:

$$G1 = (\text{pwmSp} \cdot \text{pwmTn} \cdot \text{VCD6} \cup \text{pwmTp} \cdot \text{pwmSn} \cdot \text{VCD2}) \cdot \text{RLp} \quad (1)$$

For the intervals L_n , Gate Pulses $G4$ are generated corresponding to the logical function:

$$G4 = (\text{pwmSp} \cdot \text{pwmTn} \cdot \text{VCD3} \cup \text{pwmTp} \cdot \text{pwmSn} \cdot \text{VCD5}) \cdot \text{RLn} \quad (2)$$

The result of the functions (1) and (2) for the intervals $T2(L_p)$ and $T3(L_n)$ can be seen from the waveforms, shown in Fig. 9.

The inner configuration of Subsystem Gate Pulses 3-6 and Subsystem Gate Pulses 5-2 coincides with those shown in Fig. 8. The generation of Gate Pulses 3-6 and Gate Pulses 5-2 is similar to the described above, taking into account the corresponding input signals.

D. Simulation results for the output voltage

The waveform of the output voltage V_{out} on the load resistor R_{load} is shown in Fig. 10.

It is pulsing as in the three-phase bridge rectifier with a frequency 6 times higher than the mains frequency.

Due to the sinusoidal PWM, the mean value of V_{out} for each period of the modulating frequency, remains a constant value

III. CONCLUSION

A three-phase BUCK rectifier with sinusoidal PWM that improves the power factor has been considered in the present paper. The building blocks are described and the algorithm for control is synthesized. A Matlab-Simulink model is constructed based on this algorithm. The simulation results are given illustrating the mode of operation of the functional blocks and the waveforms of the signals are presented.

REFERENCES

- [1] Power Factor Correction (PFC) Handbook, ON Semiconductor, Rev.4, Feb 2011, www.onsemi.com/pub/Collateral/HBD853-D.PDF
- [2] P.M. Barbosa, "Three-Phase Power Factor Correction Circuits for Low-Cost Distributed Power Systems", PhD diss., Virginia Polytechnic Institute and State University, 2002.
- [3] R.W. Erickson, Some Topologies of High Quality Rectifiers, First International Conference on Energy, Power, and Motion Control, May 5-6, 1997, Tel Aviv, Israel. (pp. 1-6).
- [4] T. Nussbaumer, J.W. Kolar, Advanced Modulation Scheme for Three-Phase Three-Switch Buck-Type PWM Rectifier Preventing Mains Current Distortion Originating from Sliding Input Filter Capacitor Voltage Intersections, Power Electronics Specialist Conference, 2003. PESC'03, 2003 IEEE 34th Annual, vol. 3, pp. 1086-1091, 2003.
- [5] B.N Singh, A. Chandra, K. Al-Haddad, A. Pandey, D.P. Kothari, A Review of Three-Phase Improved Power Quality AC-DC Converters, IEEE Transactions on Industrial Electronics, v. 51, n.3, pp. 641-660, 2004.

Microprocessor-based Apparatus for Electrical Stimulation of Ruminant Meat

Ivan Maslinkov¹ and Krassimir Kolev²

Abstract – A microprocessor-based device for electrical stimulation of ruminant meat is designed by AT89C2051 microcontroller. The paper considers the action principle by structural and time diagrams of ruminant meat stimulator. The microprocessor-based apparatus stimulates the meat with a safety low voltage. The designed apparatus has six different stimulation modes. The schematic diagram and an algorithm description of designed apparatus are given. Analyses and recommendations are made.

Keywords – Electrical stimulation, Microprocessor-based apparatus, Meat of ruminant animals.

I. INTRODUCTION

Electrical stimulation of ruminant meat is a world-wide established operation where electrical current (pulses) of certain parameters [1-4] is applied through the carcass (or parts thereof). As a result, the technological cycle is shortened, the quality of meat and the hygiene are improved, etc. [1].

Advancements in the electrical engineering, electronics and automation resulted in an increased number of mass produced and marketed devices (or assemblies and parts for such devices) equipped with standardized inputs and outputs, allowing for programming (setting up) of wide ranges and various modes and fitted with built-in logical functions, etc. [2,3].

The aim of this paper is to present a microprocessor-based device for electrical stimulation of ruminant meat incorporating a mass produced microcontroller AT89C2051.

II. DESIGN DIAGRAM AND OPERATING PRINCIPLE

Requirements to parameters of the device for electrical stimulation using low (amplitude of electrical pulses up to 100 ÷ 110 V) voltage are [3]:

- process duration is within 60 s ;
- voltage pulse amplitude (U_{MAX}) minimum 60÷70 V ;
- current pulse amplitude minimum 50 mA ;
- pulse duration (t_{PLS}) about 5÷10 ms ;
- recommended pulse repetition frequency (f) 10÷100 pulses/s, no operation under 10 pulses/s since the carcass

¹Ivan Maslinkov is with the Technical Faculty at University of Food Technologies Plovdiv, 26 Maritsa Blvd, Plovdiv 4000, Bulgaria E-mail: imm@uft-plovdiv.bg.

²Krassimir Kolev is with the Technical Faculty at University of Food Technologies Plovdiv, 26 Maritsa Blvd, Plovdiv 4000, Bulgaria E-mail: k_kolev@uft-plovdiv.bg.

contracts at each pulse and the contractions, particularly in the beginning, are strong and bone fractures may occur ;

- rectangular pulse shape.

It should be noted that the shape of the pulses is not of significance but the most commonly used shape is rectangular as it is easier to obtain [3, 4]. The polarity of the pulses is also of no significance, however (heteropolar) pulses are recommended having alternating polarity to reduce the impact of polarization effects [5].

The maximum output current for the low-voltage stimulators does not exceed 1 A [3, 4] which must be borne in mind when selecting the stimulator components.

There are also other requirements to the electrical stimulation apparatuses, such as:

1. In the first 5÷7 s the pulse amplitude must increase from 10÷20 V to 60÷70 V, and the by the end of the stimulation it reaches 80÷90 V (or up to 110 V, if the effective voltage value is safe) [5]. This is to avoid the violent and abrupt contractions of the carcass at the start of the stimulation;

2. In [3] there is a recommendation to stimulate using electrical pulses with gradual (the said paper specifies exponential) reduction in their frequency from 100 pulses/s at the start of the stimulation to 10 pulses/s at its end since muscle fatigue occurs during the process (and they cannot respond effectively to the higher frequencies) and habituation to unvaried stimuli. It is advisable to reduce the frequency when the amplitude is increased.

Fig. 1 shows the block diagram of the proposed microprocessor-based apparatus, and Fig. 2 shows time-diagram of its output electrical pulses (u_{out}) with which the meat is being treated.

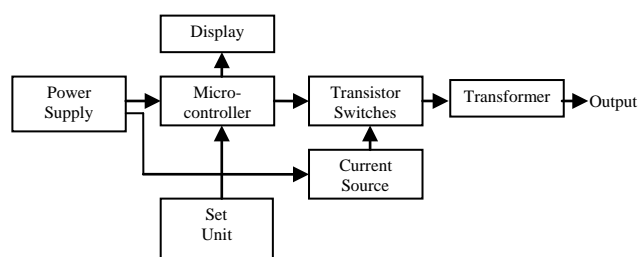


Fig. 1. Block diagram

Both figures illustrate the principle of operation of the proposed apparatus where the stimulation was performed with rectangular heteropolar pulses

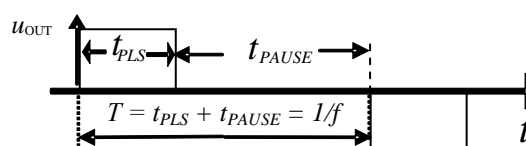


Fig. 2. Time-diagram of output pulses

The apparatus in Fig.1 consists of:

- power supply which provides safe continuous voltage of 9 V for the operation of the stimulator;
- microcontroller to control and form the string of pulses (t_{PLS}) and pauses (t_{PAUSE}) between them as well as the frequency of pulse repetitions (f) to control the transistor switches;
- transistor switches which perform switching action and produce the output rectangular pulses;
- current source for constant safe charge;
- set unit for selecting the stimulation mode;
- display to show the selected stimulation mode.

III. DESIGN OF THE APPARATUS

The second voltage which must supply the transformer is selected so as to ensure the minimum of the pulses' amplitude at the output of the apparatus ($U_{MAX} \geq 60\div 70$ V) while their effective value (U) must not exceed the safe 24 V. The latter depends on the amplitude, duration, shape and the repetition frequency of the pulses used [5]. The following formula applies:

$$U = U_{MAX} \sqrt{f \cdot t_{HMI}} \quad (1)$$

If, for example, $U \approx 24$ V, $U_{MAX} \approx 90$ V and $f = 15$ pulses/s are to be selected, the pulse duration for this configuration is $t_{PLS} \approx 5$ ms. For this configuration it is better to increase the duration $t_{PLS} \approx 7$ ms in order for it not to be at the lower limit and to decrease the frequency ($f = 12$ pulses/s) and the amplitude of the output pulses ($U_{MAX} = 80$ V). It is apparent that the power of the transformer is under 50 VA and the price is around EUR 25 [6].

It is advisable that the transistor switches, in addition to conforming with the specified current and voltage, be able to switch on and off with small losses, i.e. to have the so called soft switching.

Each electrical apparatus needs a suitable housing and power supply of 9 V DC which in this case are expected to cost around EUR 35.

The minimum pulse amplitude value provided in the beginning has any significance only if the output current is being monitored in the stimulator. In fact, it would be more precise to state that only by ensuring minimum value of the current density will it be possible to provide quality stimulation [5]. The design of the microprocessor stimulator is based on a low-budget widely available microcontroller AT89C2051 by Atmel at a price of EUR 1 [6]. The AT89C2051 provides the following standard features: 2K bytes of Flash, 128 bytes of RAM, 15 I/O lines, two 16-bit timer/counters, a five vector two-level interrupt architecture, a full duplex serial port, a precision analog comparator, on-chip oscillator and clock circuitry. The Port 1 is an 8-bit bi-directional I/O port. Port pins P1.2 to P1.7 provide internal pull-ups. P1.0 and P1.1 require external pull-ups. P1.0 and P1.1 also serve as the positive input (AIN0) and the negative input (AIN1), respectively, of the on-chip precision analog

comparator. The Port 1 out-put buffers can sink 20 mA and can drive LED displays directly. When 1s are written to Port 1 control register, its pins can be used as inputs. When pins P1.2 to P1.7 are used as inputs and are externally pulled low, they will source current because of the internal pull-ups [7]. The basic schematic diagram of the stimulator is shown on Fig.3. The microcontroller IC1 (AT89C2051) is programmed to generate rectangular pulses at its outputs Rx and Tx upon pressing the start S1 button. These pulses control the MOSFET transistors T1 (IRF540) and T2 (IRF540) which switch the voltage over to the primary winding of the TR1 transformer. The transformer is a step-up line audio with transformer ratio of ten and power of 30 W. The magnitude of the output current is determined by a current source consisting of the transistor T3 (BD140) and the passive components R1, R3 and C6. The current source charges the capacitor C6 to a safe charge. The voltage of this capacitor is used to supply the transistor switches T1 and T2. The circuitry shaping the output pulses is designed as a traditional push- pull topology converter with transformer galvanic isolation. The maximum energy transferred for a switching cycle is:

$$E = \frac{C \cdot U^2}{2}, \quad (2)$$

where C is the capacity of capacitor C6, and U is the supply voltage.

With the values thus selected, the maximum transferred energy is $E=4.05mJ$, which is way under the permissible threshold value of 300mJ for the electrical safety of electrical stimulators [8]. This ensures that the device is safe as it provides reduction of the transferred energy for each switching cycle.

A question may be asked as to why a microcontroller is being used to generate pulses when this can be done using timer integrated circuits of the 555 type. In addition to the selected controller being sold on the market at a price comparable to the one of the timer integrated circuits, it is possible to introduce additional software-based features and various stimulation modes. Moreover, in case of fault, the microcontroller stops the execution of the system software and the generation of pulses to the transistor switches, i.e. the frequency and the cycle of pulses do not depend on external time-setting components.

The S2 button (PROG) is used to select among the six stimulation modes (1÷6) which are displayed on the 7-segment LED indicator LD1. If no mode has been selected, the indicator displays zero and the simulator cannot be started. After selecting a mode, the stimulation process is initiated using S1 (START). The duration of the stimulation process is 60 seconds according to the technology [5].

The pulses are of duration t_{PLS} and variable frequency f in order to form variable intensity of meat treatment for the six different modes. Fig. 4 shows the diagrams for the intensity of treatment for the different program modes.

LED D2 indicates that the stimulator functions properly. The C3 and R5 group is standard for the processor and produces the signal for the initial resetting after the switch on of the power supply.

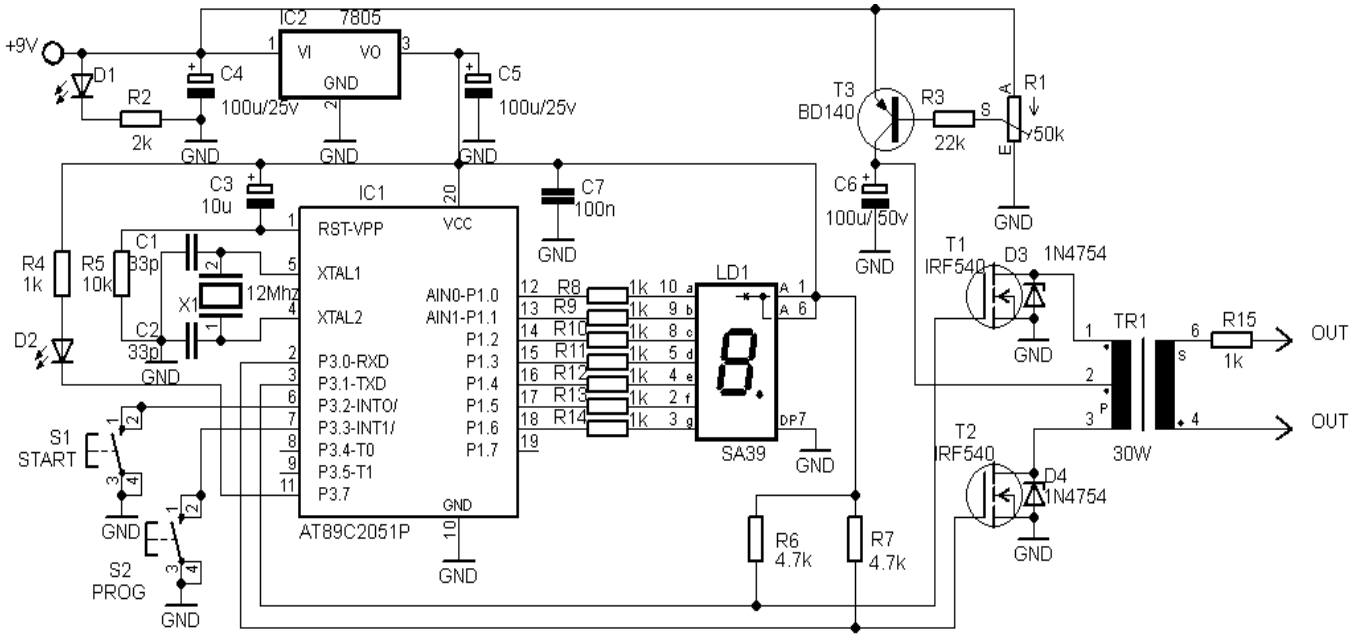


Fig. 3. Schematic diagram of the microprocessor stimulator

A 12 MHz quartz resonator has been selected and the internal system microprocessor clock is with precise value of $1 \mu\text{s}$ for all microcontroller subsystems.

The value of the active electronic components of the presented ruminant meat stimulator is under EUR 10 [6]. Hence the total costs of the materials do not exceed EUR 75. If the labor costs are to be taken into account, the total value of the designed multifunctional apparatus can reach around EUR 110.

The software consists of a main program and an interrupt service routine.

The main program performs initialization, allows interrupts of the timer and the external inputs P3.2 and P3.3. The interrupt service routine controls all processes in real time such as monitoring the stimulation time, servicing the buttons and generation of rectangular pulses at outputs P3.0 и P3.1. The internal timer 0 operates in mode 3 where its clock frequency 1 MHz is divided by 256 [9]. The timer 0 generates an interrupt each $256 \mu\text{s}$. Interrupts are counted and the circuitry is controlled. The program actually comprises a finite-state machine which activates outputs P3.0 and P3.1 in sequential order. The P3.0 output is established at high level every odd cycle of t_{PLS} generation, and the P3.1 output at high level every even cycle of t_{PLS} generation.

The value of t_{PLS} is set in a table format based on the number of interrupts from timer 0 for each stimulation mode based on the desired pulse duration. The numbers of interrupts are equal to the desired t_{PLS} in ms multiply by 1000 and divide to 256. For example, for $t_{PLS} = 7 \text{ ms}$ we set 27 interrupts for timer 0 by look-up table in the program read only memory on AT89C2051. The number of interrupts forming the pause cycle are equal to $1/f$ multiply by 15625 divide to 4 minus number of interrupts for t_{PLS} .

Processing time is fixed for all operation modes and is obtained after producing 234375 interrupts.

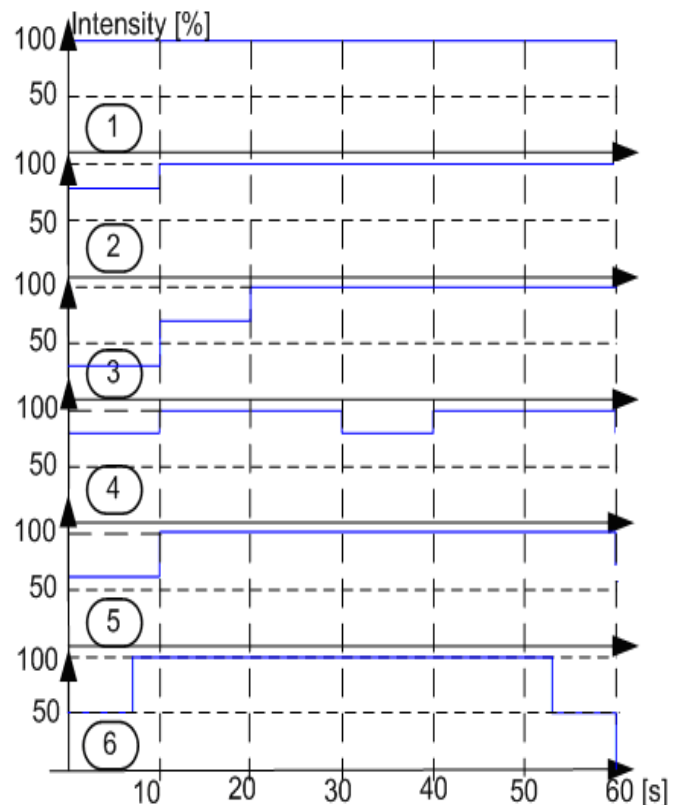


Fig. 4. Operation modes

The program allows for the processing to be interrupted by pressing again the S1 or S2 buttons. Figure 5 shows the algorithmic diagram for the interrupt service routine.

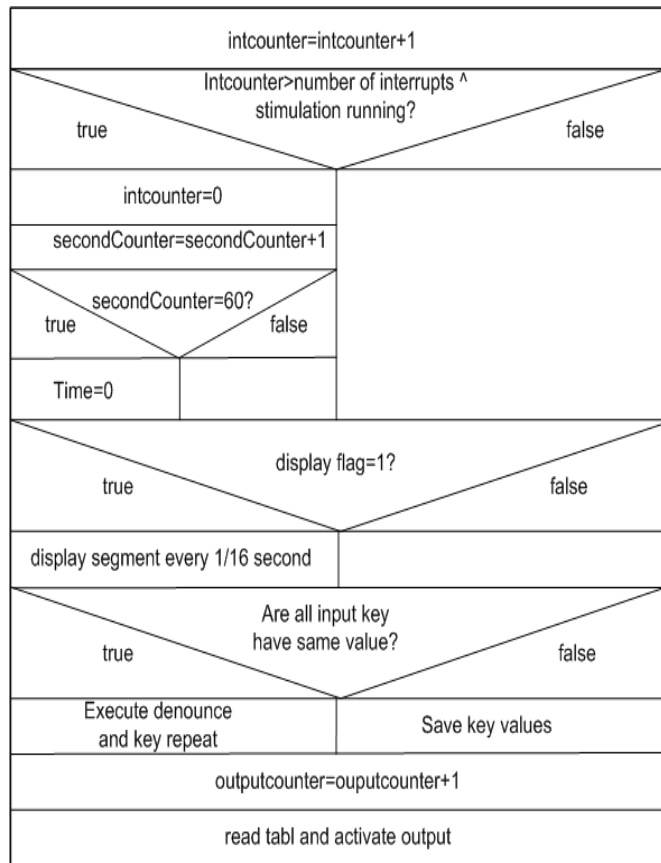


Fig. 5. Algorithmic diagram for interrupt service routine

The intcounter monitors the number of pulses per second. The secondCounter is used to set and monitor the fixed processing time. At any time, using the S1 and S2 buttons, it is possible to interrupt the servicing of the timer and stop the stimulation process. Based on the produced timer interrupts, values controlling the outputs for the next produced cycle are loaded from a table located in the internal program read only memory.

The main program checks whether a specific button has been pressed. The program operates in an infinite loop until a button is pressed.

Firmware of the proposed microprocessor-based apparatus is written in C programming language using freeware Crimson editor [10] and burn to the microcontroller by using Willar SP200S programmer [11].

Before operating the apparatus, the personnel must be made aware of the electrical safety precautions and only a certification safe double galvanically decoupled source of 9 V dc with power of 50 W must be used [12]. The selection of transistors and diodes is not crucial and other types may be used considering switching currents and supply voltages.

IV. CONCLUSION

This paper discusses a microprocessor based design and configuration of an apparatus for electrical stimulation of ruminant meat built using a mass produced, widely available and low-budget microcontroller AT89C2051.

The operating principles and manner of its construction have been explained. The presented stimulator supports six program selectable stimulation modes. Since the program modes are implemented through software, it is possible, without making changes in the circuitry, to expand the set programs up to fifteen. If a second seven segment indicator element is added, the selectable programs can be increased up to ninety-nine. The cost of the proposed device is around EUR 110.

REFERENCES.

- [1] A. Asghar, R. L. Henrickson. Post-mortem Electrical Stimulation of Carcasses: Effects on Biochemistry, Biophysics, Microbiology and Quality of Meat, Tech. Bulletin T-156, April, 1982, AES, Oklahoma State University, Oklahoma, USA..
- [2] D. Tsankov, Iv. Maslinkov, G. Mihov. Improved Method for Electrical Stimulation of Beef and Lamb Carcasses, 33rd International Congress of Meat Science and Technology, 2-7.08.1987, Helsinki, Finland, vol. I, 128-130.
- [3] D. Tsankov, I. Maslinkov. Apparatus for Electric Stimulation of Meat by Means of Alternating Frequency Impulses, Scientific Works of Higher Institute of Food and Flavour Industries, Plovdiv, 1991, Vol. XXXVIII, Roll 1, 239-245. (in Bulgarian)
- [4] D. Tsankov, I. Maslinkov. Apparatus for Meat Stimulation by Means of Electric Pulses with a Random Law Changing Frequency, Scientific Works of Higher Institut of Food and Flavour Industries, Plovdiv, 1993, Vol. XXXX, 413-419. (in Bulgarian)
- [5] I. Maslinkov, Electronic Apparatus for Electrical Stimulation of Meet of Ruminant Animals, International Scientific Conference "Unitech 2013", 22-23.10.2013, Gabrovo, Vol. I, 211-215. (in Bulgarian)
- [6] Comet Electronics katalogu, (www.comet.rs), 2014.
- [7] Atmel, AT89C2051 Microcontroller 0368H-MICRO-6/08 data sheet, 2008.
- [8] International Electrotechnical Commission, International Standard IEC 60601-1, Edition 3.1, Geneva, Switzerland, 2012.
- [9] M. A. Mazidi, R. D. McKinlay, J. G. Mazidi, The 8051 Microcontroller: A Systems Approach, Pearson, 2013.
- [10] I. Kang, Crimson Editor, www.crimsoneditor.com , 2014.
- [11] F. Liu, Willar SP200S programmer manual, www.willar.com, 2014.
- [12] D. Prutchi, M. Norris. Design and development of medical electronic instrumentation: a practical perspective of the design construction and test of material devices, John Wiley & Sons Inc., New Jersey, 2005.

A Microprocessor System for Food Quality Evaluation by Hyperspectral Images

Krassimir Kolev¹

Abstract – The paper reports on the development of a microprocessor system base on video signal processor DM642 for food quality evaluation by hyperspectral images processing. The presented microprocessor system captures hyperspectral sliced images and makes images processing. The schematic diagram of the microprocessor system, hardware structure description, algorithm description for preprocessing by wavelet transformations and quality features reduction are given. Quality features reductions are made by extraction transformations. Experiments show that the microprocessor system has a good performance for objective quality evaluation of meat products.

Keywords – Microprocessor system, hyperspectral images, food quality.

I. INTRODUCTION

Acquisition and processing of hyperspectral images is a new promising technology successfully combines the advantages of computer vision and spectroscopy methods for modern objective contactless quality food evaluation. Hyperspectral technology is a contactless nondestructive, requires no pre-treatment of samples obtained both spatial and spectral information for foods allows a more complete description of the constituent concentration and distribution in heterogeneous foods. Hyperspectral technology is very sensitive to detect small components in the samples and allows examination of foods with different geometries. Processing of hyperspectral images of food requires fast image processing hardware. Many authors report that they use hyperspectral images for food evaluation, but they have not published details of their computer systems for processing [1]. The goal of this paper to report a microprocessor system for food quality evaluation by hyperspectral images processing.

The author designs a full working microprocessor system and implements algorithms for preprocessing and features extraction for food assessment. The author uses a digital signal processor (DSP) for his proposed microprocessor system, because modern DSPs are flexible and suitable to extremely complex math intensive tasks such as hyperspectral image processing. The presented system is suitable for testing and grading for all types of food by conveyer moving. Hyperspectral scanning is not matter of this paper. Some basic algorithms are developed for system performance tests,

¹Krassimir Kolev is with the Technical Faculty at University of Food Technologies Plovdiv, 26 Maritsa Blvd, Plovdiv 4000, Bulgaria, E-mail: k_kolev@uft-plovdiv.bg.

because we know that microprocessor are useless without software.

II. DESIGN DIAGRAM AND COMPONENTS

Considering the details of the different scanning systems for obtaining hyperspectral images is possible to synthesize modern model of computer platform for objective non-destructive quality assessment of food by processing hyperspectral images. Computer platform for determining the quality characteristics of foods consist of interconnection hardware and software components.

A model design diagram of computer platform for food quality evaluation is given in Fig.1.

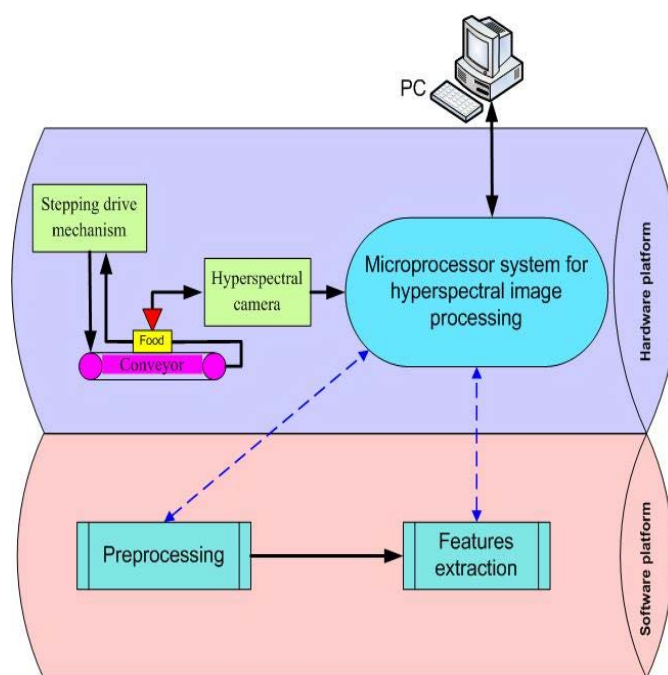


Fig.1. Design diagram of the computer platform

Presented model of the computer platform in Fig.1 shows that the hardware platform consists of stepping drive mechanism, conveyor, hyperspectral camera and microprocessor system for hyperspectral image processing. The paper highlights subsystems making hyperspectral image processing. Hardware subsystem (microprocessor system for hyperspectral image processing) consists of a high performance DSP for image processing.

Software subsystem is divided into algorithmic modules (preprocessing and features extraction) according to the tasks performed by the software associated with the preprocessing hyperspectral images and reduction of feature space.

Diagram of the hardware subsystem is shown in Figure 2.

The MT9V022 image sensor was chosen for hyperspectral camera due to its suitability for hyperspectral imaging, because it can be used in the wavelength range from 300 nm to 1100 nm of the spectrum [2]. The image sensor provides a resolution of 10 bits per pixel, is able to capture both continuous video and single frames progressively.

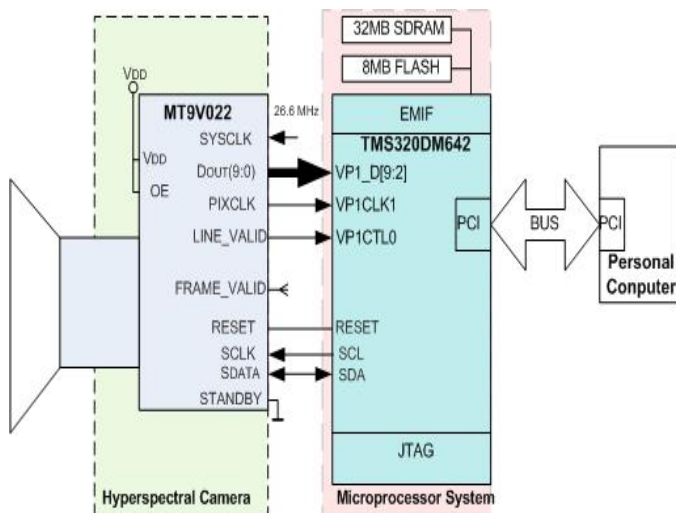


Fig. 2. Diagram of the hardware subsystem

All image sensor registers are written and read through the I²C serial interface. The I²C address of the MT9V022 is fixed and consists of seven bits of address and 1-bit of read/write direction. Full registers descriptions are given in datasheet of MT9V022 [2]. The image sensor interfaced to the microprocessor system through the video port of DSP TMS320DM642 (DM642). The FRAME_VALID signal on the MT9V022 is unconnected because no input exists on the DM642 which can take advantage of this signal. However, the FRAME_VALID line is not needed since the information necessary for proper operation with the DM642 is carried on the LINE_VALID signal. Recall that the LINE_VALID and FRAME_VALID signals indicate that a line and frame of valid pixel data is available on the data bus. Because the DM642 samples data when VP1CTL0 is active, proper video port and MT9V022 operation requires that the LINE_VALID signal to be connected to the VP1CTL0 signal [3].

I use the high performance DSP chip TMS320DM642 of Texas Instrument (TI) as a core, design and realize a whole hardware subsystem. The TMS320DM642 (or DM642) offers cost-effective solutions to high-performance DSP programming challenges with up to 5760 MIPS at a clock rate of 720 MHz. Its core processor has 64 general-purpose registers of 32-bit word length and eight highly independent functional units—two multipliers for a 32-bit result and six arithmetic logic units [4]. The VelociTI™ extensions in the eight functional units include new instructions to accelerate the performance in video and imaging applications and extend the parallelism of the VelociTI™ architecture. The DM642 can produce four 16-bit multiply-accumulates (MACs) per cycle for a total of 2880 million MACs per second (MMACS), or eight 8-bit MACs per cycle for a total of 5760 MMACS. The DM642 uses a two-level cache-based architecture and has a powerful and diverse set of peripherals. It also has a 64-bit

seamless External Memory Interface (EMIF), which can interface to synchronous and asynchronous memories and peripherals. The TMS320DM642 DSP is IEEE-1149.1 JTAG boundary scan compatible. In order to support multimedia applications, the DM642 device has been integrated with 3 configurable Video Port (VP0, VP1, and VP2) peripherals and Multi-Channel Audio Serial Port (MCASP). The inter-integrated circuit (I²C) module provides an interface between a DM642 and other devices compliant with Philips Semiconductors Inter-IC bus (I²C bus). The I²C port on the TMS320DM642 allows the DSP to easily control peripheral devices. The PCI port for the DM642 supports connection of the DSP to a PCI host via the integrated PCI master/slave bus interface. For the DM642, the PCI port interfaces to the DSP via the EDMA internal address generation hardware. This architecture allows for both PCI Master and Slave transactions, while keeping the EDMA channel resources available for other applications [5, 6].

III. DESIGN OF THE SYSTEM

A. Hardware Structure

Schematic diagram of the designed microprocessor system for food quality evaluation is given in Fig. 1.

The microprocessor system has a large byte addressable address space. Program code and data can be placed anywhere in the unified address space. The given system incorporates a 64 bit wide external memory interface.

Addresses are always 32-bits wide. By default, the internal memory sets at the beginning of the address space. The EMIF (External Memory Interface) has 4 separate addressable regions called chip enable spaces (CE0-CE3). The DM642 uses chip enables CE0, CE1, and CE3. The SDRAM occupies CE0 while the Flash is mapped to CE1. DM642 signals CE2 and CE3 can be used for extra components connection and expanded RAM. The microprocessor system has 32 megabyte SDRAM realized by IC7, IC8. The bus uses an external phase lock loop (PLL) device to operate the SDRAM at 133 megahertz for optimal performance. Refresh for SDRAM is handled automatically by the DM642. The PLL used for the EMIF is the IC5. The input clock to this ICS512 is 25 Megahertz via IC4. The system has 8 megabytes of Flash external memory (not shown in diagram) and connected as SDRAM to address and data bus and activates by CE1. The DM642 directly supports a PCI interface. Cross Bar Technology (CBT) mux and switches are used to separate the PCI bus from the DM642 so that the CBT's also provide +5 volt interface logic support for the PCI interface. The CBT's are automatically configured for PCI operation when the board is plugged into a PCI slot via the PCI-Detect signal. The DM642 has an internal PLL which can multiply the input clock to generate the internal clock. The PLL multiplier is set via the CLKMODE0 and CLKMODE1 pins on the DM642 device. At reset these pins are sampled, and this determines the PLL multiplier for the internal CPU clock. EEPROM IC9 connects to DM642 via I2c and it has clock generator IC10. IC6 generates reset signal for the system.

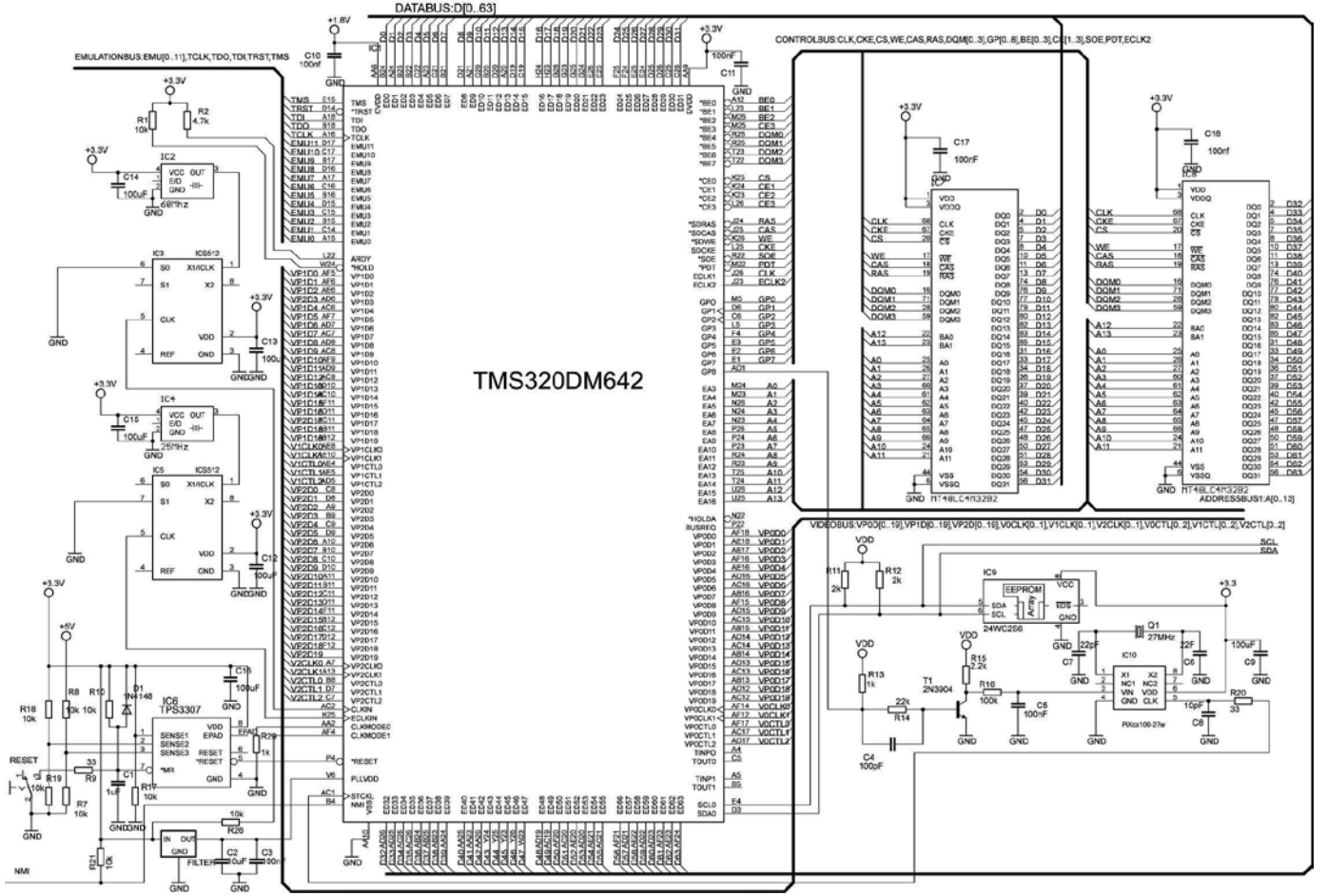


Fig. 3. Schematic diagram of the microprocessor system

B. Software Structure

Preprocessing

The hyperspectral images of food taken down in steps constitute two-dimensional images subdivided in subspaces by using multiple-resolution approximation of the initial space into low-frequency components – constituting optimum approximation and into high-frequency components constituting detailed information of the original signal [7]. The decomposition coefficients in the wavelet orthogonal basis are divided by:

$$c_{j,k,l} = \sum_{m=-\infty}^{+\infty} \sum_{n=-\infty}^{+\infty} h_{m-2k} h_{n-2l} c_{j-1,m,n} \quad (1)$$

$$d_{j,k,l}^1 = \sum_{m=-\infty}^{+\infty} \sum_{n=-\infty}^{+\infty} h_{m-2k} g_{n-2l} c_{j-1,m,n} \quad (2)$$

$$d_{j,k,l}^2 = \sum_{m=-\infty}^{+\infty} \sum_{n=-\infty}^{+\infty} g_{m-2k} h_{n-2l} c_{j-1,m,n} \quad (3)$$

$$d_{j,k,l}^3 = \sum_{m=-\infty}^{+\infty} \sum_{n=-\infty}^{+\infty} g_{m-2k} g_{n-2l} c_{j-1,m,n} \quad (4)$$

, where c_j are approximation coefficients, d_j are the detailing coefficients.

The sequence $H = \{h_k \mid k = \dots, -2, -1, 0, 1, 2, \dots\}$ is designated as a scaling filter.

The sequence $G = \{g_k \mid k = \dots, -2, -1, 0, 1, 2, \dots\}$ is designated as a wavelet filter.

For Haar wavelet $h_0 = 1/\sqrt{2}$, $h_1 = 1/\sqrt{2}$, $g_0 = 1/\sqrt{2}$ and $g_1 = 1/\sqrt{2}$.

The filters divide the input signal into frequency bands. The filtered signals at the exit of the filters are obtained with double length, so after the filtration decimation is performed, i.e. removal of all odd coefficients.

The high-frequency filter (H) is related to $\psi(t)$, while the low-frequency filter (L) is related to $\phi(t)$.

The processing of images $f(x, \lambda)$ with an array of dimensionality (N,M) is performed separately by rows and columns, by first performing 1-D convolution with coefficients $h_0(k)$ /low-frequency filter L/ and $h_1(k)$ /high-frequency filter H/. After that follows a decimation with a factor 2 i.e. a new array is obtained (N/2,M).

Upon processing by columns also 1-D convolution $h_0(k)$ /low-frequency filter L/ is applied and $h_1(k)$ /high-frequency filter H/ and then decimation with a factor 2.

Thus a single high-scale approximation is performed. As approximating coefficients C_1 are in a matrix form with dimensionality $(N/2, M/2)$. It is possible to apply for a second time high-scale approximation on the matrix with approximation coefficients whereby a new reduction of the feature space is obtained up to approximation coefficients C_2 . This process of dual-scale approximation has been illustrated in Figure 4.

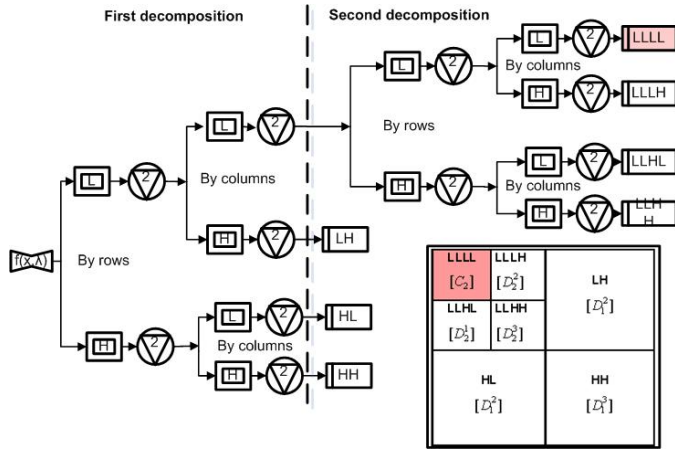


Fig. 4. Diagram of two levels transform of sliced hyperspectral image

Feature Extraction by Independent Component Analysis (ICA)

To estimate n independent components, the algorithm is run for n times. The steps of Fast-ICA for separating an independent component are shown.

1. Pre-whiten the observed image data to obtain a whitened signal v .
2. Take a random initial vector $w(0)$ and normalize it to unity, i.e., $w(0) = w(0) / \|w(0)\|$, and set $j = 1$.
3. Set $w(j) = E\{v(w(j-1)^2 v)\} - 3w(j-1)$. The expectation operator can be estimated using a large number of samples.
4. Set $w(j) = w(j) / \|w(j)\|$ i.e., normalize $w(j)$.
5. If $|w^T(j)w(j-1)|$ is not close to 1, then set $j = j+1$ and repeat step 3. Otherwise output vector $w(j)$.
6. Using $w(j)$, one of the separated signals is given by

$$s(k) = w^T(j)v(k), \quad k = 1, 2, \dots$$

An orthogonalizing projection has to be added inside the recursive loop of this algorithm to estimate different components each time.

C. Testing of the System

The development test of the proposed microprocessor system was made by JTAG emulator XDS560 connected between DM642 and personal computer ASUS M51AC i7.

The performance of data processing is tested in real-time. The connection of Video Port 1 to hyperspectral camera is

similar to the way described in this paper. The data for test is 320x240x16bits video stream from hyperspectral camera CCD sensor. In the experiment 24 linearly scanned hyperspectral images were used of ready-to-cook minced meat products. The algorithms are realized in C program environment for digital signal processor DM642 of Texas Instruments. The analysis of the video signal is line oriented. Table 1 shows the results obtained per time for machine processing for one step of scanning /one slice/ for each of the algorithms realized upon fixed eight features of reduction.

TABLE 1
VALUES OF PROCESSING TIME IN HARDWARE IMPLEMENTATION

Algorithms	Machines cycles	Processing Time Value [s]
Initialization	2125	$1.53 \cdot 10^{-06}$
Preprocessing (dual-scale Wavelet)	169444444	0.061
Features Extraction	6337722222	2.28158
Total:	6507168791	2.34258

The actual power consumption in this experiment with proposed microprocessor system based on DM642 is 6.47 W. The total maximum power consumption of all components of the microprocessor system is less than 9 W, according to component manufacturers.

IV. CONCLUSION

The performance test result shows that this microprocessor system has total processing time under 120 seconds per 50 slides quality tracking. This system could be applied to build computer platform for fast objective quality food evaluation by hyperspectral image processing. The proposed microprocessor system based on high performance video signal processor DM642 has small size and can use as mobile quality evaluation platform on production lines and shops.

REFERENCES

- [1] D. Sun, Hyperspectral Imaging for Food Quality Analysis and Control, Elsevier, 2010.
- [2] Aptina Imaging Corporation, MT9V022 Digital Image Sensor Data sheet MT9V022_DS - Rev.H 6/10 EN, USA, 2006.
- [3] M. Hernandez, Interfacing a CMOS Sensor to the TMS320DM642 Using Raw Capture Mode, Texas Instruments Inc., 2004.
- [4] M. Qadri, I. Usmani, M. Khan, S. Mehmood, IPTV using DM642 Multimedia Processor and Bluetooth, International Conference on Machine Learning and Computing IPCSIT, IACSIT Press, Singapore, vol.3, p.466-471, 2011.
- [5] TMS320DM642 Video/Imaging Fixed-Point Digital Signal Processor Data Manual, Literature Number: SPRS200E.
- [6] S. Qureshi, Embedded Image Processing on the TMS320C6000™ DSP, Springer Science+Business Media, New York, USA, 2005.
- [7] K. Kolev, Reducing the hyperspectral feature spaces of ready-to-cook minced meat products, International Journal „Agricultural Science And Technology“, Vol. 5, No. 1, p. 121-125, 2013.

Preparation of Germanium Photo Detectors and Photovoltaics

Silvija Letskovska¹ and Kamen Seymenlijski¹

Abstract – The design and technology of Germanium based photo devices are described. They could work as photo detectors – resistors and diodes, and in photovoltaic mode. The main laboratory works are made using mono crystal Ge for photo resistors and the system nGe–Metal (Ag) Schottky junction. The photo parameters are measured in the range of 0.6 ÷ 2.0 micrometer.

Key words - photo detectors, germanium, infrared detectors, germanium photocell.

I. INTRODUCTION

Germanium is one of the first semiconductor materials for electron devices (p/n junctions). The distance between E_C and E_V , $\Delta E = 0.65(eV)$ makes germanium suitable for photo devices in infrared range of light – $\lambda > 0.8 \mu m$ [1].

Under cooling in liquid nitrogen germanium photo devices can work up to $\lambda = 4 \div 5 \mu m$ [2].

There are several types of germanium devices:

- Ge - photo resistors;
- Ge - photodiodes;
- Ge avalanche photodiodes, as infrared detectors– Fig. 1 [3, 4, 9];
- Ge – photovoltaic.

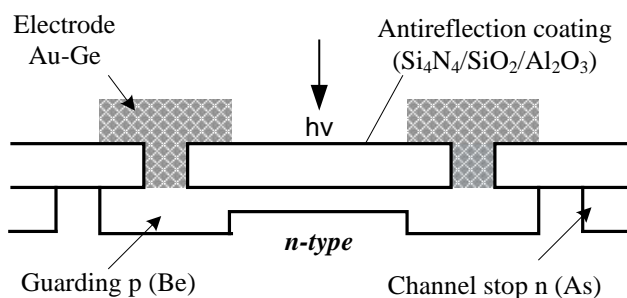


Fig. 1. Typical germanium avalanche photodiode.

Avalanche germanium diodes have the best parameters but very complicated technology.

The advantages and disadvantages are connected with price, construction and the area of application.

¹Ludwig Lubich is with the Faculty of Telecommunications at Technical University of Sofia, 8 Kl. Ohridski Blvd, Sofia 1000, Bulgaria, E-mail: icest@tu-sofia.bg.

²Ivo Dochev is with the Faculty of Telecommunications at Technical University of Sofia, 8 Kl. Ohridski Blvd, Sofia 1000, Bulgaria.

The goal of this work are germanium photo devices – resistors and diodes.

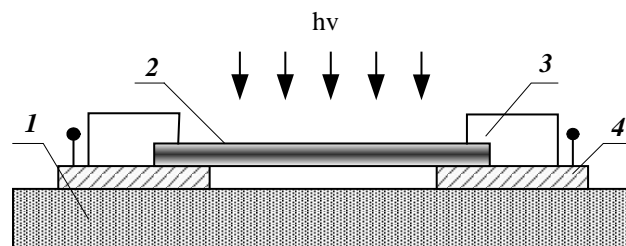
The last ones are based on the system Ag-Ge which is not classical p/n junction but metal – semiconductors barrier Schottky.

The samples have been prepared for student laboratory classes and for laboratory use in infrared range of the light.

II. DESIGN AND TECHNOLOGY OF GE - PHOTO DEVICES

A. Germanium photo resistors

The most popular construction of Ge photo resistors is a rectangular plate with two electrical contacts at the opposite ends - Fig. 2.



1 – Insulating substrate; 2- Ge crystal–detectors; 3 – Ohm contacts; 4 - External leads.

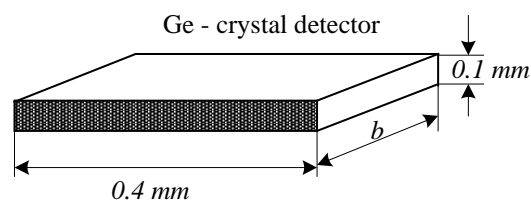


Fig. 2. Rectangular plate with two electrical contacts at the opposite ends

The nominal value of the resistance ($T=20^{\circ}C$ without light) can be calculated as $R_0 = \rho_{Ge} \cdot A$ (where A is coefficient of the geometry).

The germanium used in the experiments are crystals (size $0.4 \times b \times 0.1$ mm), n - type and specific resistance – $\rho = 0.1 \div 10$ (Ωcm). It is clear (Table 1) that the nominal values of R_0 are between $10 \div 8000$ ohms.

The electrical (ohm) contacts are made using eutectic Au – Ge plus Sb.

TABLE I
VALUES OF R_0 (Ω)

ρ (ohm.cm)	b (cm)			
	0.05	0.1	0.2	0.4
0.1	80	40	20	10
0.2	160	80	40	20
0.5	400	200	100	50
1.0	800	400	200	100
2.0	1000	800	400	200
5.0	4000	2000	1000	500
10.0	8000	4000	2000	1000

B. Germanium Schottky photodiodes

The cross - section of germanium Schottky photo diodes is shown on Fig. 3.

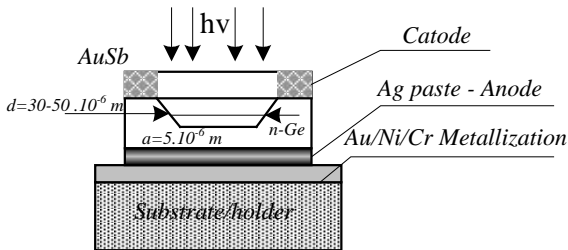


Fig. 3.a. – Cross section of Germanium Schottky devices.

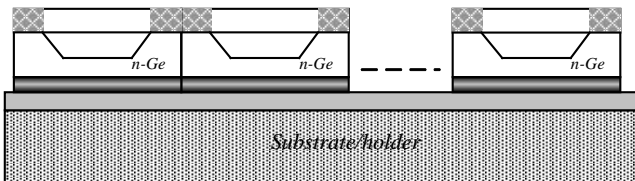


Fig. 3.b. Photocell with multiple photovoltaic – parallel and serial connection.

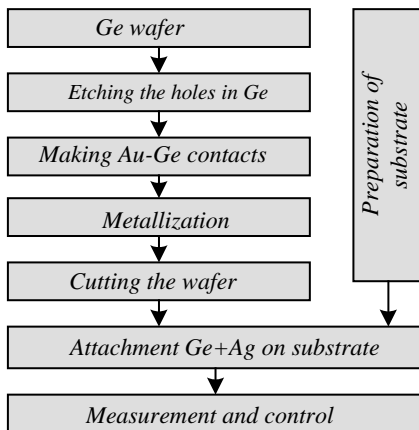


Fig. 4. Ge-Ag photo devices fabrication.

Usually, it is considered that Ge–Ag barrier is “sharp” p/n junction and parameters such as U_{BR} , I_S and C_O will depend only on Ge properties (ρ).

It could be calculated that $U_{BR}=83.4.\rho^{0.61}$. The technology consist next important steps - Fig. 4:

Metallization of Ge devises has two main applications: ohmic contacts and Schottky contacts [5 - 8].

III. CONCLUSION

The measurements of so prepared photo detectors show that the response in infrared light is sufficient for laboratory use and student education - Fig. 5.

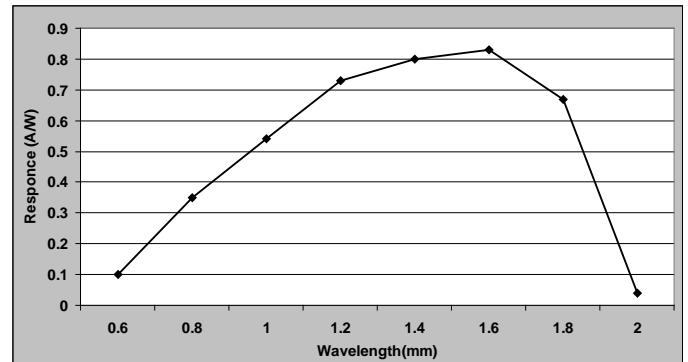


Fig. 5. The measurements of so prepared photo detectors

The measurements of so prepared photo detectors show that the response in infrared light is sufficient for laboratory use and student education - Fig. 5.

The voltage from single element is 0.1 V in visible light and 0.08 V if $\lambda=0.8\div 1.0 \mu\text{m}$.

Photovoltaic based of germanium could be successfully used for space applications.

REFERENCES

- [1] <http://www.judsontechnologies.com>.
- [2] <http://www.spectrolab.com>
- [3] <http://www.blogs.intel.com>
- [4] G. Masini, L. Colace, H-C Luan, L.C. Kimerling, "High-performance p-i-n Ge on Si photodetectors for the near infrared: from model to demonstration", IEEE Tran. Electr. Devices, 48, 1092 (2001).
- [5] P. Rahnev, N. Simeonova, S. Letskovska, Flexible Untergründe organischer Herkunft für hybride Schaltkreise, TECHNOMER 2003, Germany.
- [6] P. Rahnev, S. Letskovska, Germanium photo detectors - IR range, Annual book 2007, Burgas Free University - Bulgaria.
- [7] P. Rahnev, S. Letskovska, Germanium Photo Detectors, XLIII ICEST 2008, Nis, Serbia.
- [8] P. Rahnev, S. Letskovska, D. Parachkevov and K. Seymenliyski, Sputtering of Thin Films on Flexible Substrates, XLVIII ICEST, 2013, Ohrid, Macedonia.
- [9] <http://www.pvmaterials.umicore.com/productsServices/GermaniumSubstrates>.

AUTHOR INDEX

A

Al Rasheed, O., 321
Aleksieva, V., 31
Anastasov, J., 15, 203
Andreev, R., 251
Angelov, K., 191
Angelov, M., 27
Angelova, T., 421
Armenski, G., 307
Atanasković, A., 131
Atanasov, I., 67, 71
Atanasovski, M., 157, 391
Atanassov, A., 450

B

Bankov, N., 467, 471
Bjekić, M., 395
Blau, K., 131
Bonev, B., 151, 191
Borisova, L., 450
Božić, M., 61
Božić, M., 395
Brodic, D., 373
Brusev, T., 463

C

Cajić, M., 286
Carvalho, J., 211
Csizmadia, G., 185
Cvetković, A., 15, 203
Cvetković, N., 360

Ć

Ćirić, T., 127

D

Denić, D., 409
Dimcev, V., 113
Dimitrijević, B., 325
Dimitrijević, S., 437
Dimitrijević, T., 147
Dimitrov, K., 413
Dimitrova, E., 288
Dimov, D., 169
Dimova, T., 151
Dobrev, D., 195, 199
Dobrev, R., 333
Docheva, L., 377, 381
Dončov, N., 139, 147, 343, 347, 355
Donevski, A., 79
Doshev, J., 251
Drača, D., 207
Draganov, N., 421, 429
Drajić, D., 321

Đ

Đorđević-Kozarov, J., 417
Đorđević, LJ. G., 91
Đorđević, T. G., 19, 321
Đorđević, N., 255
Đorđević, V., 135
Đorić, A., 131
Đošić, D., 329
Đošić, S., 91

F

Frtunić, M., 105

G

Gajić, D., 121
Ganev, Z., 341
Gavrovski, C., 113
Gega, V., 87
Gegov, B., 157
Georgiev, D., 443
Georgiev, G., 425
Georgiev, P., 263
Gergov, V., 282
Goranov, G., 259
Guliashki, V., 37, 169
Gusev, M., 41, 45, 79, 83, 307
Guseva, A., 45

H

Hristov, V., 367
Hristova, G., 263
Hristova, R., 259
Hubenova, Z., 282

I

Ilić, M., 57
Iliev, I., 143, 191
Iliev, T., 337
Iontchev, E., 267, 271
Ivaniš, P., 321
Ivanov, M., 67
Ivanov, S., 425

J

Janevski, T., 23
Janković, D., 97
Janjić, A., 403
Janjić, I., 165
Joković, J., 147
Jolevski, I., 87
Jordanova, L., 195, 199
Jovanović, A., 7
Jovanović, G., 221
Jovanović, M., 49, 117
Jovanović, M., 91
Jurukovski, A., 292

K

Karpov, G., 195
Kenov, R., 267, 271
Kim, T., 127
Kirilov, L., 37, 247
Kiryakova, D., 450
Kokolanski, Z., 113
Kolev, K., 483, 487
Komitov, N., 475
Kostić, M., 139
Kostoska, M., 307
Kostov, M., 157
Koteska, B., 41
Kovacheva, M., 225
Kovačević, M., 109
Krastanov, N., 71
Krishnan, A., 3
Kunov, G., 463, 479

L

Labura, S., 311
Laskov, L., 199
Lazarević, M., 286
Letskovska, S., 315, 491

M

Madankov, Y., 471
Madzharov, N., 458
Maleš-Ilić, N., 131
Marinković, Z., 127, 135
Marinova, G., 303
Markov, B., 274, 278
Markov, E., 143
Marković, G., 11
Marković, I., 61
Marković, V., 127, 135
Maslinkov, I., 483
Michalev, T., 443, 446
Mihajlović, V., 109
Mihaylov, G., 337
Mihaylov, V., 413
Miladić, S., 11
Milenković, A., 97
Miletiev, R., 267, 271
Milić, D., 161, 165, 203, 329
Milijić, M., 127, 351
Milivojević, Z., 373, 385, 437
Milosevski, M., 391
Milošević, N., 325
Milovanović, B., 131, 147, 343, 347, 351
Milovanović, I., 347
Milovanović, M., 215
Milović, D., 165, 203, 215
Miljković, G., 409
Mitev, Y., 247
Mitić, D., 417
Mitrevski, P., 75
Mitrovski, C., 157
Mitsev, T., 413

N

Nagy, S., 185
Naumović, M., 311
Nedelchev, M., 143
Nedev, N., 454
Nedkov, T., 433
Nenov, H., 263
Nenov, T., 454
Nenova, Z., 425, 454
Neshov, N., 177
Nešić, A., 351
Nikolić, Z., 325
Nikolij, V., 23
Nikolova, B., 463

P

Pacheco, C., 211
Panajotović, A., 207
Pandiev, I., 225
Panov, V., 274
Pavlović, V., 161
Pencheva, E., 67, 71
Perić, Z., 7
Petkov, P., 151, 153, 191
Petković, M., 15, 19
Petkovski, M., 157, 292
Petrov, I., 443, 446
Pejchev, I., 443, 446
Pleshkova-Bekjarska, S., 367, 433
Poulkov, V., 191
Prinčević, B., 373
Pronić-Rančić, O., 127, 135

R

Radenković, D., 329, 417
Radić, M., 399
Radmanović, M., 121
Rahnev, P., 315
Rajković, P., 97
Rančić, D., 105, 109, 255
Rankovska, V., 299
Reis, A., 211
Ristić, A., 360
Ristov, S., 41, 45, 79, 83, 307
Ristović, M., 311
Rosić, M., 395

S

Savić, S., 403
Savov, S., 341
Sekulović, N., 207
Seymenliyski, K., 315, 491
Shoshkov, T., 241
Simeonov, I., 267, 271
Simić, M., 409
Simić, N., 215
Simić, R., 255
Simjanoska, M., 83

Smiljaković, V., 229, 233
Sovilj, P., 417
Spalević, P., 329
Spasić, S., 181
Spirov, D., 475
Srbinovska, E., 75
Srbinovska, M., 113
Stajić, Z., 399
Stanković, J., 61
Stanković, M., 403
Stanković, V., 57
Stanković, Z., 139, 343, 347
Stefanović, Č., 19, 329
Stoilković, M., 343, 347
Stoimenov, L., 105
Stojanović, D., 101
Stojanović, I., 91
Stojanović, M., 61
Stojanović, M., 360
Stojanović, N., 101
Stojanović, V., 437
Stojčev, M., 221
Stojković, M., 97
Stošić, B., 161, 355
Stoumenov, E., 225
Stoyanov, I., 251
Stoyanov, N., 303

T

Tančić, M., 7
Tatić, D., 121
Todosijević, D., 49, 117
Trpezanovski, Lj., 391

V

Valchanov, H., 27
Valkov, G., 237
Vasić, B., 3
Veiga, H., 211
Velchev, Y., 413
Veličković, Z., 385
Velimirović, L., 403
Velkoski, G., 41, 83
Veljanovski, A., 97
Veljković, M., 165
Vietzorreck, L., 127
Vuchev, A., 467, 471
Vuchev, S., 463, 479
Vučković, D., 360
Vučković, V., 53, 181
Vujičić, V., 417

Z

Zdravković, N., 19

Ž

Živanović, D., 409
Živanović, Z., 229, 233